Mathematical Techniques for Assessing Cardiac Wavefront Dynamics

Caroline Helen Roney

Department of Bioengineering

Imperial College London

A thesis submitted for the degree of

Doctor of Philosophy

Declaration

I declare that all work in this thesis is my own, unless clearly referenced or stated otherwise.

The copyright of this thesis rests with the author and is made available under a Creative Commons Attribution Non-Commercial No Derivatives licence. Researchers are free to copy, distribute or transmit the thesis on the condition that they attribute it, that they do not use it for commercial purposes and that they do not alter, transform or build upon it. For any reuse or redistribution, researchers must make clear to others the licence terms of this work.

To my family.

Acknowledgements

This PhD thesis would not have been possible without the help of many people and I would like to express my gratitude.

First of all, I would like to thank my supervisors Dr Jennifer Siggers, Professor Nicholas Peters and Dr Fu Siong Ng for their invaluable advice, guidance and career support over the course of my PhD. In particular, I am grateful to Jennifer for providing a supportive research environment and for teaching me how to write a thesis. I would like to thank Nick for helping me keep the bigger picture of my research in mind, for the number of research opportunities he has given me, and for his many great ideas. Thanks to Fu for all his help and input when going through countless graphs, for keeping me motivated, and for continuously guiding my research.

I would like to acknowledge the British Heart Foundation Centre of Research Excellence at Imperial College London for funding my research, and thank the Department of Bioengineering and the National Heart and Lung Institute for supporting my studies.

I am indebted to Dr Chris Cantwell for all of his help and his guidance. His idea generation and problem solving meetings have been invaluable, and I have really enjoyed collaborating on a range of projects.

To Eugene and Rheeda, bastions of Imperial College, I would like to say thank you for all of your help and support. I have really enjoyed working with you through all the ups and downs. It would not have been the same without you. Thanks also to Kishan and team Phys Sci. In addition, I am grateful to Jennifer's research group, including Olga, Ani, Kritsada, Sang, Sophie, Yean, Nico, Maryam and Karla, for their many helpful suggestions over the years.

I would also like to thank the other members of Nick Peters' lab. In particular, I am grateful to Rasheda for teaching me about biological experimental techniques and for being so generous with her time and experimental data. I would like to thank Emman for many insightful discussions about rotors and HL1 cells. I would also like to thank Mike and Junaid for their experimental data, and Pravina for always being

on hand to help. I am very grateful to Norman and Boon for explaining many clinical concepts to me, for inspiring and exchanging research ideas, and for their careful data collection and understanding of data requirements.

I am grateful for the input of other researchers into my work including Professor Kim Parker, Dr Ken Macleod, Professor Spencer Sherwin, Professor Kim Christensen and Dr Anil Bharath.

Finally I would like to thank my family and friends for all their support and encouragement. In particular, my parents, my brother and Tim for always being there for me.

Abstract

Electrical signals measured during cardiac arrhythmias may be difficult to analyse and there are multiple challenges associated with their interpretation, including noise, variability between and within datasets, data resolution, and complicated wavefront behaviour. This thesis aimed to develop and test techniques for analysing cardiac electrical wavefront dynamics applied to *in vitro*, *in silico* and *in vivo* data.

One such technique was developed to determine conduction velocity and to estimate the location of the origin of a focal source, assuming either a planar or circular wavefront, measured from any arbitrary arrangement of recording points. This algorithmic technique performed well on simulated and clinical data, and was extended to incorporate curvature of the atrium.

The sensitivity to filtering and post-processing parameters of a technique for tracking rotational sources in optical mapping experiments was investigated, and an optimal parameter set was determined. This was used alongside a technique developed to calculate the distribution of new wavefront initiation sites, in order to gain insight into the mechanisms sustaining atrial fibrillation. The technique for tracking rotational sources was extended to work for unipolar and bipolar electrogram data. This extension was tested in simulation against action potential data, where the modalities (unipolar electrogram, bipolar electrogram and action potential phase) were found to perform similarly; and then applied to experimental and clinical electrograms. Rotational content and activation maps were found to be similar for clinical unipolar and bipolar phase.

The developed techniques were used to investigate the effects of spatial resolution on the identification of rotors and focal sources, as a function of the distance between successive wavefronts. A technique was presented to estimate this distance from a small number of measuring points, providing experimental and clinical utility. These requirements were then tested for simulated high-density mapping catheters and basket catheters, where all catheters provided sufficient resolution.

Contents

Abbreviations **xvii**

1 Introduction **1**
1.1 Overview . . . 1
1.2 Cardiac conduction and arrhythmias . . . 2
1.3 Electrical recordings . . . 3
1.3.1 Action potential . . . 3
1.3.2 Unipolar electrogram . . . 5
1.3.3 Bipolar electrogram . . . 7
1.3.4 Monophasic action potential . . . 8
1.3.5 Electrocardiogram . . . 8
1.4 Mechanisms of atrial fibrillation . . . 8
1.4.1 The "mother rotor" hypothesis . . . 9
1.4.2 Focal sources . . . 10
1.4.3 The "multiple–wavelet" hypothesis . . . 10
1.4.4 Endo-epi dissociation . . . 10
1.5 Factors affecting arrhythmia susceptibility . . . 11
1.5.1 Dispersion of repolarisation . . . 11
1.5.2 Action potential duration restitution slope . . . 12
1.5.3 Intracellular calcium cycling dynamics . . . 13
1.5.4 Conduction velocity restitution . . . 13
1.5.5 Gap junctional coupling . . . 13
1.5.6 Electrical remodelling . . . 14
1.5.7 Structural remodelling . . . 14
1.6 *In vitro* modalities for investigating electrical activity . . . 15
1.6.1 Optical mapping . . . 15
1.6.2 Microelectrode arrays . . . 15
1.7 *In silico* modalities for investigating electrical activity . . . 17
1.7.1 Cell models . . . 17
1.7.2 Cardiac tissue electrophysiology . . . 20
1.7.3 Three-dimensional electrophysiological models . . . 21
1.7.4 Patient specific modelling . . . 22
1.8 *In vivo* modalities for investigating electrical activity . . . 23
1.8.1 Clinical electroanatomic mapping systems . . . 23
1.8.2 Non contact mapping . . . 24
1.8.3 Basket catheter mapping . . . 25

1.8.4 Noninvasive inverse mapping . . . 25
1.9 Clinical treatment strategies for persistent AF . . . 25
1.9.1 Eliminating "triggers": pulmonary vein isolation . . . 25
1.9.2 Linear ablation lines . . . 26
1.9.3 Targeting complex fractionated atrial electrograms . . . 26
1.9.4 Targeting sources: stable rotors and focal sources . . . 27
1.9.5 Targeting sources: regions of high driver content . . . 27
1.9.6 Targeting sources: dominant frequency mapping . . . 28
1.10 Analysing wavefront dynamics overview . . . 28
1.11 Activation time calculations . . . 29
1.11.1 Motivation and overview . . . 29
1.11.2 Standard definitions . . . 30
1.11.3 Non-linear energy operator . . . 30
1.11.4 Time-delay cross-correlation . . . 31
1.11.5 Local activation times . . . 31
1.12 Conduction velocity calculations . . . 31
1.12.1 Triangulation . . . 32
1.12.2 Finite difference . . . 33
1.12.3 Smoothed finite difference . . . 33
1.12.4 Polynomial surface fitting algorithms . . . 34
1.12.5 Cosine-fit techniques . . . 37
1.12.6 Time delay analysis . . . 39
1.12.7 Ensemble vector directional analysis . . . 39
1.12.8 Radial basis function interpolation . . . 39
1.12.9 Isopotential line techniques . . . 40
1.12.10 Analysis of arbitrary scalar fields . . . 41
1.12.11 Analytic expressions . . . 41
1.12.12 Vector field analysis . . . 41
1.12.13 Choice of method for calculating conduction velocity . . . 42
1.13 Rotor tracking . . . 45
1.13.1 Motivation and overview . . . 45
1.13.2 Phase mapping background . . . 45
1.13.3 Phase mapping: choice of zero mean signal . . . 50
1.13.4 Phase mapping: empirical mode decomposition . . . 51
1.13.5 Rotor tip identification: phase singularity identification . . . 52
1.13.6 Rotor tip identification: isopotential line method with zero normal velocity . . . 52
1.13.7 Rotor tip identification: other techniques . . . 53
1.13.8 Spiral wave trajectories . . . 53
1.13.9 Phase singularity chirality . . . 54
1.13.10 Phase singularity birth and annihilation . . . 54
1.13.11 Three-dimensional scroll waves . . . 55
1.13.12 Choice of atrial model and modelling electrical remodelling . . . 55
1.14 Scope of thesis . . . 57

2 Numerical methods for simulation, and techniques for post-processing, rotor tracking and visualisation 59
2.1 Introduction . . . 59
2.2 Cardiac cell models, including the Courtemanche et al. (1998) human atrial cell model . . . 61
2.3 Single cell solution methods . . . 64
2.4 Computational methods for solving the monodomain model . . . 66
2.4.1 One dimensional cable . . . 66
2.4.2 Two dimensional sheet . . . 67
2.4.3 Discussion of the suitability of the methods . . . 69
2.4.4 Boundary and initial conditions . . . 69
2.4.5 Time and space step . . . 70
2.5 Spectral/*hp* element methods . . . 70
2.6 Pacing protocol for spiral wave initiation . . . 70
2.7 Postprocessing: action potential duration and conduction velocity restitution . . . 72
2.8 Postprocessing: calculating bipolar electrograms and p-ECGs . . . 73
2.9 Phase mapping: Hilbert transform . . . 73
2.10 Phase mapping: creating a zero mean signal . . . 74
2.11 Phase mapping: calculating the phase singularity line integral . . . 77
2.12 Phase mapping: phase interpolation . . . 79
2.13 Isopotential line method for rotor tip tracking . . . 79
2.14 Surface flattening . . . 82
2.14.1 Introduction . . . 82
2.14.2 Mesh generation . . . 83
2.14.3 Distance-preserving mapping . . . 86
2.14.4 Distance distortion measure . . . 86
2.15 Summary . . . 88

3 Wavefront velocity and focal source estimation from clinical multipolar catheters 91
3.1 Introduction . . . 91
3.2 Methods: equation derivation . . . 92
3.2.1 Case 1: planar wavefront with circular catheter . . . 93
3.2.2 Case 2: planar wavefront with spiral catheter . . . 95
3.2.3 Case 3: circular wavefront emanating from a point source with circular catheter . . . 97
3.2.4 Case 4: circular wavefront emanating from a point source with spiral catheter . . . 99
3.2.5 Case 5: planar wavefront with arbitrary measuring points . . . 101
3.2.6 Case 6: circular wavefront with arbitrary measuring points . . . 103
3.3 Methods: implementation and testing . . . 104
3.3.1 Fitting the measuring positions to a plane . . . 104
3.3.2 Calculating geodesic distances . . . 106
3.3.3 Applying the conduction velocity algorithms . . . 109
3.3.4 Simulation details . . . 109

3.3.5 Clinical data analysis . . . 110
3.3.6 Analytic testing . . . 110
3.3.7 Ensuring the correct time window for analysis . . . 110
3.3.8 Modelling catheter arrangements . . . 114
3.4 Results . . . 115
3.4.1 Simulated data at exact electrode locations . . . 115
3.4.2 Clinical data at exact electrode locations . . . 116
3.4.3 Effect of electrode location measurement error . . . 117
3.4.4 Effect of catheter deformation . . . 118
3.4.5 Effect of catheter choice when over focal source . . . 118
3.4.6 Assigning activation direction in atrial tachycardia . . . 120
3.4.7 Rotor core location estimation . . . 124
3.4.8 Effect of number of measuring points . . . 126
3.4.9 Clinical atrial tachycardia activation time mapping using a geodesic flattening . . . 128
3.5 Discussion . . . 130
3.5.1 New methodology . . . 130
3.5.2 Summary of findings . . . 130
3.5.3 Comparison with other methods . . . 132
3.5.4 Limitations and future work . . . 133

4 Assessing the effects of parameter choices in rotor tracking analysis of optical mapping data 135
4.1 Introduction . . . 135
4.2 Methodology . . . 136
4.2.1 Experimental preparation and overview of methodology . . . 136
4.2.2 Filtering techniques . . . 140
4.2.3 Phase calculation . . . 143
4.2.4 Phase binning . . . 150
4.2.5 Phase singularity detection . . . 151
4.2.6 Phase singularity tracking . . . 154
4.2.7 Calculating the number of rotations . . . 164
4.2.8 Heat map binning . . . 166
4.2.9 Regional analysis . . . 166
4.3 Results . . . 167
4.3.1 Parameter sensitivity analysis overview . . . 167
4.3.2 Dominant frequency maps . . . 169
4.3.3 Cycle length maps calculated from voltage . . . 170
4.3.4 Cycle length maps calculated from phase . . . 171
4.3.5 Number of phase singularities . . . 172
4.3.6 Number of phase singularities by duration and number of rotations . . . 175
4.3.7 Maximum and mean duration and number of rotations . . . 177
4.3.8 Phase singularity heat maps: spatial smoothing of heat maps . 179
4.3.9 Phase singularity heat maps: duration and number of rotations thresholds . . . 182

4.3.10 Phase singularity heat maps: effects of voltage and phase bin size . . . 188
4.3.11 Phase singularity heat maps: effects of filter settings . . . 190
4.3.12 Phase singularity heat maps: phase calculation settings . . . 192
4.3.13 Additional validation . . . 194
4.4 Discussion . . . 196
4.4.1 Summary of findings . . . 196
4.4.2 Data filtering . . . 196
4.4.3 Phase calculation and phase tracking . . . 197
4.4.4 Number of rotations . . . 199
4.4.5 Heat maps . . . 199
4.4.6 Parameter sensitivity . . . 200
4.4.7 Limitations and future work . . . 200

5 Optical mapping analysis: classifying arrhythmia mechanisms by comparing distributions and timings of phase singularities and new wavefronts 203
5.1 Overview . . . 203
5.2 Methods . . . 206
5.2.1 Detecting instances of new wavefronts . . . 206
5.3 Results . . . 209
5.3.1 Stability over time: dominant frequency . . . 209
5.3.2 Stability over time: phase singularity density maps . . . 212
5.3.3 Stability over time: new wavefront locations . . . 216
5.3.4 Correlation between frequency, phase singularity distribution maps and new wavefront sites . . . 218
5.3.5 Phase singularity number and number of rotations . . . 218
5.3.6 Initial attempts to determine AF mechanisms . . . 219
5.3.7 Frequency of electrical quiescence . . . 222
5.3.8 Frequency of new wavefront initiation following electrical quiescence . . . 222
5.3.9 Comparing new wavefront and rotor cycle lengths . . . 224
5.4 Discussion . . . 225
5.4.1 Summary of findings . . . 225
5.4.2 Dominant frequency stability . . . 225
5.4.3 Stability of phase singularity distribution . . . 226
5.4.4 New wavefront stability . . . 226
5.4.5 The origin of new wavefronts: triggered, transmural conduction, or rotors? . . . 227
5.4.6 Correlation between frequency, phase singularity distribution maps and new wavefront initiation distribution maps . . . 228
5.4.7 Initial attempts to determine AF mechanisms . . . 228
5.4.8 Limitations . . . 229

6 Electrogram Phase **231**
6.1 Introduction . . . 231
6.2 Simulated data . . . 232
6.2.1 Methods: simulation details . . . 232
6.2.2 Methods: bipolar electrogram filtering . . . 235
6.2.3 Methods: bipolar phase calculation . . . 237
6.2.4 Methods: unipolar phase calculation . . . 240
6.2.5 Methods: phase interpolation and phase singularity identification . . . 240
6.2.6 Methods: error quantification . . . 240
6.2.7 Results: overview for simulated data . . . 244
6.2.8 Results: single rotor detection . . . 246
6.2.9 Results: overall phase singularity distribution . . . 248
6.2.10 Summary of simulated data findings . . . 251
6.3 Microelectrode array data . . . 253
6.3.1 Methods: data overview . . . 253
6.3.2 Problems with calculating field potential MEA phase using the techniques developed for simulated data . . . 253
6.3.3 Calculating phase from the filtered derivative of unipolar signals 256
6.3.4 Phase interpolation . . . 260
6.3.5 Bipolar phase calculation . . . 260
6.3.6 Circular correlation coefficient . . . 260
6.3.7 Results: multi-electrode array phase mapping . . . 263
6.3.8 Summary of multi-electrode array findings . . . 263
6.4 Clinical data . . . 266
6.4.1 Methods: data overview . . . 266
6.4.2 Methods: QRS subtraction . . . 266
6.4.3 Methods: modifications to the phase calculation . . . 271
6.4.4 Methods: data projection and interpolation . . . 274
6.4.5 Unipolar phase method with 10Hz filter . . . 274
6.4.6 Validation using atrial tachycardia data . . . 276
6.4.7 Results: number of phase singularities . . . 281
6.4.8 Results: phase angle correlation . . . 283
6.4.9 Results: activation time map correlation . . . 285
6.4.10 Results: investigating segments of low correlation between unipolar and bipolar phase . . . 287
6.4.11 Summary of clinical findings . . . 288
6.5 Applying the clinical algorithms to left-atrial simulation data . . . 290
6.6 Discussion . . . 294
6.6.1 Overview . . . 294
6.6.2 Comparison to action potential phase calculations . . . 294
6.6.3 Comparison of simulated, experimental and clinical algorithms 294
6.6.4 Comparison with other published methodologies . . . 295
6.6.5 Limitations and future work . . . 299

7 Assessing the effects of spatial resolution on wavefront dynamics 301
7.1 Introduction . . . 301
7.2 Methods for determining spatial resolution requirements assuming a regular grid . . . 303
7.2.1 Simulation . . . 304
7.2.2 Data downsampling . . . 305
7.2.3 Phase singularity calculations . . . 305
7.2.4 Phase interpolation . . . 305
7.2.5 Conduction velocity . . . 305
7.2.6 Divergence of conduction velocity . . . 305
7.2.7 Calculating wavelength . . . 307
7.2.8 Estimating wavelength . . . 310
7.2.9 Selection criteria for determining required resolutions . . . 312
7.3 Results for determining spatial resolution requirements, assuming a regular grid . . . 314
7.3.1 APD and CV restitution . . . 314
7.3.2 Full resolution . . . 314
7.3.3 Estimating wavelength . . . 317
7.3.4 Error upon downsampling: spiral wave . . . 320
7.3.5 Error upon downsampling: focal source . . . 325
7.4 Testing derived spatial resolution requirements using data from realistic catheter arrangements . . . 328
7.4.1 Methods for modelling realistic catheter arrangements: Lasso, Afocus and PentaRay catheters . . . 328
7.4.2 Results for modelling realistic catheter arrangements: Lasso, Afocus and PentaRay catheters . . . 328
7.4.3 Methods for modelling realistic catheter arrangements: patient geometry with basket catheter . . . 331
7.4.4 Results for modelling realistic catheter arrangements: patient geometry with basket catheter . . . 339
7.5 Discussion . . . 346
7.5.1 Main findings . . . 346
7.5.2 New developments . . . 346
7.5.3 Expected spatial wavelengths in human AF . . . 346
7.5.4 Spatial wavelength scaling across species . . . 348
7.5.5 Required resolution for regular grids of data . . . 349
7.5.6 Using the conduction velocity divergence to identify focal sources 349
7.5.7 Realistic mapping catheters – required resolutions . . . 350
7.5.8 Choice of interpolation method . . . 351
7.5.9 Feasibility of estimating wavelength to calculate resolution requirements . . . 351
7.5.10 Implications for various mapping modalities . . . 352
7.5.11 Limitations and extensions . . . 353

8 Conclusions **355**
8.1 Summary of key findings . . . 355
8.2 Novel techniques . . . 358
8.2.1 Visualising three-dimensional left atrial cardiac activation data in two dimensions with minimal distance distortion . . . 358
8.2.2 Estimating conduction velocity and the location of the origin of a focal source, for either a planar or circular wavefront, measured from any arbitrary arrangement of recording points 359
8.2.3 Assessing the spatio-temporal distribution of dominant frequency, phase singularities and new wavefront initiation locations in order to gain insight into arrhythmia mechanisms . . 361
8.2.4 Calculating phase and tracking phase singularities from simulated, cell culture and clinically acquired electrogram data . . 363
8.2.5 Estimating spatial wavelength . . . 365
8.3 Questions addressed . . . 366
8.3.1 Effects of post-processing techniques and importance of parameter choice for rotor tracking analysis . . . 366
8.3.2 Determining the relationship between resolution requirements and wavefront spatial wavelength for identifying rotors and focal sources . . . 367
8.4 Open problems and challenges . . . 369
8.5 Study limitations . . . 369
8.5.1 Limitations of recording techniques: two-dimensional measurements of a three-dimensional substrate . . . 369
8.5.2 The lack of gold standard measurement . . . 370
8.5.3 Requirement of a single macroscopic wavefront under the recording points for the conduction velocity algorithm . . . 371
8.6 Future directions . . . 371
8.6.1 Calculating conduction velocity and estimating locations of sources using sequentially collected data in fibrillation . . . 371
8.6.2 Extending the spatial resolution requirement investigations . . 372
8.7 Concluding remarks . . . 372

A Preliminary investigations into the choice of method and parameter choices for rotor core location identification **405**
A.1 Preliminary findings . . . 405
A.1.1 Effects of rotor tip identification method . . . 405
A.1.2 Voltage-Calcium mapping in simulated data . . . 409
A.1.3 Calcium mapping in HL1 cells . . . 410
A.1.4 Effects of fibroblast coupling . . . 410
A.1.5 Effects of resolution . . . 411
A.1.6 Summary . . . 413

B Permissions to use figures **415**

List of Abbreviations

Greek Symbols

λ	Spatial wavelength
τ	Time delay

Acronyms

ACh	Acetylcholine
AE	Angle error
AF	Atrial fibrillation
AP	Action potential
APD	Action potential duration
AT	Atrial tachycardia
CFAE	Complex fractionated atrial electrogram
CL	Cycle length
CV	Conduction velocity
DF	Dominant frequency
DI	Diastolic interval
ECG	Electrocardiogram
ERP	Effective refractory period
FIRM	Focal impulse and rotor modulation
FSDE	Focal source distance error
LA	Left atrium
LAT	Local activation time
LGE-MRI	Late-gadolinium enhanced magnetic resonance imaging

LIPV	Left inferior pulmonary vein
LSPV	Left superior pulmonary vein
MAP	Monophasic action potential
MEA	Microelectrode array
MRI	Magnetic resonance imaging
NLEO	Non-linear energy operator
ODE	Ordinary differential equation
PDE	Partial differential equation
PS	Phase singularity
PVI	Pulmonary vein isolation
PV	Pulmonary vein
RBF	Radial basis function
Res	Residual
RIPV	Right inferior pulmonary vein
RP	Refractory period
RSPV	Right superior pulmonary vein
VFCL	Ventricular fibrillation cycle length
VFDF	Ventricular fibrillation dominant frequency
VF	Ventricular fibrillation
VT	Ventricular tachycardia
WF	Wavefront

List of Figures

1.1 Human ventricular and atrial action potentials and associated currents, reproduced from Nerbonne and Kass (2005) 4
1.2 Schematic to show different action potential morphologies seen in different regions of the human heart, reproduced from Nerbonne and Kass (2005) 5
1.3 Definition of activation times of action potential, unipolar electrogram and bipolar electrogram data, from Cantwell et al. (2015b) 6
1.4 Schematic to show the mechanisms of Atrial Fibrillation 9
1.5 Microelectrode array set-up and field potential characteristics 16
1.6 Cardiac cell models action potentials from Cherry and Fenton (2008) 18
1.7 Focal Impulse and Rotor Modulation mapping technology 27
1.8 Rotor identified using phase mapping and ECGi technology 28
1.9 Conduction velocity calculation using triangulation 32
1.10 Conduction velocity calculation using finite difference techniques . . . 34
1.11 Two variable FitzHugh state space from Iyer and Gray (2001) 47
1.12 Phase of optical mapping fluorescence from Gray et al. (1998) 48
1.13 Diagram to illustrate poor choice of time shift for state space mapping, from Bray and Wikswo (2002a) 49
1.14 Range of spiral tip trajectories exhibited by biophysical cell modes . . 54
1.15 Spiral trajectories for variants of the Courtemanche et al. (1998) and Nygren et al. (1998) models, from Cherry and Evans (2008). 56

2.1 Schematics to show the Courtemanche et al. (1998) human atrial cell model 63
2.2 Spiral wave initiation following an *S1–S2* extra-stimulus pacing protocol 71
2.3 Definition of APD, DI and activation time 72
2.4 Regular mean: phase shows incomplete progressions 75
2.5 Moving mean removal results in clean phase in simulated data 76
2.6 A mapping is introduced for phase interpolation 80
2.7 Isopotential line method of rotor-core identification 81
2.8 Different isopotential lines using the Kay and Gray (2005) method . . 82
2.9 Example mapping of left atrium to two-dimensional surface representation 84
2.10 Cuts in the mesh from the mitral valve to the ends of the pulmonary vein sleeves, allowing a mapping which is distance-preserving 85
2.11 Example geodesic distance contours 85

2.12 Localised distance distortion calculated using the Sammon mapping criterion 87

3.1 Planar wavefront and circular catheter 94
3.2 Planar wavefront and spiral catheter 95
3.3 Planar wavefront and spiral catheter: trigonometry 96
3.4 Circular wavefront and circular catheter 98
3.5 Circular wavefront and spiral catheter 100
3.6 Planar wavefront and arbitrary arrangement of measuring points . . . 102
3.7 Circular wavefront and arbitrary arrangement of measuring points . . 103
3.8 Methodology for calculating conduction velocity from anatomically accurate left atrial simulation data 105
3.9 Catheter on curved part of geometry: need for geodesic distances – outline of methodology 107
3.10 Calculation of the conduction velocity of a spiral wavefront 112
3.11 Simulation set-up showing pacing location 115
3.12 Planar and circular results for three patients. 116
3.13 Focal source estimation from clinical data. 117
3.14 Analytical results: effects of electrogram location perturbations from a perfect spiral catheter 118
3.15 Effect of catheter shape on prediction of focal sources under catheter. 119
3.16 Atrial tachycardia wavefront direction map calculated using the circular wavefront algorithm 120
3.17 Atrial tachycardia wavefront direction map in which activation directions calculated using unipolar and bipolar activation times agree well and spatial heterogeneity in conduction speed is observed 121
3.18 Atrial tachycardia conduction velocity estimates for unipolar and bipolar recordings 122
3.19 Atrial tachycardia beat-to-beat variation in wavefront direction 123
3.20 Spiral wave location estimation using the circular wavefront algorithm with a spiral catheter 125
3.21 CV and wavefront direction depend on the number of measuring points included in the fit 127
3.22 Surface flattening used to plot an LAT map for a clinical atrial tachycardia using a geometry derived from an electro-anatomic mapping system 129

4.1 Photo to show the canine left atrial preparation used for optical mapping 137
4.2 Photo to show the canine left atrial preparation used for optical mapping divided into regions for calculating the correlation between structural and functional features 138
4.3 Schematic to show steps involved in analysis, along with associated default parameter values 139
4.4 Mask used for thresholding data 140
4.5 Convolution matrices 141
4.6 Increasing the voltage bin size from 3-by-3 pixels to 9-by-9 pixels leads to an increased spatial smoothing of the fluorescence 141

4.7 Steps for filtering optical mapping fluorescence 142
4.8 Phase calculation steps 144
4.9 Redefining maxima following the deletion of maxima-minima or minima-maxima pairs that fail to meet the amplitude threshold 144
4.10 Calculating thresholds for the high-band of the temporal filter, and the window length and amplitude thresholds for the phase calculation 145
4.11 Phase calculation: effects of reducing amplitude deletion threshold . . 147
4.12 Phase calculation: effects of reducing window length threshold and reducing amplitude deletion threshold 147
4.13 Phase calculation: effects of increasing amplitude deletion threshold . 148
4.14 Phase calculation: effects of reducing window length threshold and increasing amplitude deletion threshold 148
4.15 Phase calculation for a regular signal 149
4.16 Phase binning was applied to reduce noise in the raw phase angle . . 150
4.17 Phase singularities were defined based on the number of neighbouring candidate phase singularities 151
4.18 Phase singularity detection: using the threshold allowance and neighbourhood rule identifies phase singularities that would otherwise be masked by noise 152
4.19 Phase singularity detection: requiring that a phase singularity has three neighbouring pixels that satisfy a phase value threshold prevents false detections due to noise 152
4.20 Larger contour size phase singularity detection 153
4.21 Phase singularity detection using wavefronts. 154
4.22 Schematic to show the steps involved in constructing the phase singularity trajectory matrices 156
4.23 Missing detection allowance 157
4.24 Calculating distances using convolution operators 158
4.25 Measured distance movement between occupied frames of each trajectory 159
4.26 Distance matrix of 5-by-5: PS assigned incorrectly to new trajectory . 160
4.27 Distance matrix of 11-by-11: new PS incorrectly assigned to complete PS trajectory 161
4.28 Deletion of PS trajectory subsets 162
4.29 Deletion of short-lived PS pairs: trajectories 163
4.30 Calculating the number of rotations 165
4.31 Schematic to show the parameters varied at each stage of the analysis protocol, the permissible values for each parameter, and the outputs measured for each variation 168
4.32 Dominant frequency maps with varied voltage bin size are visually similar, although there is more noise content for smaller bin sizes. . . 169
4.33 Dominant frequency maps with different high-band filter settings, where filtering at 100% removes the high frequency content 170
4.34 Effects of voltage bin size and filter settings on median cycle length . 171
4.35 Effects of window length and amplitude settings on median cycle length and amplitude 172

4.36 Overall number of PSs depends on voltage, filter and phase binning settings . . . 173
4.37 Mean number of PS depending on window length and amplitude settings 173
4.38 Combined effects of parameter changes on overall number of PSs: voltage and phase bin size are not independent . . . 174
4.39 Number of PS by duration and number of rotations for different voltage bin sizes . . . 176
4.40 Number of PS by duration and number of rotations for different phase bin sizes . . . 176
4.41 Number of PS by duration and number of rotations for different filter settings . . . 177
4.42 Maximum and mean duration and number of rotations for different voltage and phase bin sizes . . . 178
4.43 Heat map smoothed with different bin sizes, along with the correlations between the resulting heat maps . . . 180
4.44 Heat map smoothing with varied phase and voltage bins . . . 181
4.45 Heat maps with varied PS duration and number of rotation thresholds and localised correlations . . . 183
4.46 Regional analysis for duration and number of rotation thresholds: densities and percentages . . . 185
4.47 Regional analysis for duration and number of rotation thresholds: ranking and top three . . . 186
4.48 Regional analysis for duration and number of rotation thresholds: region maps correlations and number of PSs by number of rotations . 187
4.49 Regional analysis for different phase and voltage bin sizes . . . 189
4.50 Regional analysis for various filter settings . . . 191
4.51 Regional analysis and heat map correlations for varied parameters in the phase calculation . . . 193
4.52 Effects of random spatial permutation of pixels . . . 195

5.1 Active pixels are defined at an isophase value of $-\frac{\pi}{2}$ and pixels are considered as belonging to a propagated wavefront if there is a nearby active pixel in the previous frame . . . 207
5.2 New wavefronts are identified as instances of active pixels that cannot be explained by propagation from active pixels in the previous frame, and occur during existing AF, or following electrical quiescence in the mapping field . . . 208
5.3 Examining the stability of DF over time: DF maps, values, area and centre of mass trajectories . . . 210
5.4 DF stability: values, island area and centre of mass trajectories . . . 211
5.5 PS density map stability over time: density maps, overall correlations and regional analysis . . . 213
5.6 PS distribution map stability over time: overall correlations and regional analysis . . . 214
5.7 Stability of PS trajectory start and end locations: regional analysis . 215

5.8 Three out of four of the preparations had clear sites of new wavefront initiation . . . 216
5.9 Stability over time of focal source locations for LA1 . . . 217
5.10 Mean number of phase singularities and number of rotations for each preparation . . . 218
5.11 Number of rotors, PSs, active tissue and new wavefronts over time: attempting to determine AF mechanisms, LA1 . . . 220
5.12 Number of rotors, PSs, active tissue and new wavefronts over time: attempting to determine AF mechanisms, LA4 . . . 221
5.13 Frequency of electrical quiescence within the mapping field as a function of average duration without activity . . . 222
5.14 Density of new wavefront initiation and of reinitiations in the preferential region compared to the rest of the tissue, as a function of the area of each region . . . 223
5.15 Comparing average rotor cycle length and average cycle length of the new wavefront hot spot region . . . 224

6.1 Summary of simulation data types: action potential, unipolar electrograms and bipolar electrograms . . . 234
6.2 Bipolar electrogram filtering steps for 2mm and 4mm inter-electrode spacing. . . . 235
6.3 Electrogram filtering for 6, 8 and 10mm spacing. . . . 236
6.4 Amplitude dependence of bipolar electrograms on wavefront direction. 237
6.5 Calculation of bipolar electrogram phase with 2 or 4mm interelectrode spacing. . . . 238
6.6 Calculation of bipolar electrogram phase with 6, 8 or 10mm interelectrode spacing . . . 239
6.7 Bipolar electrogram with 8mm inter-electrode spacing: large number of double potentials at 20Hz. . . . 241
6.8 Steps for calculating unipolar electrogram phase. . . . 242
6.9 Measures used for error quantification . . . 243
6.10 Results overview for 2mm interelectrode spacing . . . 245
6.11 As grid spacing increases, rotor trajectories for AP, unipolar electrogram and bipolar electrogram phase become less like the gold standard trajectory . . . 247
6.12 Isophase maps for AP, unipolar electrogram and bipolar electrogram data . . . 249
6.13 Heat maps for AP, unipolar electrogram and bipolar electrogram phase at spacings of $2-10$mm . . . 250
6.14 Unipolar multi electrode array phase calculated for the signal low-pass filtered at 10Hz. . . . 254
6.15 Unipolar MEA phase calculated for the 10Hz filtered signal leads to incorrect phase assignment in the case of a noisy baseline . . . 255
6.16 Method for calculating unipolar electrogram phase from MEA data using the electrogram derivative . . . 257

6.17 Using tagged points in the raw signal as target times improves robustness to baseline noise . . . 258
6.18 Steps involved in calculating MEA electrogram phase . . . 259
6.19 Criterion for point exclusion in phase interpolation . . . 260
6.20 Example bipolar MEA electrogram coloured by phase . . . 261
6.21 Calculation of the correlation coefficient for phase requires the use of a circular correlation coefficient. . . . 262
6.22 MEA unipolar and bipolar phase singularity trajectory comparison . 264
6.23 Patient left atrial geometry, electrode locations and example electrograms . . . 267
6.24 Steps involved in ventricular template subtraction . . . 269
6.25 QRS subtraction for a signal with a large ventricular component . . . 270
6.26 Capping the derivative at zero prevents the algorithm from picking positive deflections . . . 272
6.27 Pre-processing steps required in order to calculate the phase of clinical unipolar electrograms . . . 272
6.28 Outline of steps applied to calculate phase of filtered bipolar electrograms or the filtered derivative of unipolar electrograms . . . 273
6.29 Clinical unipolar and bipolar electrograms coloured by phase . . . 274
6.30 Unipolar phase method with electrogram filtering at 10Hz correlates poorly with bipolar electrogram phase . . . 275
6.31 Isochronal map example for validation of use of phase for atrial tachycardia data . . . 278
6.32 Isochronal map correlation and number of pixels overlap for bipolar voltage and phase comparison . . . 279
6.33 Directions measured using voltage (activation times), unipolar electrogram phase and bipolar electrogram phase show a similar global pattern. . . . 281
6.34 Average number of phase singularities per frame is shown per catheter for both unipolar and bipolar phase for three patients . . . 282
6.35 Average number of phase singularities per frame is shown per catheter for both unipolar and bipolar phase as a scatter plot and as a histogram 283
6.36 Correlation plot between unipolar and bipolar phase angles for an example catheter and histogram of all correlations for all catheters . . 284
6.37 Histogram to show the median correlation coefficient between activation maps from bipolar and unipolar phase . . . 285
6.38 Methodology used to determine suitable time windows to construct activation time maps from unipolar and bipolar phase and to assess their correlation . . . 286
6.39 Investigating segments of low correlation between unipolar and bipolar phase: missing detection on unipolar electrogram . . . 287
6.40 Investigating segments of low correlation between unipolar and bipolar phase . . . 288
6.41 Differences in wavefront dynamics and PS positions computed using unipolar electrogram, bipolar electrogram and AP data were not clinically relevant in an MRI-derived left atrial simulation with two rotors 293

7.1 Definition of spatial wavelength . . . 303
7.2 Comparison of linear, cubic and spline interpolation techniques . . . 306
7.3 Finite difference technique for calculation of conduction velocity . . . 307
7.4 Calculation of divergence . . . 308
7.5 Calculation of the divergence of a downsampled focal source . . . 309
7.6 Calculation of the wavelength of a spiral or focal wavefront . . . 309
7.7 Estimation of cycle length . . . 311
7.8 Methodology for defining success or failure of rotor core identification 313
7.9 APD and CV restitution plots . . . 315
7.10 Full resolution rotor tip trajectories for nine wavelengths . . . 316
7.11 Estimated spatial wavelengths agree well with calculated spatial wavelengths and vary between parameter sets . . . 319
7.12 Phase singularity locations and rotor trajectories to show the resolution at which the error in the centre location exceeds threshold . . . 320
7.13 Figure to show phase singularity resolutions for every level of downsampling from 1 to 25mm for one parameter set . . . 321
7.14 Phase singularity distributions at 5, 10, 15, 20 and 25mm resolution for each spiral parameter set . . . 322
7.15 Phase singularity locations and histograms to show the resolution at which the number of false detections exceeds threshold . . . 323
7.16 Required resolution for spiral wave detection . . . 324
7.17 The effects of spatial wavelength on resolution requirements for a focal source . . . 326
7.18 Required resolution for focal source detection . . . 327
7.19 The effects of choice of catheter on spiral tip trajectories . . . 330
7.20 Basket catheter arrangement in human left atrial geometry: selection of electrode recording points . . . 332
7.21 Flattening of the left-atrial mesh to preserve geodesic distances . . . 334
7.22 Filtering for unipolar simulated electrograms . . . 335
7.23 Steps to calculate phase for unipolar simulated electrograms . . . 336
7.24 Calculating rotor trajectories using surface flattening techniques . . . 338
7.25 Box and whisker diagram to show the distances between electrodes in a basket catheter . . . 340
7.26 Realistic catheter arrangement: basket catheter in left-atrial geometry, results overview for longer wavelength . . . 341
7.27 Realistic catheter arrangement: basket catheter in left-atrial geometry, results overview for shorter wavelength . . . 342
7.28 Rotor locations for gold-standard and basket electrodes and false detection histograms for long wavelength simulation . . . 343
7.29 Rotor locations for gold-standard and basket electrodes and false detection histograms for short wavelength simulation . . . 344
7.30 Phase singularity locations for thirty second basket simulation: average path and area calculation . . . 345

A.1 Spiral tip trajectories for different isopotential lines . . . 406
A.2 Rotor tip trajectories for different amplitude deletion thresholds . . . 407

A.3 Mean difference in rotor core location between different phase amplitude deletion and isopotential lines 408
A.4 Rotor tip locations for the isopotential line method and for voltage and calcium phase 409
A.5 Phase singularity locations calculated from calcium optical mapping of HL1 cells 410
A.6 Rotor tip locations for the isopotential line method with and without fibroblast coupling 411
A.7 A rotor and focal source were identifiable down to 15mm, when it became difficult to visually distinguish between a spiral and focal source. 412
A.8 Complex wavefront interactions were lost at 9mm. 412

B.1 Permission to use Fig. 1.4, from Eckstein et al. (2008). 416
B.2 Permission to use Fig. 1.5, from Reppel et al. (2004). 417
B.3 Permission to use Fig. 1.8, from Haissaguerre et al. (2013). 418
B.4 Permission to use Fig. 1.11, from Iyer and Gray (2001). 419
B.5 Permission to use Fig. 1.12, from Gray et al. (1998). 420
B.6 Permission to use Fig. 1.13, from Bray and Wikswo (2002a). 421
B.7 Permission to use Fig. 1.15, from Cherry and Evans (2008). 422
B.8 Permission to use Fig. 2.1(B), from Ashihara et al. (2012). 423

List of Tables

1.1 List of conduction velocity estimation techniques detailing their advantages, disadvantages, data suitabilities and requirements 44

2.1 Average distance distortion under mappings 88

3.1 Summary statistics for simulated data 116

6.1 Error in centre location of isolated rotor and maximum radius of phase singularity trajectory 246
6.2 Framewise mean distance error and standard deviation for the isolated rotor 248
6.3 Mean number of PSs per frame, for different inter-electrode spacings . 248
6.4 Correlation of heat maps for subsampled data with full-resolution AP data distribution 249

7.1 Wavelengths for spiral wave simulations 317
7.2 Wavelengths for focal source simulations 318

Chapter 1

Introduction

Abnormal heart rhythms (cardiac arrhythmias) are a major health burden. Examples include atrial fibrillation (AF), which increases the risk of stroke; and ventricular fibrillation (VF), which is a major cause of sudden cardiac death. Successful treatment requires understanding of electrical data recorded during arrhythmias, which is often made difficult by noise and variability; the limitations of recording techniques; and that the underlying rhythm may be complicated. This thesis aimed to develop techniques for analysing electrical arrhythmia data, as well as assessing the effects of data type, resolution and parameter choices on these analyses. Novel techniques were developed to estimate the speed of propagation of the electrical signal; to estimate the location from which an arrhythmia initiates; and to track rotational propagation from different electrical datasets. Research questions addressed included determining the effects of data resolution on correct interpretation of arrhythmia data, and the parameter sensitivity of algorithms for tracking rotational propagation. Overall, this thesis contributes novel methodologies for arrhythmia data analyses, as well as assessing resolution requirements and parameter sensitivity for algorithm development.

1.1 Overview

Electrical signals measured during cardiac arrhythmias may be difficult to analyse and the resulting wavefront patterns can be challenging to interpret. Optimal ablation therapy for atrial fibrillation (AF) requires an understanding of the electrical activity, including the identification of any electrical sources maintaining the arrhythmia. Findings differ in the literature with regards to the underlying mechanisms for AF, which may be explained by the complicated arrhythmogenic substrate, patient variability, and the variety of recording techniques and post-processing methodolo-

gies applied. Thus the challenge is to analyse and identify mechanisms given a dataset of limited resolution, from a variety of modalities.

There are a number of challenges in arrhythmia interpretation. This includes visualisation of the electrical activity on the three-dimensional atrial surface, which typically requires multiple viewpoints simultaneously. In addition, it is difficult to estimate conduction velocity accurately, where areas of conduction slowing may indicate a more diseased substrate. Locating electrical drivers during tachycardia or fibrillation is difficult due the sequential nature of clinical data collection and the complexity of signals. Furthermore, analysis protocols contain many parameters and the sensitivity of the observed dynamics to these parameters is critical, since analysing the interplay between phase singularity distributions and new wavefront initiation locations may elucidate the mechanisms sustaining AF. Finally, data should be of high enough resolution to distinguish rotors and focal sources, and so knowledge of the resolution requirements is important.

The overall aims of this thesis are to develop and test techniques for assessing cardiac electrical wavefront dynamics applied to *in vitro*, *in silico* and *in vivo* data. The questions of the measurements required, the most appropriate post-processing protocols and the influence of parameter choice within analysis protocols are investigated, along with the development of novel techniques for measuring CV, for estimating focal source location, for phase mapping of electrogram data, and for assessing arrhythmia mechanisms.

In this chapter, the relevant background literature for addressing the aims of this thesis are presented, including the electrical recordings currently available, the mechanisms proposed to underlie AF, clinical treatment strategies, techniques for measuring conduction velocity and for locating the cores of electrical rotors.

1.2 Cardiac conduction and arrhythmias

Fibrillation is a *cardiac arrhythmia*, or abnormal heart rhythm, in which fragmented electrical waves propagate over the conducting tissue of the heart in a disordered way. The presence of these disorganised waves in the atria (*atrial fibrillation*, AF) increases the risk of stroke, while ventricular fibrillation (VF) is a major cause of sudden cardiac death (Pastore et al., 1999). Analysis of the wavefront dynamics of these disorganised waves is required to inform treatment strategies.

1.3 Electrical recordings

Electrical activation can be measured at different scales, ranging from the signal at the cellular level to the body surface.

1.3.1 Action potential

The *action potential* (AP) of a cardiac cell represents the movement of ions across the cell membrane, causing a sudden increase in the membrane potential to a positive value. The action potential, also known as the *transmembrane potential*, consists of five phases (see Fig. 1.1):

- **Phase 4, resting phase:** the resting membrane potential is around −80mV, which is a result of the high intracellular potassium concentration compared to extracellular potassium concentration.
- **Phase 0, AP upstroke, rapid depolarisation:** an inward current (either an applied stimulus, or from a neighbouring cell) increases the membrane potential to a threshold value (around −60mV). This causes the sodium channels to open, resulting in a sudden influx of sodium ions, and the membrane rapidly depolarises (increases in potential) until it reaches a positive overshoot of between 20mV and 30mV. The sodium current, I_{Na}, reaches a large peak magnitude and quickly inactivates ($\approx$ 1ms).
- **Phase 1, brief spike, initial repolarisation:** the sodium channels close and the potassium transient outward current (I_{to}) channels open, allowing potassium to leave the cell. Consequently the membrane partially repolarises to between −20mV and 0mV. This *notch* in the action potential morphology is only present in cells in which the transient outward current is expressed.
- **Phase 2, plateau:** the slow calcium L-type channels (I_{Ca}) open to provide a depolarising current against the repolarising potassium currents (rapid I_{Kr} and slow I_{Ks}) and there is a plateau in the potential, during which it remains stable for 200–400 ms.
- **Phase 3, repolarisation:** the L-type calcium channels close and the membrane repolarises (decreases in potential, predominantly due to the inward rectifier potassium channel I_{K1}). The rate of repolarisation is slower than the rate of depolarisation seen in phase 0.

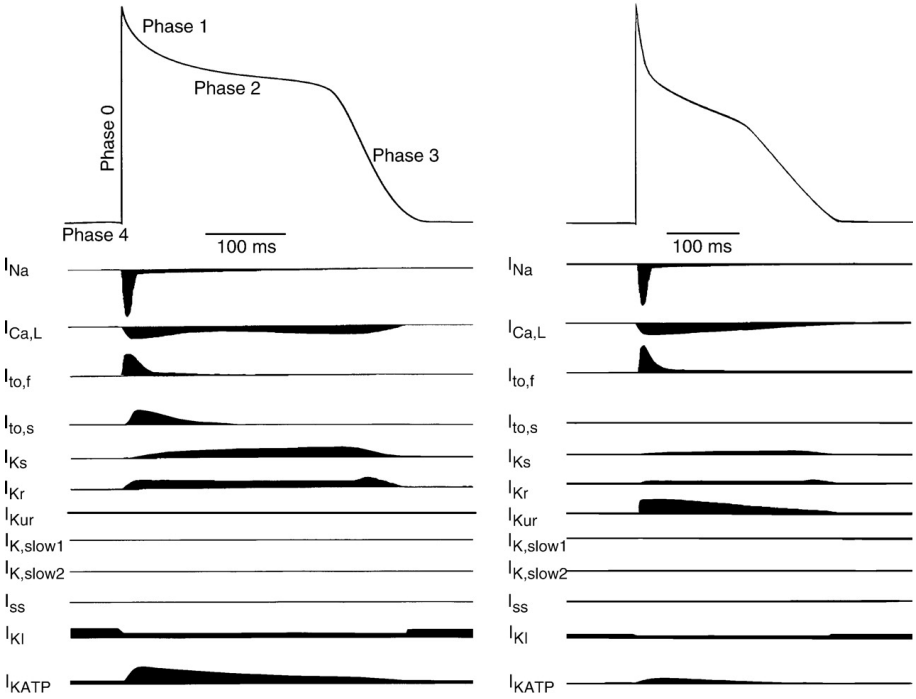

Figure 1.1: Human ventricular (left) and atrial (right) action potentials and associated currents, reproduced from Nerbonne and Kass (2005). Sodium and calcium currents are seen have similar time and voltage dependent properties between ventricular and atrial cell types, whilst potassium currents exhibit differences.

The *refractory period* is the time following depolarisation of the cell during which the cell cannot generate a full action potential. This is composed of an initial time period when the cell is completely unexcitable (the *absolute refractory period*), and a small time period following this when the cell is still repolarising but a sufficiently large stimulus may cause a partial action potential (the *relative refractory period*).

The action potential morphology varies across species and between the different cell types in the heart (see Fig. 1.2).

The duration of the action potential, measured at a particular level of repolarisation (for example 90%, see Section 2.7), is the *action potential duration* (APD), and the time interval between action potentials is the *diastolic interval* (DI).

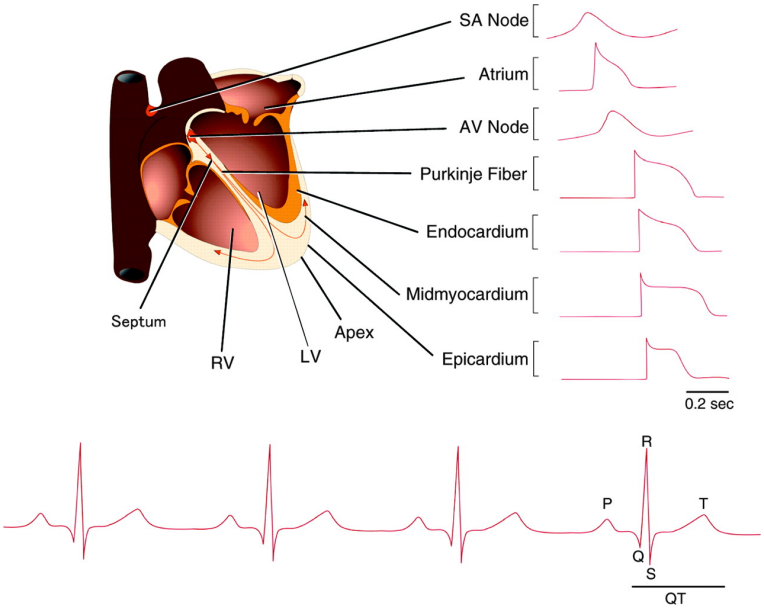

Figure 1.2: Top: Schematic to show different action potential morphologies seen in different regions of the human heart. Bottom: example surface ECG trace. Reproduced from Nerbonne and Kass (2005).

1.3.2 Unipolar electrogram

Both unipolar and bipolar electrograms represent the summation of electrical activity from all of the cells within the field of view of the catheter. Unipolar electrograms represent the difference between a recording electrode placed on the tissue surface and an indifferent electrode placed a large distance away from the tissue. The sensing electrode is connected to the positive input of a differential amplifier and the indifferent electrode is connected to the negative input, in order to produce the unipolar signal (Shenasa et al., 2013).

Spach and Kootsey (1985) investigated the relationship between the time of peak sodium current, the slope of the action potential, and the slope of the extracellular electrogram in a uniform cable model, and found that the maximum positive slope of the action potential, the maximum negative slope of the extracellular electrogram and the peak sodium current all coincide in time. Since the peak sodium current corresponds to the maximum rate of increase of the depolarising current, this can be defined to be the *activation time*. This leads to the standard definition of the activation time of an action potential being the time point of maximum slope, while for a unipolar extracellular electrogram it is the point of maximum negative slope. These definitions of activation time are illustrated in Fig. 1.3.

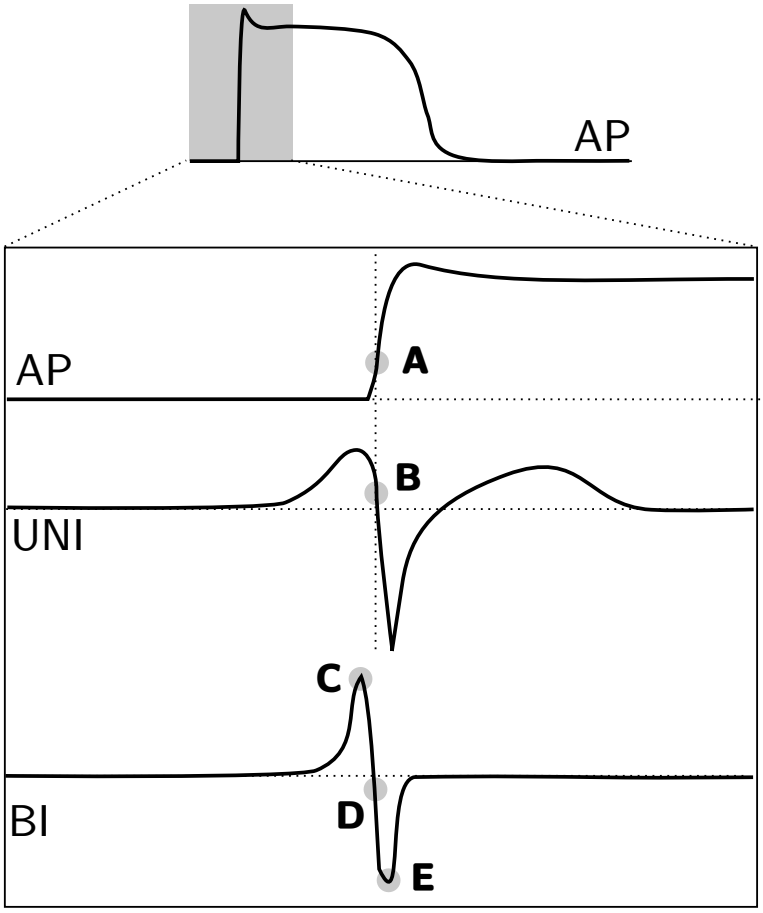

Figure 1.3: Definition of activation times of action potential (AP), unipolar electrogram (UNI) and bipolar electrogram data (BI), from Cantwell et al. (2015b). (A) Time of maximal gradient for action potential data; (B) Time of maximum negative gradient for unipolar electrogram data; (C) Maximum voltage point for bipolar electrogram data; (D) Time of maximum negative gradient for bipolar electrogram data; (E) Maximum negative voltage point for bipolar electrogram data. For bipolar electrograms the time point of maximum amplitude (C) is often used as the activation time.

Advantages of unipolar electrograms include that they give an accurate measure of the activation time of the underlying tissue, and that their morphology is easy to interpret as the passing of a wave across the electrode. In addition, unipolar electrograms can be used for identifying repolarisation of the tissue. The *activation-recovery interval* (the time between the maximum negative derivative and the maximum positive derivative, which occurs close to the repolarisation wave peak) has been shown to correlate with the duration of the cellular action potential (Coronel et al., 2006; Vigmond et al., 2009). However, unipolar electrograms have the disadvantage that they may also include far-field activity, representing electrical activity from tissue a considerable distance from the recording electrode, which can make the analysis of unipolar signals difficult, particularly for atrial signals, which often include far-field signals from the larger ventricular depolarisation.

1.3.3 Bipolar electrogram

For bipolar electrograms, the two electrodes are placed close to each other, usually within a few millimetres. This has the advantage that it removes most of the far-field signal because this is similar at the two electrodes, leaving the local activity. The bipolar electrogram approximates the first derivative of the unipolar electrogram (Shenasa et al., 2013). Although the definition for activation time of the action potential and unipolar electrogram have a theoretical basis, there is no such definition for the bipolar electrogram. Activation time in bipolar electrograms is typically defined as the time of maximum amplitude, although there are other definitions in the literature (Biermann et al., 2003). Additional techniques for assigning activation times are discussed in Section 1.11.

The main disadvantage of the bipolar electrogram is that the signal is dependent on the direction of the wavefront, and for example in the case that the wavefront is parallel to the bipolar electrodes, the wavefront will not be detected on the resulting bipolar electrogram. Furthermore, it is more difficult to determine the activation time and to interpret the morphology of the signal. In addition, bipolar electrograms are sensitive to inter-electrode spacing (Ndrepepa et al., 1995). Unipolar and bipolar electrograms may be used in tandem, where the bipolar signal is used to identify the local activation complex, and the unipolar signal is used to define the activation time more accurately.

1.3.4 Monophasic action potential

Monophasic action potentials (MAPs) are extracellular electrograms whose morphology is similar to the cellular action potential. MAPs are calculated as the difference between closely spaced electrodes, where one of the electrodes is pushed onto a small region of tissue. There is still uncertainty in the literature as to the correct physical basis of MAP catheter recordings, including which of the electrodes is the recording electrode (Vigmond and Leon, 1999; Kondo et al., 2004; Coronel et al., 2006).

MAPs have been used to study changes in the action potential duration with pacing, and the maximum slope of this relationship was found to indicate susceptibility of a premature beat to initiate AF in paroxysmal patients (Narayan et al., 2008); while alternating APD, as identified by MAP catheters, was found to precede all AF episodes (Narayan et al., 2011b).

1.3.5 Electrocardiogram

The electrocardiogram (ECG) is measured non-invasively using electrodes on the body surface. The output from each pair of electrodes is known as a lead, and there is a total of twelve leads. The angle of view of the lead depends on the location of the electrodes that make up the lead; for example, lead I is measured from the left arm to the right arm and is defined as having an angle of view of 0° (Levick, 2009). The main components of the ECG signals are the P wave, which represents atrial depolarisation; the QRS complex, which is the ventricular depolarisation; and the T wave, which represents ventricular repolarisation (see Fig. 1.2). Atrial repolarisation is not seen on the ECG leads as it is hidden within the larger ventricular depolarisation (QRS).

1.4 Mechanisms of atrial fibrillation

In humans, AF is the most common sustained cardiac arrhythmia, with a prevalence close to 20% in those aged 85 and above (Heeringa et al., 2006). It is a major risk factor for stroke and is associated with an increased risk of morbidity and mortality (Ezekowitz and Levine, 1999). Current antiarrhythmic drug therapies have limited efficacy, and many are not specific for atrial electrical activity leading to serious proarrhythmic effects, while a multicentre study reported that an average of 30% of patients who are treated by catheter ablation require a repeat procedure (Cappato et al., 2010). Increased understanding of the mechanisms underlying AF initiation and maintenance may aid in developing new and adapting existing thera-

pies. However, there are multiple hypotheses for the mechanistic basis of AF, and it is likely that in humans several mechanisms for AF exist. Different mechanisms are illustrated in the following schematic (Fig. 1.4).

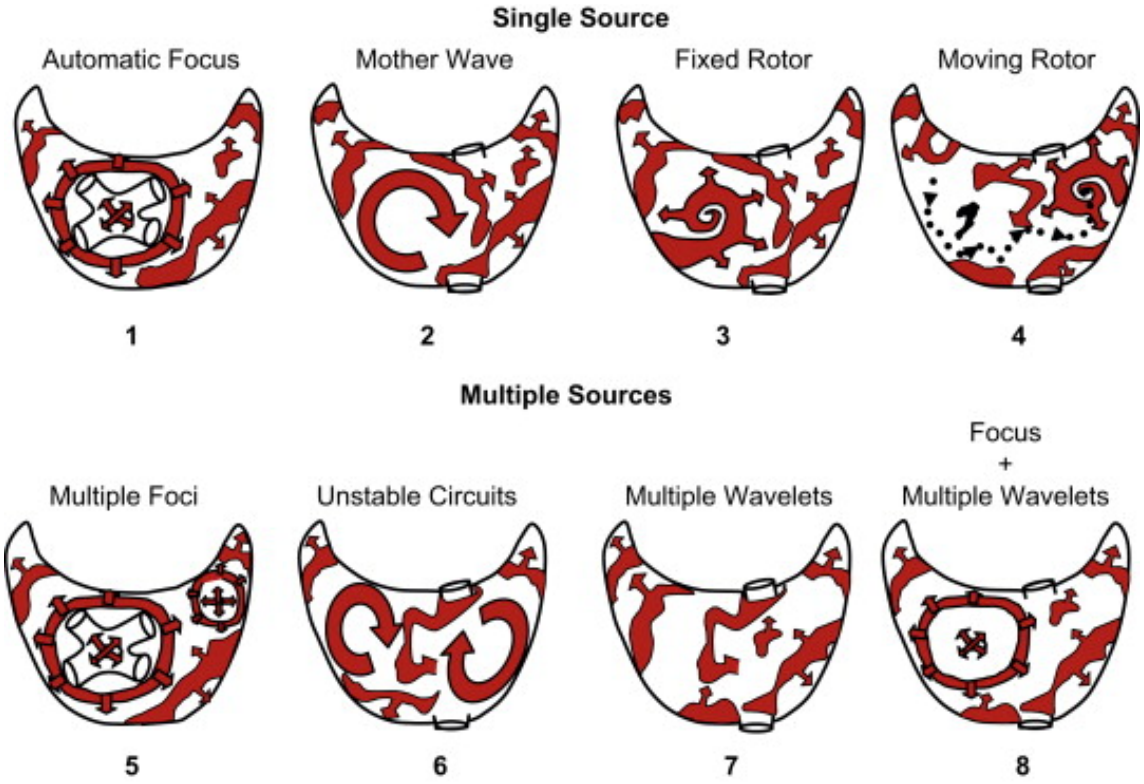

Figure 1.4: Schematic to show the mechanisms of Atrial Fibrillation. Reproduced from Eckstein et al. (2008).

1.4.1 The "mother rotor" hypothesis

The *mother rotor* hypothesis proposes that AF is not entirely random, but that hierarchical periodic rotors drive the AF, acting as sources of high frequency wavefronts (Jalife et al., 2002). A rotor is defined to be the organising source of functional reentrant activity, and the wave of excitation emitted by the rotor is a spiral wave in 2D, or a scroll wave in 3D (Vaquero et al., 2008). The wavefronts produced by the rotors may break into wavelets upon collision with obstacles (Vaquero et al., 2008).

Despite the presence of rotors in animal experimental studies (Davidenko et al., 1990), little evidence had been found for the existence of rotors in humans (Allessie et al., 2010), until Narayan et al. (2012b) recently presented a clinical computational mapping tool to identify rotors and focal sources in the atria, which were then ablated. In their study they located sources for AF in 96% of patients. They

demonstrated the potential for clinically targeting rotors. However their studies use simultaneous collection from most of the atrium using a 64 pole basket catheter, while many centres only have the technology for sequential mapping; thus an important question is whether rotors can be located using sequentially collected data.

1.4.2 Focal sources

Focal sources sustaining persistent AF have been identified in patients and these were ablated (Narayan et al., 2012b). A second mapping methodology of a non-invasive vest of electrodes has also found evidence for both focal sources and electrical rotors (Haissaguerre et al., 2013).

1.4.3 The "multiple–wavelet" hypothesis

The *multiple–wavelet* hypothesis was initially proposed by Moe and Abildskov (1959) to explain the persistence of AF; here atrial fibrillation is assumed to be a disorganised anarchical atrial rhythm in which there are multiple random wavelets of activation. The activity is assumed to be self-sustaining and independent of the initiating event, and Moe et al. (1964) developed a computer model of a non-homogeneous excitable substrate which predicted that at least 26 wavelets are required to sustain the arrhythmia. Experimental support for this hypothesis came from the Allessie group who found that between four and six wavelets were required to sustain turbulent atrial arrhythmia with the application of acetylcholine to dog hearts (Verheule et al., 2010). However, the multiple wavelet hypothesis does not explain the origin of the activity that causes the wavelets; if there were a small number of wavelets, then one would expect them to coalescence and annihilate AF (Jalife et al., 2002). In addition, the structural and electrical requirements needed to sustain such wavelets should be considered.

1.4.4 Endo-epi dissociation

Allessie *et al.* found no evidence for the presence of stable foci or rotors in a human epicardial mapping study (Allessie et al., 2010). Instead, they proposed a novel theory for the development of AF in structural heart disease, where the endocardium and epicardium of the atrium become electrically dissociated and *epicardial breakthrough* leads to fibrillatory waves (de Groot et al., 2010). These findings were from a high resolution mapping catheter.

There is conflicting evidence regarding the different mechanisms underlying AF. Studies using low-resolution global modalities tend to report hierarchical rotors and

focal sources; whereas studies using high-resolution mapping catheters tend to report anarchical multiple wavefronts. One important question is whether these differences are affected by the data resolution, field of view or post-processing techniques applied.

1.5 Factors affecting arrhythmia susceptibility

There are a multitude of factors affecting arrhythmia susceptibility, making AF a complicated disease to treat since it is multifactorial. Some of the factors are detailed in this section.

1.5.1 Dispersion of repolarisation

One feature shown to be involved in the vulnerability of cardiac tissue to fibrillation is dispersion of repolarisation. Repolarisation alternans, or just *alternans*, are beat-to-beat alternations in the duration or amplitude of the action potential (AP) of a cell. Alternans can be spatially *discordant*, where regions of the cardiac tissue alternate out of phase with each other (with one area alternating long-short-long, while an adjacent area simultaneously alternates short-long-short); otherwise they are known as *concordant*. Discordant alternans can produce spatial gradients of repolarisation large enough to cause unidirectional block (Fox et al., 2002) and ventricular tachycardia (VT). In addition, the occurrence of alternans has been implicated in the initiation of fibrillation in many experimental (Pastore et al., 1999), modelling (Karma, 1994; Fox et al., 2002), and clinical studies (Narayan et al., 2011b).

Spatially discordant alternans cause large spatial gradients of repolarisation, leading to an increased probability that ectopic beats cause functional block and reentry; particularly at the line separating discordant regions, the *nodal line*, where the spatial gradients in APD and intracellular calcium transient amplitude are steepest (Weiss et al., 2006). Narayan et al. (2008) proposed that the mechanism behind paroxysmal AF initiation from ectopic beats from the pulmonary veins is the ectopic beat encountering tissue with large APD oscillations, where the APD restitution slope is greater than one. However this mechanism does not explain incidences of persistent AF from ectopics, as the restitution curve was found to be flatter for these patients.

Arrhythmia does not require ectopic beats; in the presence of heterogeneity of susceptibility to alternans within the tissue, the amplitude of alternans can grow large enough that the DI following the longer APD goes to zero and conduction block of the short APD occurs. This in turn may lead to reentrant propagation

from the surrounding tissue, which is less susceptible to alternans, to the blocked region.

In a study of AF vulnerability, two mechanisms were found linking APD alternans to AF; the first was by spontaneous premature atrial beats when the maximum gradient of the restitution curve was greater than one, while the second was by amplified or complex APD oscillations (Narayan et al., 2011b). The spatiotemporal heterogeneity of repolarisation caused by discordant alternans has been suggested to form a substrate for fibrillation from fast pacing (Hiromoto et al., 2005) and for the transition from atrial flutter to fibrillation (Narayan, 2002).

1.5.2 Action potential duration restitution slope

Alternans can be induced by fast pacing in an experimental set-up, or increasing the heart rate in a clinical setting, and the heart rate threshold at which alternans occur correlates with risk of arrhythmia. A further increase in heart rate can lead to loss of spatial organisation of repolarisation of the myocardium, resulting in discordant alternans.

The first mathematical explanation for the relationship between heart rate and alternation of the action potential was given in 1968 by Nolasco and Dahlen who derived a criterion relating the rate adaptation of cardiac cells (*restitution*) to the occurrence of alternans and the electrical stability of the heart (Nolasco and Dahlen, 1968). Action potential duration restitution determines how the APD of a cell depends on the preceding interval between consecutive APs, the diastolic interval (DI). A restitution curve is a plot of APD against DI. Cardiac cells exhibit a form of rate adaptation, such that for a large range of longer DIs, APDs are long and there is a shallow relationship between DI and APD; while for shorter DIs there is a steep relationship. Physiologically, this allows the body to adapt to increased heart rates; while mechanistically, it occurs because there is a reduced current available at high heart rates, since the ion channels have had insufficient time to fully recover from inactivation.

Nolasco and Dahlen (1968) used a graphical method to hypothesise that restitution gradients greater than one lead to persistent repolarisation alternans. Consequently, clinical pharmacologic development was targeted at flattening the restitution curve to prevent wave breakup, with the aim of reducing the incidence of fibrillation (Garfinkel et al., 2000; Weiss et al., 2000). However, this critical gradient rule is not always observed; experimental studies have shown the existence of very steep restitution curves where alternans do not occur, and also the incidence of alternans when the restitution curve is shallow (Banville and Gray, 2002).

1.5.3 Intracellular calcium cycling dynamics

The mechanisms behind the generation of arrhythmias are multifactorial, and intracellular calcium cycling is another cellular property for which regional variations may lead to discordant alternans implicated in arrhythmia. Some studies have proposed that intracellular calcium cycling is more important than APD restitution in the initiation of alternans. For example, Pruvot et al. (2004) found that APD alternans and Ca^{2+} alternans usually happen together and the myocytes that were most susceptible to alternans suffered from disturbances in intracellular calcium cycling, but did not have the steepest restitution curves. Further evidence for the role of calcium is that repolarisation alternans are affected by drugs that change the intracellular calcium cycling (Saitoh et al., 1988).

In a combined clinical and modelling study, Bayer et al. (2010) showed that the differences seen between control and heart failure patients in the rate dependence of alternans of AP voltage are predicted by a mathematical model with abnormal calcium handling in the form of reductions in the sarcoplasmic reticulum calcium dynamics. One hypothesis explaining the progression from concordant to discordant alternans is regional heterogeneities in the expression of calcium cycling proteins and repolarising currents, with a study in guinea pigs finding transmural differences in sarcoplasmic reticulum Ca^{2+} cycling proteins as a possible molecular basis for spatially heterogeneous susceptibility to AP alternans (Wan et al., 2005).

1.5.4 Conduction velocity restitution

A further factor thought to affect the progression of concordant alternans to discordant alternans that lead to arrhythmia is the degree to which the speed of conduction through the myocardium changes with pacing rate. The velocity at which the activation front propagates (*conduction velocity*, CV) has restitution properties, and the interplay of CV restitution with APD restitution dynamics can affect alternans. In particular when CV slows in some areas, the DI prolongs and spatial inhomogeneity of DI exists, which can in turn lead to spatial discordance of APD (Walker and Rosenbaum, 2005). Echebarria and Karma (2007) demonstrated that CV restitution alone could produce discordant alternans in a rabbit ventricular model.

1.5.5 Gap junctional coupling

Furthermore, the degree of intercellular gap-junctional coupling may affect the transition to discordant alternans. Electrotonic effects act to homogenise cellular properties including APD, so a reduction in gap-junctional coupling leads to both a

reduction in CV (Kléber and Rudy, 2004) and facilitates spatial differences in AP alternation. Cellular uncoupling occurs during ischemia and Kjolbye et al. (2008) discovered that the gap-junction opener Rotigaptide reversed CV slowing and suppressed discordant alternans. Though intercellular coupling attenuates differences in repolarisation between cells, discordant alternans can occur in conditions of normal coupling, and hence abnormal intercellular coupling cannot completely account for the formation of discordant alternans (Tan and Joyner, 1990).

1.5.6 Electrical remodelling

Electrical remodelling occurs during AF. Changes in the ionic conductance of multiple ion channels have been shown to occur during chronic AF, including I_{K1}, I_{KACh}, I_{Na}, I_{CaL}, I_{to} and I_{Kur} (see Table 1 of Workman et al. (2008) for a comprehensive collation of findings in the literature).

I_{K1} is the main determinant of the resting potential, and it has been shown to increase in chronic AF. Modelling studies have found that increasing I_{K1} reduced spiral wave meander and hence stabilised reentry (Pandit et al., 2005a), as well as increasing the dominant frequency, which has been shown to occur because of changes in APD and its rate dependence (Sánchez et al., 2012). I_{CaL} is reduced in chronic AF; it affects the AP plateau but has a smaller effect than I_{K1} (Pandit et al., 2005a).

1.5.7 Structural remodelling

Structural remodelling also plays an important role in AF, including an increase in cell size (Eckstein et al., 2011); a change in cell-to-cell coupling and connexin expression; and fibrosis (Mahnkopf et al., 2010). The extent of fibrosis has been shown to increase the risk of reentry and wave break (ten Tusscher and Panfilov, 2003; Kawara et al., 2001), with interactions of waves with fibrotic patches controlling fibrillation in some cases (Tanaka et al., 2007). In a computer modeling study, Engelman et al. (2010) showed that structural discontinuities in their model of cardiac tissue increased the probability for discordant alternans occurring at high stimulation rates since the random barriers to excitation cause large spatial differences in activation time distribution, providing a substrate for reentry.

Thus there are many factors ranging from those at the cellular to the tissue level that affect arrhythmia susceptibility and maintenance, making AF a difficult disease to interpret. Increased understanding of the disease can be provided by experiments in the basic research environment, the use of computational models,

and clinical research; and, in each case, analysis of the wavefront dynamics will provide important information to aid interpretation of the arrhythmia dynamics.

1.6 *In vitro* modalities for investigating electrical activity

In vitro studies have the advantage that they are more controllable. Experiments can be undertaken at a range of spatial scales, from the single cell level, to the level of the organ. There are two commonly used technologies that enable access to information on the action potential and electrogram.

1.6.1 Optical mapping

Optical mapping uses potentiometric dyes in order to visualise changes in measures such as transmembrane voltage or intracellular calcium concentration. It can be used for cell cultures, tissue slices, or for Langendorff whole heart preparations (Efimov et al., 2004). Dyes are chosen such that changes in the intensity of the fluorescence signal emitted from a voltage sensitive dye is proportional to changes in the transmembrane voltage (or to the calcium concentration of the cytosol in the case of a calcium sensitive dye). These recordings represent a summation of the transmembrane voltage for all of the cells within a volume of tissue corresponding to the recording pixel (Walton et al., 2012).

1.6.2 Microelectrode arrays

Microelectrode arrays consist of a grid, or array, of electrodes that record extracellular field potentials. The technique has the advantage that it is non-invasive as it does not damage the cell membrane, allowing for longer experiments. Field potentials can be post-processed to determine activation patterns and conduction velocities across the array. These arrays can be on a fixed plate for use in cell culture, or on a flexible array for use with a Langendorff set-up.

Halbach et al. (2003) related the components of field potentials from mouse embryonic cardiomyocytes to characteristics in the action potential, and found that the time of the minimum voltage of the field potential (FP_{min}) and the time of maximum voltage (FP_{max}) correlated well with the depolarisation and repolarisation of the action potential respectively (see Fig. 1.5). Consequently the field potential duration shows a close correspondence to the action potential duration. In addition, Halbach et al. (2003) found there is a linear relationship between the *rise time* (time

for depolarisation, FP_{rise}, in Fig. 1.5) of the field potential and the rise time (duration of the upstroke) of the action potential.

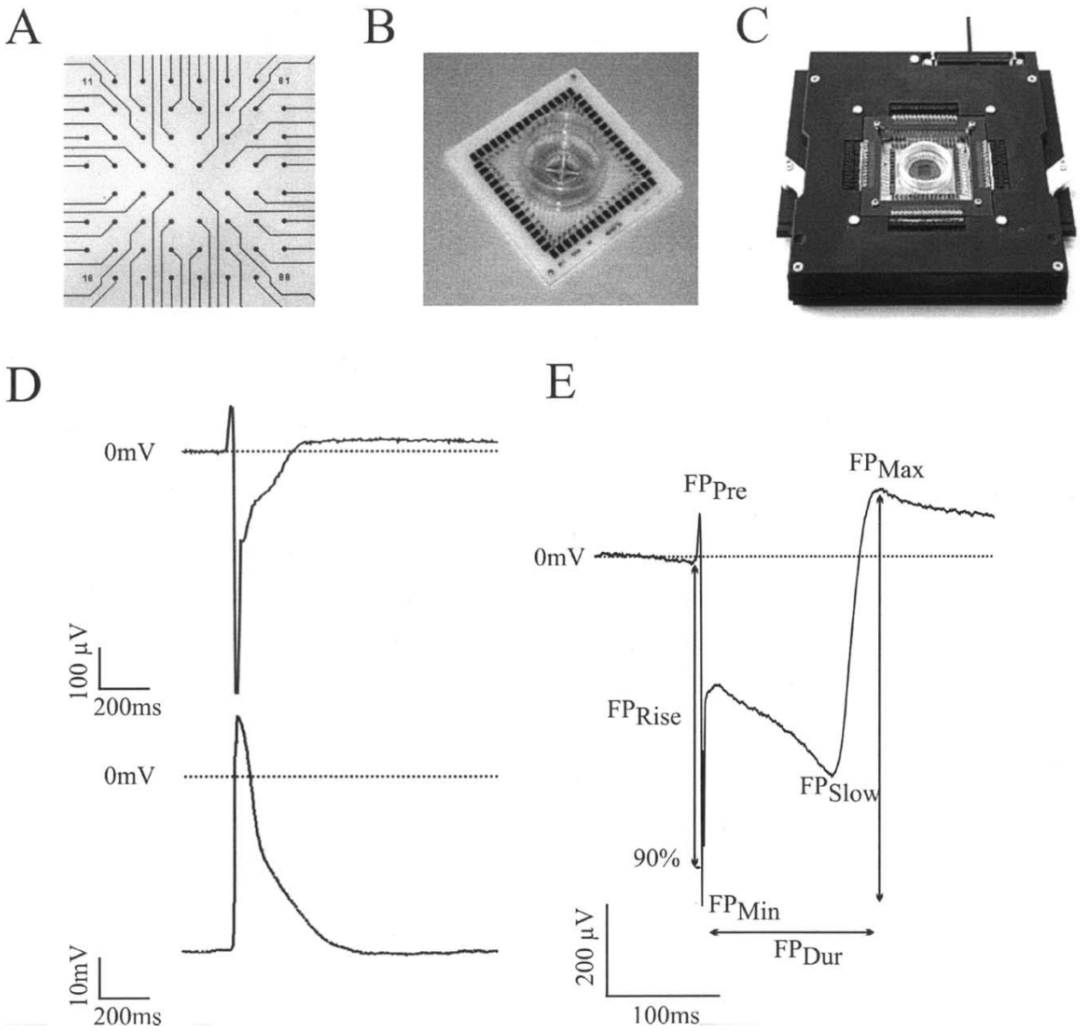

Figure 1.5: Microelectrode array set-up and field potential characteristics. (A) Electrode array containing 60 electrodes in an 8-by-8 grid (with corner electrodes missing); (B) MEA plate; (C) Filter amplifier (MultiChannel Systems (Reutlingen, Germany)); (D) Field potential (top) and action potential (bottom), for which the activation and depolarisation, and recovery and repolarisation are seen to coincide in time, respectively. (E) Components of the field potential, as defined by Halbach et al. (2003), are marked showing the rise (FP_{rise}), time of minimum voltage (FP_{min}) and time of maximum voltage (FP_{max}). Image reproduced from Reppel et al. (2004).

1.7 *In silico* modalities for investigating electrical activity

Computational modelling is a widely used research tool in electrophysiology, which aids in the generation of hypotheses and predictions, explanation of experimental results and integration of data across many spatial and temporal scales. The field stems from the Nobel Prize winning work of Hodgkin and Huxley, who in 1952 created the first mathematical model of excitable current in nerve cells (Hodgkin and Huxley, 1952). Noble (1960) went on to use these equations as a basis for the first model of a cardiomyocyte action potential in 1960. With an increase in both computational power and experimental data, the field has flourished, with over 100 different cardiac action potential models now available in the literature. Meanwhile the solution domain now ranges from the single cell, right up to the whole heart level.

Cardiac models typically contain a representation of cellular membrane excitability, with an equation for how this propagation spreads over the cardiac tissue. Thus developing a model requires the choice of an action potential cell model, equations for how the electrical signal propagates and a geometry on which to solve. Here we first outline two types of action potential models (biophysically detailed and phenomenological), followed by some notable findings and methodologies for three-dimensional anatomically detailed models and patient specific modelling.

1.7.1 Cell models

There are a plethora of models available for representing cardiac membrane dynamics. A curated database of published cell models can be found on the CellML model repository website (Lloyd et al., 2008). Example biophysical and phenomenological cardiac cell models are shown in Fig. 1.6.

Biophysically detailed electrophysiology models

Biophysically detailed models contain voltage- and time-dependent currents derived from experimental studies, typically using single cell patch clamp data. Action potential models represent different species, from mouse to canine to human, and different cell types, including sinoatrial-nodal, atrial and ventricular cells. The models are typically for the undiseased state, though it is possible to change ion channel conductances to represent changes that happen in disease – for example, Courtemanche et al. (1999) proposed changes to their model for chronic AF by altering the

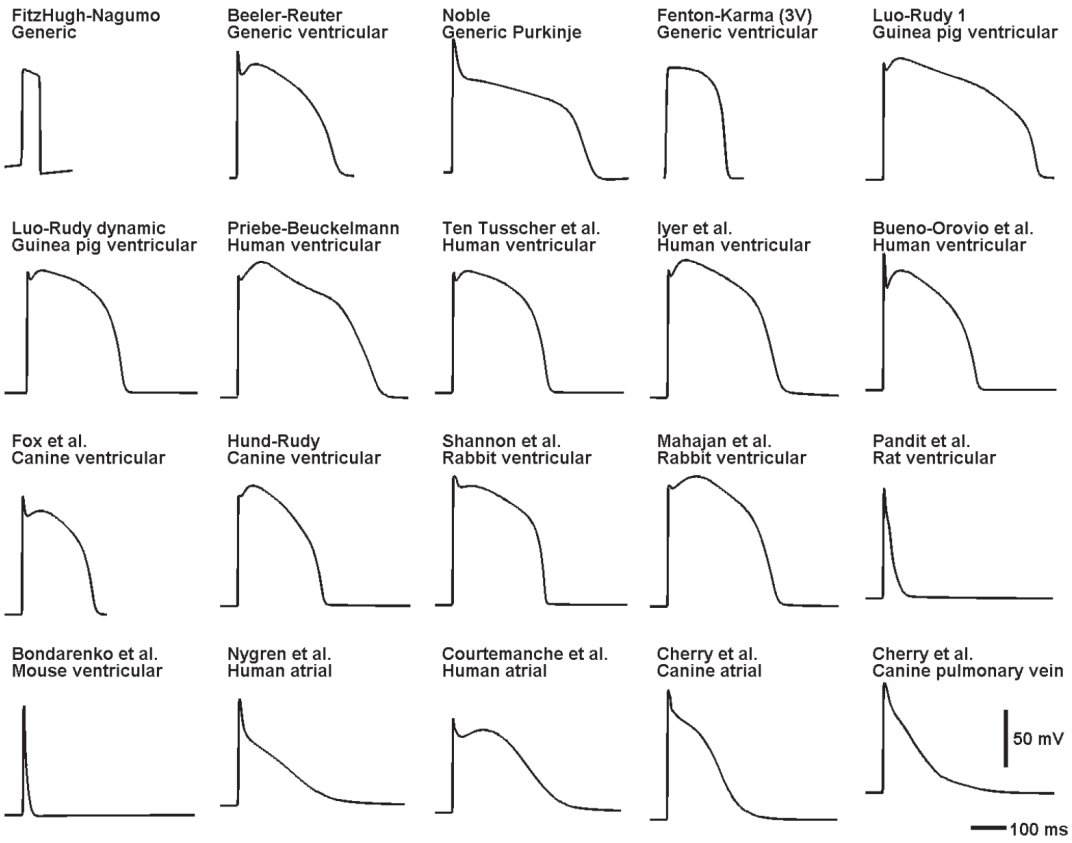

Figure 1.6: Cardiac cell models action potentials from Cherry and Fenton (2008).

conductance of several ion channels. In addition, biophysical models may include detailed intracellular calcium cycling (Bayer et al., 2010; ten Tusscher and Panfilov, 2006).

One use of biophysically detailed models is in making predictions. For example, several studies have used computational models to simulate the effects of drugs on particular ion channels, considering how this affects the action potential and manifests at the tissue and whole heart level (emergent properties), thus also linking spatial scales. Moreno et al. (2011) used this approach to simulate the action of the anti-arrhythmic drug flecainide on cardiac sodium channels, and how this manifests at the whole heart level.

Despite being developed to model the action potential of a particular species, models may contain a hybrid of data from many species, recorded at different temperatures. For example, Niederer et al. (2009) analysed the origin of data used in the ten Tusscher et al. (2004) human ventricular model and found that it came from a wide range of species and temperatures, either because of lack of available human data at the time of model construction, or due to inheritance of elements of the model from other models. This may limit the use of these models in drug toxicity studies. The O'Hara et al. (2011) dynamic model is based entirely on healthy human ventricular data.

Biophysical models are computationally expensive to solve, so various simplifying assumptions are sometimes adopted; one approach is to keep the main dynamics of the model the same but to eliminate gating variables, or to take intracellular concentrations to be constant (Clayton et al., 2011). An alternative is to use a phenomenological model.

Phenomenological models

As well as being computationally less expensive and improving modelling feasibility, *phenomenological models* can be used to study tissue level properties of the tissue, such as the response of the APD and CV to changes in stimulation frequency (Cherry and Fenton, 2004). These models typically contain variables that represent summed currents, rather than representing individual currents. A disadvantage of this is that it is more difficult to change individual ion channels to see, for example, the effects that a drug has on impulse propagation.

The Fenton and Karma (1998) model is a widely used three variable phenomenological model. Echebarria and Karma (2007) used different parameter sets for this model to investigate the effects of APD and CV restitution on spiral wave breakup in tissue, to elucidate the mechanisms underlying the breakup. Cherry and Fenton

(2004) investigated the influence of short-term pacing history (*memory*) and electrotonic effects on the occurrence of action potential alternans using a model based on the Fenton and Karma (1998) model, with different parameter sets to vary these factors independently. This demonstrates one advantage of modelling, which is that it is possible to vary factors independently to see the effects of each in a controlled environment, which is difficult to do experimentally. Varying factors independently may offer mechanistic insight, though it is important to keep the model assumptions in mind when interpreting the results.

The Bueno-Orovio et al. (2008) model is a recent development of the Fenton and Karma (1998) model that includes a fourth variable which allows the model to be accurately fit to match AP morphology; for example, to represent epicardial, endocardial and mid-myocardial cells. Furthermore, it is possible to perform parameter fitting to match the action potential morphology and restitution curves of experimental results, or other computational models. A recent study developed a stochastic version of the deterministic Bueno-Orovio et al. (2008) model to capture beat-to-beat variations in action potential morphology and duration (Walmsley et al., 2010).

1.7.2 Cardiac tissue electrophysiology

Discrete models

One of the earliest computational models of AF was that by Moe et al. (1964), which elegantly proposed, using a simple cellular automata model of non-homogeneous excitable tissue, that at least 26 wavelets are required to sustain AF. Cellular automata, which model a lattice of cells in a finite number of states of excitation, updated at each time step, have also been used to study spiral wave generation in a heterogeneous substrate, where the resulting simulations were compared to experimental results from monolayers of embryonic chick cells (Bub et al., 2002). Disadvantages of cellular automata models are the lack of electrotonic interactions and that it is challenging to incorporate restitution properties in the model (Clayton et al., 2011).

Continuum models

Other mathematical descriptions of electrical signal propagation in cardiac tissue include the eikonal equation (Jacquemet, 2010); discrete formulations with representations of individual cells coupled by gap junctions (such as the model of Stinstra et al. (2010)); and continuum models, including the monodomain and bidomain equations.

Continuum models are reaction–diffusion type equations that consider the heart as a functional syncytium with propagating waves on the macroscopic scale. The *bidomain* model includes an intracellular and extracellular domain that are overlapping and continuous, but separated by a cell membrane. Under the assumption of equal anisotropy of the intracellular and extracellular domains, the bidomain model can be simplified from two to just one partial differential equation (PDE), which is for the transmembrane potential – this is the *monodomain* equation. The monodomain model is generally a good approximation to the bidomain model (Colli Franzone et al., 2005), and is also numerically easier to solve; however, the bidomain model must be used to study defibrillation (Trayanova, 2006). It is possible to incorporate tissue anisotropy, heterogeneities in cell type (for example fibroblasts (MacCannell et al., 2007; Sachse et al., 2009)), wavefront curvature, and gradients of repolarisation into the model.

The resulting PDEs and ordinary differential equations (ODEs) are typically solved using finite difference, finite element (Vigmond et al., 2002) or finite volume techniques (Trew et al., 2005). Finite difference methods are generally easiest to implement; however, finite element and finite volume methods facilitate implementation of more complex geometries and boundary conditions. Several software packages have been developed to implement these methods for simulating cardiac electrophysiology on different geometries, including: Nektar ++ (Cantwell et al., 2015a), Chaste (Pitt-Francis et al., 2009), and CARP (Vigmond et al., 2003). There has been a recent drive for benchmarking within the field (Niederer et al., 2011). In addition, there is an international collaboration for building multiscale cardiac models called the Cardiac Physiome Project (Bassingthwaighte et al., 2009).

Action potential models can be incorporated into tissue and solved in a 1D cable, 2D or 3D. The geometry can either be idealised, such as a 2-D sheet, or anatomically detailed, based on histology or imaging data.

1.7.3 Three-dimensional electrophysiological models

Realistic anatomical models based on MRI and histology have been developed and these can be used for in silico electrophysiology experiments. Examples of whole ventricular myocardium models include the UCSD rabbit (Vetter and McCulloch, 1998) and Auckland swine (Stevens et al., 2003), which are based on histological sectioning data; and the Oxford rabbit, JHU canine, and JHU human (Vadakkumpadan et al., 2010), which are constructed from imaging data. Using imaging, typically the MRI structural image is segmented, a finite element mesh is then generated and fibre orientations are assigned based on DT-MRI data. Alternatively, histological

sectioning data can be used for the mesh and for assigning fibre orientations. Models based on MRI and DT-MRI data of heart failure or infarcted hearts have also been created. In addition, structural MRI data can be combined with data from histology to generate high-resolution histo-anatomical models (Plank et al., 2009).

A three-dimensional human ventricular model with realistic anatomy derived from histology was used alongside human *in vivo* VF data to demonstrate that human VF has a simpler spatial organisation compared to VF of large animal hearts. Human VF was found to be driven by approximately 10 reentrant sources, compared to approximately 50 in canine and swine hearts – which are commonly used animal experimental models for studying human VF. The effects of different factors on the number of rotors were investigated in the model, including anisotropy, excitability, maximum APD restitution slope and minimum APD. The study found that minimum APD had the greatest influence (ten Tusscher et al., 2007, 2009).

A further application of three-dimensional models is investigating the impact of structural heterogeneities on arrhythmia susceptibility. Pop et al. (2011) constructed models of two infarcted swine hearts – one of which had noninducible ventricular tachycardia (VT) *in vivo*, while the other had macrorentrant VT – using MRI for structural information and DT-MRI for fibre orientations. Simulation results accurately reproduced the cycle lengths and outcomes of the cases.

In addition, using a high-resolution model generated from confocal images of a transmural infarct zone, Rutherford et al. (2012) found that structural heterogeneity alone is a sufficient substrate for reentry by isolating the effects of structural changes.

Structural data for anatomically accurate models for human atria are typically from MRI or CT scans (see Table 1 in Dössel et al. (2012) for an extensive list of geometries used by different studies). Aslanidi et al. (2011) developed a three-dimensional computer model of human atria, with geometry from the visible human dataset, while fibre orientation for the sino-atrial node and surrounding right atrium were based on DT-MRI data of this tissue. Heterogeneous AP models were used for different regions of the atrium, and ECGs were calculated by embedding the atria in a torso model.

1.7.4 Patient specific modelling

Patient specific models offer a bridge between computational models and data from the catheter laboratory and imaging. With advances in imaging and computational technologies, it is hoped that patient specific modelling can aid clinical treatment strategies, lead to more detailed diagnosis and improve treatment. However, patient specific modelling is very challenging due to the following difficulties: constructing a

geometric mesh from in vivo clinical scans of limited resolution; obtaining accurate fibre orientations; and finally performing simulation experiments fast enough to be clinically useful, as simulations that extend treatment times are not clinically acceptable. The ultimate aim is for patient specific modelling to be routinely used in clinical practice.

McDowell et al. (2012) recently published a patient specific model of human atria for a patient with persistent AF, which was the first model to include an accurate distribution of fibrotic tissue. The model used images from LGE-MRI, where the contrast agent allows quantification of the distribution of fibrosis. The LGE-MRI was segmented and fibrotic regions defined based on signal intensity, to give a computational mesh. Fibre orientation was added to the mesh by tagging landmark points on both the patients geometry and an atlas geometry which contains fibre orientations (Krueger et al., 2011), then deforming the fibre orientations to estimate fibre orientations for the geometry of the patient. Other features such as myofibroblasts were added to the model, and a reentrant arrhythmia following pulmonary vein ectopy initiated in the model, demonstrating its utility. Due to the resolution available being on a similar scale to atrial wall thickness, DT-MRI is not yet usable for determining the fibre orientation of the whole *in vivo* atria.

Studies by Rotter et al. (2007) and Ruchat et al. (2007) tested the effects of varying ablation line patterns in patient specific models of AF and showed that this is feasible, with simulation results reproducing clinical outcomes, suggesting the potential of models to optimise ablation patterns.

1.8 *In vivo* modalities for investigating electrical activity

In vivo studies offer the least control and the strictest research protocols; however, they also provide the most valuable datasets, which may be complicated to interpret. Data come from a variety of mapping modalities, depending on what is available at the clinical centre.

1.8.1 Clinical electroanatomic mapping systems

Electroanatomic mapping systems allow the integration of electrical and location data, in order to provide the clinician with a more detailed picture of the patient's electrical characteristics. These systems are particularly useful during complicated cases such as AF. The method used to determine the location data depends on the

choice of electroanatomic mapping systems, and there are two techniques commonly used.

Ensite NavX Velocity (St Jude Medical, Inc., St Paul, MN, USA) determines the location of catheters by using three pairs of skin patches, arranged in orthogonal planes (Eitel et al., 2010). Specifically, three-dimensional catheter position is located by applying a signal across pairs of patches to create a voltage gradient, and the amplitude of the voltage of each electrode is compared to this gradient to estimate the catheter position. In order to build up a patient-specific map, the roving catheter is moved along the endocardial surface to create the geometry, and then sequential mapping is performed.

Carto (Biosense Webster, Baldwin Park, CA, USA) uses magnetic fields to determine the spatial location of the electrode catheter and its orientation.

Both Ensite Velocity and Carto are sequential mapping systems, where the electrical signals for a small area of the tissue are collected using a multipolar catheter, and then the catheter is moved to a new location. For stable rhythms, this approach works well, as relatively high resolution data can be acquired and pieced back together by the electroanatomic mapping system into a global map. Examples of multipolar mapping catheters used clinically include the circular Lasso catheter, the spiral-shaped AFocus II and the five-spline PentaRay catheter, which are approximately 2cm in diameter.

1.8.2 Non contact mapping

There are also non-contact mapping systems available, which have the advantage that they enable the simultaneous acquisition of a large number of electrograms. As such, activation maps can be built using just a single beat of activity, which is particularly useful for mapping atrial tachycardia (AT). An example of such a system is EnSite 3000 (Endocardial Solutions), which allows the generation of 3360 virtual electrograms measured using a multi electrode array catheter (Schilling et al., 1998). The recorded signals are of lower amplitude and frequency than surface endocardial electrograms, and so an inverse solution technique is used to enhance these signals. A disadvantage of the system is that if the distance from the electrode array to the endocardial surface is greater than 34mm, accuracy of activation times of the reconstructed electrograms are reduced.

1.8.3 Basket catheter mapping

A mapping modality that enables low resolution global mapping of the endocardial surface of the atrium is the *basket* catheter, composed of eight splines each with eight electrodes. The catheter is available in several sizes including 48mm diameter (4mm interelectrode spacing) and 60mm diameter (5mm interelectrode spacing). This catheter was used in the first cases to identify electrical rotors in human AF (Narayan et al., 2012b) and is currently used by several centres to identify and target electrical rotors and focal sources (Baykaner et al., 2014).

1.8.4 Noninvasive inverse mapping

A noninvasive mapping system which consists of a vest containing an array of 252 body surface electrodes (ECVUE, CardioInsight Technologies Inc, Cleveland, OH) can be used along with a CT scan to provide detailed electroanatomic maps. The technology uses inverse solution techniques originally pioneered by Rudy and Messinger-Rapport (1988) to determine the origin of cardiac arrhythmias. The ECGi technology has been used to identify the spatiotemporal distribution of focal sources and rotors during AF, with ablation focussed on the high density regions (Haissaguerre et al., 2013, 2014a).

These recording techniques provide electrical information during clinical treatment, for which there are several different treatment strategies.

1.9 Clinical treatment strategies for persistent AF

1.9.1 Eliminating "triggers": pulmonary vein isolation

Pioneering work by Haïssaguerre et al. (1998) in 1998 demonstrated the importance of ectopic beats from the myocardial sleeves of the pulmonary veins (PVs) for triggering AF in humans. Radiofrequency catheter ablation to isolate the PVs (*pulmonary vein isolation*, PVI), and eliminate the ectopic focal drivers, is a successful treatment for paroxysmal AF (Haïssaguerre et al., 2000); however patients with persistent AF will often require multiple procedures and antiarrhythmic drug therapy. Hence it is likely that mechanisms other than focal triggers from the pulmonary veins are responsible for the maintenance of persistent AF, where longer AF duration has led to electrical and structural changes.

1.9.2 Linear ablation lines

Following PVI, linear ablation may be performed, with common ablation lines being a roof line and a mitral valve line. There are conflicting studies on the effects of these additional ablation lines on clinical outcome (Knecht et al., 2008; Arbelo et al., 2014).

1.9.3 Targeting complex fractionated atrial electrograms

Konings et al. (1997) introduced a classification system for unipolar electrograms, separating them into single, short-double, long-double and fragmented electrograms, with fragmented electrograms showing multiple negative deflections over a long activation complex, and said to represent either slow conduction or reentrant wavelet pivot points.

Current ablation strategies include using techniques other than pulmonary vein isolation (PVI), such as targeting the ganglionated plexi and *complex fractionated atrial electrograms* (CFAE). Nademanee et al. (2004) proposed that fragmented electrograms represent areas where AF is perpetuated. They defined CFAEs as atrial electrograms which satisfy at least one of the three following conditions: either having mean *cycle length* (interval between activation times) less than 120ms, or having continuous activity for the 10 second electrogram duration, or the electrogram has two or more consecutive deflections. Ablation of CFAEs terminated AF in 95% of the patients in their study. However, other groups have failed to replicate this success. For example, Estner et al. (2008) saw conversion to sinus rhythm following CFAE ablation alone in only 25% of patients, while the combined approach of PVI and CFAE ablation, targeting so called triggers and substrate, led to a much higher success rate of 74% of patients in sinus rhythm nineteen months after treatment (where PVI alone had a success rate for treating persistent AF of only 20%) (Oral, 2002). One confounding factor is that there are different definitions of fractionated electrograms, with the clinically used electroanatomic mapping softwares NavX and Carto using different algorithms to calculate CFAE scores, which have been shown to correlate poorly with each other and with conduction velocity and number of waves per AF cycle (Lau et al., 2015).

In addition, it is difficult to separate the mechanisms underlying electrogram morphology. Narayan et al. (2011a) mapped local refractoriness of atrial tissue using MAP catheters to help to classify the fractionation of bipolar electrograms, finding that far field signals account for 67% of fractionation, while other CFAE types include rapid localised AF sites (8%), spatial disorganisation (17%), and CFAE

following AF acceleration, which is often accompanied by MAP alternans (8%). A high-density mapping study of patients during AF, sinus rhythm and paced rhythms showed that CFAE distribution is highly variable (Jadidi et al., 2012). Paced and sinus rhythm fractionation was attributed primarily to wave collision, and Jadidi et al. (2012) suggest that CFAEs are functional, with dynamic sites.

1.9.4 Targeting sources: stable rotors and focal sources

Focal Impulse and Rotor Modulation (FIRM) is a clinical mapping system that utilises a basket catheter and phase mapping technology to identify rotors and focal sources in patients undergoing ablation for AF (Narayan et al., 2012b). The technology has found that AF is sustained by an average of $2-3$ rotors or focal sources, within areas of 2.2 ± 1.4 cm^2, which can then be ablated (Baykaner et al., 2014). The technology has shown an improved clinical outcome compared to conventional ablation in many studies; however, a recent study showed that catheter ablation of sites identified by FIRM mapping terminated AF in only a minority of patients (Benharash et al., 2015).

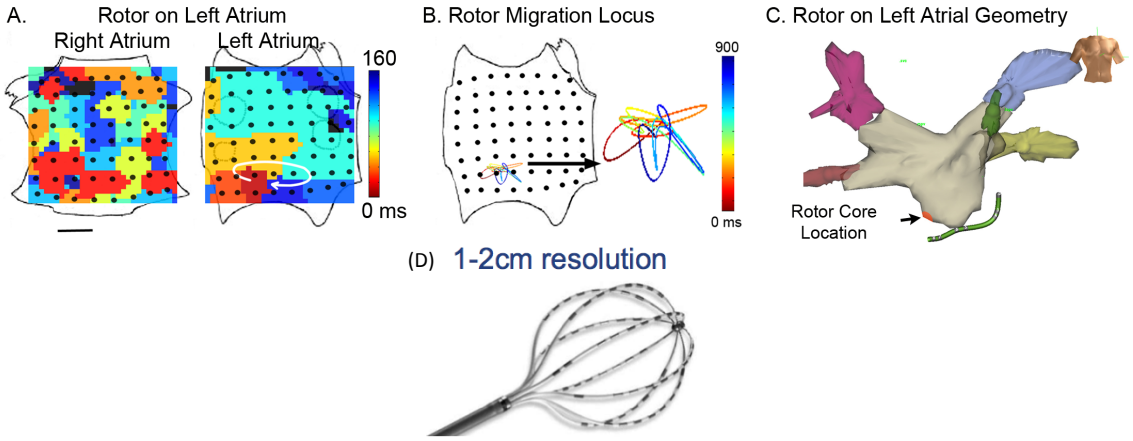

Figure 1.7: Focal Impulse and Rotor Modulation mapping technology. (A) Rotor identified on the left atrium using activation maps; (B) The trajectory of the rotor is determined; (C) Rotor shown on the left atrial geometry. (D) Photo of a basket catheter. Adapted from Narayan et al. (2012a).

1.9.5 Targeting sources: regions of high driver content

Cumulative spatial distributions of rotors and focal sources are used clinically by centres using the non-invasive ECGi technology to determine ablation targets (Haissaguerre et al., 2013, 2014a). In the studies of Haissaguerre et al. (2013), the atria

are divided into seven regions and ablation starts by targeting the region with the highest density of *drivers*, which are defined as focal sources or reentrant sources with greater than one rotation. An example rotor identified using the technology is shown in Fig. 1.8.

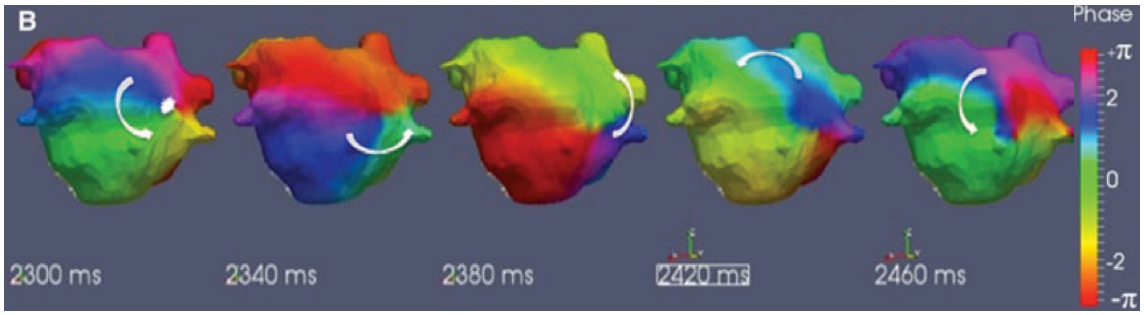

Figure 1.8: Rotor identified using phase mapping and ECGi technology. Figure reproduced from Haissaguerre et al. (2013).

1.9.6 Targeting sources: dominant frequency mapping

The *dominant frequency* (DF) of an electrogram is the frequency with the highest power in the frequency spectrum. Areas of high DF are thought to indicate areas of driver activity (Mansour et al., 2001), and some clinical studies have targeted these areas. Jarman et al. (2012) found that areas of high DF are not spatiotemporally stable, suggesting that they do not represent a fixed driver.

Multiple treatment strategies with varying success highlight the challenges associated with understanding AF, for which improved methods for analysing wavefront dynamics are critical.

1.10 Analysing wavefront dynamics overview

Analysis of propagation patterns – including calculating wavefront velocity, features of the velocity field, and using phase to identify rotational activity – can aid in understanding functional and structural factors underlying arrhythmia, as well as offering insight into the mechanisms perpetuating the fibrillation. In the following sections, techniques available in the literature for defining activation times, for calculating conduction velocity and for identifying rotor cores will be presented.

1.11 Activation time calculations

1.11.1 Motivation and overview

Conduction velocity (CV) describes the speed and direction at which the activation wavefront propagates. CV is a quantitative physiological measure that gives an indication of the underlying properties of cardiac tissue, where an area of reduced CV may indicate an area of increased fibrosis (Kawara et al., 2001). In addition, an estimation of the direction and distance to an electrical source during ventricular tachycardia (VT) or AF can guide ablation. Thus CV is important for both understanding arrhythmia mechanisms and for treatment, offering functional and structural insight into the initiation and perpetuation of cardiac arrhythmias. Experimental, clinical or simulated data can be either unipolar electrogram, bipolar electrogram or action potential data (and activation times are defined according to the type of data, see Fig. 1.3), with different spatial distribution, number and resolution of recording points. The most appropriate algorithm to calculate CV will depend on these factors, and also on the curvature and number of underlying wavefronts. Overall, limitations in data resolution, and uncertainty in recording location and activation time make calculating conduction velocity accurately a challenge.

In this section and the following Section 1.12, techniques available in the literature for defining activation time of electrical recordings and for calculating CV are presented, and their suitability for different data types, rhythms and data resolutions are discussed. These two sections formed the basis for a review of conduction velocity techniques for which I was second author: *Techniques for automated local activation time annotation and conduction velocity estimation in cardiac mapping*, published in Computers in Biology and Medicine (Cantwell et al., 2015b).

In the simplest case, conduction speed can be measured by taking two recording points chosen such that the line joining the points is perpendicular to the wavefront, and then dividing the length of this line by the difference in the activation times of the points. This is appropriate for propagation that is predominantly one-dimensional and uniform, for example in lines of cardiac cells in tissue culture (Dhillon et al., 2013). In two and three dimensional preparations, it is often difficult to determine the path of activation and thus it is hard to get an accurate measure of distance that the wavefront has travelled. However, the first challenge is to accurately measure the activation time of each electrogram.

There are standard definitions of the point on either an action potential, unipolar electrogram or bipolar electrogram that are typically used as the activation time in basic science or in the clinical set-up, as shown in Fig. 1.3 and discussed in

Section 1.11.2. However, other definitions may be more accurate or appropriate in the case of fractionated multicomponent electrograms, for which it is challenging to define the activation time, or for low temporal sampling rate.

1.11.2 Standard definitions

As detailed in Fig. 1.3, the standard definition for the time of cellular activation is the point of steepest gradient on the action potential. The point of maximum negative slope on the unipolar electrogram has been shown to match with the activation time measured using the action potential of the underlying cells. There is no such correspondence for the bipolar electrogram, although one commonly used choice for the activation time of bipolar electrograms is the time of maximum amplitude.

There are many different algorithms for detecting activation time in unipolar and bipolar electrograms and these have been compared in the laboratory (Pieper et al., 1993) and in computer simulations (Steinhaus, 1989). One such definition for bipolar electrograms is the point which equally divides the modulus of the signal into two; the so-called *centre of mass* (Sandrini et al., 2002). This point was found to coincide with the point of maximum negative slope on the unipolar electrogram (El Haddad et al., 2013). This choice has been shown to show closer correspondence with unipolar activation times than other markers of bipolar activation (Pieper et al., 1993; Langston et al., 1994).

1.11.3 Non-linear energy operator

Kaiser (1990) originally proposed using the non-linear energy operator (NLEO) as a measure of the energy of a signal which is proportional to the amplitude squared multiplied by the frequency squared. It is defined for a signal x as

$$E(t) = x(t)^2 - x(t+1)x(t-1). \tag{1.1}$$

The NLEO can be used to segment the bipolar electrogram signal into active and inactive regions. Schilling et al. (2009) calculated the proportion of the electrogram that is active (the *activity ratio*) as a classification for CFAE. Similar to the centre of mass approach, both Weber et al. (2010) and Burdumy et al. (2012) used the barycenter of the filtered NLEO as the activation time. According to Weber et al. (2010), activation times defined using the barycentre of the NLEO may be closer to representing tissue activation for the point between electrodes for bipolar electrograms than the time of the maximum amplitude.

1.11.4 Time-delay cross-correlation

Electrogram data may be collected with a low temporal sampling rate, and for standard techniques the activation time position is limited by the sampling rate of the data. Cross-correlation is a technique that was original developed by Shors et al. (1996) to overcome limitations associated with low sampling rate. It works on the basis that electrograms measured from recording points that are close together may have similar enough morphologies to work out the time delay between the electrograms using cross correlation. The data are filtered, the cross-correlations are calculated and then the zero-crossings of the linearly interpolated Hilbert transform of the cross-correlation are taken as the time delays. The results of cross correlation were found to have a smaller standard deviation than that of maximum negative slope of the electrogram, suggesting that this method is more accurate. However, the technique only works when the signal morphologies are sufficiently similar, which is often not the case for large inter-electrode distances or diseased tissue (Fitzgerald et al., 2001). Shors et al. (1996) make the point that this method may be more appropriate in the case of heterogeneous tissue, for which the maximum negative slope of the unipolar electrogram is not necessarily the activation time; however, intracellular recordings are required to see how the time delays relate to the cellular activation.

1.11.5 Local activation times

The *local activation time* (LAT) of a unipolar or bipolar electrogram is the time of activation of the tissue in the locality of the recording electrode. In clinical procedures, electroanatomic mapping systems provide the ability to construct activation time maps, for which the activation time at a roving electrode is referenced to a time point in an ECG signal or stable intracardiac electrogram. This necessities the presence of a stable rhythm; for example, sinus rhythm, paced rhythms and some tachycardias.

1.12 Conduction velocity calculations

In a two-dimensional preparation, recordings from three non-collinear electrodes may be sufficient to provide an accurate CV vector. However, in the case of heterogeneous tissue, fractionated electrograms, uncertainty in recording location or complicated activation patterns, more sophisticated methodologies for calculating CV are required. These include a variety of techniques, which are introduced, along

with their data requirements and suitabilities in the following sections. Finally the techniques are compared.

1.12.1 Triangulation

Triangulation is a technique to calculate CV vectors from triads of non-collinear points. It is suitable for clinical data and has been applied to global sequentially acquired local activation time maps during sinus rhythm and paced rhythms (Kojodjojo et al., 2006; Ravelli et al., 2011; Sawa et al., 2008). Triangles of points can be constructed using either Delaunay triangulation (Delaunay, 1934) or edge completion (Barr et al., 1980). Points were only included in a triad if they were less than 20mm apart and had a local activation time difference of greater than 3ms (Kojodjojo et al., 2006). A local CV is assigned to these three points using a trigonometric technique (see Fig. 1.9 and see Cantwell et al. (2014a) for equations). An advantage of triangulation is that a large number of CV vectors can be assigned to the data, giving a measure of local CV, which can be used for localised correlation with other functional and structural measures (Ali et al., 2014). However, this method may be more sensitive to errors in local activation time assignment because only three points are included in each vector calculation. This method has recently been automated by Cantwell et al. (2014a).

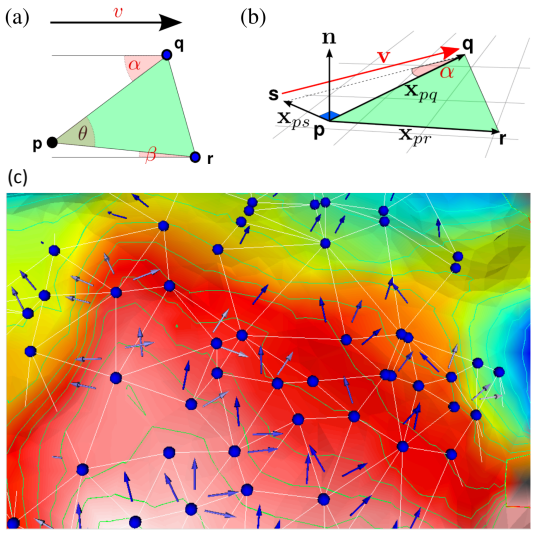

Figure 1.9: Conduction velocity calculation using triangulation. Figure reproduced from Cantwell et al. (2014a).

1.12.2 Finite difference

Optical mapping data, multi electrode data, and simulated data that have been solved using a finite difference numerical technique are often arranged on a regular grid. As such, finite difference techniques, which calculate derivatives at grid points using a stencil, are applicable. A vector is calculated for each point on the grid by considering the activation time of the point and its four neighbours, as in Salama et al. (1994).

Using a standard first-order finite-difference stencil (see Fig. 1.10 A), the horizontal component of the gradient of activation is:

$$\mathbf{G}_x = \frac{1}{2}\left[\frac{t_{i+1,j} - t_{i,j}}{d} + \frac{t_{i,j} - t_{i-1,j}}{d}\right]\mathbf{i} = \frac{t_{i+1,j} - t_{i-1,j}}{2d}\mathbf{i}, \tag{1.2}$$

similarly the vertical component is

$$\mathbf{G}_y = \frac{t_{i,j+1} - t_{i,j-1}}{2d}\mathbf{j}. \tag{1.3}$$

The conduction speed $|\mathbf{u}|$ is then

$$|\mathbf{u}| = \frac{1}{|\mathbf{G}_A|} = \frac{1}{\sqrt{\mathbf{G}_x^2 + \mathbf{G}_y^2}}, \tag{1.4}$$

and the unit vector in the direction of activation, $\hat{\mathbf{n}}$ is

$$\hat{\mathbf{n}} = \mathbf{i}\frac{\mathbf{G}_x}{\sqrt{\mathbf{G}_x^2 + \mathbf{G}_y^2}} + \mathbf{j}\frac{\mathbf{G}_y}{\sqrt{\mathbf{G}_x^2 + \mathbf{G}_y^2}}, \tag{1.5}$$

leading to a velocity of

$$\mathbf{u} = |\mathbf{u}|\,\hat{\mathbf{n}} = \mathbf{i}\frac{\mathbf{G}_x}{\mathbf{G}_x^2 + \mathbf{G}_y^2} + \mathbf{j}\frac{\mathbf{G}_y}{\mathbf{G}_x^2 + \mathbf{G}_y^2}. \tag{1.6}$$

An example of this technique applied to optical mapping data is shown in Fig. 1.10. Similar to triangulation, the finite difference technique has the advantage that it can be used to assess local heterogeneity of CV, and has the disadvantage that it is sensitive to errors in activation time assignment.

1.12.3 Smoothed finite difference

One method for reducing the effects of localised noise in activation time is to smooth the velocity field. For example, Laughner et al. (2012) applied a Gaussian filter for smoothing CV vectors from optical mapping data. Paskaranandavadivel et al. (2012)

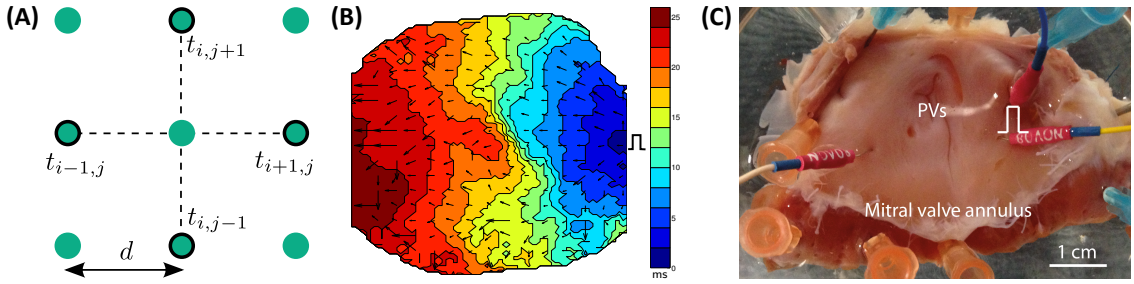

Figure 1.10: Conduction velocity calculation using finite difference techniques. (A) Finite-difference stencil (from Cantwell et al. (2015b)); (B) Isochronal map with CV arrows overlaid; (C) Canine optical mapping preparation used for the analysis (also see Chapters 4, 5 for analysis of data from this experimental preparation).

also smoothed the velocity field V_x, V_y, calculated using a finite difference technique with missing points filled in using inverse distance squared interpolation, again using a Gaussian filter.

1.12.4 Polynomial surface fitting algorithms

Polynomial surface fitting algorithms determine CV vector fields by fitting one or more polynomial surfaces $T_k(\mathbf{x})$ to subsets of space-time coordinates $(\mathbf{x}, t)$, where $\mathbf{x}$ is the electrode position, t is the wavefront activation time and k is the order of the polynomial surface. These techniques have been applied to two- and three-dimensional data, with a linear, quadratic or cubic polynomial surface.

Bayly et al. (1998a) initially developed this technique for determining velocity vector fields of high density unipolar electrogram data in two-dimensions, for which CV vectors were calculated from the quadratic polynomial surfaces. Unipolar electrograms were defined to be *active* at time t_i if they satisfy $\frac{\mathrm{d}V}{\mathrm{d}t} < -0.5$ V/s. For a given time t_i, wavefronts were defined as being at active locations where there had been no activity in the preceding 40ms. A wavefront is selected within windows $\Delta x_{\max}$, $\Delta y_{\max}$, $\Delta t_{\max}$ and fit to the following Equation:

$$T(x, y) = ax^2 + by^2 + cxy + dx + ey + f. \tag{1.7}$$

For the resolution and wavelength of data in the study conducted by Bayly et al. (1998a), $\Delta x_{\max} = \Delta y_{\max} = 4$mm and $\Delta t_{\max} = 16$ms were used. However this is specific to the resolution of data and wavelength of the activation wavefronts.

This quadratic fit requires at least six measuring points, and Bayly et al. (1998a) found that twenty points were usually required for a good least squares fit.

The velocity vector is then:

$$\frac{\mathrm{d}x}{\mathrm{d}t} = \frac{T_x}{T_x^2 + T_y^2}, \tag{1.8}$$

$$\frac{\mathrm{d}y}{\mathrm{d}t} = \frac{T_y}{T_x^2 + T_y^2}. \tag{1.9}$$

Three dimensional extension

Barnette et al. (2000) extended and generalised this technique to work in three-dimensions, and applied the method to sinus rhythm and paced plunge needle unipolar electrograms in canine myocardium. In this case, a least squares technique was used to fit subsets of data from a given wavefront, within spatial and temporal windows, to the following equation:

$$T(x, y, z) = ax^2 + by^2 + cz^2 + dxy + exz + fyz + gx + hy + iz + j. \tag{1.10}$$

For data containing noise, at least twenty points should be used to fit the ten coefficients. In particular, if data points are linearly dependent, more recordings are required for the fit. The velocity vectors are then:

$$\frac{\mathrm{d}x}{\mathrm{d}t} = \frac{T_x}{T_x^2 + T_y^2 + T_z^2}, \tag{1.11}$$

$$\frac{\mathrm{d}y}{\mathrm{d}t} = \frac{T_y}{T_x^2 + T_y^2 + T_z^2}, \tag{1.12}$$

$$\frac{\mathrm{d}z}{\mathrm{d}t} = \frac{T_z}{T_x^2 + T_y^2 + T_z^2}. \tag{1.13}$$

Barnette et al. (2000) found that their method was reasonably accurate for simulated data, however some sinus rhythm and paced rhythms were found to be too complex for the technique. A limitation of polynomial surface fitting algorithms is that the resolution and number of data points required to apply these methods often exceeds what is available. This is particularly true for curved wavefronts or those with short wavelength features.

Comparing linear, quadratic and cubic fits

Krüger (2012) compared both a cubic and a linear fit to the quadratic fit suggested by Barnette et al. (2000); that is:

$$T(x,y,z) = ax^3 + by^3 + cz^3 + dx^2y + ex^2z + fy^2x + gy^2z + hz^2x + iz^2y + jxyz + kx^2 + ly^2 + mz^2 + nxy + oxz + pyz + qx + ry + sz + u, \quad (1.14)$$

and

$$T(x,y,z) = ax + by + cz + d. \quad (1.15)$$

The cubic fit (Equation 1.14) has twenty unknowns, while the linear (Equation 1.15) has four (compared to ten for the quadratic fit, Equation 1.10). In particular, Krüger (2012) found that the linear fit gave a more detailed CV field close to the borders of the domain, but it sometimes gave erroneous results, while there was little difference between the quadratic and cubic fits. The cubic fit may give a more accurate measure of CV for complex activation patterns (for example wavefronts with multiple bends) where the curvature cannot be captured by the quadratic fit; however, it requires more data points. All three fits were found to underestimate curvature, and the linear fit also resulted in some incorrect speeds. Hence the most accurate fit will depend on the curvature, wavelength and spatial resolution of data.

Linear fits for small datasets

For a high resolution of data, it is possible to have an overdetermined system (more recordings than parameters to fit: four, ten or twenty for linear, quadratic or cubic 3D fits respectively) resulting in an accurate estimate of CV; however, clinically this resolution is often not available. Fitzgerald et al. (2001) considered how to estimate CV from small datasets of between four and seven electrograms and compared these estimates to the CV calculated using a higher resolution of data. The Bayly et al. (1998a) method was adapted to provide the high resolution CV, using a quadratic fit to time delays for measurements from the full resolution dataset. For points $(x_1, y_1, T_1), (x_2, y_2, T_2)$, the polynomial surface is as follows:

$$T_2 - T_1 = a(x_2^2 - x_1^2) + b(y_2^2 - y_1^2) + c(x_2y_2 - x_1y_1) + d(x_2 - x_1) + e(y_2 - y_1). \quad (1.16)$$

Subsets of between four and seven electrograms were chosen to lie on a 2.5mm diameter circle. Using only four to seven electrograms, it is not possible to fit to a model with curvature; hence the points were fit to a plane wave:

$$T_2 - T_1 = a(x_2 - x_1) + b(y_2 - y_1). \quad (1.17)$$

Parametric version to incorporate surface curvature

For whole heart optical mapping data, the curvature of the heart surface is also an important consideration when calculating CV. Sung et al. (2000) performed optical mapping of rabbit hearts and calculated the CV on each reconstructed geometry by developing a parametric version of the Bayly et al. (1998a) method, where activation times were written as a function of the local finite element co-ordinates of the heart geometry. This gives a more accurate measure of distance compared to if the recording points were projected onto the (x, y) plane of best fit, which leads to some distortion in distance. The study also showed that activation times measured optically showed close agreement with times from bipolar electrograms. Parametric mapping techniques are not widely available (Laughner et al., 2012).

Advantages and disadvantages of the method

Polynomial surface algorithms have the advantages that they are robust to outliers; they do not require regularly spaced data, whereas, finite difference requires a regular grid; and it is possible to use the residual to assess the quality of the fit. In addition, the approach is smoothing in the case that the system is overdetermined. Disadvantages are that the method may require more points than are available and it can be difficult to define a suitable time and space window for analysis.

Comparison of regular finite difference, smoothed finite difference and polynomial surface fitting

Paskaranandavadivel et al. (2012) compared regular finite difference, smoothed finite difference and the Bayly et al. (1998a) method, in the context of gastric slow wave propagation, and concluded that smoothed finite difference gave the most accurate results.

1.12.5 Cosine-fit techniques

Weber et al. (2010) developed an automated technique for estimating the speed and direction of a planar wavefront from a multipolar circular mapping catheter. Due to the low density and number of data points available, this technique was developed to detect a single macroscopic wavefront only. It was initially tested on simulated data with artificial noise and then applied to clinical data to see whether the method could distinguish activity from the four pulmonary veins. Activation times were determined using the non-linear energy operator technique discussed in

Section 1.11.3. For a planar wave intersecting a circle of recording points, it can be shown that the activation times satisfy:

$$t(n) = t_c - A\cos\left[\phi(n) - \phi_0\right], \tag{1.18}$$

where t_c is the centre activation time; $\phi(n)$ is the angle of electrode n; A is the wave amplitude; and ϕ_0 is the angle of earliest activation. Assuming a constant offset between recording electrodes, γ, the activation times can be fit to the following:

$$t(n) = t_c - A\cos\left[\gamma \cdot (n-1) - \phi_0\right]. \tag{1.19}$$

Initial values can be estimated from the data and then a least squares fit is performed to find the unknown parameters t_c, A, ϕ_0, γ. The CV is then r/A, where r is the radius of the recording electrode.

Thirty-six different pacing positions were tested in the simulated set-up, and the effects of random errors in the form of Gaussian noise applied to the activation times and the angle between electrodes were evaluated (Weber et al., 2010). The error in angle increased with increasing noise, but was less than 10° for all of the cases tested. To evaluate how curvature affected the fit, CV was calculated for a simulated stimuli 25mm and 50mm from the recording catheter, where it was observed that the average directional error only increased by 1.5° for the closer stimulus. In the clinical set-up, the initial guess for γ was calculated from the electroanatomic mapping electrode positions, which were projected onto the plane of best fit. For the clinical activation time fits, the residuals were an order of magnitude larger than the simulated data.

The main limitation of the method is that it assumes a single wavefront is under the catheter; thus the method does not work for two colliding wavefronts, where in this case a large residual would indicate a poor fit. In addition, for a spiral wavefront the estimated angle of incidence may not align with the spiral core, which may also be true for a focal source if the conduction is anisotropic. A minor limitation is that the angle of incidence is measured relative to the catheter.

This method was applied to investigate human conduction velocity restitution properties using a circular multipolar catheter. Weber et al. (2011) found that the method is robust to a small degree of curvature in the wavefront, and so it is appropriate when the pacing is a distance from the catheter.

This technique was applied to clinical circular catheter data during both sinus rhythm and paced rhythms to compare clinical data to patient specific simulated data by Burdumy et al. (2012). One limitation of the cosine-fit technique is that it assumes data are on a circular catheter; the authors point out that it would be

useful to extend the technique for use with other catheter arrangements, such as a spiral or five-spline PentaRay, which are commonly used clinically.

1.12.6 Time delay analysis

Dubois et al. (2012) proposed two methods for creating activation maps from clinically acquired global electrogram data. The first performs a least squares fit to all of the time delays to find the activation times (for the system $T_j - T_i = \tau_{ij}$); as such it is global. The second assumes that activation can be approximated as a plane wave locally in a homogeneous medium and a least squares fit is performed to find the local activation vectors from the time delays between neighbouring electrodes. A similar technique has been applied to optical mapping data (Walton et al., 2013).

1.12.7 Ensemble vector directional analysis

Another method for assigning activation direction is by plotting a vector loop for two orthogonal bipoles (Kadish et al., 1986, 2003). The orientation of this vector loop gives the activation direction. Kadish et al. (1986) compared the activation directions resulting from the vector loop at single measuring sites to isochronal maps and showed a good agreement. In a later study, an electrode plaque of 112 electrodes was used to investigate the consistency of direction in AF by using vector loops to assign normalised activation vectors, and then defining an ensemble vector index as a measure of direction variability (Kadish et al., 2003).

Schoenwald et al. (1994) created vector loops to find activation directions in three-dimensions using six unipolar signals to create three orthogonal bipoles. This extension of the 2D method of Kadish et al. (1986) was used to investigate non-random behaviour in 15 minute recordings of AF (Schoenwald et al., 1998).

Horner et al. (1997) developed a catheter consisting of three recording electrodes in an equilateral triangle, with a central reference electrode, to measure three monophasic action potential recordings from which CV and repolarisation could be investigated simultaneously.

1.12.8 Radial basis function interpolation

Radial basis functions (RBF) provide a technique for interpolating local activation times across the endocardial surface, and this interpolation can be assessed to detect activation patterns, including wavefront collision. This technique has the advantage that it does not require as high a resolution of data as the surface fitting algorithms; for example, Masè et al. (2009) used it to calculate the CV field for a single PentaRay

catheter. Masé and Ravelli (2010) applied radial basis function interpolation to find activation times for any point on the atrial surface using a global LAT map. The function has the constraint that it should equal the known activation times at the clinical data points p:

$$T(x_p, y_p, z_p) = LAT_p \quad \text{for} \;\; 1 \leq p \leq N, \tag{1.20}$$

and the interpolation function is:

$$T(x, y, z) = \sum_{i=1}^{N} \alpha_i R_i \left(\|\mathbf{X} - \mathbf{X_p}\| \right) + \sum_{j=1}^{M} \beta_j \phi_j(x, y, z). \tag{1.21}$$

Here the R_i are the radial basis functions which depend only on the Euclidean distance between the point and the measuring points and ϕ_j are the polynomials. α_j and β_j are found by applying the constraint in Equation 1.20 and by enforcing that the basis functions are orthogonal. Since $T(x, y, z)$ is analytic, the velocity is found as before using Equations 1.11, 1.12 and 1.13. This method has the advantage that it makes no assumptions on the arrangement and spacing of the recording points. It also enables the calculation of a high resolution velocity field that can be used to examine properties such as the divergence and curl of the field (Masè et al., 2009).

Comparing radial basis function interpolation and cosine-fit methods

Weber (2011) used RBF interpolation to detect wavefront collision under a circular catheter, which could not be resolved using the cosine-fit technique. Weber (2011) showed that the RBF method has the advantage that it can be used for any shape of catheter, since it works for sparse irregularly spaced points; whereas, the cosine-fit technique of Weber et al. (2010) can only be used for a circular catheter. One additional factor to consider is the distortion in catheter shape seen when the measured electrogram positions are projected onto a plane; this may lead to incorrect distances and a change in CV estimate. Thus in some cases it may be more accurate to model the catheter as for example a perfect circle (Burdumy et al., 2012).

1.12.9 Isopotential line techniques

Kay and Gray (2005) developed a technique to estimate CV by considering the distance travelled by an isopotential line in a voltage map over a fixed time interval. For each time instant, isopotential nodes for a chosen potential were located and joined using a parametric spline. Calculation of the distance travelled in the direction

normal to the isopotential line over a fixed time window gives the CV at a particular point. The normal vector is calculated analytically from the equation for the spline. This technique requires a higher resolution of data than is clinically available, and is used on transmembrane potential data, limiting it to simulated or optical mapping data.

1.12.10 Analysis of arbitrary scalar fields

Mourad and Nash (2007) generalised the isopotential line technique to work for any scalar field for which a constant value can be used to define wavefronts. Examples of such fields include phase and detrended voltage. CV calculated using these fields was shown to be equivalent to that calculated from activation times.

1.12.11 Analytic expressions

Mazeh et al. (2013) derived equations to find the wavefront speed, direction and radius of curvature from activation times at just four or five sites. This method is much simpler than polynomial surface fitting methods and was applied to simulated data. Their method assumes that the radius of curvature is large enough that the wavefront can be approximated locally as circular.

1.12.12 Vector field analysis

The features of local normalised CV vector fields can be analysed by applying vector calculus operations. The divergence of the two-dimensional CV vector field,

$$\nabla \cdot \mathbf{v} = \frac{\partial v_x}{\partial x} + \frac{\partial v_y}{\partial y},$$

can be used to distinguish between focal sources and areas of collision, where normalisation ensures only the direction of the vectors influences the divergence. At a source, all of the conduction velocity vectors point outwards resulting in a positive divergence; at a sink or area of collision, the divergence will be negative.

The curl of a two-dimensional CV vector field is

$$\nabla \times \mathbf{v} = \left(\frac{\partial v_y}{\partial x} - \frac{\partial v_x}{\partial y} \right),$$

where positive curl indicates counterclockwise rotation and negative curl indicates clockwise rotation.

The divergence and curl operators have been applied to CV vector fields from simulated data (Rousakov et al., 1999; Masè et al., 2009), canine epicardial electrograms (Fitzgerald et al., 2005) and human atrial local activation time maps (Fitzgerald et al., 2005). These operators require a regular grid of CV vectors, which can be obtained from irregularly arranged data in several ways. Radial basis function interpolation (Section 1.12.8) can be applied to the activation times, followed by finite difference methods (Weber et al., 2011) (Section 1.12.2) or polynomial surface fitting methods (Masè et al., 2009) (Section 1.12.4) to calculate the CV vectors. Fitzgerald et al. (2005) calculated the divergence of human atrial LAT data from the electroanatomic system Carto by fitting the electrogram positions to an ellipsoid, projecting onto a two-dimensional plane, spatially interpolating the LATs and finally using a linear polynomial fit to the data (Fitzgerald et al., 2001). In order to accurately locate ectopic foci, spatial resolution can be improved by Delaunay triangulation and cubic interpolation (Fitzgerald et al., 2005). In addition, the use of the Radon transform has been suggested to allow more accurate localisation of areas of high divergence (Weber et al., 2011). Ectopic foci have been successfully identified using divergence maxima, providing that the CV vectors surround the foci (Fitzgerald et al., 2005; Masè et al., 2009; Weber et al., 2011). Uniform spacing is not required and this technique has been applied to simulated data and high-density circular, spiral and five-spline PentaRay mapping catheters (Masè et al., 2009; Weber et al., 2011). For human clinical data, divergence was low in areas of collisions (which were confirmed by double potentials on the electrograms), but curl did not indicate any central obstacles in reentrant circuits (Fitzgerald et al., 2005).

1.12.13 Choice of method for calculating conduction velocity

The most appropriate technique to use for assigning activation time and calculating CV depends on the data modality, data resolution and underlying rhythm. The following Table 1.1 summarises the advantages and disadvantages of different conduction velocity methods, as well as their requirements in terms of input data.

The optimal choice of algorithm depends on a balance between the CV vector field resolution required and the required accuracy. For example, triangulation will provide a localised measurement appropriate for localised correlation with functional and structural measures, such as fibrosis (Ali et al., 2014); however, estimates are only based on three times and so are susceptible to error. On the other hand, cosine-fit techniques provide a CV estimate that is based on more measurements and so is less susceptible to errors in the activation times; however, it only provides one

vector per catheter.

The expressions for the CV vector are the same for the finite difference technique (Equations 1.6) and for polynomial surface fitting (Equations 1.8, 1.9). However, in the case of polynomial surface fitting, these gradients are evaluated analytically on the surface, allowing evaluation at any point to be performed easily. In the case that there are more data points than parameters for the fit, the polynomial surface fitting is also noise smoothing and so may result in a different CV vector to the corresponding vector from the finite difference technique.

It is worth noting that cardiac wavefront propagation is a three-dimensional wave in most tissues; however, most measuring modalities allow surface measurement only. As such, conduction velocity estimates for wavefronts that are not tangential to the surface of measurement may be inaccurate. This is a particular problem at wavefront breakthrough locations – for example, at Purkinje-myocardial junctions during regular rhythms, or in the atria during AF – for which many techniques may overestimate conduction velocity. This is a limitation inherent to the recording modality and not necessarily to the conduction velocity methodology; several algorithms can be extended to work with three-dimensional measurements (Barnette et al., 2000).

Table 1.1: List of conduction velocity estimation techniques detailing their advantages, disadvantages, data suitabilities and requirements.

Method	Advantages	Disadvantages	*Suitability* & Requirements
Triangulation. Horner et al. (1997); Kojodjojo et al. (2006); Ravelli et al. (2011); Sawa et al. (2008); Cantwell et al. (2014a)	Local score, Examine regional heterogeneities, Any arrangement of points, Uses actual LATs.	Sensitive to error in LAT, Difficult to automate.	*Clinical* $3 \geq d \geq 20$mm, LAT differences $>$ 3ms.
Finite difference. Salama et al. (1994); Laughner et al. (2012)	Local score, Examine regional heterogeneities, Easy to implement, Uses actual LATs.	Sensitive to noise / missing data, Fails if times are identical, Requires regular grid.	*Optical mapping* *Multielectrode arrays* 4 points, Sufficient temporal resolution to avoid adjacent equal activation times.
Polynomial Surface. Bayly et al. (1998a); Barnette et al. (2000); Fitzgerald et al. (2001); Sung et al. (2000); Laughner et al. (2012)	Any arrangement of points, Robust to noise, Allows missing data points, Residual to assess quality of fit.	May require more points than available, Requires choice of $\Delta X, \Delta T$.	*Optical mapping* *Multielectrode arrays* 3D: linear (4 points), quadratic (10 points), cubic (20 points), More points needed for complicated rhythms.
Cosine-fit. Weber et al. (2010, 2011); Burdumy et al. (2012); Roney et al. (2014a)	Measure of curvature and distance to focal source, Any arrangement of points, Robust to noise, Residual to assess quality of fit.	Single macroscopic wavefront only, No collision, One vector per catheter.	*Clinical* 10 points.
Vector loops. Kadish et al. (1986, 2003); Schoenwald et al. (1994)	Does not require LAT assignment.	Requires specific catheter.	*Clinical* 2 orthogonal pairs of bipoles.
Radial Basis. Masè et al. (2009); Masé and Ravelli (2010)	Multiple wavefronts, Use to find LATs anywhere on surface, No assumption on arrangement and spacing, High resolution velocity field (div, curl).	Computationally demanding.	*Clinical* Any arrangement.
Isopotential lines. Kay and Gray (2005)	Accurate wavefront curvature estimation, Robust to spatial noise.	Requires measurement of membrane potential, Requires high resolution, LATs do not always coincide with isopotential lines.	*Optical Mapping* High resolution.
Arbitrary scalar fields. Mourad and Nash (2007)	Extends CV calculation from isopotential lines to use other variables	Requires measurement of another scalar field	Scalar field (e.g. activation time, electrical potential, phase).
Time delays. Dubois et al. (2012)	Uses neighbouring location information, Can deal with incorrect LATs, Local score, Any arrangement of points.	Assumption of plane wave locally.	*Clinical*
Analytic expressions. Mazeh et al. (2013)	Velocity and curvature from 4/5 points, Low density data, Simple to apply.	Points must lie on a square, Radius of curvature must be large, Requires accurate LATs.	*Optical mapping* *Multielectrode arrays* Points on a square.

1.13 Rotor tracking

1.13.1 Motivation and overview

Spiral waves are ubiquitous in nature and excitable media; for example, occurring in chemical reactions (e.g. Belousov-Zhabotinsky), morphogenesis of amoeba (Pálsson and Cox, 1996), mitochondrial calcium waves in frog eggs (Falcke et al., 1999) and chicken retina (Yu et al., 2012). Spiral waves are also known to play a role in cardiac arrhythmias including VF. Recent clinical studies have suggested that spiral waves, also known as electrical *rotors*, may be important in sustaining AF (Narayan et al., 2012d). Assessing the location and stability of rotors can help the targeting of ablation therapy for AF.

1.13.2 Phase mapping background

Despite fibrillation being a seemingly random process, Gray et al. (1998) developed a technique to analyse fibrillatory signals to translate periodicity in the signals into loops in a two variable state space that represents the system. The phase angle is then measured as the angle around this trajectory for each point in the domain, and a spatial singularity in phase then corresponds to the centre of a rotating wave. This landmark paper revealed a degree of spatiotemporal organisation in fibrillation and the technique used to reveal this organisation is one method that can be used to locate the tip of spiral waves and analyse their dynamics.

Transmembrane potential does not uniquely define the state of the tissue

One motivation for the state space technique is that at a fixed time point the transmembrane potential does not uniquely define the state of the tissue, because a particular voltage could refer to either depolarisation or repolarisation. Computationally, we can consider the system to be multidimensional, consisting of the transmembrane potential and the gating variables for the various ion channels of the action potential model. During fibrillation, the multidimensional state space collapses so that a realistic representation of the system is attained using only two dimensions and the state of a cell can be uniquely defined in terms of these two dimensions (Efimov et al., 2004). Following the trajectory in state space then gives a unique time course for the action potential.

Two-dimensional state spaces

For cardiac cell models that use two state variables only (for example the Aliev and Panfilov (1996) model), the state space representation of the action potential is found by plotting one variable against the other (in which typically one of the variables is a fast variable representing excitability and the other is a slow variable representing recovery). Iyer and Gray (2001) considered the Bär and Eiswirth (1993) two variable model and these two variables completely define the state space.

Phase angle definition

To parameterise the position on the state space trajectory, a phase angle is defined as the angle from a prescribed origin to the position on the trajectory at that time point. This then identifies the state of the tissue, and thus the spatial and temporal dynamics of the signal propagation can be studied using the phase angle variable. The phase angle can be calculated at every point in the tissue at any time, $\theta(x, y, z, t)$. The phase is a continuous and periodic function. For a two-variable model with excitability variable e and recovery variable g, for example, the FitzHugh-Nagumo model (shown in Figure 1.11) the phase angle for a particular point is given by:

$$\theta(t) = \text{arctan2}[g(t) - g^*, e(t) - e^*], \tag{1.22}$$

where (e^*, g^*) is the origin and arctan2 is the four-quadrant inverse tangent, giving $\theta \in (-\pi, \pi]$ depending on the signs of x and y.

Other topologically equivalent state spaces

Most cardiac models are multidimensional, containing many gating variables and there is no immediate choice for the slow and fast variable to plot the state space. Similarly, experimentally and clinically the true state space is not available since typically only voltage is measured. Thus it is necessary to process the voltage to attain a suitable second variable. The simplest two variables to consider for the state space are either the voltage and first derivative of the voltage, or the voltage and a time shifted voltage. It can be shown that both of these state spaces are topologically equivalent to the true state space, as would be defined by a two variable system (Takens, 1981; Packard et al., 1980).

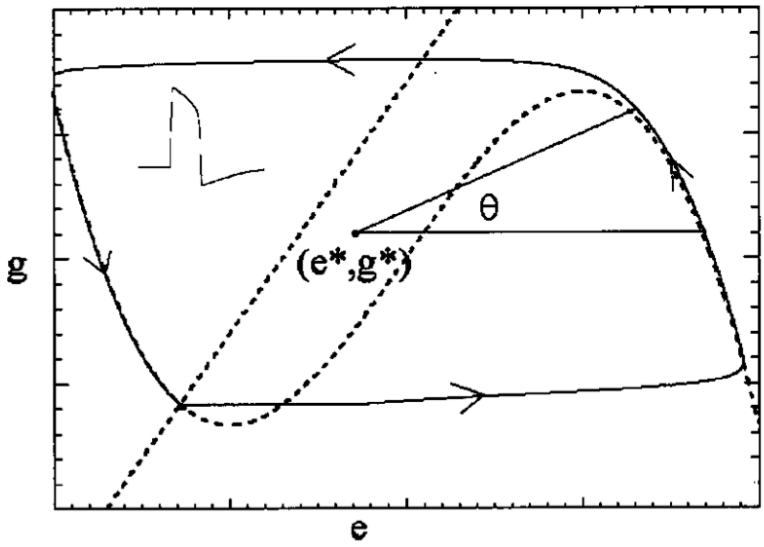

Figure 1.11: Two variable FitzHugh state space from Iyer and Gray (2001). True state space diagram for the two variable FitzHugh model (Fitzhugh, 1961). The dotted lines are the nullclines, representing no change in the excitability variable e and recovery variable g respectively with time, while the solid line shows the trajectory traced during the action potential. The system will stay at the steady state value until a suprathreshold stimulus is applied to perturb the system – the excitable system then undergoes a large excursion representing the action potential. The angle θ is the phase angle, measured from the origin point (e^*, g^*) to the point on the trajectory. This angle gives a unique representation over the action potential time course.

Using time shifted fluorescence as the second variable in optical mapping experiments

In the first paper to explore these techniques, Gray et al. (1998) plotted the fluorescence signal $F(t)$ from optical mapping experiments against the time shifted signal $F(t+\tau)$ to reveal attractors in this state space (Fig. 1.12). Action potentials manifest as loops in the state space, revealing each activation. As well as giving a unique location for each point in the action potential, these techniques have the additional advantage that the great variability in action potential duration and duration between activations in fibrillation does not affect the state space map. Each action potential is seen as a 2π loop, and subthreshold stimuli do not result in loops in the state space, so long as the time shift τ and origin of the phase map are chosen correctly. In this case, the phase angle is defined as:

$$\theta(t) = \arctan2[F(t-\tau) - F_{\text{mean}}, F(t) - F_{\text{mean}}]. \tag{1.23}$$

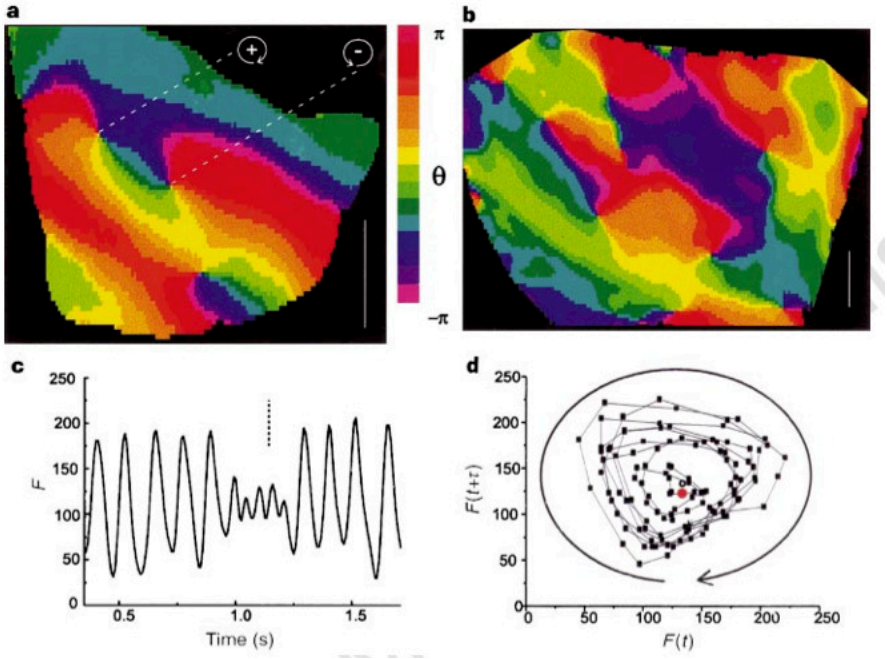

Figure 1.12: Phase of optical mapping fluorescence from Gray et al. (1998). (a) Phase from rabbit with two phase singularities marked, and (b) phase from sheep. (c) Fluorescence signal and (d) state space. The low amplitude area is found close to the centre of the state space (dashed line in (c) and red dot in (d)). From Gray et al. (1998)

Choosing the correct time shift for the second variable

One disadvantage of using the time shifted signal is the difficulty associated with choosing the correct time shift. Ideally the time shift should be chosen such that the signals are as close to independent as possible (Brown et al., 1993). However, Iyer and Gray (2001) showed that choosing an embedded time delay value such that the autocorrelation between the signals is zero leads to overlapping state space trajectories and non-uniqueness. On the other hand, if τ is too small, the signals will be too similar ($V(t) \approx V(t+\tau)$), and this results in trajectories fixed along a diagonal in the state space. Thus Iyer and Gray (2001) chose to use a time shift of 2ms, which is the time of the upstroke in their model, because this is the greatest time shift for which the phase loops do not overlap. Gray and Jalife (2001) showed that phase loops overlap for time shifts greater than the action potential upstroke. Phase loops are stretched for large values of τ. In addition, the optimal choice of τ may change during fibrillation.

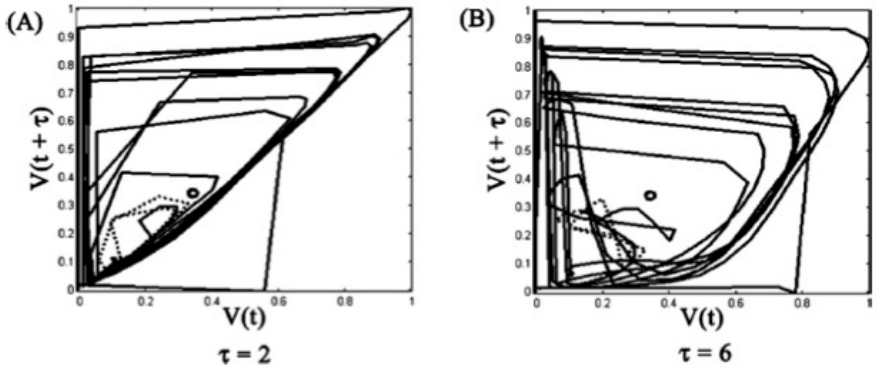

Figure 1.13: Diagram to illustrate poor choice of time shift for state space mapping, from Bray and Wikswo (2002a). (a) Trajectory mainly along the diagonal as τ is too small; (b) trajectory stretched and deformed as τ is too large.

Using the first derivative of fluorescence for the second variable

Using the first derivative of fluorescence (or voltage) as the second variable in optical mapping experiments does not have the difficulty associated with picking the correct time shift; however, it has the limitation that the first derivative is sensitive to noise (Rosenbaum and Jalife, 2001). Tissue depolarisation corresponds to $\frac{\mathrm{d}F}{\mathrm{d}t} > 0$, while repolarisation corresponds to $\frac{\mathrm{d}F}{\mathrm{d}t} < 0$.

Challenge of ensuring the state space trajectories circle the origin

Another potential issue is trajectories not encircling the origin if the signal amplitude is below the chosen threshold – this leads to an incorrect parametrisation for the position on the trajectory. Action potentials close to the rotor tip on the tissue will have smaller amplitudes and so result in small phase loops in the state space; therefore, it is important to define the origin such that these trajectories still encircle the origin, to ensure that the phase angle can be calculated correctly. Different approaches have been employed to pick a suitable origin. This is a particular problem when the spiral meanders.

Hence there are two main challenges for phase mapping. The first is the choice of signal to plot against the voltage signal; in particular the choice should give complete phase loops; the second is applying appropriate pre-processing techniques to ensure that all trajectories encircle the origin of the state space.

1.13.3 Phase mapping: choice of zero mean signal

There are many approaches in the literature for addressing these two challenges, with different choices of second variable to plot against the voltage, and several published methods for generating a phase plot with a stable centre. Rogers (2004) suggest the use of the integral of the voltage as the second function for the state space plot, with the justification that integration reduces noise and so is a preferred choice of variable compared to the differential. In order to ensure that the phase plot has a stable centre location, the mean voltage over each action potential should be zero, which requires a pre-processing step. Activations within the signal were identified by tagging peaks of $\frac{\mathrm{d}V}{\mathrm{d}t}$ using a moving window of length 80ms. These activation points were then joined using a piecewise linear curve and this was then removed from the voltage, resulting in a signal of zero at activation times with action potentials centred around zero. This step is called *linear detrending*. The integral of this zero mean signal was then plotted against the zero mean signal to give trajectories, where the angle around the trajectory was the phase angle.

Nash et al. (2006) adapted the linear detrending step of Rogers (2004) to include a quadratic term, in order to ensure that the resulting signal had a mean of zero when applied to unipolar electrograms. This step ensured the voltage was zero at the unipolar electrogram activation times, which were defined using the conventional minimum $\frac{\mathrm{d}V}{\mathrm{d}t}$. The application of the Hilbert Transform to this signal resulted in a suitable second signal for the phase plane plot.

1.13.4 Phase mapping: empirical mode decomposition

The Hilbert-Huang method combines an empirical mode decomposition technique that produces a zero-mean signal (in order to achieve a stable centre for the trajectories), with the application of the Hilbert Transform of this signal to give a suitable second signal for the phase plane plot (Huang et al., 1996). The empirical mode decomposition breaks down the signal into a series of functions, known as intrinsic mode functions. This step is performed by identifying all maxima and minima in the signal, joining the maxima using a cubic spline (the *upper envelope*) and joining the minima using a cubic spline (the *lower envelope*). The maxima and minima lines are averaged to give a mean for the signal, which is then subtracted from the signal. This resulting signal is then checked to see if it satisfies the properties of intrinsic mode functions, which are that the number of extrema and the number of times the function crosses zero should differ by at most one and that the mean of the upper and lower envelopes should be zero everywhere in the signal (symmetry about zero). If these properties are satisfied, the signal is an intrinsic mode function; if not, the steps are repeated in a process called *sifting* until a stoppage criterion is reached. The intrinsic mode functions give a basis for the signal, where each represents an oscillation frequency within the data, and the Hilbert transform is applied successfully to each intrinsic mode function, since each is symmetric about zero.

Potential disadvantages of the method and suggested modifications

The Hilbert-Huang method overcomes both of the aforementioned challenges in that it generates signals that can be plotted against each other to give proper trajectories in the phase plane that encircle a fixed origin. However, the method treats every oscillation in the data as important, which is not appropriate for cardiac action potential data (Bray and Wikswo, 2002a), where small changes in voltage that do not correspond to action potentials may not warrant a full trajectory in the phase plane. For cardiac data, it is necessary to decide which oscillations within the data are physiologically relevant and so should be assigned a full change in phase. To achieve this, Bray and Wikswo (2002a) suggest performing a pseudo-empirical mode decomposition; maxima and minima are tagged using a moving window of a length equal to half of the average cycle length, with the motivation of including double potentials that may occur during reentry in the phase plane. The maxima and minima are then joined using cubic splines, and then the mean of these lines is removed from the signal to produce a zero mean signal. Thus the first step of the empirical mode decomposition is performed, but the algorithm stops at this stage. The choice of window length determines which fluctuations in the action potential

data are present in the phase.

1.13.5 Rotor tip identification: phase singularity identification

A *rotor* is defined as the organising source of functional reentrant activity, and the wave of excitation emitted by the rotor is a *spiral wave* in 2D, or a *scroll wave* in 3D (Pandit and Jalife, 2013). Phase singularities (PSs) are locations where the phase is considered arbitrary or undefined, and the phase changes by 2π as the point is circled around in either the anticlockwise or clockwise direction. Typically the wavefront rotates around a phase singularity. Mathematically, a phase singularity is defined at a site where the line integral of the gradient of the phase around a closed contour around that location is $\pm 2\pi$. If this line integral is performed along any contour not containing a phase singularity, the integral will be 0. So the line integral quantity is as follows:

$$\oint_c \nabla\theta \cdot \mathrm{d}\mathbf{r} = \begin{cases} \pm 2\pi & \text{if PS in C} \\ 0 & \text{if no PS in C.} \end{cases} \tag{1.24}$$

This quantity divided by 2π is defined to be the *topological charge* (Bray and Wikswo, 2002b).

Phase singularities are necessary for rotor formation; however, they are not sufficient since often a phase singularity location will be transient rather than indicating that a wave is rotating around that point.

1.13.6 Rotor tip identification: isopotential line method with zero normal velocity

Fenton and Karma (1998) define the rotor tip as the point where depolarised ($\mathrm{d}V/\mathrm{d}t > 0$) and repolarised tissue ($\mathrm{d}V/\mathrm{d}t < 0$) meet; hence the position of ($\mathrm{d}V/\mathrm{d}t = 0$) where $\mathrm{d}V/\mathrm{d}t$ is measured along a line of fixed voltage (zero normal velocity). This can be thought of as tracing the spiral, by drawing along one isopotential line, and then taking the point on this line where the wavefront and waveback meet at $\mathrm{d}V/\mathrm{d}t = 0$. Thus, for each time point, the position (x, y) is found such that:

$$V(x, y, t) - V_{\text{iso}} = \frac{\mathrm{d}V(x, y, t)}{\mathrm{d}t} = 0, \tag{1.25}$$

for a given potential V_{iso}. It is clear that the spiral centre position will depend on the choice of V_{iso}. However, how much the positions differ between isopotential lines

depends on the choice of ionic model. For phenomenological models in which both the wavefront and waveback are thin boundary layers, such as the FitzHugh Nagumo model, the value of V_{iso} will not have a great effect on the calculated positions (Fenton and Karma, 1998); however for ionic models where the waveback is spread over a larger area, the choice will have a larger effect. Fenton and Karma (1998) show that the wave tip meander pattern is independent of the isopotential line. These techniques can also be used for scroll wave detection (Clayton and Holden, 2002a); for example Clayton and Holden (2003) identified scroll wave filaments for the Fenton-Karma model using an isoptential line of -20mV.

1.13.7 Rotor tip identification: other techniques

Instead of finding the point with zero normal velocity along an isopotential line, the state of neighbouring cells can be used to define a rotor tip. Zhang and Holden (1995) found the point where the wavefront and waveback of an isopotential line met by identifying a cell that had neighbouring cells in four different states – undergoing excitation, excited, refractory and resting – defined according to the sign of $\frac{\mathrm{d}V}{\mathrm{d}t} = 0$ and the value of V. A similar method was used by Biktashev et al. (1994). Beaumont et al. (1998) consider the point of null curvature on an isopotential line (-30mV) to be the position of the spiral wave centre (*spiral tip*). In the case of a two variable system, such as the FitzHugh Nagumo model, spiral tip location can be identified as the intersection of contours of the two variables (Barkley et al., 1990), or as the location of the maximum of the cross-product of two chemical gradients (Jahnke et al., 1989).

1.13.8 Spiral wave trajectories

The location of a spiral tip can be identified over time as a trajectory. A range of spiral tip trajectories are seen in cardiac cell models (Fenton et al., 2002; Cherry and Fenton, 2008) and observed experimentally (Davidenko et al., 1992a; Kim et al., 1997; Wu et al., 1998). These include circular, epicycloidal, cycloidal, hypocyclodial, hyper meandering and linear, where examples are shown in Fig. 1.14. Trajectories in excitable media, such as the Belousov-Zhabotinsky reaction, are often circular, but those observed in cardiac tissue are typically linear (Davidenko et al., 1992b). Efimov et al. (1995) showed that circular trajectories transition via a Hopf bifurcation to meandering trajectories (epicycloidal, cycloidal and then hypocyclodial) and then to linear trajectories, as the sodium conductance of the Beeler-Reuter model was increased. The trajectory observed depends on both the excitability (determined

by sodium dynamics) and wavelength (calcium and potassium dynamics) (Cherry and Fenton, 2008). Simulations of long QT syndrome by modifying conductance of I_{Na}, I_{Kr} and I_{Ks} affected spiral wave trajectories (Clayton et al., 2001). Cell model parameters, the initial conditions of the simulation and the geometry used for the simulation have all been shown to affect the number and lifetimes of three-dimensional rotor trajectories (scroll wave filaments) in simulations of VF (Clayton, 2008).

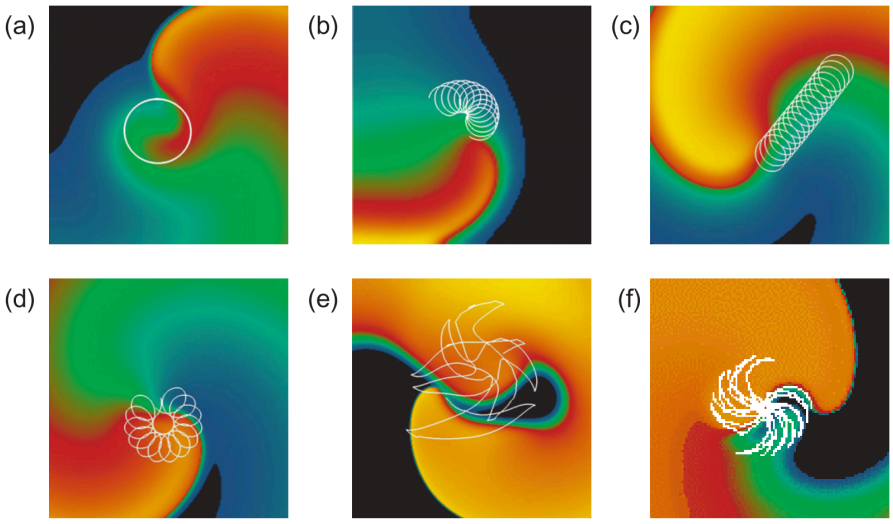

Figure 1.14: Range of spiral tip trajectories exhibited by biophysical cell modes. (a) Circular; (b) epicycloidal; (c) cycloidal; (d) hypocycloidal; (e) hypermeandering; (f) linear; reproduced from Cherry and Fenton (2008).

1.13.9 Phase singularity chirality

The chirality of a phase singularity indicates the sense of rotation, that is clockwise or anti-clockwise. The sign of the topological charge integral, Equation 1.24, indicates the chirality, with a positive integral signifying clockwise rotation, and a negative integral signifying anti-clockwise rotation.

1.13.10 Phase singularity birth and annihilation

Due to topological constraints, activation wavefronts must either be a closed loop, end on a boundary, or end on a phase singularity. In the case that both ends of an activation wavefront are phase singularities, they must be of opposite chirality. In addition, phase singularities are created and destroyed as pairs of opposite chirality.

As such, a pair of phase singularities of opposite chirality will mutually *annihilate* upon collision; a singularity will also terminate if it meets a no flux boundary (Rogers, 2004).

1.13.11 Three-dimensional scroll waves

In three dimensions, waves emitted by rotors are known as scroll waves, where each wave rotates around a filament of phase singularities. These filaments exist in different forms following topological constraints, as either I shaped, leading to phase singularities on both the epicardial and endocardial surface; U shaped, consisting of two phase singularities on one surface and focal activation on the other; or O shaped, which are intramural filaments leading to focal activations on both surfaces (Clayton et al., 2006).

1.13.12 Choice of atrial model and modelling electrical remodelling

Three families of models of human atrial cells have been developed to date: Nygren et al. (1998), Courtemanche et al. (1998) and Grandi et al. (2011). The Grandi et al. (2011) model is based on different experimental data to the Nygren et al. (1998) and Courtemanche et al. (1998) models. The Nygren et al. (1998) model has been extended to include new experimental rate dependence data by Maleckar et al. (2009) and this model was again extended to include atrial-specific characteristics of the sarcoplasmic reticulum by Koivumäki et al. (2011). These models and their chronic AF variants are compared by Wilhelms et al. (2012). Krummen et al. (2012) adapted the Courtemanche et al. (1998) model to produce a better fit to rate dependent data and to model extracellular potassium accumulation during rapid pacing.

The Nygren et al. (1998) and Courtemanche et al. (1998) models have different AP morphology, APD and CV restitution properties, intracellular calcium handling and dynamics in tissue despite being largely based on the same experimental data and containing twelve equivalent transmembrane currents. The models have been compared in detail by Cherry and Evans (2008). Some of the differences between the models may be down to the techniques for modelling intracellular calcium cycling.

Electrical remodelling is known to happen in chronic AF and studies have incorporated some changes in maximum channel conductances to model these effects. In particular, Courtemanche et al. (1999) suggest a decrease in the maximum conductance of I_{to} and I_{Kur} by 50%, while decreasing I_{CaL} by 70%. These changes are included in the model of persistent AF used in this thesis.

Different action potential models exhibit different spiral wave dynamics in tissue. For example, the Courtemanche *et al.* model without any modifications exhibits wave breakup, while the Nygren model and Courtemanche-AF model give stable spiral wave trajectories, of differing shapes with the Nygren model giving circular trajectories, while the Courtemanche-AF model gives a linear-petal trajectory. This is shown in Fig. 1.15. Thus an additional motivation for using the modified Courtemanche *et al.* model is to track stable spiral wave dynamics.

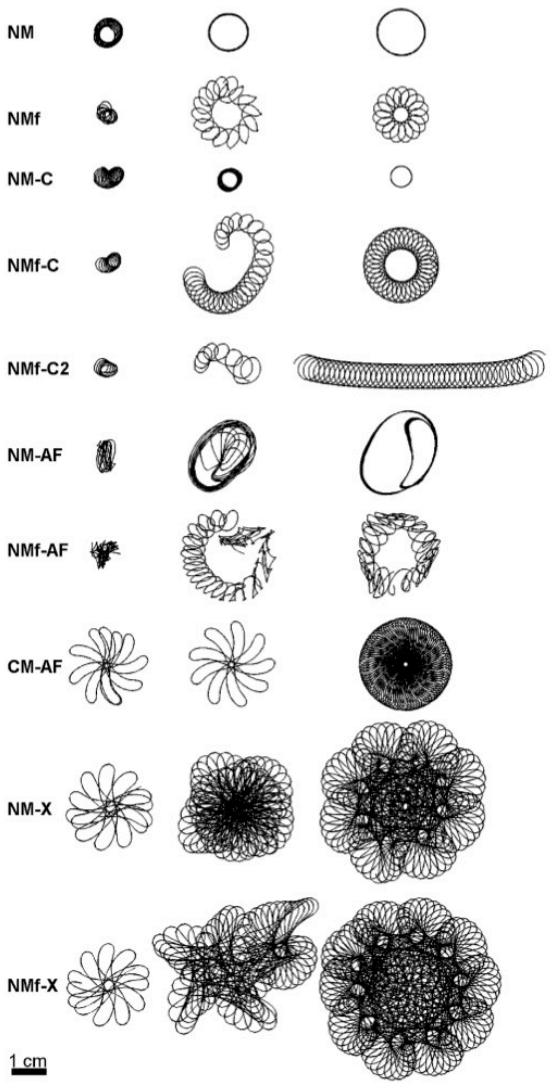

Figure 1.15: Spiral trajectories for variants of the Courtemanche et al. (1998) and Nygren et al. (1998) models, from Cherry and Evans (2008). The model implemented in this thesis is the CM-AF model, with dynamics being closest to the leftmost figure which shows the dynamics after $0.6 - 1.8$ seconds.

1.14 Scope of thesis

The overall motivation of this thesis is to address some of the challenges associated with interpreting signals and wavefront patterns during cardiac arrhythmias, by developing techniques for assessing cardiac electrical wavefront dynamics measured in various simulated, experimental and clinical environments. In particular, the aims are to develop techniques for improved visualisation of atrial surface data in two-dimensions; to calculate conduction velocity and estimate focal source location from multipolar catheter data; for phase mapping of electrogram data; and for assessing arrhythmia mechanisms by comparing distributions and timings of phase singularities and new wavefronts. In addition, the questions of the effects of post-processing techniques and the importance of parameter choice in phase mapping; and of the resolution requirements for identifying rotors and focal sources were addressed. As such, the specific aims are as follows:

- to develop an algorithm to rapidly estimate conduction velocity and the location of the origin of a focal source, for either a planar or circular wavefront measured from any arbitrary arrangement of recording points (Chapter 3);
- to develop a protocol for assessing wavefront dynamics in optical mapping data, including phase singularities, and frequency analysis, and to assess the effects of parameter choices within this protocol in order to determine an optimal set of parameters (Chapter 4);
- to develop a computational method for assessing the spatio-temporal distribution of dominant frequency, phase singularities and new wavefront initiation locations in order to gain insight into arrhythmia mechanisms (Chapter 5);
- to develop and test a technique to track phase singularities from simulated, cell culture and clinically acquired electrogram data, and to determine the effect of data modality on the observed dynamics (Chapter 6);
- to determine the resolution requirements for identification of spiral waves and focal sources as a function of the distance between successive wavefronts (the *spatial wavelength*), and to develop a method for estimating the spatial wavelength (Chapter 7).

This thesis is arranged as follows:

Chapter 2 outlines numerical techniques that are each used in multiple chapters of this thesis. This includes the numerical methods that are used to solve the monodomain equation; the general techniques used for phase mapping; and the

method applied for visualising three-dimensional surface data in two dimensions. Analysis of the effects of different cuts in the mesh on the distance distortion caused by the surface flattening mapping are presented for the cases of inclusion or exclusion of the pulmonary veins.

In Chapter 3, algorithms are presented for estimating CV and the location of the origin of focal sources from an arbitrary arrangement of points, where either a planar or a circular wavefront is assumed. The robustness of the technique to noise is determined for simulated data, and the technique is then applied to clinical data.

In Chapter 4, a methodology is presented for analysing optical mapping data, including calculating dominant frequency and phase singularity distributions. The sensitivity of the protocol to parameters within the analysis are presented, and a suitable set of parameters is suggested.

This methodology is then built on in Chapter 5, and a method to detect instances of new wavefronts and determine arrhythmia mechanisms by examining the relationship between phase singularity distributions, dominant frequency (DF) sites, and new wavefront locations is presented. In particular, the method could be used to identify arrhythmogenic foci.

Techniques for calculating phase of unipolar and bipolar electrograms are presented in Chapter 6, where a comparison is shown between phase singularities calculated using the electrogram phase and those measured using action potential phase in simulated data. The techniques are then adapted for cell culture and clinical electrograms, where the differences between unipolar and bipolar recordings are assessed.

The relationship between the distance between successive wavefronts (the *spatial wavelength*) and the resolution required for identifying rotors and focal sources are determined for a regular grid of data in Chapter 7. These requirements are then tested for arrangements corresponding to high-density mapping catheters and basket catheters. Preliminary investigations into the effects of parameter choices and spiral core detection method, as well as the effects of resolution are presented in Appendix A.

Finally, conclusions are presented in Chapter 8.

Chapter 2

Numerical methods for simulation, and techniques for post-processing, rotor tracking and visualisation

2.1 Introduction

Cardiac tissue can be modelled as a continuum, to represent propagating waves on a macroscopic tissue level, where it is considered to behave as a functional syncytium of coupled cells. Neu and Krassowska (1993) first derived the continuous bidomain equation by homogenising a discrete representation of tissue. The bidomain model includes an intracellular and extracellular domain that are overlapping and continuous, but separated by a cell membrane. Under the assumption of equal anisotropy of the intracellular and extracellular domains, the bidomain model can be simplified from two to just one partial differential equation (PDE), giving the monodomain equation for the transmembrane potential. The monodomain model is in general a good approximation to the bidomain model (Colli Franzone et al., 2005), and is also numerically easier to solve.

Cardiac continuum models typically consist of a system of ordinary differential equations (ODEs) that represent the myocardial cell, coupled to a partial differential equation (PDE) that describes the flow of electricity through the tissue. For the simulations in this thesis, the Courtemanche et al. (1998) human atrial model is used as the system of ODEs for the cell model, coupled to the monodomain PDE for the tissue model. Data from these simulations are used to develop and test techniques for CV estimation and rotor tracking, as well as to investigate the data

requirements for wavefront identification (in Chapters 3, 6, 7 and A).

Post-processing of action potential data enables the investigation of the pacing dependent properties of the tissue by calculating restitution curves, used in Section 7.3; and the generation of pseudo-electrograms, used for testing the unipolar and bipolar phase algorithms developed in Chapter 6 and for testing spatial resolution requirements in Section 7.4.3.

Spiral waves can be generated in simulations using extra-stimulus protocols. Rotor-core location can be identified using the techniques discussed in Section 1.13, which includes the isopotential line method and phase singularity tracking. These rotor tracking techniques are also used to address questions (such as the data resolution required for accurate rotor-core identification), and are applied and further developed to work with other datatypes in Chapters 4, 5, 6, 7 and A.

Electro-anatomic mapping and medical imaging systems, used during clinical procedures for treatment of atrial arrhythmias, frequently record and display measurements on an anatomical surface of the left atrium. As such, obtaining a complete picture of activation necessitates simultaneous views from multiple angles. In addition, post-processing of three-dimensional surface data is challenging, since algorithms are typically applicable to planar or volumetric data. In this chapter, a surface flattening methodology is applied to medical imaging data and electro-anatomic mapping data to generate a two-dimensional representation that best preserves distances, since the calculation of many clinically relevant metrics, including conduction velocity requires an accurate representation of distance. The effects of exclusion of the pulmonary veins on the distance distortion are also presented. Specifically, the technique is applied to clinical local activation time map data in Section 3.4.9 and to rotor-core trajectories in Section 7.4.3. The same techniques are also used for calculating geodesic distances and mapping to two dimensions for conduction velocity calculations in Chapter 3; for analysing atrial tachycardia wavefront direction and phase maps in Section 6.4.6; and for displaying maps from a basket recording catheter in Section 7.4.3.

In this chapter, the general numerical methods used to solve a system of ODEs representing the transmembrane voltage for a single cell (Sections 2.2, 2.3), and the monodomain model for a one-dimensional cable and two-dimensional sheet are outlined (Section 2.4). In addition, the stimulus protocols used to simulate spiral waves are outlined (Section 2.6), and post-processing techniques are detailed; including for generating restitution curves (Section 2.7) and for calculating pseudo-electrograms (Section 2.8). Next, rotor tracking techniques are detailed, including phase mapping (Sections 2.9, 2.10, 2.11, 2.12) and the isopotential line method (Section 2.13).

Finally, a surface flattening methodology that best preserves distances is applied to left-atrial geometries (Section 2.14).

2.2 Cardiac cell models, including the Courtemanche et al. (1998) human atrial cell model

For a single cardiac myocyte cell, the equation for the transmembrane potential is independent of space; it is a first-order ODE in time. The following differential equation is solved to find the transmembrane potential, V, of a single cell:

$$\frac{\mathrm{d}V}{\mathrm{d}t} = -\frac{I_{\text{ion}} + I_{\text{stim}}}{C_{\text{m}}}, \tag{2.1}$$

where I_{ion} represents the sum of the ionic currents, which depends on the choice of ionic model, I_{stim} is the stimulus current, and C_{m} is the membrane capacitance. The ionic currents depend on *gating variables* and ionic concentrations, which are also represented by ODEs.

The conductance of each ion channel are represented as a function of gating variables, that is for an ion channel, k, the conductance is:

$$g_k = \bar{g}_k f_k(y_1, y_2, \dots), \tag{2.2}$$

where $\bar{g}_k$ is the maximum conductance, and f_k scales the conductance depending on the gating variables y_i.

We consider the simplest model for ion channel conductance, for which the channel is assumed to be in one of two states: open (O) or closed (C). In this case, $\mathrm{C} \underset{\beta(V)}{\overset{\alpha(V)}{\rightleftharpoons}} \mathrm{O}$, and then letting g be the proportion of channels that are open (and $1-g$ the proportion that are closed), we have the following:

$$\frac{\mathrm{d}g}{\mathrm{d}t} = \alpha(V)(1-g) - \beta(V)g. \tag{2.3}$$

Thus gating variables y_i follow first-order kinetics and satisfy ODEs of the form:

$$\frac{\mathrm{d}y_i}{\mathrm{d}t} = \alpha_i(1-y_i) - \beta_i y_i, \qquad j = 1, 2, \dots, n_y, \tag{2.4}$$

where the rate constants α_i and β_i are voltage dependent.

Overall, the cell model presents as an initial value problem of the form:

$$\frac{\mathrm{d}\mathbf{y}}{\mathrm{d}t} = \mathbf{f}(t, \mathbf{y}), \qquad \mathbf{y}(0) = \mathbf{y}_0, \qquad t \in [t_0, t_f], \tag{2.5}$$

where $\mathbf{y}$ is a system of coupled nonlinear ODEs representing the transmembrane voltage V, ionic concentrations and gating variables.

The system in Equation 2.5 is given by the following equations for the transmembrane voltage and ionic concentrations $\mathbf{c}$:

$$\frac{\mathrm{d}V}{\mathrm{d}t} = -\frac{1}{C_\mathrm{m}} \sum_{i=1}^{n_\mathrm{ion}} I_i(V, \mathbf{y}, \mathbf{c}, t), \tag{2.6}$$

$$\frac{\mathrm{d}c_j}{\mathrm{d}t} = g_j(c_j, \mathbf{y}, V, t), \qquad j = 1, 2, \ldots, n_c, \tag{2.7}$$

as well as equations for the gating variables (Equation 2.4).

The Courtemanche et al. (1998) human atrial cell model

The ionic model used for most of the simulations in this thesis is the Courtemanche et al. (1998) human atrial cell model. Motivations for choosing this model are detailed in Section 1.13.12. The model consists of 21 ODEs, of which fifteen are gating variables (Equation 2.4), five represent ionic concentrations (Equation 2.7), and the final ODE is for the transmembrane voltage (Equation 2.6). The following ionic currents are included in the Courtemanche et al. (1998) model:

$$\begin{aligned} I_\mathrm{ion} = {} & I_\mathrm{Na} + I_\mathrm{K1} + I_\mathrm{to} + I_\mathrm{Kur} + I_\mathrm{Kr} + I_\mathrm{Ks} + I_\mathrm{Ca,L} \\ & + I_\mathrm{p,Ca} + I_\mathrm{NaK} + I_\mathrm{NaCa} + I_\mathrm{b,Na} + I_\mathrm{b,Ca}. \end{aligned}$$

This is shown in the schematic in Fig. 2.1.

The ionic concentrations included in the model are intracellular sodium, potassium and calcium, as well as calcium uptake and release from the sarcoplasmic reticulum.

The fast sodium current has three gating variables (m, h and j). There are four time-dependent potassium currents, with a total of six associated gating variables: transient outward (o_a, o_i); ultra rapid delayed rectifier (u_a, u_i); rapid delayed outward rectifier (x_r); and slow delayed outward rectifier (x_s). The L-type calcium current has three gates (d, f, f_{Ca}); and the ionic current representing calcium release from the sarcoplasmic reticulum also has three gates (u, v and w). Full details of the equations are given in Courtemanche et al. (1998).

Electrical remodelling during chronic AF was included in some simulations following Courtemanche et al. (1999); reducing the ionic conductances of I_to, I_Kur and I_CaL by 50%, 50% and 70% respectively.

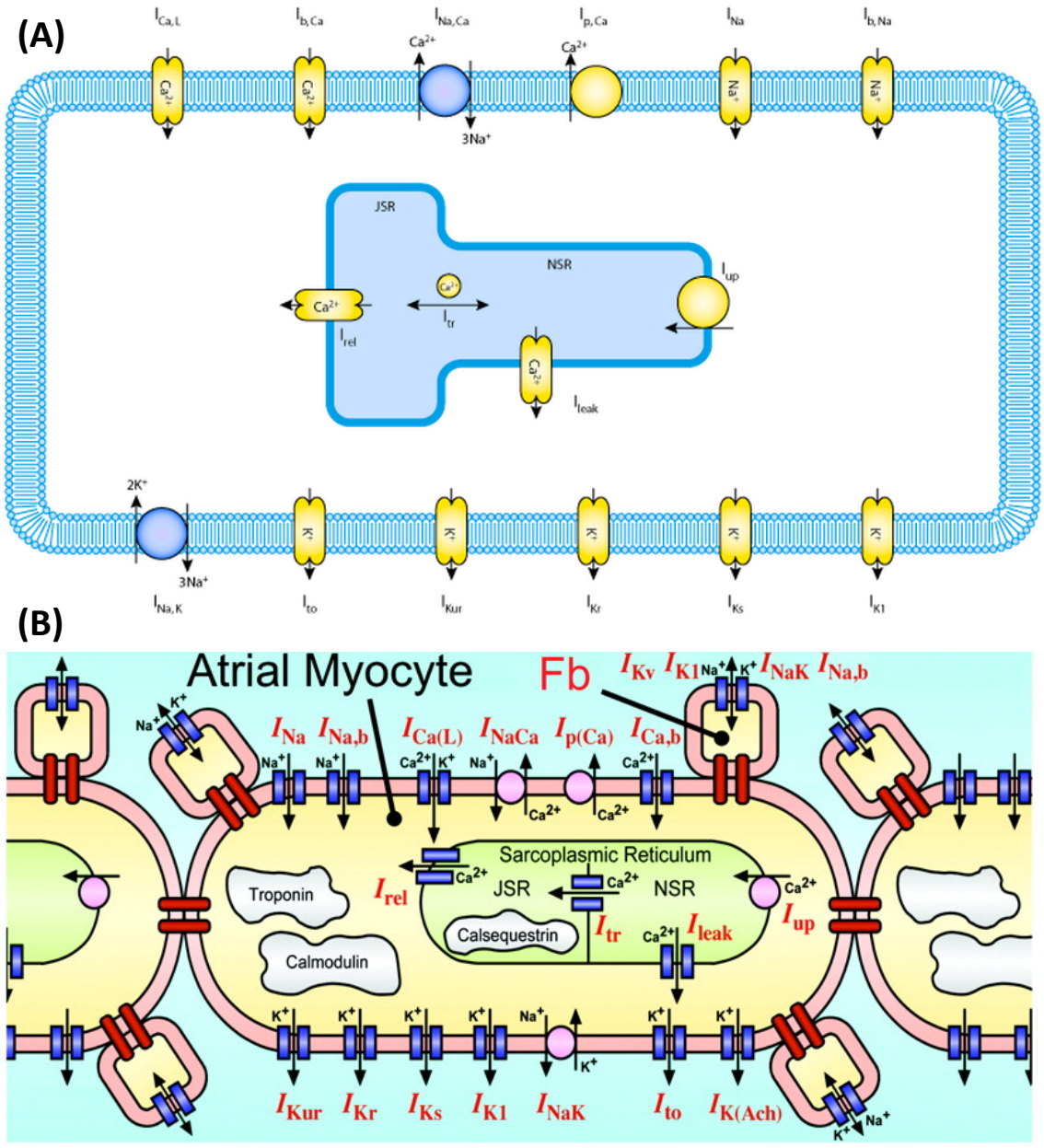

Figure 2.1: Schematics to show the Courtemanche et al. (1998) human atrial cell model. (A) Reproduced from the CellML model repository website (Lloyd et al., 2008; Noble, 2015). (B) Schematic to show a Courtemanche et al. (1998) human atrial myocyte coupled to fibroblast cells (labelled Fb), modelled using the MacCannell et al. (2007) fibroblast cell model; reproduced from Ashihara et al. (2012).

One further change is made from the original Courtemanche et al. (1998) formulation to treat the sodium and potassium concentrations as fixed constants. This adaptation is used in Cherry and Evans (2008) to eliminate the drift of these concentrations.

For a subset of simulations, fibroblasts were included in the model (see Appendix, Section. A.1.4), by coupling Courtemanche et al. (1998) human atrial myocytes to between one and four MacCannell et al. (2007) fibroblast cells, following Ashihara et al. (2012). This is shown in the schematic in Fig. 2.1(B).

2.3 Single cell solution methods

The system of ODEs representing the single cell model are non-linear and have a wide range of timescales, which results in a *numerically stiff* system, where the step size required is limited by stability rather than accuracy (Spiteri and Dean, 2008). This results in a system that is challenging to solve.

In order to solve the set of equations for the transmembrane voltage, ionic concentrations and the gating variables (Equations 2.6, 2.7 and 2.4 respectively), we use finite difference numerical methods.

Specifically, we use a partitioned method that treats the gating variable ODEs differently to the transmembrane voltage and ion concentration equations, following Rush and Larsen (1978a). The ODEs for the gating variables are solved numerically using an exponential integrator, whilst the ODEs for the transmembrane voltage and ion concentration are solved numerically using a forward Euler integrator.

Forward Euler

Equations 2.6 for the transmembrane voltage and Equation 2.7 for the ion concentrations are solved as follows:

$$\begin{aligned} \mathbf{y}_{n+1} &= \mathbf{y}_n + \Delta t_n \cdot \mathbf{f}(t_n, \mathbf{y}_n), \\ t_n &= t_{n-1} + \Delta t_n. \end{aligned}$$

This integration is combined with integration of the gating variables, using the steps outlined below.

Rush–Larsen method

The idea behind the Rush–Larsen method is that the equations for the gating variables (Equation 2.4) would be simple to solve if the rate constants α and β were constant, as in this case there is an analytical solution to the linear ODEs. The Rush–Larsen method works by picking a time step small enough that we can assume α and β are constant over that time step. The technique is as follows: pick a small time increment Δt over which α and β can be assumed constant. At each time step we rearrange Equation 2.4 to give,

$$\frac{\mathrm{d}y}{\mathrm{d}t} + (\alpha + \beta)y - \alpha = 0,$$

which we multiply by $e^{(\alpha+\beta)t}$ and solve using the method of integrating factors:

$$\frac{d(e^{(\alpha+\beta)t}y)}{dt} = \alpha e^{(\alpha+\beta)t},$$

then integrating gives

$$e^{(\alpha+\beta)t}y = \frac{\alpha e^{(\alpha+\beta)t}}{\alpha+\beta} + C,$$

$$\Rightarrow y = \frac{\alpha}{\alpha+\beta} + Ce^{-(\alpha+\beta)t}.$$

Applying the initial condition that at $t = 0$, $y = y_0$, gives:

$$y = \frac{\alpha}{\alpha+\beta} + (y_0 - \frac{\alpha}{\alpha+\beta})e^{-(\alpha+\beta)t}.$$

Finally, defining the time constant $\tau = \frac{1}{\alpha+\beta}$ and the asymptotic value $y_\infty = \frac{\alpha}{\alpha+\beta}$, leads to

$$y = y_\infty + (y_0 - y_\infty)e^{-\frac{t}{\tau}}. \tag{2.8}$$

In the following, we outline the steps for simultaneously solving the system of equations for the transmembrane voltage (Equation 2.6) and ionic concentrations (Equation 2.7), along with the gating variables (Equation 2.4):

Step 1: Define constants C_m, Δt, and those from the ionic model.

Step 2: For each time increment $1, 2, \ldots n$ complete steps 3 - 7 below.

Step 3: Use the value of V_{n-1} to calculate α and β for each gating variable.

Step 4: Calculate τ and y_∞ for each gating variable.

Step 5: Calculate the next values for each gating variable using Equation 2.8.

Step 6: Use the new values of the gating variables to calculate $\mathrm{I_{ion}}$.

Step 7: Calculate V_n using the forward Euler approximation: $V_n = -\frac{\Delta t}{C_m} I_{\mathrm{ion}} + V_{n-1}$.

2.4 Computational methods for solving the monodomain model

2.4.1 One dimensional cable

We now consider a one dimensional continuous cable, where we assume that the potential depends only on the length along the cable and has no radial or angular dependence (the core conductor assumption, (Keener and Sneyd, 2009)). This partial differential equation (PDE) contains an ionic term, as for the single cell Equation 2.1, but also contains a spatial term for diffusion, in one dimension. Thus,

$$\frac{\partial V}{\partial t} = -\frac{I_{\mathrm{ion}} + I_{\mathrm{stim}}}{C_m} + D\frac{\partial^2 V}{\partial x^2}, \tag{2.9}$$

where D is the diffusion coefficient for the electrical signal, V is the transmembrane voltage, I_{ion} is the sum of the ionic currents, I_{stim} is the stimulus current, and C_{m} is the membrane capacitance, as before.

We apply Neumann (no flux) boundary conditions at both ends of the cable, that is no current flow is permitted through the ends of the cable, and an initial condition is applied to the entire cable.

Method of solution: We use an operator splitting algorithm proposed by Qu and Garfinkel (1999) to consider the diffusion and ionic parts of the equation separately. This splits the system into an uncoupled linear parabolic PDE and a system of nonlinear ODEs.

Step 1: Use the result at time $t(n)$ as the initial condition to integrate $\frac{\partial V}{\partial t} = D\frac{\partial^2 V}{\partial x^2}$ for a step length $\Delta t/2$ (use the Crank-Nicolson numerical technique; see below for further explanation).

Step 2: Use the resulting value of V from step 1 as the initial condition for solving the ionic part of the equation for a step length Δt:

$$\frac{\mathrm{d}V}{\mathrm{d}t} = -\frac{I_{\mathrm{ion}} + I_{\mathrm{stim}}}{C_{\mathrm{m}}},$$

$$\frac{\mathrm{d}y_i}{\mathrm{d}t} = \alpha_i(1 - y_i) - \beta_i y_i, \quad i = 1, \ldots, M,$$

(using Rush Larsen and forward Euler, as for a single cell above).

Step 3: Use the resulting V from step 2 as the initial condition to integrate $\frac{\partial V}{\partial t} = D\frac{\partial^2 V}{\partial x^2}$ for a step length $\frac{\Delta t}{2}$.

This gives the value of V at time $t(n) + \Delta t$. These steps are then repeated.

Crank–Nicolson: We use the Crank–Nicolson numerical scheme (Press et al., 2007) on

$$\frac{\partial V}{\partial t} = D\frac{\partial^2 V}{\partial x^2},$$

to give

$$\frac{V_{n+1}^j - V_n^j}{\Delta t} = \frac{D}{2}\left[\frac{(V_{n+1}^{j+1} - 2V_{n+1}^j + V_{n+1}^{j-1}) + (V_n^{j+1} - 2V_n^j + V_n^{j-1})}{(\Delta x)^2}\right]$$

Defining $\eta = \frac{D\Delta t}{2(\Delta x)^2}$ and rearranging we find:

$$-\eta V_{n+1}^{j-1} + (1 + 2\eta)V_{n+1}^j - \eta V_{n+1}^{j+1} = \eta V_n^{j-1} + (1 - 2\eta)V_n^j + \eta V_n^{j+1}$$

This can be written in the form:

$$M_1 V_{n+1} = M_2 V_n,$$

where M_1 is a tridiagonal matrix with $-\eta$, $1 + 2\eta$ and $-\eta$ on the lower, main and upper diagonals, respectively; and M_2 is also a tridiagonal matrix with η, $1 - 2\eta$ and η on the lower, main and upper diagonals, respectively. We now have a matrix equation of the form $Ax = b$ with $A = M_1$, $b = M_2 V_n$ and we solve for $x = V_{n+1}$ using inbuilt Matlab commands.

2.4.2 Two dimensional sheet

In two dimensions, the monodomain equation (2.9) becomes:

$$\frac{\partial V}{\partial t} = -\frac{I_{\text{ion}} + I_{\text{stim}}}{C_m} + D_1\frac{\partial^2 V}{\partial x^2} + D_2\frac{\partial^2 V}{\partial y^2}, \tag{2.10}$$

where D_1 and D_2 are the diffusivities in the x and y directions, respectively. Here we have assumed the sheet is aligned with the axes, so that there are no cross derivative terms.

As for the one-dimensional cable equation, we use an operator splitting technique and follow the steps in Section 2.4.1. For Crank-Nicolson on the two dimensional equation,

$$\frac{\partial V}{\partial t} = D_1 \frac{\partial^2 V}{\partial x^2} + D_2 \frac{\partial^2 V}{\partial y^2},$$

we get

$$\begin{aligned} \frac{V_{n+1}^{j,l} - V_n^{j,l}}{\Delta t} &= D_1 \frac{(V_{n+1}^{j,l+1} - 2V_{n+1}^{j,l} + V_{n+1}^{j,l-1}) + (V_n^{j,l+1} - 2V_n^{j,l} + V_n^{j,l-1})}{2(\Delta x)^2} \\ &+ D_2 \frac{(V_{n+1}^{j+1,l} - 2V_{n+1}^{j,l} + V_{n+1}^{j-1,l}) + (V_n^{j+1,l} - 2V_n^{j,l} + V_n^{j-1,l})}{2(\Delta y)^2}. \end{aligned}$$

Defining $\eta = \frac{D_1 \Delta t}{2(\Delta x)^2}$ and $\zeta = \frac{D_2 \Delta t}{2(\Delta y)^2}$ and rearranging with V_{n+1} on the left and V_n on the right gives:

$$\begin{aligned} -\eta V_{n+1}^{j,l-1} - \zeta V_{n+1}^{j-1,l} + (1 &+ 2\eta + 2\zeta) V_{n+1}^{j,l} - \zeta V_{n+1}^{j+1,l} - \eta V_{n+1}^{j,l+1} \\ &= \eta V_n^{j,l-1} + \zeta V_n^{j-1,l} + (1 - 2\eta - 2\zeta) V_n^{j,l} + \zeta V_n^{j+1,l} + \eta V_n^{j,l+1}. \end{aligned}$$

We now change the indexing system to convert the 2D domain into a 1D vector. Consider a point at (j, l) and its four neighbours (above is $(j-1, l)$, below is $(j+1, l)$, left is $(j, l-1)$ and right is $(j, l+1)$). We transform using a new variable $i = (l-1)J + j$, where J is the number of rows in the 2D sheet. Our equation becomes:

$$\begin{aligned} -\eta V_{n+1}^{i-J} - \zeta V_{n+1}^{i-1} + (1 &+ 2\eta + 2\zeta) V_{n+1}^{i} - \zeta V_{n+1}^{i+1} - \eta V_{n+1}^{i+J} \\ &= \eta V_n^{i-J} + \zeta V_n^{i-1} + (1 - 2\eta - 2\zeta) V_n^{i} + \zeta V_n^{i+1} + \eta V_n^{i+J}. \end{aligned}$$

As for the one-dimensional cable, this can then be written in the form:

$$M_1 V_{n+1} = M_2 V_n.$$

Each matrix has five diagonals; we use the alternating-direction implicit method to convert it to a tridiagonal system following Press et al. (2007), dividing each time

step into two of size $\frac{\Delta t}{2}$:

$$\begin{aligned} -\eta V_{n+\frac{1}{2}}^{i-J} + (1+2\eta)V_{n+\frac{1}{2}}^{i} &- \eta V_{n+\frac{1}{2}}^{i+J} \\ &= \zeta V_n^{i-1} + (1-2\zeta)V_n^i + \zeta V_n^{i+1}, \end{aligned}$$

and

$$\begin{aligned} -\zeta V_{n+1}^{i-1} + (1+2\zeta)V_{n+1}^{i} &- \zeta V_{n+1}^{i+1} \\ &= \eta V_{n+\frac{1}{2}}^{i-J} + (1-2\eta)V_{n+\frac{1}{2}}^{i} + \eta V_{n+\frac{1}{2}}^{i+J}. \end{aligned}$$

The alternating direction implicit solution method alternates in solving the ODEs and the PDE, and we implement this solution using inbuilt Matlab commands.

2.4.3 Discussion of the suitability of the methods

Forward Euler is explicit and known to be suboptimal for stiff problems (Maclachlan et al., 2007). Rush–Larsen has been shown to outperform other solution methods when applied to moderately stiff ODEs, such as the Courtemanche et al. (1998) model (Marsh et al., 2012), providing the best combination of stability and expense per step. Rush–Larsen has also been shown to be the most efficient in the case of constant step size (Spiteri and Dean, 2008). Disadvantages of the Rush–Larsen technique include that it is only first order accurate and it is not expected to provide an efficient solution in the case when the model stiffness is not captured by gating variables. A limitation of the methods used here is that cell model sub-stepping is not included.

2.4.4 Boundary and initial conditions

Neumann (no flux) boundary conditions are applied to all edges of the domain to impose no current leak.

Prepacing

Results are quoted after pacing to steady state which can take several cycles to reach. For computational efficiency when solving for a cable or 2D sheet, initial conditions were applied to the entire domain which corresponded to the steady state results

for a single cell paced at that cycle length; a process called *prepacing* (Sato et al., 2009). Using this technique means the domain reaches a steady state more quickly. The initial conditions for prepacing were taken from the CellML model repository website (Lloyd et al., 2008).

2.4.5 Time and space step

Simulations were run with a space step of 0.1mm and a time step of 0.01ms.

2.5 Spectral/hp element methods

Anatomically accurate left-atrial mesh simulations were run using the open source *Nektar++* finite element solver (Cantwell et al., 2014b). The solver uses finite element methods, for which the domain is subdivided into elements, which can be different shapes and sizes. The solution to the monodomain equation on each element is represented by a space of hierarchical high-order polynomials. At the boundaries between elements, the solution is assumed to be continuous. Finite element methods have the advantage that the left atrial geometry can be modelled accurately.

In particular, Nektar++ uses a spectral/hp element method, where h indicates the ability to change the size of elements, and p indicates the polynomial order for the solution. These methods have the advantage that they have exponential convergence of the solution with increasing polynomial order.

2.6 Pacing protocol for spiral wave initiation

Spiral waves were initiated using an extra-stimulus protocol, *S1–S2 pacing*, in which the S1 stimulus represents a regular paced beat, and the S2 stimulus is an extra stimulus beat. For spiral wave initiation in a two-dimensional sheet, an S1 stimulus was applied along the whole left hand edge of the domain to produce a planar wave, and once the repolarisation of the wave reached the centre of the domain, an S2 beat was applied parallel to the S1 beat, but only for three quarters of the height of the sheet. The timing of this beat was chosen such that the tissue ahead of the stimulus was still refractory, in order to create a spiral wave re-entry. This is illustrated in Fig. 2.2.

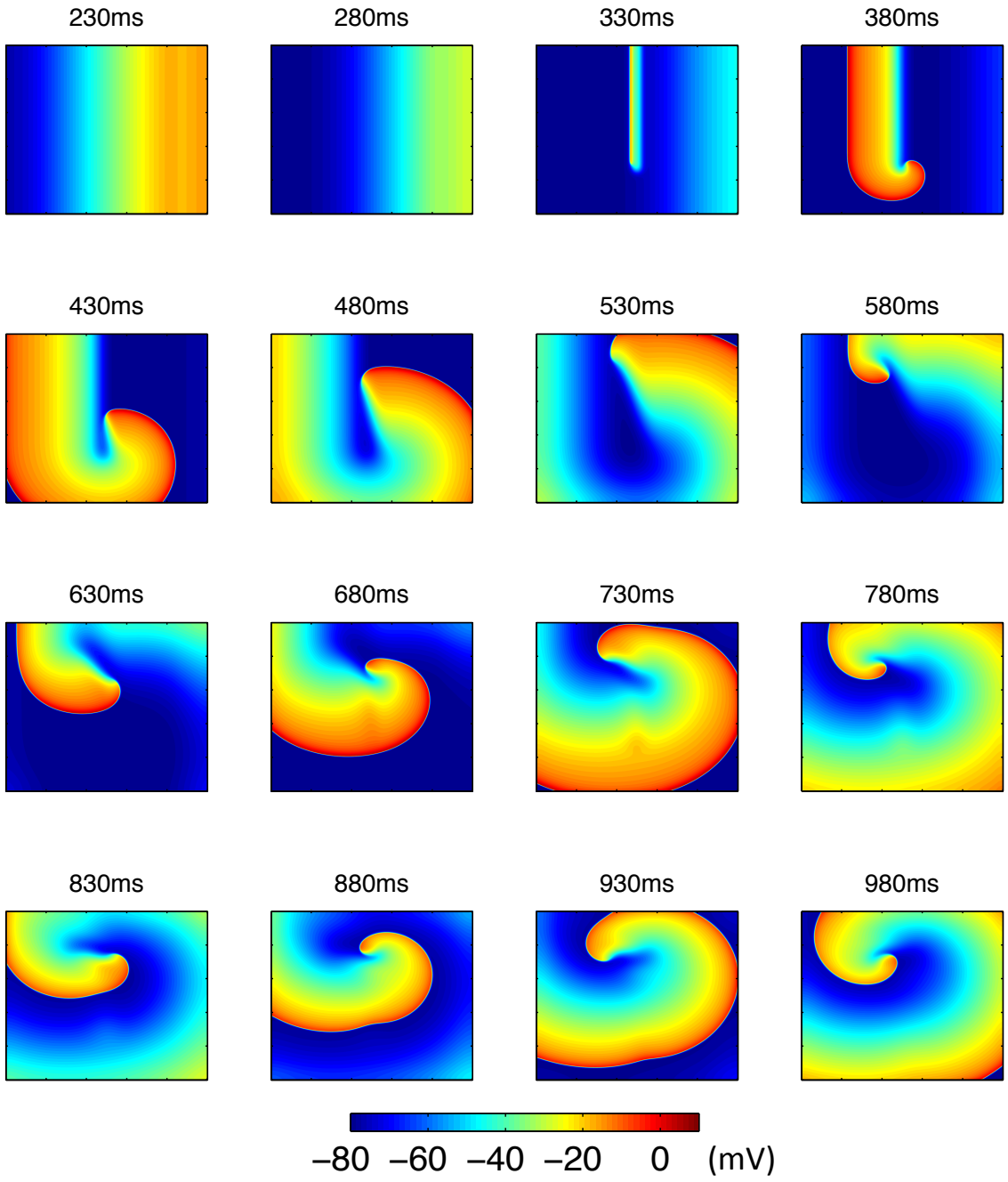

Figure 2.2: Spiral wave initiation following an *S1–S2* extra-stimulus pacing protocol. A planar S1 stimulus is applied to the entire left hand edge of the domain at time 0, which can be seen in the first two frames. A second S2 stimulus is applied parallel to the S1 beat, but only three quarters of the height of the sheet, at a time point such that the tissue ahead of the stimulus is still refractory (third frame; 330ms). This creates a spiral wave re-entry. The domain size shown here is 10cm-by-10cm.

2.7 Postprocessing: action potential duration and conduction velocity restitution

APD and CV restitution properties were calculated in a 2cm one-dimensional cable. An S1-S2 pacing protocol was performed consisting of 100 beats at a cycle length (CL) of 500ms (the S1 beats), followed by an extrastimulus (S2) at the S1–S2 interval. Initial conditions were from the cell model repository CellML (Lloyd and Noble, 1998). APD90 and DI (Fig. 2.3) were calculated for a point at the centre of the cable using the voltage threshold for 90% repolarisation for the S1 beat, to allow for differences in amplitude and resting membrane potential (Cherry and Evans, 2008). CV was calculated by considering the difference in activation times between points at 0.5cm and 1.5cm along the cable (Gong et al., 2007), where activation time was taken to be the time point of maximum temporal gradient (T_{ACT} in Fig. 2.3).

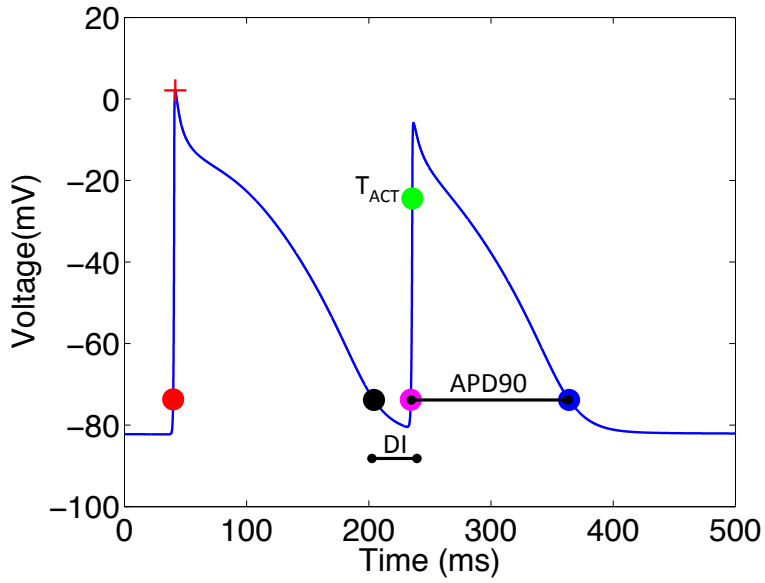

Figure 2.3: Definition of APD, DI and activation time. APD90 and DI were calculated using the final S1 beat of the pacing train (first AP in diagram) and the S2 beat (second AP in diagram). The voltage threshold for 90% repolarisation was calculated for the final S1 beat as the black dot, using the amplitude measured from the baseline to the red cross. The voltage value for this 90% repolarisation point was then used to define the start and end of the S2 beat; the purple and blue points, respectively. APD90 is then the time difference between the blue and purple dots, and DI is the time difference between the purple and black dots. Activation time was defined as the time point of maximum gradient (T_{ACT}, green dot).

2.8 Postprocessing: calculating bipolar electrograms and p-ECGs

Electrograms were calculated, following Sato et al. (2009), using the following formula:

$$\Phi_e(x_p, y_p, z_p) = \mathrm{D} \int \int_A (\nabla V).(\nabla \left(\frac{1}{R}\right)) \mathrm{d}x\mathrm{d}y, \tag{2.11}$$

where $R = \sqrt{(x - x_p)^2 + (y - y_p)^2 + (z - z_p)^2}$ is the distance from the location of the electrode at (x_p, y_p, z_p), A is the area of the sheet, and D is the diffusion coefficient and V is the transmembrane potential, as before. Unipolar electrograms were calculated one cell radi (5μm) above the domain and bipolar electrograms were calculated as the difference between unipolar electrograms. Simulated electrograms in this thesis are in arbitrary units since a scalar constant premultiplying this equation, which determines the units, has been arbitrarily set to 1 following Varela and Aslanidi (2014).

2.9 Phase mapping: Hilbert transform

In the following sections, the techniques used for rotor tip identification will be presented. As discussed in Section 1.13, one difficulty with phase calculation is picking the correct time delay for the shifted signal $V(t + \tau)$. Application of the Hilbert Transform creates a suitable signal for state space analysis and phase calculation, without the need to specify a time shift τ. This approach was suggested by Bray and Wikswo (2002a) and we will use several of the techniques that they have developed.

As for the time-shifted signal (Section 1.13, Fig. 1.13), the Hilbert Transform, H, of the signal is plotted against the signal to give attractors in this state space. Again a phase angle is defined from the origin as:

$$\theta(t) = \arctan2[V^*(t), H[V^*(t)]], \tag{2.12}$$

here V^* is $V - V_{mean}$ so that the origin is at $(0, 0)$.

The Hilbert transform of a function is orthogonal to the function itself which means that plotting one against the other will give loops in the state space (Umapathy et al., 2010). It is given as:

$$H[V(t)] = \frac{1}{\pi} \ p.v. \int_{-\infty}^{\infty} \frac{V(T)}{t - T} \mathrm{d}T, \tag{2.13}$$

where $p.v$ is the Cauchy principal value of the integral. A signal can be combined

with the Hilbert transform of itself to give an analytic signal as follows:

$$z(t) = V^*(t) + i \cdot H[V^*(t)] = A(t)e^{i\theta(t)}, \tag{2.14}$$

where $A(t)$ gives the amplitude of the signal, and $\theta(t)$ is the phase (Umapathy et al., 2010).

Application of the Hilbert Transform requires a zero mean signal. However, simply subtracting the mean of the entire signal over time at each spatial point leads to miscalculations in phase close to the rotor tip, as will be discussed in the following section.

2.10 Phase mapping: creating a zero mean signal

Simply removing the mean of the signal can lead to incomplete loops in the state space and activations that do not experience a full 2π change in phase. An example where this occurs is shown in Fig. 2.4. In order to ensure that all activations experience a full change in phase, a processing step is required in order to ensure the mean of each action potential is zero. This is performed using a technique similar to that used by Bray and Wikswo (2002a) (see Section 1.13.4).

For our application, several modifications to the approach of Bray and Wikswo (2002a) were required. First of all, the maxima of the signal are tagged using a moving window, and the minima are then defined as the locations of the minimum value between each pair of maxima. This ensures that the number of maxima and minima differs by at most one. This step requires the choice of a window length, such that adjacent maxima are separated by at least that many samples. As a second additional step, an amplitude threshold is set for which minima-maxima pairs of amplitude less than this threshold are deleted. Thus maxima and minima are assigned in the signal based on both the temporal difference between the maxima (or minima) and the amplitude of fluctuations within the signal. This enables more control over which deflections are considered to represent activations, since thresholds can be set on both the amplitude of fluctuations that are considered physiologically relevant, and the timing between such fluctuations.

As in Bray and Wikswo (2002a), the maxima and minima are each joined by cubic splines and the mean line is then removed from the signal, to create a zero mean signal. The Hilbert transform of this zero mean signal is then plotted against the zero mean signal to give trajectories in the state space. The angle around this trajectory gives the phase angle, as explained in Section 1.13.2. The steps involved in calculating the phase angle by subtracting a moving mean are shown in Fig. 2.5.

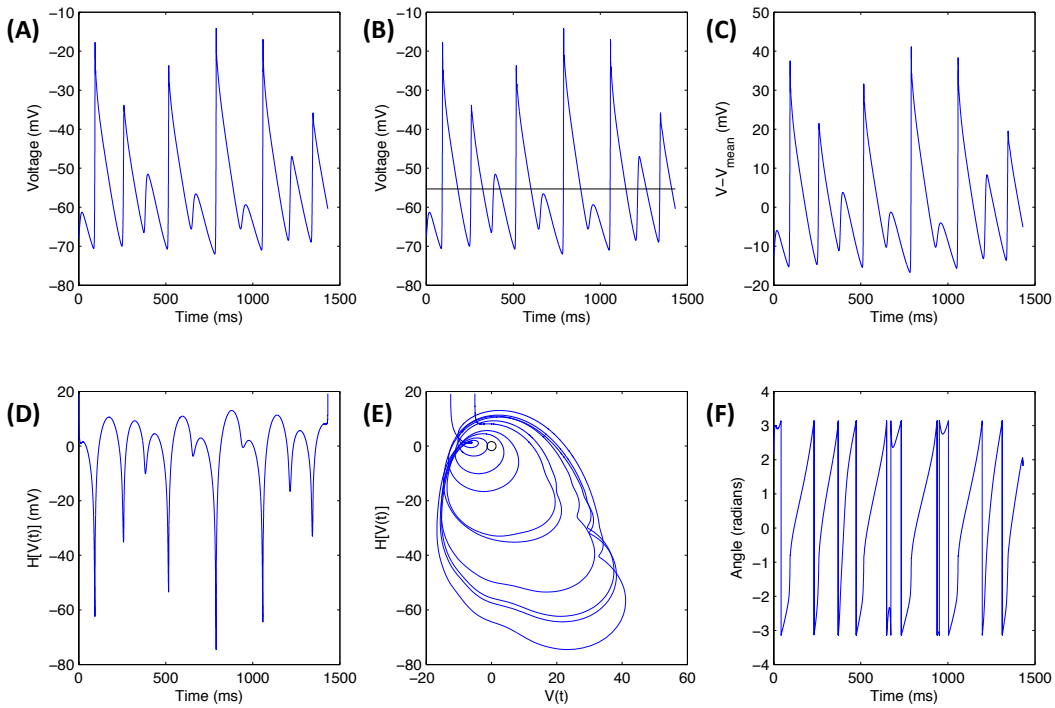

Figure 2.4: Regular mean: phase shows incomplete progressions. When the regular mean is taken, the origin lies outside of some of the trajectories and the phase shows incomplete progressions. The results after subtracting a moving mean are shown in Fig. 2.5. (A) Voltage signal; (B) Voltage signal with straight mean marked; (C) Voltage with straight mean subtracted; (D) Hilbert transform of straight mean subtracted signal; (E) Plotting the zero-mean signal against its Hilbert transform creates phase loops, where some loops do not encircle the origin (marked by black circle); (F) Resulting phase.

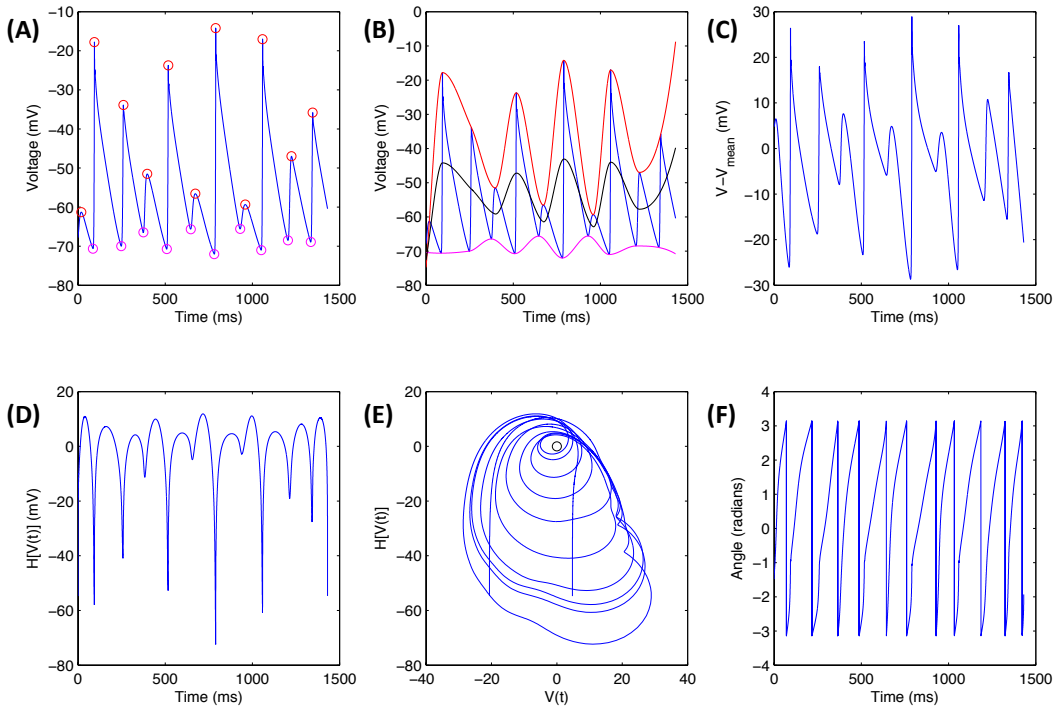

Figure 2.5: Moving mean removal results in clean phase in simulated data. (A) Voltage signal, with maxima (red circles) and minima (purple circles) marked; (B) Voltage signal with maxima (red) and minima (purple splines), as well as the average of these (black line), which gives the moving mean; (C) Moving mean subtracted voltage; (D) Hilbert transform of moving mean subtracted signal; (E) Plotting the zero-mean signal against its Hilbert transform creates phase loops, where all loops encircle the origin; (F) Resulting phase. Compare to using a regular mean on this signal in Fig. 2.4.

This approach to tagging the maxima and minima to determine which deflections to keep in the phase signal has the advantage that the effects of varying the window length and amplitude thresholds can be tested. It is difficult to assign a universal window length parameter that works for all points in space and time; thus, testing the effects of this are important. The effects of these parameters are investigated in Chapter 4 and Appendix, Section A.1.1.

2.11 Phase mapping: calculating the phase singularity line integral

To calculate the integral given in Equation 1.24, we use the technique given in Bray and Wikswo (2002b). Here we consider the topological charge in Equation 1.24, multiplied by 2π. By Green's theorem, this integral is

$$\oint_c \nabla\theta \cdot \mathrm{d}\mathbf{r} = \iint_D (\nabla \times \nabla\theta) \cdot \hat{\mathbf{z}} \, \mathrm{d}A. \tag{2.15}$$

By the properties of scalar fields, if θ is differentiable, $\nabla \times \nabla\theta = 0$. Thus the topological charge is zero everywhere when θ is differentiable. Hence the integral will be non-zero just if it contains a phase singularity, which would correspond to where θ is not differentiable.

In the limit as the area goes to zero, the integral on the right hand side is equal to the integrand; i.e. $(\nabla \times \nabla\theta) \cdot \hat{\mathbf{z}}$. Defining $k(x, y, t) \equiv \nabla\theta(x, y, t)$, then this can be rewritten as

$$(\nabla \times \nabla\theta) \cdot \hat{\mathbf{z}} \equiv (\nabla \times k) \cdot \hat{\mathbf{z}} = \left(\frac{\partial k_y}{\partial x} - \frac{\partial k_x}{\partial y} \right) \hat{\mathbf{z}}. \tag{2.16}$$

The above expression can be numerically evaluated for values of θ on a finite difference grid, in order to identify phase singularities. Since the integral is performed on a finite-difference grid, the integral is not expected to be exact. Instead a threshold allowance is used such that integrals within a threshold of $\pm 2\pi$ are assumed to contain phase singularities.

The numerical method developed here is based on a path length of eight, along a three-by-three square around each point in the domain. The method makes use of certain computationally efficient operators known as convolution operators. A convolution operator is a matrix M applied to another matrix N via $*$, the convolution operator. M acts as a stencil, replacing each point in the matrix N with a linear

sum of its neighbours. For example if the matrix M were as follows,

$$M = \begin{pmatrix} 0 & 0 & 0 \\ 1 & 0 & 0 \\ 0 & 0 & 0 \end{pmatrix} \tag{2.17}$$

then the convolution operator would replace each point in N with its neighbour on the left. Convolution operators can be applied efficiently in Matlab using the `conv2` command.

The method is applied at some time point t, for which the domain of θ on a regular square grid can be thought of as a matrix $\theta[x, y]$. Two further matrices corresponding to the partial derivatives k_x and k_y are numerically calculated for each element of the matrix as follows:

$$k_x[x, y] = \nabla\theta_x[x, y] = \theta[x + 1, y] - \theta[x, y], \tag{2.18}$$

and

$$k_y[x, y] = \nabla\theta_y[x, y] = \theta[x, y + 1] - \theta[x, y]. \tag{2.19}$$

For efficient computation of $\frac{\partial k_y}{\partial x}$ and $\frac{\partial k_x}{\partial y}$, the following convolution operators are defined respectively as:

$$\nabla_x = \begin{pmatrix} -\frac{1}{2} & 0 & +\frac{1}{2} \\ -1 & 0 & +1 \\ -\frac{1}{2} & 0 & +\frac{1}{2} \end{pmatrix}, \nabla_y = \begin{pmatrix} +\frac{1}{2} & +1 & +\frac{1}{2} \\ 0 & 0 & 0 \\ -\frac{1}{2} & -1 & -\frac{1}{2} \end{pmatrix}. \tag{2.20}$$

They are combined with the convolution operator in the following way in order to calculate the curl of k:

$$(\nabla \times k) \cdot \hat{\mathbf{z}} = \left(\frac{\partial k_y}{\partial x} - \frac{\partial k_x}{\partial y} \right) \hat{\mathbf{z}} = \nabla_x * k_y + \nabla_y * k_x. \tag{2.21}$$

Since there is a branch cut in the phase angle between π and $-\pi$, care has to be taken when taking the difference in phase between adjacent matrix elements because a small change in phase could be computed as a large jump in the phase, if this is not corrected for. In order to account for this, instances of the differences k_x and k_y for which the absolute values are greater than π are changed to instead be the difference between their 2π complements, which is easily implemented using the matlab function `WrapTo2Pi`. For example, $k_x[x, y] = \nabla\theta_x[x, y] =$ `WrapTo2Pi`$(\theta[x + 1, y])$ − `WrapTo2Pi`$(\theta[x, y])$.

Longer path lengths can also be considered; for example, Bray and Wikswo

(2002b) give possible convolution operators for a path length of twelve. Using a longer path length may be less sensitive to noise, however this may also lead to a less accurately defined position (Iyer and Gray, 2001), and issues in the case that multiple phase singularities are contained within the contour. In Section 4.2.5, the effects of path length are investigated where a path of 5-by-5 is considered using the following convolution kernels:

$$\nabla_x = \begin{pmatrix} -\frac{1}{2} & 0 & 0 & 0 & +\frac{1}{2} \\ -1 & 0 & 0 & 0 & +1 \\ -1 & 0 & 0 & 0 & +1 \\ -1 & 0 & 0 & 0 & +1 \\ -\frac{1}{2} & 0 & 0 & 0 & +\frac{1}{2} \end{pmatrix}, \nabla_y = \begin{pmatrix} +\frac{1}{2} & +1 & +1 & +1 & +\frac{1}{2} \\ 0 & 0 & 0 & 0 & 0 \\ 0 & 0 & 0 & 0 & 0 \\ 0 & 0 & 0 & 0 & 0 \\ -\frac{1}{2} & -1 & -1 & -1 & -\frac{1}{2} \end{pmatrix}. \tag{2.22}$$

2.12 Phase mapping: phase interpolation

In Chapters 6 and 7, results for data on larger grid spacings need to be compared to those on smaller grid spacing; thus, phase interpolation is required. To avoid the issue of interpolation across the phase angle branch cut, it was necessary to convert the phase angle (θ) to exponential form ($e^{i\theta}$) before interpolation. The mapped data was then interpolated, and finally converted back to phase angles between $-\pi$ and π. This is shown in Fig. 2.6, comparing interpolating θ (left) with mapping to $e^{i\theta}$, interpolating, and then mapping back to θ (right). Errors associated with the phase discontinuities in the direct interpolation become significantly more pronounced as the resolution is reduced.

2.13 Isopotential line method for rotor tip tracking

Tracking the intersection of an isopotential line with the point of zero normal velocity is another technique developed to identify spiral (or rotor) tips (Section 1.13.6). This technique is implemented here in order to compare the spiral tip locations using different choices of isopotential line, to the phase singularity locations calculated using the method described in Sections 2.9 to 2.11.

The first challenge is to identify an isopotential line in discrete data. Since the model has been solved at discrete spatial points, positions where the voltage equals the chosen isopotential value lie in general between points at which the equation has been solved. This is particularly critical at the wavefront, since there is a steep

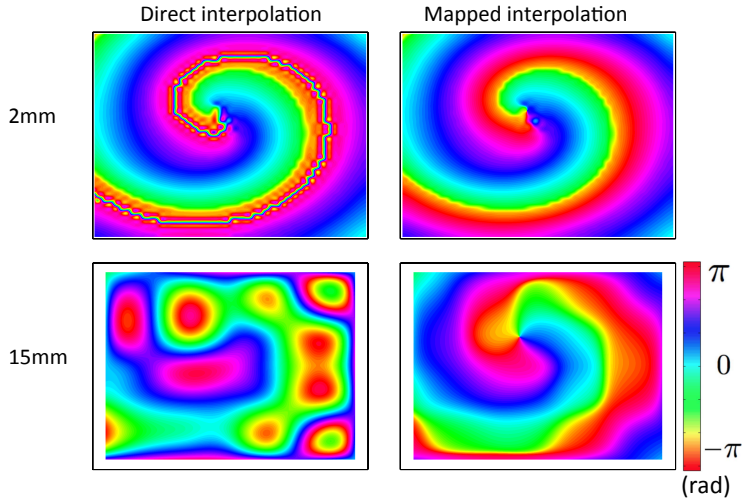

Figure 2.6: A mapping is introduced for phase interpolation. Direct interpolation of the phase angle θ leads to issues when interpolating, in the instance that neighbouring points are close to π and $-\pi$ (left). Mapping to the exponential form ($e^{i\theta}$), interpolating this and then converting back to a phase angle removes the issue with phase angle discontinuities (right). The errors become larger as the grid spacing is increased (bottom). The domain size shown here is 10cm-by-10cm.

change in voltage over a small area. Two methods were compared for circumventing this problem.

The first spatially interpolates the voltage, so that an additional 9 points are added between solution points, and then points in the mesh are logged if the voltage is within 0.3mV of the isopotential value. This gives a visually continuous isopotential line.

The second method does not involve any interpolation, but instead a point at (x, y) is logged at a time t if the following two criteria, from an approach suggested by Kay and Gray (2005), are satisfied:

1. $V(x, y) > V_{iso}$,
2. between one and three of the four pixels neighbouring (x, y) have a voltage which is less than V_{iso}.

This method produces a one pixel wide line of constant potential and has the advantage that is computationally fast. However, since the line follows the discreteness of a grid with 0.25mm inter-point distance, in this case, it is not smooth but rather step-like. Example isopotential lines with or without interpolation are shown in Fig. 2.7.

The second challenge is to find the point of zero temporal derivative. Points on the isopotential line were classified as either $\frac{\mathrm{d}V}{\mathrm{d}t} > 0$, $\frac{\mathrm{d}V}{\mathrm{d}t} < 0$, or indeterminate

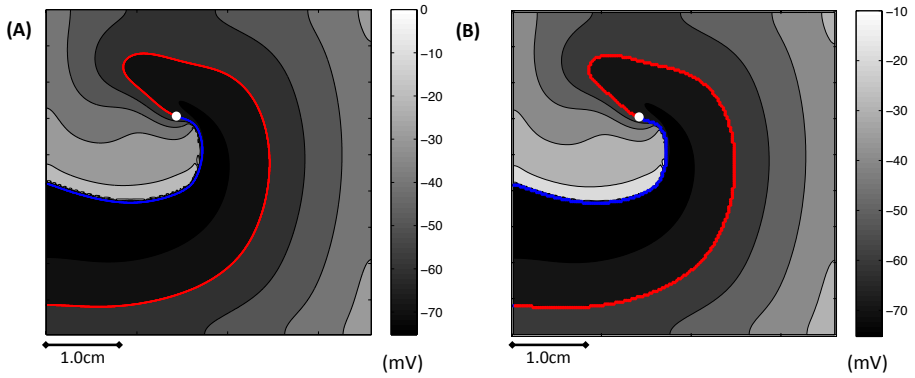

Figure 2.7: Isopotential line method of rotor-core identification. (A) Isopotential line using the Kay and Gray (2005) method on the interpolated data (0.1mm). (B) Isopotential line without any interpolation (0.25mm) using the Kay and Gray (2005) method. Waveback position is shown in red; while wavefront is shown in blue. The wave tip point where the wavefront and back meet is shown in white. The average distance between the two cases over the simulation is 0.4 mm.

(possible spiral tip positions). The motivation for this is that the isopotential line can be separated into two segments corresponding to the wavefront ($\frac{\mathrm{d}V}{\mathrm{d}t} > 0$) and waveback ($\frac{\mathrm{d}V}{\mathrm{d}t} < 0$), with the tip position as the intersection of these two lines (Fenton and Karma, 1998). Due to the discreteness of the data, points were not classified as wavefront or waveback based strictly on the $\frac{\mathrm{d}V}{\mathrm{d}t}$ value, but rather by the number of neighbouring pixels for which $\frac{\mathrm{d}V}{\mathrm{d}t} < 0$. Here a neighbourhood of eight neighbouring pixels was considered and a point at (x, y) was considered as part of the wavefront or waveback depending on the thresholds F and B.

1. if the number neighbours $< F$, then (x, y) is part of wavefront
2. if the number neighbours $> B$, then (x, y) is part of waveback
3. if $B <$ number neighbours $\leq F$, then (x, y) is tip

For the full resolution data, $F = 8$ and $B = 7$ were used.

Points for which a wavefront point is neighbouring a waveback point (from a neighbourhood of eight) are also classified as spiral tip. This method essentially finds the point of wave break, where the wave front meets the wave back. Examples of isopotential lines corresponding to different potentials are shown in Fig. 2.8.

Fenton et al. (2002) say that the Fenton and Karma (1998) isopotential line with zero temporal derivative method is independent of spatial resolution.

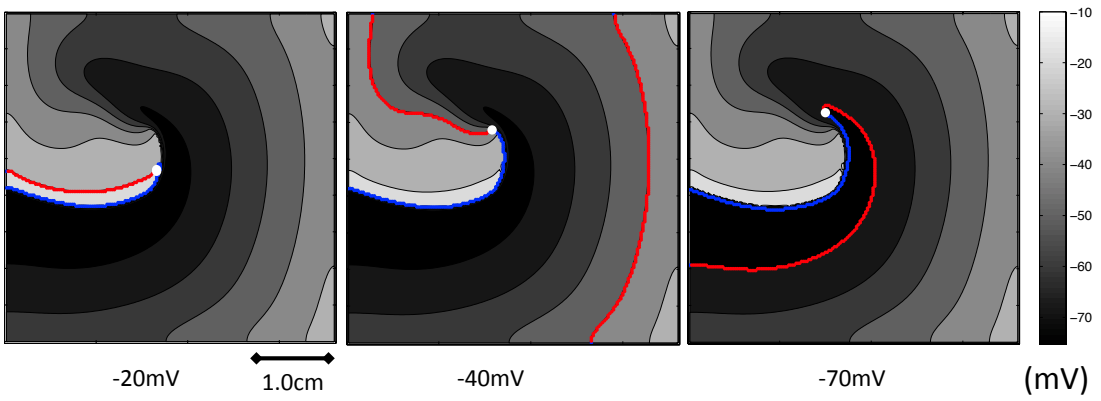

Figure 2.8: Different isopotential lines using the Kay and Gray (2005) method. Here the original data resolution is used (0.25mm).

2.14 Surface flattening

In order to visualise surface data in two dimensions and to apply two-dimensional algorithms to three-dimensional data, a surface flattening technique is applied to map surface data to the two-dimensional co-ordinates that best preserve geodesic distances. This application is motivated, presented, and the associated distance distortions are quantified, in the following sections. This work has been accepted for presentation at the IEEE Engineering in Medicine and Biology conference and will be published as conference proceedings; it is the work of the author unless stated otherwise.

2.14.1 Introduction

Electro-anatomic mapping systems and medical imaging used during clinical procedures for the treatment of atrial arrhythmias typically record measurements on the surface of the left atrium. These electrical and structural data are located in three dimensions on an anatomical surface representing the left-atrium. As such, visually interpreting data across the complete chamber requires multiple simultaneous views of the atrium. In addition, many algorithms developed to analyse such data are commonly designed to work with planar or volumetric data, rather than on anatomical surfaces. Examples of clinically relevant metrics include the spread of the electrical activation wavefront and its conduction velocity. In order to identify areas of slow conduction, indicated by the bunching of isochrones, or to calculate conduction velocity, distances need to be conserved.

Local analysis is frequently performed on a projection of the data onto a plane

of best fit when there is little surface curvature; for example, a single multipolar catheter on the posterior wall. However, this technique is not suitable for generating a projection of the entire atrium. Ventricle data are often projected onto a cone-shaped surface which is subsequently projected onto a circular two-dimensional polar plot (Nash et al., 2006), or a circumferential polar plot known as a *bull's eye* display (Cerqueira et al., 2002). Alternatively, a direct representation can be achieved by transforming from Cartesian coordinates (x, y, z) to spherical coordinates (θ, ϕ, r) and plotting in the θ-ϕ plane (Lou et al., 2008). A further technique is a parametric method used for optical mapping that initially fits to a finite element mesh using prolate spheroidal coordinates and then conduction velocity calculations are expressed in terms of the two local finite-element coordinates (Sung et al., 2000). These methods are more challenging to apply to the complicated atrial morphology.

Karim et al. (2014) applied a surface mesh parameterisation method to unfold the left atrium to a square using a technique which aims to preserve angles and areas; the mitral valve was mapped to the edges of the square, and other cuts performed so as to map the veins to the middle of the square. These requirements inevitably cause distance distortion, although the choice of the quantities to conserve will depend on the application. Zigelman et al. (2002) applied a surface flattening technique to arbitrary surfaces that minimised distance distortions, but did not specifically assess its use for the cardiac anatomy.

In this study, we apply a modified version of the Zigelman et al. (2002) technique to specifically map the left atrial surface to a two-dimensional representation. Distance distortion is quantified in the cases where the pulmonary veins are included or excluded from the mesh. This approach is applied to electro-anatomic mapping data (in Section 3.4.9) and to simulated fibrillation on a surface derived from magnetic resonance imaging (MRI) to illustrate its feasibility for left atrial analysis (in Section 7.4.3).

2.14.2 Mesh generation

All clinical data used in this thesis were obtained with informed consent under ethical approval from the Health Research Authority Ref 13/LO1169. Surface triangulations of the left atrium were obtained either through segmentation of MRI data using ITK-snap software (Yushkevich et al., 2006), or through exporting the geometry from the Ensite Velocity (St Jude Medical, Inc) electro-anatomic mapping system. Cuts were performed, using the mesh manipulation package Blender, on the closed surface at the mitral valve and the four pulmonary veins in order to produce a topologically accurate mesh of the atrial chamber and pulmonary vein sleeves. The

surface was remeshed using Gmsh to produce a coarser triangulation with elements of approximately equal characteristic length, suitable for use with a high-order spectral element discretisation (Cantwell et al., 2014b). MeshLab was used to create a second mesh, used for surface mapping, in which cuts were added on either side of the atrium from the mitral valve up to the ends of the pulmonary vein sleeves (see Figs. 2.9 and 2.10). MRI segmentation was performed by clinical electrophysiologist Dr Norman Qureshi, and the surface cuts were performed by masters student Konstantinos Tzortzis.

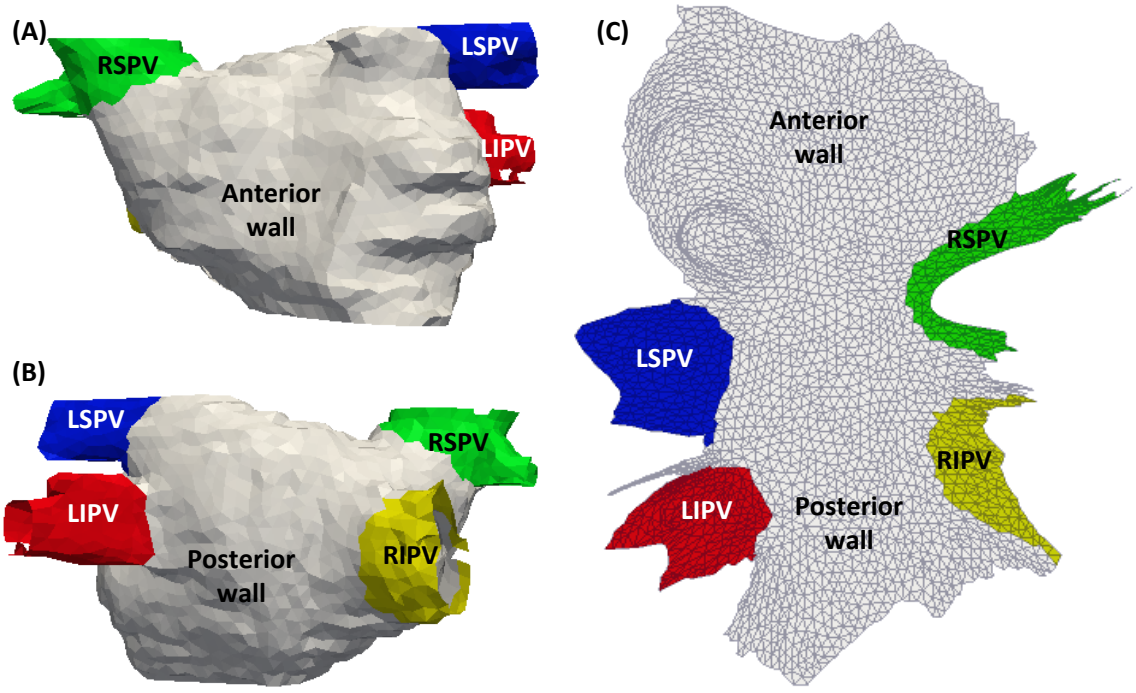

Figure 2.9: Example mapping of left atrium to two-dimensional surface representation. The left inferior (red), left superior (blue), right inferior (yellow) and right superior (green) pulmonary veins are indicated on the MRI-derived geometry (A, B) (which show an anterior and posterior view), as well as on the flattened representation (C). Distortion is identifiable in (C) by regions of irregular triangle size.

The three-dimensional coordinates of mesh vertices were mapped to a planar surface following the methodology of Zigelman et al. (2002) (see Section 2.14.3). Geodesic distances between all n vertices on the mesh were first calculated by using a fast marching algorithm (Peyre, 2015) (example path shown in Fig. 2.11(A)). This leads to an $n \times n$ distance matrix, D.

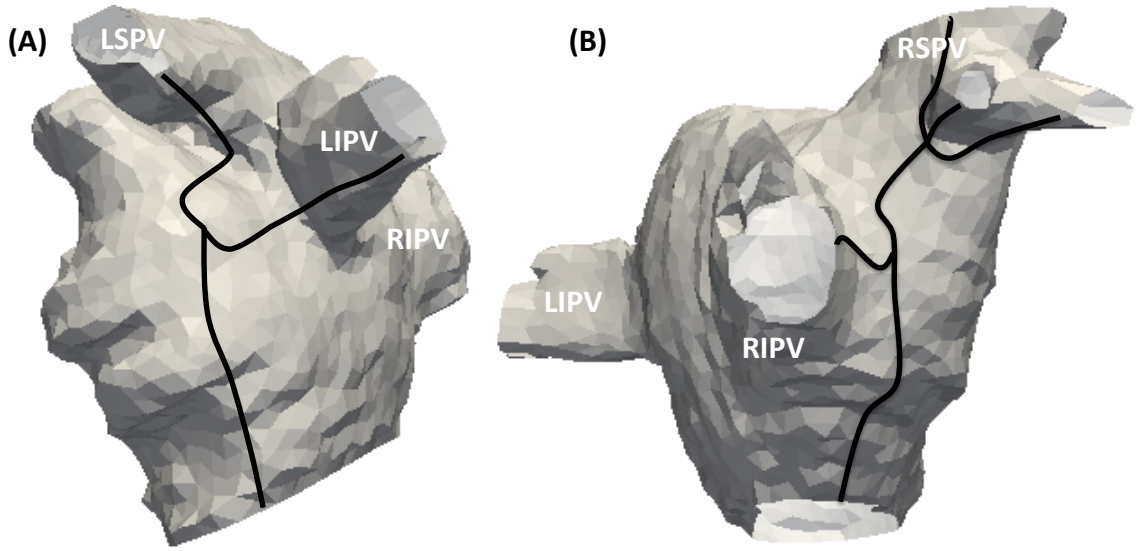

Figure 2.10: Cuts in the mesh from the mitral valve to the ends of the pulmonary vein sleeves, allowing a mapping which is distance-preserving.

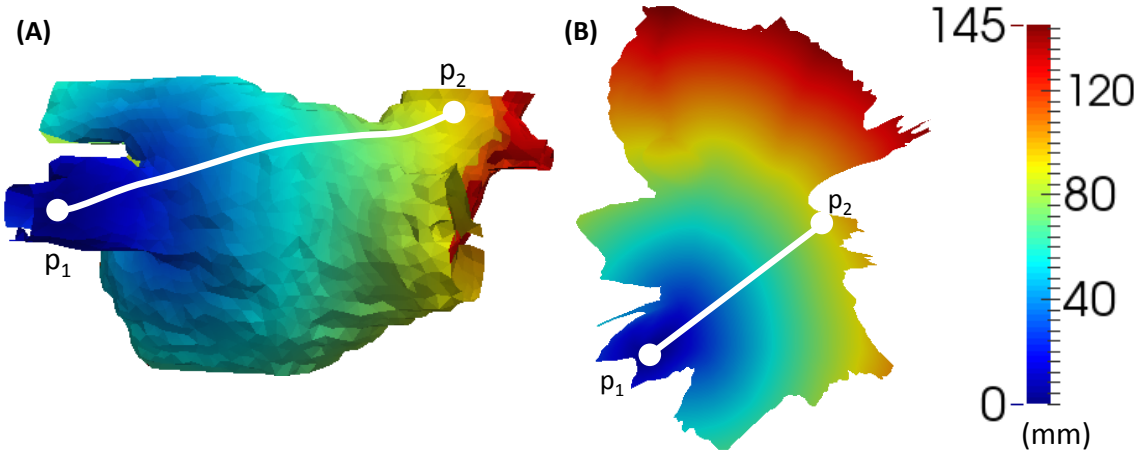

Figure 2.11: Example geodesic distance contours. (A) Geodesic distance contours calculated by solving an eikonal equation with a source point at the desired starting point (p_1). The path between two vertices (p_1 and p_2) is shown, and the corresponding Euclidean path in two-dimensions is shown in (B).

2.14.3 Distance-preserving mapping

A multi-dimensional scaling technique was then applied to map three-dimensional vertices onto a two-dimensional plane, in a way that best preserved D. The aim is to approximate D with a matrix of rank two. This is achieved using spectral decomposition, as the two eigenvectors with largest eigenvalues. The amount of error is indicated by the sizes of the remaining eigenvalues. This was implemented using the Matlab multidimensional scaling function `mdscale` and, in contrast to Zigelman et al. (2002) who used the strain loss function, we applied Sammon's nonlinear mapping criterion, since this was found to give an improved preservation of local distances. The output is a matrix of n two-dimensional coordinates.

2.14.4 Distance distortion measure

The distance distortion introduced by the surface flattening was quantified using both a local and global measure, and the impact of removing the pulmonary veins before and after mapping was investigated. *Local distortion* for a given vertex was defined as the mean absolute difference in the pre-mapping and post-mapping distances between the vertex and each immediate neighbour. *Global distortion* is defined similarly, but between all pairs of vertices in the mesh.

A map of localised distortion is shown in Fig. 2.12(A-C) for the same geometry as shown in Fig. 2.9. In this case, cuts are made from the mitral valve and along the length of each vein sleeve, as illustrated in Fig. 2.10. In general, there is higher local distortion in areas of increased surface curvature, particularly around the pulmonary veins. We next consider the impact on the mapping of the pulmonary vein sleeves by removing them entirely down to the atrial chamber. This case is shown in Fig. 2.12(D-F), which shows a substantial reduction in local distance distortion throughout the mesh. The highest distortion is now localised around the anterior wall in the vicinity of the atrial appendage. Finally, we examine a case where cuts are not made along the pulmonary vein sleeves (Fig. 2.12(G-I)), so as to display them as holes within the flattened geometry. This results in significantly higher local distortion around the lower posterior wall and atrial appendage.

The local and global distortions in the above three cases are quantified in the first three rows of Table 2.1. Cutting along the pulmonary vein sleeves and then removing them to the level of the atrial body produced the least distortion. In addition, we also measured the average local and global distortion of the mesh in the top row of Fig. 2.12, but with the veins removed from the unwrapped geometry, post mapping. This was found to be higher than when the veins are removed prior

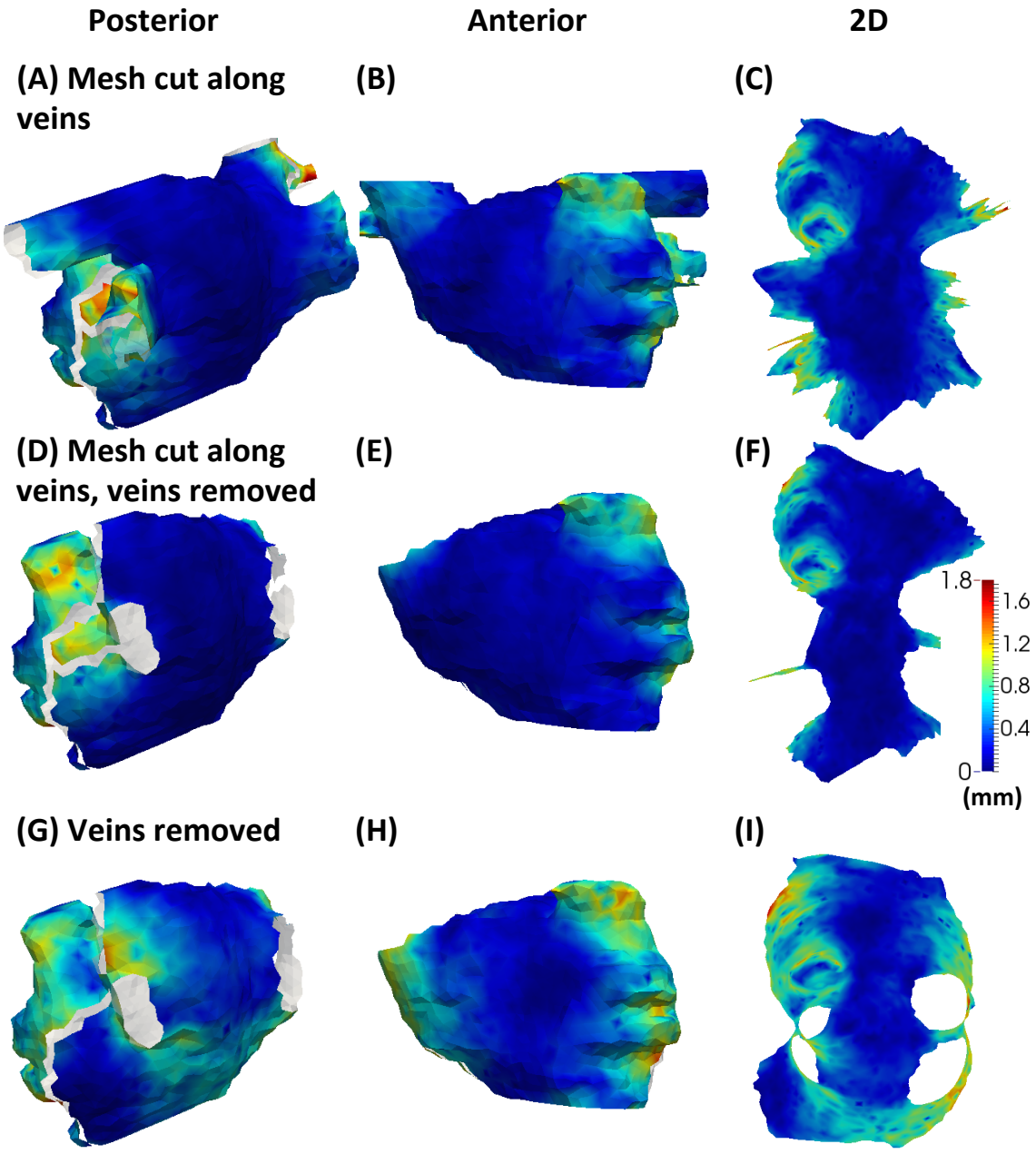

Figure 2.12: Localised distance distortion calculated using the Sammon mapping criterion with different cuts. (A-C) Mesh cut along the vein sleeves; (D-F) mesh cut along the vein sleeves together with the pulmonary veins removed to the level of the atrial body before flattening; (G-I) veins removed but no cuts along the vein sleeves.

Table 2.1: Average distance distortion (mm) under mappings

	Sammon		Strain	
	Local	Global	Local	Global
Mesh cut along veins	0.37	3.49	0.58	5.02
Mesh cut along veins, veins removed pre flat	0.28	2.34	0.50	3.29
Veins removed	0.49	5.51	0.65	5.72
Mesh cut along veins, veins removed post flat	0.31	2.89	0.49	3.34

to mapping (middle row of Fig. 2.12), indicating that the distortion is not localised to the veins but impacts the mapping of the entire geometry. Finally the distortions are shown in Table 2.1 for both the Sammon mapping criterion and the strain loss criterion used in Zigelman et al. (2002), where the Sammon criterion gives lower distance distortions in all cases.

2.15 Summary

Methods from the literature for solving the monodomain equation, for calculating pseudo-electrograms and for calculating restitution curves were presented. A technique for phase interpolation that offered increased robustness for decreased data resolution was presented in Section 2.12. Techniques for identifying rotor-cores as phase singularities were presented in Sections 2.9, 2.10 and 2.11, in which the technique developed by Bray and Wikswo (2002a) was modified to tag deflections based on both a window length and amplitude threshold. This offers more control over which deflections are considered activations, and the sensitivity of the algorithms to these parameters are investigated in Chapter 4 and Section A.1.1.

The methodology presented in Section 2.14 demonstrates a technique to visualise the left atrium in two-dimensions, with minimal distance distortion, which can also be applied to other chambers. The method is superior to existing methods in circumstances where it is important to preserve distances, such as for CV mapping. In addition, the method allows the application of two-dimensional algorithms, including interpolation and phase singularity tracking, and can be applied to improve the visualisation of phase singularity trajectories during fibrillation (see Fig. 7.24). This technique differed from that of Karim et al. (2014) since they aimed to preserve area and angles, and applied boundary conditions to fit the two-dimensional representation to a square. In this chapter, we allow a free boundary to minimise distance distortion. Cutting along the pulmonary vein sleeves and removing them

to the level of the atrial body minimised the distance distortion due to their high curvature. However, for some applications it may be important to include the veins in the map. The case in Fig. 2.12 (G-I) includes holes in the two-dimensional map representing the pulmonary veins, which is similar to the mapping of Karim et al. (2014). The effects of any distance distortion on calculated measures, including interpolation, could be reduced by weighting points by the degree of distance distortion.

Chapter 3

Wavefront velocity and focal source estimation from clinical multi-polar catheters

Part of this chapter has been published as conference proceedings; IEEE Engineering in Medicine and Biology (Roney et al., 2014a). The material presented herein is the work of the author, unless stated otherwise.

3.1 Introduction

Conduction velocity (CV), a quantitative electrophysiological measure that describes the speed of propagation of the action potential impulse across myocardium, provides important information about the underlying tissue, with areas with slower CV thought to represent more diseased myocardium (Kawara et al., 2001). Quantification of CV in clinical electrophysiology cases remains a major challenge, with no consensus on the optimal methods. A second major challenge in the cardiac catheter laboratory is the estimation of the direction and distance to a focal source during focal tachycardias to guide the ablation catheter towards that source.

As discussed in Section 1.12, the most appropriate technique to calculate CV depends on the spatial distribution of recording points (resolution and area of coverage), as well as the number of underlying wavefronts and their curvature. Existing methods include triangulation (Section 1.12.1), finite difference techniques (Section 1.12.2), polynomial surface fitting algorithms (Section 1.12.4), ensemble vector directional analysis (Section 1.12.7) and radial basis function interpolation (Section 1.12.8). However, many of these techniques have limited applicability to multipolar catheter data due to the small number of data points and irregular ar-

rangement of data. Alternatively, techniques may be too localised or computationally demanding.

Methods developed for CV estimation from multipolar clinical catheter recordings include the technique of Weber et al. (2010) which assumes a single macroscopic planar wavefront locally and estimates CV and wavefront direction from ten recordings of a circular catheter. However, wavefronts may not be planar, but rather exhibit curvature, especially in the case of a nearby focal source. In addition, catheters may be shapes other than circular; in particular a spiral-shaped or five-spline PentaRay catheter are commonly used, which may further deform upon myocardial contact.

In this chapter, the method of Weber et al. (2010) is extended in order to overcome these limitations and rapidly estimate CV and the location of the origin of a focal source, for either a planar or circular wavefront measured from any arbitrary arrangement of recording points. The algorithms are derived analytically and are tested on both numerically simulated data and on clinical recordings. The equations developed are for two-dimensional coordinates and initially the three-dimensional electrode locations are projected onto the plane of best fit, in order to apply the algorithms. The estimated focal source location in two dimensions is then projected to the closest point on the atrial geometry. This approach provided good results in the case that the focal source was close enough that the region containing the catheter and the focal source was approximately flat; however, the technique is less accurate in the case of high surface curvature, either below the catheter or between the catheter and focal source location. Hence, these techniques are then extended to instead work with surface geodesic distances, rather than three-dimensional Euclidean distances. This reduces the effect of errors caused by curvature underneath the catheter.

3.2 Methods: equation derivation

Conduction velocity algorithms are derived for either a planar or circular wavefront meeting either a circular, spiral or arbitrary arrangement of measuring points, giving a total of six cases. The approach for each of the six cases is similar and is as follows. In this section, we derive the equation for the activation time, t, of an arbitrary point. The equation is in terms of some distance R and the unknown time duration T required for the wavefront to propagate across the distance R. In Section 3.3, we use this equation to form a system of N equations for each of the N measuring points. These equations can be solved for the time T and any other

unknown parameters, and CV can be estimated as distance R divided by time T.

The cases involving circular or spiral catheters are particular instances of the case of an arbitrary arrangement of measuring points, and also a planar wavefront may be considered the limit of a circular wavefront originating a long distance away.

For these cases, the 3D coordinates of the electrode locations of the catheter are first mapped to 2D coordinates by either computing a plane of best fit onto which the points are orthogonally projected, or by finding the arrangement that best preserve the geodesic distances. The 2D electrode locations are denoted $\boldsymbol{x}_i = (x_i, y_i)$ and are ordered by their corresponding known time of activation, t_i.

3.2.1 Case 1: planar wavefront with circular catheter

We present here a derivation for the equation used in the method of Weber et al. (2010). We start with the equation of a plane wave, which is as follows:

$$u(z,t) = A_0 \cos(kz - \omega t + \varphi), \tag{3.1}$$

where varying the parameter z moves the point along lines that are perpendicular to the plane waves (the wave is travelling in the positive z direction); ω is the angular frequency of the wave; φ is the phase shift of the wave; and t is a point in time.

We track the wavefront $u(z,t) = A_0$. This holds when $kz - \omega t + \varphi = 0$, which implies that

$$t = \frac{k}{\omega} z + \frac{\varphi}{\omega}. \tag{3.2}$$

Referring to Fig. 3.1, let R be the radius of the circular catheter, and take the origin $z = 0$ to be at the point where the plane wave first crosses the circular catheter, which does not necessarily correspond to a measuring point. We define ϕ to be the angle of inclination of the z axis, which gives the angle of wave propagation. Angle θ parametrises the circle and the z coordinate of points on the circle can be expressed in terms of θ, where z represents the perpendicular distance travelled by the wavefront when it reaches the given measuring point.

For the lower half plane (Fig. 3.1 (A)), define $\hat{\theta} = \phi - \theta + \pi$, then:

$$z = R - R\cos\hat{\theta}. \tag{3.3}$$

For the upper half plane (Fig. 3.1 (B)), define $\hat{\theta} = \phi - \theta$, then:

$$z = R + R\cos\hat{\theta}. \tag{3.4}$$

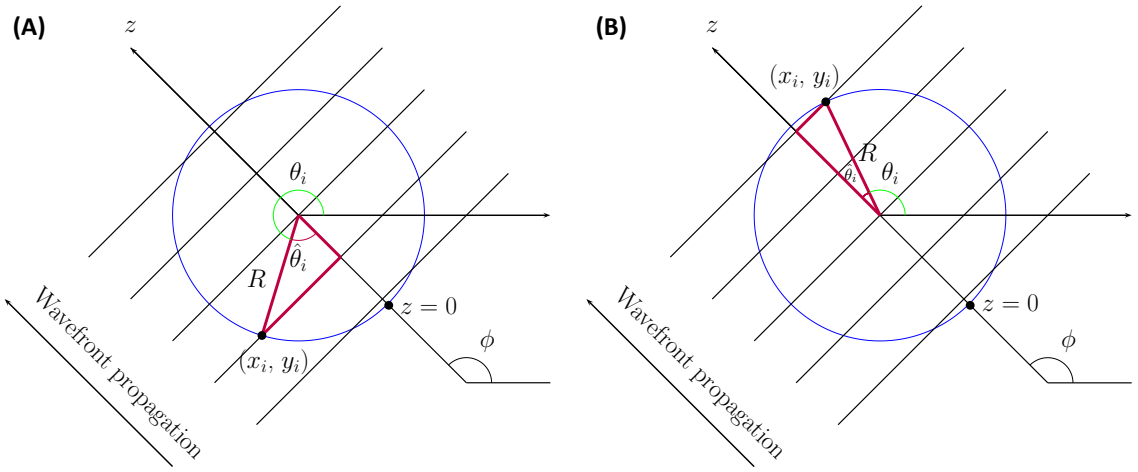

Figure 3.1: Planar wavefront and circular catheter. (A) Case in which the measuring point (x_i, y_i) is the lower half plane; (B) Case in which the measuring point (x_i, y_i) is the upper half plane. The parameter z represents the perpendicular distance travelled by the wavefront when it reaches the given measuring point, where $z = 0$ at the earliest measuring point; R is the radius of the circular catheter; ϕ is the angle of inclination of the z axis; and θ_i gives the angle of the measuring point (x_i, y_i) on the circular catheter.

We combine these conditions, to give for the lower half plane $z = R - R\cos(\phi - \theta + \pi) = R + R\cos(\phi - \theta)$. Thus, in general:

$$z = R(1 + \cos(\phi - \theta)), \tag{3.5}$$

and Equation 3.2 becomes for our system of recording points (x_i, y_i) with times t_i:

$$t_i = \frac{kR}{\omega}\left(1 + \cos(\phi - \theta_i)\right) + \frac{\varphi}{\omega}. \tag{3.6}$$

We now apply boundary conditions. Let t_c be the activation time of the centre of the circular catheter and T be the time taken for the wave to travel from the edge of the catheter to the centre, then at $z = 0$, $t = t_c - T$; thus substituting in to Equation 3.2, we see that $\frac{\varphi}{\omega} = t_c - T$. For the second boundary condition, we use that at $z = R$, $t = t_c$, which implies that $t_c = \frac{k}{\omega}R + (t_c - T) \implies \frac{k}{\omega} = \frac{T}{R}$. So, $t = \frac{T}{R}(R + R\cos(\phi - \theta)) + t_c - T$, and we have a final expression for t_i

$$t_i = t_c + T\cos(\phi - \theta_i), \tag{3.7}$$

with $CV = \frac{R}{T}$ and angle of wavefront propagation ϕ.

3.2.2 Case 2: planar wavefront with spiral catheter

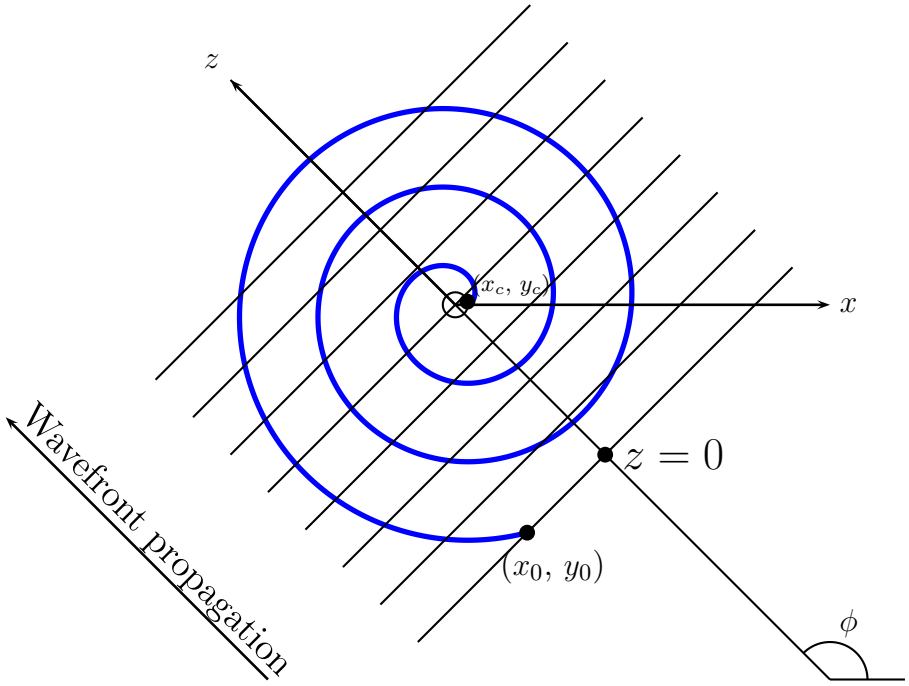

Figure 3.2: Planar wavefront and spiral catheter.

Next we consider the case of a planar wavefront meeting a spiral catheter, where the spiral catheter is modelled as an involute of a circle. The involute of a circle is the spiral traced out by the end of a piece of thread kept taut as it is unwrapped around a reel. It has the property that the line segment from any point on the involute to the centre circle, which is tangent to the centre circle has length equal to the radius of the centre circle multiplied by the angle, since it is equal to the length of unwound thread. It has the cartesian equations:

$$x = a(\cos\theta + \theta\sin\theta) \tag{3.8}$$

$$y = a(\sin\theta - \theta\cos\theta), \tag{3.9}$$

where a is the radius of the centre circle and θ is the angle in radians.

We use the same approach as for Case 1, converting recording points on the spiral to a z value, where the z parameter is the distance traversed perpendicular to the plane waves. Referring to Fig. 3.2, we measure θ from the positive x-axis about the centre of the involute circle. As for case 1, we set $z = 0$ at the point where the plane wave first crosses the spiral catheter (which again does not necessarily correspond to a measuring point). We define ϕ to be the angle of inclination of the z line, which

again gives the angle of propagation of the planar wavefront.

First we find the perpendicular distance R from the centre of the catheter to where the wave first meets the spiral catheter, perpendicular to the direction of wavefront propagation (see Fig. 3.3). We will use this distance to set $z = 0$ for the point where the plane wave first crosses the spiral catheter, and consider other points relative to this. See Fig. 3.3 for the two similar triangles we consider to find R.

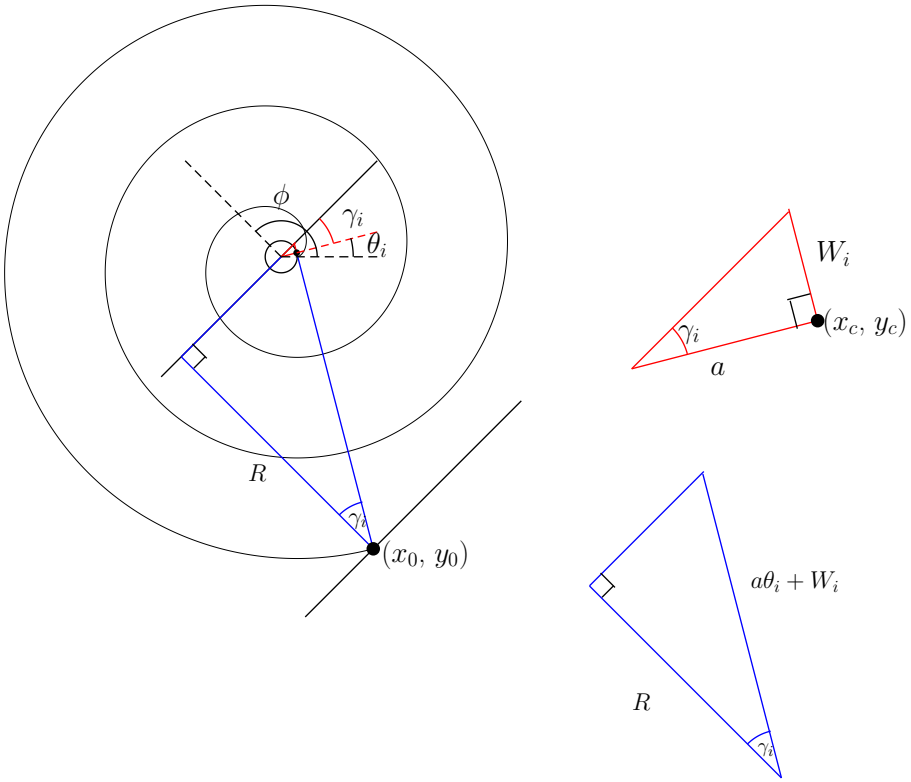

Figure 3.3: Planar wavefront and spiral catheter: trigonometry.

To find R in the large blue triangle (Fig. 3.3), we need to find W_i using the small triangle (shown in red in Fig. 3.3). The small triangle is a right angled triangle, since a tangent to the circle will meet the radius at a right angle (at point (x_c, y_c) in Fig. 3.3); by trigonometry, $W_i = a \tan \gamma_i$. Then for the second triangle we have $R_i = (a\theta_i + W_i) \cos \gamma_i$. Substituting in our equation for W_i, we have $R_i = (a\theta_i + a \tan \gamma_i) \cos \gamma_i = a\theta_i \cos \gamma_i + a \sin \gamma_i$. Now we also have that $\gamma_i = \phi - \frac{\pi}{2} - \theta_i$, and so $R_i = a\theta_i \cos(\phi - \frac{\pi}{2} - \theta_i) + a \sin(\phi - \frac{\pi}{2} - \theta_i)$, or

$$R_i = a\theta_i \sin(\phi - \theta_i) - a \cos(\phi - \theta_i). \tag{3.10}$$

Thus the distance to the centre of the involute circle is $a\theta_0 \sin(\phi - \theta_0) - a \cos(\phi - \theta_0)$,

where θ_0 is the angle for the point of earliest activation. Since z is defined as the distance from this point,

$$z = a\theta_0 \sin(\phi - \theta_0) - a\cos(\phi - \theta_0) - (a\theta \sin(\phi - \theta) - a\cos(\phi - \theta)). \tag{3.11}$$

Similarly it can be shown that this holds in all quadrants.
As for case 1, $t = \frac{k}{\omega}z + \frac{\varphi}{\omega}$. Define T to be the difference between the time that the planar wave first hits the catheter and the time when the wave crosses the centre of the involute circle (t_c); then at $z = 0$, $t = t_c - T \implies t = \frac{k}{\omega}z + (t_c - T)$.
Also at $z = a\theta_1 \sin(\phi - \theta_0) - a\cos(\phi - \theta_0) := R$, $t = t_c$, which implies that $\frac{k}{\omega} = \frac{T}{R}$.
Substituting, we have $t = \frac{T}{R}z + (t_c - T) = \frac{T}{R}(R - a\theta\sin(\phi - \theta) + a\cos(\phi - \theta)) + t_c - T$.
Hence simplifying, for a point at (x_i, y_i) with measuring time t_i:

$$t_i = t_c + \frac{T}{R}(a\cos(\phi - \theta_i) - a\theta_i \sin(\phi - \theta_i)), \tag{3.12}$$

where a is the radius of the circle, t_c is the activation time of the centre of the catheter, T_1 is the time at which the plane wave first crosses the catheter, $T = t_c - T_1$, and $R = a\theta_1 \sin(\phi - \theta_0) - a\cos(\phi - \theta_0)$, where θ_0 is the angle parameterising the point on the spiral where the plane wave first hits the spiral.

For a measure of CV we consider the time it takes for the wave to travel from the point at which it first meets the catheter to the centre point, as we know this distance is R.

$$CV = \frac{a\theta_0 \sin(\phi - \theta_0) - a\cos(\phi - \theta_0)}{T_1 - t_c} = \frac{R}{T}. \tag{3.13}$$

We assume that a and θ_i are known from the catheter and then fit to estimate t_c, T, R and ϕ_0.

3.2.3 Case 3: circular wavefront emanating from a point source with circular catheter

We start with the equation of a circular point source wave:

$$u(x, y, t) = A_0 \cos(k\sqrt{x^2 + y^2} - \omega t + \varphi), \tag{3.14}$$

where varying the parameter $z = \sqrt{x^2 + y^2}$ moves the point along rays, which are defined as being rays perpendicular to the waves, and originating from the point source, $\mathbf{s} = (s_x, s_y)$. Compare this to the plane wave where the parameter z corresponds to different translations; here it is different rays with the origin at $\mathbf{s}$. Again, the radius of the circular catheter is defined to be R.

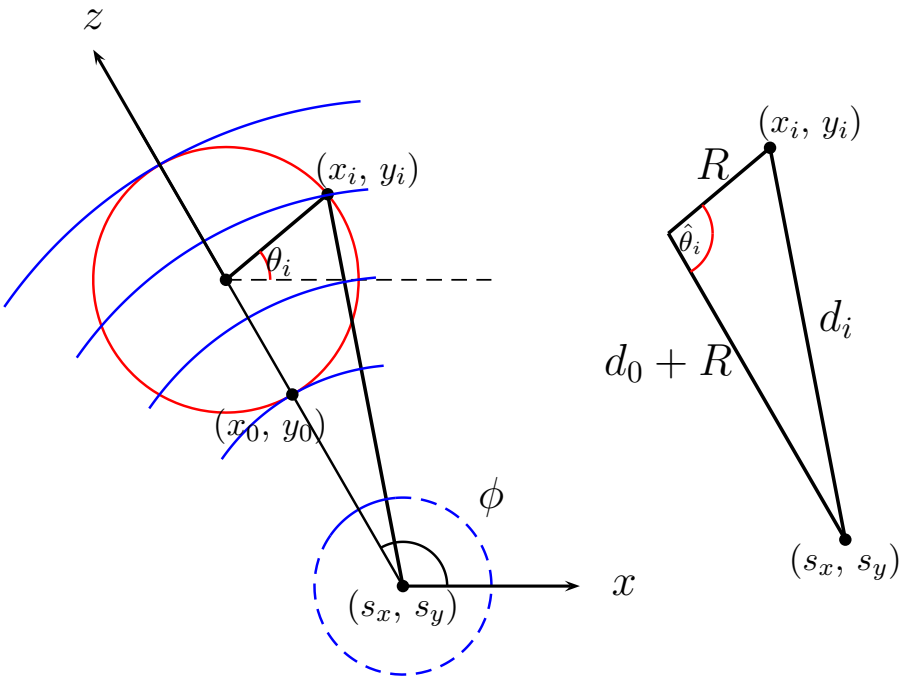

Figure 3.4: Circular wavefront and circular catheter.

Thus we assume that the waves emanate from the point **s**, and are arcs with centre that point. We define ϕ to be the angle of the ray from the point source which crosses the centre of the circular catheter (which will also cross the point of earliest contact – by symmetry of the circular catheter).

Referring to Fig. 3.4, let d_0 be the distance along this ray from the point source **s** to the point at which the plane wave first crosses the catheter (x_0, y_0); then we can form the triangle with sides $d_0 + R$, R and d_i, where d_i is then the radius of the arc which intersects the circle at the measuring point (x_i, y_i). This triangle has angle $\hat{\theta}_i$ between the sides $d_0 + R$ and R. As for case 1, we parametrise the circle using θ_i in the usual way. Thus d_i corresponds to the distance along the $z = \sqrt{x^2 + y^2}$ axis that we need for the point on the circle at some angle θ_i.

Using the cosine rule on this triangle, we find d_i: $d_i^2 = R^2 + (d_0 + R)^2 - 2R(d_0 + R)\cos\hat{\theta}_i$

$$d_i = \sqrt{R^2 + (d_0 + R)^2 - 2R(d_0 + R)\cos\hat{\theta}_i}, \tag{3.15}$$

where $\hat{\theta}_i = \pi + \theta_i - \phi_0$. As for cases 1 and 2, we track the wavefront by considering when $u(x, y, t) = A_0$, implying $k\sqrt{x^2 + y^2} - \omega t + \varphi = 0$. So,

$$t = \frac{k}{w}\sqrt{x^2 + y^2} + \frac{\varphi}{\omega}. \tag{3.16}$$

We now apply boundary conditions: when $\sqrt{x^2+y^2} = d_0 + R$, then $t = t_c$ and so

$$t_c = \frac{k}{w}(d_0 + R) + \frac{\varphi}{\omega}. \tag{3.17}$$

As a second boundary condition, when $\sqrt{x^2+y^2} = d_0$, then $t = t_c - A$, which gives

$$t_c - T = \frac{k}{w}d_0 + \frac{\varphi}{\omega}. \tag{3.18}$$

Equation 3.17 minus equation 3.18 gives $T = \frac{k}{w}R$, then substituting this in equation 3.17 $\implies$ $t = \frac{T}{R}\sqrt{x^2+y^2} - \left(\frac{T}{R}(d_0 + R) - t_c\right)$. Thus we have the final expression for t_i,

$$t_i = t_c - \frac{T}{R}(d_0 + R - \sqrt{x_i^2 + y_i^2}) \tag{3.19}$$

where $\sqrt{x_i^2+y_i^2} = \sqrt{R^2 + (d_0+R)^2 - 2R(d_0+R)\cos\hat{\theta}_i}$, (from Equation 3.15) and $\hat{\theta}_i = \pi + \theta_i - \phi_0$, where θ_i is the angle that parameterises the circular catheter at (x_i, y_i). We assume that R and θ_i are known from the catheter, and fit to find t_c, T, d_0, ϕ. The conduction velocity is R divided by T.

3.2.4 Case 4: circular wavefront emanating from a point source with spiral catheter

We start with the equation of a circular point source wave:

$$u(x, y, t) = A_0 \cos(k\sqrt{x^2+y^2} - \omega t + \varphi), \tag{3.20}$$

where the $z = \sqrt{x^2+y^2}$ parameter is the distance from the point source. Thus we assume that the waves emanate from a point $\mathbf{s} = (s_x, s_y)$ and are arcs, with centre that point. As before, we define ϕ to be the angle of the ray from the point source $\mathbf{s}$ which crosses the centre of the involute circle.

Referring to Fig. 3.5, letting the distance along the ray from the point source $\mathbf{s}$ to the centre of the catheter be R and considering a measuring point (x_i, y_i), we can form the triangle with sides R, r_i and d_i, where d_i is the radius of the arc which intersects the involute of a circle at the point corresponding to angle θ_i, where θ parameterises the involute of a circle. The distance d_i corresponds to the distance from the point source to the measuring point (x_i, y_i) at angle θ_i. The angle between R and r_i is defined as $\hat{\theta}_i$.

We first find r_i which is the length of the vector from the centre of the circle for the involute, to the point (x_i, y_i) on the trajectory. Letting (X_i, Y_i) be cartesian

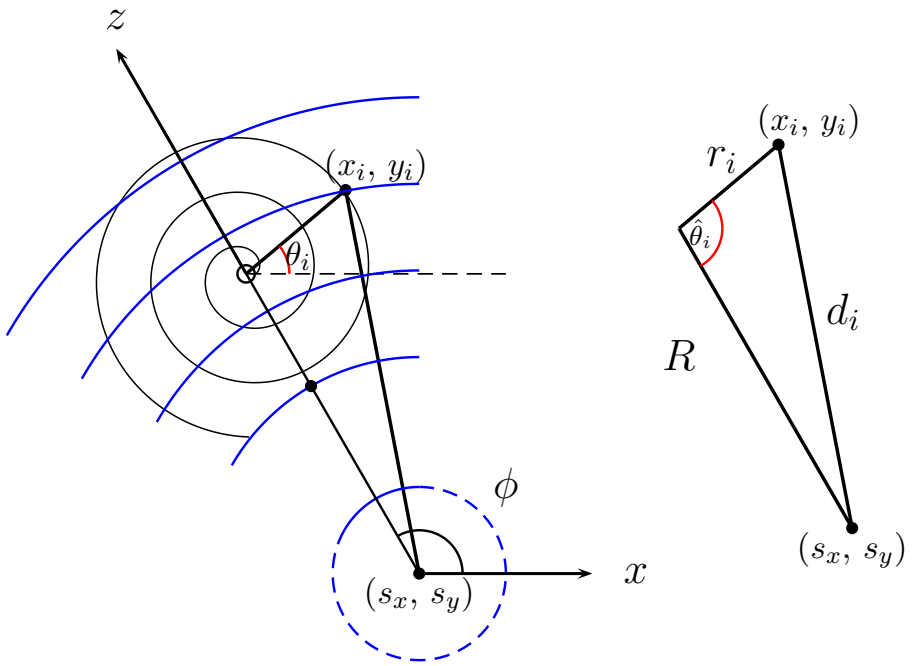

Figure 3.5: Circular wavefront and spiral catheter.

coordinates for (x_i, y_i) with origin relocated to the centre of the circle of the involute, then:

$$X_i = a(\cos\theta_i + \theta_i \sin\theta_i) \tag{3.21}$$

$$Y_i = a(\sin\theta_i - \theta_i \cos\theta_i). \tag{3.22}$$

Then the distance to centre of circle is $\sqrt{X_i^2 + Y_i^2}$, which simplifies to $a\sqrt{1+\theta_i^2}$. Thus $r_i = a\sqrt{1+\theta_i^2}$. We also have $\hat{\theta}_i = \pi + \theta_i - \phi$. So now we use the cosine rule to find d_i:

$$d_i^2 = r_i^2 + R^2 - 2Rr_i\cos\hat{\theta}_i = a^2(1+\theta_i^2) + R^2 - 2Ra\sqrt{1+\theta_i^2}\cos\hat{\theta}_i.$$

Thus,

$$\sqrt{x_i^2 + y_i^2} = \sqrt{a^2(1+\theta_i^2) + R^2 - 2Ra\sqrt{1+\theta_i^2}\cos\hat{\theta}_i}. \tag{3.23}$$

As for cases 1 and 2, we track the wavefront by considering when $u(x, y, t) = A_0$, so when $k\sqrt{x^2+y^2} - \omega t + \varphi = 0 \implies t = \frac{k}{w}\sqrt{x^2+y^2} + \frac{\varphi}{\omega}$.

We now apply the boundary conditions:
when $\sqrt{x^2+y^2} = 0,\ \ t = \hat{T} \implies \hat{T} = \frac{\varphi}{\omega} \implies t = \frac{k}{w}\sqrt{x^2+y^2} + \hat{T}$.
Also when $\sqrt{x^2+y^2} = R,\ \ t = t_c \implies t_c = \frac{k}{\omega}Y + \hat{T} \implies \frac{k}{\omega} = \frac{t_c - \hat{T}}{Y}$.

Hence we have the final expression:

$$t_i = \hat{T} + \frac{t_c - \hat{T}}{R}\sqrt{a^2(1+\theta_i^2) + R^2 - 2Ra\sqrt{1+\theta_i^2}\cdot\cos(\pi + \theta_i - \phi)} \tag{3.24}$$

where θ_i is the angle that parameterises the spiral catheter at (x_i, y_i) and R is the distance from the point source to the centre of the catheter. We assume that a and θ_i are known from properties of the spiral catheter, and we fit to find $\hat{T}$, R, t_c and ϕ. Here $CV = \frac{R}{t_c - \hat{T}} = \frac{R}{T}$, where $T = t_c - \hat{T}$.

3.2.5 Case 5: planar wavefront with arbitrary measuring points

Again we start with the equation of a plane wave:

$$u(z,t) = A_0\cos(kz - \omega t + \varphi), \tag{3.25}$$

where varying the z parameter moves the point along lines that are perpendicular to the plane waves (the wave is travelling in the positive z direction); φ is the angular frequency of the wave; ϕ is the phase shift of the wave; and t is a point in time.

We track the wavefront $u(z,t) = A_0$. This holds when $kz - \omega t + \varphi = 0$, which implies that

$$t = \frac{k}{\omega}z + \frac{\varphi}{\omega}. \tag{3.26}$$

Referring to Fig. 3.6, we let the earliest point of activation (x_0, y_0) correspond to $z = 0$, and then find a general expression for the perpendicular distance X_i from the earliest measuring point (x_0, y_0) to an arbitrary measuring point, (x_i, y_i). The angle within the triangle shown is $\gamma_i = \phi - \theta_i$. Then $X_i = r_i\cos\gamma_i = r_i\cos(\phi - \theta_i)$, and $r_i = \sqrt{(y_i - y_0)^2 + (x_i - x_0)^2}$.
Thus

$$X_i = \sqrt{(y_i - y_0)^2 + (x_i - x_0)^2}\cos(\phi - \theta_i), \tag{3.27}$$

where $\theta_i = \arctan\left(\frac{y_i - y_0}{x_i - x_0}\right)$. We can simplify using the fact that:

$$\cos(\phi - \arctan\left(\frac{y_i - y_0}{x_i - x_0}\right)) = \cos(\phi)\cos(\arctan\left(\frac{y_i - y_0}{x_i - x_0}\right)) + \sin(\phi)\sin(\arctan\left(\frac{y_i - y_0}{x_i - x_0}\right))$$

$$= \cos(\phi)\frac{1}{\sqrt{1 + (\frac{y_i - y_0}{x_i - x_0})^2}} + \sin(\phi)\frac{\frac{y_i - y_0}{x_i - x_0}}{\sqrt{1 + (\frac{y_i - y_0}{x_i - x_0})^2}}$$

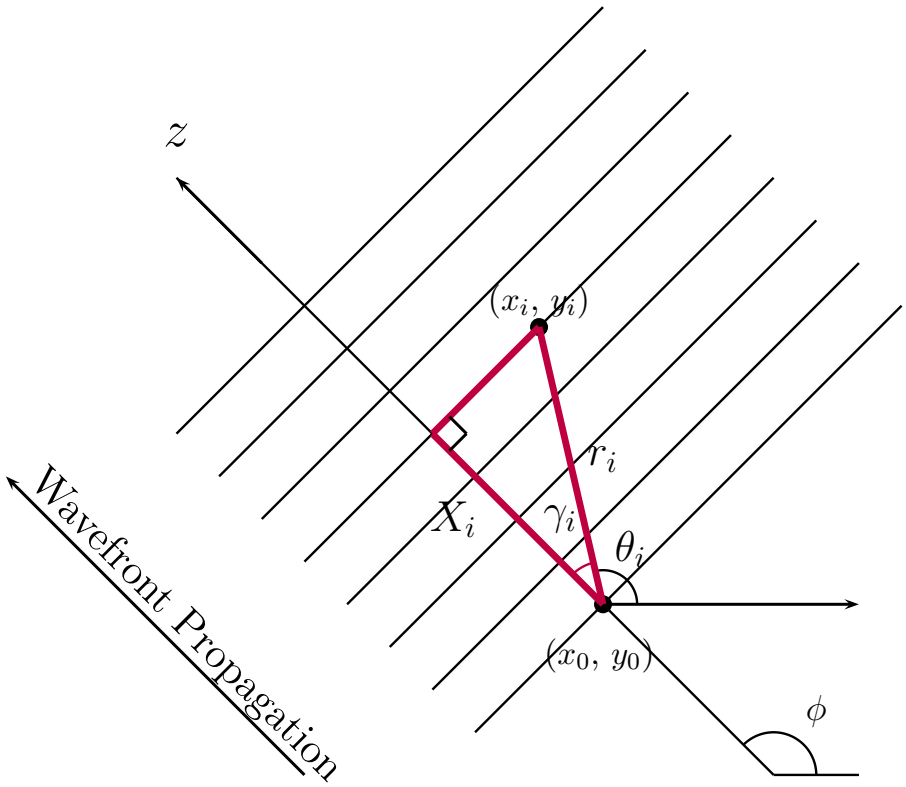

Figure 3.6: Planar wavefront and arbitrary arrangement of measuring points.

$$= \cos(\phi)\frac{x_i - x_0}{\sqrt{(x_i - x_0)^2 + (y_i - y_0)^2}} + \sin(\phi)\frac{y_i - y_0}{\sqrt{(x_i - x_0)^2 + (y_i - y_0)^2}}.$$

Thus,

$$X_i = \cos(\phi)(x_i - x_0) + \sin(\phi)(y_i - y_0). \tag{3.28}$$

We now apply the boundary condition $t = T_0$ at $z = 0$ and define $\alpha = \frac{k}{\omega}$ which imply that $t = T_0 + \alpha z$.
Thus,

$$t_i = T_0 + \alpha\cos(\phi)(x_i - x_0) + \alpha\sin(\phi)(y_i - y_0), \tag{3.29}$$

where T_0 is the earliest activation time, (x_0, y_0) is the earliest measuring point, $\alpha = \frac{k}{\omega}$ and ϕ_0 is the inclination of a line perpendicular to the wavefronts.

To calculate CV, we need to find the X distance of the first and last measuring points to be activated, then $CV = \frac{z_{t_{\max}} - z_0}{t_{\max} - T_0}$.

3.2.6 Case 6: circular wavefront with arbitrary measuring points

We derive equations for a circular wavefront measured at an arbitrary arrangement of points.

Modelling the wavefront as originating from the unknown point $\boldsymbol{s} = (s_x, s_y)$, at the unknown time T, and propagating with unknown constant speed v, then we expect an activation time at $\boldsymbol{x_i}$ of

$$\hat{t}_i = T + \frac{||\boldsymbol{x}_i - \boldsymbol{s}||}{v}. \tag{3.30}$$

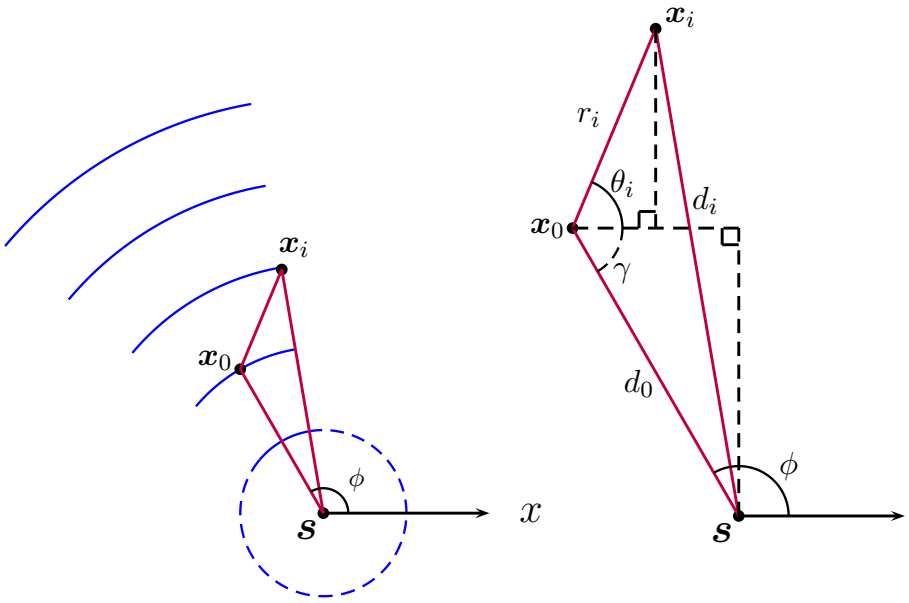

Figure 3.7: Circular point source at $\boldsymbol{s}$ measured at an arbitrary arrangement of recording points $\boldsymbol{x}_i$. Local radius of curvature d_i computed for each electrode. Length r_i is the distance to the earliest activated electrode $\boldsymbol{x}_0$.

We express this equation in terms of the unknown parameters ϕ, the angle subtended at $\boldsymbol{s}$ by the x-axis and the earliest measuring point $\boldsymbol{x}_0$, and the radius of curvature $d_0 = ||\boldsymbol{x}_0 - \boldsymbol{s}||$. Referring to Fig. 3.7, the distance d_i from $\boldsymbol{s}$ to the point $\boldsymbol{x}_i$, can be expressed in terms of ϕ, d_0 and the electrode location, using the cosine rule, as

$$\begin{aligned} d_i^2 &= d_0^2 + r_i^2 - 2d_0 r_i \cos(\theta_i + \gamma) \\ &= d_0^2 + r_i^2 + 2d_0 \left[(x_i - x_0)\cos\phi + (y_i - y_0)\sin\phi\right], \end{aligned} \tag{3.31}$$

where $r_i = ||\boldsymbol{x}_i - \boldsymbol{x}_0||$. Combining (3.30) and (3.31), we have that

$$\hat{t_i} = \beta_0 + \beta_1 \sqrt{(\beta_2^2 + \beta_3^2) + 2(\beta_2 X_i + \beta_3 Y_i) + Z_i}. \tag{3.32}$$

Here, $X_i = x_i - x_0$, $Y_i = y_i - y_0$, $Z_i = r_i^2$, and the coefficients $\boldsymbol{\beta} = [T,\ v^{-1},\ d_0 \cos\phi_0,\ d_0 \sin\phi_0]^\top$.

3.3 Methods: implementation and testing

The developed algorithms were tested on simulated data and applied to clinical data. As an overview of the methodology, electrode locations in three dimensions were converted to two dimensions by either projecting to the two-dimensional plane of best fit, or by finding the two-dimensional arrangement that best preserves geodesic distances in the locality of the catheter. The planar and circular algorithms were then applied with the data input of the two-dimensional locations, along with their activation times, to estimate the conduction velocity, wavefront direction and focal source location. These steps are outlined in Fig. 3.8 and detailed in the following sections.

3.3.1 Fitting the measuring positions to a plane

Two methods were compared for representing the 3D coordinates of the electrode locations in 2D. First, orthogonally projecting to the plane of best fit, and second using geodesic distances (the *geodesic method*, described in Sections 2.14 and 3.3.2). The projected electrode locations are denoted $\boldsymbol{x}_i = (x_i, y_i)$ and are ordered by their corresponding known time of activation, t_i.

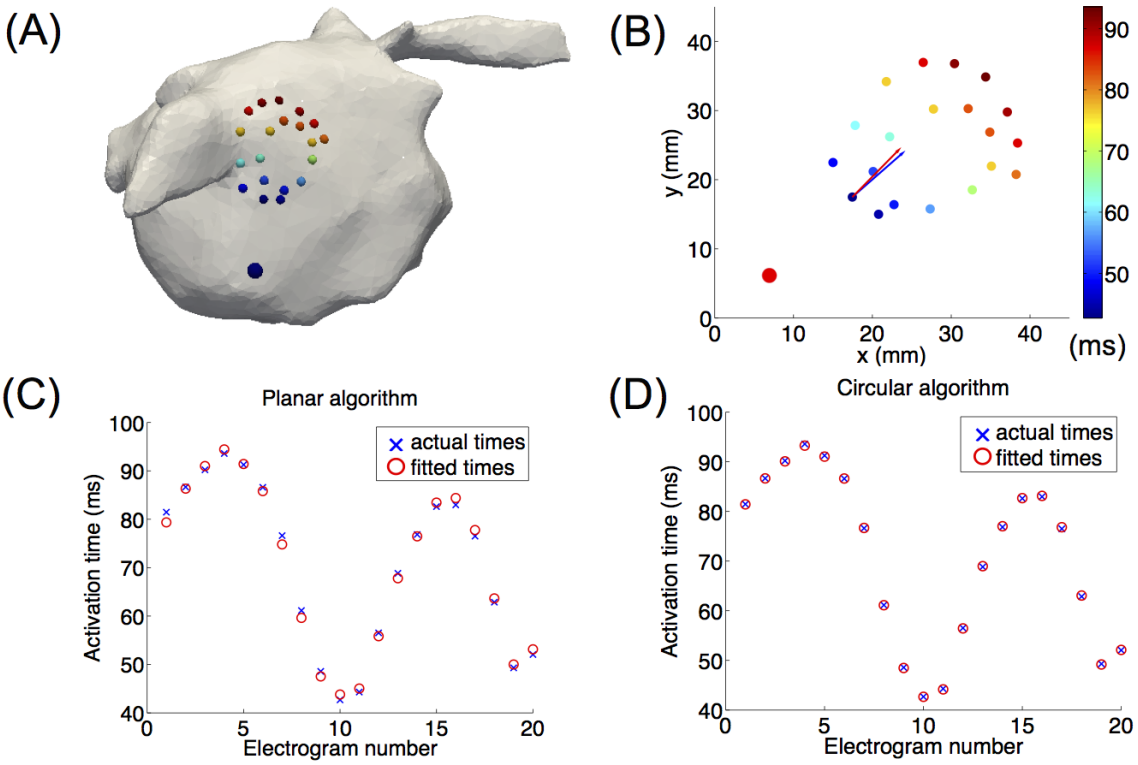

Figure 3.8: Methodology for calculating conduction velocity from anatomically accurate left atrial simulation data. (A) Left atrial patient geometry showing locations of a focal source (black dot), and one catheter position, coloured by activation time. (B) Projected 2D electrode locations with arrows showing wavefront direction for planar (blue) and circular (red) algorithms, and estimated focal source position (red dot). (C, D) show the activation times and fitted activation times for the planar and circular wave algorithms, respectively.

3.3.2 Calculating geodesic distances

In the case that the surface exhibits a high degree of curvature in the locality of the catheter or between the catheter and the focal source location, the method of projecting to a plane may not be appropriate. For example, if the catheter were located on a different side of the atrium to the focal source, a geodesic method would be required. An example of this is shown in Fig. 3.9(A), in which the catheter is on a curved part of the geometry and is also on a different side of the geometry. The geodesic method was used to reduce the dimensionality of the 3D co-ordinates to 2D space, using a representation that best preserves the geodesic distances in the locality of the catheter. The method of surface flattening using geodesic distances presented here follows Zigelman et al. (2002), and is presented in more detail in Section 2.14. Here, the two-dimensional plane method did not predict the focal source location correctly, while the geodesic method did. Note that this particular simulation is not physiologically realistic as the catheter has been placed on the mitral valve.

Calculating geodesic distances

Distances between vertices on the mesh were calculated using the techniques outlined in Section 2.14. An example of such a path is shown in Fig. 3.9(A). The output of this step is an $n \times n$ matrix of geodesic distances between every pair of vertices, where n is the number of vertices.

Multi-dimensional scaling

A multi-dimensional scaling technique was applied to flatten points on the three-dimensional geometry onto a two-dimensional plane, in a way that best preserves distances between points. This is detailed in Section 2.14, and the final output is a list of n two-dimensional coordinates.

Steps for the flattening methodology

An overview of the steps used in the flattening methodology is as follows:

1. Find the closest vertex on the left atrial surface mesh to each of the catheter electrode locations. This step is required because geodesic distances are calculated between vertices.

2. Find the geodesic distances between each pair of catheter electrode vertices by finding the shortest path between vertices. In the case that an afocus catheter

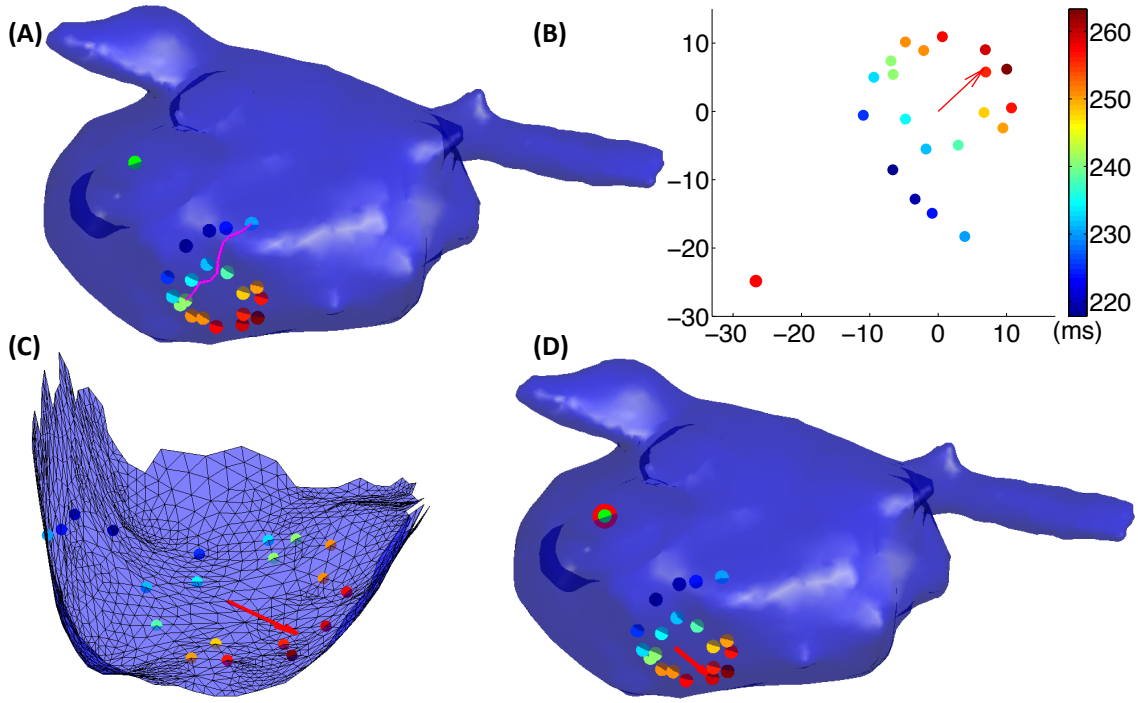

Figure 3.9: Catheter on curved part of geometry: need for geodesic distances – outline of methodology. (A) Left atrial mesh used for the simulation, with the stimulus location marked by the green dot, and the catheter location shown. The electrodes are coloured by their activation time. An example geodesic path between two vertices is also shown. (B) Electrode locations in the two-dimensional locations that best preserve geodesic distances, where points are coloured by activation time. The circular algorithm wavefront direction is shown, along with the predicted focal source location from the circular algorithm in red. (C) The section of the mesh within the bounding box of the catheter is subdivided to give an extra vertex between every pair of vertices. The wavefront direction estimated by the circular algorithm is shown as the red arrow. (D) The focal source location is predicted accurately as the red dot. Again the wavefront direction estimated by the circular algorithm is shown as the red arrow.

with twenty electrodes is analysed, this step results in a 20×20 matrix of distances.

3. A multi-dimensional scaling technique is used to find the two-dimensional coordinates that best preserve the matrix of squared distances.

4. The conduction velocity algorithms are applied to these two-dimensional coordinates and activation times to estimate the conduction speed, the wavefront direction and the focal source location.

In order to map the wavefront direction and estimated focal source location in two-dimensions to the three-dimensional mesh, the following steps were used:

1. Isolate the section of the mesh containing the catheter by constructing a bounding box and taking the vertices and faces that lie within the box.

2. Subdivide this region of the mesh to create a denser arrangement of vertices, so that the wavefront direction arrow (the *arrow*) can be defined more accurately, where the arrow is taken to be an ordered pair of vertices. A factor of two was used for this subdivision, to create an extra vertex between every two vertices (see Fig. 3.9 C). This subdivision was performed in Matlab using the file exchange tool box `geom3D` (Legland, 2015).

3. Calculate the distance in two dimensions between the two ends of the arrow and all electrodes on the catheter. The approach is to find for each end of the arrow the vertex on the mesh that best satisfies the set of distances to all electrodes on the catheter.

4. Work out the geodesic distance from each electrode vertex on the mesh to all vertices in the subdivided mesh.

5. For each end of the arrow, find the vertex for which the sum of the absolute error in distance between the desired distance to each electrode vertex and the actual distance to that vertex is smallest. This gives the two ends of the arrow in three dimensions, and the line joining these points is the required wavefront direction (see Fig. 3.9 C, D).

6. Use the same approach for the focal source location; find the point on the full mesh (that has not been subdivided) that best satisfies the distances to all electrodes.

3.3.3 Applying the conduction velocity algorithms

For planar wavefronts with an arbitrary arrangement of measuring points, Equation 3.29, is re-written in the form:

$$\hat{t}_i = \gamma_0 + \gamma_1 X_i + \gamma_2 Y_i, \tag{3.33}$$

where $X_i = x_i - x_0$ and $Y_i = y_i - y_0$ and $\boldsymbol{\gamma} = [T, v^{-1}\cos\phi, v^{-1}\sin\phi]^\top$, which can be solved for $\boldsymbol{\gamma}$ as a linear least-squares problem, and subsequently values for T, v and ϕ can be found. In this case, ϕ is the angle of incidence of the wavefront and T is the activation time of $\boldsymbol{x}_0$.

The equation for arbitrary measuring points with a circular wavefront, Equation 3.32, is posed as a non-linear least-squares problem in $\boldsymbol{\beta}$, which minimises the residual $\sqrt{\sum_{i=0}^{m-1}\left(t_i - \hat{t}_i\right)^2}$, and is solved using `lsqnonlin` in Matlab. Initial estimates for ϕ and v are derived from the planar case.

3.3.4 Simulation details

Simulations were performed on a surface reconstruction of a single patient's left atrium using the *Nektar++* high-order spectral/*hp* element solver (Cantwell et al., 2014b), with the monodomain tissue model and Courtemanche et al. (1998) human atrial cell model. The finite element mesh was constructed using a triangulation obtained from the Ensite Velocity (St Jude Medical, Inc) electroanatomic mapping system (Eitel et al., 2010). Electrode locations obtained from the system were used as recording points in the simulation and activation times were determined at these locations. The algorithms above (Sections 3.2.5, 3.2.6 and 3.3.3) were applied to the simulated recordings to determine the CV, wavefront direction (planar) and focal source location (circular).

For the circular wavefront case, with the measuring points projected to the two-dimensional plane of best fit, the estimated location of the focal source was projected to the closest vertex on the mesh, and the distance error from the true focal source location was calculated (focal-source-distance-error, FSDE). The angle error (AE) was defined as the absolute difference between the predicted angle and the angle measured from the stimulus location projected onto the 2D plane to the earliest measuring point.

3.3.5 Clinical data analysis

All clinical data used in this thesis were obtained with informed consent under ethical approval from the Health Research Authority Ref 13/LO1169. Unipolar data were collected from three patients using a 20 electrode Afocus II catheter (St. Jude Medical). Activation times were automatically assigned by the electroanatomic system (Eitel et al., 2010), at maximum negative $\mathrm{d}V/\mathrm{d}t$, and manually corrected by an experienced clinical electrophysiologist (Dr Norman Qureshi). Electrograms indicating poor contact with the tissue were removed. The recording electrode locations and the pacing electrode location were exported from the system. The algorithms were used to predict the CV, wavefront direction (planar) and estimated focal source location (circular). Results are given as mean and standard deviation.

3.3.6 Analytic testing

In order to generate exact planar and circular waves for testing the algorithms, the following equations were used, following Barnette et al. (2000):

Planar

$$f(x, y, t) = \sin\left(\omega t - k_x x - k_y y\right), \tag{3.34}$$

where the conduction speed is $c = \frac{\omega}{\sqrt{k_x^2 + k_y^2}}$.

Circular

$$f(x, y, t) = \sin\left(\omega t - k_r r\right), \tag{3.35}$$

where $r = \sqrt{(x - x_0)^2 + (y - y_0)^2}$ and the conduction speed is $c = \frac{\omega}{k_r}$.

3.3.7 Ensuring the correct time window for analysis

In order to correctly calculate conduction velocity for a given recording area, the time window for the activation times analysed must be chosen appropriately such that the activation times of each of the measuring points are from the same propagating wavefront.

For a spiral wave, this means the times should be from the same arm of the spiral; that is between the same two turns of the wavefront. This is demonstrated in Fig. 3.10 in which the top row shows an inappropriate choice of times for which some points are on one arm of the spiral and others on another, creating a discontinuity in the activation time field; the bottom row showns an appropriate choice of times. The

conduction velocity is calculated correctly in the latter case. It can be challenging to select the correct time window for analysis during complicated rhythms, such as fibrillation, and so an automated method for selection is proposed here.

First of all, the median interval between subsequent activations of all measuring points is calculated, to give an estimate of the average cycle length of the activity, which is then used as the window length, L, for analysis. Activation times for each recording point are then selected within a window starting at some initial start time, T, giving $[T, T+L]$ (in the instance that multiple activations occur within the window for a recording location, the minimum time is selected). The conduction velocity is then calculated for these times along with the residual of the fit. This is repeated for intervals of length L, for which the start point is shifted from T, in 10ms increments, until $T+L$. The time window with the lowest residual of the fit is then chosen as the optimal choice of activation times and gives the conduction velocity estimate. In the example shown in Fig. 3.10, a shift equal to half of the median cycle length from the initial start time gives the lowest residual and most appropriate choice of activation times.

For analysis of repeating wavefronts, including focal sources and spiral waves, this technique was used in order to automatically find the conduction velocity, without the need to pre-specify a time window.

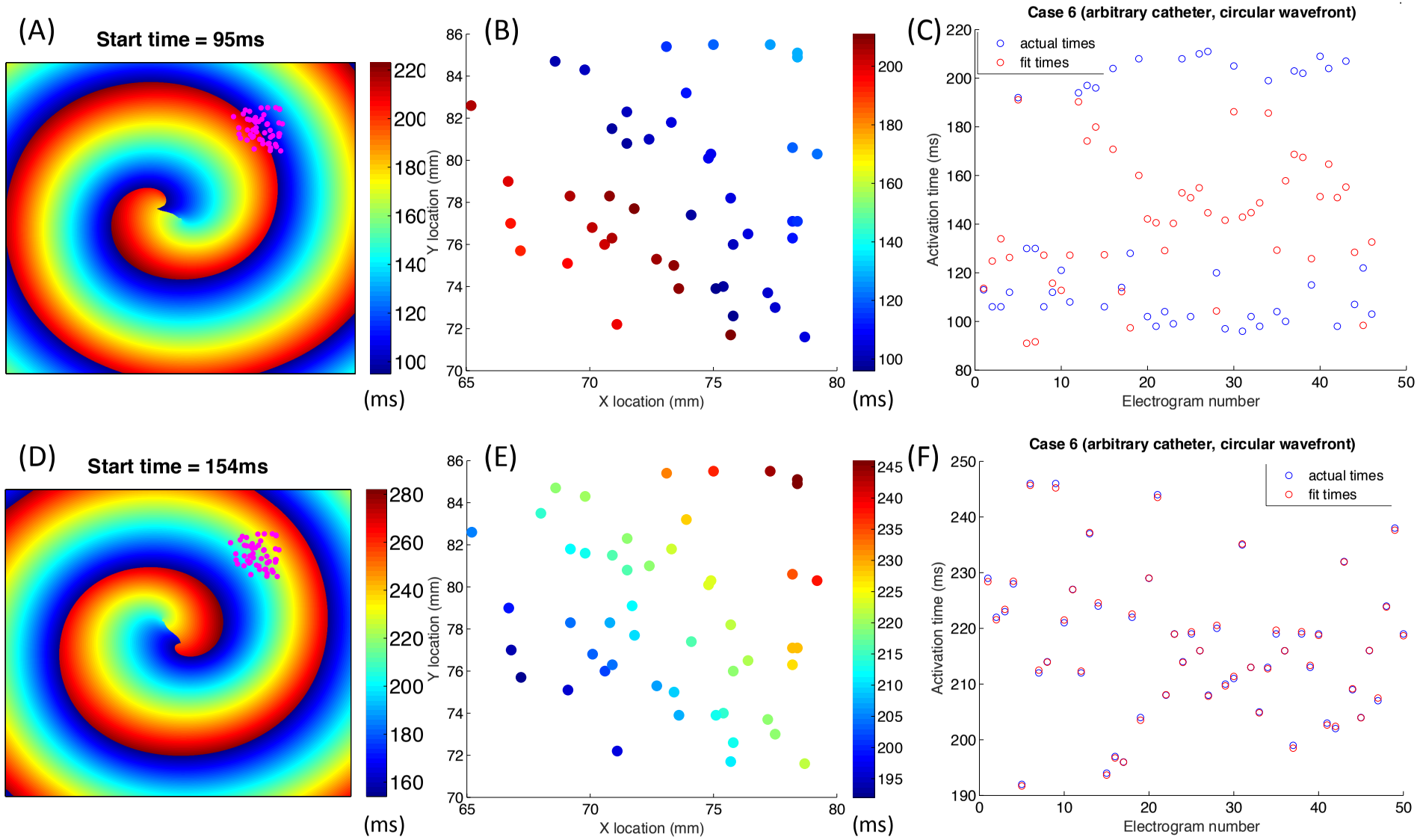

Figure 3.10: Calculation of the conduction velocity of a spiral wavefront. Caption continued on page 113.

Figure 3.10: Calculation of the conduction velocity of a spiral wavefront. Fig. on page 112. (A, D): Activation times were analysed for the points shown at the purple dots in the isochronal maps. (B, E): Locations of the points used for the fit, coloured by their activation times. (C, F): Plots to show the actual times and fitted times that result from using these points in the conduction velocity algorithm assuming a circular wavefront. (A-C) A poor fit is obtained when activation times are not on the same arm of a spiral, as the first and last measuring points to be activated are both in the centre of the arrangement of points. (D-F) Shifting by the median CL divided by two gives a time window for which the times are all on the same arm of the spiral, and a satisfactory fit is obtained. In this case, the first points to be activated are in the bottom left of the arrangement, and the last points to be activated are in the top right. The domain size shown here is 10cm-by-10cm.

3.3.8 Modelling catheter arrangements

Clinical multipolar circular (Lasso), spiral (AFocus II) and five-spline (PentaRay) catheters were modelled. Each was modelled as having a diameter of 2cm. For the modelled circular catheter, points were equally spaced on a circle of diameter 2cm. The spiral catheter was modelled as an Archimedean spiral, in which the arc length of the spiral was taken to be the length required for 19×4.5 mm spacing plus the final electrode (approximately 87mm), based on 20 electrodes with an inter electrode spacing of 4mm and electrode width of 1mm (giving 4.5mm between the centres of adjacent electrodes). The required number of electrode points were then equally spaced around this spiral, by solving for the Archimedean spiral angle, and finally the arrangement could be rescaled in the case that a different diameter of catheter was required. A PentaRay catheter was modelled as having equal spacing of 4-4-4mm along each of the equally-spaced five splines. These are shown in Fig. 3.15.

3.4 Results

3.4.1 Simulated data at exact electrode locations

We initially tested the accuracy of the planar and circular algorithms on simulated data from a focal source. The motivation for applying the planar algorithm was that far from the focal source, the wavefront was expected to be approximately planar. In addition, the planar algorithm was more computationally efficient. Pacing from three focal source locations were recorded at eight catheter locations, giving a total of twenty-four test cases. All of the catheter and focal source positions were located on the posterior or anterior walls of the atrium. Fig. 3.11 shows the activation times for one catheter location. Of the three focal sources, the locations of two were estimated correctly while the third was estimated to be 4.10 mm from the actual source.

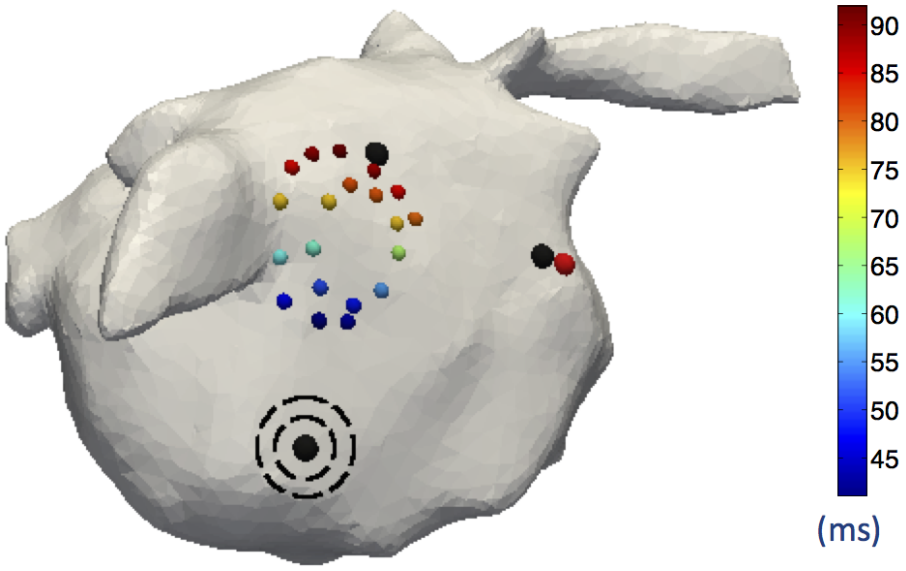

Figure 3.11: Simulation set-up showing pacing location. Left atrial patient geometry showing locations of the three focal sources (black dots), one catheter position, coloured by activation time, and estimated focal source locations from the circular algorithm (red dots). For two of the sources, the black and red dots overlap.

A summary of the results is shown in Table 3.1. Both the planar and circular algorithms computed similar CV and angle estimates; the latter achieved a lower angle error since it provided a more accurate fit, as evidenced by the lower residual. The residual is the square root of the sum of the squared errors in estimated and actual activation times. In addition, the focal source location and focal source distance error (FSDE) was calculated for the circular algorithm.

Five of the twenty-four cases were excluded from the summary statistics, since for these set-ups the focal source was located beneath the catheter. In these cases the planar wave algorithm broke down, although the focal source position was still identified accurately using the circular algorithm.

Table 3.1: Summary statistics for simulated data.

	Planar	Circular
CV (m/s)	0.50 ± 0.02	0.49 ± 0.00
Angle error (degrees)	5.06 ± 4.36	1.26 ± 1.48
Residuals (ms)	5.95 ± 2.50	0.59 ± 0.62
FSDE (mm)	n/a	2.31 ± 4.72

3.4.2 Clinical data at exact electrode locations

The planar and circular algorithms were applied to activation time data collected on the posterior wall of the left atrium, paced from the coronary sinus, for three patients. Results are presented in Figs. 3.12 and 3.13. Focal source location was predicted accurately for two of the patients using the circular algorithm (1.55mm, 3.49 mm error; within the diameter of a 4 mm ablation catheter), while for the third patient, the planar model gave a slightly improved fit to the data (lower residual, Res). Errors in the computed angle (AE) were relatively small in all cases (< 30 degrees), whilst CVs were close to typical physiological values (Kanagaratnam et al., 2002).

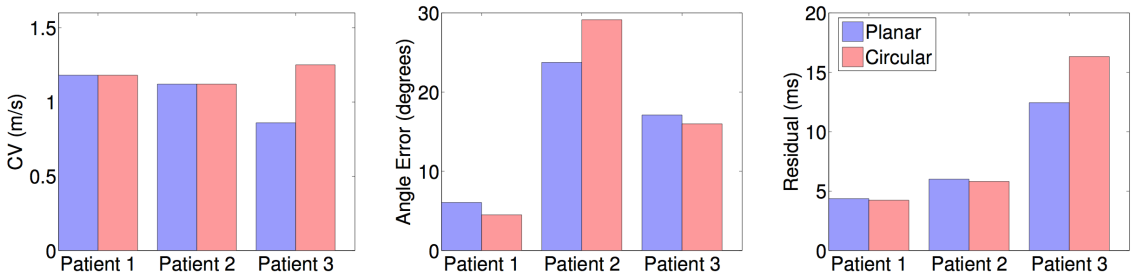

Figure 3.12: Planar and circular results for three patients.

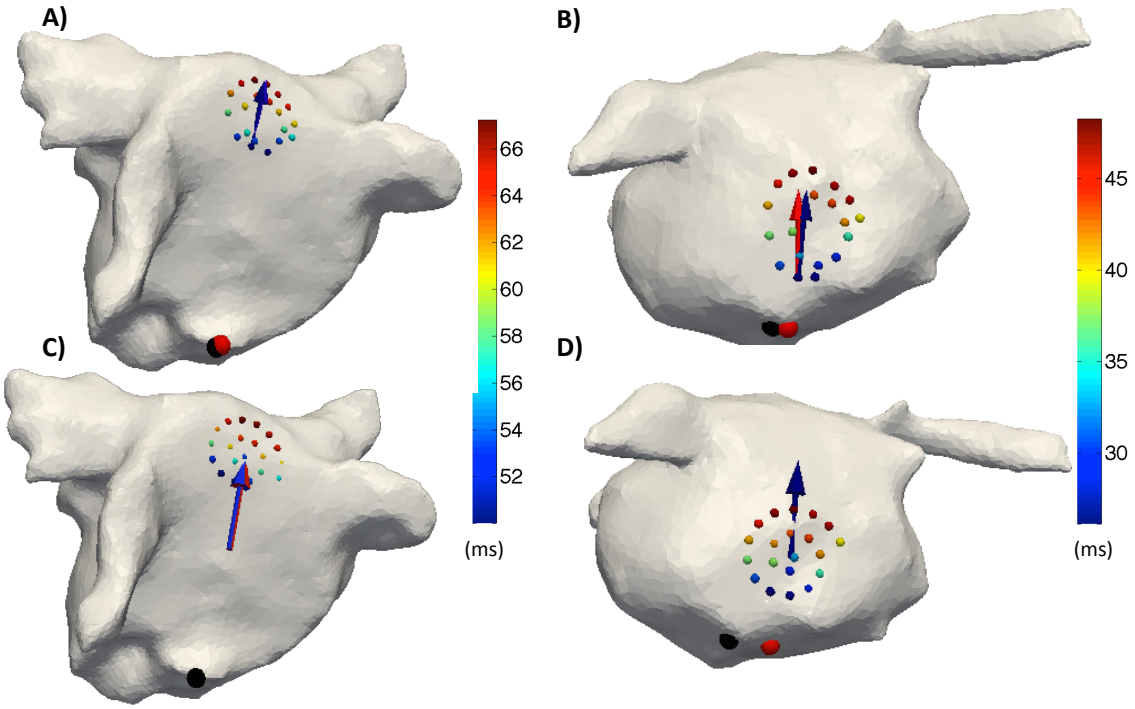

Figure 3.13: Focal source estimation from clinical data. (A,B) Focal source (black dot) for two patients was accurately predicted (red dot). (C,D) Electrode locations fitted to a spiral. Arrows show planar (blue) and circular (red) wavefront direction.

3.4.3 Effect of electrode location measurement error

In reality, the locations of the electrodes include measurement error and may not be known with great accuracy. We investigated how sensitive estimated CV, wavefront direction and focal source location are to errors in electrode positions. Calculations were performed analytically in a two-dimensional plane for a focal source. The real electrode positions were assumed to lie on a perturbed spiral, where Gaussian noise scaled by 5, 15 or 25% of the catheter diameter was added to both the x- and y-coordinates of a perfect spiral. The planar and circular algorithms were applied ten times using the original spiral recording positions, but using activation times from the perturbed recording positions. Results are shown in Fig. 3.14. Mean FSDE was less than 10% of the catheter diameter for 5% spatial noise ($9.78 \pm 8.03\%$), but for larger noise levels the focal source location estimation was unsuccessful, as the estimated radius of curvature was greater than the size of the domain.

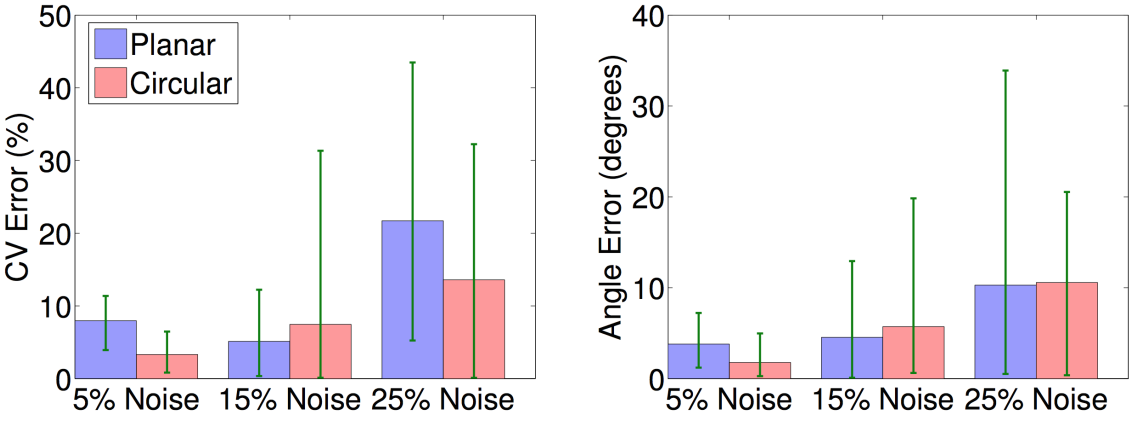

Figure 3.14: Analytical results: effects of electrogram location perturbations from a perfect spiral catheter. Results are given as mean and standard deviation.

3.4.4 Effect of catheter deformation

The spiral catheter is flexible and may deform in shape when in contact with the myocardium during data collection. We examined the effects of catheter shape deformation for the clinical data previously considered, by taking the measured electrode positions and fitting them to a spiral, equivalent to that of the undeformed catheter. The fitted positions, together with the original recorded times, were tested with the circular and planar algorithms, and the resulting change in the parameter estimates was investigated.

CV was relatively unaffected (mean change: planar 7.62%, circular 8.06%). Angle error increased (mean error: planar 13.69, circular 11.28 degrees). For the first patient, shown in Fig. 3.13(A,C), wavefront direction remained accurate (error less than 35 degrees), but radius of curvature was overestimated by 72.84 mm. For the second patient, Fig. 3.13(B,D), focal source location error was 10.19mm, which is larger than a 4mm or 8mm ablation catheter but is on the same order of magnitude. For the third patient, the radius of curvature was overestimated, and the planar model has a slightly lower residual.

3.4.5 Effect of catheter choice when over focal source

In the case where the catheter was placed over a focal source, the planar wavefront algorithm broke down, although the focal source could still be located in some cases using the circular wavefront algorithm. Here, the choice of catheter shape had a significant influence on the quality of the results.

Spiral, PentaRay and circular shaped catheters of 20mm diameter were simu-

lated. For the examples shown in Fig. 3.15, focal source locations were predicted correctly for the PentaRay and spiral catheters, but incorrectly for the circular catheters. In the case of the circular catheter in Fig. 3.15(A), the conduction velocity estimate was particularly inaccurate using both the planar and circular algorithms. For the case shown in Fig. 3.15(B), the circular CV estimate was close to the planar CV estimates for all three catheters.

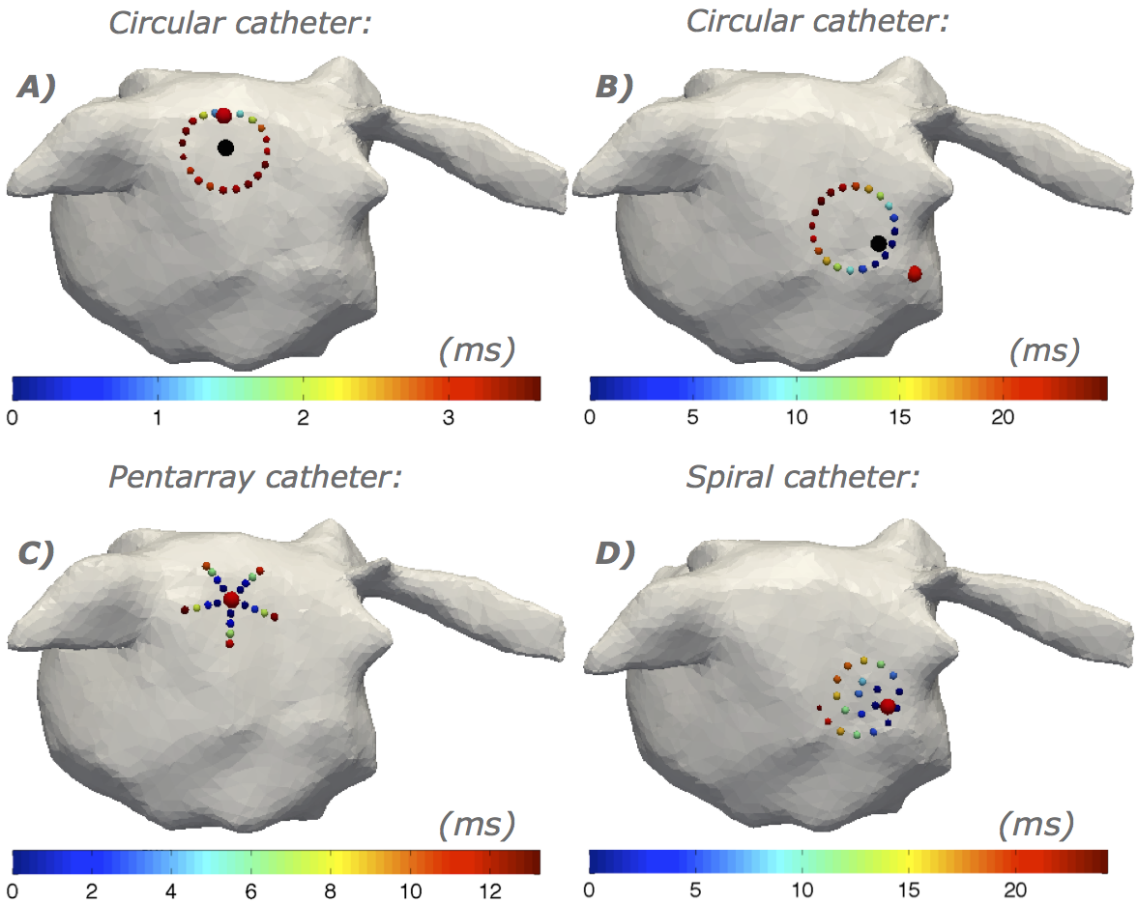

Figure 3.15: Effect of catheter shape on prediction (red dots) of focal sources (black dots) under catheter. (A,B) Circular catheter with source at centre and off-centre. (C) PentaRay catheter, (D) Spiral catheter.

3.4.6 Assigning activation direction in atrial tachycardia

The algorithm was applied to atrial tachycardia datasets for two patients. For the first patient, the input data were in the form of electrode locations along with local activation times, exported from the clinical electro-anatomic mapping system. An activation arrow was assigned for each catheter of data using the circular wavefront algorithm, and the resulting map is shown in Fig. 3.16. It can be seen that the activation is reentrant around the mitral value annulus, and the wavefronts collide on the roof.

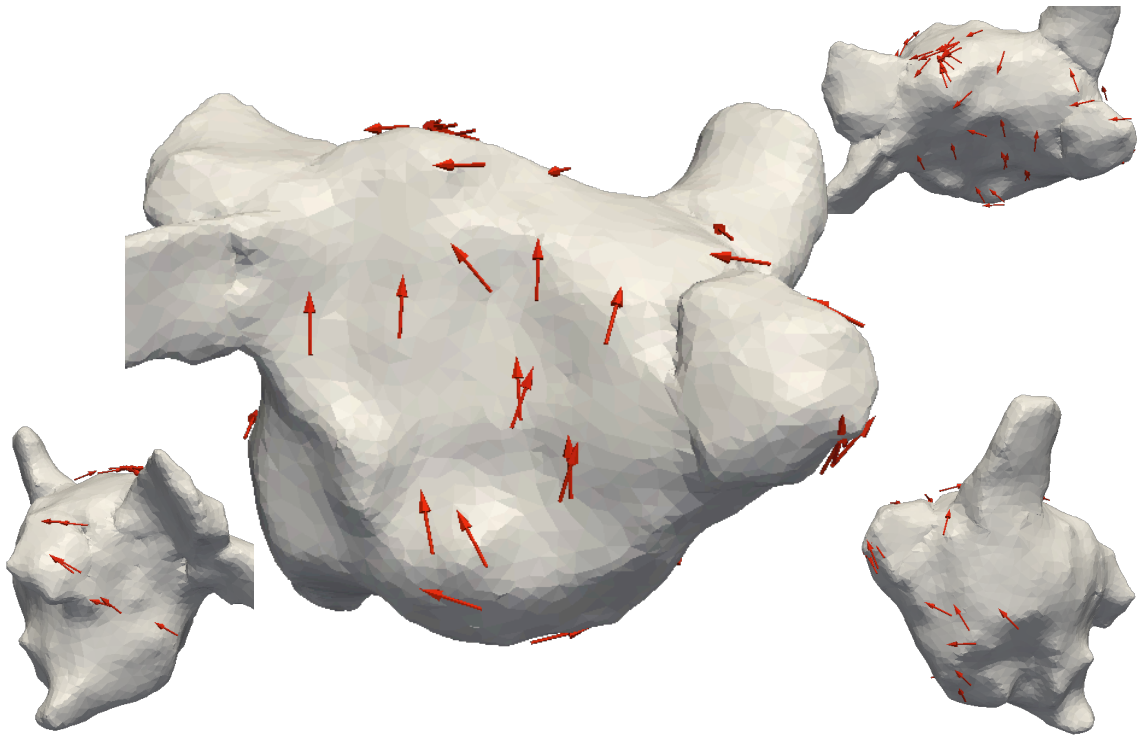

Figure 3.16: Atrial tachycardia wavefront direction map calculated using the circular wavefront algorithm. Each arrow indicates the calculated wavefront direction for activation times from one catheter of data.

For the second patient, the data were bipolar and unipolar electrograms from eleven catheter sites, for which each recording is $22.4 - 33.0$s (mean duration 27.9s), representing between 85 and 134 beats of atrial tachycardia (mean 108.4 beats). Activation times were calculated for all bipolar electrograms as the times of maximum amplitude and for unipolar electrograms as the time of maximum negative slope, in each case using a moving window of length 122.9ms (250 samples). For each catheter, the activation direction was assessed for each beat. The mean and standard deviation of the estimated CV and directions were calculated, for which the 10% of beats with the highest residual were excluded for each catheter. This

exclusion was applied to allow for a degree of error in activation time assignment.

Fig. 3.17 shows the mean direction for each of the catheters indicated by an arrow for the unipolar and bipolar recordings, where the CV arrows are coloured by the conduction speed. There is heterogeneity in CV, where the roof and floor show the highest CV. The range of CVs was $0.33 - 0.74$m/s for the unipolar recordings and $0.33 - 1.19$m/s for the bipolar recordings, with the difference arising from the CV estimates for the catheter on the roof differing between the unipolar and bipolar recordings. The CV estimates are shown on a per catheter basis in Fig. 3.18, in which a difference in CV is evident between the catheters.

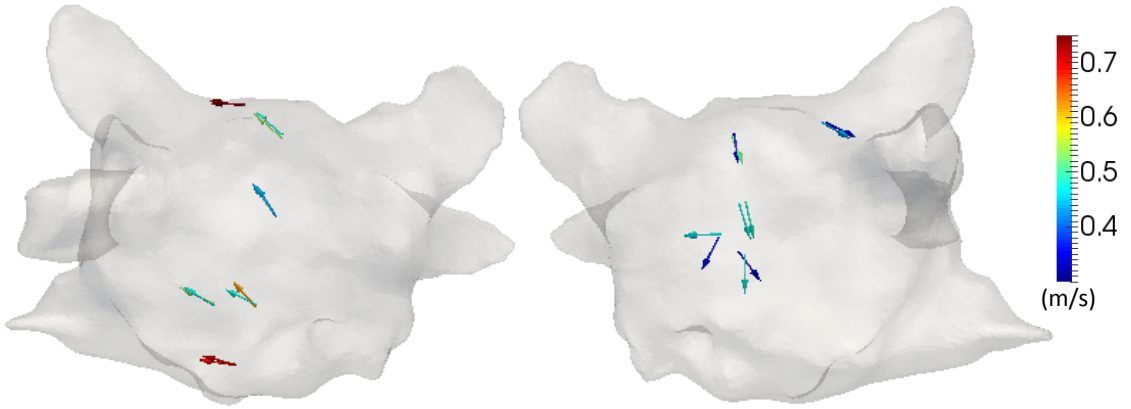

Figure 3.17: Atrial tachycardia wavefront direction map in which activation directions calculated using unipolar and bipolar activation times agree well and spatial heterogeneity in conduction speed is observed. Mean wavefront direction estimated using the circular wavefront algorithm are shown for each of the eleven catheters, with an arrow indicating the mean direction across all beats for the unipolar recordings and for the bipolar recordings. There is visually a good agreement between the directions for the two data modalities. The colour of the arrow indicates the conduction speed, for which there is heterogeneity across the atrium.

The difference in angles between the unipolar and bipolar algorithms, along with the standard deviation for each catheter are shown in Fig. 3.19. The angle estimates for the unipolar recordings show a larger variation than the bipolar recordings for nine of the eleven catheters.

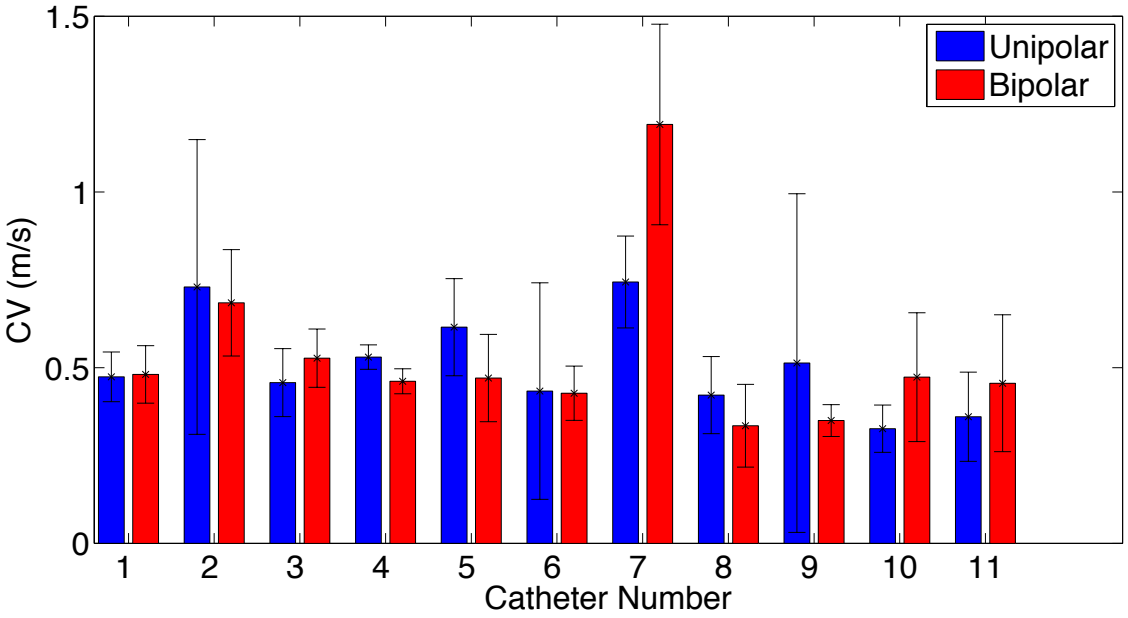

Figure 3.18: Atrial tachycardia conduction velocity estimates for unipolar and bipolar recordings. These are expressed as mean and standard deviation across each catheter over a mean of 108.4 beats (range: $85 - 134$). There is generally a good agreement between the mean value for unipolar and bipolar recordings, although differences in mean CV can been seen between the different catheters. Catheter number seven shows the largest CV and also the largest variation, and is located on the roof.

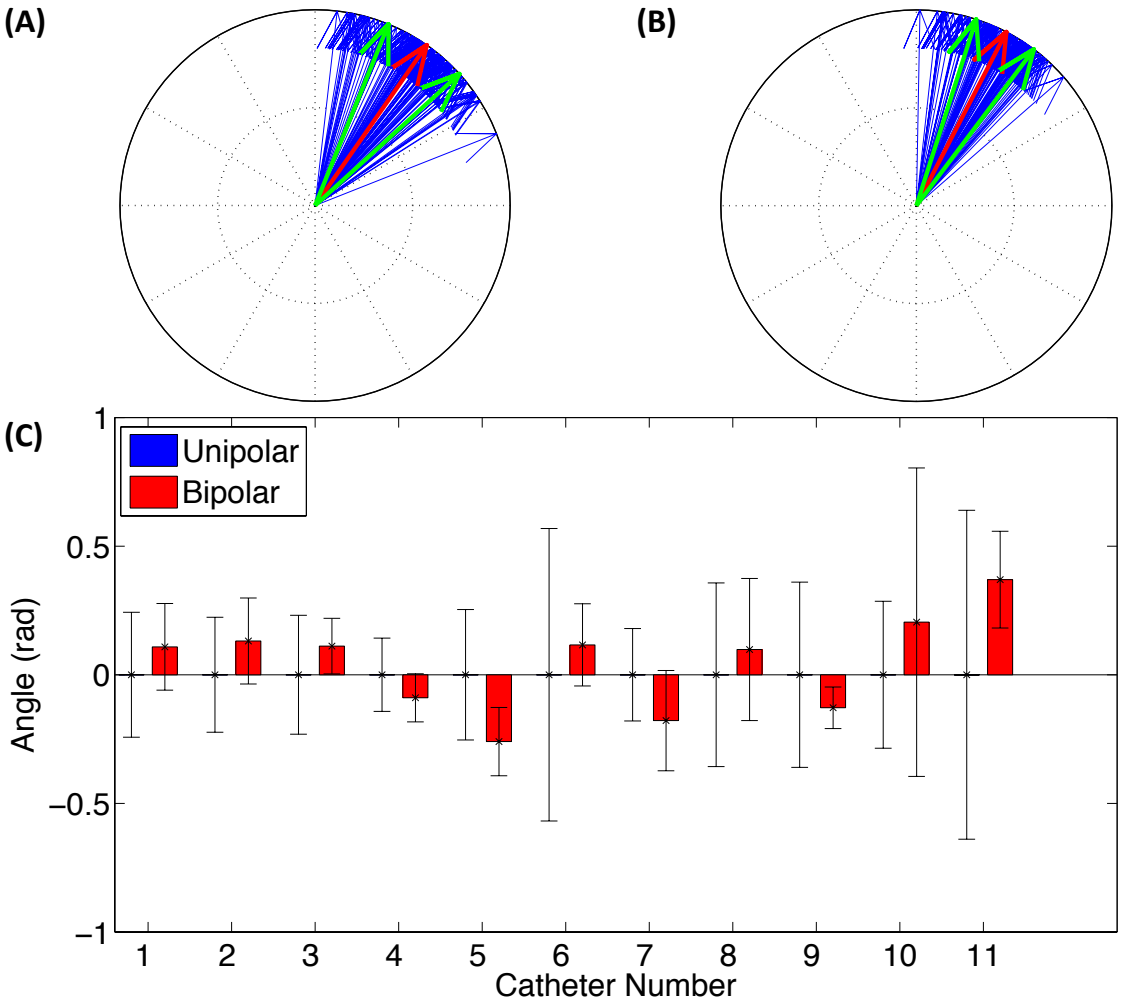

Figure 3.19: Atrial tachycardia beat-to-beat variation in wavefront direction. For each catheter, the mean and standard deviation of the wavefront direction calculated over all beats recorded for the tachycardia are calculated. (A) Compass plot to show the mean and standard deviation direction for unipolar electrograms for catheter number three; (B) Bipolar electrogram compass plot. Here the difference in the mean angle is 0.13 radians and the standard deviation for unipolar is 0.22 radians and bipolar 0.17 radians. (C) Plot to show the difference in angle between unipolar and bipolar angle (unipolar angle set to zero) and standard deviations.

3.4.7 Rotor core location estimation

The ability of the circular wavefront algorithm to locate the core of a rotor was tested using data from a two-dimensional sheet simulation in which there was a single meandering rotor. The rotor core location was tracked over time to give a trajectory (see Section 7 for simulation details and rotor tracking methods). Spiral, PentaRay and circular shaped catheters of 20mm diameter were simulated at ten random locations on the sheet, and the estimated focal source locations were compared to the calculated rotor trajectory location. Optimal time windows for analysis were automatically chosen using the techniques in Section 3.3.7.

The rotor core location was estimated accurately and reliably using all three catheter arrangements. The spiral catheter performed best with distance errors ranging from $0.05 - 2.58$mm (median 1.52mm); while errors for the circular catheter ranged from $0.47 - 3.94$mm (median 2.00mm); and for the PentaRay catheter from $0.37 - 6.47$mm (median 2.02mm). This shows that the circular wavefront algorithm can be used to locate rotor core locations in the instance of a single rotor. The locations estimated using the spiral catheter are shown in Fig. 3.20.

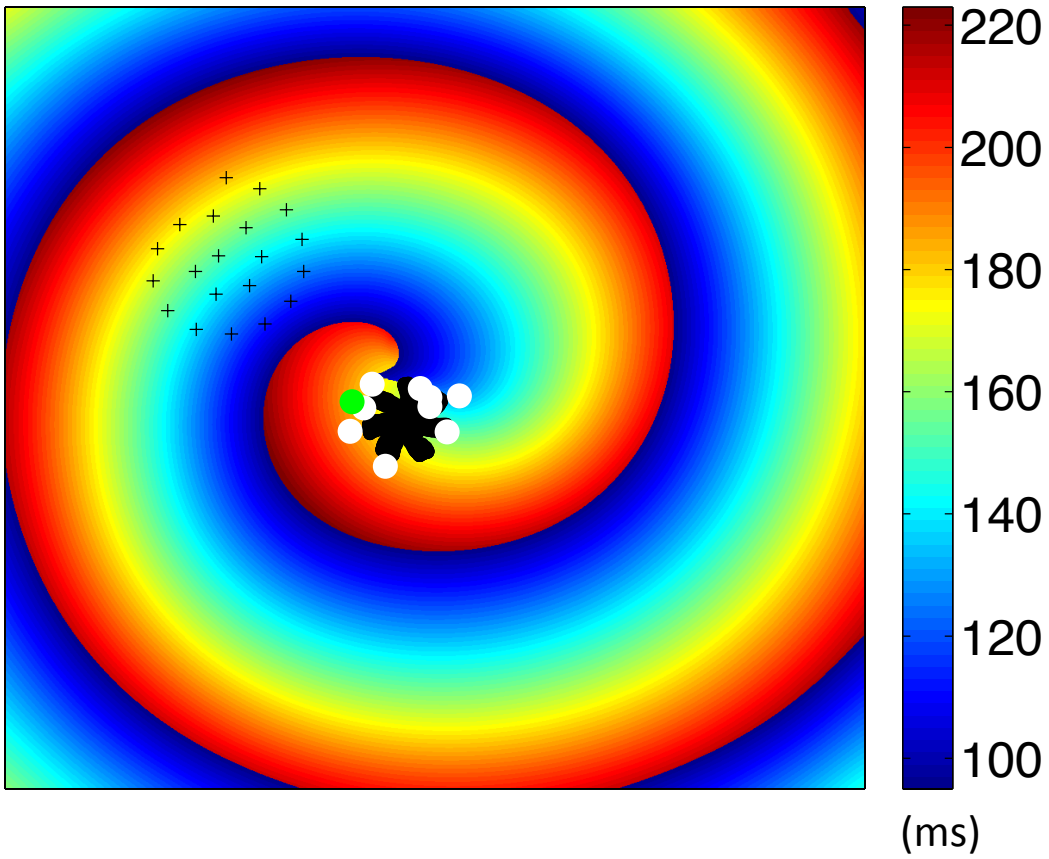

Figure 3.20: Spiral wave location estimation using the circular wavefront algorithm with a spiral catheter. A simulated spiral catheter was placed in ten random locations on the two-dimensional sheet and the activation times that give the lowest residual were chosen to give the estimated location. An example location of the spiral catheter is marked by crosses, with the estimated source location from this recording shown in green. The rotor core trajectory is shown in black and the estimated locations from the other spiral locations are shown in white. The algorithm is seen to locate the rotor core accurately and reliably. The domain size shown here is 10cm-by-10cm.

3.4.8 Effect of number of measuring points

In order to determine the number of measuring points required to reliably estimate conduction velocity and source location, five catheters of AT data, each consisting of nineteen bipolar electrograms, were analysed, and twenty-three beats were assessed for each catheter. In each case, the number of measuring points used in the fit was varied between four and nineteen, where these points were chosen randomly for each number of points, and this was repeated ten times. The percentage error in CV and the mean absolute difference in wavefront direction were calculated for each fit, compared to the corresponding values for the nineteen point arrangement. The results can be seen in Fig. 3.21. Using a cut-off of 10% mean error in CV, eight measuring points are required. In the case of a 15% error tolerance for mean CV, only five points are required. The error shows a large jump (24.5%) as the number of points is decreased from five to four points, while other changes are more gradual. The size of the standard deviation error bars decreases as the number of measuring points is increased, indicating that an increasing number of fits are accurate and reliable with increased numbers of measuring points.

The absolute error in angle also has smaller error bars as the number of points is increased. A more gradual increase in error is seen as the number of points is reduced so that changing the number of points has an incremental change, with no large jumps. For an angle error below 0.5 radians, twelve points are required.

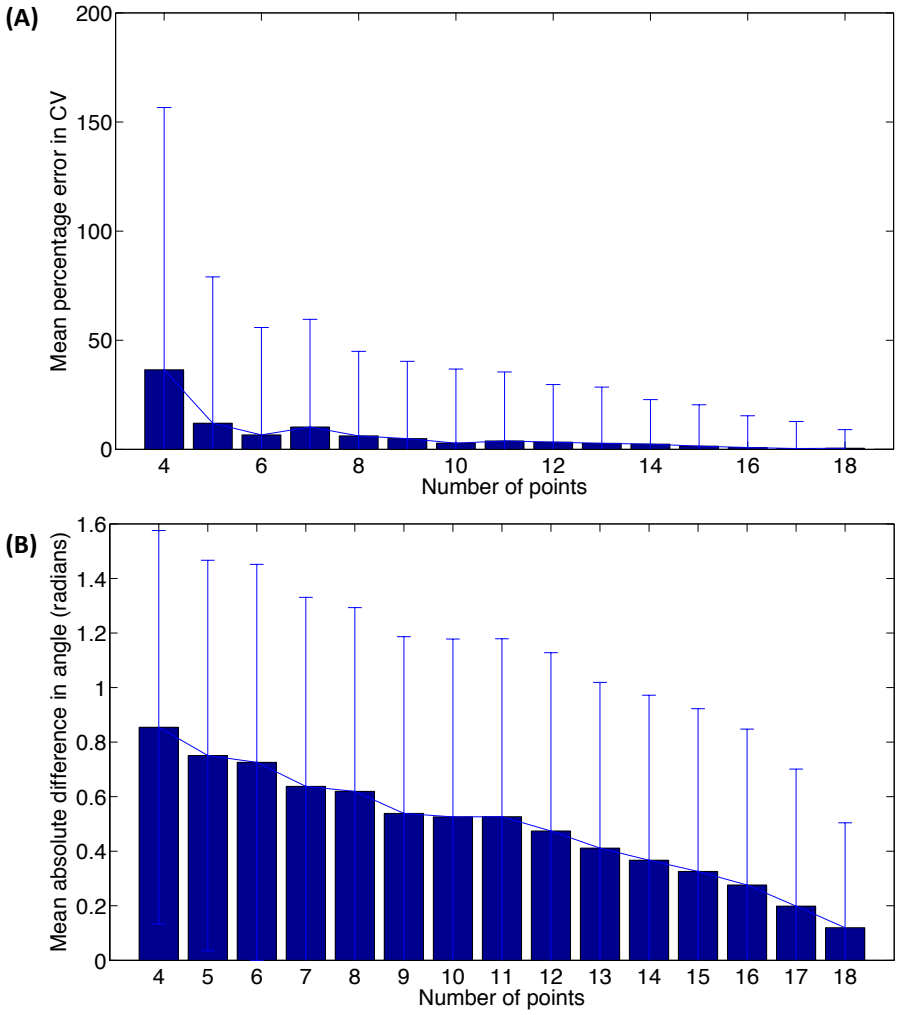

Figure 3.21: CV and wavefront direction depend on the number of measuring points included in the fit. (A) The mean percentage error in CV compared to the fit using all nineteen points calculated across five catheters using twenty-three beats for each catheter, and ten choices of points included in the fit. (B) The mean absolute difference in angle compared to the direction calculated using all nineteen bipoles. Standard deviation increases as number of points is decreased.

3.4.9 Clinical atrial tachycardia activation time mapping using a geodesic flattening

The surface flattening technique detailed in Section 2.14 can be used for two-dimensional visualisation of activation time maps. An example is shown in Fig. 3.22, in which local activation times measured from a multipolar catheter during an atrial tachycardia were analysed in two-dimensions on the flattened geometry. Displaying the two-dimensional interpolation of the times on the three-dimensional geometry (Fig. 3.22(D)) shows a good visual agreement with the recorded local activation times (Fig. 3.22(A)). Activation is seen to move from the mitral valve, up both the anterior and posterior walls to the roof, across the left veins and back down to the mitral valve. Conduction velocity algorithms could be applied to the two-dimensional representation of the data.

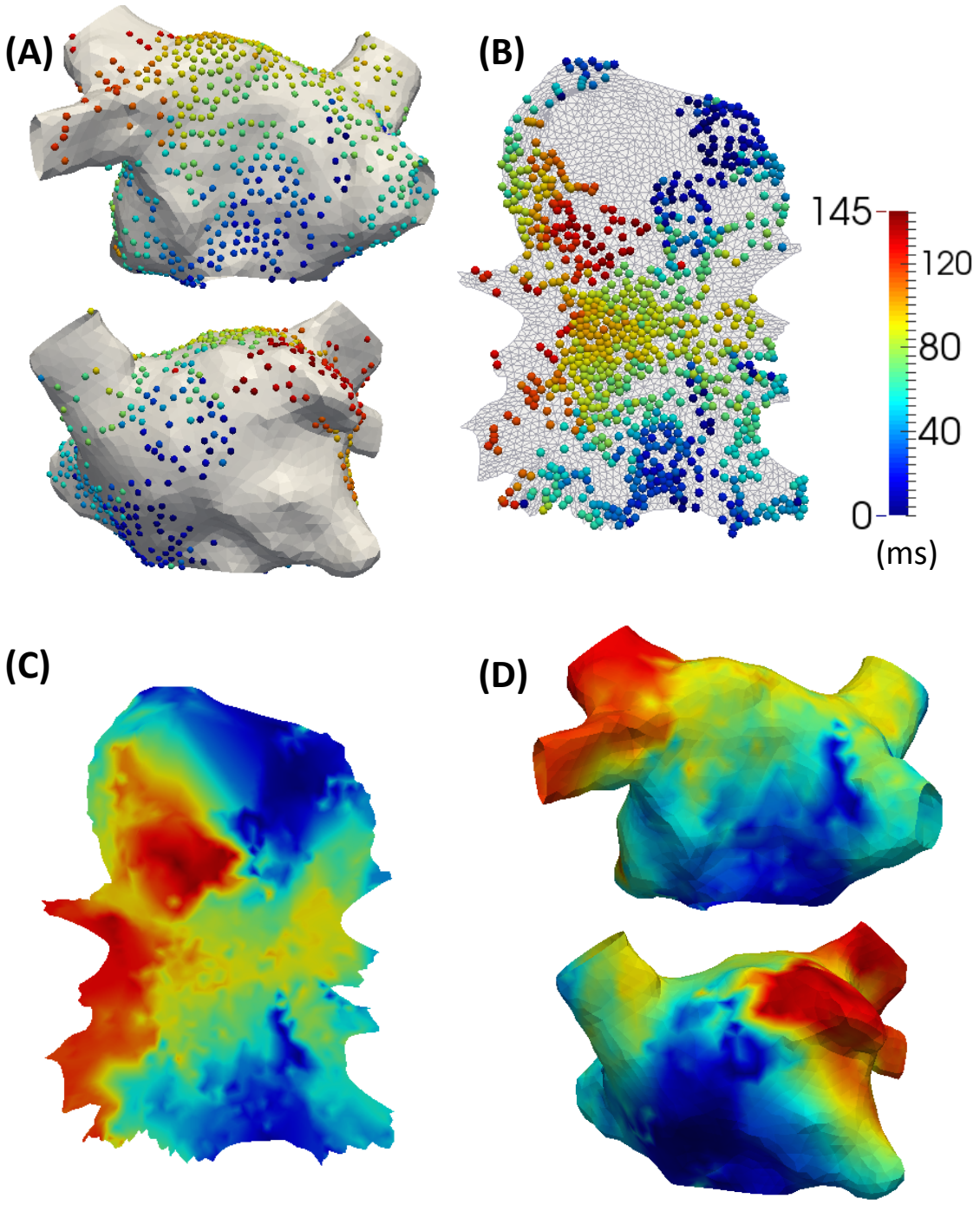

Figure 3.22: Surface flattening used to plot an LAT map for a clinical atrial tachycardia using a geometry derived from an electro-anatomic mapping system. (A) LATs for several multipolar catheters displayed on the electro-anatomic mapping system geometry. (B) Flattened geometry with corresponding LAT measurement in two-dimensions. (C) Interpolation of the LATs. (D) Interpolated LATs displayed on the three-dimensional geometry.

3.5 Discussion

3.5.1 New methodology

The equation for the technique developed by Weber et al. (2010) for estimating CV and wavefront direction for a planar wavefront with measuring points from a circular catheter was first derived. This was then extended to consider the cases of a spiral arrangement of measuring points, since spiral shaped catheters are often used clinically, with a planar wavefront and either of the catheters with a circular wavefront. The circular algorithm uses the estimated radius of curvature of the wavefront, together with the wavefront direction to estimate the focal source location. Finally these cases were generalised to consider the case of an arbitrary arrangement of points, with either a planar or circular wavefront. These final two automated algorithms can be used with any electrode configuration to calculate CV, and estimate the direction towards a focal arrhythmic source and its location (circular wavefront model), and these were tested in simulated data and for clinical data. This means the algorithms can be used for the Lasso, Afocus and PentaRay catheters and can also be used in the case that the catheter has deformed in shape upon contact with the atrial wall.

In the case of increased surface curvature, either in the locality of the catheter, or between the catheter and the focal source; or in the case that the source location and recording catheter are not on the same side of the geometry, the approach of projecting to the two-dimensional plane of best fit is not appropriate. A method to calculate the geodesic distances and to work with the two-dimensional representation that best preserves these distances was implemented.

In the case of spiral wave data or focal source data, it can be difficult to assign an appropriate time window for analysis. An automated approach to finding the CV and focal source location using the time window with the lowest residual was developed, so that the algorithm can be used without the need to pre-specify a time window.

3.5.2 Summary of findings

Testing the algorithms

Both the planar and circular algorithms with an arbitrary arrangement of points performed well for a range of simulated focal sources and catheter locations on the left atrial wall, and for two out of the three clinical data sets considered. The algorithms were extended to evaluate the effect of catheter deformation and measurement error

in the electrode locations, which predictably reduced their accuracy.

Source location estimation

The circular wavefront algorithm provided an estimate of the location from which the focal wave originates. The performance of the algorithms were reduced in the case that the catheter is placed over the focal source or rotor core. In cases when the catheter was placed over the focal source, spiral and PentaRay catheters were shown to be able to locate the source. This agrees with studies by Weber (2011) in which the ability of RBF interpolation to identify a focal source from data representing a Lasso, Afocus and PentaRay catheters placed over the focal source was investigated to find that the Lasso catheter could not identify the focal source, but rather the RBF interpolation showed a planar wave. This limitation occurs because the Lasso catheter does not contain any radial information. Similar results are found in Chapter 7, in which the effects of catheter shape on rotor tip location calculated using phase was investigated, and for twenty recording points, the Lasso catheter gave the largest error in estimated rotor centre location. Whereas focal source location was unsuccessful for the Lasso catheter placed over the focal source, the rotor tip location estimation, although more inaccurate than for the other multipolar catheters, was successful.

Calculating wavefront direction in Atrial tachycardia

The circular algorithm with geodesic distance preservation was used to compare activation directions and CV estimated using unipolar and bipolar data over many beats of an atrial tachycardia. This demonstrates the ability of the algorithm to be used for tachycardia data.

Dependence on the number of measuring points

The dependence of the algorithm on the number of measuring points was assessed using 115 beats of AT data (five catheters, twenty-three beats each), where between four and eighteen electrodes were randomly chosen from the catheter ten times for each beat analysed. Using clinical data for this analysis is preferable to using simulated data, since error in activation time assignment may occur in reality, so this provides a more realistic testing environment. Taking ten random permutations of points each time ensures that the output is not biased by the point removal. CV error showed a large jump from five to four points, suggesting that four points is too few to accurately and reliably estimate CV from clinical data, while five points

gives a mean error below 15% (12.0%). Angle error changes were more incremental, where adding additional points, decreased the angle error. Twelve points and above gave an average error below 0.5; whilst five points and above gave an error below $\pi/4$.

3.5.3 Comparison with other methods

Triangulation

Both triangulation and the methods presented here work with any arrangement of recording points and so are suitable for use with clinical data. The suitability for their use in calculating CV depends on the balance between required resolution of the CV field and accuracy. Triangulation is based on triads of points and as such many CV vectors can be assigned for a single catheter, permitting a more localised correlation with other measures, for example scar location (Ali et al., 2014). However, triangulation is more susceptible to inaccuracy due to errors in activation time assignment. The methods developed here can be applied to four or more measuring points (or three or more in the case of a planar fit); however, the technique is designed to work with a catheter of measuring points, and in this case would give a more robust estimate of CV than triangulation; however, it only provides one arrow per catheter.

Heterogeneity in CV is evident for the AT data, with the mean CV differing depending on the location of the catheter. It would be interesting to see whether further differences emerge using a more localised measure of CV, such as that provided by triangulation.

Existing cosine-fit methods

The work presented in this chapter extends the technique developed by Weber et al. (2010) to work with any arrangement of measuring points and to consider both planar and circular wavefronts, in which the circular wavefront algorithm also provides an estimate of the focal source location. The planar algorithm with arbitrary measuring points applied to a perfect circle of recording points will provide the same results as the cosine-fit technique of Weber et al. (2010). The development of the algorithm to work for any arrangement of measuring points is useful because clinically circular, spiral and five-spline catheters are used, which may also deform in shape when in contact with the tissue. Burdumy et al. (2012) discuss the need for this extension in their paper. The ability of the circular algorithm to estimate the location where a focal wave originates from is also a useful extension.

Surface fitting algorithms

One disadvantage of the method developed in this chapter is that it assumes a single macroscopic wavefront, and so the method breaks down in the case of wavefront collision. Surface fitting algorithms work in the case of wavefront collision so long as the windows in space and time for the points included in the surface fit are chosen appropriately to only include one wave in each of the polynomial surface fits (Bayly et al., 1998a). This is challenging to achieve in practice.

Radial basis function interpolation

Radial basis function interpolation works well in the case of multiple wavefronts. Weber (2011) used RBF interpolation to detect wavefront collision under a circular catheter, which could not be resolved using the cosine-fit technique (see Section 1.12.8).

Other methods for predicting the direction towards a focal source

Ganesan et al. (2015) investigated how electrogram characteristics vary with distance from a rotor core location, in particular cycle length and total conduction delay. Using simulation studies and testing on a clinical case they found that moving the catheter in the direction of the earliest activation within the catheter directed the catheter towards the source of rotational activity, and the total pairwise conduction delay was found to increase moving towards the rotational source. However their method does not give an explicit measure of the distance towards the source. Whereas, the algorithms developed in this chapter provide an estimate of the focal source location.

3.5.4 Limitations and future work

A potential limitation of our approach is that it assumes either a planar or circular wavefront. The combination of tissue heterogeneity and anisotropy, multiple layers of conducting tissue, movement of the cardiac chambers, and curvature of the atrial surface may lead to non-uniform conduction and wavefront direction, which may affect the performance of our algorithms, although they performed well in initial clinical testing.

A potential source of error in the technique in the case of the geodesic algorithm is the requirement that electrode points lie on a vertex of the atrial mesh. Electrode roving locations may be a relatively large distance from the atrial surface and this

requirement may itself introduce some distortion in distance. In addition, the algorithms assume a single underlying macroscopic wavefront, and so the collision of multiple wavefronts from different sources may produce spurious results, although this will be indicated by the residual of the fit. Furthermore, the feasibility of using our technique to locate the origin of focal tachycardias in real-time in the cardiac catheter laboratory to improve the efficacy of catheter ablation cases needs to be assessed.

The algorithm can be extended to three dimensions, however due to the limitation that most measuring techniques available clinically are limited to the endocardial or epicardial surface, three-dimensional analysis is not required. As such, propagation is assumed to be along the atrial surface, for which the geodesic extension to the algorithm is more appropriate than a fully three-dimensional approach. The limitation of not being able to capture the full three-dimensional nature of wavefront propagation is common among CV algorithms.

The requirement that activation times of measuring points come from a single wavefront imposes a constraint on the size of the measuring catheter used with this algorithm to be smaller than the spatial wavelength of the underlying activity. This is an important consideration when applying this algorithm, and the question of spatial resolution requirements are further assessed in Chapter 7. In addition, the number of measuring points required may depend on the spatial wavelength.

Extensions of the algorithm to work with fibrillation data warrant further investigation. Possible approaches include using time windows and electrode points indicated using phase analysis (see Section 6.4.6). Alternative approaches include using the residual of the fit to determine suitable window and point choices. A major challenge during fibrillation is the potential existence of fibrillatory conduction away from the core of a rotor. This may lead to multiple wavefronts underneath a catheter and a chaotic activation pattern, preventing accurate estimation of rotor-core location. Accurate estimation of rotor core location requires that the wavefront propagates approximately focally from the core to the recording catheter.

Chapter 4

Assessing the effects of parameter choices in rotor tracking analysis of optical mapping data

4.1 Introduction

Optical mapping is an effective measuring modality for analysing wavefront dynamics, and has been used to investigate driver activity at various spatial scales, ranging from cell monolayers (Campbell et al., 2012) to whole atrial preparations (Mansour et al., 2001). Optical mapping experiments on sheep ventricular muscle provided the first evidence for spiral waves in the heart (Davidenko et al., 1992a).

Analysis of optical mapping data during fibrillation is challenging due to the noise content, as well as the changing amplitude and duration of the signal. There are many approaches in the literature for filtering optical mapping data (Laughner et al., 2012) and for calculating phase (Umapathy et al., 2010). Analysis protocols contain many parameters and thresholds that need to be decided upon and the effects of these choices on the resultant dynamics need to be determined.

Preliminary investigations, shown in Appendix A, into rotor-core location techniques suggest that the calculated trajectories depended on the choice of location algorithm (phase singularity location (Section 2.11) or using the isopotential line technique (Section 2.13)), as well as the choice of parameter within these algorithms. In particular, the amplitude threshold used for including peaks within the phase affected the trajectory (see Fig. A.2); and the choice of isopotential line used for the isopotential line rotor-core location technique also affected the observed trajectory (see Figs. A.1, A.3). Furthermore, the choice of analysis variable of either voltage or calcium affected the rotor-core locations (Section A.1.2). This motivates

the importance of parameter choice within protocols for rotor tracking analysis. Furthermore, the feasibility of phase singularity identification from optical mapping data was assessed for calcium mapping in a monolayer of HL1 cardiomyocyte cells (Section A.1.3), demonstrating the techniques on simpler optical mapping data.

In this chapter, techniques are implemented and developed to investigate wavefront dynamics from optical mapping data of a canine left-atrial tissue preparation, and the effects of parameter choices within the protocol are assessed.

The aims of this chapter are:

- to develop a protocol for assessing wavefront dynamics in optical mapping data, including tracking phase singularities and frequency analysis;
- to assess the effects of parameter choices within this protocol and to determine an optimal set of parameters.

4.2 Methodology

4.2.1 Experimental preparation and overview of methodology

The experiments in this chapter were undertaken by Dr Fu Siong Ng, Dr Michael Debney and Dr Norman Qureshi. Four control canine hearts were donated by GlaxoSmithKlein. The left atrium was dissected (see Fig. 4.1) and perfused in a temperature controlled bath (37°) of Krebs-Henseleit solution as in Byrd et al. (2005); Doshi et al. (1999). Fig. 4.1 shows the preparation set-up. An electrode was attached through-out for monitoring the electrical activity. The preparation was loaded with a voltage sensitive dye (RH237) and changes in the fluorescence were recorded using a set-up containing a CMOS (complementary metal oxide semiconductor) optical mapping camera with 128-by-80 pixels. A restitution pacing protocol was performed to test the rate-dependent properties of the tissue under normal conditions. Acetylcholine was then added to the preparation and the restitution pacing protocol was repeated, where the pacing cycle length was decreased until fibrillation was induced and sustained. The dose of acetylcholine used differed between the preparations (30μM for the first two preparations; 10μM for the third and fourth preparations). Multiple sequential ten second recordings of AF were then taken, which are analysed in this chapter.

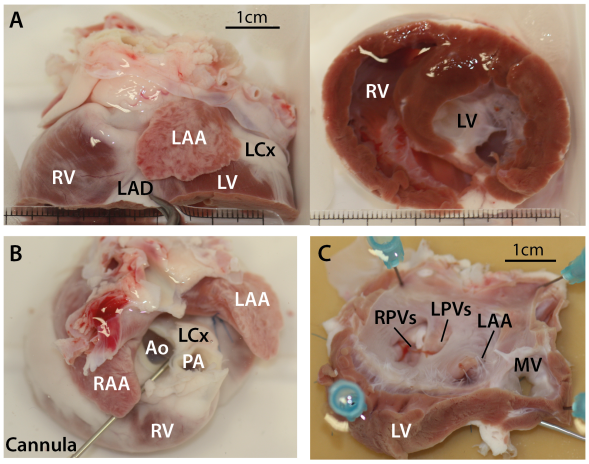

Figure 4.1: Photos to show the canine left atrial preparation used for optical mapping. RV = right ventricle; LAD = left anterior descending artery; LAA = left atrial appendage; LV = left ventricle; LCx = left circumflex artery; RAA = right atrial appendage; Ao = aorta; PA = pulmonary artery; RPVs = right pulmonary veins; LPVs = left pulmonary veins; MV = mitral value. Courtesy of Dr Fu Siong Ng.

Overview

The final output of the analysis protocol in this chapter is the arrhythmia properties of these preparations, including the number and distribution of phase singularities and the dominant frequency. These measures were calculated and assessed on a regional basis, determined by the atrial sections used for histological studies performed by other members of the research group. Fig. 4.2 shows a photo of one of the preparations, divided into nine regions for sectioning of the tissue for structural analysis.

The protocol used to locate phase singularities from the raw fluorescence signals contains many steps, with many associated parameters. The fluorescence signals are initially spatially smoothed and temporally filtered (Section 4.2.2); the phase is calculated (Section 4.2.3) and smoothed (Section 4.2.4); and phase singularities are identified (Section 4.2.5), tracked (Section 4.2.6) and the number of rotations are calculated (Section 4.2.7); and finally displayed as spatial distributions of phase singularity density (Section 4.2.8). A schematic illustrating these steps and the associated default parameters is shown in Fig. 4.3. The sensitivity of the algorithm output to parameters marked by an asterisk is assessed in the Results Section 4.3.

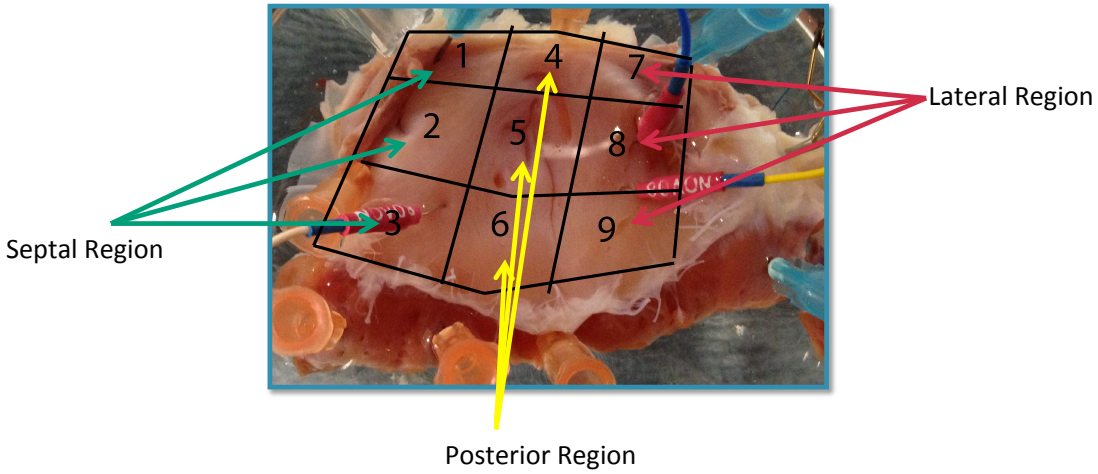

Figure 4.2: Photo to show the canine left atrial preparation used for optical mapping divided into regions for calculating the correlation between structural and functional features. Septal, posterior and lateral regions of the tissue are seen, where the pulmonary veins are located in the centre of the posterior region. Courtesy of Dr Fu Siong Ng.

			Default value
Smooth and filter voltage	Spatial binning (Section 4.2.2)	Voltage bin size*	9-by-9 pixels
	Temporal Filter (Section 4.2.2)	Low band	2Hz
		High band*	125% of DF
Calculate phase	Tag minima-maxima and remove mean signal (Section 4.2.3)	Moving mean window length threshold*	90% of estimated CL
		Moving mean amplitude threshold*	15% of median amplitude
	Smooth phase (Section 4.2.4)	Phase bin size*	9-by-9 pixels
Calculate phase singularity duration and number of rotations	PS identification (Section 4.2.5)	Threshold	Within 3.0 of ±2π
		Neighbourhood rule	≥3
		Integral contour size	3-by-3 pixels
	PS tracking algorithm (Section 4.2.6)	Distance threshold	9-by-9 pixels
		Time threshold	5 timeframes
		Deleting incorrect trajectories	Overlap >90% longer trajectory, or share >60% and < 10 pixels long
	Calculating number of rotations (Section 4.2.7)	Pixel radius	3 pixels
	PS Heat Mapping (Section 4.2.8)	Heat map bin size*	3-by-3 pixels
		Number of rotations threshold*	>0.5 rotations for inclusion in heat map

Figure 4.3: Schematic to show steps involved in analysis, along with associated default parameter values. Broadly, the raw fluorescence data are smoothed and filtered; the phase of the filtered signals are calculated; phase singularities are identified and their duration, number of rotations and distributions are calculated. The associated sections are listed in the second column, along with the parameters in the third column. Parameters that are varied in the parameter sensitivity analysis are marked with an asterisk. Default values for each parameter are listed in the final column.

4.2.2 Filtering techniques

The following data import and filtering techniques were adapted from an open source optical mapping data analysis toolbox, the *Rhythm* GUI (Laughner et al., 2012) (https://code.google.com/p/rhythm-analysis-software/).

1. *Data import:* Data from a CMOS optical mapping camera with 128 by 80 pixels and 1000Hz sampling frequency were read into Matlab and converted to matrix form. The preparation here is 3.5cm in width.

2. *Thresholding data:* To determine pixels from noise, a mask of zeros and ones was overlaid on the data, where one represented tissue. Ones were assigned to pixels over a threshold fluorescence, and holes in the mask were filled using `imfill` in Matlab (see Fig. 4.4).

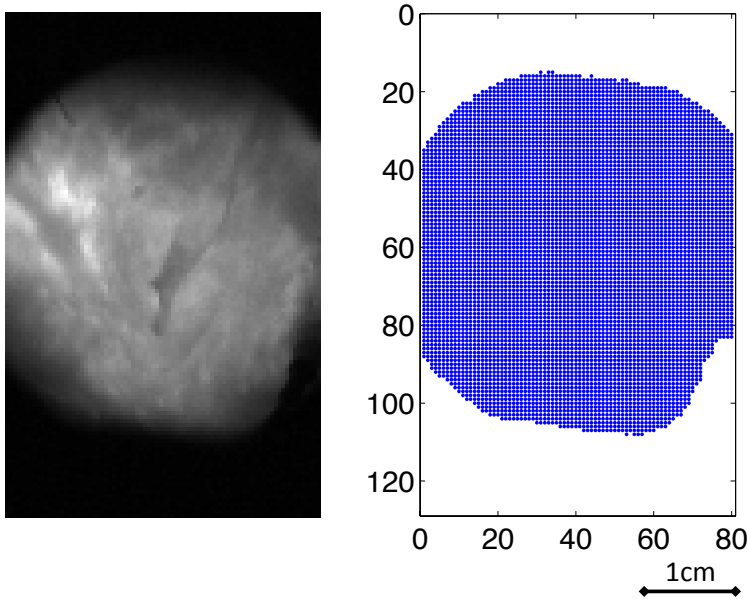

Figure 4.4: Mask used for thresholding data created from a still image at the beginning of the protocol on left; final mask used for thresholding on the right.

3. *Spatial binning:* The masked data were spatially averaged to decrease noise, by replacing the value of each pixel by an average of the data over neighbouring pixels. This was achieved using a two-dimensional convolution operator (`conv2`) with a uniform weighting (see Fig. 4.5).

   A modification was made to the *Rhythm* GUI to correctly calculate averages on the border of the mask, according the number of neighbouring tissue pixels.

A bin size of 9-by-9 pixels was used as a baseline value since it provides adequate smoothing, without over smoothing the voltage field (Fig. 4.6). The effects of varying the bin size on the observed PS dynamics are shown in the results, Section 4.3.

(A)

4%	4%	4%	4%	4%
4%	4%	4%	4%	4%
4%	4%	4%	4%	4%
4%	4%	4%	4%	4%
4%	4%	4%	4%	4%

(B)

0.1%	0.7%	1.3%	0.7%	0.1%
0.7%	5.5%	11.1%	5.5%	0.7%
1.3%	11.1%	22.6%	11.1%	1.3%
0.7%	5.5%	11.1%	5.5%	0.7%
0.1%	0.7%	1.3%	0.7%	0.1%

Figure 4.5: A convolution operator replaces a pixel by a linear sum of the surrounding pixels, according to the linear coefficients specified as entries in a separate matrix, or *convolution kernel*. When these linear coefficients sum to one, the convolution operator can be thought of as replacing a pixel with a weighted average of its neighbours, where the weights correspond to the matrix entries. (A) If a uniform 5-by-5 convolution is applied to the pixel in blue, the pixel value will be replaced with the average value of the pixels on a 5-by-5 grid centred around itself. Uniform convolutions are used in this chapter, but other convolutions exist, such as a Gaussian, (B), which gives greater weight to points closer to the original pixel.

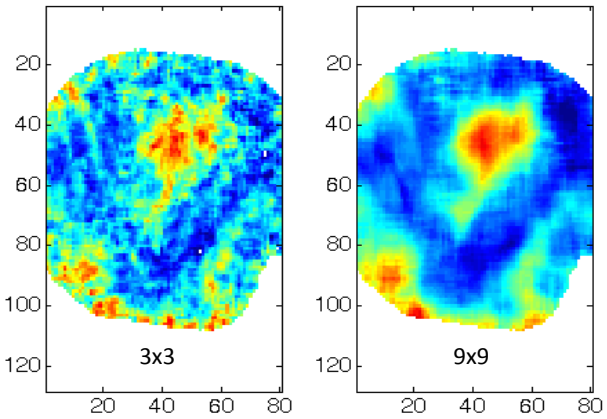

Figure 4.6: Increasing the voltage bin size from 3-by-3 pixels (left) to 9-by-9 pixels (right) leads to an increased spatial smoothing of the fluorescence. Colour scale goes from 0 to 1 (blue to red); fluorescence shown after all filtering steps in Section 4.2.2 have been applied (high-band 125%). In the case of a 3-by-3 bin-size, each pixel is replaced by the average of itself and the eight neighbouring pixels.

4. *Temporal filtering:* Each pixel was temporally filtered using a finite impulse response filter in Matlab (Parks-McClellan algorithm; `firpm`). Zero-phase filtering (`filtfilt`) was performed to minimise any temporal shifts caused by the filter. A band-pass filter was used where the low-band was 2Hz, and the high-band was taken as a percentage of a measure of the dominant frequency (DF) of the recording.

   The baseline value for the high-band of the filter was taken to be 125% of the DF, for which the DF is calculated as shown in Fig. 4.10. The effects of changing the high-band of the band-pass filter are presented in the results, Section 4.3.

5. *Drift removal:* Baseline drift was removed from each pixel by fitting a polynomial of order four, following Laughner et al. (2012), to the signal and then subtracting this from the signal.

6. *Normalisation:* Finally the signal of each pixel was normalised to be between 0 and 1 to correct for any differences in fluorescence intensity. Fig. 4.7 shows the results of applying each of the steps above to an example signal.

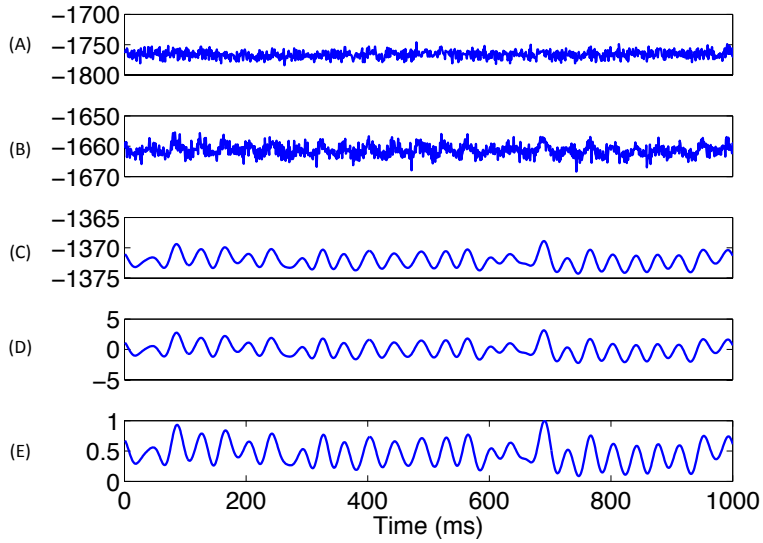

Figure 4.7: Steps for filtering optical mapping fluorescence. For a pixel at the centre of the array after applying each of the steps detailed in Section 4.2.2: (A) raw signal; (B) signal after spatial smoothing of 9 by 9 pixels; (C) after filtering with 125% of the DF for the high-band of the band-pass filter; (D) after drift removal; (E) after normalisation. (For the pixel shown here, drift removal was not required.)

4.2.3 Phase calculation

After filtering the data, the phase was calculated to analyse wavefront dynamics.

Steps for calculating the phase

In order to calculate the phase angle for each pixel, a signal with zero-mean was required. The steps to achieve this are:

1. Tag minima of the signal using a sliding window, and then tag maxima between each pair of minima (Fig. 4.8 A). A *window length threshold* was chosen such that tagged minima were separated temporally by at least that many samples.

2. Working from left to right, if any minima-maxima or maxima-minima pairs were within the *amplitude threshold*, then the pair were deleted (Fig. 4.8 B, Fig. 4.9).

3. Maxima were then redefined based on the remaining minima (Fig. 4.8 C, Fig. 4.9).

4. Cubic spline fits (`pchip`) were performed on the maxima and minima of the signal (Fig. 4.8 D). End-points were added to both ends of the signal at the median of the maximum amplitudes or median of the minimum amplitudes respectively. The average of these maxima (red) and minima (green) splines (the *mean line*, shown in black) was subtracted from the signal to give a signal of zero mean.

5. The real and imaginary parts of the Hilbert transform of this zero-mean signal were plotted in the phase plane (Fig. 4.8 E).

6. The angle around this trajectory gave the phase angle (Fig. 4.8 F).

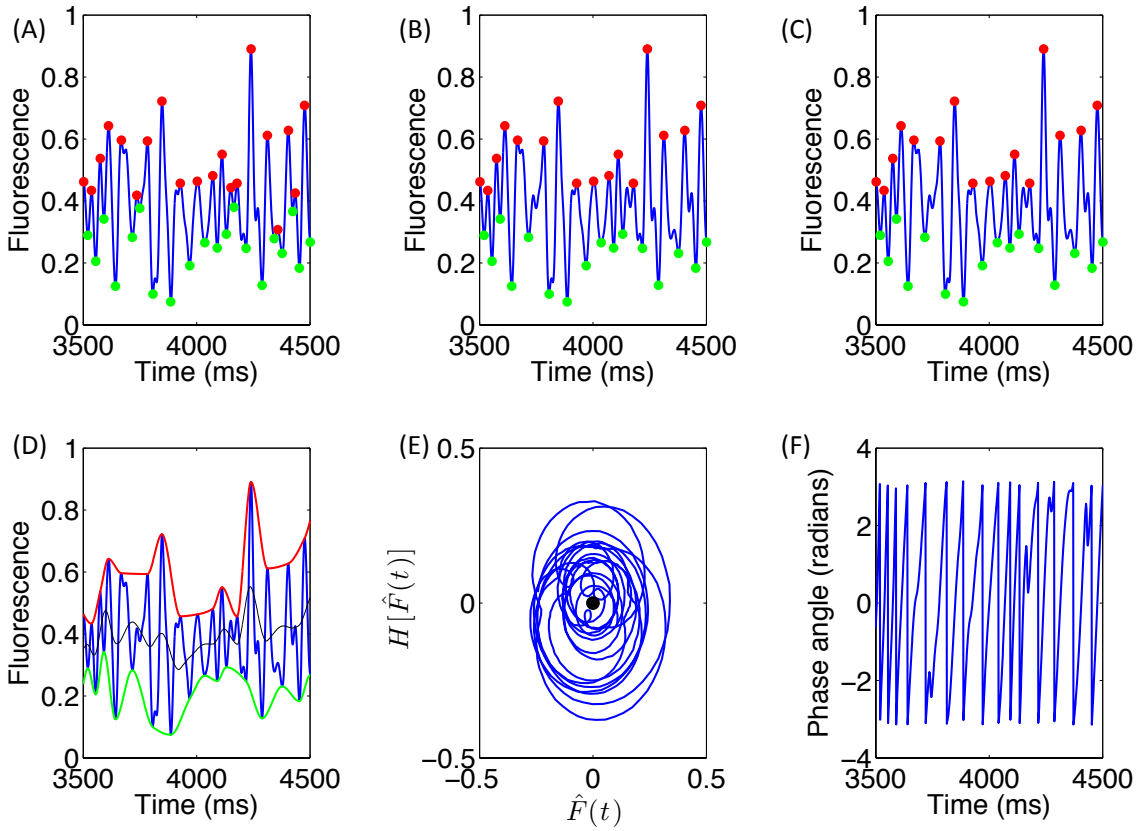

Figure 4.8: Phase calculation steps, detailed on Page 143. In this example, the window length threshold is 90% of estimated CL; amplitude threshold is 15% of median amplitude.

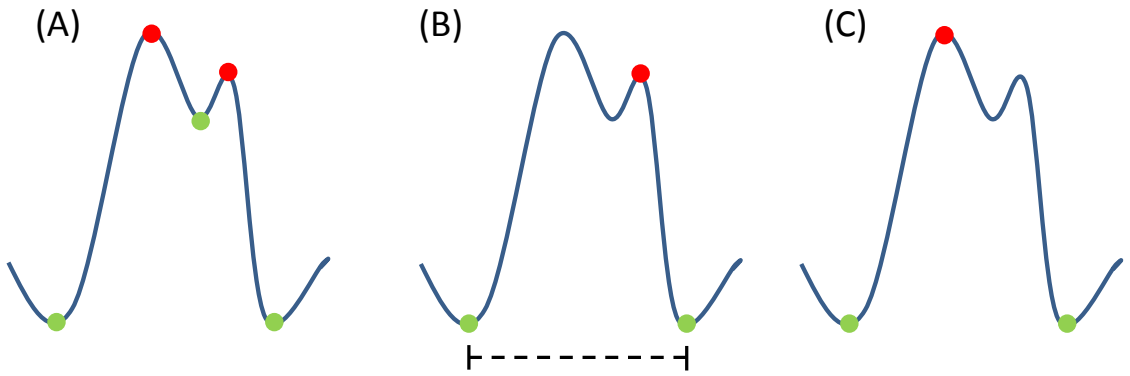

Figure 4.9: Redefining maxima following the deletion of maxima-minima or minima-maxima pairs that fail to meet the amplitude threshold. (A) A small deflection between the two maxima results in a maxima-minima pair and a minima-maxima pair below the amplitude threshold. (B) Since the deletion algorithm works from left to right, the first maxima-minima pair are deleted. (C) The remaining maxima is discarded, and recalculated as the maximum value on the interval between the two remaining minima.

Defining thresholds for the high-band of the temporal filter, and for the window length and amplitude thresholds for the phase calculation

Data-specific thresholds are required for the high-band of the temporal filter and the window length and amplitude thresholds for the phase calculation. Variability between preparations means that absolute thresholds are not appropriate. Fig. 4.10 illustrates the calculation of the data-specific thresholds.

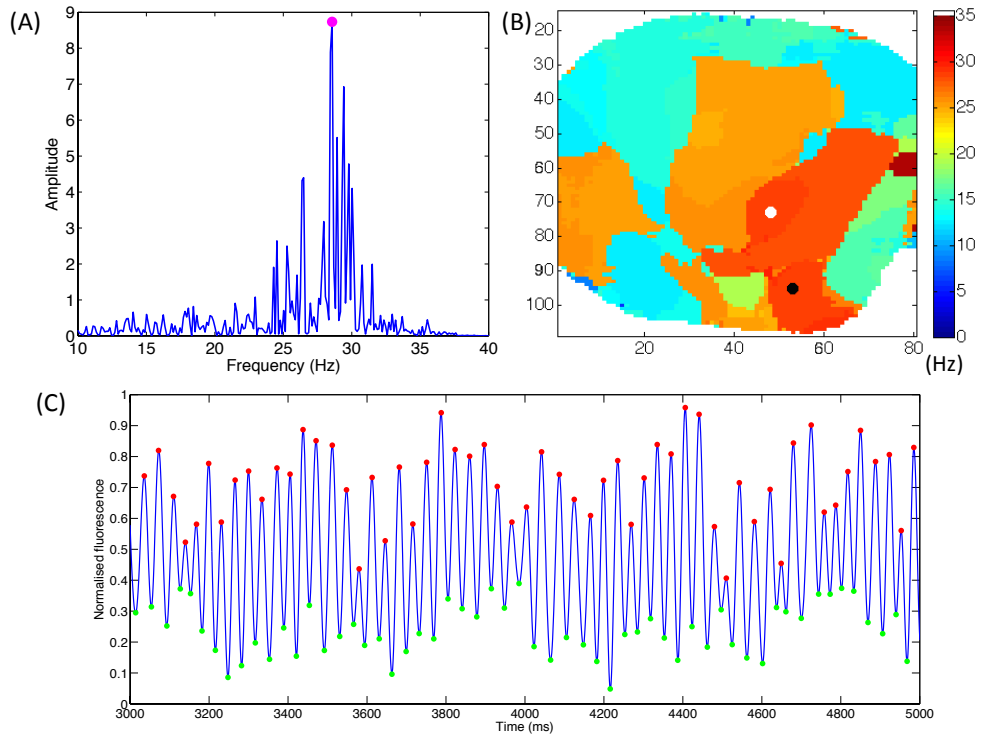

Figure 4.10: Calculating thresholds for the high-band of the temporal filter, and the window length and amplitude thresholds for the phase calculation. The overall *dominant frequency* estimate was taken to be the frequency of a pixel in the middle of an island of high frequency (black dot in (B)). The *window length threshold* is then taken as a percentage of the *cycle length*, 1000/DF. The amplitude threshold was calculated from a pixel within the island that is also close to the centre of the tissue (white dot), where a clean fluorescent signal was expected. (A) The *dominant frequency of each pixel* was defined as the peak (purple dot) with the highest amplitude in the frequency spectrum calculated by taking the Fourier transform of the signal. (B) Spatial frequency map showing the DF of each pixel. An island of high frequency is clearly visible, and the DF is 28.6Hz, giving a cycle length of 35.0ms. (C) The maxima and minima of the filtered signal at the white dot were tagged using the calculated window length. The *amplitude threshold* is taken as a percentage of the median of the paired deflections (median amplitude in this example is 0.5). In the example shown here, a filter with a high-band of 30Hz was applied.

The effects of window length and amplitude thresholds

In general, the calculated phase angle depended on the window length and amplitude thresholds used to calculate the moving mean line, because this determined which deflections were given a full trajectory in the phase plane. The effects of varying these thresholds on the signal used in Fig. 4.8 are shown in Figs. 4.11, 4.12, 4.13 and 4.14.

Window length and amplitude threshold: baseline values

For the parameter sensitivity analysis, baseline values were a window length of 90% of the estimated cycle length (CL) and an amplitude deletion threshold of 15% of the estimated median amplitude. These values were chosen because they were found to tag the deflections most likely to correspond to true activations in the points tested during the development of the algorithm. For example, Fig. 4.8 shows the most satisfactory deflection tagging of the parameters tested here; decreasing the window length tags too many double potentials that may not be deleted in later steps (Fig. 4.12), while increasing the window length would eliminate deflections closer together than the estimated DF allowance. Equally, decreasing the amplitude deletion threshold leads to the inclusion of deflections that are too small to be activations (Fig. 4.11), while increasing it deletes activations (Fig. 4.13). Hence 90% and 15% were taken as reasonable baseline values for the window length and amplitude respectively, and the effects of changing these values on the resulting PS maps are shown in the results, Section 4.3.

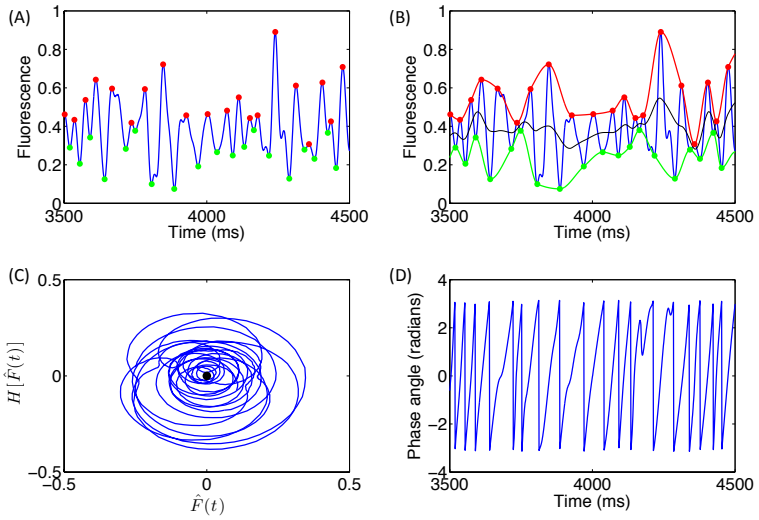

Figure 4.11: Phase calculation: effects of reducing amplitude deletion threshold. Here the window length is 90% of estimated CL, as in Fig. 4.8, while the amplitude deletion threshold is changed to 0%, so that no deflections are deleted.

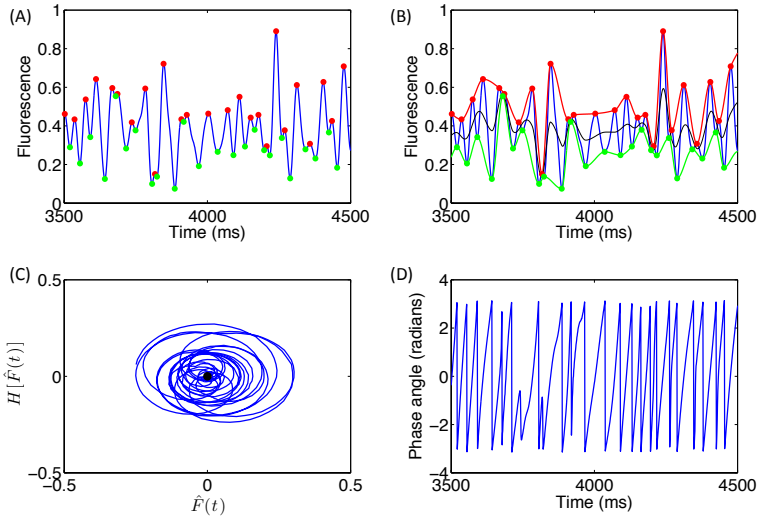

Figure 4.12: Phase calculation: effects of reducing window length threshold and reducing amplitude deletion threshold. Here the window length is reduced to 40% of the estimated CL and so more deflections are tagged in the first pass, whilst the amplitude deletion remains at 0% and no detections are deleted. Hence, this includes the maximum number of deflections of all of the parameter sets.

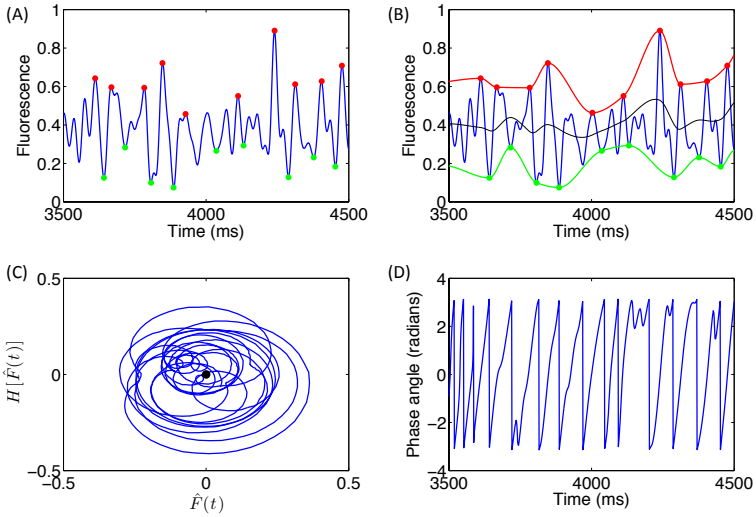

Figure 4.13: Phase calculation: effects of increasing amplitude deletion threshold. Again the window length is 90% of estimated CL, as in Figs. 4.8, 4.11, but the amplitude deletion threshold is increased to 50%, so that any minima–maxima pairs of amplitude below 50% of the estimated median amplitude are deleted, giving the pairs in (A) (compare Figs. 4.8B, 4.11A). This includes the minimum number of deflections of all of the parameter sets.

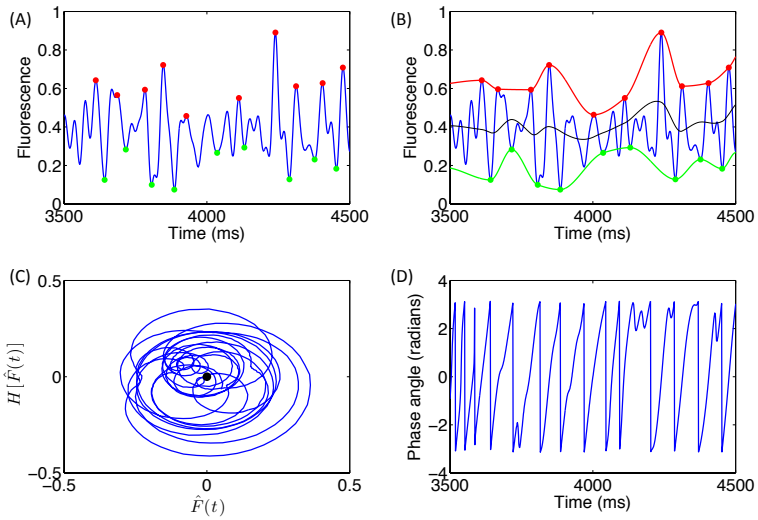

Figure 4.14: Phase calculation: effects of reducing window length threshold and increasing amplitude deletion threshold. Here the window length is again 40% of the estimated CL so that most deflections are tagged in the first pass. The amplitude deletion threshold is 50%, so that many of the tagged points are then discarded.

It should be noted that in the case that the signal is regular, the amplitude threshold will have little effect on the phase, as shown in Fig. 4.15.

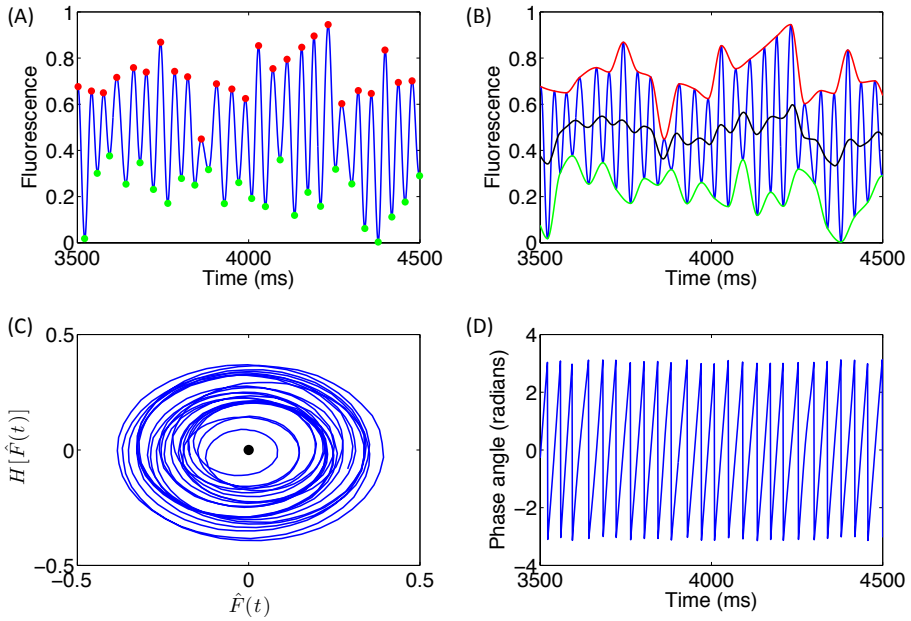

Figure 4.15: The amplitude threshold has little effect on phase calculation of a regular signal. The signal shown here has regular deflections and the originally tagged maxima and minima do not need additional correction. The phase plane plot is very clean; all trajectories encircle the origin.

4.2.4 Phase binning

The phase angle was spatially smoothed to reduce the noise content, and to improve phase singularity detection and tracking. The method used was as the same as the method used for the fluorescence (Step 3 in Section 4.2.2), except an additional mapping step was required to deal with discontinuities in phase angle due to the branch cut. The phase angle (θ) was converted to exponential form ($e^{i\theta}$) before the convolution operator was performed. The results of spatially averaging the exponential form were then converted back to phase angles between $-\pi$ and π (see Fig. 4.16). The default phase bin size was 9-by-9 and the effects of varying this on PS distributions are shown in the results, Section 4.3.10. After binning the phase, the locations of PSs were calculated.

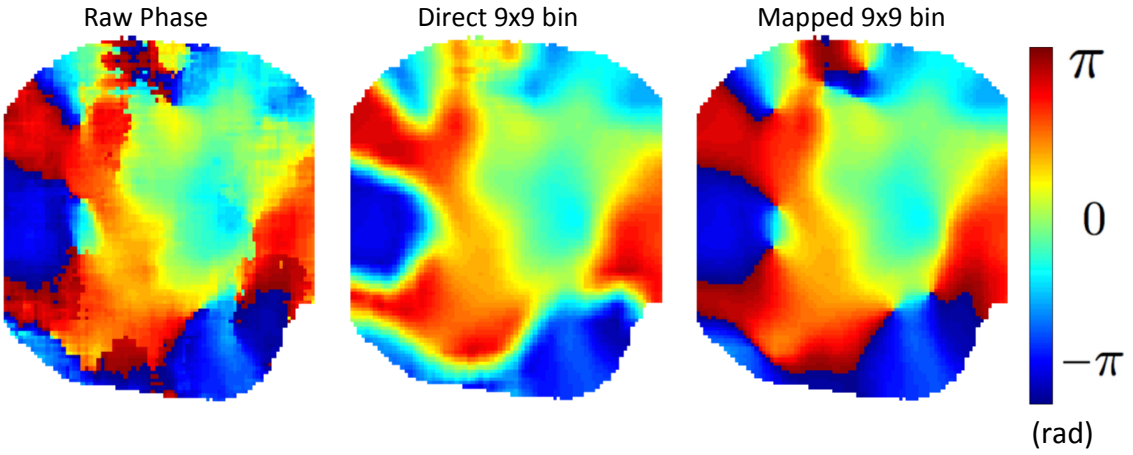

Figure 4.16: Phase binning was applied to reduce noise in the raw phase angle. Noise in the raw phase angle (left) was reduced by spatial smoothing using a 9 by 9 bin. Smoothing the phase angle θ directly (middle) leads to issues when neighbouring points are close to the branch cut at π and $-\pi$. Mapping to the exponential form ($e^{i\theta}$), smoothing this and then converting back to a phase angle (right) removes this issue. The same mapping method is used for phase interpolation in Section 7.2.4 (compare Fig. 2.6).

4.2.5 Phase singularity detection

In order to detect phase singularities, the line integral around pixels (Equation 1.24) was calculated using a 3-by-3 contour size for each pixel, using the techniques described in Section 2.11. Due to increased noise in phase from optical mapping data compared to simulated data, pixels were identified as candidate phase singularities if the integral was within a larger allowance of $\pm 2\pi$, compared to that allowed in Section 2.11. Candidate phase singularities were only identified as actual phase singularities if they lay on a neighbourhood of candidates and were the closest of their neighbours to $\pm 2\pi$. This is detailed in Fig. 4.17.

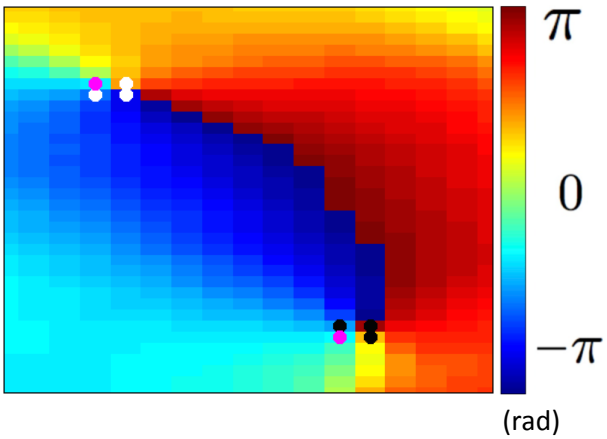

Figure 4.17: Phase singularities were defined based on the number of neighbouring candidate phase singularities. Candidate phase singularities were detected if the integral was within 3.0 of $\pm 2\pi$. A candidate phase singularity was said to belong to a neighbourhood when at least three of its eight neighbours were also candidates. The point within a neighbourhood closest to $\pm 2\pi$ was then defined as an actual phase singularity. Here, the white points are within 3.0 of -2π, signifying anticlockwise rotation and the purple dot is the closest to -2π and so is defined as the actual phase singularity. The black dots are clockwise rotation detections (2π), and the purple dot is defined as the actual phase singularity.

These additional steps make the method more robust to noise in phase. They enable phase singularities to be identified that would otherwise be masked by noise (Fig. 4.18). They also eliminate false phase singularities from isolated noisy pixels (Fig. 4.19). Any remaining false detections were eliminated at a later stage of the algorithm by taking into consideration how long phase singularities lasted for.

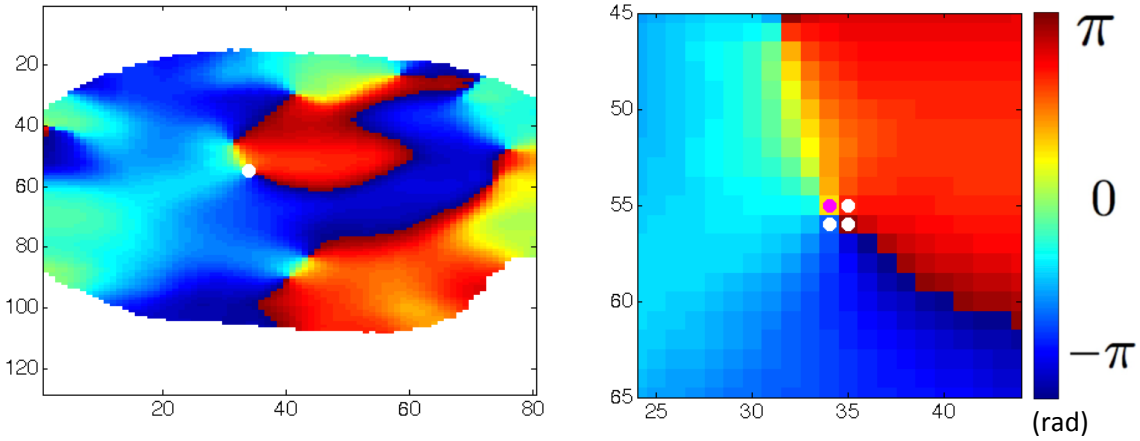

Figure 4.18: Using the threshold allowance and neighbourhood rule identifies phase singularities that would otherwise be masked by noise. In this example, a phase singularity is visually identifiable. The four neighbouring pixels have phase integrals equal to $-5.5, -5.0, -5.5, -4.1$, and so a strict value threshold from -2π would miss these points. Hence a more generous threshold of 3.0, together with the neighbourhood rule, was used to identify just one of these pixels as the actual phase singularity (purple dot in the inset).

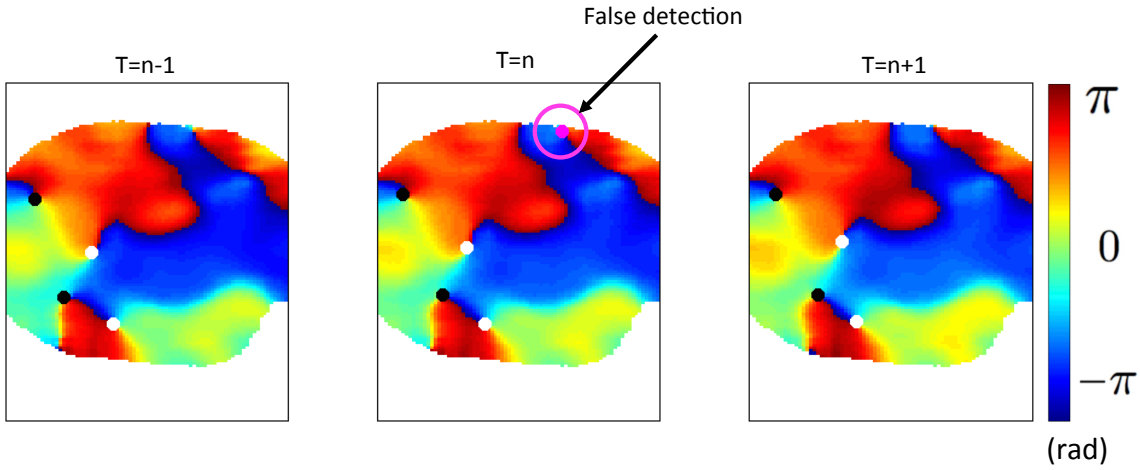

Figure 4.19: Requiring that a phase singularity has three neighbouring pixels that satisfy a phase value threshold prevents false detections due to noise. For example, the purple dot in the middle plot has an integral value of -6.0, and has been identified as a candidate. The adjacent frames (left and right) indicate that this is not a genuine phase singularity. Since the purple dot only has one neighbouring candidate, this point is discarded due to the neighbourhood rule.

Use of larger contour sizes to increase robustness to noise

An alternative method for increasing robustness to noise of phase singularity detection is to use a larger contour size for the integral in Equation 1.24. Other studies have used this approach, for example, Bray and Wikswo (2002b) show how to use an integral of 4-by-4. However, using a longer path length may lead to a less accurately defined position (Iyer and Gray, 2001). In this section, the results of using a 5-by-5 integral with a threshold allowance of 0.5 are compared to the modified 3-by-3 algorithm with neighbour information (Fig. 4.20). Using a larger integral without the neighbour requirement may be more sensitive to identified phase singularities; however, it may also lead to more false detections (Fig. 4.20).

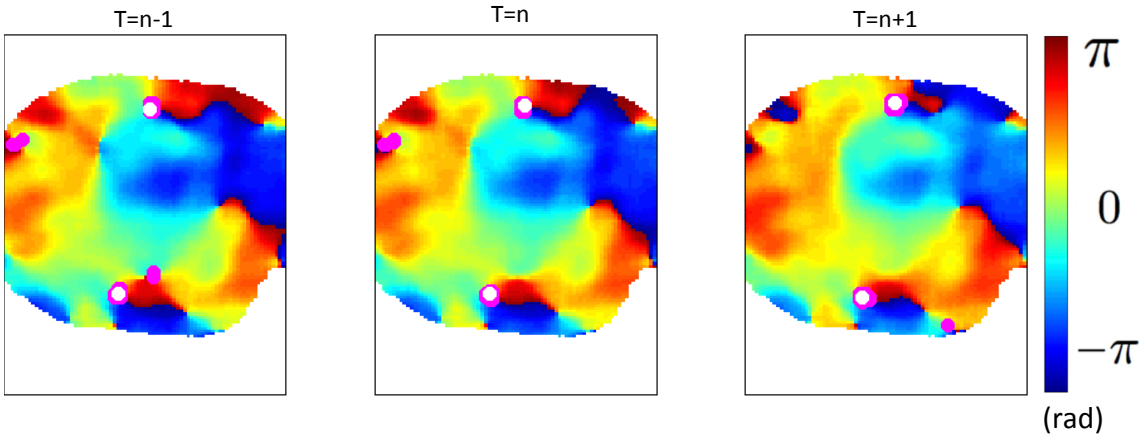

Figure 4.20: An alternative method to improving noise robustness when detecting phase singularities is to use a larger path size for the phase calculation contour integral, although this leads to more false detections in some cases. Phase singularities detected using a larger path integral of 5-by-5 with a threshold allowance of 0.5 (purple dots) are compared to those detected using a 3-by-3 path length with a threshold allowance of 3.0 with the neighbourhood rule (white dots). From the three consecutive frames here, the larger path length leads to more false detections. However, this could be improved by introducing a neighbour rule.

Phase singularity detection parameters

The threshold allowance of 3.0 and neighbourhood requirement of at least three neighbouring candidates provided adequate phase singularity identification in the data analysed and these values were fixed throughout the following parameter sensitivity analysis.

Phase singularities were stored by chirality (positive or negative spin; integral $\pm 2\pi$). The phase singularities detected on a framewise basis were next sorted into

phase singularity trajectories over time, so that the duration and behaviour of phase singularities over the course of the recording could be analysed.

4.2.6 Phase singularity tracking

In order to calculate PS lifetime and number of rotations, PSs must be tracked over time. Preliminary attempts used the technique developed by Rogers (2004) to work out PS lifetimes by tracking wavefronts. In the analysis of Rogers (2004), tracking wavefronts was preferred because PSs may jump large distances between frames, whereas wavefronts cover larger areas and may move smaller distances between frames. However, for the data analysed here, wavefront identification was more sensitive to noise in phase compared to PS identification using the phase singularity detection methodology described above (Fig. 4.21).

This was because the PS detection algorithm presented here was robust to small amounts of noise in the phase, while the same degree of noise led to wavefront break-up and misidentification of a single wavefront as two separate wavefronts. If PSs were identified as points at the ends of wavefronts, then PS detection would be affected in the same way. Hence, PSs were tracked over time without the use of wavefront information, and adaptations were included in the algorithm to circumvent problems created by missing detections and large movements between frames.

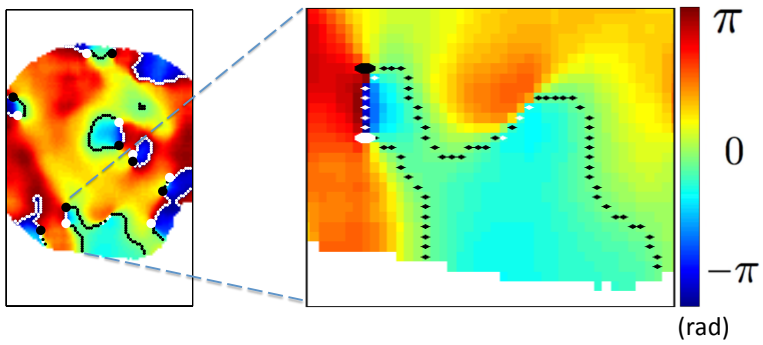

Figure 4.21: Phase singularities can also be tracked by following wavefronts, as in Rogers (2004); however, in the optical mapping data used here, noise in phase led to wavefront mis-identification. Shown here are PSs (black and white circles), the wavefront (isophase line of activation, $\pi/2$ shown as black line) and waveback (isophase line of recovery, white line). Misidentification occurs in the inset where the white pixels break up the black line into separate wavefronts. Thus defining PSs at the end of wavefronts would lead to incorrect PSs; whereas, the phase detection algorithm is robust to this noise (no false detections seen).

Steps involved in the phase singularity trajectory algorithm

The algorithm uses two storages matrices, one for positive PSs and one for negative PSs. Matrix columns refer to successive time frame numbers, and rows correspond to PS trajectories. Matrix entries record PS location in terms of its pixel index location. The steps in constructing these matrices are as follows and the method is illustrated in Fig. 4.22.

Step 1: Matrix initialisation

Each of the PSs from the first frame of the recording are assigned a separate row of the matrix corresponding to their chirality. These initial PS locations are entered for each row, forming the first column of the two matrices.

Step 2: Populating successive rows and columns

The algorithm then checks each frame of the recording chronologically. PSs from that frame are assigned to the storage matrix of the same chirality, either to an existing row if they can be identified with an existing PS trajectory, or to a new row.

Distance and time thresholds were employed to assign PS to trajectories. If a PS falls within a distance of 9-by-9 convolution pixels of a trajectory path over the last five time frames, then the PS is assigned to that trajectory. This is determined by computing the Euclidean distance of a PS location to each of the previous five entries in each matrix row. Using the previous five frames instead of just the previous frame allows for missing detections (Fig. 4.23).

There are four possibilities:

Filling in a row

The PS is assigned to just one trajectory. In this case, the PS location is recorded as the next entry of the row, corresponding to the latest position of the PS trajectory at the time frame being analysed.

New row

The PS is not assigned to any trajectory. In this case, a new row is created to indicate the start of a new PS trajectory. Historical location entries in the newly created row are populated with NA.

Multiple rows

The PS is assigned to multiple trajectories. In this case, the PS is added to each assigned row and so is logged as continuing multiple PS trajectories.

Row duplication

In the instance that multiple PSs in a given frame are allocated to the same trajectory, then the corresponding matrix row is duplicated as necessary. In this way each PS may be stored with that trajectory.

(A) PS trajectory matrix

	...	Frame(n-5)	Frame(n-4)	Frame(n-3)	Frame(n-2)	Frame(n-1)	Frame(n)
...							
PS(x-1)	...						
PS(x)	...	(x_{n-5}, y_{n-5})	(x_{n-4}, y_{n-4})	(x_{n-3}, y_{n-3})	(x_{n-2}, y_{n-2})	(x_{n-1}, y_{n-1})	(x_n, y_n)
PS(x+1)	...						

(B) Step 1: Initialise matrices

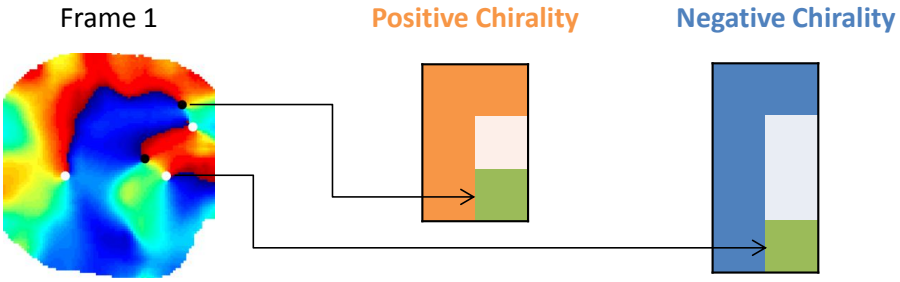

(C) Step 2: Fill in matrix

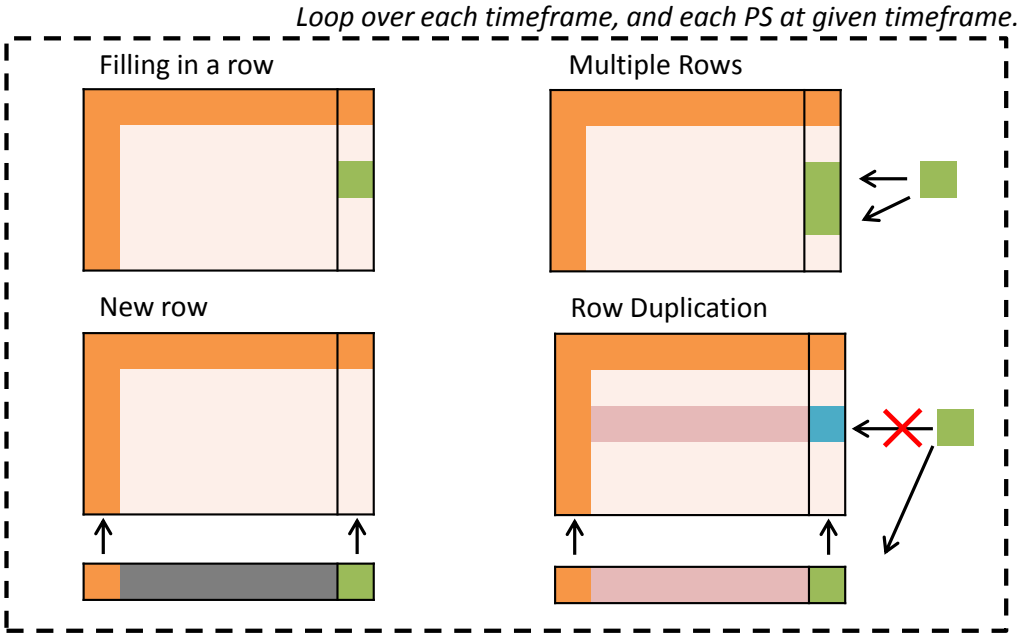

Figure 4.22: Schematic to show the steps involved in constructing the phase singularity trajectory matrices. See text on Page 155 for explanation.

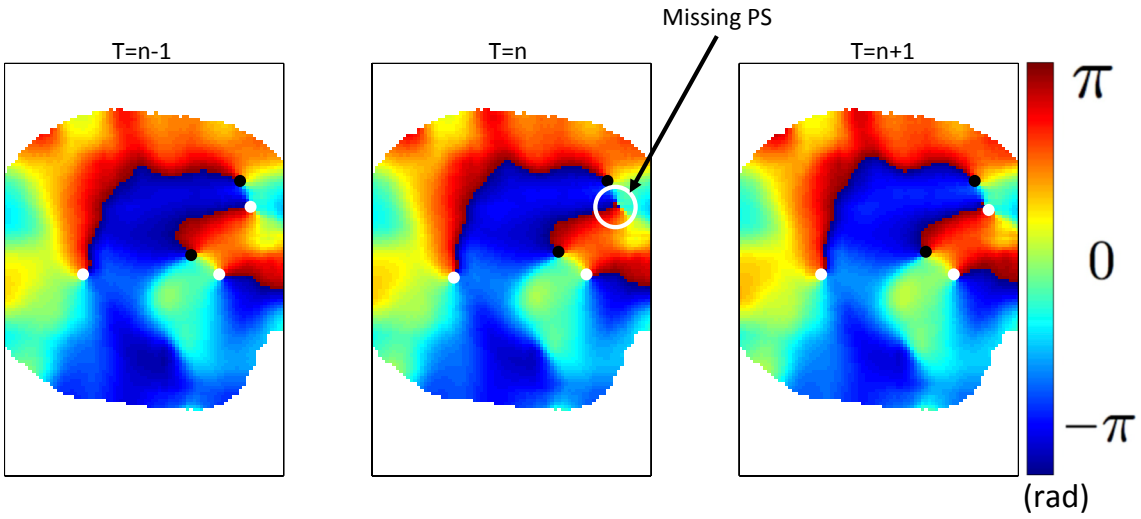

Figure 4.23: Missing frame allowance ensures missing PSs do not affect the PS trajectory lifetime. When tracking PSs, the previous five frames are checked for a candidate trajectory, since there may be frames with missing detections. For example, in the middle frame here, there is a detection missing; however, this would not affect the PS trajectory lifetime as the PS is still counted as one trajectory because a missing frame threshold of five is used.

The tracking algorithm recorded all possible trajectories allowable within the thresholds, and so multiple overlapping trajectories were obtained. Due to this, filtering was required to delete superfluous or unwanted trajectories. These additional steps are described later in the section.

Determining appropriate thresholds for the phase singularity trajectory algorithm

Appropriate values for the number of missing frames and distance movement allowance were determined. The trajectory algorithm was run using the maximum justifiable thresholds for number of missing frames and distance movement allowance, in order to generate the most comprehensive population of trajectories. The missing frames threshold used was five frames because this corresponded to 5ms of noise, during which the phase singularity was not expected to move a large distance and so a single trajectory could still be identified. The distance movement allowance used was 15-by-15 pixels to give a larger allowance than the level of spatial binning applied (9-by-9 pixels). See Fig. 4.24 for an explanation of distances.

The mean number of missing frames per trajectory was 1.51, and 3.10% of all of the frames in PS trajectories were missing a detection for that trajectory. Sequences of consecutive missing frames (*trains*) were identified across all trajectories. There

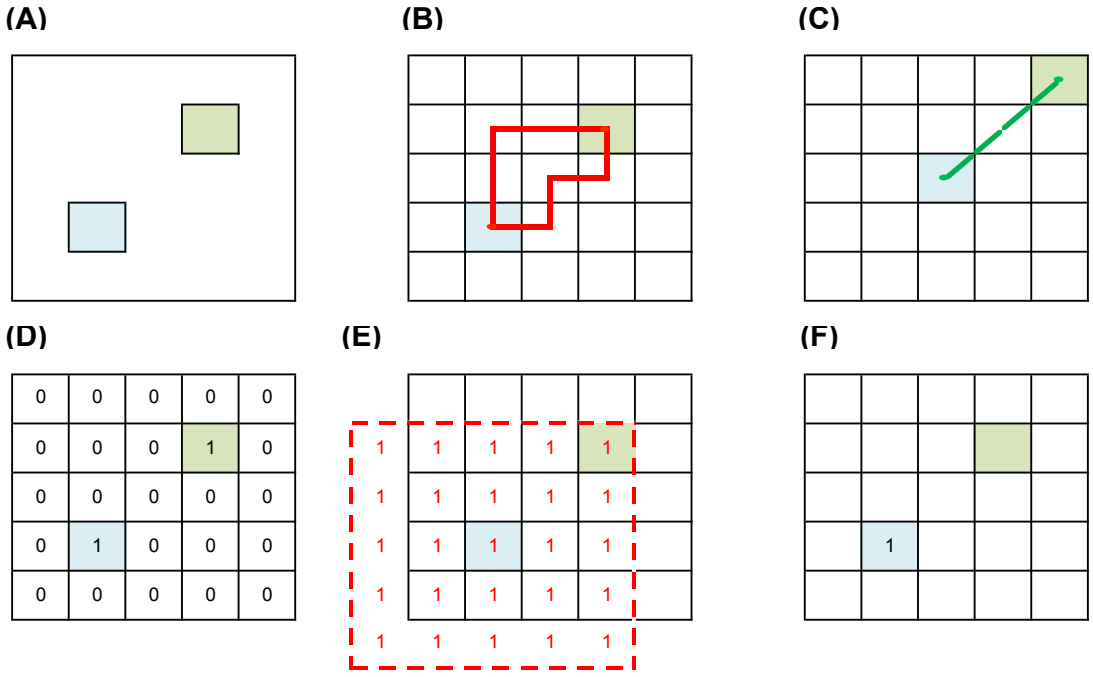

Figure 4.24: Convolution operators offer a computationally efficient way of determining if two pixels are within a distance threshold, although distance can be defined in different ways. (A) Distance is determined between the blue and green pixel. Under the norm or city-block measure of distance, these pixels are a distance of 4 pixel-lengths away as 4 adjacent pixels are required to get from one to the other. (B) Two such routes are shown in red. (C) Under Euclidean distance shown in green, the pixels are a distance of $2\sqrt{2}$ pixel-lengths away. Use of a $(2n+1)$-by-$(2n+1)$ convolution within the algorithm results in a norm distance threshold of n pixels, and a Euclidean distance threshold of $\sqrt{2}n$. Here a 5-by-5 convolution is used. (D) The two pixels are assigned value 1 and the other pixels value 0. (E) A uniform 5-by-5 matrix of ones is overlaid over the blue pixel, and under the convolution operator the blue pixel is replaced with the value of the sum of the products of each entry of the convolution matrix and the underlying values. (F) The result is 1, indicating the blue and green pixels are within the distance threshold defined. This method is more computationally efficient than calculating the distance between every pair of pixels and comparing to the threshold, as the actual distance between the two pixels is not calculated.

were 1051, 99, 99 and 173 trains of 1, 2, 3 and 4 missing frames respectively. Since there are a significant number of occurrences of 4 consecutive missing frames (12%), a frame allowance of 5 frames was used as a final parameter.

Next, the distance moved between occupied frames was calculated. The mean was 0.65 pixels and Fig. 4.25 shows the distribution. A distance allowance threshold of 9-by-9 pixels was chosen (corresponding to 5.6 pixel Euclidean distance) because firstly it matches the level of spatial binning, and secondly only 1.18% of movements are outside of this range.

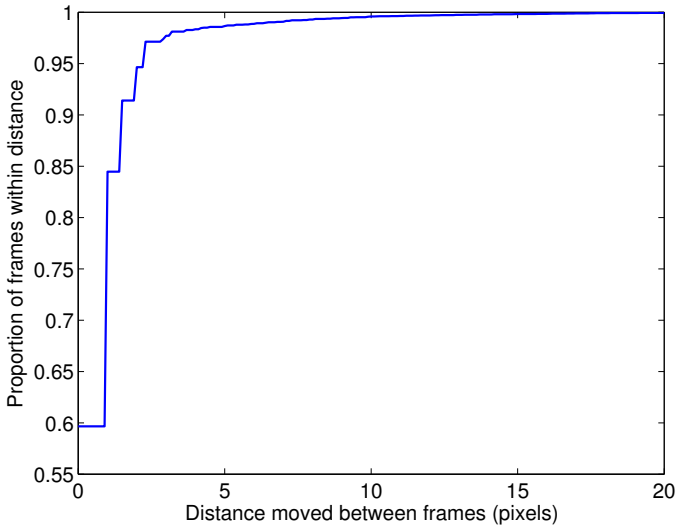

Figure 4.25: Measured distance movement between occupied frames of each trajectory. The distance movement between occupied frames in each trajectory was measured in order to set thresholds for the distance movement allowed between the PS and the trajectory in the previous 5 frames. These results are for generous distance and time thresholds of 15 pixels and 5 frames respectively, and show the proportion of frames where the PS is within a given distance.

As an additional check that the 9-by-9 distance movement allowance is appropriate, the effects of changing this choice from 3 to 15 were investigated. Five and below were found to be too small because there were movements between frames outside of these allowances where the PS clearly continued the trajectory (see Fig. 4.26). Eleven and above were found to be too large as PSs were incorrectly included in the trajectory, resulting in too long a path and the amalgamation of trajectories (see Fig. 4.27). Matrices of size 7-by-7 and 9-by-9 gave very similar results to each other for the PS trajectories.

Hence, for the remainder of the analysis, these thresholds were fixed as an allowance of five missing frames and a 9-by-9 distance movement allowance. It should

be noted that other values may give improved trajectory tracking for other smoothing and filter values; however, this was not investigated in the parameter sensitivity tests.

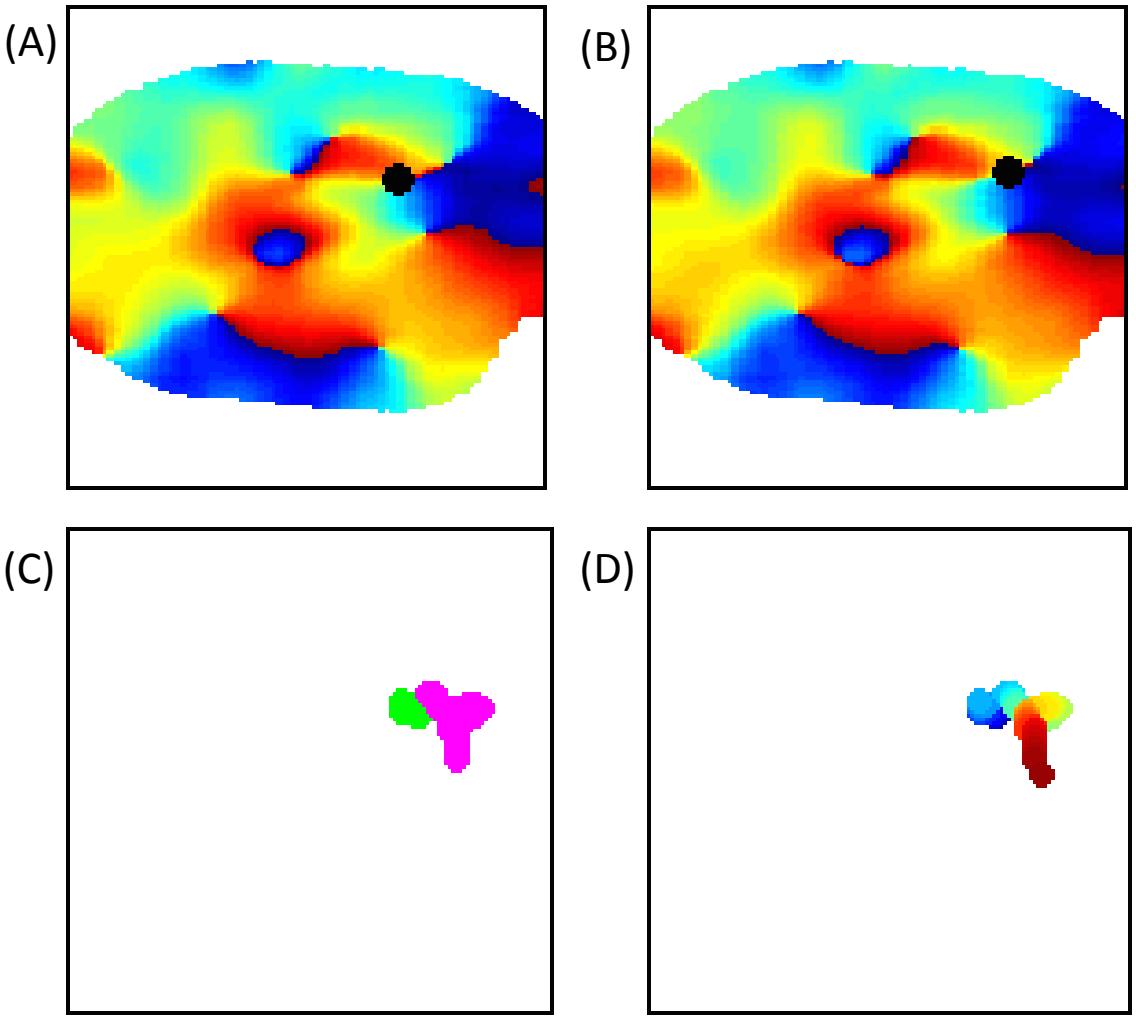

Figure 4.26: Distance matrix of 5 by 5 is too small: PS assigned incorrectly to new trajectory. (A) Frame at time point n showing a PS in black. (B) Frame at time point $n + 1$ in which the PS is outside of the distance threshold of the PS in (A). This leads to a new trajectory being started from the PS. (C) The trajectory is split into one of 32 ms (green) and one of 72ms (purple). (D) Correct trajectory, coloured by time (blue to red).

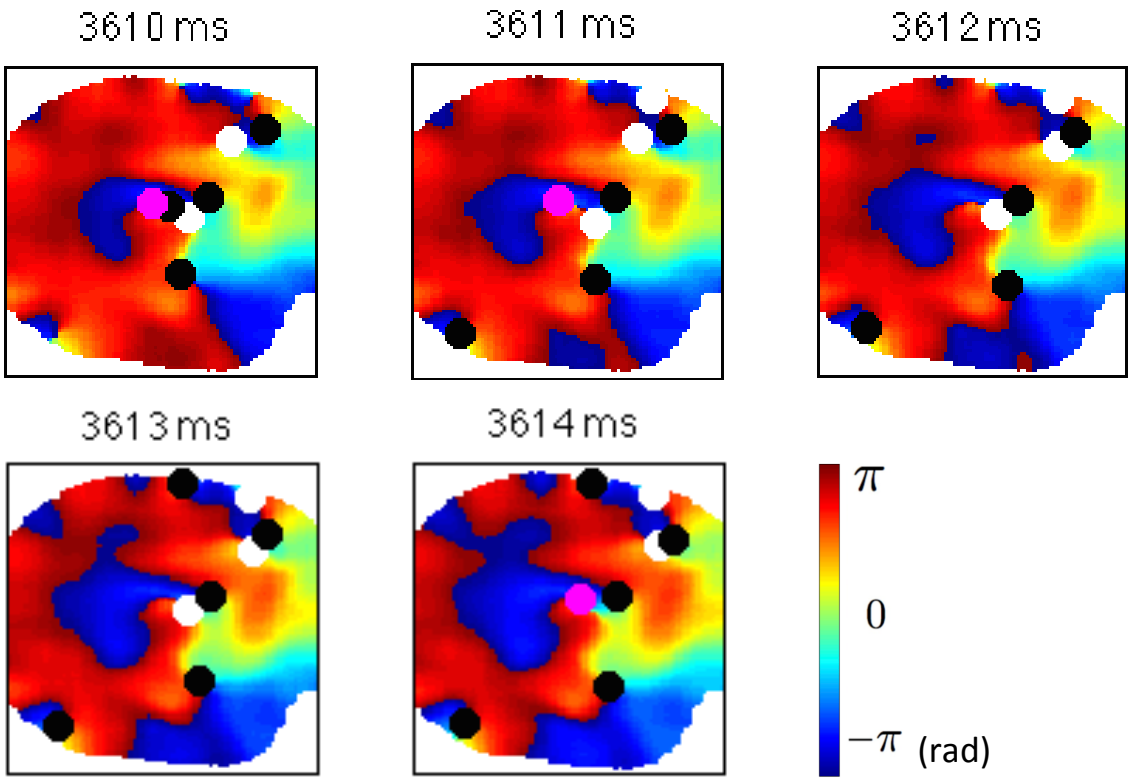

Figure 4.27: Distance matrix of 11-by-11 is too large: here a new PS is incorrectly assigned to the current trajectory. Using an 11 by 11 convolution matrix, the PS indicated by the purple circle collides with one of opposite chirality at time 3610/3611ms and the PS trajectory for this point should end here. However, the purple circle in the isophase map at 3614ms is within the allowed distance threshold and so is logged as continuing the trajectory, overestimating the trajectory lifetime.

Deleting incorrect trajectories

A trajectory may incorrectly be divided into separate trajectories if there are single frame movements outside of the distance threshold. In addition, the tracking algorithm generates all possible legitimate trajectories, and some trajectories should be discarded in favour of other more complete trajectories.

For example, during the distance allowance tests, it was observed that there are instances where a new PS trajectory is started incorrectly. This can either occur when the PS is outside of the distance allowance (Fig. 4.28) or when a false detection occurs such that there are then two candidates that could continue the PS trajectory. In both cases, the algorithm starts a new row for a new trajectory and the new trajectory shares a large amount of overlap with the original trajectory. This necessitated an additional step in the algorithm to delete the shorter of the rows. The row with a shorter lifetime is deleted, as this PS trajectory is a subset of the other, where any differences are due to noise. A row was deleted in the instance that it overlaps by greater than 90% with a longer trajectory, or if greater than 60% of its pixels match the longer trajectory and it is less than 10 pixels long.

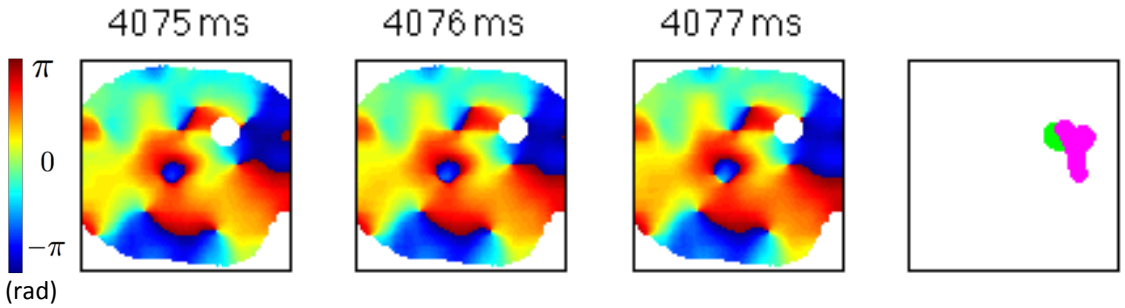

Figure 4.28: Deletion of PS trajectory subsets: PS trajectories that have a large degree of overlap with other trajectories are deleted. Here the PS at 4076ms is outside of the distance threshold matrix of 7-by-7 pixels and so is logged as a new trajectory. The PS at 4077ms satisfies both trajectories and so the trajectories match from 4077ms onwards. This creates a trajectory starting at 4076ms (purple) that repeats the existing longer trajectory (green, plus purple). The shorter trajectory does not correspond to a separate trajectory and so is deleted using overlap thresholds.

Trajectories of duration less than 3ms were discarded; these were considered to be noise and usually occur as short-lived pairs of opposite chirality. This was observed to cause problems when one of the pair of false detections is instead stored as part of another trajectory (Fig. 4.29). These PSs were removed along with any PSs of the opposite chirality within a small neighbourhood of the point, and the trajectory algorithm was then re-run excluding these phase singularities.

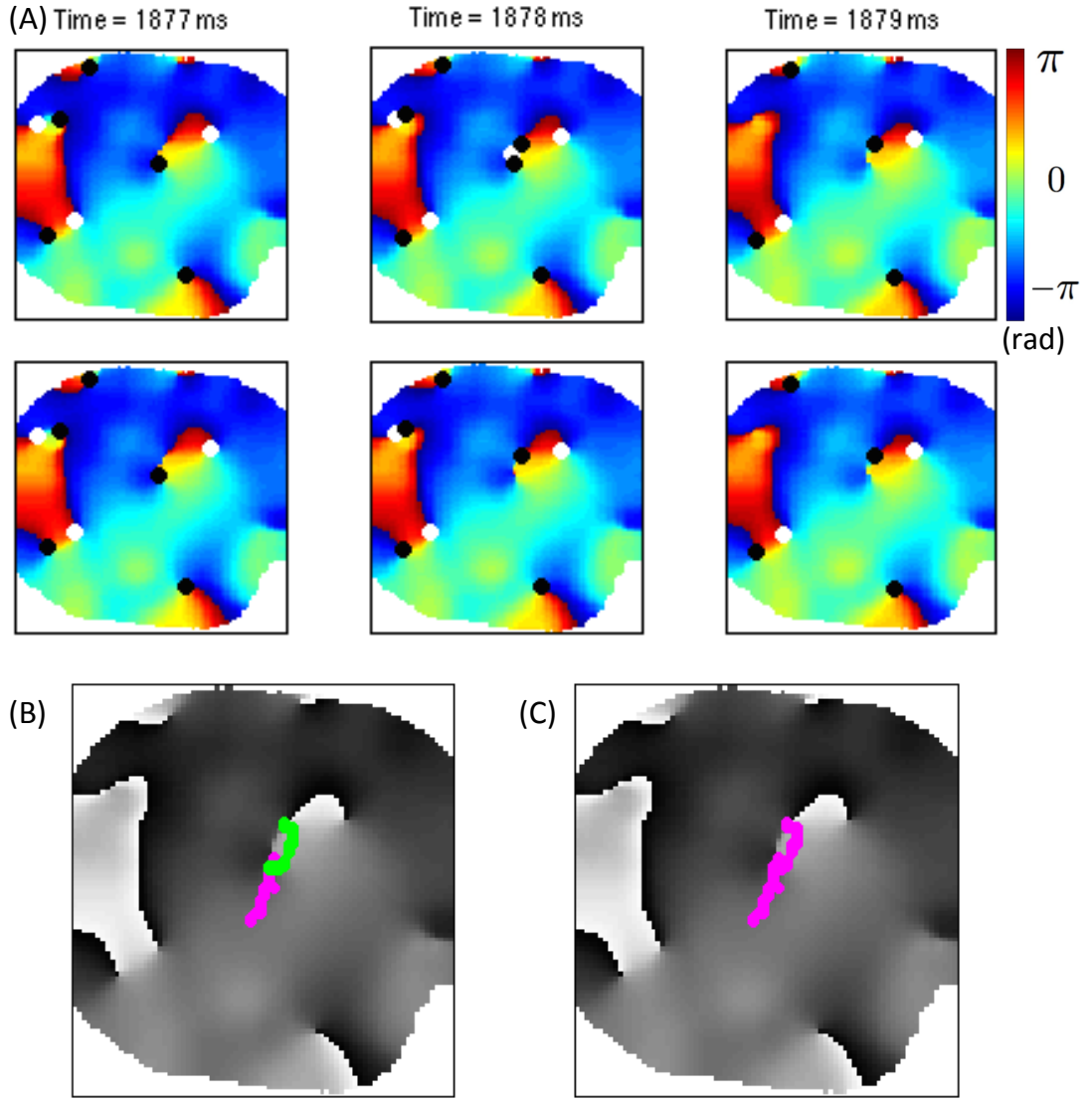

Figure 4.29: Short-lived phase singularities may be incorrectly assigned to trajectories, leading to the the creation of an extra phase singularity trajectory. In the example here, a pair occur at 1878ms in the top row and this starts a new PS trajectory for the black PS. The close by PS at 1879ms then satisfies either trajectory. This results in two PS trajectories shown in (B); the shorter being the green and the longer is the purple with green except the pixel at 1878ms. In order to obtain the correct single trajectory, the pair of phase singularities occurring at 1878ms (top row) must be deleted. These are identified by locating the short-lived white trajectory at 1878ms and deleting it plus the close by black PS. The tracking algorithm is then re-run with these PSs excluded (i.e. on the PSs in the bottom row of (A)), leading to the correct single trajectory in (C).

4.2.7 Calculating the number of rotations

A method for calculating the number of rotations of a phase singularity trajectory was developed. The phase of a pixel a set distance and angle away from the PS was tracked over time in order to estimate the changes in phase occurring around a PS (see Fig. 4.30(A)). For example, the phase of the pixel one above the PS location could be stored over time. The differences between the phase for consecutive frames were then calculated and wrapped to the range $-\pi$ to π. The sum of these differences divided by 2π then gave the number of rotations. The effects of choosing a different pixel to store; for example, the pixel below, to the left or right of the PS, as well as the distance away were investigated. An ideal distance would give a measure of the number of rotations that is not affected by the pixel location for that radius. Distances of 1, 3 and 5 pixels away, either above, below, to the left, or right of the PS were compared for all of the PSs in a recording.

There was a high correlation coefficient for the number of rotations calculated using the phase from the top pixel compared to the other three choices for each radius ($0.92, 0.95$ and 0.92 for $1, 3$ and 5) respectively. The results for an example trajectory are shown in Fig. 4.30, where the pixel choice gives similar results (Fig. 4.30 C). Equally the results for the different radii correlate well (mean correlation 1 with 3: 0.91; 3 with 5: 0.95; 1 with 5: 0.92). The results for the example shown are visually similar for radii of 1, 3 and 5 (Fig. 4.30 D); however, there is more noise for the case of 1 pixel away since this choice is close to the PS. The number of rotations is also expected to correlate well with the duration of the PS and the correlations are as follows: 0.94, 0.96 and 0.94 for 1, 3 and 5.

In the following analysis, a radius of 3 pixels was used since this was less affected by noise, and there was the highest correlation between the location choices at a 3 pixel radius (north, south, east and west), as well as the highest correlation with duration.

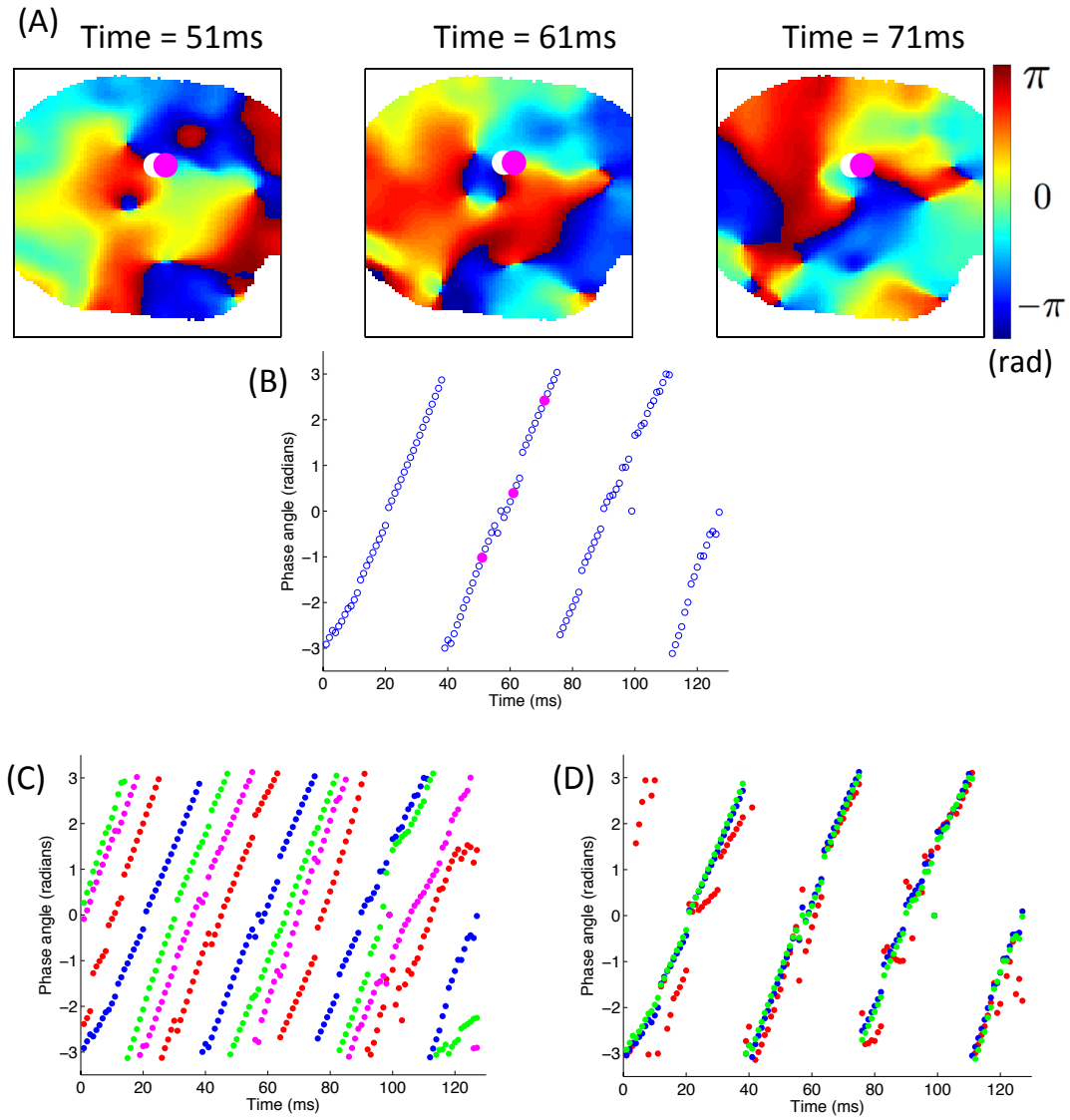

Figure 4.30: The number of rotations was calculated by tracking the phase of a pixel a set radius away from the PS. For example, (A) shows the PS location as a white dot and the pixel used for calculating the number of rotations as a purple dot. In this case it is 3 pixels to the right of the PS and the phase of this tracked pixel is shown in (B), with purple dots indicating the phase of the pixel in the time frames shown in (A). Using this pixel, the number of rotations is 3.50. The effects of different pixel choices were also investigated, and (C) shows the choice of the pixel 3 away that is above (red; 3.61 rotations), below (green; 3.60 rotations), to the left (magenta; 3.55 rotations) and to the right (blue; 3.50 rotations) of the PS. For a radius of 3, the pixel location does not have a big effect. The effect of distance of the pixel from the PS was also investigated, and (D) shows the phase at 1 (blue), 3 (red) or 5 (green) pixels away. The phase at a 1 pixel distance is more noisy, suggesting it is not a sufficient distance from the PS.

4.2.8 Heat map binning

The number and distribution of PSs were analysed by creating heat maps showing the PS density, expressed as number of PS per cm^2 per second. Heat maps were compared between parameter sets and also between recording files by computing a two-dimensional correlation coefficient of the finite tissue values, using `corr2` in Matlab. Heat maps were not expected to match on a pixel by pixel basis and so were binned before calculating the correlation coefficient, where the default bin size was 3-by-3 pixels. Phase singularities were included in heat maps in the instance that the phase singularity trajectory is above a threshold number of rotations (default value is 0.5). For each frame of the phase singularity trajectory, the count of phase singularity occurrence at the pixel location of the phase singularity was increased.

4.2.9 Regional analysis

To align with the histological analysis, PS characteristics for each preparation were calculated for each tissue region. A score was assigned per region to represent the average number of PSs, per tissue pixel, per frame of the recording.

The region assignment was based on photos showing the preparation which included lines representing where the tissue was cut for the histological analysis.

The resulting scores were a 3-by-3 matrix and the correlations between the scores obtained with different parameter sets were calculated using `corr2`.

4.3 Results

4.3.1 Parameter sensitivity analysis overview

In order to assess the suitability of the baseline parameter sets chosen for the analysis, the parameters were each varied in turn or in pairs from the baseline set and the effects on the calculated outcomes were observed. The parameters to be varied are the spatial bin size and the high-band of the temporal filter for reducing noise in the fluorescence signals; the window length and amplitude deletion thresholds for the phase calculation; the spatial bin size for smoothing the phase; the spatial bin size for smoothing the spatial distribution of phase singularities density map; and the threshold number of rotations or the duration threshold for inclusion in the distribution heat map. These are shown, along with their baseline and permissible values, in the schematic 4.31. For each parameter sensitivity analysis, all other parameters were held at default value. The sensitivity on the dominant frequency (DF) and cycle length (CL), as well as phase singularity measures were investigated.

DF and CL of the voltage are only dependent on the choice of spatial bin size and temporal filter for the voltage filtering and this is investigated in Sections 4.3.2 and 4.3.3. CL can also be calculated from phase, and the effects of the window length and amplitude thresholds on this are investigated in Section 4.3.4. All of these parameter choices (voltage bin size, temporal filter and phase calculation window length and amplitude values) along with the phase bin size, affect the phase singularities detected (Section 4.3.5). Changes in phase singularities can be quantified in terms of the number of phase singularities, as well as the number according to their duration or number of rotations and the maximum number of rotations found in the recording (Sections 4.3.6, 4.3.7). Finally, the distribution of phase singularities can be compared as spatial heat maps (Section 4.3.8), where the choice of bin size for the heat map, as well as the duration and number of rotations threshold for inclusion in the heat map will affect the overall correlation. The schematic 4.31 shows the parameters varied during the analysis protocol and the different outputs measured for variation of the different parameters.

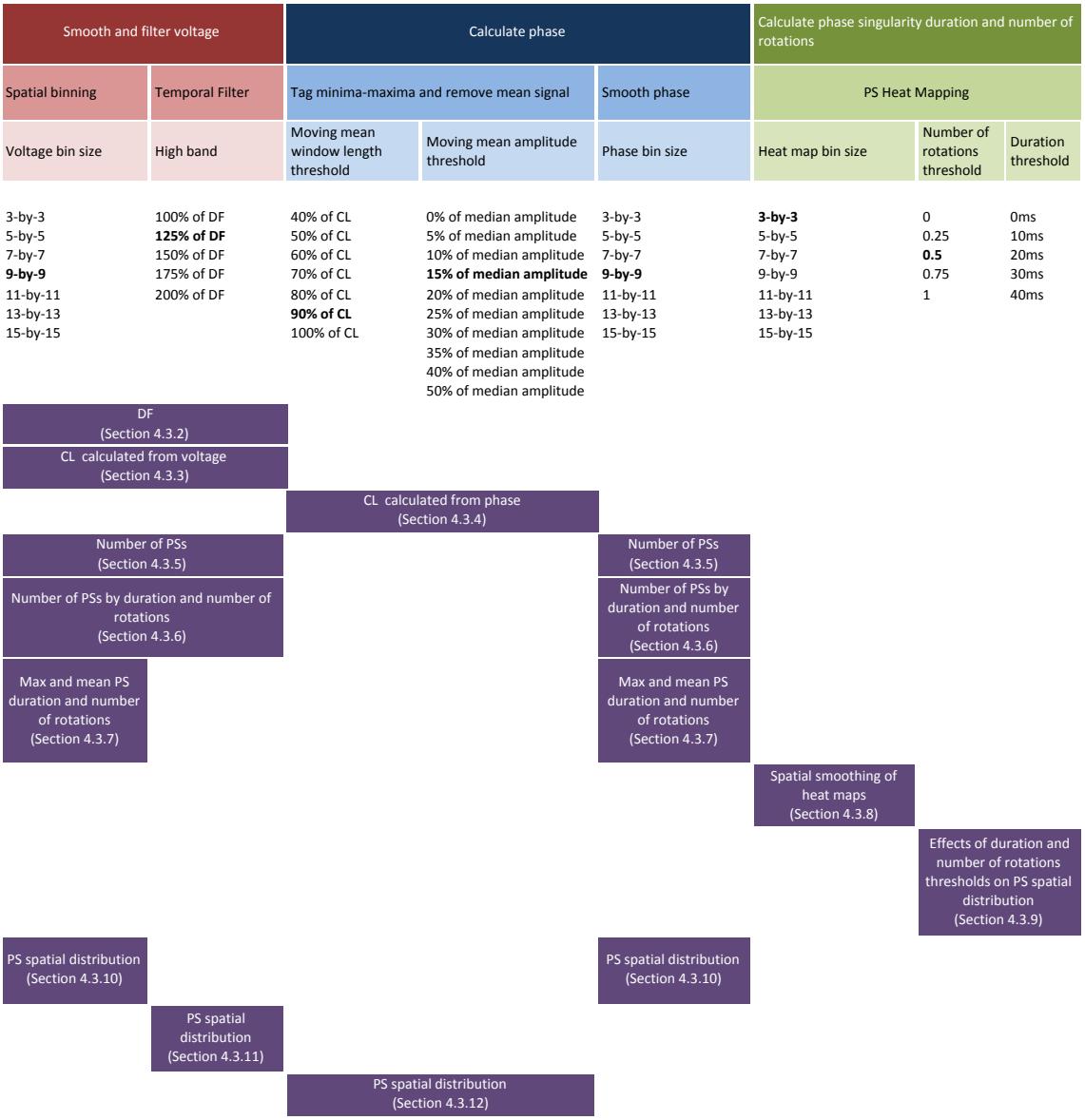

Figure 4.31: Schematic to show the parameters varied at each stage of the analysis protocol, the permissible values for each parameter, and the outputs measured for each variation. The methodology is to smooth and filter the voltage (red boxes); calculate the phase (blue boxes); and calculate the phase singularity duration, number of rotations and spatial distributions (green boxes). The parameters required for each step of the analysis are shown, with the default value in bold. In the case that one parameter is being varied, all other parameters will be fixed at their default value. Note that the duration threshold does not have a default value because the number of rotations threshold was used instead. The outputs measured for each parameter variation are shown in purple boxes, along with the associated section. The column that the purple boxes are located in indicates the parameters that are varied in each case.

4.3.2 Dominant frequency maps

Dominant frequency (DF) is often used as a measure of activity, and areas of high frequency may be used to locate drivers and be used clinically to guide ablation. As such, the DF needs to be captured properly by the chosen parameter set, giving an optimal balance between noise and information loss. The dominant frequency of the optical mapping data was affected by the voltage binning and filtering applied. The effects of varying the voltage bin size on the DF are shown in Fig. 4.32, where the maps are visually similar across bin sizes, but have more noise for the lower bin sizes (3-by-3 and 5-by-5). Likewise, the DF maps are visually similar for high-band filter settings of 125% to 200% of estimated DF (Fig. 4.33), although at 100% the higher frequencies are filtered out of the signal, since there is a small area of frequency higher than the estimated DF used for setting the filter values. This suggests that bin sizes of 7 or above and filter settings of 125% or above give acceptable measures of DF.

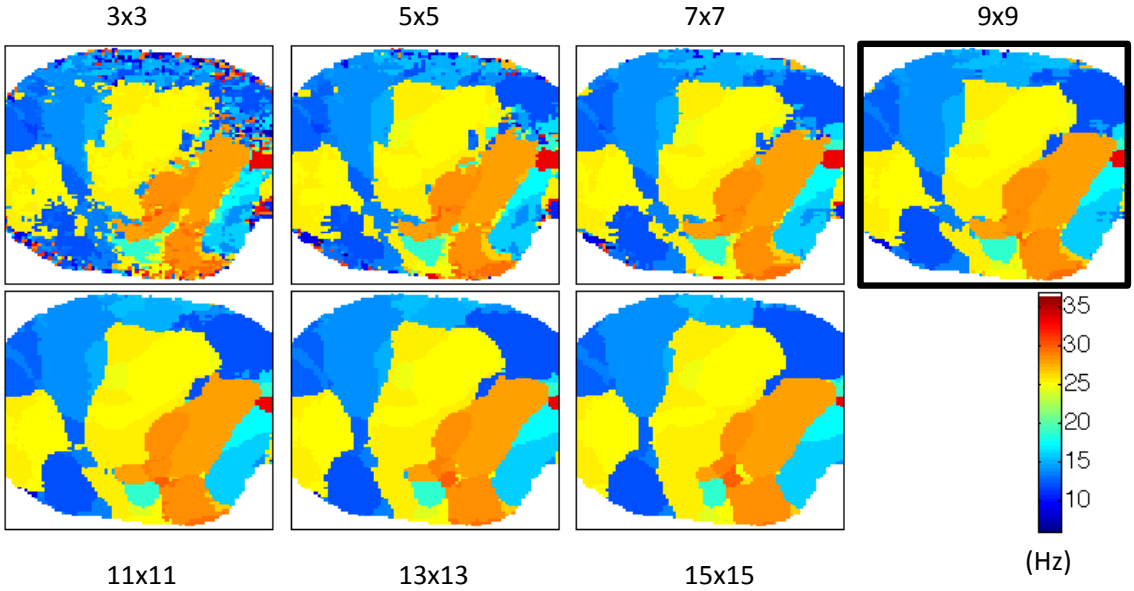

Figure 4.32: Dominant frequency maps with varied voltage bin size are visually similar, although there is more noise for smaller bin sizes. The default value is 9-by-9, shown in the black box.

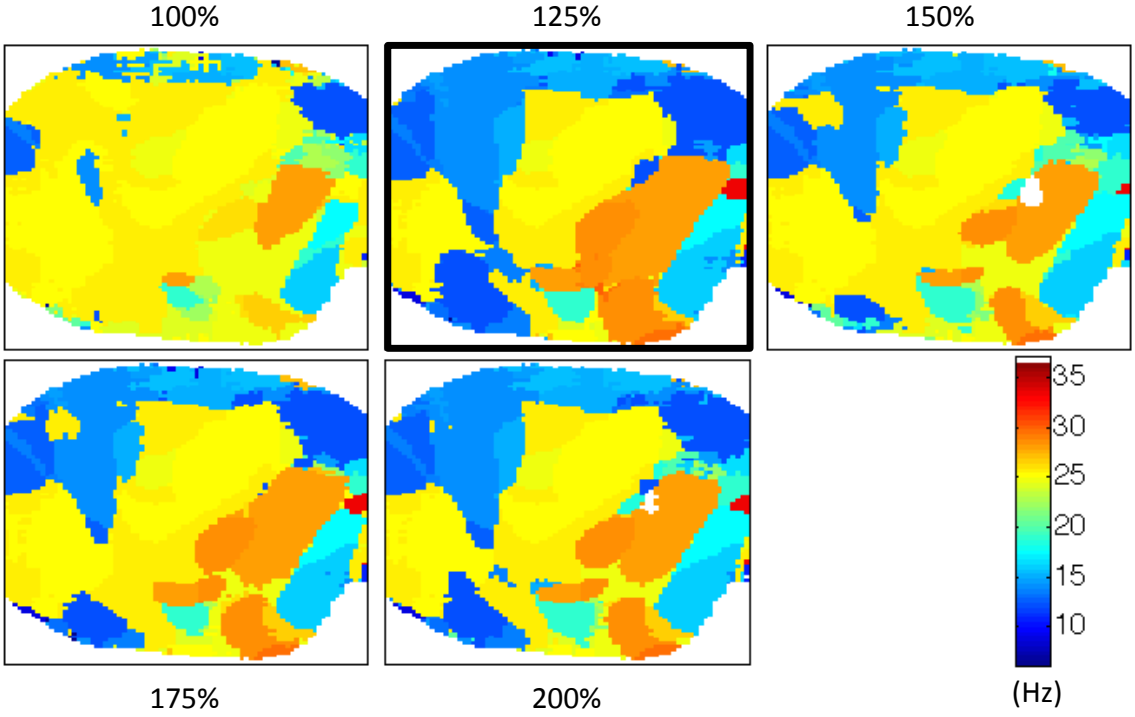

Figure 4.33: Dominant frequency maps with different high-band filter settings, where filtering at 100% **removes the high frequency content.** Default value is 125% of the DF, in black box.

4.3.3 Cycle length maps calculated from voltage

Cycle length (CL) maps give a measure of the average interval between activations in the time domain.

The effects of changing the bin size and filter setting together on the median CL were investigated. The results of combinations of all permissible bin sizes and filter settings are shown in Fig. 4.34, in which it can be seen that median CL in general decreases as the filter settings are increased from 100% to 200% and also as the bin size is decreased from 15-by-15 to 3-by-3. This is likely due to the fact that when less filtering is applied (either lower bin size, or higher percentage temporal filter), there are more small deflections in the signal, which would lower the median CL.

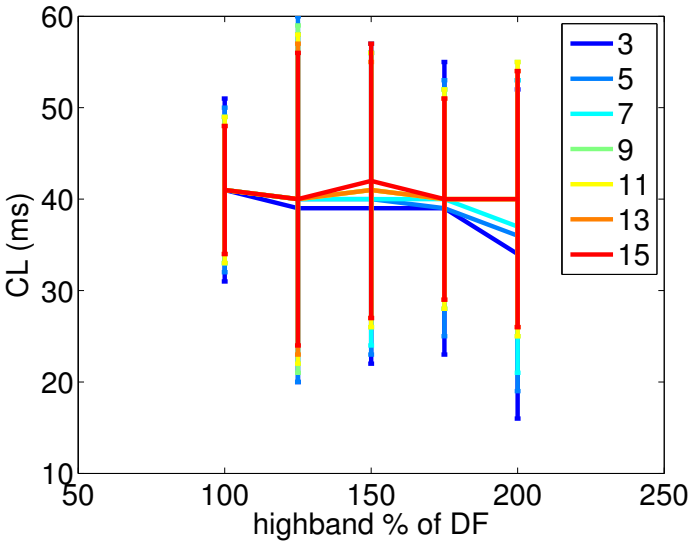

Figure 4.34: Effects of voltage bin size and filter settings on median cycle length: cycle length decreases as the high-band percentage filter increases, and as the bin size decreases. The overall range of values is small and the range at 125% filter for the different bin sizes is smaller than the equivalent range at 200%, suggesting 125% is a reasonable choice.

4.3.4 Cycle length maps calculated from phase

The effects of changing the window length and amplitude thresholds, from the baseline values of 90% and 15% respectively, on the CL measured from phase were investigated. CL in this context was defined to be the time difference between maxima tagged during the phase calculation (Section 4.2.3). The CL increases as the amplitude deletion is increased (Fig. 4.35 A), since more deflections are deleted. The CL decreases with window length as fewer deflections are tagged in the first pass. However, for the values considered here, changing the amplitude deletion percentage has a bigger effect than changing the window length deletion percentage. The average magnitude of deflections increases with window length (Fig. 4.35 B) since smaller deflections do not get tagged when the window length is increased. The amplitude also increases with increasing amplitude deletion, although the window length has a bigger effect. This suggests that the deletion only offers some correction.

The baseline values of 90% for the window length and 15% for the amplitude deletion value correspond to stable areas of the plot (Fig. 4.35 A), where the values match the CL calculated from the voltage. Changes in amplitude are graded (Fig. 4.35 B), and the baseline choice seems justified.

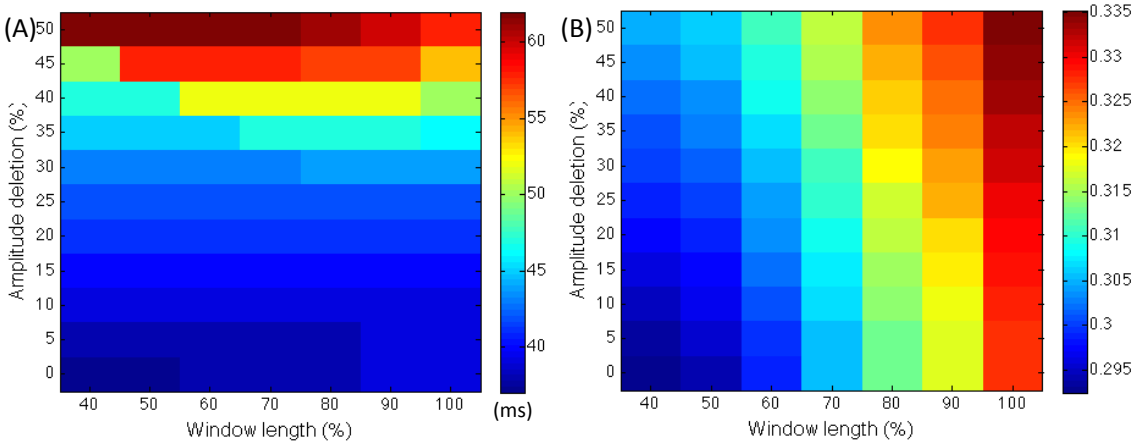

Figure 4.35: Effects of window length and amplitude settings on median cycle length (A) and amplitude (B).

4.3.5 Number of phase singularities

One measure of how the results change with parameter settings is the change in average number of phase singularities per frame. The number of phase singularities detected depends on the voltage bin size and voltage temporal filter, as well as the window length and amplitude thresholds for the phase calculation, and also the bin size for the phase smoothing.

Effects of varying parameters separately

The effects of varying each of the voltage bin size, temporal filter and phase bin size, while holding the other parameters at baseline are shown in Fig. 4.36. The number decreases with increasing bin size Fig. 4.36(A) as noise is reduced and small wavefronts may be lost. The trend is very similar for phase binning Fig. 4.36(C); whereas, the temporal filter has a much smaller effect Fig. 4.36(B).

Varying the window length and amplitude thresholds did not have a big effect on the mean number of PSs (Fig. 4.37). The number of PS increases as amplitude deletion increases above 15% and also as it is decreased to 5% or 0%. This may be due to increased noise in the resulting phase due to incorrectly tagged deflections. This suggests the baseline values are justified.

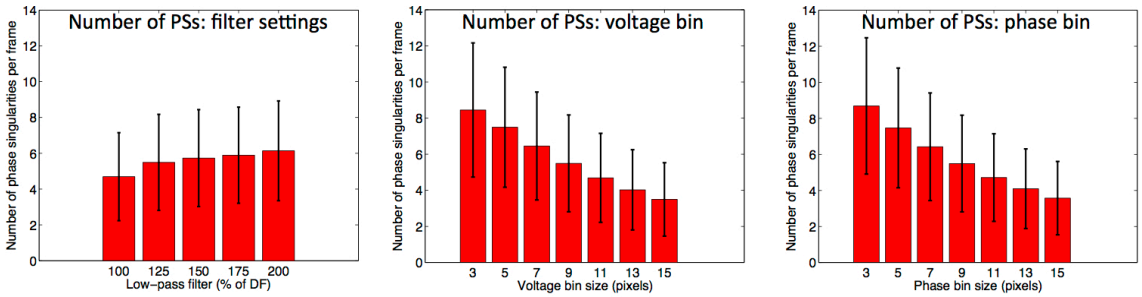

Figure 4.36: The number of PSs decreases with increasing voltage or phase bin size; whereas, the high-band filter setting has a much smaller effect. (A) Effects of filter settings on overall number of PSs; (B) effects of voltage bin size on overall number of PSs; (C) effects of phase bin size on overall number of PSs.

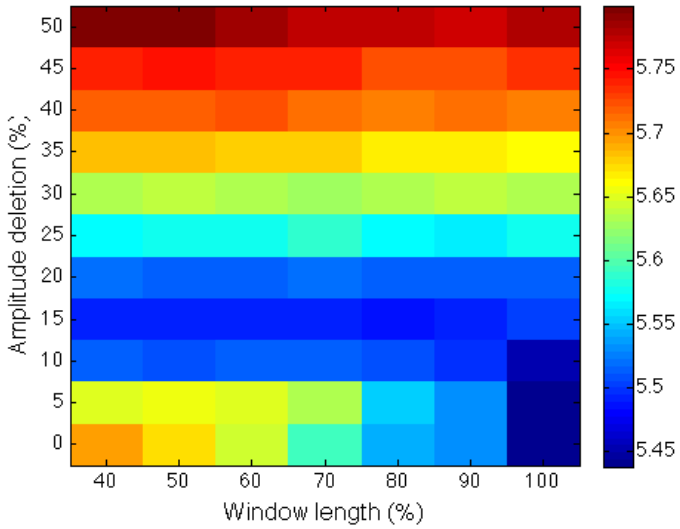

Figure 4.37: Amplitude deletion threshold affects mean number of PSs, whilst window length threshold has little effect. The baseline value of 15% amplitude deletion, 90% window length represent a stable part of the plot.

Effects of varying parameters in combination

To check whether the voltage, filter and phase trends are general, the effects of varying voltage bin size and temporal filter together, and voltage and phase bin together were investigated (Fig. 4.38). For a given voltage bin size, varying the temporal filter had little effect on the number of PSs (Fig. 4.38 A). This confirmed the finding for the baseline voltage value hold true at other voltage values. The number of PSs shows a similar dependence on voltage bin size across the temporal filter settings. This suggests that the choice of temporal filter was not as important as voltage or phase bin size.

Considering changes in voltage bin size and phase bin size together shows that they are not independent (Fig. 4.38 B). The number of PSs when both bin sizes are five is considerably larger than for the other bin sizes; one question is whether the additional PSs at lower bin sizes are short-lived false detections and this is investigated in the following section.

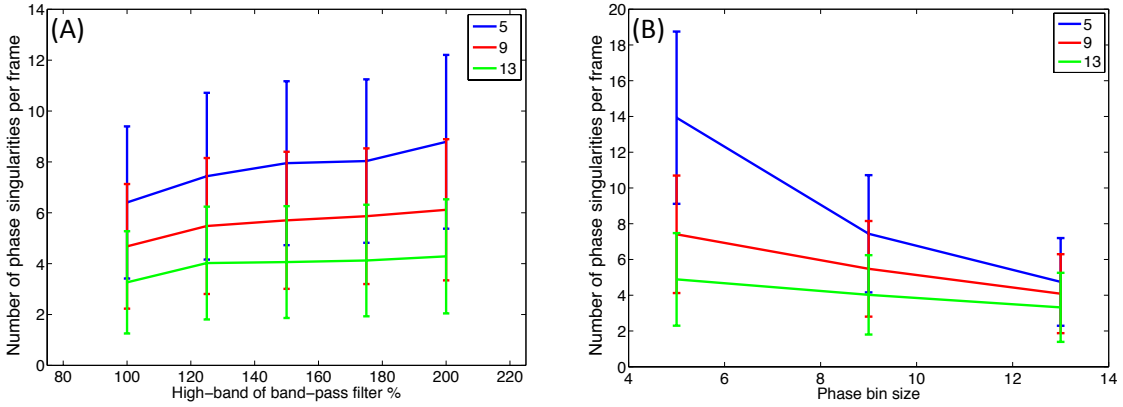

Figure 4.38: Combined effects of parameter changes on overall number of PSs: voltage and phase bin size are not independent. (A) Effects of voltage bin size and filter settings on overall number of PSs; (B) effects of voltage bin size and filter settings on overall number of PSs. When a large bin size of 13-by-13 is applied to either the voltage or the phase, the average number of PSs per frame is reduced and the choice of bin size for the other variable has little effect.

4.3.6 Number of phase singularities by duration and number of rotations

To investigate whether the increased number of phase singularities for small voltage and phase bin sizes are due to an increased number of short-lived false detections, or are true phase singularities that are lost with increased binning, the number of phase singularities of different durations and numbers of rotations were calculated.

Dependence on voltage bin size

First of all, trajectory durations were calculated for a phase bin size of 5-by-5 pixels with varied voltage bin sizes, and for a voltage bin size of 5-by-5 pixels with varied phase bin sizes, with the motivation that the overall number of PSs was much higher for a voltage and phase bin size of 5-by-5 than for larger bin sizes. There were a large number of PSs that last for a short duration (for example between 0 and 20ms) for the small bin sizes, suggesting that there were lots of additional short-lived PS detections for the lower bin sizes (Fig. 4.39 A).

The number of rotations shows the same trend, suggesting that these additional PSs are not of physiological relevance (Fig. 4.39 C). The same trends are seen when the phase bin size is changed to the baseline size of 9-by-9 pixels (Fig. 4.39 B, D). That is for lower voltage bins, there are more detections of a small number of rotations, whilst the number of PSs detected that have a larger number of rotations does not change as much. The results are similar for duration and number of rotations.

Dependence on phase bin size

A similar relationship is seen for a fixed voltage bin of either 5-by-5 pixels or 9-by-9 pixels with varied phase bin size. Again there are more PSs of a short duration and number of rotations for lower bin sizes (Fig. 4.40). Voltage and phase bin sizes had a larger effect than filter settings on the number of PSs and were not independent; binning each at 5-by-5 led to a larger number of PSs than at 9-by-9 (13.9 vs 5.5 per frame), which were short-lived (1.2 vs 1.4 per frame $\geq$ 50ms). Bin sizes of 9-by-9 were found to be sufficient to identify true PSs, without over-smoothing. Mean duration increased for larger bin sizes as PSs became easier to track (17.3 ± 16.6 vs 20.8 ± 19.5ms, 5-by-5 vs 9-by-9).

Dependence on temporal filter settings

There is a different pattern when the voltage and phase bin sizes are fixed at baseline and the filter settings are varied, in which the overall number of PSs increases and

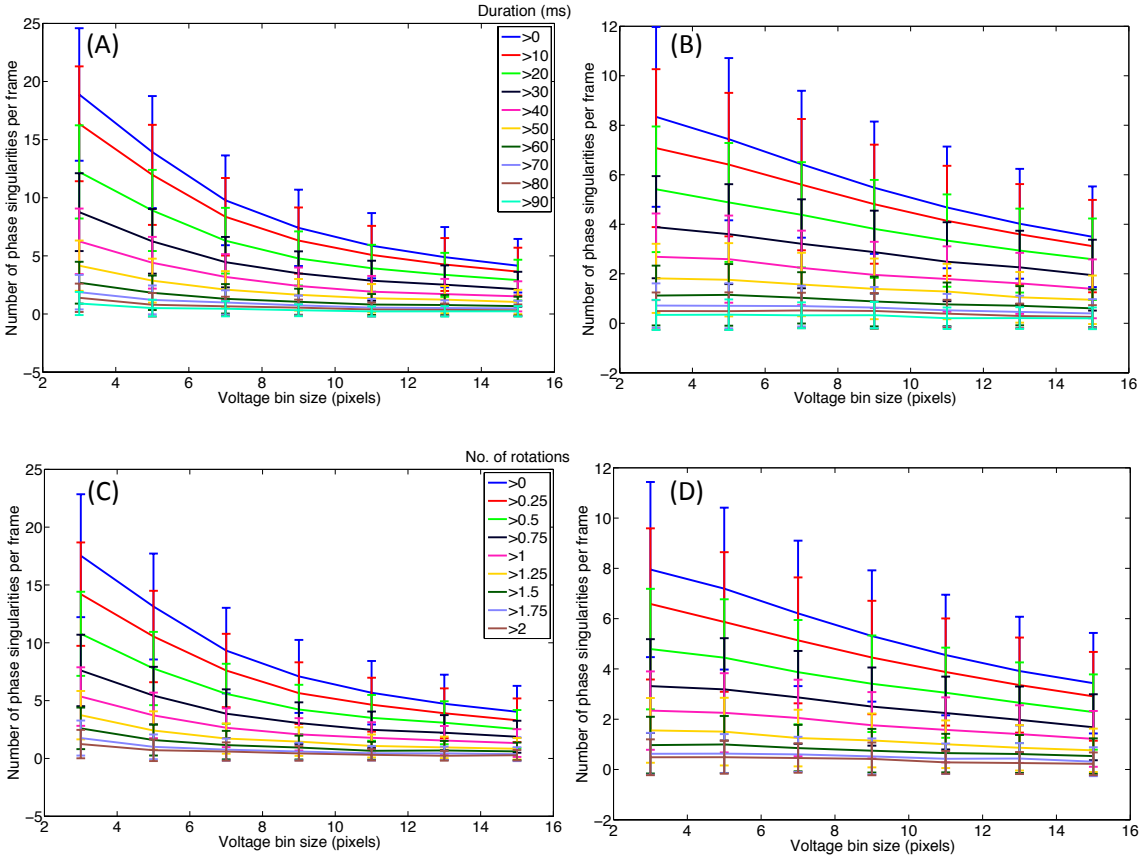

Figure 4.39: Quantifying the number of PSs by duration shows that there are an increased number of false detections for small bin sizes. Number of PSs by duration for various voltage bin sizes with a phase bin size of 5-by-5 pixels (A) or 9-by-9 pixels (B); number of PSs by number of rotations for various voltage bin sizes with a phase bin size of 5 by 5 pixels (C) or 9-by-9 pixels (D).

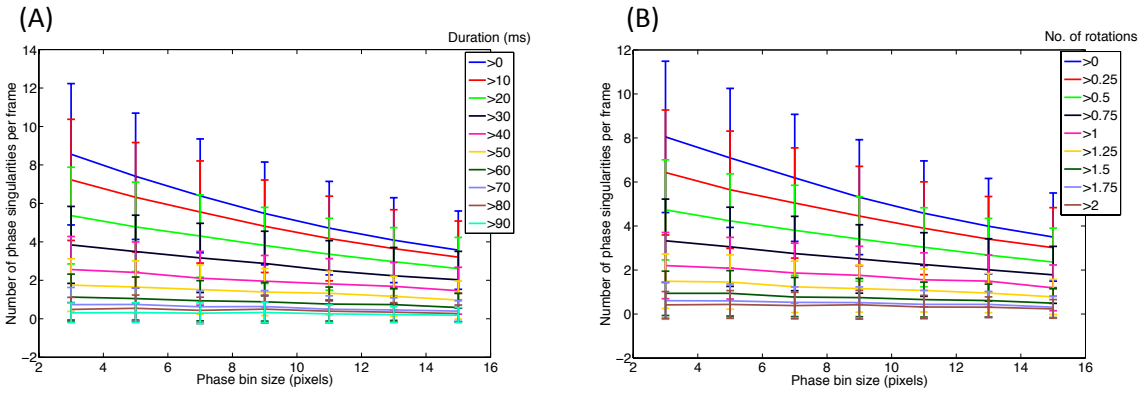

Figure 4.40: For phase bin sizes, number of PSs by duration (A) and by number of rotations (B).

those of longer duration decrease as the filter settings are increased (Fig. 4.41). This is most likely due to more noise at the higher filter percentages, leading to more PSs and also a concomitant decrease in the ability of the algorithm to track the longer lasting PSs. This indicates that a choice of 125% is reasonable.

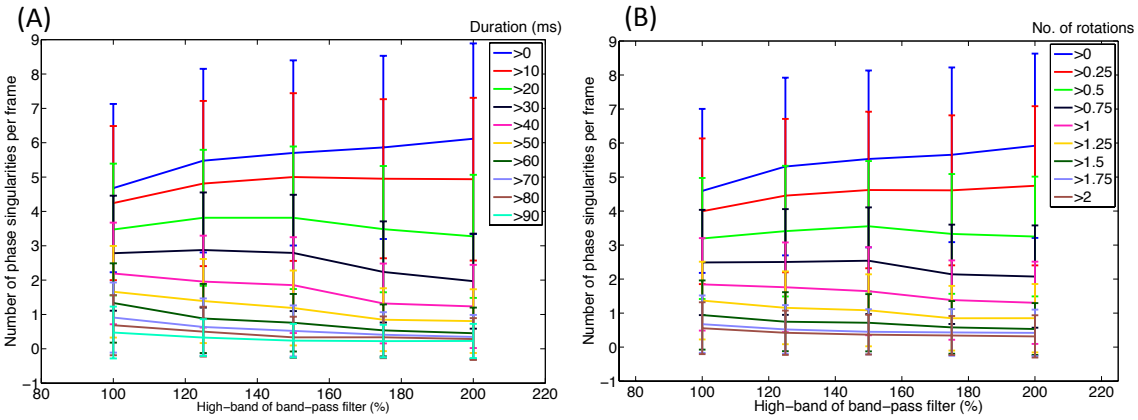

Figure 4.41: For various filter settings, number of PSs by duration (A) and by number of rotations (B).

4.3.7 Maximum and mean duration and number of rotations

Along with the number of PSs, it is also important that the maximum PS duration and number of rotations are captured accurately with the chosen parameter set, because these PSs may be considered the most important in tissue. The mean duration and mean number of rotations were also calculated. There is no clear trend in maximum duration or number of rotations with voltage or phase bin size for this data file (Fig. 4.42 A, B), suggesting that the parameter sets perform equally. On the other hand, the mean duration and mean number of rotations both increase with increasing voltage bin size and with increasing phase bin size (Fig. 4.42 C, D). This is expected since PSs are easier to track with increased smoothing of the voltage and phase field, since their movement is smoother and there are fewer other PSs complicating the analysis. Again the results are similar for duration and number of rotations.

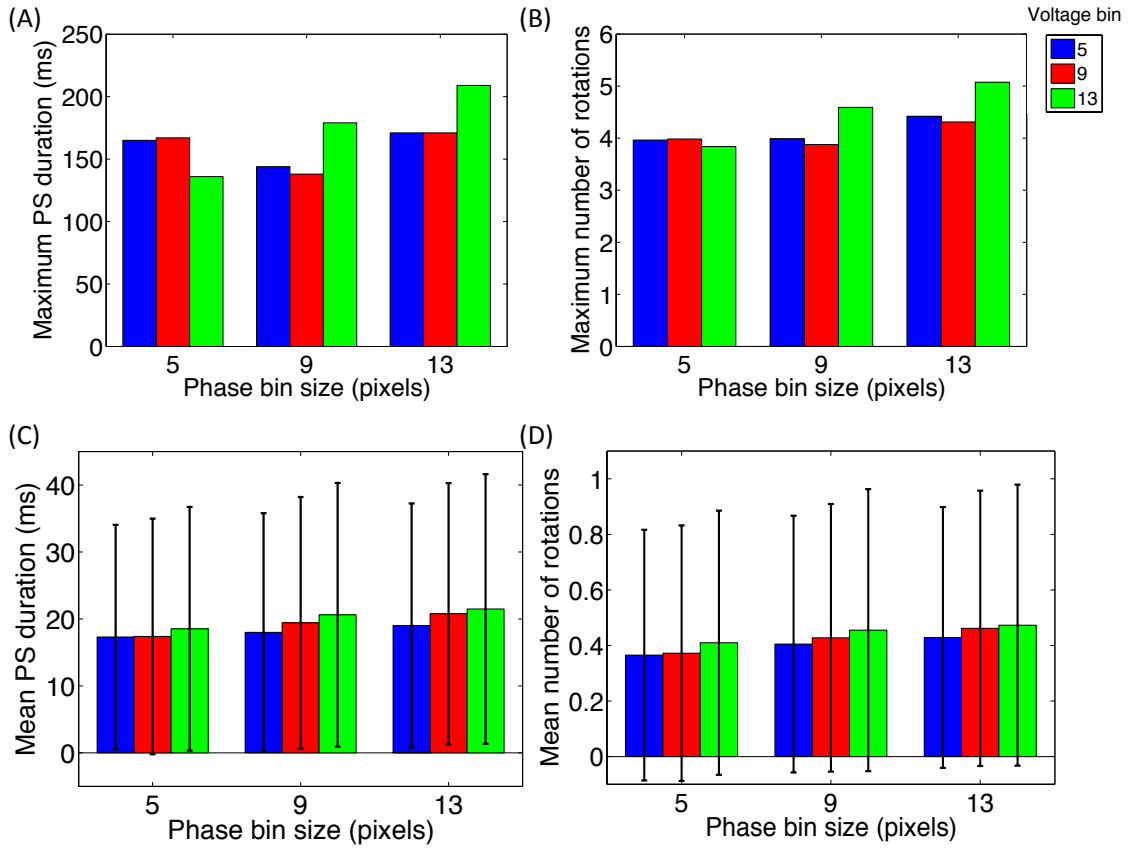

Figure 4.42: Maximum and mean duration and number of rotations for different voltage and phase bin sizes. For voltage and phase bin sizes of 5, 9 and 13: (A) maximum PS duration; (B) maximum number of rotations; (C) mean PS duration; (D) mean number of rotations.

4.3.8 Phase singularity heat maps: spatial smoothing of heat maps

As well as the number, duration and number of rotations of PSs, it is necessary to consider the spatial distribution of PSs (*heat maps*). The distribution was assessed by plotting spatial heat maps showing the counts of occurrence over time. The differences in heat maps between parameter sets were assessed visually and quantitatively, for different duration and number of rotation thresholds, on both a localised level, as well as on a regional level. The assessment on a localised level was done to investigate how the spatial distribution of PSs changes with choice of parameter set. For the regional analysis, the tissue was divided into nine regions as shown in Fig. 4.2 and a score was assigned to each of the nine regions for comparison with the structural features of the tissue, which were assessed using histology in parallel studies performed by other members of the research group.

For the local analysis, due to the different amounts of smoothing between parameter sets, heat maps are not expected to correlate on a pixel-by-pixel basis and thus the heat maps are spatially smoothed before correlations were calculated between the parameter sets as well as for the later analysis between recording files. In order to determine an appropriate bin size, the effects of varying the amount of spatial smoothing of the heat map were investigated. Fig. 4.43 shows the effects of varying the bin size along with the resulting correlations between the heat maps. Visually, larger bin sizes above 9-by-9 appear to be too smoothed, while it is more difficult to identify high-density areas when no binning is applied (1-by-1). Heat maps for bin sizes other than 1-by-1 correlate well with each other. The chosen bin level needs to be large enough that a correlation is measurable, and small enough that this correlation captures local aspects of the map. This was tested for heat maps where the voltage and phase bin sizes were varied (Fig. 4.44). The differences in the heat maps are most easily observed in the correlation chart for 3-by-3 pixels heat map binning and visually it is easy to identify hot spots in maps binned at this level (Fig. 4.44, top panel), thus this value is chosen for all subsequent analyses.

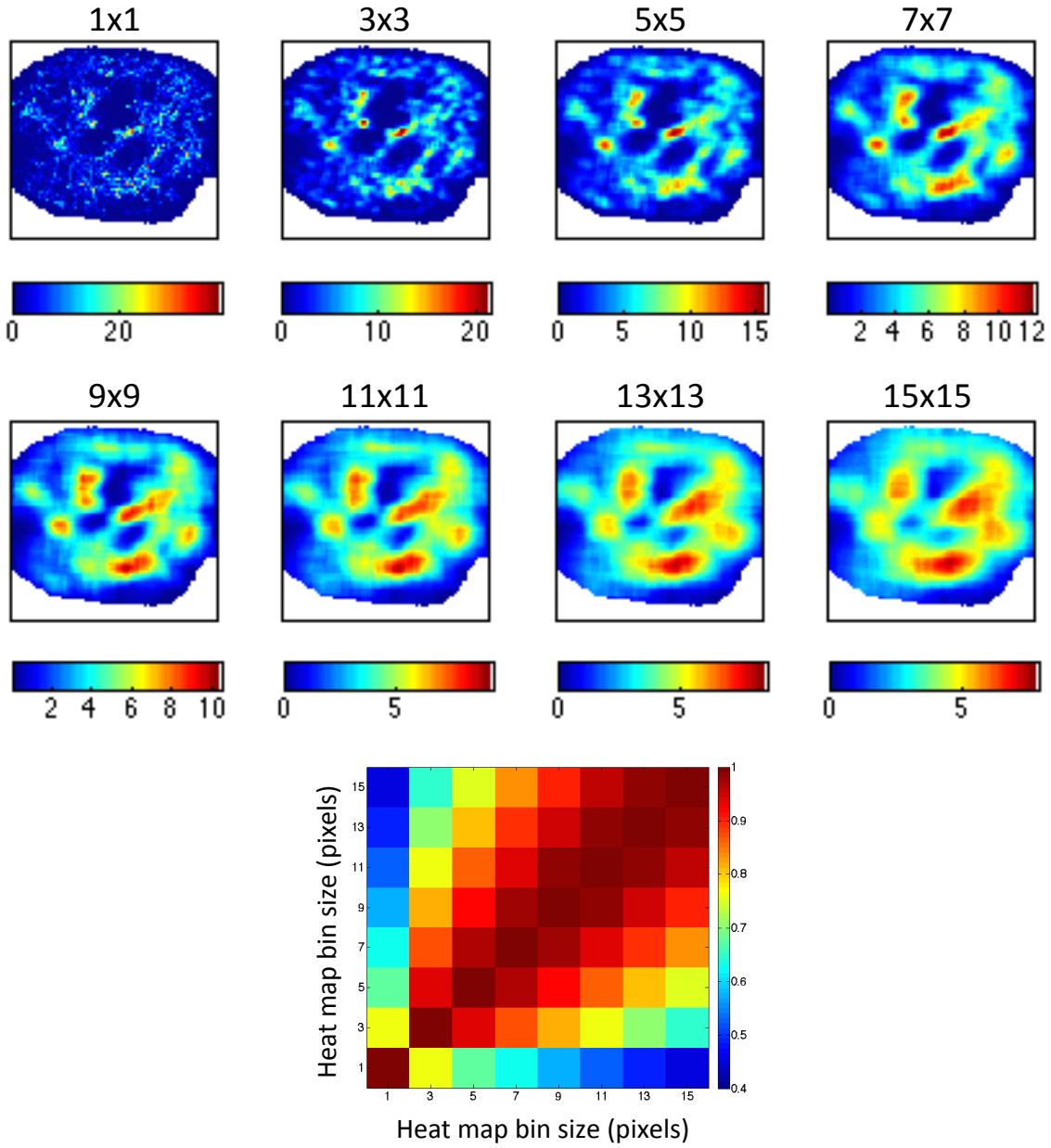

Figure 4.43: Heat map smoothed with different bin sizes, along with the correlations between the resulting heat maps. A value of 3-by-3 was chosen as it is visually easy to identify hotspots in maps binned at this level.

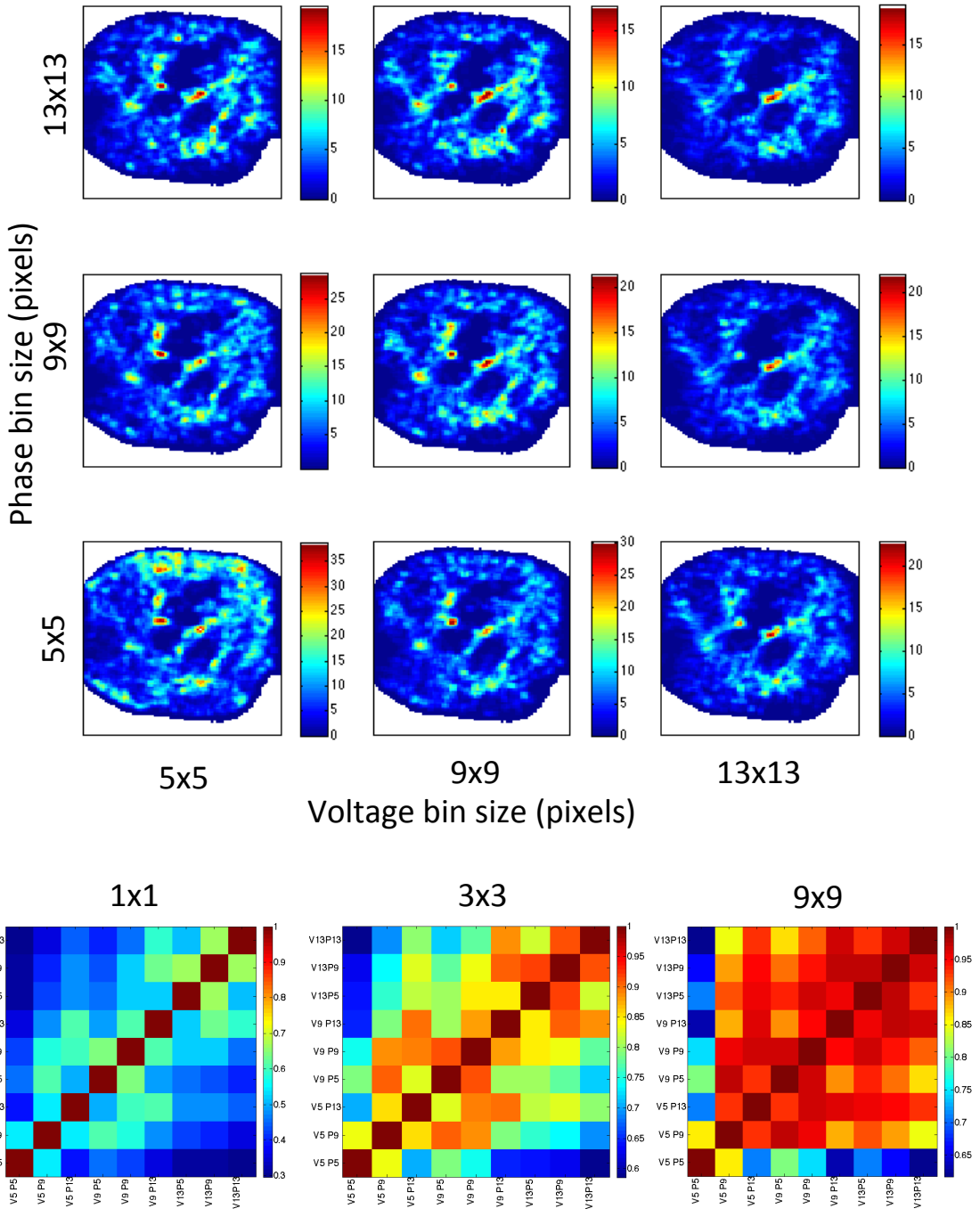

Figure 4.44: Heat map smoothing with varied phase and voltage bins. Top: Heat maps smoothed with a bin size of 3-by-3 pixels, with various voltage and phase bin sizes. Bottom: correlations between heat maps for voltage and phase bin sizes of 5-by-5, 9-by-9 and 13-by-13, where the heat maps are smoothed using a bin size of either 1-by-1 (no binning), 3-by-3 or 9-by-9. These results are for PS with at least 0.5 rotations. It is easiest to see differences between the correlations for 3-by-3 binning, indicating it is a suitable choice.

4.3.9 Phase singularity heat maps: duration and number of rotations thresholds

The results have so far been similar when considering equivalent cut offs for PS duration compared to number of rotations. Thus the first step is to compare the heat maps for PSs above threshold durations and number of rotations for the baseline parameter set. The values chosen for the initial check were $0, 0.25, 0.5, 0.75$ and 1 rotation or durations of $0, 10, 20, 30$ and 40ms. Using either set of measures for the threshold should give similar results because the median CL is around 40ms. Here the localised correlation score was calculated as well as the regional scores.

The heat maps represent the count of PSs at each pixel, where the count for any given pixel increases by one each time a PS trajectory of sufficient duration or number of rotations crosses that pixel. The map can be thought of as a sum of all the PS trajectories.

Overall assessment

Heat maps showing PS distribution over the entire recording for PSs above the duration and rotation thresholds, smoothed using a bin size of 3-by-3 pixels are shown in Fig. 4.45. For example, for a cut off level of 0.5 rotations, only PSs that last for 0.5 rotations or more are included in the map. Maps are visually similar to maps for their neighbouring durations and number of rotations and these similarities are quantified by the correlation chart (Fig. 4.45, bottom), where correlations are high for maps with their neighbouring durations, and equivalent and neighbouring rotations. This chart is a correlation of the heat maps binned at 3-by-3 pixels, so can be thought of as capturing how well the maps match on a local level.

Regional assessment

A regional assessment was also done using the nine regions shown as black lines on the heat maps in Fig. 4.45, and also illustrated in Fig. 4.2. For each of the regions in the original heat maps (no smoothing applied), the total of all of the pixel counts were calculated and divided by the number of tissue pixels in that region, to give an average PS count per pixel (Fig. 4.46, top). Since these pixel counts are higher for the lower inclusion thresholds, it is difficult to compare between the duration and number of rotation thresholds, and instead the maps were normalised to give an average tissue pixel density percentage per region (Fig. 4.46, bottom). This score gives a measure of the percentage of PSs locations that are in each region. To aid with visualisation, these percentages can then be ranked in order to assign each of

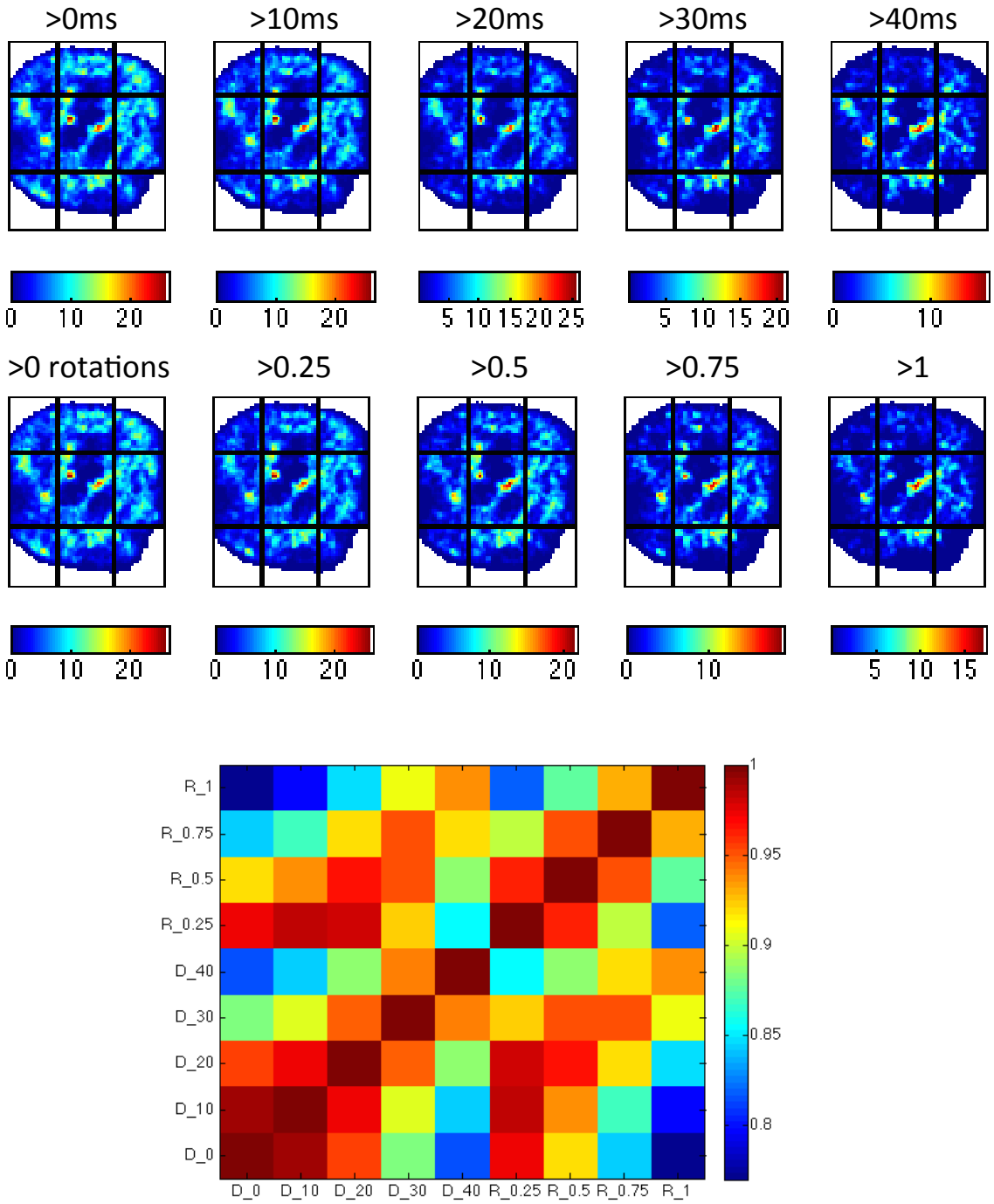

Figure 4.45: Heat maps with varied PS duration and number of rotation thresholds correlate well. Top: Heat maps (smoothed with bin size 3 by 3 pixels) with PSs included according to duration and number of rotations thresholds. Black lines show how the tissue is divided for regional analysis. Bottom: Correlation chart shows localised correlations between maps where PSs are included when they exceed a threshold duration, in the case that a duration threshold is used, or a threshold number of rotations. Maps thresholded by duration are labelled D_n with the duration (for example D_{10} included PSs that last at least 10ms); whilst those thresholded by number of rotation are labelled R_n. Correlations are high for maps with their neighbouring durations or number of rotations. Maps are also high between maps for equivalent duration to number of rotations thresholds (for example, a duration of 40ms is approximately 1 rotation as the mean rotational CL is approximately 40ms, and these maps correlate well).

the regions their ranking from 1 to 9 of lowest density to highest density (Fig. 4.47, top). The top three regions by density can also be determined (Fig. 4.47, bottom). Maps for thresholds of 20ms and above and for 0.25 rotations and above look visually similar and have the same three regions in the top three. This similarity is quantified by calculating the correlations between each of the maps, shown in Fig. 4.47. The correlations between maps other than the heat map containing all PSs (no duration or number of rotations cut off) are high (0.95 ± 0.05; minimum including this map 0.60; minimum excluding this map 0.80), showing a good match (Fig. 4.48). This suggests that for the regional analysis, duration thresholds of 20ms and above and number of rotation thresholds of 0.25 and above all give similar results.

Number of trajectories of different numbers of rotations

The percentage of PS trajectories above various number of rotations were calculated (Fig. 4.48, bottom), and it can be seen that for number of rotation thresholds of 0.25, 0.5, 0.75 and 1, the percentages of trajectories in the corresponding map are: 59.2, 34.1, 20.2, 11.9%. All other parameter set heat maps were compared for heat maps consisting of only those phase singularities that last for greater than 0.5 rotations. This choice should give similar results to other thresholds, and 0.5 rotations and above suggests physiological relevance.

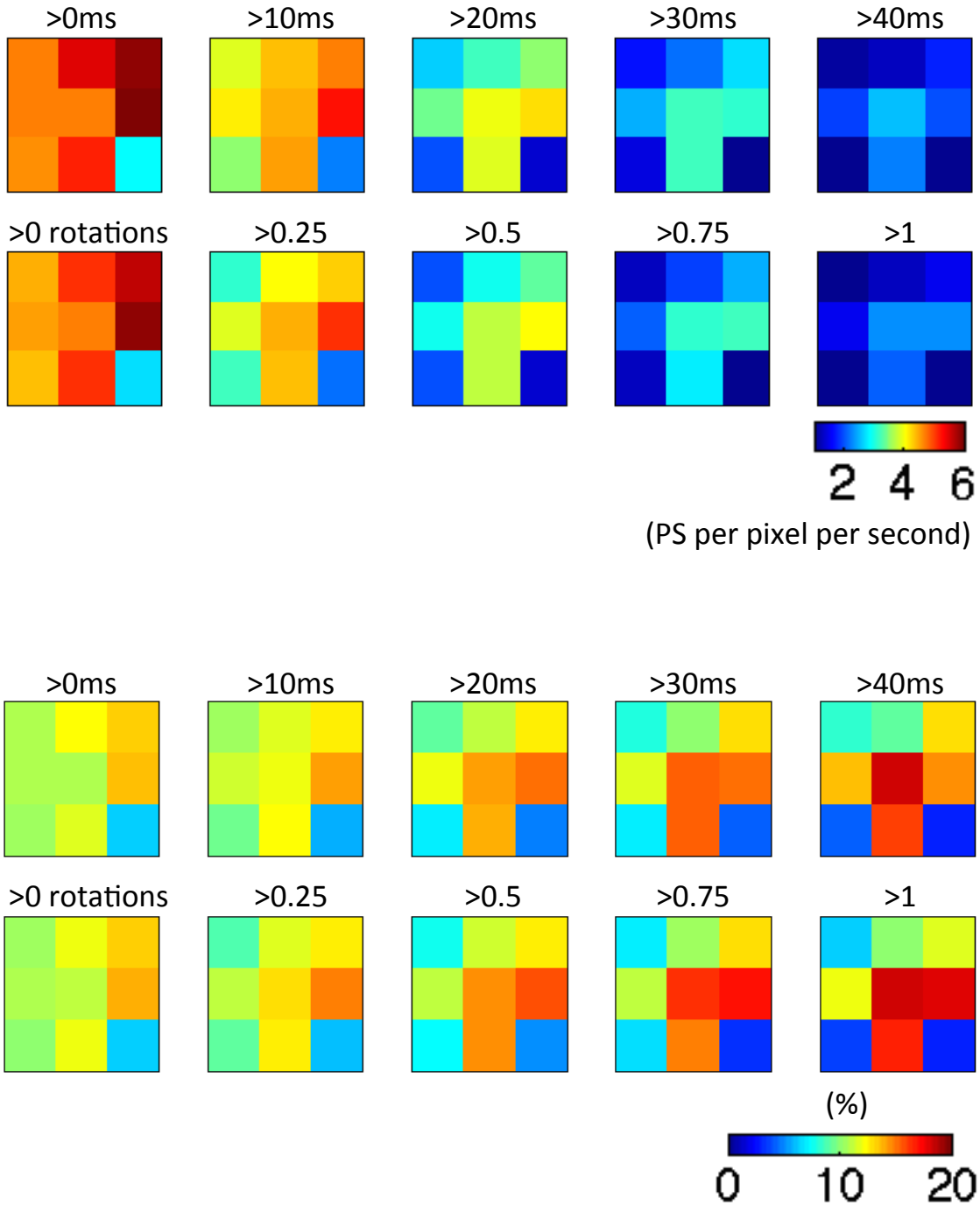

Figure 4.46: Regional analysis for duration and number of rotation thresholds: densities and percentages. Top: Average number of PS per pixel per second in each region for each of the duration and number of rotation thresholds. Bottom: Maps to show the percentage of the total number of PSs found in each region, for each of the duration and number of rotation thresholds.

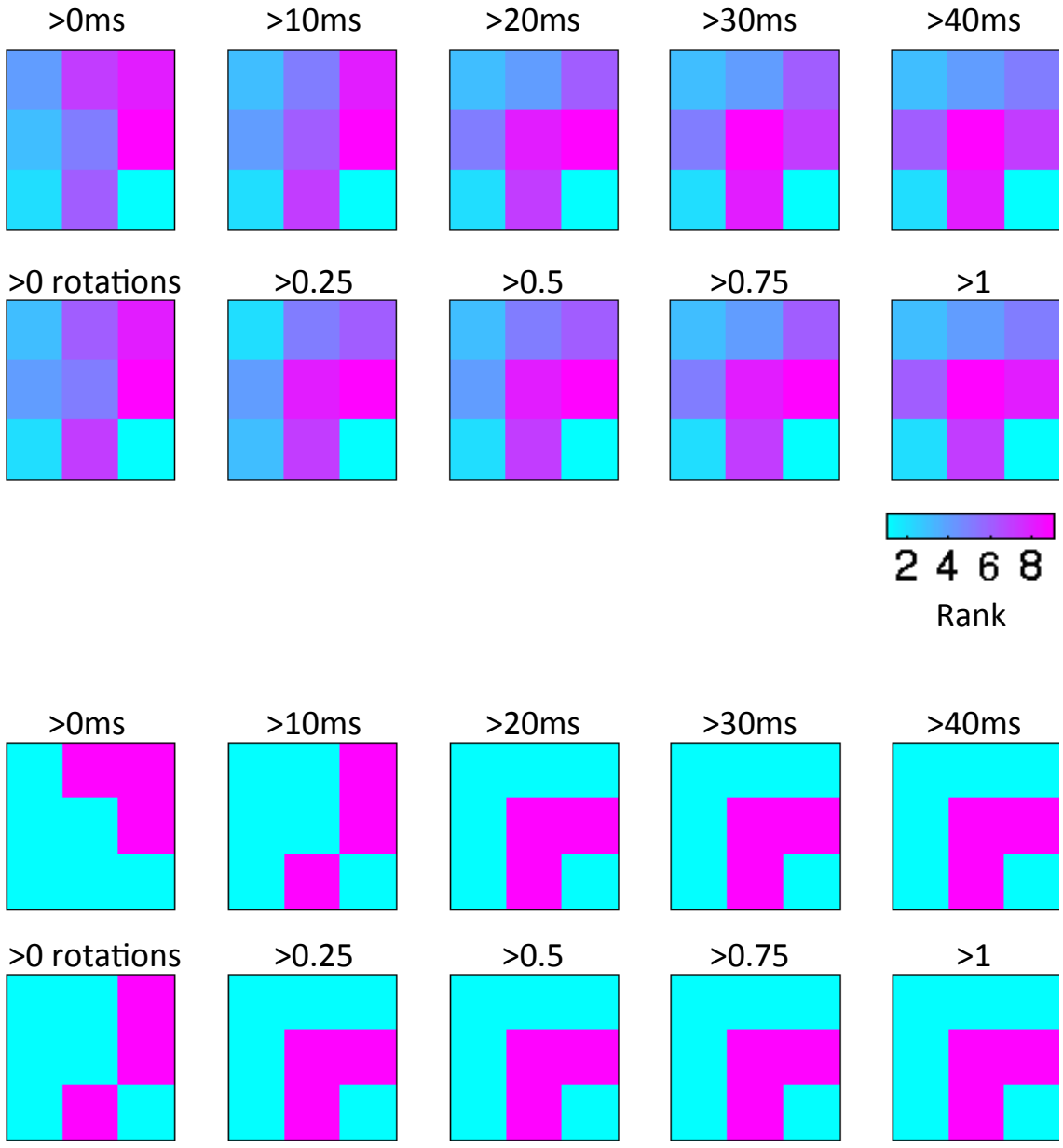

Figure 4.47: Regional analysis for duration and number of rotation thresholds: ranking and top three. Top: Ranking from one to nine (low to high) to show ranked PS density in each region. Bottom: The top three regions by PS density are shown in purple.

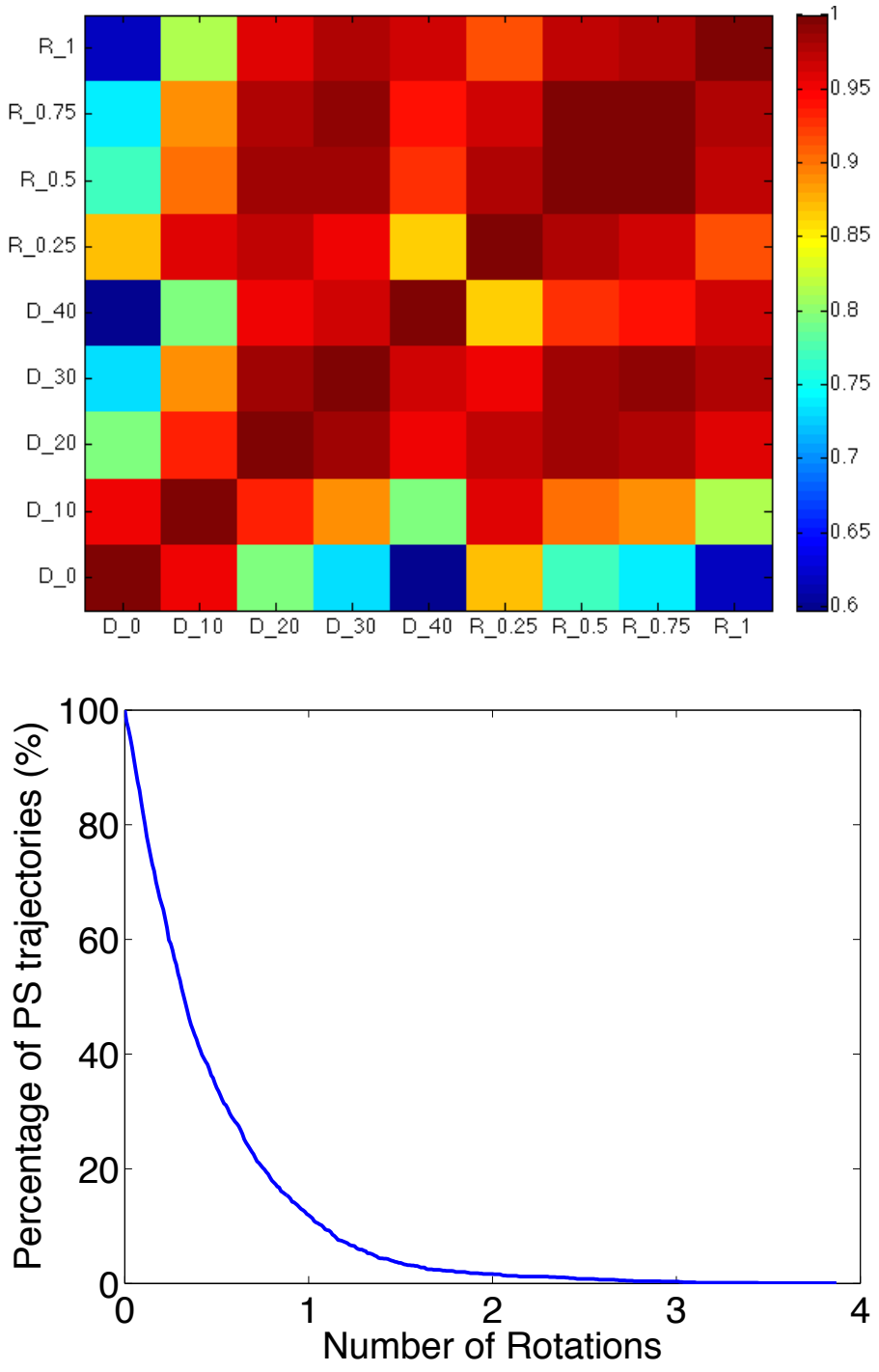

Figure 4.48: Regional analysis for duration and number of rotation thresholds: region maps correlations and number of PSs by number of rotations. Top: Correlation chart for the regional PS densities (see Fig. 4.46 top). Bottom: Percentage of the PS trajectories that are greater than a given number of rotations. From this, for number of rotation cut-offs of 0.25, 0.5, 0.75 and 1, the percentages of trajectories in the corresponding map are: 59.2, 34.1, 20.2, 11.9%.

4.3.10 Phase singularity heat maps: effects of voltage and phase bin size

In order to determine the effects of voltage and phase bins on the spatial distribution of PSs, heat maps were computed for low (5-by-5), medium (9-by-9) and high (13-by-13) binning of voltage and phase (Figs. 4.44 and 4.49). The maps have visually similar high-density regions, and correlate well (> 0.58) on a localised level (Fig. 4.44). The maps were then divided into nine regions and the PS densities calculated for the regional analysis, where the maps match well visually when either the voltage or phase bin are 13, as well as when both are binned at 9 (Fig 4.49 B, C). This suggests that binning both voltage and phase at 9-by-9 pixels is sufficient, without requiring a higher bin size of 13, which may over-smooth the data. The correlation for 5-by-5 with other bin combinations is substantially lower than other combinations (Fig 4.49 D, E), suggesting it is an inferior choice. Voltage and phase bin sizes of 9-by-9 are chosen.

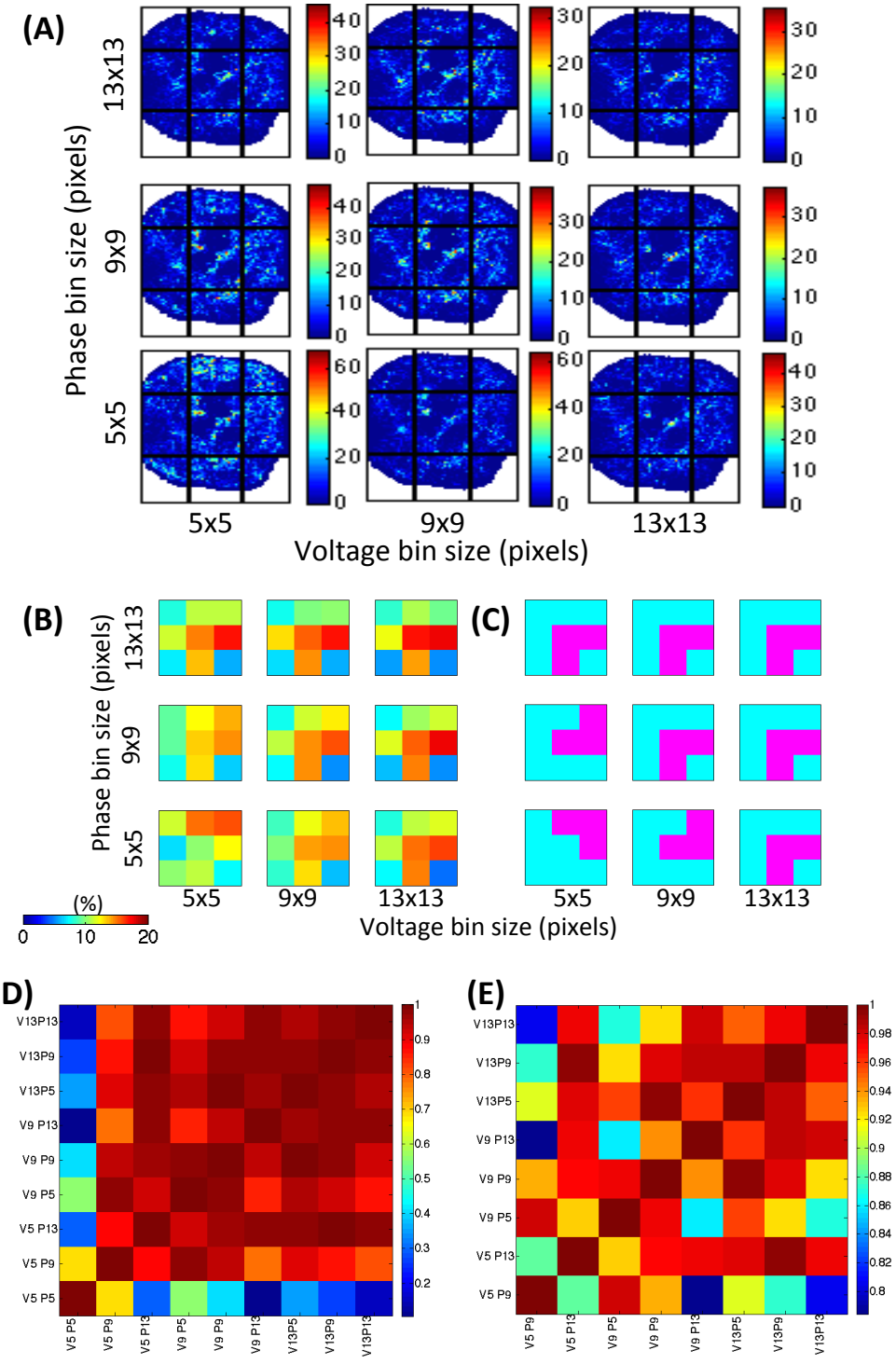

Figure 4.49: Regional analysis for different phase and voltage bin sizes. (A) Heat maps with no smoothing for voltage and phase bin sizes of 5-by-5, 9-by-9 and 13-by-13 (compare Fig. 4.44 for maps smoothed using a bin size of 3), where the black lines denote the lines between the different regions. (B) Percentage of PS density in each region. (C) Top three regions by PS density for each of the bin sizes shown in purple. (D) Regional correlations between the nine region PS densities (shown in B); compare to the localised correlation score shown in Fig. 4.44. (E) Since the map binned using 5-by-5 for both voltage and phase correlates poorly with the other maps, this is removed from the correlation table (D) in order to see the differences between the other correlations.

4.3.11 Phase singularity heat maps: effects of filter settings

Although the number of PSs were found to depend on the choice of filter only moderately (Fig. 4.41), the effect on the spatial distribution was still checked for high-band filter settings of $100, 125, 150, 175$ and 200% of the estimated DF. The heat maps visually have similar areas of high-density. The correlations between each of the heat maps are moderate to high (0.81 ± 0.12), especially for 125% and above (0.87 ± 0.08). The regional correlations between the PS densities for the nine regions show a similar trend. Although the top three regions change depending on the filter settings, the actual density maps visually and quantitatively correlate well (Fig. 4.50). Here a choice of 125% is used for further analysis.

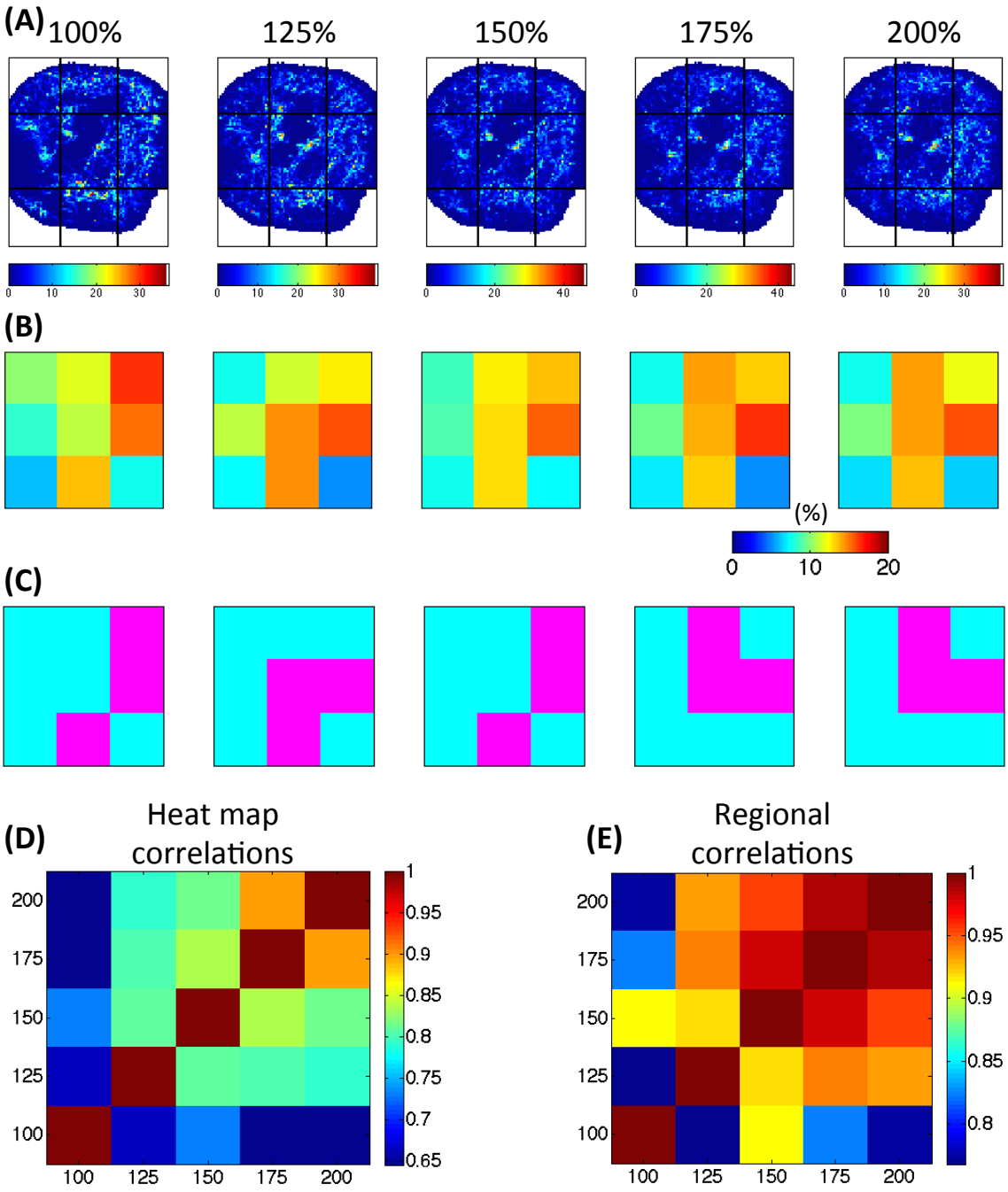

Figure 4.50: Regional analysis for various filter settings. (A) PS heat maps for various filter settings for PS trajectories of 0.5 rotations or more; (B) PS density percentages by region; (C) Top three regions marked in purple; (D) Correlations for heat maps; (E) Correlations of PS density maps for average density of nine regions.

4.3.12 Phase singularity heat maps: phase calculation settings

Finally the effects of window length and amplitude settings were tested, for low values, the baseline values and values higher than the baseline values (Fig. 4.51). The heat maps look very similar between the settings (Fig. 4.51 A) and quantifying this gives high correlations ($0.69-0.99$ for regional correlations) for all of the combination of settings (Fig. 4.51 D). Unlike other heat maps where adjacent values correlate more with each other than non-adjacent values, here there is no clear pattern. For the regional analysis, all of the choices have the middle region and the middle right region in the top three densities regions. The density grids correlate well and again there is a pattern. For future analysis, 90% and 15% are used for the window length and amplitude deletion thresholds, respectively.

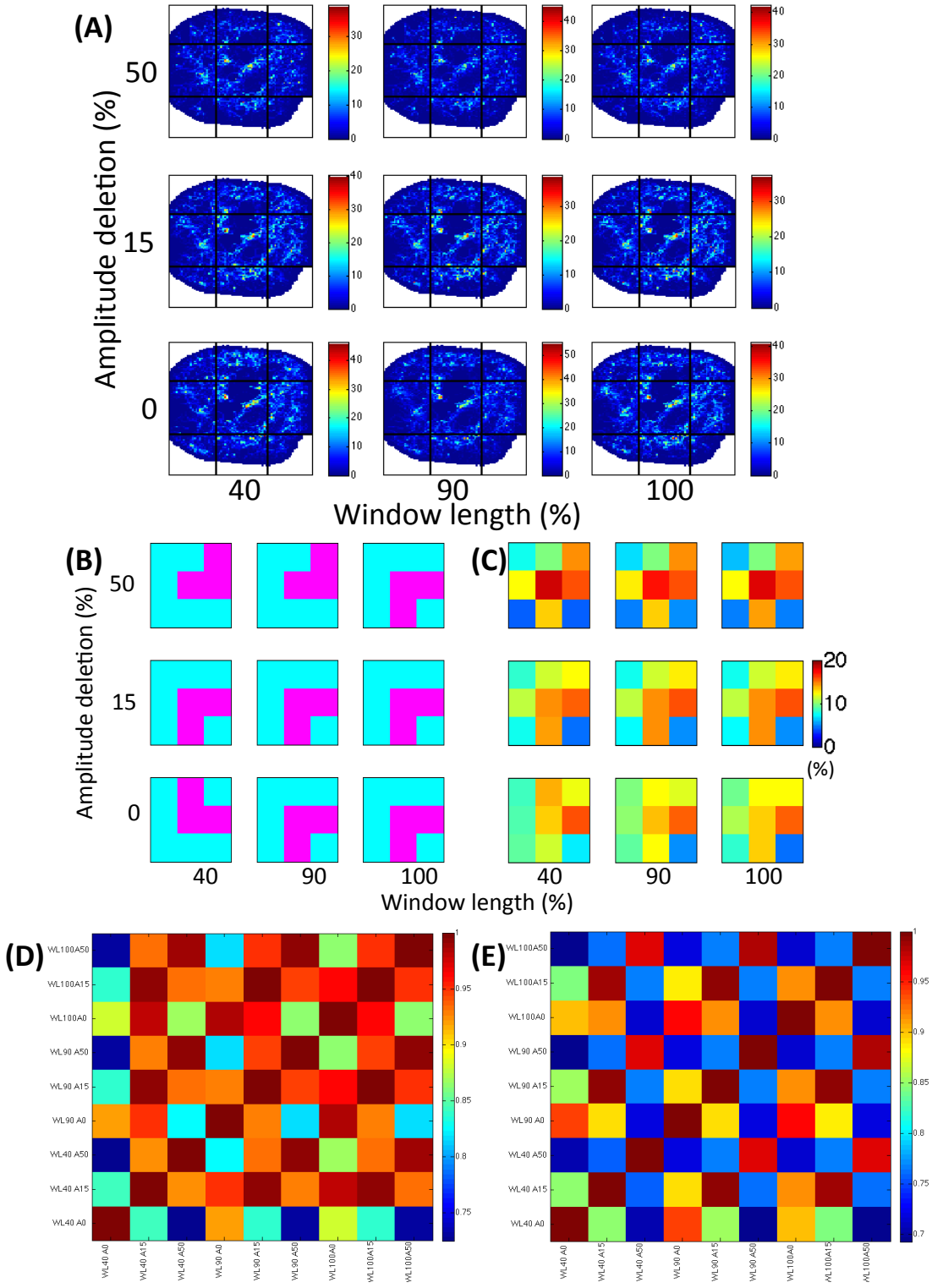

Figure 4.51: Regional analysis and heat map correlations for varied parameters in the phase calculation. Window length and amplitude thresholds for the phase calculation were varied to values less than and greater than the baseline values of 90% and 15% respectively. (A) Heat maps; (B) top three regions by density shown in purple; (C) PS average density by region; (D) Correlations for heat maps; (E) Correlations of PS density maps for average density of nine regions.

4.3.13 Additional validation

As an additional check that the method works and that the resulting phase maps could not be generated from noise alone, the locations of raw fluorescence pixels were randomly rearranged and all of the analysis steps were applied. This was done by taking each tissue pixel location and mapping it to another pixel location, where the new location is determined by a random permutation of the pixel locations. Thus each pixel has a fluorescence recording that is from a true recording, but the pixels are arranged randomly. Applying the filtering, phase calculation and phase singularity location algorithms to this new phase arrangement leads to frames that either average to a relatively uniform phase value with few phase singularities present in the frame, or to what appears as a noisy arrangement with a large number of PSs present (Fig. 4.52). However, these PSs do not last more than a couple of frames and so there are no PSs that last more than 0.5 rotations, resulting in an empty heat map. Fig. 4.52 shows the average number of PSs per frame over the recording for the true pixel distribution as well as the number for the random pixel permutation.

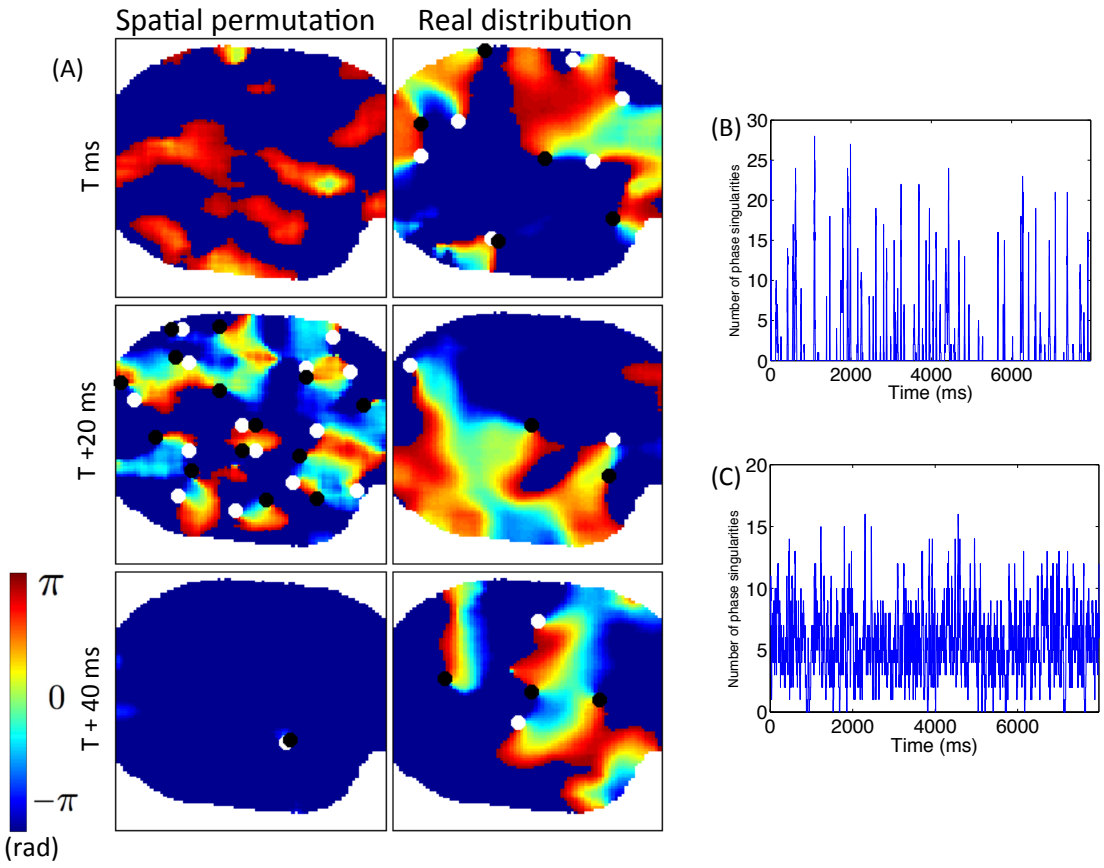

Figure 4.52: Random spatial permutation of pixels offers validation of the algorithm. Randomly permuting the raw fluorescence pixels and applying the algorithms leads to frames with either a reasonably uniform phase and few PSs (A, left hand side, top and bottom), or frames with a high number of PSs (A, left hand side middle), which do not last (not present 20ms before or 20ms after). The isophase maps for the original data distribution are shown on the right hand side of (A). (B) Number of PSs over time for the random spatial permutation of data, where there are sudden peaks in the number that do not last, and (C) number of PSs for the original data.

4.4 Discussion

4.4.1 Summary of findings

In this chapter, a protocol was presented for assessing wavefront dynamics in optical mapping data, including frequency analysis and phase singularity analysis. This involved developing a method to detect and track phase singularities that is robust to noise. A method was also developed for calculating the number of rotations of phase singularities. Finally, the effects of changing the parameters within this protocol were also assessed. The parameters were varied either individually or in combination and the effects on the measured DF maps, and phase singularity numbers, durations, number of rotations and distributions were assessed. The protocol used, the default and permissible values for the parameters, and the measured outputs are all detailed in schematic Figs. 4.3 and 4.31. The effects of varying each of the following parameters on the DF, the number of PSs and the spatial distribution were tested and the following values were chosen: spatial bin size for voltage (9-by-9 pixels); temporal filter for voltage (125%); moving mean window length (90%) and amplitude deletion threshold (15%) for phase calculation; spatial bin size for phase (9-by-9 pixels); spatial bin size for heat map (3-by-3 pixels); duration or number of rotation threshold for inclusion in heat map (0.5 rotations). The final protocol with determined parameters is used to assess features of the arrhythmia dynamics for this experimental preparation in Chapter 5.

4.4.2 Data filtering

Spatial binning

In this chapter, a spatial bin size of 9-by-9 was found to be optimal for binning both the voltage and then the phase signal. Laughner et al. (2012) advise that spatial binning can cause broadening of the AP upstroke, which can lead to inaccuracies in activation time estimation. In this chapter, the interest is overall wavefront dynamics, such that small errors in AF cycle length estimation are permissible. Laughner et al. (2012) suggest the use of Gaussian convolution matrices as an improved method of spatial binning to the uniform convolution matrices used here. Phase is not typically smoothed spatially due to the difficulties associated with the fact that phase angle is discontinuous. In this chapter, a method was proposed to overcome these difficulties (Section 4.2.4), which allowed spatial smoothing of phase and easier phase singularity identification.

Temporal filtering

For temporal filtering of voltage, a band-pass filter was used where it was found that a high-band value of 125% of the estimated DF was optimal. Filtering at 100% of the DF removed some required frequencies from the signal (Fig. 4.33), while there were still some small deflections in the signal upon filtering at 200% of the estimated DF (equivalent to around 60Hz), which would make the phase calculation step more difficult (Fig. 4.7). Overall, the choice of filter within the range tested ($100 - 200\%$ of the estimated DF) did not have a large effect on the calculated PSs (Figs. 4.41). DF in this example is estimated as 28.6Hz, so a high-band filter setting of 125% is equivalent to filtering at 35.7Hz. This is lower than the value used by Laughner et al. (2012) who compared the effects of filter settings on optical mapping data from mouse, rabbit and human and suggest filtering at 100Hz, since all of the relevant physiological frequencies in the frequency spectrum are below 100Hz. Rodrigo et al. (2014) compared the effects of no filtering and filtering at the highest DF for localisation of PSs on the atria from surface mapping data in clinical and computational studies, and found that unstable wave patterns were seen in the unfiltered data, while filtering at the highest DF allowed the identification of rotors that would otherwise be hidden by irregular activity at other frequencies.

4.4.3 Phase calculation and phase tracking

Phase calculation window length and amplitude thresholds

Calculating the phase required the choice of a window length for tagging extrema of the signal, as well as an amplitude threshold to determine which tagged maxima-minima pairs to delete; the remaining extrema were used to calculate a moving mean of the signal that could then be subtracted to give a zero-mean signal. A window length of 90% of the estimated median cycle length and amplitude deletion threshold of 15% of the median amplitude were decided on (Fig. 4.51, Section 4.2.3).

The phase calculation method is based on Bray and Wikswo (2002a), with the extension that small amplitude detections are deleted. In their paper, Bray and Wikswo (2002a) use a window length of 50% of the estimated cycle length, with the justification that this would include double potentials that occur during reentry in the final phase signal. Here window lengths smaller than 90% of the estimated median cycle length were found to include too many additional deflections within the signal, and it is preferable with the data used here to lose a small number of double potentials due to re-entry in order to avoid the inclusion of many incorrectly assigned deflections.

Phase singularity identification

Phase singularities were identified using an adaptation of the method of Bray and Wikswo (2002b). Noise within optical mapping data means that alterations to the algorithm are required for robust phase singularity detection. Methods suggested in the literature include using larger contour sizes for the identification integral (Equation 1.24) (Bray and Wikswo, 2002b); however, this may lead to a less accurately defined position (Iyer and Gray, 2001).

In this chapter, an alternative method was developed where PSs are defined based on a neighbourhood requirement. This method was shown to be reasonably robust to noise; allowing discrepancies due to noise from the calculated integral, as long as neighbouring pixels were also close enough, and it also eliminated false PSs in areas where only a few pixels were erroneous (Figs. 4.18, 4.19). This technique was compared to using a larger contour size of 5-by-5 without the neighbourhood requirement, where the larger contour size was shown to lead to more false detections (Fig. 4.20). The value allowance of 3.0 and neighbourhood requirement of at least three neighbours provided adequate PS identification in the preliminary data analysed; however different thresholds may be more suitable for other datatypes.

Phase singularity trajectory methods

Phase singularity trajectories were calculated using a method modified from Rogers (2004); the primary difference being that Rogers (2004) tracked wavefronts in order to follow PSs, whilst here PSs are tracked directly, without the use of wavefront information. In contrast to Rogers (2004) who found wavefronts easier to track than PSs, in the work presented here, noise in phase lead to wavefront mis-identification in some cases (Fig. 4.21). The neighbourhood modifications made to the phase singularity identification algorithms here are robust to this level of noise, meaning that PS identification is more reliable than wavefront identification, and so PSs were tracked without the use of wavefront information. In order to achieve this, thresholds had to be set for the distance movement allowed between frames and the number of missing frames permissible. The effects of the choice of these thresholds are discussed in Section 4.2.6, where the values chosen are optimal for this dataset and the baseline parameter set, although other values may give improved trajectory tracking for other parameter settings and datatypes. Other phase singularity tracking methods include those of Chen et al. (2000) and Clayton and Holden (2002b).

4.4.4 Number of rotations

A novel method was developed for calculating the number of rotations (Section 4.2.7), where the effects of choice of pixel location were investigated. Studies typically estimate the number of rotations using the trajectory duration and frequency (Rodrigo et al., 2014). This is a reasonable approach for rotors where it is possible to estimate the rotor frequency; however it is impractical for short-lived trajectories, where it is difficult to estimate the frequency; assuming all PSs rotate at the DF of the tissue may not be true in all cases. The method developed in this chapter estimates the number of rotations using the phase adjacent to each rotor, so should be more accurate.

It is important to calculate the number of rotations as well as the duration for PS trajectories because changes in rotational frequency will change their relationship. For example, Sarmast et al. (2003) found that the duration of trajectories decreased with increasing Acetylcholine, whilst the number of rotations increased because the frequency increased. Further, rotors are often defined as PSs that last more than one rotation (Sarmast et al., 2003; Rodrigo et al., 2014), so it is necessary to have an accurate measure of number of rotations in order to correctly classify PS trajectories as rotors.

4.4.5 Heat maps

Cumulative spatial distributions of rotors and focal sources are used clinically by centres using the non-invasive ECGi technology to determine ablation targets (Haissaguerre et al., 2013, 2014a). In the studies of (Haissaguerre et al., 2013), the atria are divided into seven regions and ablation starts by targeting the region with the highest density of *drivers*, which are defined as focal sources or reentrant (greater than one rotation) sources.

In this chapter, our analysis is similar in that it divides the left atrium into regions and the spatial distribution of reentrant sources and focal sources are considered. However, here the regional analysis is split into nine regions for comparison with histological analysis. Furthermore, phase singularity heat maps are defined with an inclusion threshold of half a rotation, rather than one rotation, and only phase singularities are considered in this chapter (see Chapter 5 for focal sources). Other studies also define rotors based on a full rotation criterion (Rodrigo et al., 2014).

4.4.6 Parameter sensitivity

To summarise, referring back to schematic 4.31, the effects of varying each of the following parameters on the DF, number of PSs and spatial distribution were tested and the following values were chosen as the baseline: spatial bin size for voltage (9-by-9 pixels); temporal filter for voltage (125% of the DF); moving mean window length (90% of the median CL) and amplitude deletion threshold (15% of the median amplitude) for phase calculation; spatial bin size for phase (9-by-9 pixels); spatial bin size for heat map (3-by-3 pixels); duration or number of rotation threshold for inclusion in heat map (0.5 rotations).

Duration and number of rotations of phase singularities

The maximum duration and number of rotations are important because these phase singularities may be targeted clinically, and there was no clear trend in the effects of voltage and phase bin size on these numbers, suggesting the choices performed equally. The mean duration and mean number of rotations both increase with increasing voltage bin size and with increasing phase bin size (Fig. 4.42 C, D). This is expected since phase singularities are easier to track with increased smoothing of the voltage and phase field, since their movement is smoother and there are fewer other phase singularities to complicate the analysis. This finding is similar to that of Rodrigo et al. (2014), in which phase singularities were more evident upon filtering at the highest DF.

4.4.7 Limitations and future work

A major limitation is that there is no absolute gold standard for determining the wavefront dynamics, so the results from various parameter sets had to be compared to each other. In addition, it can be difficult to determine the DF of noisy data, which may result in errors in the estimated DF used for the filter settings.

Several parameters were set during the methods development study based on the optimal values for the baseline parameter set. These included the value threshold and number of neighbours threshold for the phase singularity identification algorithm, as well as the distance movement between frames and number of missing frames allowed in the phase singularity tracking algorithm. Other values may indeed give improved PS identification and tracking for other smoothing and filter values, particularly since PSs movement between frames may be sensitive to this preprocessing. This may bias some of the results towards the baseline parameters being chosen as optimal parameters. Out of necessity, only a subset of possible parameter combinations were

tested.

As an extension, the interaction between phase singularities could be plotted as a directed graph, similar to the graphs plotted by Clayton and Holden (2004) to show the birth, death, bifurcation and amalgamation of filaments, to see how this output varies with parameter set.

Chapter 5

Optical mapping analysis: classifying arrhythmia mechanisms by comparing distributions and timings of phase singularities and new wavefronts

5.1 Overview

The understanding of the electrical substrate during AF is important because it may provide mechanistic insight and inform treatment strategies. Areas of high dominant frequency may coincide with electrical drivers; however, there is conflicting evidence regarding the stability of such sites (Sanders et al., 2005; Salinet et al., 2014). In addition, phase singularity analysis has been used in several clinical centres to indicate areas of rotational activity, where stable regions of high rotational or focal content are targeted during ablation therapy (Narayan et al., 2012b; Haissaguerre et al., 2013).

A multitude of mechanisms proposed for AF have been observed in simulated, experimental and clinical studies; including multiple wavelets (Moe et al., 1964; Verheule et al., 2010), multiple foci (Lee et al., 2013), and rotational activity (Narayan et al., 2012b). Disparate findings may be due to differences between the experimental models used, subject variability, and the variety of recording and analysis techniques employed.

Application of acetylcholine (ACh) leads to a dose-dependent decrease in APD because it activates the potassium acetylcholine channel, I_{KACh}. This decrease in

APD leads to an increase in AF vulnerability (Schuessler et al., 1992). As well as reducing APD, which increases the frequency and stability of reentry, ACh also increases resting membrane potential (Shumaker et al., 1993). No structural remodeling is required for AF induction with ACh, making it a sensible model for the control canine subjects studied. ACh has been used in many experimental models of AF, including the study that provided support for multiple wavelet hypothesis, where four to six wavelets were necessary to sustain AF in the dog atria (Verheule et al., 2010). Schuessler et al. (1992) found that with increasing concentrations of ACh in an isolated canine right atrial preparation, multiple reentrant circuits during tachyarrhythmia changed to a single stable reentrant circuit, which sustained AF. In this case, the mechanism for AF perpetuation was not multiple wavelets, but rather a single reentrant circuit. Modelling studies have shown that uniform ACh dose can reduce spiral wave core meander (DF 6.5Hz increased to 17Hz and core meander reduced by 70% (Kneller et al., 2002)). In both paroxysmal and persistent AF, adenosine, which also activates I_{KACh}, was found to increase AF frequency, and in the case of paroxysmal AF it increased the spatial gradient in refractory periods (Atienza et al., 2006). Here the mechanism is again high-frequency reentrant drivers.

Rotational waves during ventricular fibrillation (VF) consist of three-dimensional filaments around which scroll waves rotate. These filaments can be I shaped, leading to phase singularities on both the epicardial and endocardial surface; U shaped, consisting of two phase singularities on one surface and focal activation on the other; or O shaped, which are intramural filaments leading to focal activations on both surfaces (Clayton et al., 2006). A combined clinical and experimental study of human VF, measured the average number of epicardial rotors occurring in human VF at any one time to be around six rotors, while simulation studies suggested that the actual number of rotors is 1.4 ± 0.12 times this number, leading to an estimated average of 9.0 ± 2.6 sources during human VF (ten Tusscher et al., 2009). The atria are a much thinner walled structure, and as such filaments are shorter (Clayton and Nash, 2015). Epicardial breakthrough has been observed in both VF (Nash et al., 2006) and AF (Eckstein et al., 2013). In addition, the electrical activity on the endocardium and epicardium of the atrium during AF have been shown to exhibit degrees of discordance, in which there are periods where the surfaces show the same wavefront pattern, and times when they have different wavefront patterns (Gutbrod et al., 2015). These differences have been suggested to be due to the location of rotational filaments (Berenfeld et al., 2014). As such, recordings from both walls of the atria and through the tissue depth are required in order to fully interpret arrhythmia wavefront patterns.

Most mapping modalities are restricted to recording measurements from a single surface of the atrium only, and consequently for focally propagating wavefronts, it is difficult to distinguish between their potential causes, which are: triggered beats; breakthrough because of transmural conduction from the other surface of the atrium; intramural reentry; and rotors for which the filaments are either U or O shaped. In the case of electrogram measurements, electrogram morphology may distinguish between these, with an R/S morphology suggesting transmural propagation (Eckstein et al., 2013). Regardless of causation, new wavefront initiation locations may be in sites distinct to areas indicated by phase singularities or dominant frequency, and as such are another important measure.

With these motivations, this chapter firstly considers the stability of wavefront dynamics in terms of the dominant frequency and the distributions of phase singularities, for the canine cholinergic AF preparation analysed in Chapter 4. The distribution of new wavefront initiation locations were also assessed, as well as the spatial correlations between each of the measures. The optical mapping protocol and parameter choices determined in Chapter 4 were used. In addition, during AF it is often difficult to distinguish continuous rotor or multiple wavelet activity from new wavefronts following electrical quiescence in the mapping field, arising from breakthrough, focal activity or sites of U/O shaped filaments. These mechanisms may be visually indistinguishable; however, areas of new wavefronts may represent critical regions responsible for sustaining AF that are not detected by phase singularity density maps or DF maps. In particular, identification of foci responsible for sustaining AF may have clinical utility as potential ablation targets.

The aims for this chapter are as follows:

- to develop a method to detect instances of new wavefronts;
- to examine the stability of phase singularity distributions, dominant frequency (DF) sites, and new wavefront locations over time for each of the experimental preparations, as well as the correlation between these measures;
- to develop a computational method for identifying foci responsible for sustaining AF;
- to develop a tool to gain insight into arrhythmia mechanisms.

5.2 Methods

Data from four canine left-atrial cholinergic AF preparations were post-processed, and DF maps and phase singularity distribution maps were calculated, using the techniques in Chapter 4. The dose of acetylcholine varied between preparations (30μM for the first two preparations; 10μM for the third and fourth preparations).

5.2.1 Detecting instances of new wavefronts

Instances of new wavefronts on the endocardium were identified as areas of active tissue where there were no active tissue pixels in the vicinity in the previous frame. This was achieved by defining active tissue pixels as those at an isophase value of $-\frac{\pi}{2}$; see Fig. 5.1 for an example. To calculate an acceptable isophase line without the need to interpolate the data, the method suggested by Kay and Gray (2005) was used. Pixels are defined as belonging to an isophase line of a given value θ if the pixel phase lies within the range $[\theta - 0.5, \theta]$, and between one and three of its four adjacent neighbouring pixels have a value greater than θ.

For each wavefront within a given frame, there are three possibilities: the wavefront is an existing wavefront, present in the previous frame (*propagated wavefront*, see Fig. 5.1); the wavefront is a new wavefront and there are other wavefronts present within the mapping field (*new wavefront, existing AF*, see Fig. 5.2); the wavefront is a new wavefront and there are no other active pixels present within the mapping field in the preceding frame (*new wavefront following electrical quiescence in mapping field*, see Fig. 5.2). To identify new wavefronts, each of the active pixels at a given frame were checked for the existence of active pixels in a neighbourhood threshold of the pixel in the preceding frame (implemented using a convolution operator). Pixels without a neighbouring active pixel in the previous frame were defined as new wavefront pixels; otherwise pixels were identified as belonging to a propagated wavefront. The locations and timings of these new wavefront initiation points were saved in order to plot spatial maps of new wavefront sites and in order to analyse the new wavefront timings.

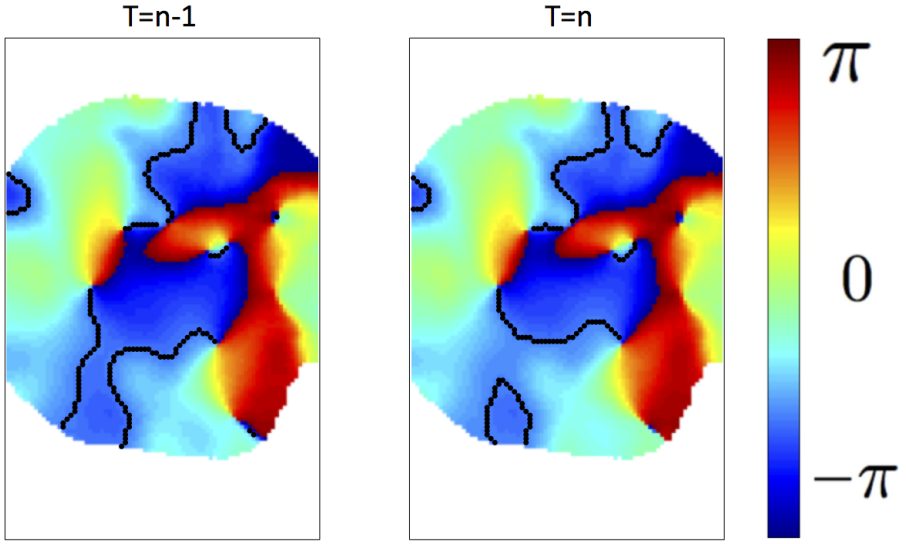

Figure 5.1: Active pixels are defined at an isophase value of $-\frac{\pi}{2}$ and pixels are considered as belonging to a propagated wavefront if there is a nearby active pixel in the previous frame. Here all of the wavefronts in the frame at $T = n$ can be explained by a propagated wavefront in the frame $T = n - 1$, and all of the active pixels have a nearby active pixel in the previous frame.

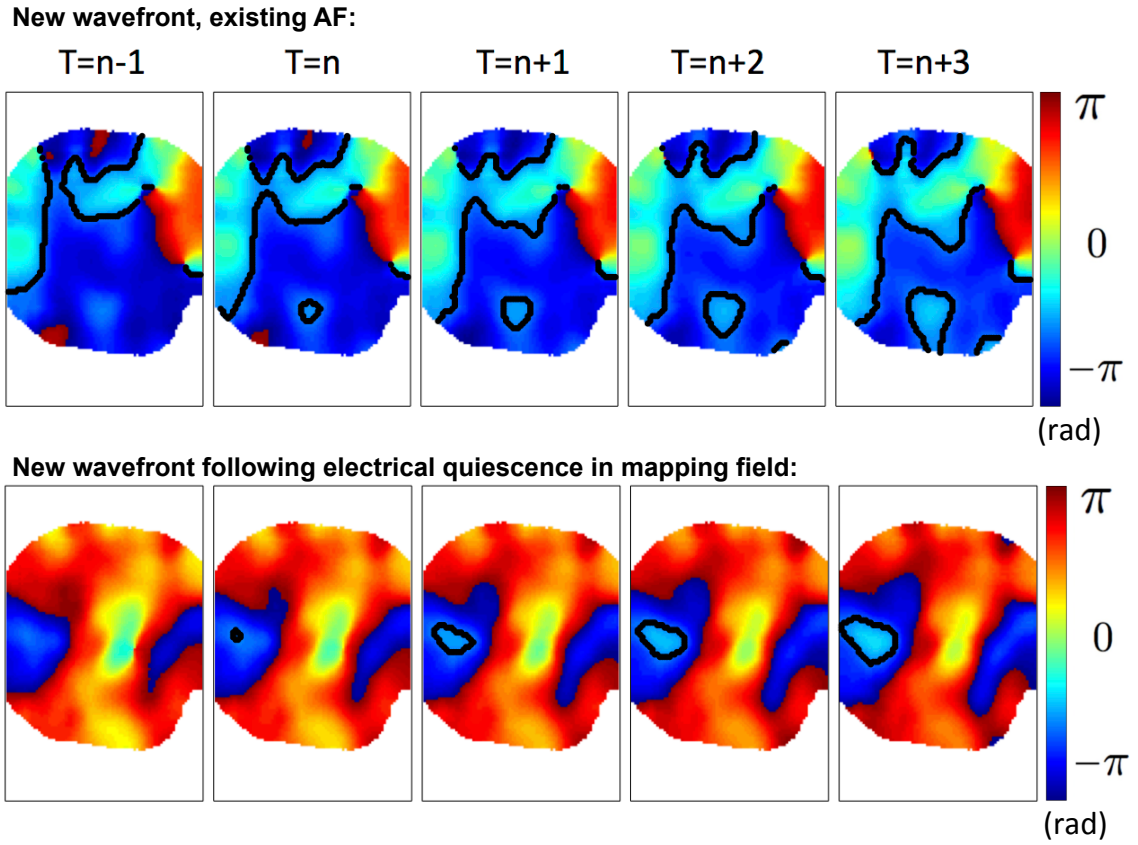

Figure 5.2: New wavefronts are identified as instances of active pixels that cannot be explained by propagation from active pixels in the previous frame, and occur during existing AF or following electrical quiescence in the mapping field. Sequential frames are shown in which a new wavefront in the mapping field is seen in frame $T = n$, which cannot be explained by any nearby active pixels in frame $T = n - 1$. The new wavefront is seen to propagate focally. Top row: there are other wavefronts within the mapping field at $T = n - 1$, and so this is termed to be a new wavefront, in which there is existing AF. Bottom row: there are no active pixels in frame $T = n - 1$, and so this is termed to be a new wavefront following electrical quiescence in the mapping field.

5.3 Results

Four experimental preparations were assessed, labelled here as LA1 (left atrial preparation number one), LA2, LA3 and LA4. For each of the preparations, between eight and fourteen ten-second recordings were taken and eight seconds of each recording were analysed offline. Full results are shown for LA1; and summary results are presented for LA2, LA3 and LA4.

5.3.1 Stability over time: dominant frequency

To investigate whether AF frequency is stable over time, DF distribution maps (defined as per Fig. 4.10) were calculated for each of the recordings and the stability of the value and location of the DF island were compared between recordings.

In general, DF value and island location show a degree of stability for all preparations (Figs. 5.3, 5.4), whilst DF area fluctuates (Figs. 5.3, 5.4). The mean DF is different for each preparation, covering a wide range from 14.5Hz (Fig. 5.4 B) to 33.8Hz (Fig. 5.3). In one of the four preparations, there is an instance of two DF islands (Fig. 5.4 B).

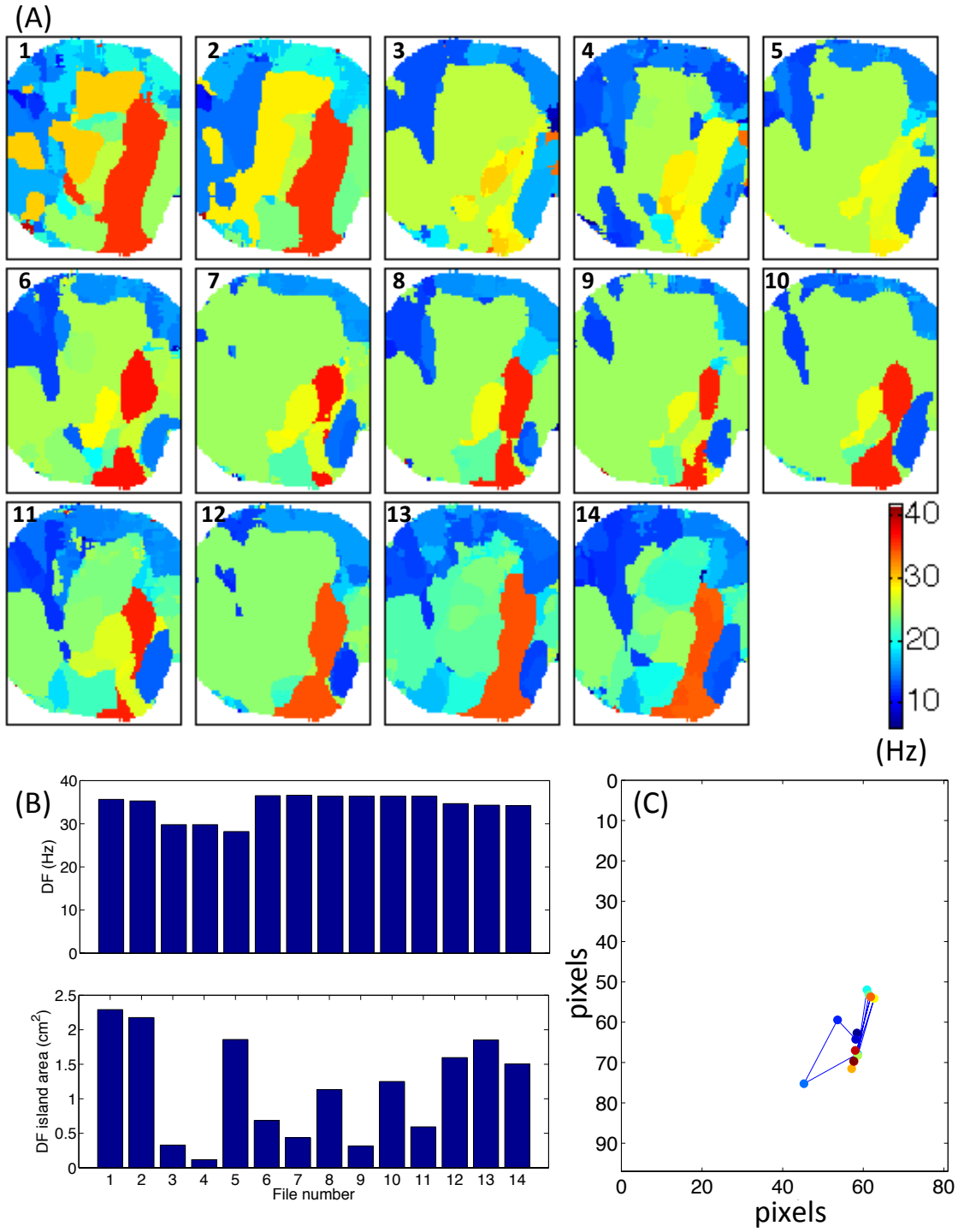

Figure 5.3: The DF value and location is stable over time, whilst DF area fluctuates for LA1. (A) DF maps for LA1, where the fourteen maps refer to sequential ten second files, which visually exhibit a degree of stability, particularly for recordings number six onwards, and have clear islands of high DF. (B) The value and area of the islands of high DF are shown. The DF area fluctuates within a narrow range ($< 2\text{cm}^2$). (C) The centre of the DF island for each file is shown, where the trajectory is seen to be localised to a small area.

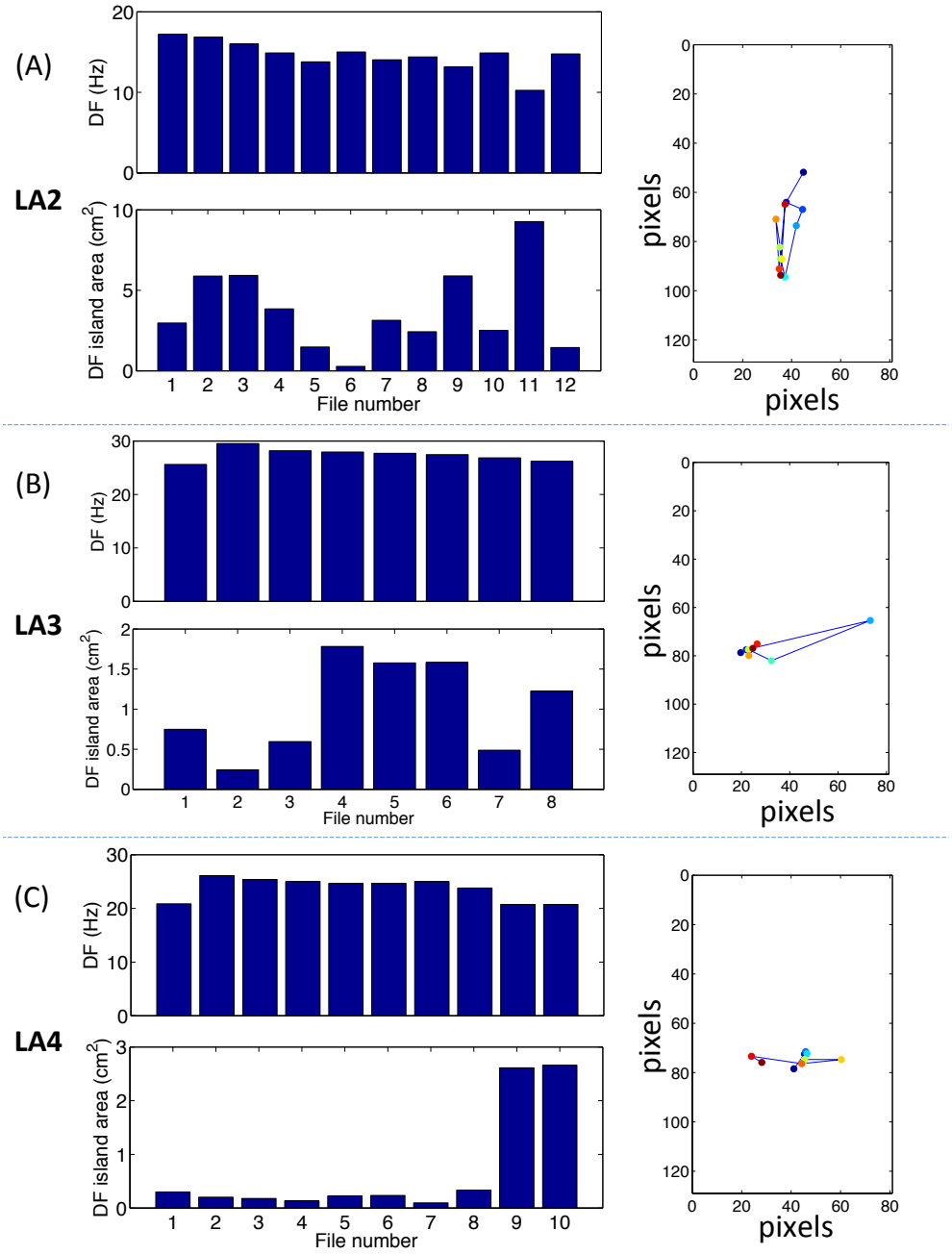

Figure 5.4: DF exhibits stability over time. DF islands were identified for each file, and the value, area and centre of mass were quantified for: (A) LA2, (B) LA3 and (C) LA4. The DF of LA2 (A) was lower than for the other three preparations (14.5Hz versus 33.8Hz, 27.5Hz and 24.4Hz). For preparation LA2, the DF island area also exhibited larger fluctuations between the twelve files, and the trajectory also covered a larger area, showing that the DF was most variable in this preparation. For preparation LA3 (B), there were two islands of the same dominant frequency, which can be seen in the centre of mass trajectory, where the island on the left-hand side is larger for seven of the eight files, while the other island is chosen for one of the files. For preparation LA4 (C), the DF is very stable for files two through eight, while the island increases in size and the DF is lower for the final two files.

5.3.2 Stability over time: phase singularity density maps

Although the DF showed a degree of stability over the duration of the experiments, the question remains as to whether PS distributions show any degree of stability or repeatability over time. There is in general a strong correlation between recording files for the same preparation (Figs. 5.5 and 5.6), and the greatest correlations are observed between the middle recording files (all files vs middle recording files only: 0.63 ± 0.13 vs 0.76 ± 0.11; 0.55 ± 0.15 vs 0.63 ± 0.15; 0.69 ± 0.13 and all > 0.54; 0.58 ± 0.18 vs 0.70 ± 0.14). This is hypothesised to occur because this is when the preparation is most stable.

Inspecting the regional densities, all four preparations have a low PS density on the left hand side of the preparation, which corresponds to the septal region (Figs. 5.5, 5.6). However the preferential regions with highest PS density vary between preparations between the lateral regions (Figs. 5.5, 5.6 (A, B)) and the posterior regions (Fig. 5.6 (A, C); see also Fig. 4.2). Therefore phase singularity distributions do show degrees of stability and preferential sites.

Start and end points maps

To isolate the starting and end point positions of the PS trajectories from the entire path, density maps of the start and end locations, respectively, of trajectories that last at least 0.5 rotations were calculated, with the motivation that there may be preferential spots for the creation or annihilation of PSs. The start location densities show a closer match between files than the PS trajectory distribution maps do (compare Figs. 5.5(C) and 5.7 (A)). There is more variability between the end point location densities (compare Fig. 5.7 (B) and (A)).

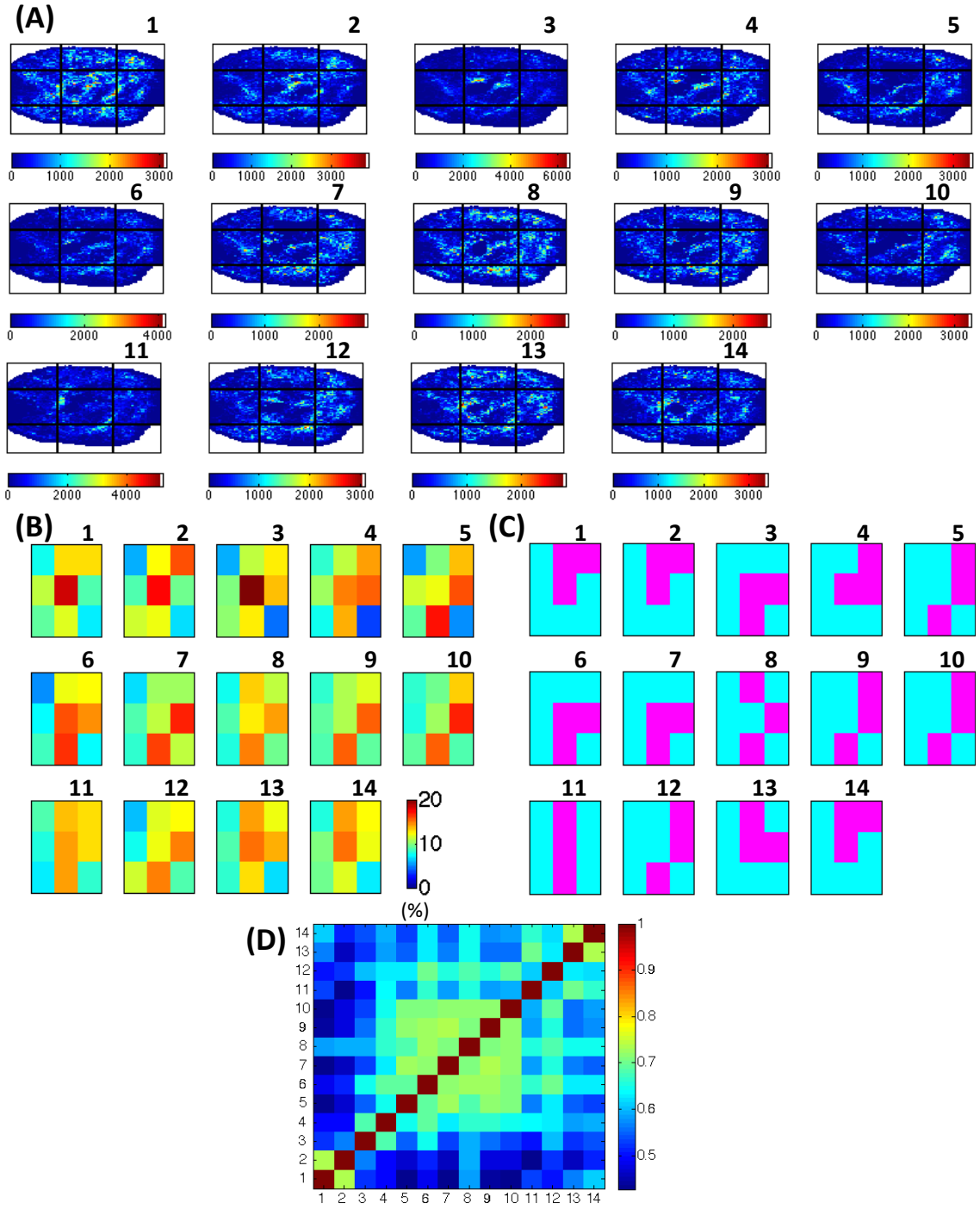

Figure 5.5: Regions of high PS density show a degree of stability over time. (A) Distribution maps of PS trajectories for each of the fourteen files for LA1 are shown here; region boundaries are marked as black lines; (B) the percentage PS density for each region; (C) the top three regions by density; (D) the global correlation of the density maps binned at a level of 3 by 3 pixels for all file combinations. Files five to ten are seen to correlate well with each other. Thus for these files the DF and PS distributions are stable. The other files show a lower overall correlation, although files one and two, and thirteen and fourteen also correlate well, respectively. Regarding the regional densities, the middle of the lateral region (middle right) has a high density of PSs for ten of the fourteen recordings and the bottom of the lateral region (bottom right) has a high density for nine of the recordings.

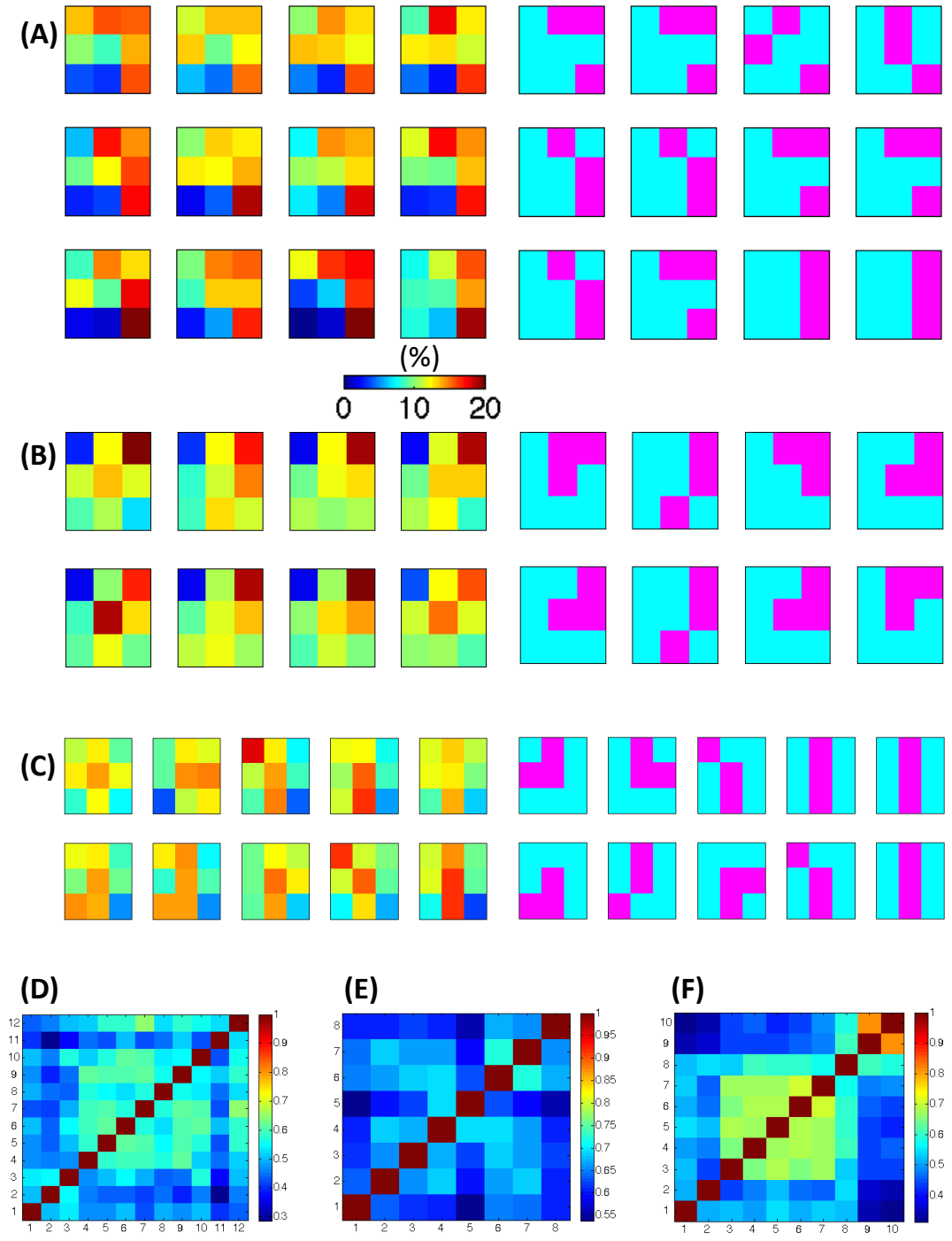

Figure 5.6: Regions of high PS trajectory density vary between preparations. Regional analysis in terms of percentage PS density (left) and top three regions (right) for: (A) LA2, (B) LA3 and (C) LA4. Correlation matrices for the overall density maps are shown: (D) LA2, (E) LA3 and (F) LA4. LA2(D) and LA4(F) show a similar trend where the middle recording files are better correlated with each other than the beginning or end files. LA3(E) does not show such a trend, where all of the files show a reasonable correlation. The PS distribution maps for LA3(B) all have a high-density region in the upper lateral region and are again low for the septal region (this is similar to Fig. 5.5 (C)). For LA2(A), the lateral region, as well as the top of the posterior region region have a high PS density for all of the files, demonstrating a degree of PS distribution map stability over time. For LA4(C), the posterior regions tend to have higher densities in the PS distribution maps.

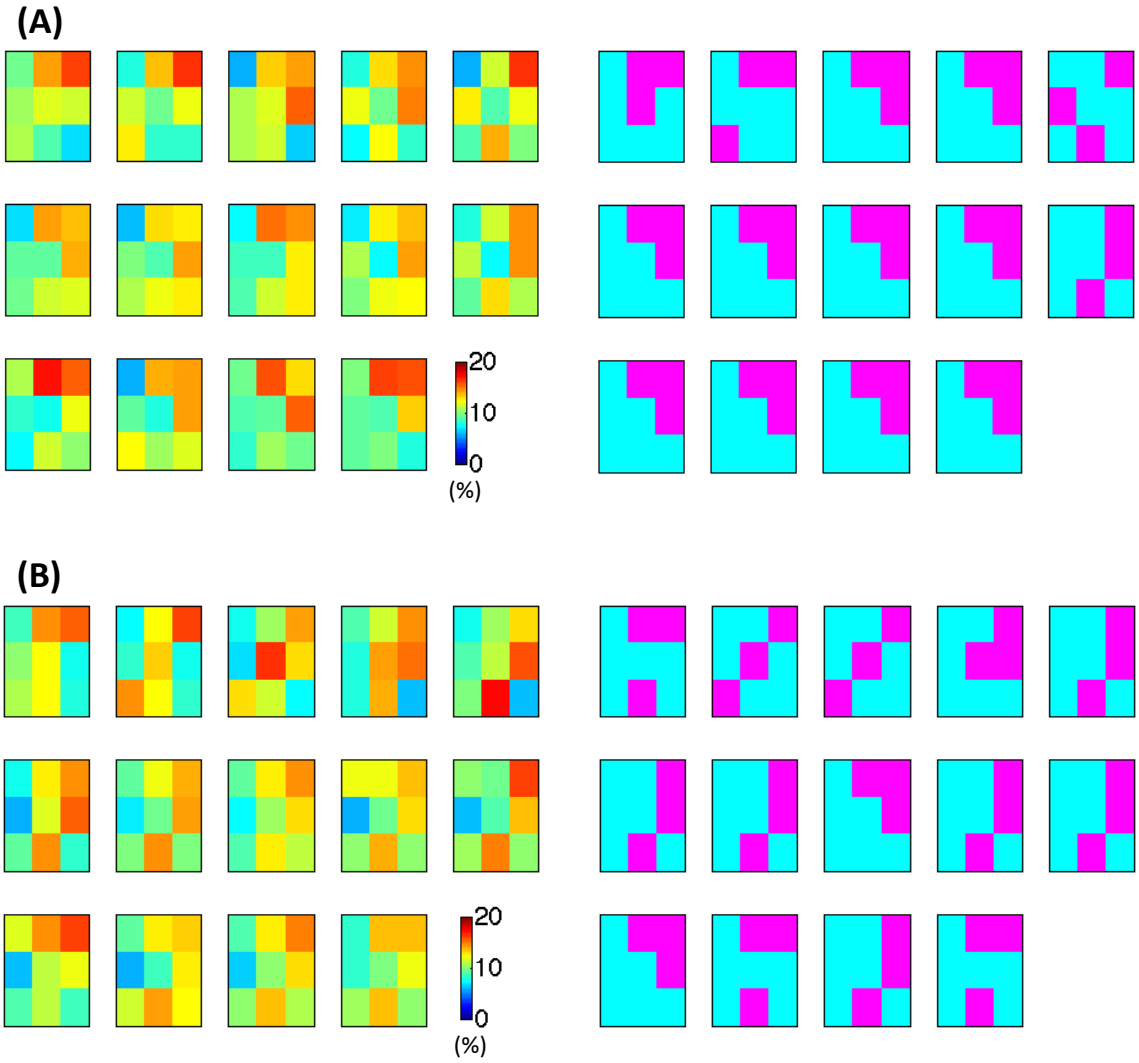

Figure 5.7: Start locations of PS trajectories exhibit stability over time, whilst the distribution of end locations of PS trajectories exhibit more variability. Regional analysis in terms of percentage density (left) and top three regions (right) for PS trajectory start point locations (A) and end point locations (B), for LA1. Only points for PS trajectories that last at least half a rotation are included here. Ten of the fourteen files have the same top three regions for start locations, in the upper lateral side of the domain. The start location densities show a closer match between files than the PS trajectory distribution maps do (compare (A) with Fig. 5.5). The end point locations show more variability between files (B).

5.3.3 Stability over time: new wavefront locations

As well as DF and PS distribution stability, a further property of the tissue that warrants investigation is the stability of new wavefront initiation locations. Three out of four preparations have clear areas with a high-density of new wavefront initiation sites. Two of the preparations (LA1 and LA2) exhibit a single preferential site, whilst one of the preparations (LA3) exhibits multiple sites of high-density (see Fig. 5.8). The final preparation (LA4) did not have any clear preferential regions (Fig. 5.8). In general, there is a strong correlation observed over time between recording files of a single preparation for the preparations with preferential sites (example shown in Fig. 5.9 for LA1). For two of the preparations (LA1 and LA2), the strongest correlations are between a set of files in the middle of the fibrillation episode (perhaps when the preparation is most stable). The properties of the high-density regions of new wavefront initiations are further investigated in Section 5.3.6.

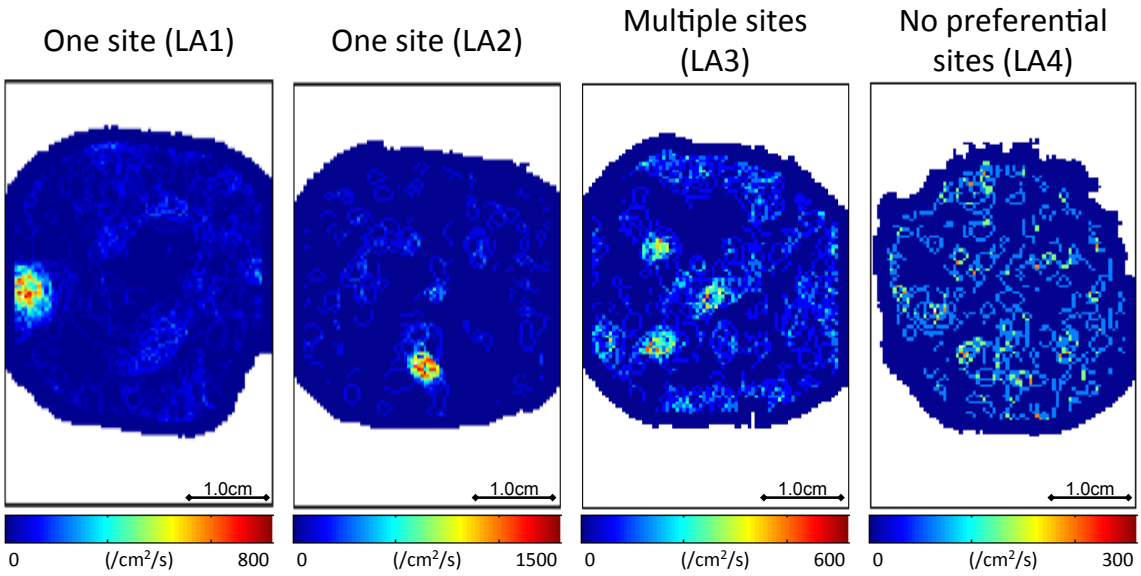

Figure 5.8: Three out of four of the preparations had clear sites of new wavefront initiation. Two of the preparations had a single high-density new wavefront initiation site (LA1 and LA2); one preparation had multiple preferential sites (LA3); and one preparation had no preferential sites.

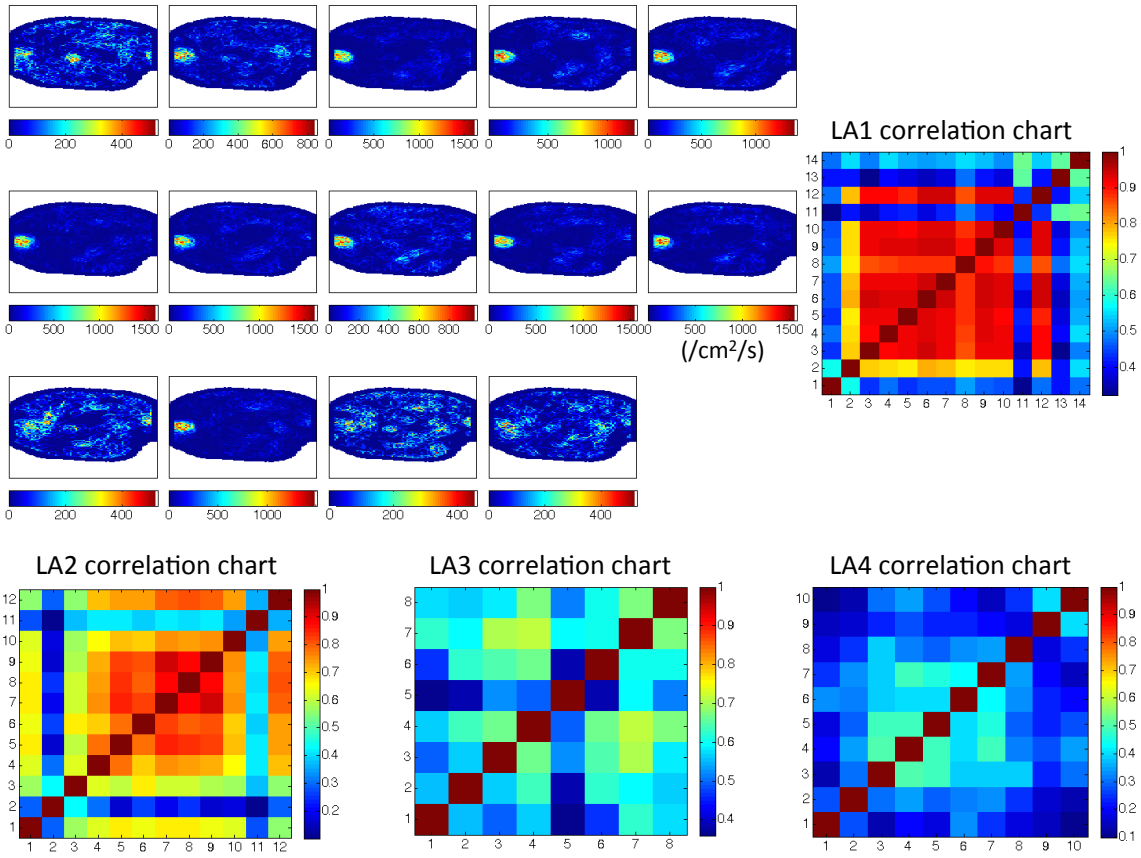

Figure 5.9: Distribution maps of new wavefront initiation locations are stable over time. Maps which show the spatial distribution of new wavefront locations for LA1. A high-density region is clearly visible in the septal region of ten of the fourteen recordings and the new wavefront distribution maps of these files correlate well. Distribution maps for LA2 show a similar relationship, in which recording files from the middle of the AF episode duration correlate well with each other. LA3 does not show such a pattern. Files for LA4 exhibit a lower correlation.

5.3.4 Correlation between frequency, phase singularity distribution maps and new wavefront sites

Similar patterns in the stability of the preparations were noted for the dominant frequency, PS distribution maps and new wavefront location maps. The correlation between dominant frequency, PS distribution maps and new wavefront location maps were calculated for each of the files and the mean values for each of the hearts were low (< 0.11 for DF and PS distribution maps; < 0.13 for PS distribution maps and new wavefront locations; and < 0.25 for DF and new wavefront locations).

5.3.5 Phase singularity number and number of rotations

The overall mean number of PSs per cm^2 per ms across all of the recordings were calculated for each of the preparations, and are shown as those that last less than a rotation and those that last for more than a rotation in Fig. 5.10, where the shorter lasting PSs represent short-lived wavefronts. The mean number of rotations (including PSs that last at least one rotation only) are also shown in the figure. The preparation that did not have any preferential sites of new wavefront initiations (LA4) has a greater number of PSs per unit area measured on the endocardium than the other three preparations (0.81 ± 0.34 vs $0.45 \pm 0.23, 0.61 \pm 0.28, 0.59 \pm 0.28$ PS $/cm^2/ms$). This suggests that the nature of AF may exhibit differences between the preparations.

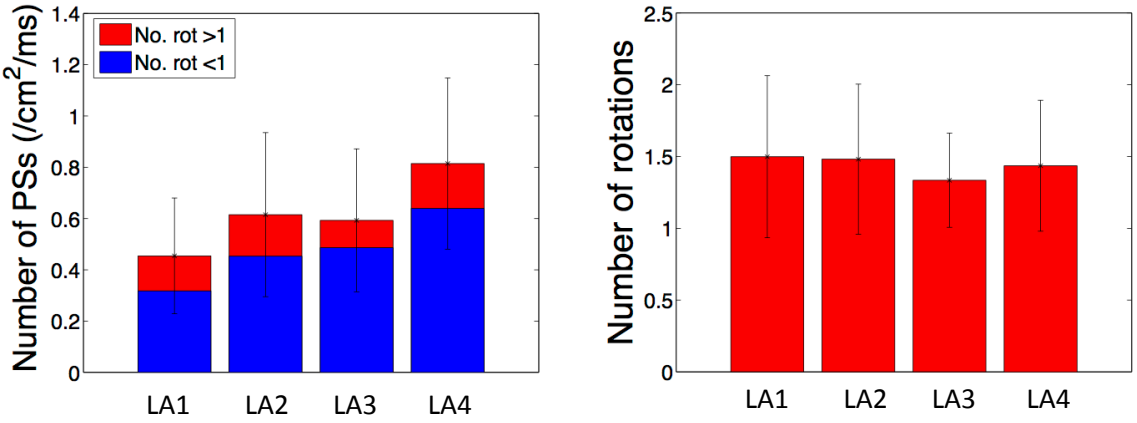

Figure 5.10: Mean and standard deviation of number of phase singularities (A) and number of rotations for each preparation (B).

5.3.6 Initial attempts to determine AF mechanisms

The differences between the preparations in terms of the number of PSs and the number of new wavefront initiations were calculated in order to investigate the mechanisms for AF. The motivation here is not to determine the exact nature of the sustaining mechanism of AF in these preparations, but rather to illustrate the utility of the techniques developed in this chapter and Chapter 4 to provide some elucidation. Namely, by considering the number of PSs that last for greater than one rotation, the total number of PSs and the new wavefront activation times, it should be possible to discern whether the activity on the endocardium is maintained by rotors, multiple wavelets or focal wavefronts, respectively.

LA1 has a lower average number of phase singularities measured on the endocardium (Fig. 5.10) and a clear preferential site for new wavefront initiations (Fig. 5.9). The mechanisms for sustaining AF in LA1 were investigated initially for a one second segment, shown in Fig. 5.11. The number of PSs and the number of PSs that last greater than one rotation are shown in Fig. 5.11(A), where there are instances when there are a large number of PSs with greater than one rotation, which are known as rotors (up to six rotors at any one time). During these times, the activity is hypothesised to be maintained by these electrical rotors. However, there are also times during the recording when the number of PSs with greater than one rotation drops down to zero, suggesting that at these times AF is not sustained by of rotor activity on the endocardium.

This can be further investigated by considering the number of active tissue pixels, which are defined here as pixels with an isophase value of $-\frac{\pi}{2}$ (see Section 5.2.1). When this number drops to zero, there are no more activation wavefronts within the mapped endocardial region, and there are instances when this can be seen to happen in Fig. 5.11(B). In this instance, AF would terminate unless a wavefront enters the mapping the field from the surrounding tissue, or there is a new focal beat on the mapped surface in the tissue arising from a triggered beat, transmural activation or rotors (U or O shaped filaments).

In order to discern the influence of wavefronts from the preferential site of new wavefront initiations, the activation times from all beats in the locality of the preferential site (shown as the red square in Fig. 5.11C) were analysed. The time intervals between each of the activations from this region are shown in Fig. 5.11(D), in which it can be seen that the cycle length is close to 40ms; with multiples also present, presumably due to times when the tissue is in a refractory state. In Fig. 5.11(B), the activation times from this area are plotted alongside the number of active pixels in the tissue, and it can be seen that increases in activity from the state where there

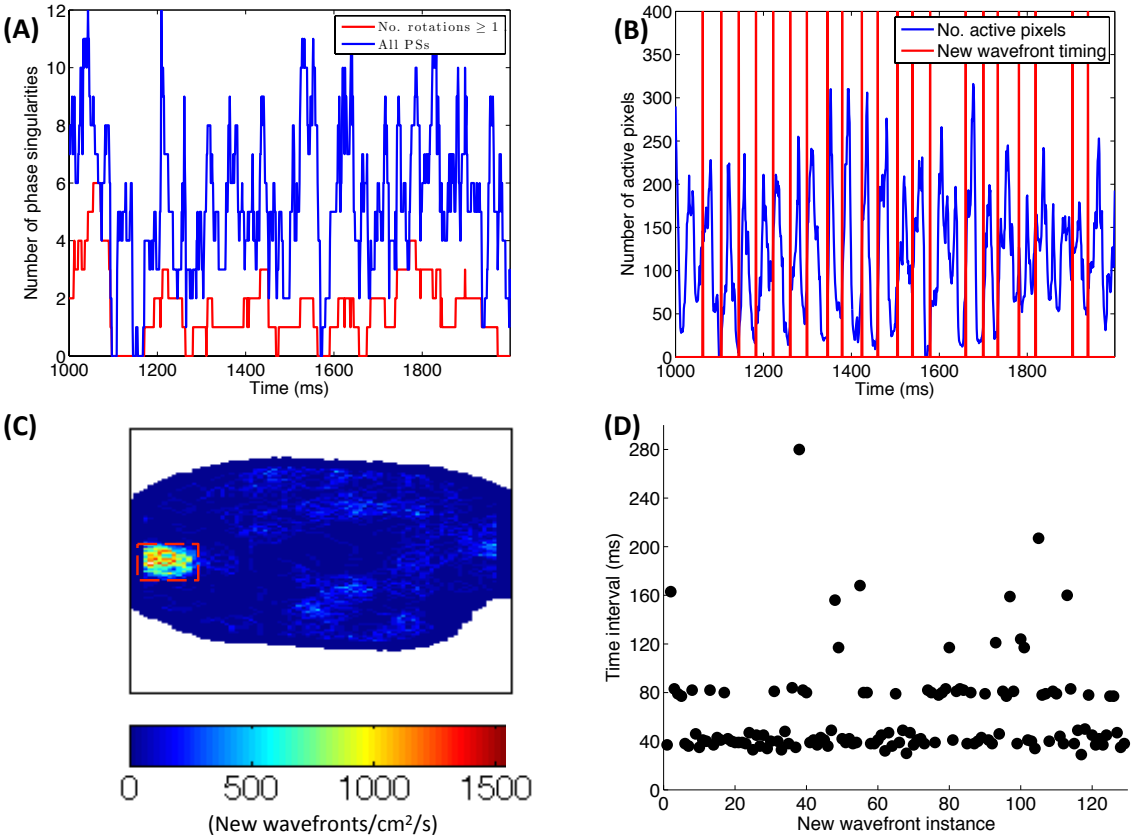

Figure 5.11: Investigating the number of rotors, PSs, active tissue pixels and new wavefronts over time indicates that timings of the new wavefront area coincide with times when the number of active tissue pixels drops to zero, sustaining AF in the mapping field. (A) Number of rotors (PS lasting greater than one rotation) and number of PSs over time; (B) number of active pixels in blue and timings of new wavefront initiations in red. The timings of the new wavefront initiations can be seen to coincide with times when the number of active tissue pixels drops to zero, triggering the re-initiation of AF in the mapping field. (C) New wavefront initiation location distribution map. (D) The activation times of the high-density region in the red box (in (C)) show the source has a CL of approximately 40ms.

are no activation wavefronts (electrical quiescence) can be attributed to the new wavefronts from this area. Thus for preparation LA1, there are a number of rotors and many wavefronts on the endocardial surface, but there are also times when there is electrical quiescence in the mapping field. Electrical activity in the mapping field appears to restart due to new wavefront initiations from the identified preferential site.

In contrast, LA4 did not have any clear preferential sites of new wavefront initiations. In this case, the number of active tissue pixels tended to be higher (Fig. 5.12 B). Activation times for all new wavefront initiations, regardless of location, were plotted alongside the number of active pixels in Fig. 5.12 B. For this preparation, new wavefronts do not appear to play a dominant role in the activity observed on the endocardial surface, and there is a higher density of endocardial PSs than for the other preparations (Fig. 5.10).

Thus there are differences between the preparations in terms of the number of PSs and the number of new wavefront initiations measured on the endocardial surface, which suggests there are differences in the nature of AF. In order to quantitatively determine the influence of preferential new wavefront sites on the maintenance of AF on the endocardial surface, the frequency of instances of no electrical activity (electrical quiescence) and the frequency of new wavefront initiation from these sites following electrical quiescence were calculated.

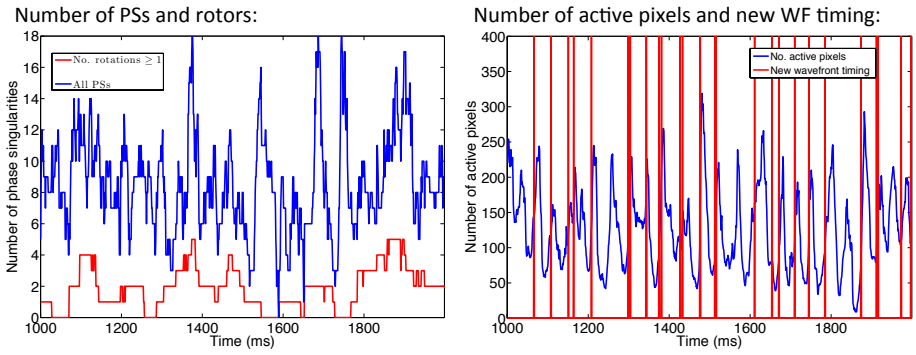

Figure 5.12: The preparation without preferential new wavefront locations (LA4) has a higher number of PSs, and the number of active tissue pixels also tends to be higher. Left: number of rotors (PS lasting greater than one rotation) and number of PSs over time. Right: number of active pixels in blue and timings of new wavefront initiations in red, where the new wavefront initiations can occur anywhere in the domain. In this preparation, new wavefront initiations do not appear to play a dominant role in the wavefront patterns observed on the endocardium.

5.3.7 Frequency of electrical quiescence

The frequency of electrical quiescence within the mapping field was calculated in order to identify periods of no electrical activity (shown in Fig. 5.13). The frequency was found to be higher for the first two preparations in which there was a single preferential site for new wavefront initiation (LA1 and LA2). For the final preparation in which there are no preferential sites of new wavefront initiation (LA4), there is a much lower incidence of electrical quiescence within the mapping field, which agrees with the hypothesis that AF is sustained by rotational activity occurring on the endocardium in this preparation.

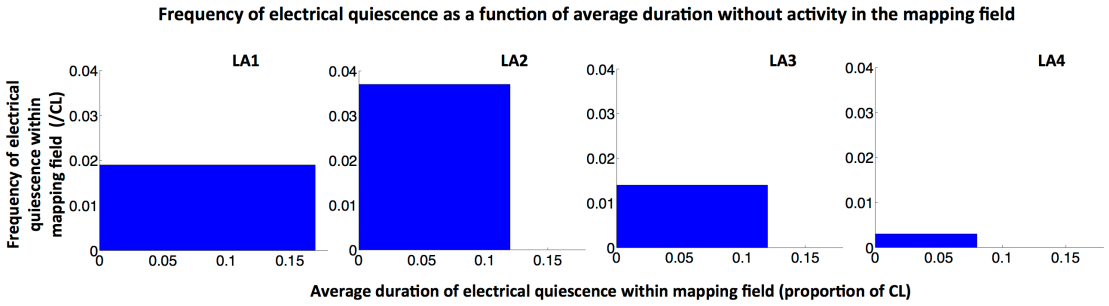

Figure 5.13: Histograms of frequency of electrical quiescence within the mapping field as a function of average duration without activity; the preparation without preferential new wavefront locations (LA4) has a much lower frequency. The area of each bar indicates the proportion of time without activity in the mapping field. Electrical quiescence within the mapping field is most frequent for LA2, but it also reinitiates more quickly than for LA1. LA4 has a lower incidence, which agrees with the hypothesis that AF is sustained by rotational activity in this preparation.

5.3.8 Frequency of new wavefront initiation following electrical quiescence

In order to assess the contribution of the preferential sites for new wavefront initiations to the number of new wavefronts initiated in the tissue, the density was compared for the preferential sites to the rest of the tissue, as a function of the area of each region. For all three preparations that visually exhibit preferential sites (LA1, LA2, LA3, see Fig. 5.8), the preferential region shows a significantly higher density of new wavefronts than the rest of the tissue (Fig. 5.14 A-C). In the case of multiple sites (LA3), the largest of the sites was chosen for analysis.

To determine whether the new wavefronts in the preferential sites were responsible for restarting the electrical activity following electrical quiescence in the mapping

field, the location of where the electrical activity originated from were assessed. In two of the preparations (LA1 and LA2), the density of new wavefronts following electrical quiescence was significantly higher in the preferential region than in the rest of the tissue (Fig. 5.14 D-E). The area of the bars in the plot indicate the number of new wavefronts following electrical quiescence in the preferential region and in the rest of the tissue, and indicate that the high-density site plays a relevant role in both preparations. For the third preparation (LA3), the analysed site showed a similar density of new wavefronts following electrical quiescence to the rest of the tissue, suggesting that although there is an increased number of new wavefronts in this region, these may not be functionally relevant. The two preparations with preferential regions of new wavefronts following electrical quiescence (LA1 and LA2) had a clear single high-density site, while the third had multiple high-density sites (and only one of these sites was used for analysis), which may explain the differences in the importance of the analysed preferential regions.

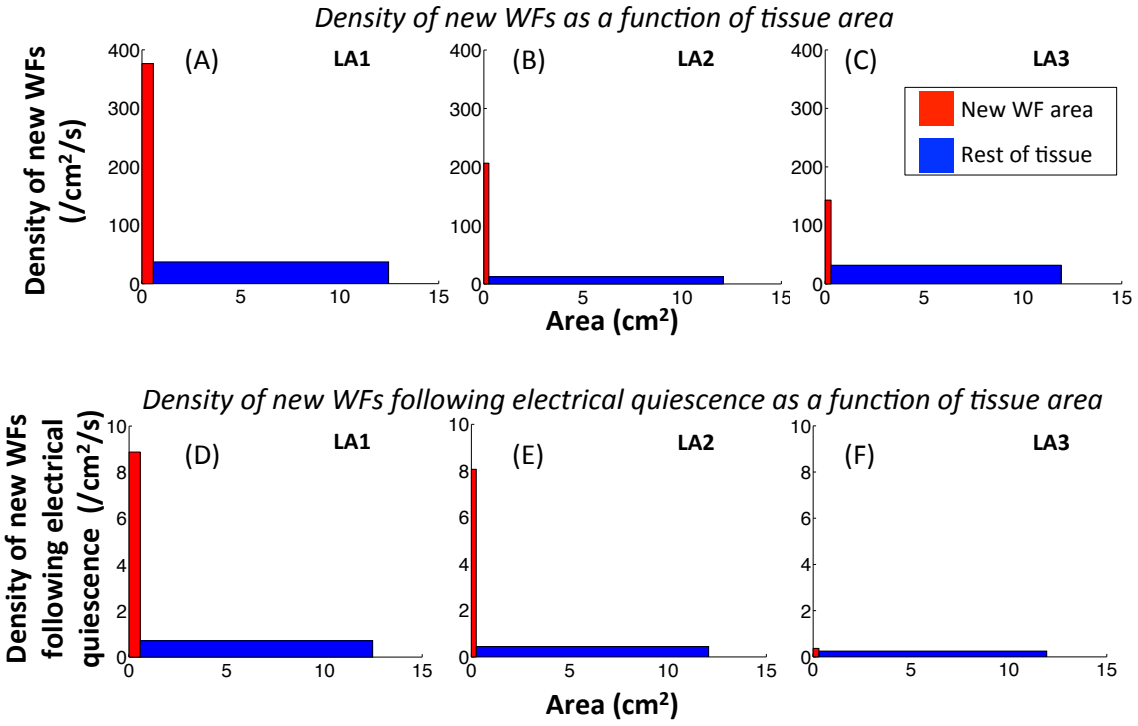

Figure 5.14: In the two preparations with one new wavefront site, the density of new wavefronts following electrical quiescence was significantly higher in this site than in the rest of the tissue, showing that this region plays a relevant role in arrhythmia maintenance. Plots to show the density of new wavefront initiation (A-C), and of new wavefront initiation following electrical quiescence (D-F) in the high-density preferential site (red) compared to the rest of the tissue (blue), as a function of the area of each region, for LA1, LA2 and LA3. The area of each bar indicates the number of new wavefronts arising in each region.

5.3.9 Comparing new wavefront and rotor cycle lengths

For one of the preparations with one preferential site of new wavefront initiations (LA2), the high-density site was found to have an equal median cycle length to the median rotor cycle length (78ms and 77ms; p= 0.73, by Mood's median test, a non-parametric test for determining whether medians of two distributions are equal). For the other preparation with one preferential site of new wavefront initiations (LA1), the median cycle lengths were unequal, but of similar magnitude (new wavefront cycle length 45ms; rotor cycle length 38ms; p< 0.005, Mood's median test). For this preparation, the new wavefront area cycle length was observed to cluster at harmonics (see Fig. 5.15). For the preparation with multiple sites (LA3), the largest site was found to have a higher cycle length than the average rotor cycle length (110ms vs 41ms; p< 0.005, Mood's median test). This agrees with the observation that the largest site did not play a dominant role in maintaining the arrhythmia following electrical quiescence. The rotor cycle lengths varied between preparations in line with the DF variation.

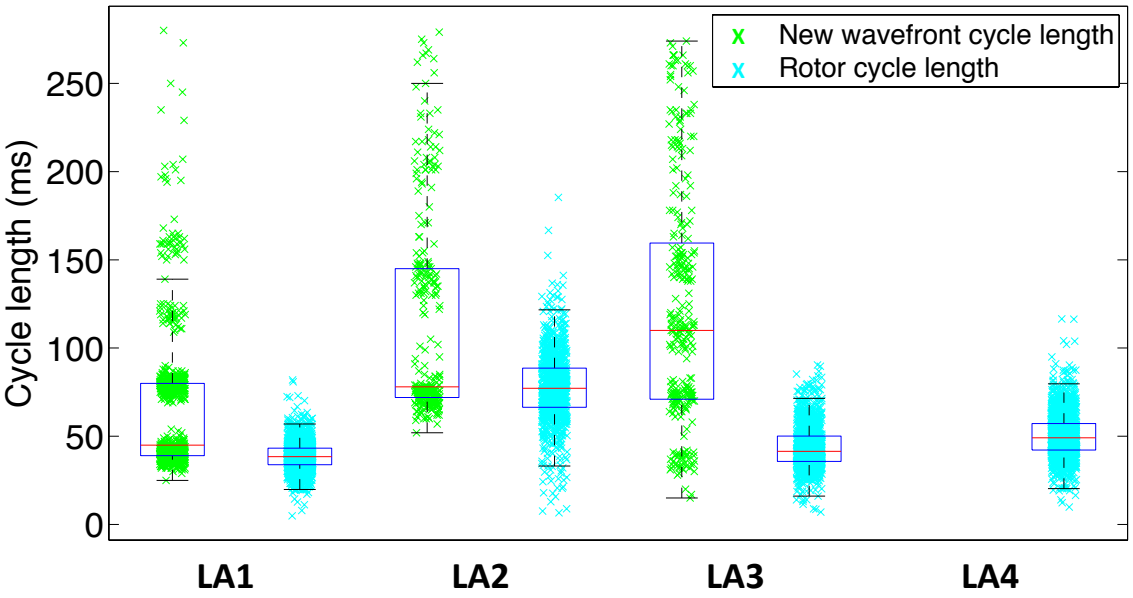

Figure 5.15: Distributions of cycle lengths for the high-density site of new wavefronts and for rotors exhibit differences between preparations. Cycle lengths measured during the recordings are marked as crosses, with box and whisker plots overlaid to mark the median value (red line) and lower and upper quartiles (blue box). For LA4, there were no preferential sites of new wavefront initiations, so only the distribution of rotor cycle lengths is considered. See text above for interpretation.

5.4 Discussion

5.4.1 Summary of findings

The stability of DF maps, phase singularity maps and new wavefront distribution maps over time for each of the preparations, as well as the correlations between each of the electrical measurements, were examined. All three measures were shown to exhibit stability over time. Preferential PS sites exist with low PS density on the septal region of all preparations. Three out of four preparations had preferential regions exhibiting a high density of new wavefront initiations, for which two of the preparations had a single site which was responsible for maintaining the arrhythmia, whilst the third preparation had multiple sites of new wavefront initiations. In contrast, for one of the preparations there was a lower incidence of electrical quiescence in the mapping field, and AF was hypothesised to be maintained by rotational activity on the endocardium.

5.4.2 Dominant frequency stability

DF was found to be relatively stable for each preparation over the AF duration (Section 5.3.1). There is conflicting evidence in the literature for the stability of DF during AF; Sanders et al. (2005) found DF was stable in human AF, whilst Salinet et al. (2014) found frequency to be temporally unstable. The duration of AF studied in this chapter is a short-duration of AF and most of the DF locations were found to be localised.

Similar to the study of Sarmast et al. (2003), which investigated the effects of ACh concentration on DF and arrhythmia dynamics in a Langendorff perfused sheep model, multiple frequency domains were observed in our study. However, in the four preparations here the frequency variations cannot be explained by the ACh concentration, since LA2, which had a ACh concentration of 30μM, had a lower DF than both LA3 and LA4, for which a concentration of 10μM ACh was used. In the study of Sarmast et al. (2003), DF plateaued at 4μM in a sheep atrial preparation, with a maximal value of 33Hz; thus it is likely that the DF had reached a maximal value in each of the preparations here, where the range of DFs was 14.5Hz to 33.8Hz. It should be noted that 33Hz is not expected at physiologic levels of cholinergic input (Sarmast et al., 2003). Atienza et al. (2006) also saw an increase in DF with adenosine infusion. Differences in the frequency measured across the preparations may be due to a heterogeneous spatial density of ACh receptors, which may increase spatial dispersion of refractory periods. Changes in DF island size over time may

represent further wavefront break-up; Bradley et al. (2011) found that the size of the largest DF domain decreased during ischemia as VF became more fragmented.

5.4.3 Stability of phase singularity distribution

All preparations exhibit preferential regions for PS location and a degree of stability in distribution over time. Preparations LA1, LA2 and LA4 all show a similar trend where the middle recording files from the fibrillation episode are better correlated with each other than the beginning or end files (Figs. 5.5 D, 5.6 D, F). This suggests the validity of the analysis protocol developed here, since files that are closer together temporally tend to show a closer agreement. For three of the preparations (LA1, LA2 and LA3), the PS density is low in the septal region of the tissue. Similar to our findings, some studies have suggested that AF driver locations show a degree of spatio-temporal stability on a regional basis (Narayan et al., 2012b; Haissaguerre et al., 2013).

The number of rotations required for a phase singularity to be defined as a rotor varies among the literature, with some studies counting all phase singularities as rotors (ten Tusscher et al., 2009), whilst others require at least one rotation (ten Tusscher et al., 2007). Further, Kay et al. (2006) define *compound rotors* to be a single organising center for which the phase singularity may change over time in the instance of wavefront fragmentation or collision. In this chapter, we defined rotors as phase singularities undergoing one or more rotations, and phase singularities that lasted at least half a rotation were included in density maps, since this threshold was determined appropriate in Sections 4.2.7 and 4.3.9. The threshold for the number of rotations required for a phase singularity to be termed a rotor and to be included in density maps will affect the results (see Section 5.4.6).

Sarmast et al. (2003) found that increasing acetylcholine concentration increased the number of PSs (0.1μM: 2.9$\pm$0.6 PS/cm^2/s; 4μM: 13.5$\pm$ 1.8 PS/cm^2/s), decreased the rotor duration (171$\pm$28ms to 79$\pm$3ms), and increased the number of rotations (1.62$\pm$0.12 to 2.27$\pm$0.07). This trend was not observed in our data, in which the number of PSs in LA4 was higher than for LA1 and LA2, whilst LA4 had a lower dose of acetylcholine; furthermore, the number of rotations was similar between preparations that had different doses of acetylcholine.

5.4.4 New wavefront stability

A method was developed in this chapter to identify new wavefronts from phase (Section 5.2.1). This has the great advantage that it does not require any activation

time assignment. The method is sometimes over-sensitive, however clear patterns are seen in the many of the new wavefront spatial distribution maps, demonstrating efficacy of the technique (Figs. 5.8, 5.9). Other studies also define wavefronts as isophase lines (Nash et al., 2006; Rogers, 2004).

In three of the four preparations examined in this chapter, there were preferential sites of new wavefront initiation. Similar to the observation for PS distribution map changes over time, where the middle files for LA1 and LA2 showed greater similarity, while for LA3 all of the files showed similar correlations, this is again the case for the new wavefront distributions. The new wavefront preferential regions are not as clear for LA3 compared to the LA1 and LA2, however there are some repeated areas. In contrast, LA4 does not have clear new wavefront regions (Fig. 5.8). The preferential region of new wavefront initiation in LA1 was shown to be involved in maintaining the arrhythmia in the endocardial mapping field (Section 5.3.6).

Focal sources have also been identified in many other studies (Haissaguerre et al., 2013; Narayan et al., 2012b; Kurotobi et al., 2014). New wavefronts due to endocardial-epicardial dissociation have been observed, although in contrast to the findings here, these are not in repeated locations (Eckstein et al., 2013). There are some studies with new wavefronts occurring in repeated locations, including the study of Filgueiras-Rama et al. (2011) in which organised focal wavefronts were detected at the same site and with the same direction over four or more sequential beats.

5.4.5 The origin of new wavefronts: triggered, transmural conduction, or rotors?

New wavefront initiation sites were found to be functionally important in sustaining AF in the endocardial mapping field in three of the four preparations investigated here. However, the source of these new wavefronts are unknown. In particular, it is unclear whether they are due to triggered activity, rotors with U or O shaped filaments, or transmural conduction. Although some studies have observed isolated trigger activity and late-phase early after depolarisations in acetylcholine induced fibrillation (Burashnikov and Antzelevitch, 2003; Schuessler et al., 1991; Sharifov et al., 2000), acetylcholine is known to suppress triggered activity (de Carvalho et al., 1969; Gutbrod et al., 2015) and thus it is unlikely that new wavefronts are due to a triggered source with fixed cycle length. Acetylcholine application is associated with reentry, rather than repetitive focal sources. Scroll waves have been shown to exhibit as focal wavefronts in the case of U or O shaped filaments (Berenfeld et al., 2014), and simulation studies have investigated the effects of tissue thickness

on the number of filaments exhibiting as phase singularities on the tissue surface (Clayton and Holden, 2002c). The preparations were from control canine, meaning there is no reason to suppose there is any structural remodelling that would explain endocardial-epicardial dissociation, which would result in transmural conduction (de Groot et al., 2010). Electrogram morphology may indicate the source of the waves as triggered or breakthrough; however, in this study, only optical mapping recordings were analysed.

5.4.6 Correlation between frequency, phase singularity distribution maps and new wavefront initiation distribution maps

There was very little correlation between dominant frequency, PS distribution maps and new wavefront sites in the preparations studied here. This is somewhat surprising since drivers, whether focal or reentrant, are typically thought to coincide with areas of high-frequency (Filgueiras-Rama et al., 2012; Mansour et al., 2001). PS distribution maps with a different threshold for PS inclusion (for example, requiring PSs to undergo a full rotation) may show an improved correlation; however, the change is expected to be minimal as PS maps with thresholds of half a rotation and a full rotation matched well in initial parameter testing (see Section 4.3.9).

5.4.7 Initial attempts to determine AF mechanisms

Initial attempts to determine AF mechanisms suggest the applicability of the techniques developed in this chapter to provide some elucidation on the wavefront dynamics in the preparation studied here. In particular, by considering the number of PSs that last for greater than one rotation, the total number of PSs and the new wavefront activation times, it should be possible to discern whether the activity is maintained within the mapping field by rotors, multiple wavefronts or focal sources, respectively. By assessing the frequency of arrhythmia termination, the frequency of new wavefronts from the high-density regions and the frequency of new wavefronts following electrical quiescence in the mapping field, the mechanisms sustaining AF can be determined, and foci responsible for near-instantaneous reinitiation of AF can be identified. This suggests that the techniques developed here can be used to probe the wavefront dynamics and to investigate the differences between preparations.

Several studies have quantified how the number of filaments, the number of wavefronts and the DF change over the course of VF, in order to determine the nature of fibrillation (Clayton and Holden, 2002a,c; Nash et al., 2006; Bradley et al.,

2011; Clayton, 2013; Kazbanov et al., 2014).

5.4.8 Limitations

A key limitation of the work presented here is the inability to discern the cause of new wavefronts. Mapping of both the endocardial and epicardial surface using optical mapping or electrode arrays would help with the interpretation of the origin of new wavefronts. Other methods for determining the origin of these focal wavefronts include applying a range of doses of acetylcholine, with the motivation that acetylcholine suppresses triggered activity, and so the attenuation of preferential sites for new wavefronts with increased acetylcholine dose would suggest triggered activity as the causation. In addition, the application of ion channel blockers may aid with this interpretation.

Chapter 6

Electrogram Phase

Part of this chapter (Section 6.2) has been published as conference proceedings; Computing in Cardiology (Roney et al., 2014b). The material presented herein is the work of the author, unless stated otherwise.

6.1 Introduction

Phase mapping is a technique for analysing fibrillatory signals, in which spatial singularities in phase correspond to the centres of rotational waves (Gray et al., 1998). Identification of phase singularities is one approach that can be used to locate the tip of spiral waves. Many optical mapping and simulation studies have used these techniques to analyse wavefront dynamics from action potential (AP) data (Clayton et al., 2006).

In the clinical environment, voltage data are recorded in the form of unipolar and bipolar electrograms. Techniques to analyse fibrillatory bipolar electrogram data include frequency analysis, such as dominant frequency or organisational index calculations (Sanders et al., 2005); fractionation scoring analysis (Nademanee et al., 2004); Shannon entropy analysis (Ganesan et al., 2013); and peak-to-peak voltage calculations (Marcus et al., 2007). However, these techniques typically assign a single time-independent score per electrode, and have shown limited success in designing ablation strategies. In addition, it is difficult to assign activation times to multi-component electrograms arising during fibrillation, and furthermore the process is challenging since activation time mapping requires the selection of an appropriate time window.

Phase mapping has the potential to overcome these limitations as it provides both spatial and temporal information. Recently, phase mapping using unipolar electrograms has been applied to VF (Nash et al., 2006) and AF data (Haissaguerre

et al., 2013; Kuklik et al., 2014). However, the correct calculation of electrogram phase during AF is difficult due to several factors, including the non-sinusoidal and fractionated nature of the electrograms, and the direction-dependency of bipolar electrogram amplitude.

In this chapter, techniques were initially developed to track phase singularities from simulated electrogram data, at various inter-electrode spacings to assess their theoretical suitability for use in a clinical environment. Computed wavefront dynamics and singularity positions for simulated action potential (AP), unipolar and bipolar electrogram data are compared, to assess the effects of datatype and inter-electrode spacings on the observed results. The techniques were then adapted for, and applied to, multi-electrode array cell-culture data and finally to clinically acquired signals, for which metrics assessing the numbers of singularities and wavefront dynamics are compared between unipolar and bipolar electrogram phase. The chapter is arranged by the data acquisition environment (*in silico*, *in vitro* and *in vivo*), building in complexity, starting with simulated data (Section 6.2), then cell-culture (Section 6.3) and finally clinically acquired data (Section 6.4).

6.2 Simulated data

6.2.1 Methods: simulation details

Data for testing the algorithms were generated from a simulation initiated with two fixed rotors on a 10cm×10cm two-dimensional domain, Ω. The monodomain tissue model and the Courtemanche et al. (1998) human atrial cell model were used to model the tissue and cellular membrane dynamics, respectively; electrical remodelling in AF was represented by reducing the ionic conductances of I_{to}, I_{Kur} and I_{CaL} (by 50%, 50% and 70% respectively (Courtemanche et al., 1999)) in the cell model. In addition, the conductance of I_{K1} was doubled on the right side of the domain, reducing the action potential duration (APD) (Pandit et al., 2005b), and allowing rotors with two different frequencies to be established. A smooth transitional region was included along the centre of the domain. Two rotors were initiated using an S1-S2 protocol (see Section 2.6). This resulted in a simulation with a stable rotor with a longer APD on the left side of the domain, whilst on the right side of the domain, the initial rotor fragmented, resulting in multiple unstable rotors, with collisions along the boundary (see Fig. 6.1).

The model was discretised using finite differences with a 0.1mm spatial resolution. Voltages and ionic concentrations were advanced using forward Euler and gating variables using the Rush-Larsen scheme (Rush and Larsen, 1978b), both with a

time-step of 0.01ms (see Chapter 2).

The action potential (AP) data were post-processed to derive extracellular unipolar electrograms, such that an electrogram at a point (x_p, y_p, z_p) is calculated as:

$$\Phi_e(x_p, y_p, z_p) = D \int \int_{\Omega} \nabla V_m \cdot \nabla \left(\frac{1}{R} \right) \, \mathrm{d}x \, \mathrm{d}y, \tag{6.1}$$

where V_m is the transmembrane voltage, $R = \sqrt{(x - x_p)^2 + (y - y_p)^2 + (z - z_p)^2}$ is the distance from the electrode and D is the diffusion coefficient (Sato et al., 2009) (Section 2.8). Unipolar electrograms were measured at recording locations on a regular grid of points with 2mm spacing, one cell radius (5μm) above Ω. Bipolar electrograms (Figs. 6.1E) were calculated as the difference of two unipolar electrograms (Fig. 6.1D), where electrograms were paired from left to right. Bipolar electrograms were calculated at inter-electrode spacings of 2, 4, 6, 8 and 10mm. An example showing 6mm spacing is given in Fig. 6.1.

In order to assess the use of unipolar electrogram phase and bipolar electrogram phase for tracking wavefront dynamics, results were compared to those from a gold standard measurement. In this case, the full resolution (0.1mm grid spacing) AP data were post-processed to calculate AP phase using the methods detailed in Sections 2.9 and 2.10, and this provided the *gold standard*. The phase of unipolar electrograms measured on the 2mm regular grid, and the phase of bipolar electrograms with inter-electrode spacings of 2, 4, 6, 8 and 10mm were each calculated using the methods detailed in the following sections. In order to isolate the effects of data resolution from signal type, subsets of AP phase and unipolar electrogram phase signals at grid spacings corresponding to bipolar electrogram inter-electrode spacings of 2, 4, 6, 8 and 10mm were considered. In each case, the phase of the AP, unipolar electrogram and bipolar electrogram data were interpolated to 0.1mm resolution, in order to compare the results to the gold standard arrangement. The methodologies for calculating phase, interpolating phase and the measures used for comparing the results from the different data types and resolutions are discussed in the next sections.

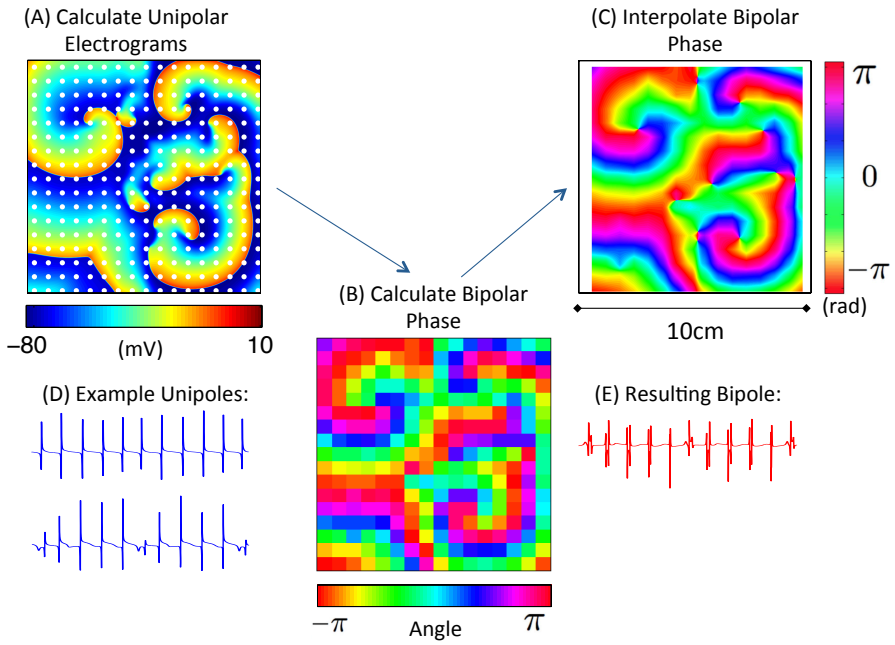

Figure 6.1: Summary of simulation data types: action potential, unipolar electrograms and bipolar electrograms. (A) Unipolar electrograms are calculated from AP data at the white dots (sub-selection of points at 6mm inter-electrode spacing shown here). (B) Bipolar electrogram phase, where bipolar electrograms are calculated from paired unipolar electrograms. (C) Interpolated bipolar phase at the original grid resolution (bipolar electrogram phase shown here; steps are equivalent for unipolar electrogram phase or action potential phase). (D) Example unipolar electrograms. (E) Bipolar electrogram calculated as the difference of unipolar electrograms.

6.2.2 Methods: bipolar electrogram filtering

Before calculating the phase of the bipolar electrogram, a series of filters were applied to the signal to make it more sinusoidal and appropriate for phase analysis. This was motivated by preprocessing steps typically applied for dominant frequency analysis.The sequence of filters suggested by Ng et al. (2006) were used:

1. Bandpass filter at $40 - 250$Hz;
2. Take the absolute value of the signal (rectification);
3. Lowpass filter at 20Hz.

The effects of each of these filtering steps are shown in Fig. 6.2. This sequence works well for 2 and 4mm spacing (see Fig. 6.4 for an example isopotential map at 2mm inter-electrode spacing).

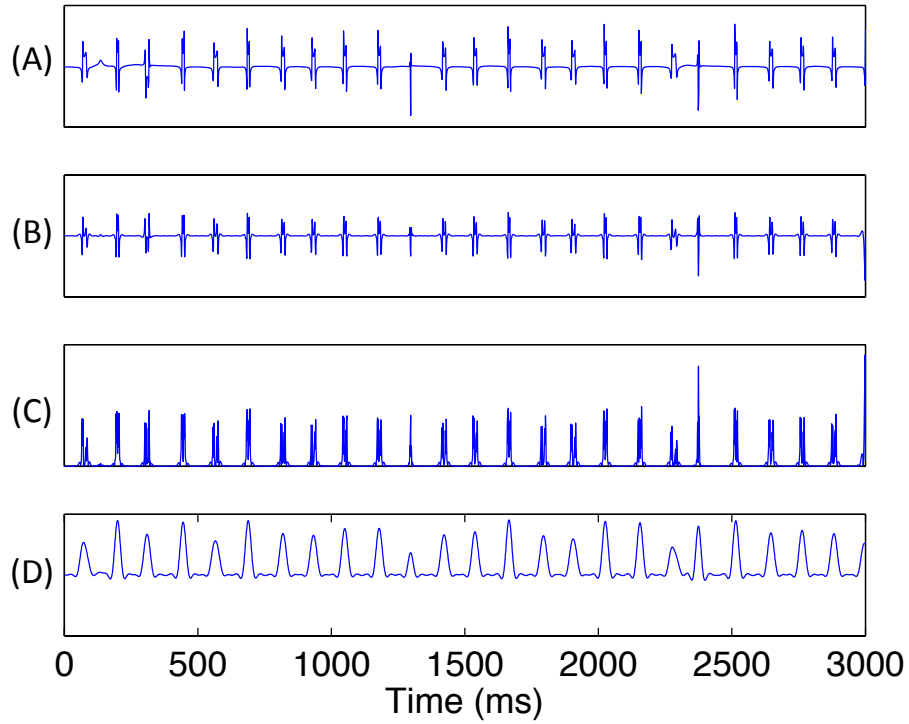

Figure 6.2: Bipolar electrogram filtering steps for 2 and 4mm inter-electrode spacing. (A) Raw signal; (B) Bandpass filter from $40 - 250$Hz; (C) Take the absolute value of the signal (rectification); (D) Lowpass filter at 20Hz.

For signals with large inter-electrode spacings ($>$ 4mm), electrograms filtered using the above filters were seen to contain many double potentials, leading to a split in the isopotential field (Fig 6.3B). In order to reduce the number of double potentials, the lowpass filter was changed from 20Hz to 10Hz for inter-electrode

spacings of 6, 8 and 10mm. This was seen to eliminate many of the double potentials and smooth the isopotential field (Fig 6.3C).

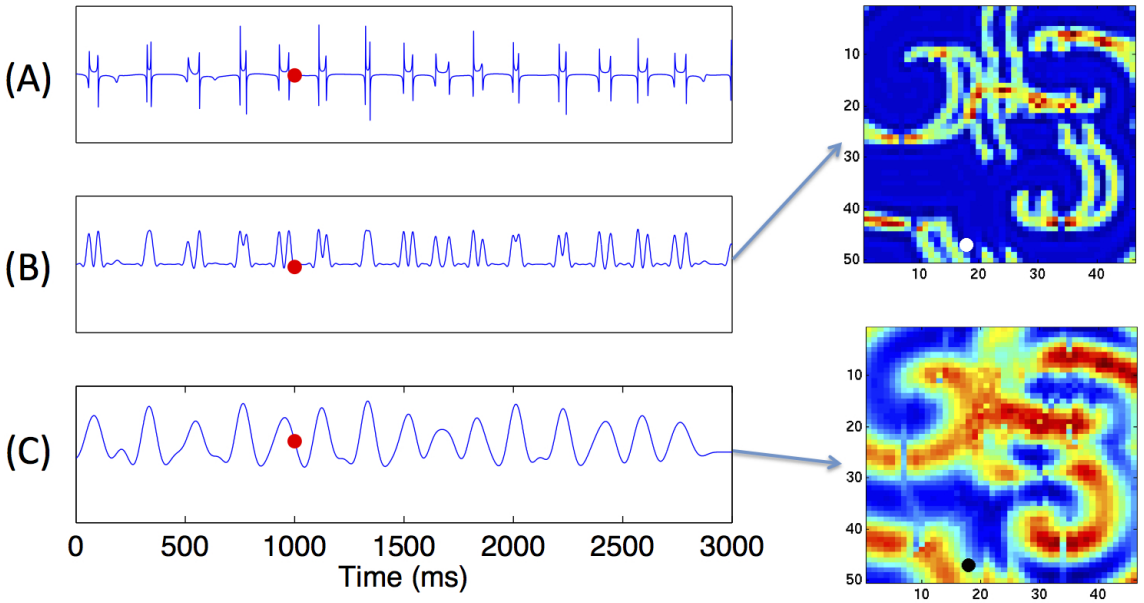

Figure 6.3: Electrogram filtering for 6, 8 and 10mm spacing. (A) Raw signal; (B) 20Hz lowpass filter signal containing a large number of double potentials and a split potential field; (C) 10Hz lowpass filter signal without double potentials and a smooth isopotential field. Red dots indicate time point for the isopotential field plot, and black and white dots indicate measuring location for the bipolar electrogram.

6.2.3 Methods: bipolar phase calculation

To identify rotor cores and track wavefront dynamics, the phase of the voltage signal was calculated (either AP, unipolar electrogram or bipolar electrogram). A signal with zero-mean was necessary to correctly compute the phase angle (Section 2.10). This was accomplished by calculating a moving mean, which was then removed from the signal. One challenge was identifying which deflections in a multi-component signal should be included in the final phase, which was further complicated by the fact that the amplitude of bipolar signals was dependent upon the wavefront direction, relative to the position of the two electrodes. An illustrative example is shown in Fig 6.4, in which the amplitude of the bipolar electrogram shown is small because the wavefront is parallel to the pair of unipolar electrograms. Signals that were small in amplitude due to wavefront direction were still included in the phase.

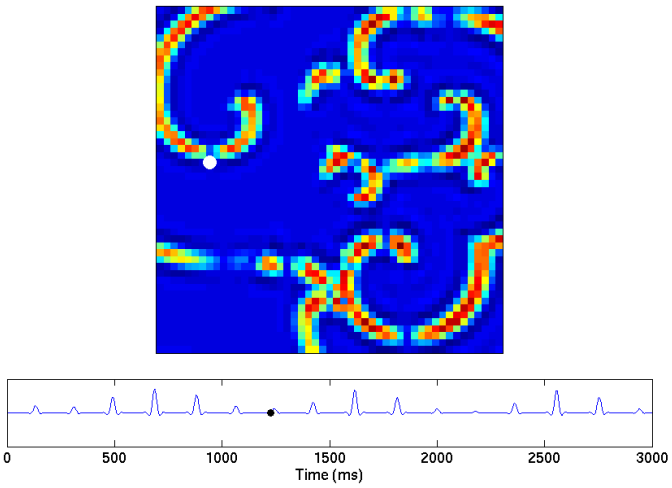

Figure 6.4: Amplitude dependence of bipolar electrograms on wavefront direction. Isopotential map, with the measuring location of the filtered electrogram below marked as the white dot. The time point of the isopotential map is indicated by the black dot on the filtered electrogram. Unipolar electrograms are paired left-to-right, and here it can be seen that the resulting bipolar electrogram is lower in amplitude at this time-point than for later deflections, as at that point the wavefront is parallel to the electrode locations. It is challenging to include these activations that are low in amplitude due to wavefront direction in the final phase.

The method used to calculate the zero-mean signal differed depending on the electrode spacing and the filtering applied. For small electrode spacings, where a 20Hz lowpass filter had been applied, a piecewise cubic hermite polynomial spline was fit to the maxima in the signal, where maxima were tagged according to thresholds that included signals that were small in amplitude due to direction. The maxima

line was used to normalise the signal (the minima line was taken as the zero-line), and subsequently a straight mean was removed (Figs. 6.5A and 6.5B).

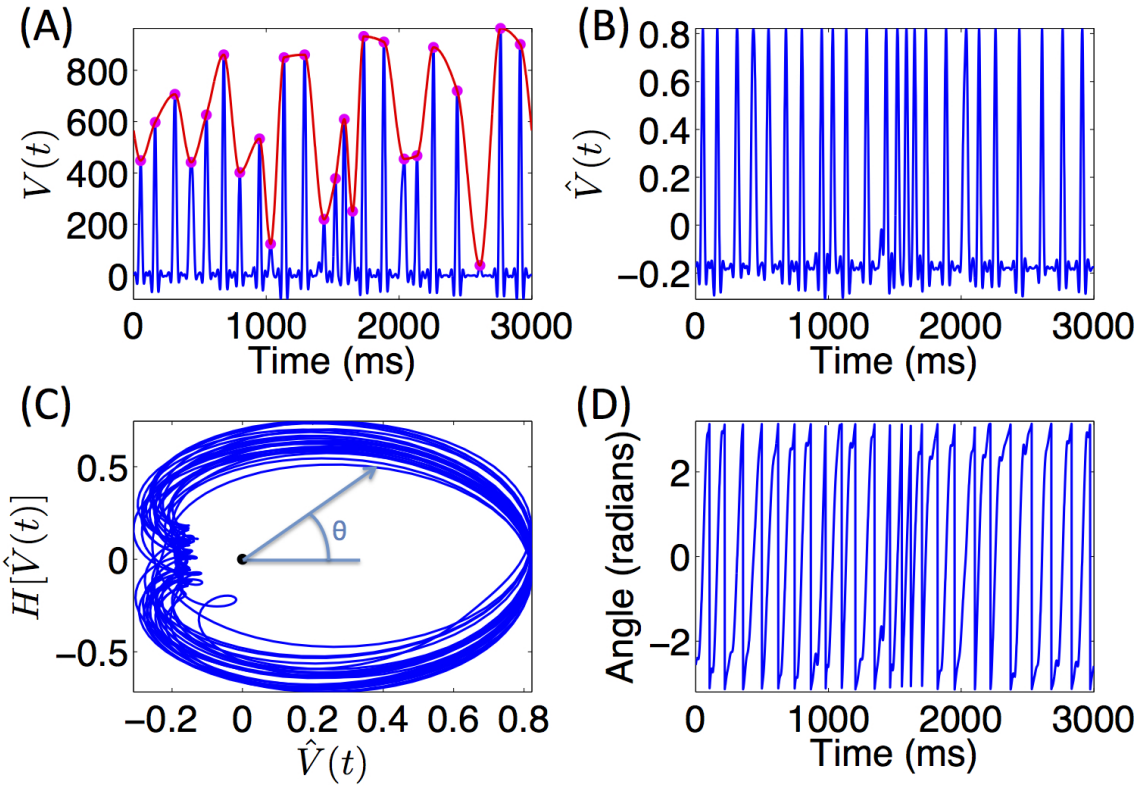

Figure 6.5: Calculation of bipolar electrogram phase with 2 or 4mm inter-electrode spacing. (A) Tagged maxima, joined using a cubic spline. (B) Signal after normalisation using the maxima line and with straight mean removed. (C) Real and imaginary parts of the Hilbert-transformed signal plotted in the phase plane. (D) Phase angle.

For large electrode spacings, where a 10Hz lowpass filter had been applied, a slightly different approach was used. Maxima were assigned using a window size of 70ms and the minima between each pair of maxima were also tagged (Fig. 6.6A). Maxima-minima pairs for which the amplitude difference was small were deleted (Fig. 6.6B), and the maxima were temporally shifted to be centred between adjacent minima (Fig. 6.6C). The maxima and minima points were again joined using splines (Fig. 6.6D), and used to normalise the signal (Fig. 6.6E). This signal was then squared to reduce the effects of noise, and finally the overall mean was removed (Fig. 6.6F).

In both cases, the real and imaginary parts of the Hilbert transform of the zero-mean signal were plotted in the phase plane (Fig. 6.5C, Fig. 6.6G) (Bray and Wikswo, 2002a), and the angle around this trajectory was the phase angle (Fig. 6.5D,

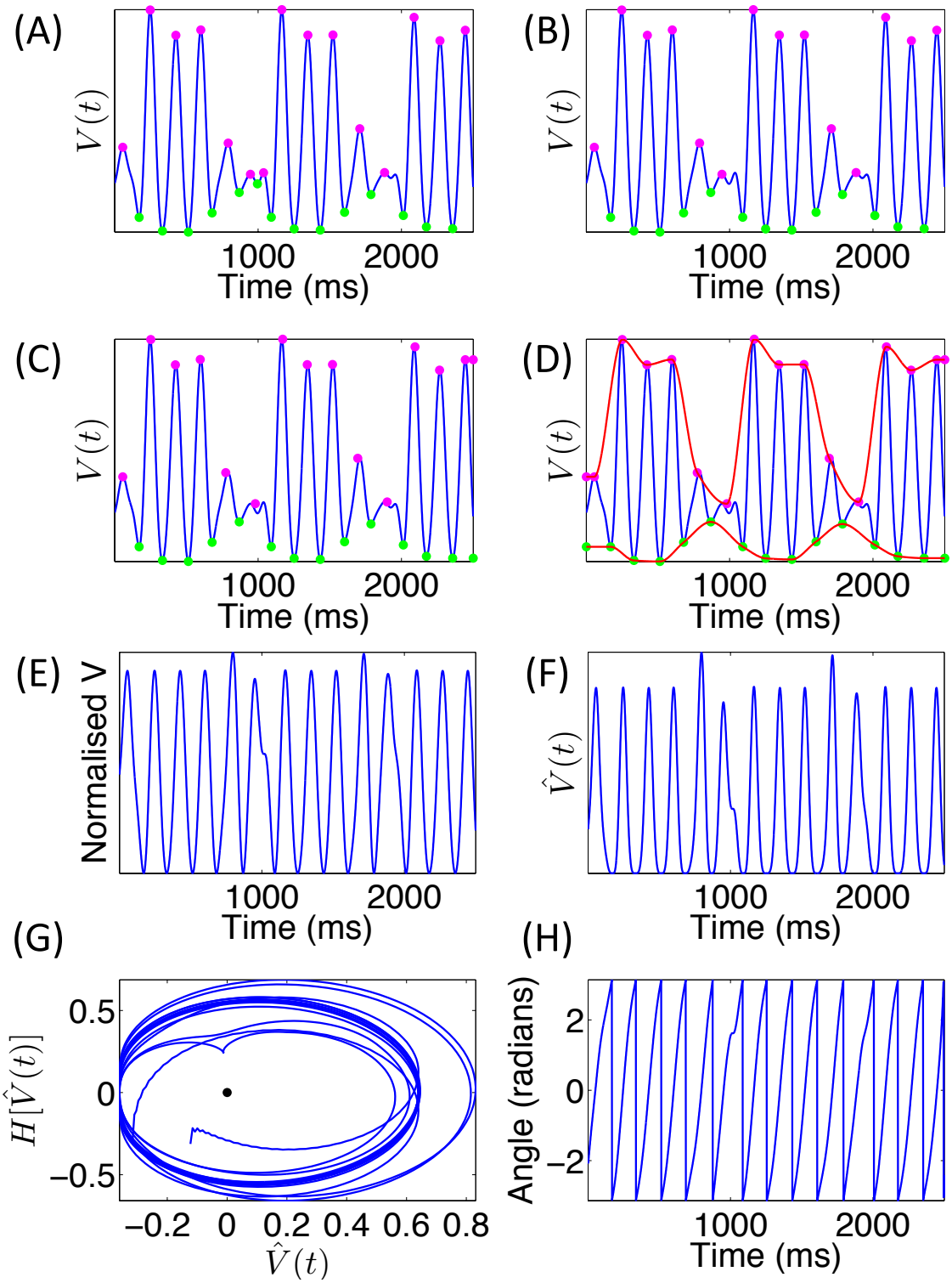

Figure 6.6: Calculation of bipolar electrogram phase with 6, 8 **or** 10mm **interelectrode spacing.** (A) Maxima and minima tagged; (B) Small amplitude pairs deleted; (C) Maxima temporally shifted mid-way between adjacent minima; (D) Maxima and minima joined by cubic splines; (E) Signal normalised; (F) Signal squared and overall mean removed ($\hat{V}(t)$ = Normalised $V(t)^2$ − mean[Normalised $V(t)^2$]); (G) Real and imaginary parts of the Hilbert-transformed signal plotted in the phase plane; (H) Phase angle measured from origin of phase loop.

Fig. 6.6H).

The effects of changing the lowpass filter and phase calculation method for large inter-electrode spacings are shown in Fig. 6.7 for 8mm spacing, where there are a large number of double potentials in the voltage when filtered at 20Hz (Fig. 6.7A) that are also seen in the resulting phase (Fig. 6.7B), which are eliminated when filtered at 10Hz (Fig. 6.7C), leading to the correct assignment of phase (Fig. 6.7D).

6.2.4 Methods: unipolar phase calculation

Similar techniques were used to calculate the AP phase and unipolar electrogram phase. Briefly, unipolar electrogram signals were initially filtered using a lowpass filter at 10Hz. As for the bipolar electrograms with large inter-electrode spacing ($6 - 10$mm), maxima were tagged using a window size threshold and minima between each pair of maxima were also tagged (Fig. 6.8A). Tags associated with small amplitude deflections were deleted (Fig. 6.8B), and the maxima and minima lines were joined using splines (Fig. 6.8C). The maxima and minima lines were used to normalise the signal (Fig. 6.8D) and then the phase angle was calculated as before (Fig. 6.8F).

6.2.5 Methods: phase interpolation and phase singularity identification

For all three data modalities (action potential, unipolar electrogram, bipolar electrogram) and for all measurement spacings (2, 4, 6, 8 and 10mm), the spatial phase maps were interpolated to the gold standard data resolution (0.1mm) using the techniques described in Section 2.12, and phase singularities were detected using the techniques described in Section 2.11.

Phase singularity locations calculated using the phase calculated from AP data at a grid spacing of 0.1mm were used as the gold standard locations. For each measurement spacing, the phase singularity locations of all three data modalities were compared in order to measure the capabilities of the unipolar and bipolar electrogram algorithms to identify rotor-cores and assess wavefront dynamics.

6.2.6 Methods: error quantification

Phase singularity locations for the interpolated AP, unipolar or bipolar electrogram phase at various spacings were compared to the locations obtained from full resolution (0.1mm) AP data. The following quantities were calculated: the error in

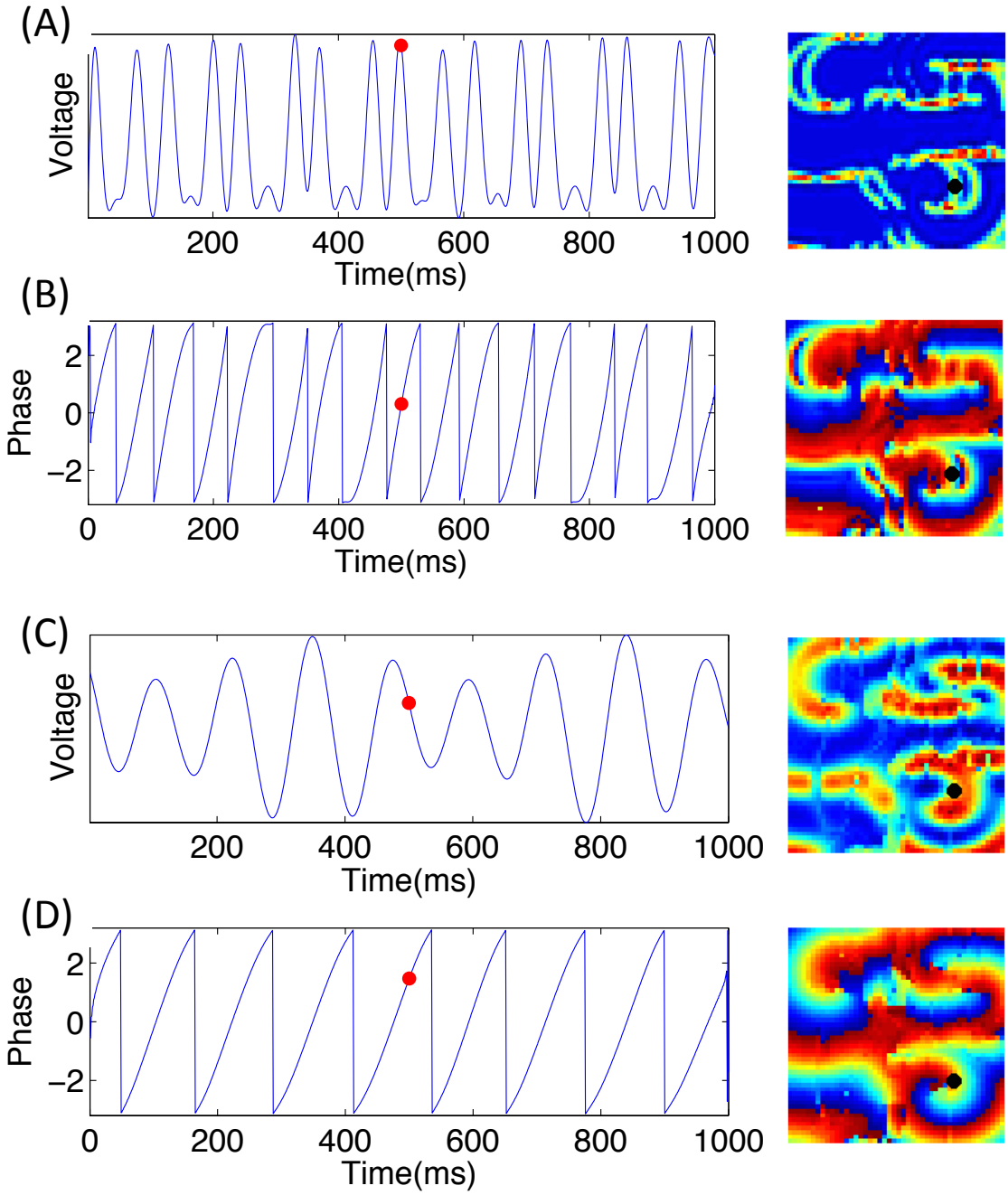

Figure 6.7: Bipolar electrogram with 8mm **inter-electrode spacing: large number of double potentials at** 20Hz**.** (A) Bipolar electrogram with 8mm inter-electrode spacing filtered at 20Hz, for which a large number of double potentials are seen. (B) Corresponding 20Hz phase where the influence of double potentials are seen. (C) Filtering the electrogram at 10Hz eliminates the double potentials. (D) Corresponding 10Hz phase. Red dots indicate time point for isopotential and isophase maps, and black dots indicate measurement location for the bipolar electrogram.

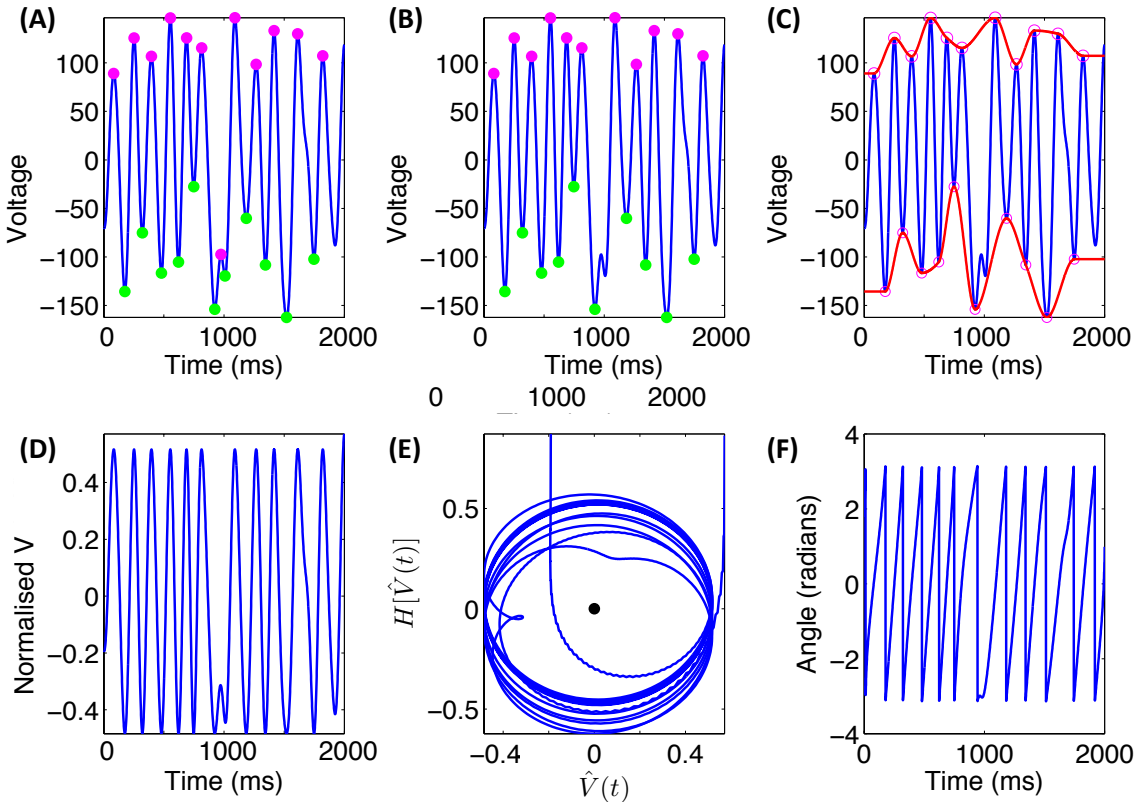

Figure 6.8: Steps for calculating unipolar electrogram phase. Detailed on Page 240.

the centre of the isolated rotor trajectory; the mean error in location per frame; the mean number of phase singularities per frame; and the correlation of the spatial heat maps. Fig. 6.9 explains the definitions used for centre error and maximum radius of the trajectory for the isolated rotor. The number of false phase singularity detections were indicated by the mean number of phase singularities per frame compared to the gold standard.

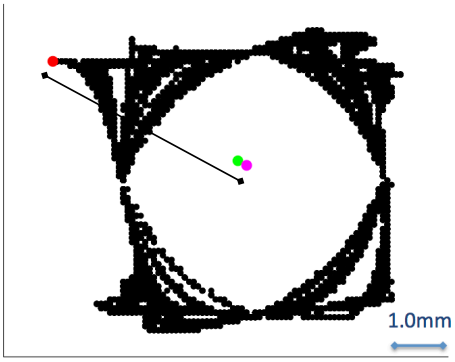

Figure 6.9: Measures used for error quantification. Differences between the trajectories were calculated in terms of the error in the centre location compared to the full resolution case and by comparing the maximum radius of the trajectories. The centre error here is the distance between the full resolution centre (green) and the bipolar 6mm centre (purple) (0.22mm). The maximum radius is the distance from the purple point to the furthest point on the trajectory, which is shown in red (4.39mm).

6.2.7 Results: overview for simulated data

Fig. 6.10 gives an overview of the simulated data results for comparing phase mapping modalities (AP, unipolar electrogram and bipolar electrogram). The left-hand side of the domain, which maintained a single isolated rotor throughout the simulation without the presence of wavefront collisions, was used to assess the accuracy of PS identification, for rhythms in which a single rotor dominates. Example rotor trajectories are shown in the top row of Fig. 6.10, where the first column shows the gold standard results. Next, the entire domain was used to give the overall distribution of PSs for more complicated dynamics, including multiple rotors and collisions, which can be seen in the middle row. The middle and bottom rows of Fig. 6.10 show respectively isophase maps and heat maps giving a count of PS positions over time (as per Section 4.2.8).

For each investigation, the isolated rotor core trajectory for the action potential, unipolar electrogram and bipolar electrogram phase at different inter-electrode spacings were compared to the gold standard full resolution AP positions. In order to assess whether these differences were due to the datatype (AP, unipolar electrogram or bipolar electrogram phase), or due to resolution, the trajectories for all three datatypes were calculated.

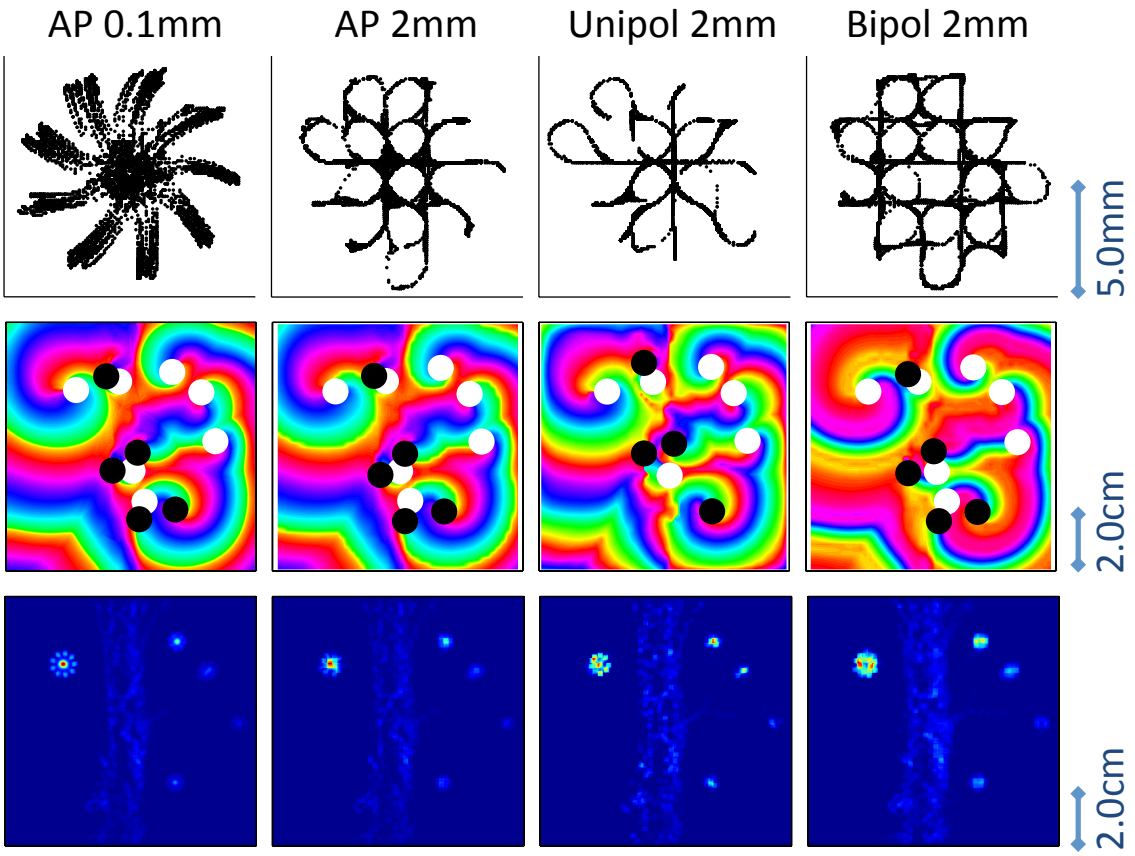

Figure 6.10: Results overview for 2mm interelectrode spacing. Top: Rotor trajectories. Middle: Isophase maps with phase singularities marked as black and white dots depending on chirality. Bottom: Phase singularity heat maps. The first column forms the gold standard results (AP, 0.1mm resolution).

6.2.8 Results: single rotor detection

The location of the PS corresponding to the isolated rotor was extracted for each frame of the simulation. Fig. 6.10 (top) shows the rotor core trajectories, calculated at a fixed inter-electrode spacing of 2mm, for the different signals. Each of the trajectories are seen, to some extent, to align with the 2mm grid. The trajectory calculated from the full-resolution data is also shown for comparison. Rotor trajectories for all inter-electrode spacings are shown in Fig. 6.11; qualitatively, the trajectories become more dissimilar to the full resolution trajectory as the inter-electrode spacing increases.

To quantify these differences, the centre of each trajectory was calculated. The centre error and the maximum radius of the trajectory, for each datatype and inter-electrode spacing, is given in Table 6.1. In general, for each datatype, the error in the location estimation increased with larger spacing, as expected. The bipolar algorithm provided an improved prediction, in general, of rotor-core centre location than unipolar data. The maximum radius of the trajectories were larger at the coarser resolutions, particularly for AP data. In addition, the error in the PS location was quantified on a frame-by-frame basis, shown as mean and standard deviation in Table 6.2. Error was seen to increase with increasing inter-electrode spacing. The bipolar algorithm provided a slight improvement in its PS location estimate for larger electrode spacings, compared to the unipolar case.

Table 6.1: Error in centre location of isolated rotor and maximum radius of phase singularity trajectory (5.71mm **at full-resolution) for different inter-electrode spacings.**

	Error in centre (mm)			Max radius (mm)		
	AP	Unipol	Bipol	AP	Unipol	Bipol
2mm	0.08	0.15	0.13	5.58	5.80	5.64
4mm	0.33	0.83	0.11	5.41	4.03	8.65
6mm	0.59	0.36	0.22	7.54	4.39	5.00
8mm	0.66	0.50	0.83	11.44	5.43	7.45
10mm	1.25	2.11	1.61	14.17	8.18	8.15

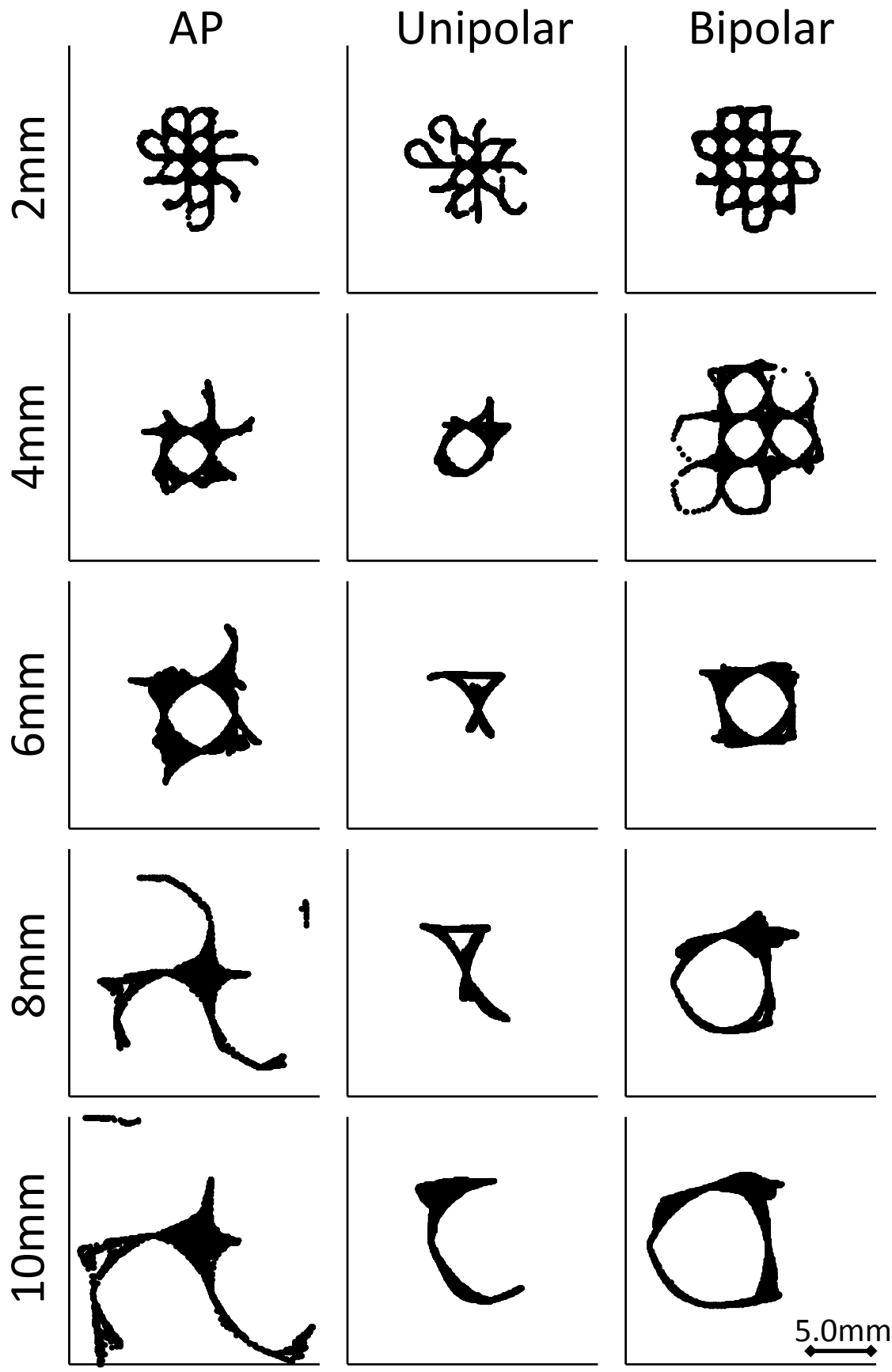

Figure 6.11: As grid spacing increase, rotor trajectories for AP, unipolar electrogram and bipolar electrogram phase become less like the gold standard trajectory. Shown for spacings of $2-10$mm; gold standard trajectory in the top left of Fig. 6.10.

Table 6.2: Framewise mean distance error and standard deviation (mm) for the isolated rotor, for different inter-electrode spacings.

	AP	Unipolar	Bipolar
2mm	1.31 ± 0.81	1.57 ± 0.99	2.22 ± 1.08
4mm	2.15 ± 0.96	2.76 ± 1.49	2.68 ± 1.37
6mm	2.64 ± 1.24	3.04 ± 1.50	2.84 ± 1.46
8mm	3.25 ± 1.55	3.42 ± 1.56	2.77 ± 1.43
10mm	3.40 ± 2.11	4.58 ± 2.09	3.92 ± 2.15

6.2.9 Results: overall phase singularity distribution

A comparison of the overall distribution of phase singularities, calculated for each signal type and at each inter-electrode spacing was then used to assess how well the algorithm performed for more complicated dynamics, including multiple rotors and wavefront collisions. Example isophase maps are shown in Fig. 6.12 (and the middle row of Fig. 6.10). Qualitatively, at coarser resolutions, AP and unipolar electrogram data had more PS detections than bipolar electrogram phase. The mean and standard deviation of the number of PS per frame was 9.62 ± 2.72 for the full resolution AP data; other results are shown in Table 6.3. Both AP and unipolar electrogram data had an increased number of PSs at coarser resolutions, while fewer PS per frame for the equivalent resolution bipolar electrogram phase were detected.

Table 6.3: Mean number of PSs per frame, for different inter-electrode spacings.

	AP	Unipolar	Bipolar
2mm	9.45 ± 2.57	9.46 ± 2.81	9.56 ± 2.59
4mm	9.66 ± 2.59	10.06 ± 2.99	9.50 ± 2.62
6mm	9.88 ± 2.59	10.61 ± 2.97	9.27 ± 2.53
8mm	12.27 ± 3.32	11.62 ± 3.52	8.84 ± 2.38
10mm	11.64 ± 2.95	12.11 ± 3.72	8.33 ± 2.41

However, the metric of average number of phase singularities does not give an indication of whether the phase singularities detected are correct. Therefore phase singularity heat maps were also calculated, showing the spatial distribution of PSs throughout the simulation (Fig. 6.13). The maps were smoothed with a bin-size of 2mm to reduce artefacts introduced by the use of different inter-electrode spacings. The isolated rotor is clearly seen in each map. Heat maps were calculated for all datatypes (Fig. 6.13) to assess whether differences were due to datatype or resolution. Table 6.4 shows correlations between each map and the full-resolution map (shown in bottom left of Fig. 6.10). These decreased with increasing inter-electrode spacing and again were similar between signal types.

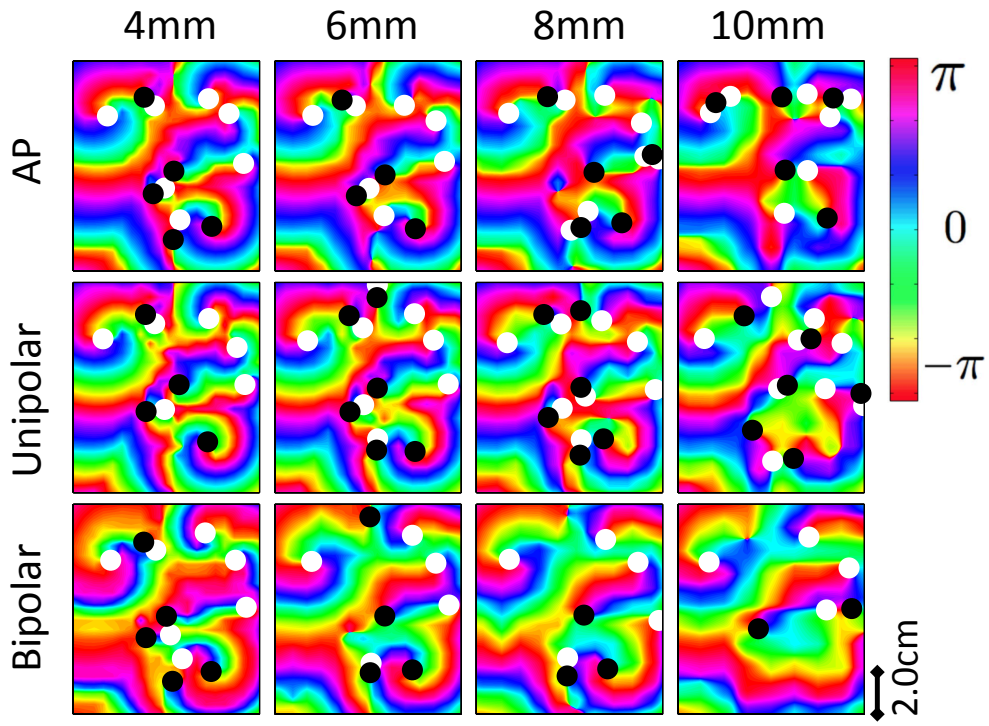

Figure 6.12: Isophase maps for AP, unipolar electrogram and bipolar electrogram data, where phase singularities are marked as black and white dots, depending on chirality.

Table 6.4: Correlation of heat maps for subsampled data with full-resolution AP data distribution.

	AP	Unipolar	Bipolar
2mm	0.91	0.81	0.80
4mm	0.65	0.56	0.60
6mm	0.54	0.66	0.52
8mm	0.48	0.50	0.43
10mm	0.38	0.29	0.29

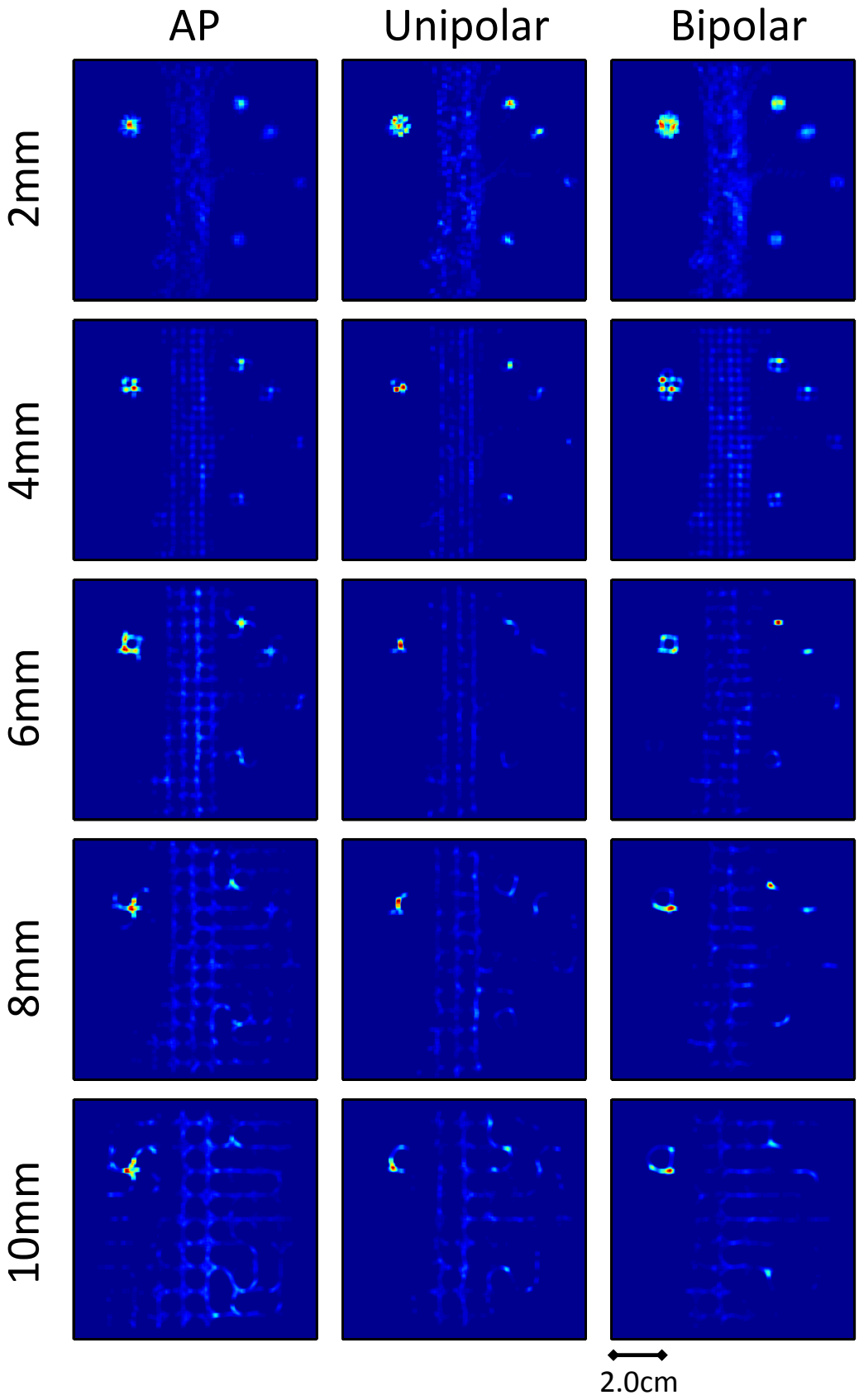

Figure 6.13: Heat maps for AP, unipolar electrogram and bipolar electrogram phase at spacings of $2-10$mm, showing the overall distribution of phase singularities, where the isolated rotor on the left-hand side of the domain is clearly seen in each map. See Fig. 6.10 for the gold standard heat map.

6.2.10 Summary of simulated data findings

An approach was presented to identify rotor core locations using phase computed from unipolar and bipolar electrograms, and the algorithms were tested on simulated data. To assess whether observed differences were due to differences in the signal type used (AP, unipolar electrogram or bipolar electrogram) or due to differences in the data resolution, phase singularity locations calculated using phase of bipolar electrograms with inter-electrode spacings of 2, 4, 6, 8 and 10mm were compared to those calculated using action potential phase or unipolar electrogram phase calculated at the same grid spacings. Therefore, results from the different signal types recorded at the same resolutions could be compared, where the phase data were first interpolated to a grid spacing of 0.1mm in each case in order to compare the results to the gold standard (AP at the full resolution of 0.1mm grid spacing). Both unipolar and bipolar electrogram phase were observed to be as effective as AP phase for rotor tip detection, suggesting either may potentially be used clinically as a method to locate rotor phase singularities in AF.

The filtering applied to the electrogram data differed between unipolar and bipolar electrograms, and was also different for small and large inter-electrode spacings for bipolar electrogram signals. Specifically, for bipolar electrograms with small inter-electrode spacings (2 and 4mm) a sequence of filters typically used for dominant frequency analysis was applied, in which the final low-pass filter was applied at 20Hz. For bipolar electrograms with large inter-electrode spacings (6, 8 and 10mm), the low-pass filter was changed to 10Hz, in order to eliminate double potentials in the signal. For unipolar electrograms, a single filter was applied (10Hz low-pass filter). Different methods were used to normalise the filtered bipolar electrograms with small inter-electrode spacings, bipolar electrograms with large inter-electrode spacings and unipolar electrograms because the signals had different morphologies. For both unipolar and bipolar electrogram phase, the signals were normalised using the maxima and minima splines and a straight mean was then removed. This is different from the method used for calculating AP phase, where the moving mean calculated using the maxima and minima splines was removed from the signal.

Errors in calculated phase singularity locations were generally similar for AP, unipolar and bipolar electrogram phase at a given measurement spacing. The magnitude of the error in the centre locations are not considered to be of clinically relevant magnitude since they are significantly less than the diameter of an ablation catheter (< 4mm). In general, the maximum radius of the trajectories increased with increasing measurement spacing, and were largest for AP data at large measurement spacing. Errors in rotor core location for the isolated rotor on a frame-by-frame ba-

sis were slightly smaller for bipolar electrogram phase than for unipolar electrogram phase at increased measurement spacing. The mean number of phase singularities per frame increased for AP and unipolar electrogram data with increasing measurement spacing, which indicates that the number of false detections increased. A similar increase was not seen for bipolar electrogram phase, suggesting it may result in fewer false phase singularity detections at larger inter-electrode spacings than the equivalent resolution AP or unipolar electrogram phase. Differences between data types may be due to the differences in the field of view of the measurement, with AP data offering the most localised measurement.

Unipolar and bipolar electrogram phase perform similarly to AP data in simulated data, suggesting they are suitable for testing in experimental data.

6.3 Microelectrode array data

6.3.1 Methods: data overview

The techniques developed for phase mapping of unipolar and bipolar electrograms in simulated data were adapted for, and applied to, field potentials from microelectrode arrays (MEAs), measured from a fibrillating monolayer of HL-1 cardiomyocytes. These data provided a bridge to clinical data because the environment was controlled but exhibited more biological variation and signal complexity than simulated data. The electrode array consisted of 60 electrodes, arranged in an 8-by-8 grid (with corner electrodes missing), with $200\mu m$ inter-electrode spacing and an electrode diameter of $30\mu m$, resulting in a 1.4mm $\times$1.4mm array (see Fig. 1.5). The MEA data used in this section were from experiments performed by Dr Rasheda Chowdhury, in which 0.5cm^2 of confluent cells were seeded at the centre of the MEA plate. Fibrillation occurred spontaneously in the preparation analysed here, and MEA recordings of 10 second duration were exported for analysis.

The method developed for calculating the phase of simulated unipolar electrograms (Section 6.2.4) did not perform well (see Section 6.3.2). Consequently, in Section 6.3.3, an alternative method is proposed for calculating MEA unipolar electrogram phase that is closer to the method used to calculate the phase of simulated bipolar electrograms. A similar method is then found to be suitable for calculating the phase of bipolar MEA electrograms (Section 6.3.5) constructed from pairs of unipolar MEA electrograms. Finally, phase singularity results from unipolar and bipolar electrograms are compared.

6.3.2 Problems with calculating field potential MEA phase using the techniques developed for simulated data

The techniques developed for calculating unipolar electrogram phase in simulated data (Section 6.2.4), for which the first step was to low-pass filter the data at 10Hz, were applied to MEA data. Low-pass filtering of the MEA field potentials at 10Hz did not capture sharp deflections representing local activation (Fig. 6.14), which in turn led to a uniform phase assignment for the local activation complex; hence, losing the features of local activation. In addition, for some electrograms with a large degree of baseline noise, the 10Hz filter was found to miss some true activations, and instead pick up baseline deflections (Fig. 6.15). An improved method is therefore required for calculating the phase of unipolar field electrograms.

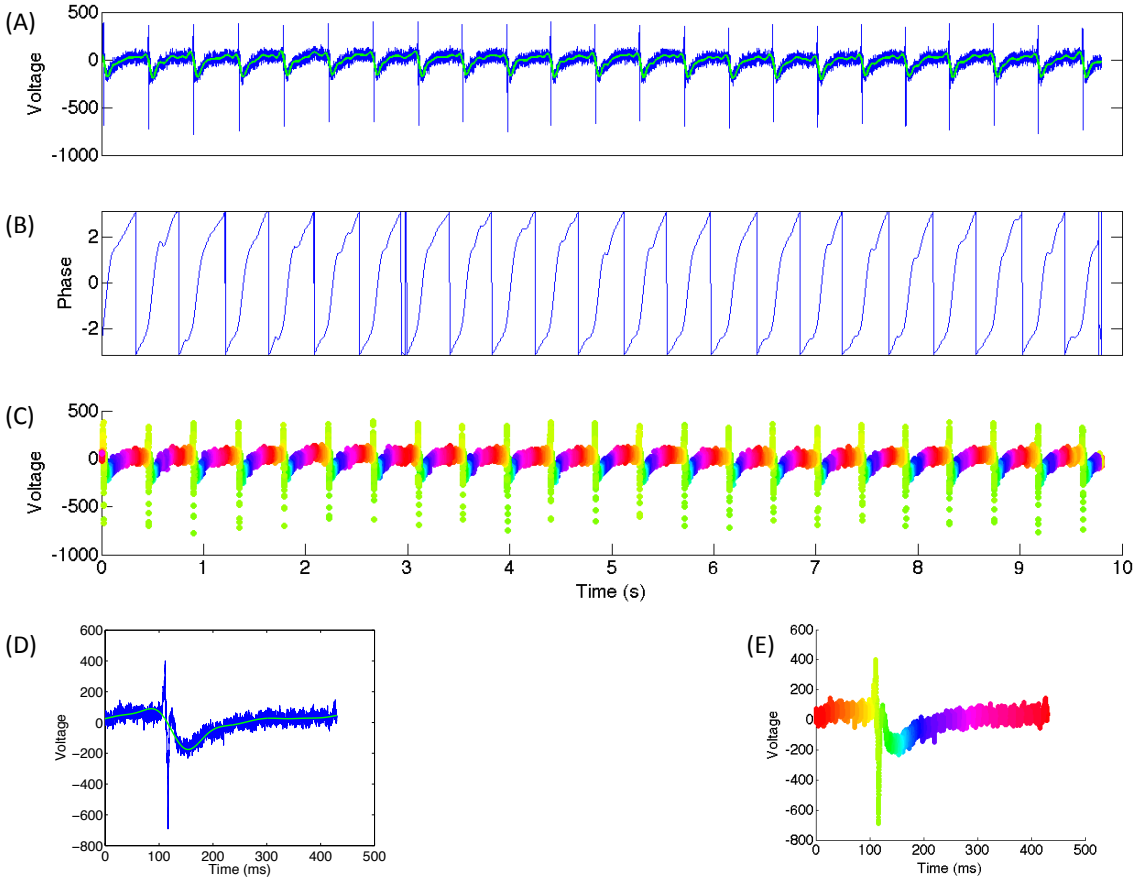

Figure 6.14: Unipolar MEA phase calculated for the signal low-pass filtered at 10Hz did not capture features of local activation. (A) Raw signal (blue), with signal low-pass filtered at 10Hz overlaid (green). (B) Corresponding phase of 10Hz filtered signal. (C) Raw unipolar signal coloured by phase angle. (D) Raw signal (blue) and filtered signal (green) for one beat (from (A)). (E) Raw unipolar signal coloured by phase angle for one beat (from (C)). The local activation complex has a uniform phase (green), and thus features of local activation are not captured by this method.

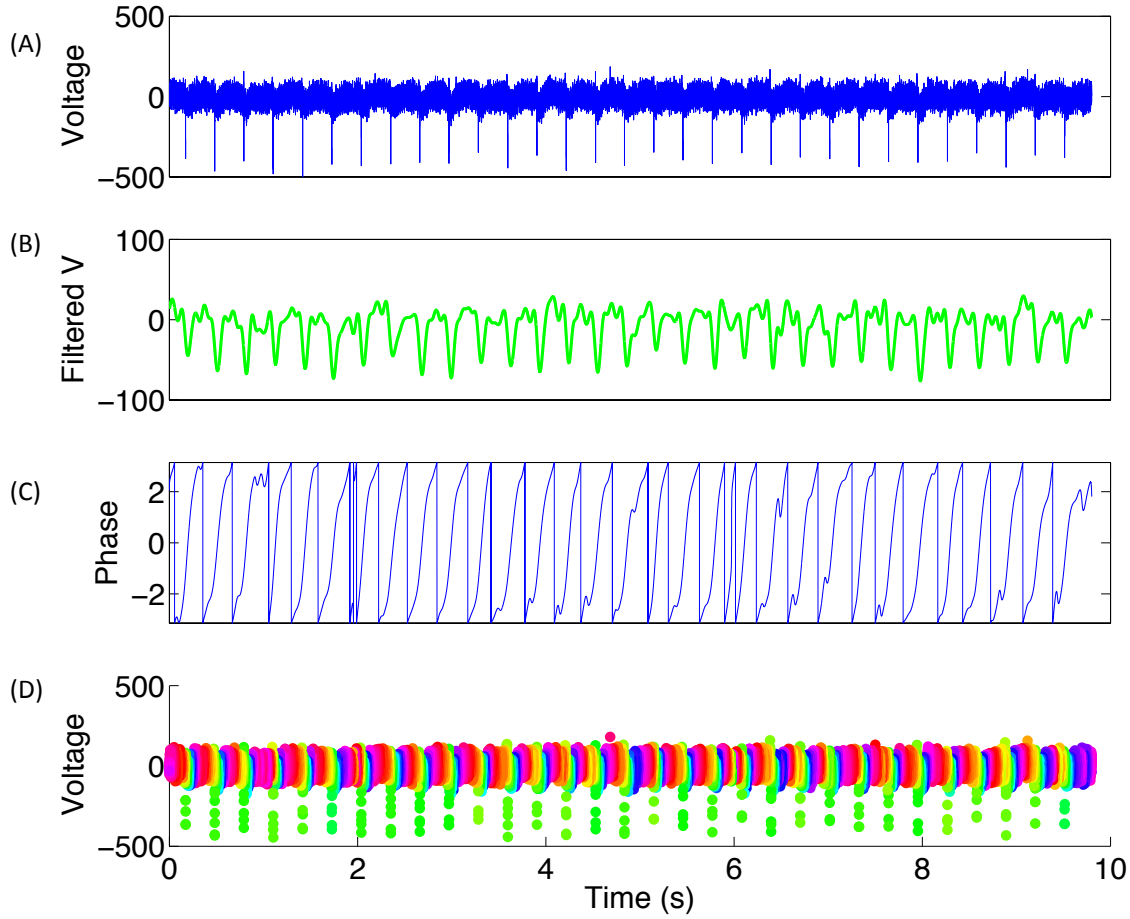

Figure 6.15: Unipolar MEA phase calculated for the signal low-pass filtered at 10Hz leads to incorrect phase assignment in the case of a noisy baseline. (A) Raw electrogram that has a noisy baseline; (B) electrogram filtered at 10Hz has multiple small deflections; (C) phase has extra trajectories; (D) voltage coloured by phase in which extra activations are seen caused by the additional trajectories.

6.3.3 Calculating phase from the filtered derivative of unipolar signals

A novel method is developed for calculating unipolar electrogram phase using the electrogram derivative, with the rationale that peaks of negative slope represent activation. This introduces the challenge of identifying peaks from a noisy derivative signal, which is not sinusoidal. In order to make the derivative signal more sinusoidal, the derivative was filtered using the sequence of filters used on bipolar electrograms, which are detailed below (Fig. 6.16 C). In order to identify peaks of the filtered derivative signal, a sequence of steps similar to those used for calculating bipolar phase of simulated data were then applied. These steps result in a phase assignment that differentiates between the components of local activation (Fig. 6.16 D).

The first step was to determine *target times* to aid the identification of peaks of the filtered derivative by determining the minima of the electrogram signal (notch filtered at 50Hz) using a moving window. These minima were used as target times for identifying peaks of the filtered derivative within a window of each target time. This step was added to the algorithm because taking the derivative increased the amount of noise in the signal, and in some cases introduced additional candidate peaks. Electrograms for which it is difficult to assign peaks in the noisy derivative often have identifiable minima in the raw signal (Fig. 6.17), and so these times from the raw signal were used to guide the selection of activation complexes in the derivative.

Steps for calculating phase are as follows. The raw signal was smoothed using a five-point moving average and the approximate derivative calculated using the difference between adjacent temporal samples. This derivative signal was then bandpass filtered ($40 - 250$Hz), rectified and lowpass filtered at 10Hz. For each target time obtained from the raw signal, a maximum was tagged in the differentiated signal within a window of $\pm$100ms of the target time. The minimum was then found between each pair of maxima (Fig. 6.18 B). The signal was then normalised using cubic splines of the maxima and minima (Fig. 6.18 B, C). In order to ensure only the tagged deflections contributed to the final phase, the signal was raised to the power of six, to amplify the selected deflections (Fig. 6.18 C). Any portions of the signal where the signal is of greater magnitude than the maxima line will be greater than one after the normalisation step. To correct for this, the normalised signal was capped at one. Finally a straight mean was removed from this signal, and the Hilbert transform of the resulting signal was plotted against the signal to give the phase angle (Fig. 6.18 D-F).

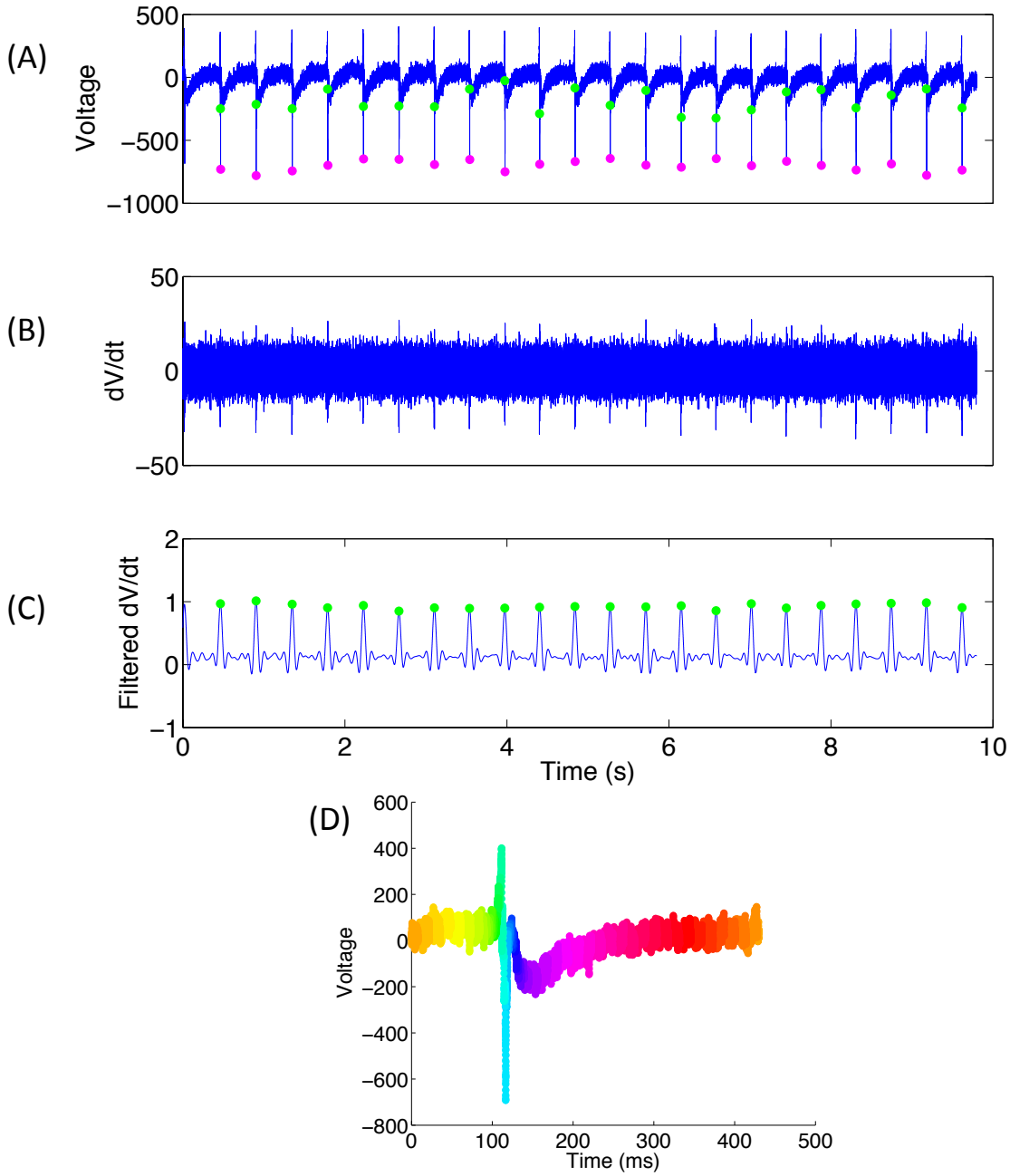

Figure 6.16: Method for calculating unipolar electrogram phase from MEA data using the electrogram derivative. See Fig. 6.14 for the 10Hz filter method applied to this electrogram. (A) Raw unipolar electrogram with target times marked in purple. The green dots show the activation times calculated as the peaks of the filtered derivative signal. (B) Derivative of voltage. (C) Filtered derivative of voltage, with peaks marked as green dots. (D) Electrogram coloured by phase, for which differences in phase are seen within the local activation complex (green through blue).

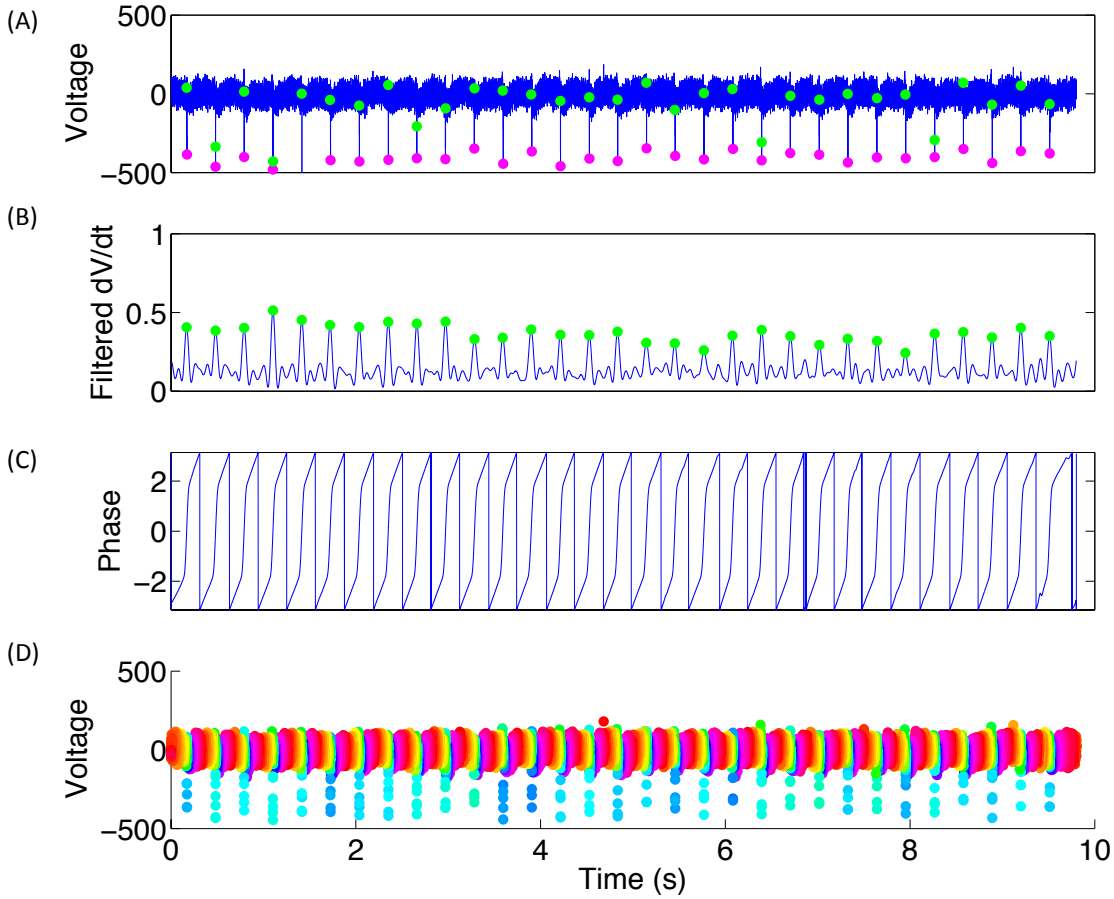

Figure 6.17: Using tagged points in the raw signal as target times improves robustness to baseline noise. (A) Raw signal where minima are tagged (purple dots). (B) Filtered derivative with maxima within a window around each of the tagged times marked in green (also marked in green in (A)). (C) Phase; (D) voltage coloured by phase. Only one maxima is tagged per target time to give the regular phase in (C) and the correct phase assignment of the voltage in (D).

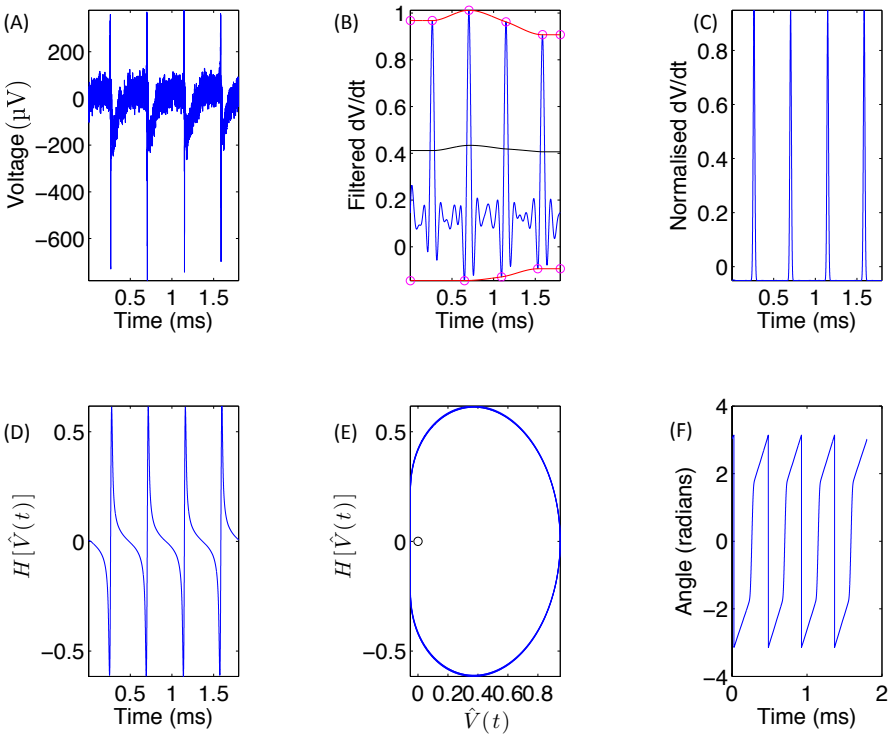

Figure 6.18: Steps involved in calculating MEA electrogram phase. (A) Raw signal. (B) Filtered derivative of voltage, with maxima and minima splines shown. (C) Signal is normalised using the maxima and minima splines, raised to the power of six to amplify deflections, and capped at one. (D) Hilbert transform of the normalised signal. (E) Plotting the Hilbert transform of the normalised signal against the normalised signal gives phase loops and the angle from the origin is the phase angle (F).

6.3.4 Phase interpolation

Some electrodes within the multielectrode array were too noisy to use. These points were automatically excluded from phase interpolation by identifying the number of activations within the phase signal (where activations occur at phase $\pi/2$) and excluding a recording if the number of activations was above a threshold (Fig. 6.19).

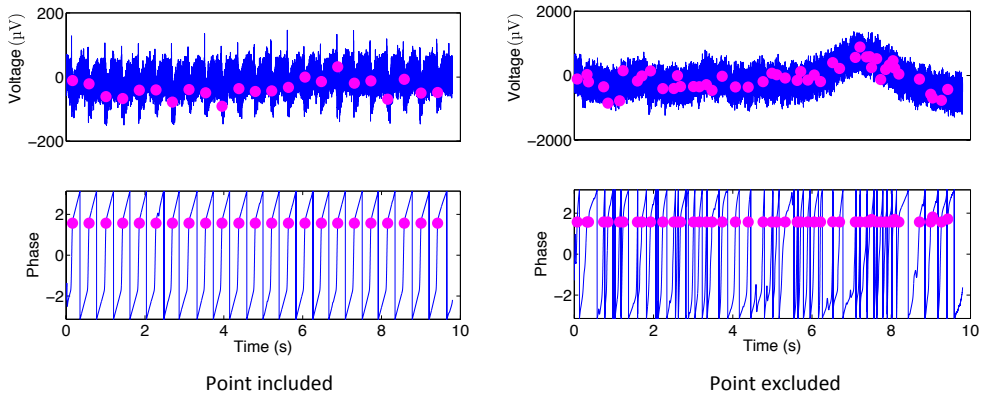

Figure 6.19: Criterion for point exclusion in phase interpolation. Points of phase $\pi/2$ were tagged in the phase of each electrogram (bottom) to represent activations in the raw signal (top). Electrograms with more tagged points than a threshold of 3.6 activations per second (threshold chosen based on DF of activity for this MEA plate) were excluded from phase interpolation and further analysis (right).

6.3.5 Bipolar phase calculation

Bipolar electrograms were constructed from the unipolar electrograms by taking the difference between neighbouring unipolar electrograms. The sequence of filters and steps applied to the derivative of the unipolar electrogram in Section 6.3.3 were also used on the bipolar electrogram. These were applied to the bipolar electrogram directly, and not its derivative. Phase of an example bipolar electrogram is shown in Fig. 6.20.

6.3.6 Circular correlation coefficient

In order to assess whether the phase values calculated using the unipolar and bipolar electrogram phase were similar, the correlation between the phase angle maps was calculated. This required the use of a circular correlation coefficient because, as an angle, values corresponding to zero, low and high do not translate to the linear scale. For example, difficulties arise for areas close to the branch cut at $\pm\pi$, which

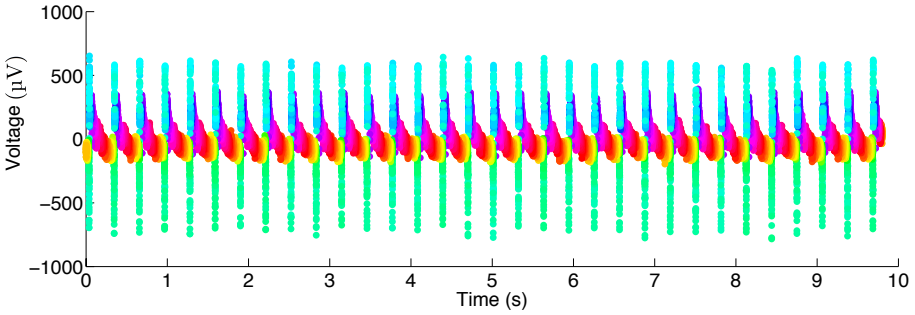

Figure 6.20: Example bipolar MEA electrogram coloured by phase angle.

are close in state, but will give rise to an artificially low correlation if correlation is measured on a linear scale.

For matrices A and B, the linear correlation coefficient is defined as follows:

$$r = \frac{\sum_m \sum_n (A_{mn} - \bar{A})(B_{mn} - \bar{B})}{\sqrt{\left(\sum_m \sum_n (A_{mn} - \bar{A})^2\right)\left(\sum_m \sum_n (B_{mn} - \bar{B})^2\right)}}, \tag{6.2}$$

where $\bar{A}$ and $\bar{B}$ represent the mean of A and B.

To correlate angles, a circular correlation measure is used as described in Jammalamadaka and Sengupta (2001) and available on the Matlab File exchange (Berens, 2012). The formula is as follows:

$$r = \frac{\sum_m \sum_n \sin\left(A_{mn} - \bar{A}\right)\ \sin\left(B_{mn} - \bar{B}\right)}{\sqrt{\sum_m \sum_n \sin^2\left(A_{mn} - \bar{A}\right)\ \sin^2\left(B_{mn} - \bar{B}\right)}}, \tag{6.3}$$

where $\bar{A}$ and $\bar{B}$ represent the mean of A and B calculated using an exponential mapping (as in Sections 2.12, 4.2.4). Similar to the linear correlation coefficient, the circular correlation coefficient takes values between -1 and 1. The strongest correlation of 1 is obtained when there is a perfect relationship, modulo 2π.

Linear and circular correlation coefficients are shown for a ten second MEA recording in Fig. 6.21, in which it can be seen that there is generally only a small difference (median absolute difference = 0.05) in the calculated coefficients; however, there are also instances where there is a large difference. An example is shown in Fig. 6.21 where the circular correlation coefficient is more than double the linear due to the effect of the branch cut; hence, motivating the use of the circular correlation coefficient.

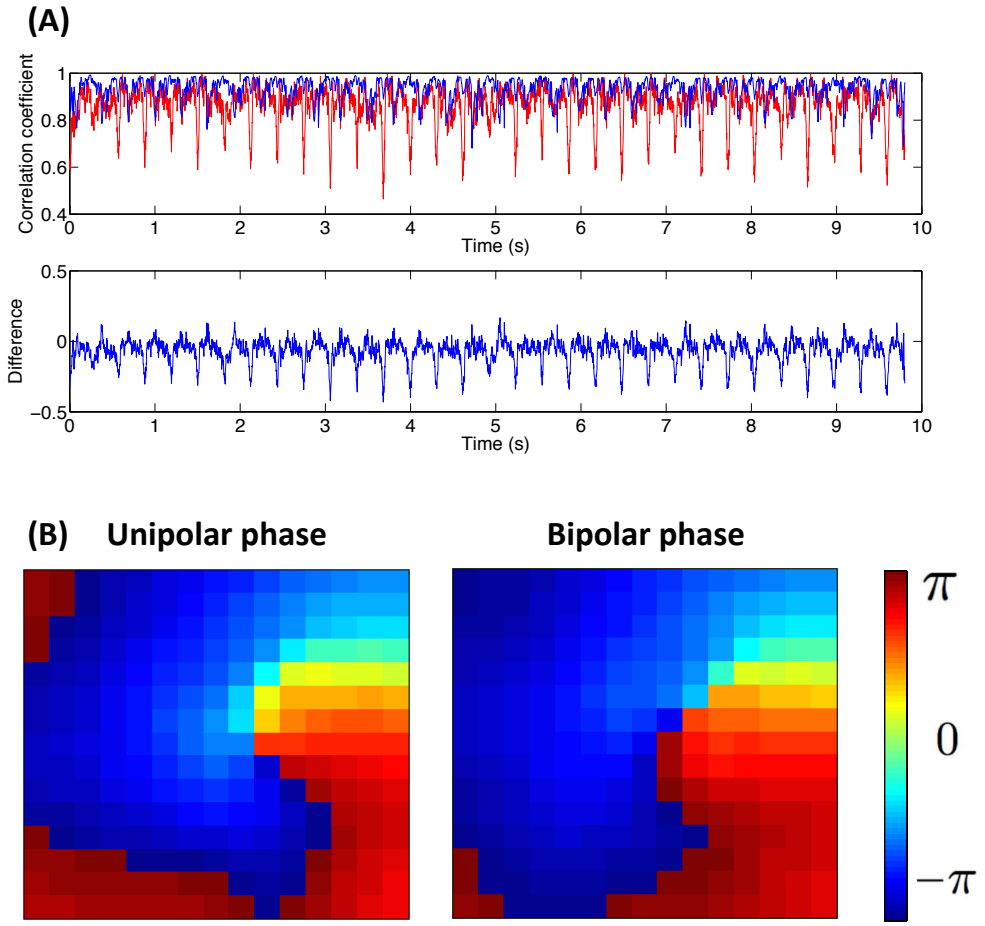

Figure 6.21: Calculation of the correlation coefficient for phase requires the use of a circular correlation coefficient. (A) Correlation coefficient over time using a linear correlation (red) or circular correlation (blue), where the calculated difference (lower plot) is large for some frames. There are instances for which this difference is large for frames where unipolar phase and bipolar phase match well visually (B). For this example, the linear coefficient is small (0.46) due to some pixels swapping between $\pm\pi$, which represent the same state; however, they are far apart on a linear scale. These values are correctly located on a circular scale and the circular coefficient is 0.90.

6.3.7 Results: multi-electrode array phase mapping

A ten-second MEA recording was analysed for which there was a single meandering rotor within the recording area. Phase singularity locations calculated using unipolar and bipolar phase mapping are shown in Fig. 6.22, in which it can be seen that the rotor core trajectory covers a similar area for each modality. Quantitatively, the mean difference on a frame-by-frame basis of the rotor core location measured using unipolar or bipolar electrogram phase is $210 \pm 173\mu$m, and the difference in the location of the centre of mass of the trajectory is 153μm, which are both similar in magnitude to the inter electrode spacing (200μm). The median circular correlation coefficient between the phase measured using unipolar and bipolar electrogram phase is 0.95, showing the unipolar phase is very similar to the bipolar phase.

6.3.8 Summary of multi-electrode array findings

In vitro multi-electrode array data provided a bridge from *in silico* to *in vivo* data. The unipolar electrogram phase method developed for simulated data was not appropriate for MEA field potential data because low-pass filtering at 10Hz did not capture the sharp depolarisation component of the electrogram ($\mathrm{FP}_{\mathrm{min}}$, see Fig. 1.5). This motivated the development of an alternative algorithm for calculating unipolar phase based on electrogram slope rather than amplitude.

A novel method similar to that applied to simulated bipolar electrograms was applied to the derivative of unipolar MEA electrograms, in order to identify activations as points of steep slope as maximum absolute derivative. Adaptions of the simulated bipolar algorithm were required to deal with the increased level of noise in MEA data. Specifically, the unipolar derivative signal or bipolar signal were band-pass filtered from 40-250Hz and rectified as per the simulated algorithm, and then low-pass filtered at 10Hz. The choice of low-pass filter was the same as for the simulated bipolar data with larger inter-electrode spacing because of the degree of noise in the experimental data. As per the simulated bipolar algorithm with large inter-electrode spacing, both the maxima and minima splines were used to normalise the data. An additional step was required for the experimental phase analysis in which the normalised signal was raised to the power of six. This acted to amplify the amplitude of tagged deflections, to ensure that only tagged activations are given a full change in phase; this was required because the noise in experimental data provided additional deflections in the filtered signal. In the case of unipolar MEA analysis, a further step was required to tag minima in the original signal as target times for assigning maxima to the filtered derivative because differentiating

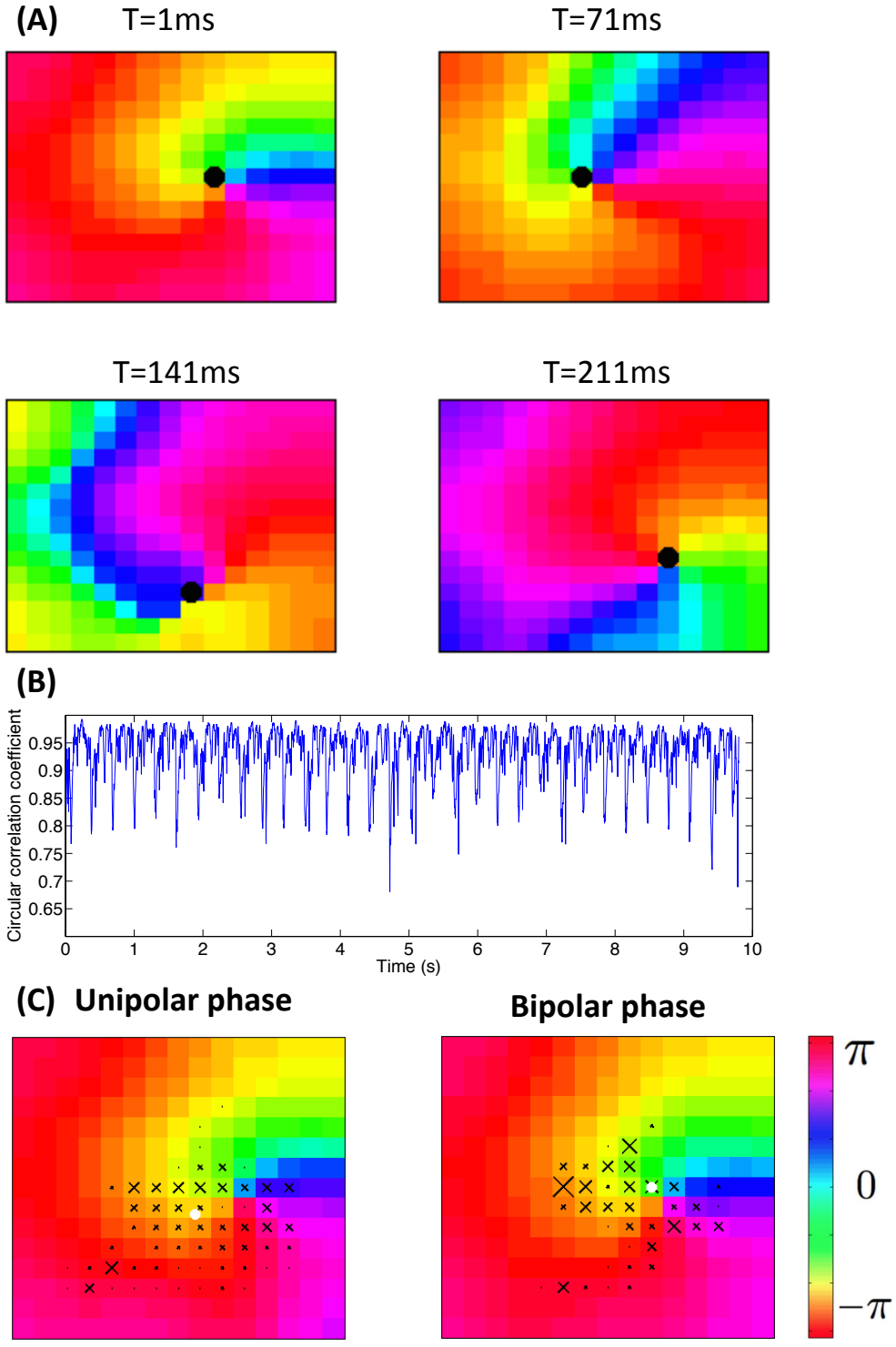

Figure 6.22: MEA unipolar phase and bipolar phase lead to similar phase singularity locations. (A) The rotor cycle length here is approximately 280ms; isophase maps are shown every 70ms to show progression of the rotor over time, with the phase singularity rotor core marked in black. (B) The circular correlation coefficient between unipolar and bipolar phase varies over time but is generally high, with a minimum value of 0.66 and a median of 0.95. (C) Phase singularity locations are indicated by a cross, for which the size indicates the number of occurrences at that location. The centre of the trajectory is indicated by the white dot. The domain size is 1.4mm×1.4mm.

the signal amplified noise. This represents a disadvantage of the method in that the original signal was also required in order to guide the tagging of peaks of the filtered derivative signal.

Phase mapping results obtained using unipolar field potentials and bipolar electrograms matched well. This shows that the methods are applicable and justifies their use on clinical data. However, it should be noted that the data were from a single meandering rotor, which presented the simplest case for testing.

The repolarisation element of the HL-1 electrograms are small because the field potential duration is short, at around 50ms (Dias, 2011) (that is, FP_{max} is difficult to detect, see Fig. 1.5). The refractory period of HL1 cells is much longer than the field potential duration at around 200ms, and the calcium transient duration is a similar length (Dias, 2011). As such, it is difficult to assign phase angles to the field potential according to field potential activation and recovery. Phase mapping, in this case, can be thought of as indicating propagation of the activation wavefront only.

6.4 Clinical data

6.4.1 Methods: data overview

The phase mapping techniques were next adapted for, and applied to, clinical electrograms. Clinical data used in this section were provided by clinicians Dr Norman Qureshi and Dr Phang Boon Lim. All clinical data used in this thesis were obtained with informed consent under ethical approval from the Health Research Authority Ref 13/LO1169. Multipolar spiral (Afocus) catheter data were collected at the beginning of procedures for ablation therapy of AF, with the catheter placed at multiple sites on the posterior wall and roof of the left atrium. Unipolar and bipolar electrograms were recorded simultaneously for approximately thirty seconds in duration (range $16 - 106$s; mean 34s). In this chapter, data from eleven patients were analysed, for which between six and seventeen catheter locations were provided per patient (the total number of catheters analysed is 127). An example of a left atrial geometry from the Ensite Velocity system (St Jude Medical, Inc), with electrode locations marked is shown in Fig. 6.23.

The algorithms developed for calculating MEA phase were also applied to clinical electrograms with a few modifications, detailed in the following sections. An additional requirement for the calculation of unipolar phase was that the method should not depend on the signal amplitude because far-field ventricular signals may be higher in amplitude than local deflections. Unipolar and bipolar phase mapping, calculated using the methods in this section, are then assessed in terms of the number of phase singularities detected, and the correlations are calculated between the phase calculated with unipolar and bipolar electrogram data, and also for the activation time maps calculated from unipolar and bipolar phase.

6.4.2 Methods: QRS subtraction

Unipolar atrial signals are often contaminated by far field ventricular depolarisation, and so a technique called QRS subtraction is required. There are several methods available for this process, which include techniques that replace the intracardiac electrogram signal with a spline (either linear or cubic) during the time segment corresponding to the QRS complex on an ECG lead (Ahmad et al., 2011; Salinet et al., 2013), or by subtracting a template representing the average ventricular signal from the electrogram (Shkurovich et al., 1998; Ng et al., 2007). Replacing the signal by either a linear or cubic spline did not give an appropriate differential. In addition, for some of the electrograms, the QRS and T wave durations covered most

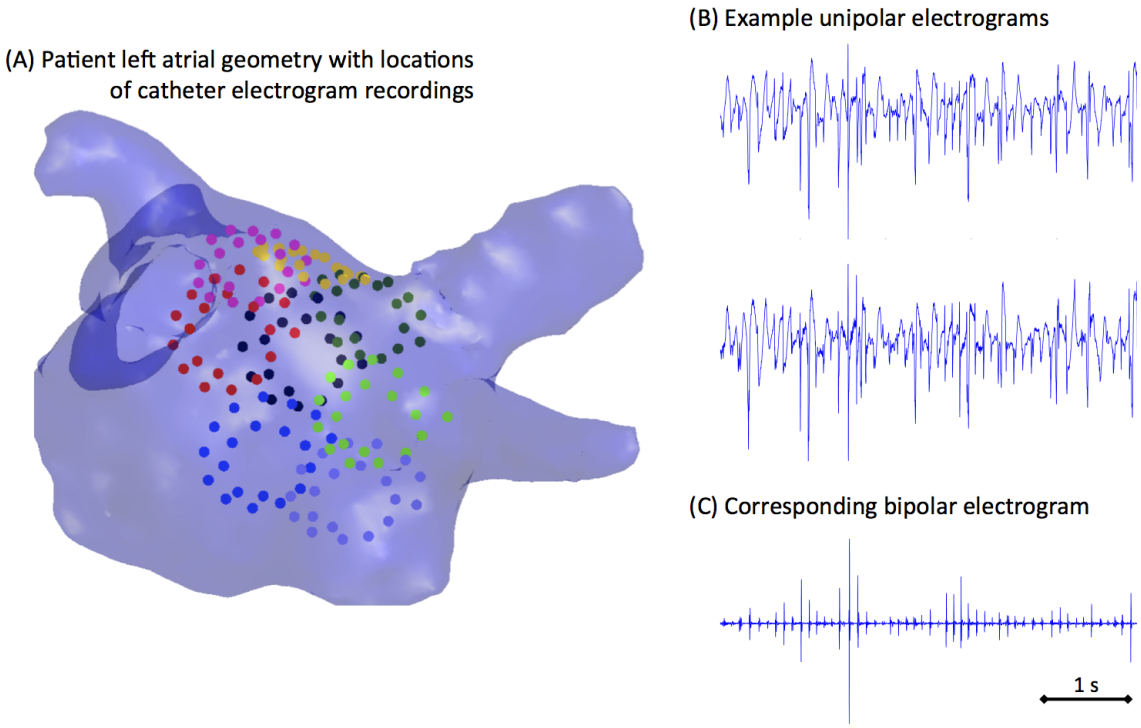

Figure 6.23: Clinical data: Patient left atrial geometry, electrode locations and example electrograms. (A) Mesh representing the left atrial geometry of a patient undergoing ablation therapy for atrial fibrillation, exported from the En-site Velocity electro-anatomic mapping system and plotted using Matlab, showing the locations of the Afocus spiral catheter during the data collection procedure, where different colours indicate sequential recording sites. Simultaneous unipolar (B) and bipolar (C) electrogram data of approximately thirty seconds in duration (approximately 150 AF cycles) were analysed from each of these sites.

of the electrogram duration, and so replacing these components by a spline is not recommended.

The QRS subtraction technique used in this chapter was initially developed by Shkurovich et al. (1998) and then used by Ng et al. (2007). The QRS complexes for ECG lead I were tagged by finding the points of steepest negative slope (Figs. 6.24A, 6.25A). The minimum of the intervals between tagged R waves (minimum R-R interval) was then taken as the window length, $R_{\min}$, for working out the ventricular component of the signal. This was a modification of the original method, which uses the average R-R interval, since there was a large variability in R-R interval for some patients, and using the average value for the template length in these cases caused windows to have a significant amount of overlap. Signals of window length $R_{\min}$ were selected where each window was positioned with 30% of the signal before the tagged time points of the QRS complexes and 70% after. The median signal of these windows was then calculated to give a template, which was repeated, aligned to the windows used for the analysis (Figs. 6.24C, 6.25C). This was then subtracted from the signal to remove the ventricular component and leave the atrial signal (Figs. 6.24D, 6.25D). The degree of ventricular contamination varied between patients and between catheters, with some signals having a relatively small ventricular component (Fig. 6.24 B), and others having a ventricular component that was larger in amplitude than the atrial signal (Fig. 6.25 B).

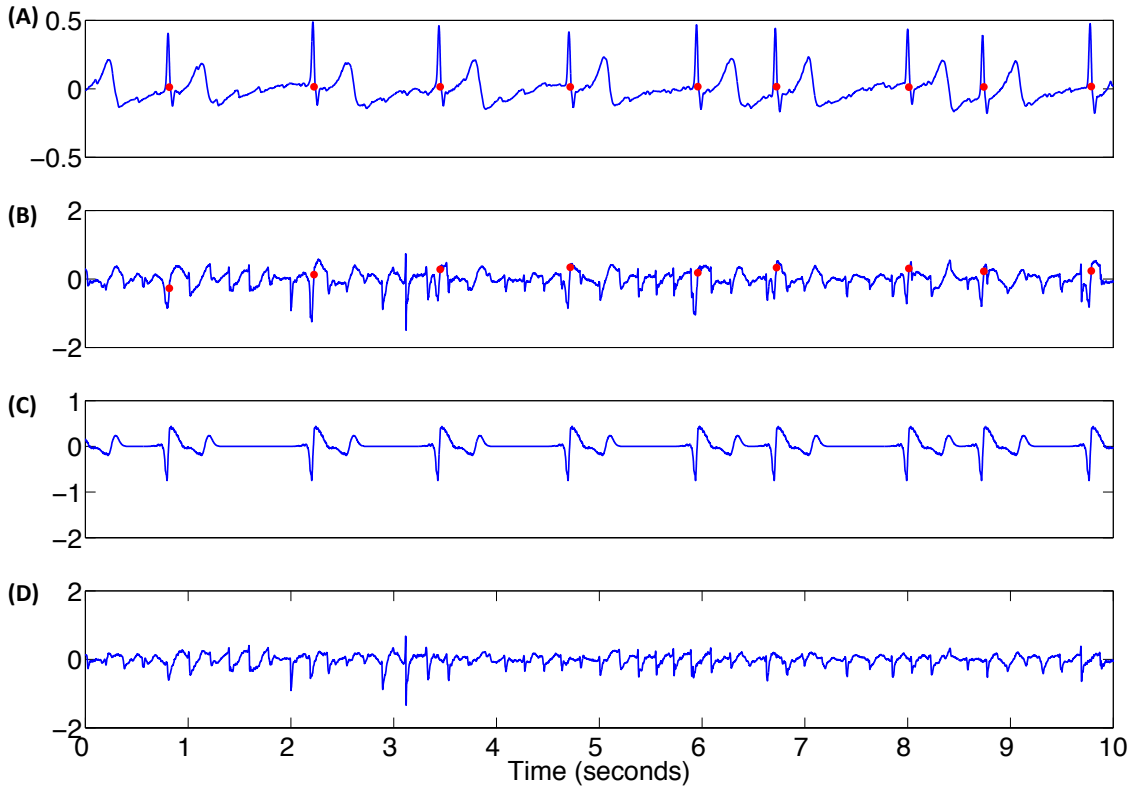

Figure 6.24: Steps involved in ventricular template subtraction for removing the ventricular component from atrial electrograms. (A) R waves are tagged in ECG lead I as the locations of steepest negative slope (red dots). (B) Atrial signal where the minimum interval between R waves (between the red dots in (A)) is used as the window length to remove the ventricular component. The intracardiac unipolar electrogram signal being analysed was split into segments of this window length at windows positioned with 30% of the window before the red dot and 70% after. (C) A template representing the ventricular component was created as the point-wise median of the signals, which was repeated, aligned to the windows used for the analysis. (D) The final signal was calculated as the original signal (B) minus the template signal (C).

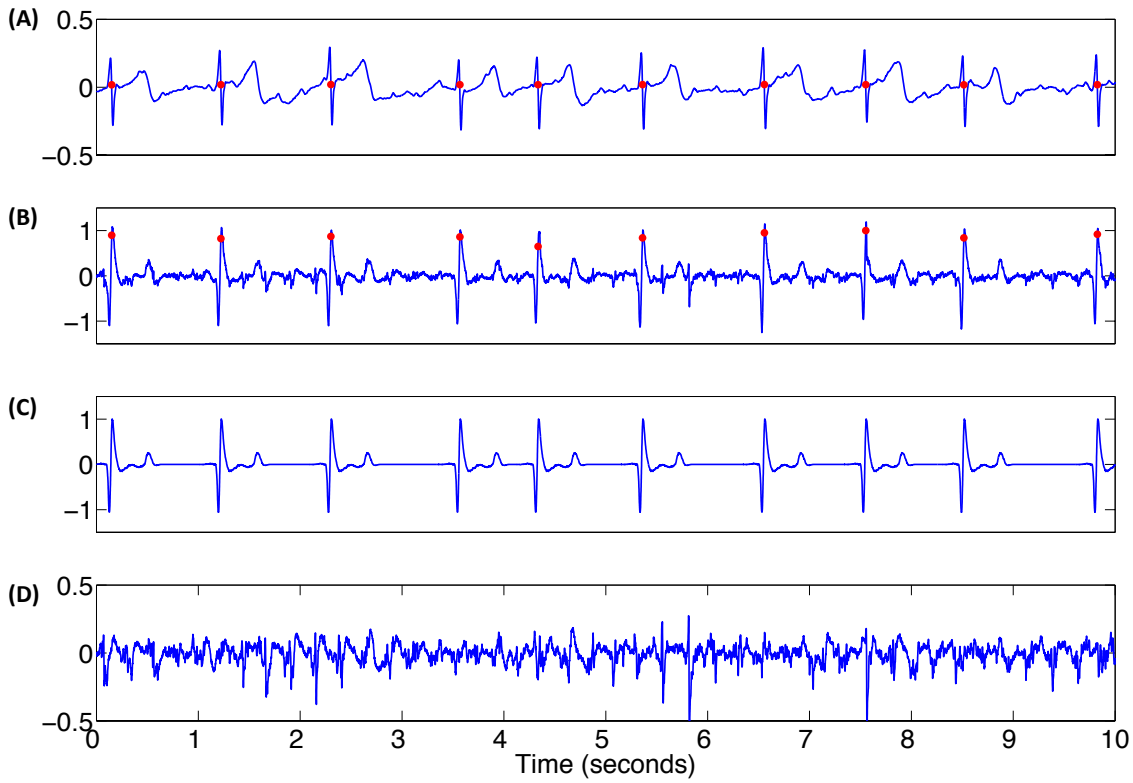

Figure 6.25: QRS subtraction for a signal with a large ventricular component. Some electrograms have a large ventricular component and the atrial signal is only evident after QRS subtraction; compare (B) and (D). (A) ECG lead I; (B) raw unipolar electrogram; (C) ventricular template; (D) QRS subtracted electrogram. Further explanation is given in the legend for Fig. 6.24.

6.4.3 Methods: modifications to the phase calculation

Previously, phase of MEA electrograms was calculated by identifying locations of maximum amplitude (bipolar) or maximum gradient (unipolar). For clinical data, a modification was required for calculating the phase of clinical unipolar electrograms in order to identify maximum negative gradient only since activation is defined as the point of steepest negative slope (see Section 1.3.2). In order to prevent the algorithm from selecting points of positive slope, the derivative was capped above at 0 before applying the set of filters. An example to show the effects of this is illustrated in Fig. 6.26. A further modification to the algorithm for unipolar phase of MEA electrograms for the application to clinical data was that target times were not used, as activation tagging was easier to perform on the filtered derivative signal. An example showing the raw unipolar electrogram, QRS subtracted signal, capped derivative and filtered derivative are shown in Fig. 6.27.

In order to calculate bipolar phase, the same sequence of filters and analysis steps were applied to the raw bipolar electrogram signal directly, rather than the capped derivative. The steps that were applied to the filtered unipolar derivative and the filtered bipolar electrogram signal are shown in Fig. 6.28. An example unipolar and bipolar electrogram coloured by their phase are shown in Fig. 6.29.

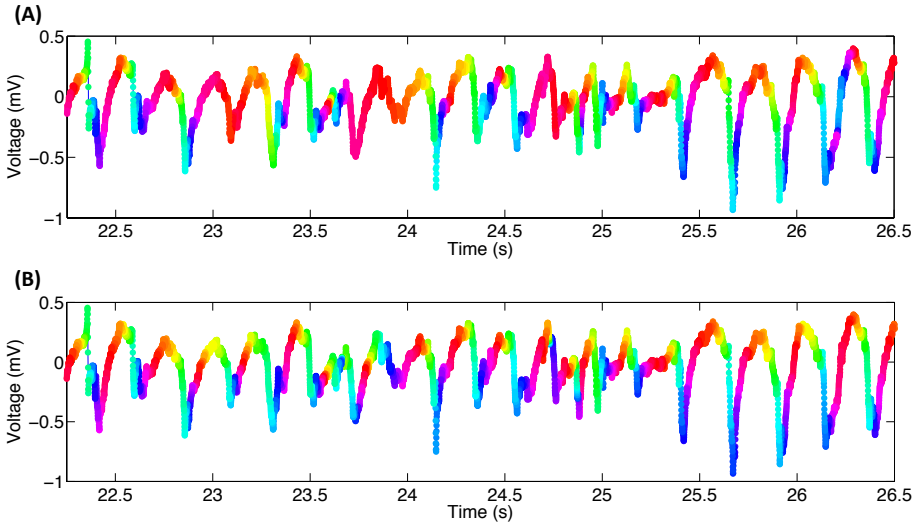

Figure 6.26: Capping the derivative at zero prevents the phase calculation algorithm from assigning areas of positive gradient as activations. (A) The voltage signal coloured by phase calculated without the capping step. There are several activations missing from the phase without the additional capping step and there is also an instance of a positive slope being tagged as an activation (at around 26.25s). (B) The voltage signal coloured by phase calculated with the capping at zero step. The cap at zero means the missing activations are detected and the false positive slope is assigned the correct phase.

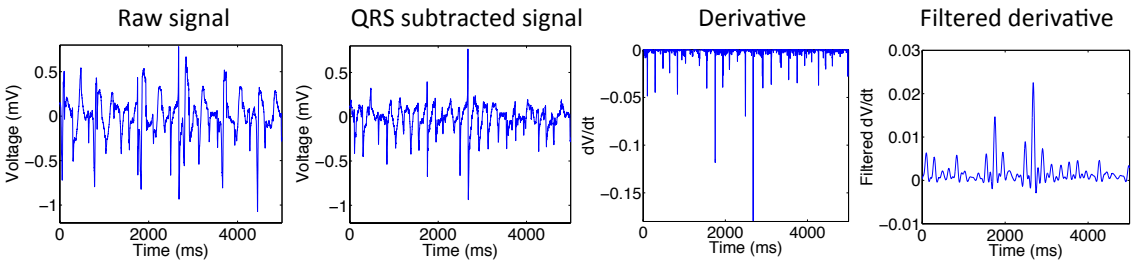

Figure 6.27: Several pre-processing steps are required in order the calculate the phase of clinical unipolar electrograms. The ventricular component of clinical unipolar electrograms is removed using QRS subtraction. The derivative of this signal is calculated and it is capped at zero. The capped derivative signal is then filtered, and the phase of this filtered derivative signal is calculated using the steps in Fig. 6.28.

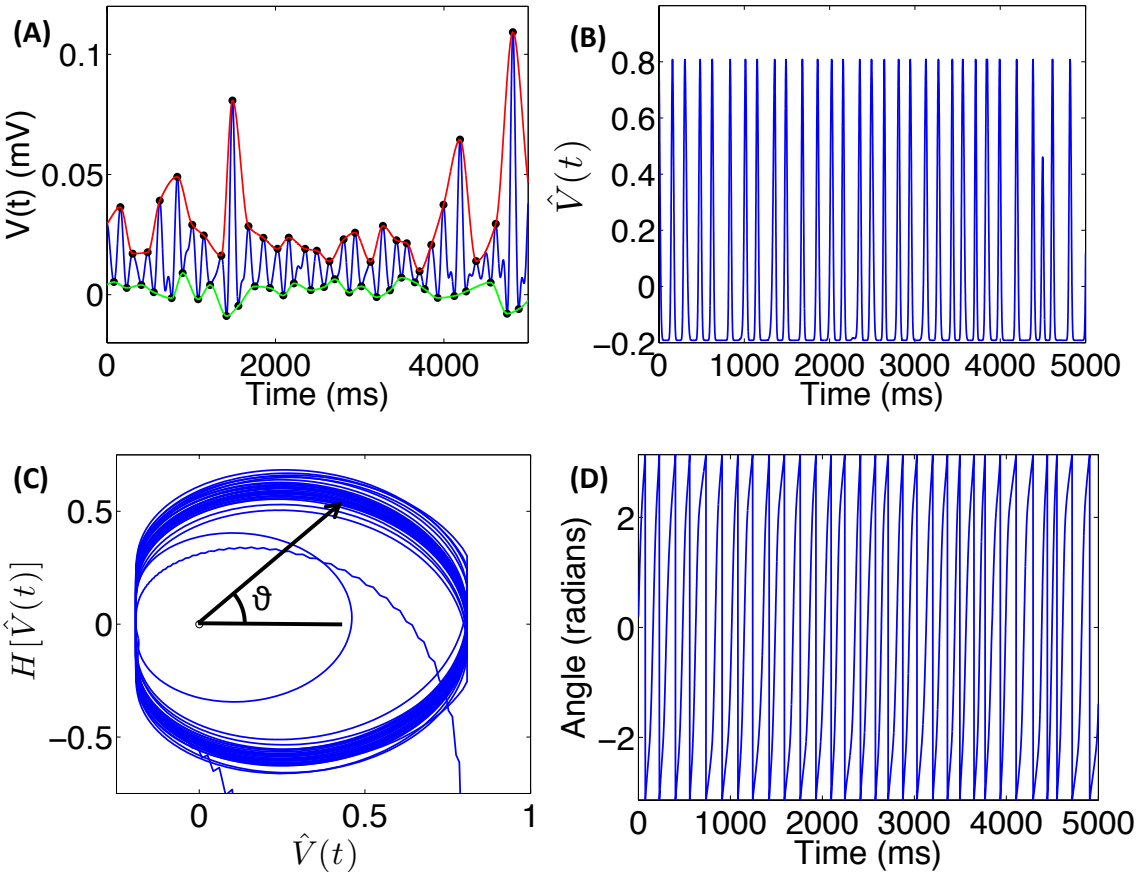

Figure 6.28: Outline of steps applied to calculate phase of filtered bipolar electrograms or the filtered derivative of unipolar electrograms. The example here is for a bipolar electrogram. (A) Maxima and minima of the signal are tagged and joined using cubic splines, respectively. (B) The maxima and minima splines are used to normalise the signal, which is then raised to the power of six to reduce the effects of noise, and finally a straight mean is removed to ensure the signal is zero mean. (C) The Hilbert transform of this zero mean signal is plotted against itself to give phase loops, and the angle around this trajectory is the phase angle in (D).

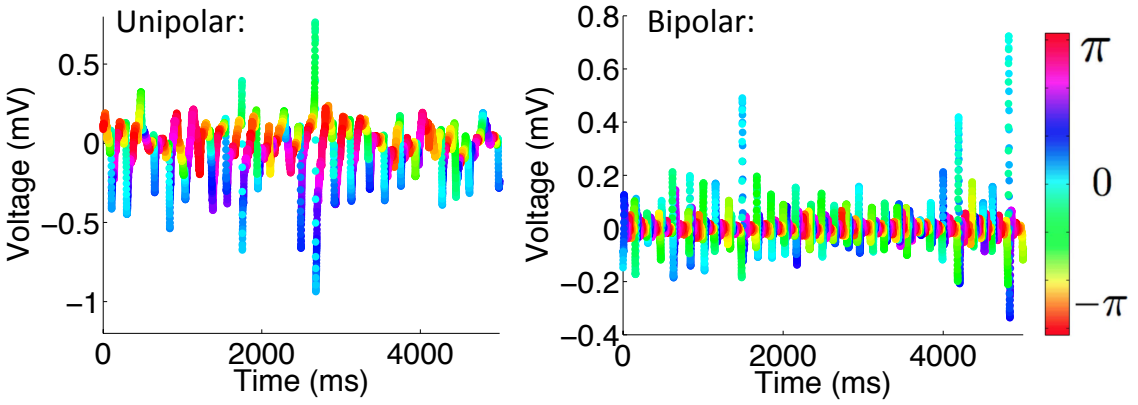

Figure 6.29: Example unipolar and bipolar electrograms coloured by phase.

6.4.4 Methods: data projection and interpolation

Three-dimensional electrode locations for unipolar electrodes were projected to the two-dimensional plane of best fit. Bipolar electrode locations in two dimensions were assumed to lie equidistant between the two corresponding unipolar locations in two dimensions. Phase data were interpolated using the matlab function `griddata` with cubic interpolation and phase angle correction (Section 2.12). The data were then spatially smoothed using a 5-by-5 bin size (Section 4.2.4). Bipolar electrograms indicating poor contact with the tissue, identified as low amplitude using a patient-specific amplitude threshold, were removed from the interpolation. For each low-amplitude bipolar electrogram, the two unipolar electrograms corresponding to the bipolar electrogram were also removed from the unipolar electrogram interpolation.

6.4.5 Unipolar phase method with 10Hz filter

The unipolar phase method developed for simulated data, for which a 10Hz filter was applied and phase was assigned based on signal amplitude, gave a poor correlation (0.16) with bipolar electrogram phase. Example phase assignment and the correlation for one catheter are shown in Fig. 6.30. This confirms that this is not a suitable method for calculating phase of clinical unipolar electrograms.

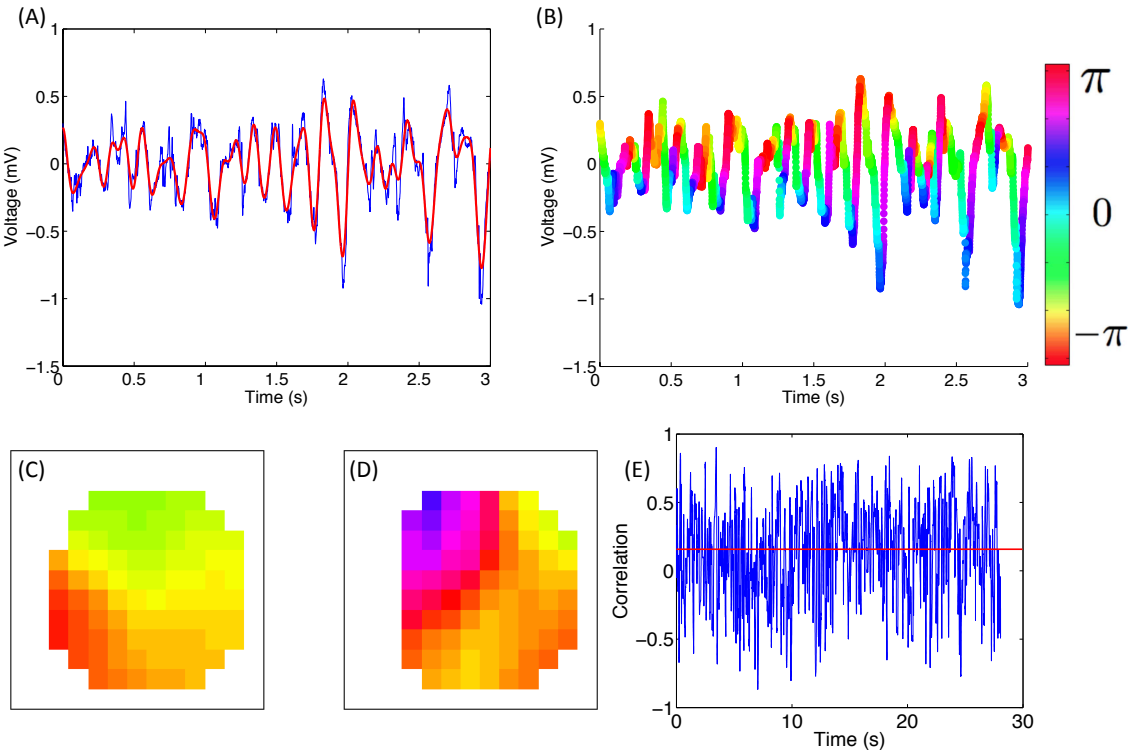

Figure 6.30: Unipolar phase method with electrogram filtering at 10Hz following QRS subtraction correlates poorly with bipolar electrogram phase. (A) Unipolar electrogram signal for which QRS subtraction has been performed (blue), with signal after 10Hz filtering shown (red). (B) Unipolar signal coloured by phase. (C) Example isophase map for unipolar phase; (D) corresponding time point for bipolar phase. (E) Circular correlation coefficient of bipolar and unipolar phase over the recording is poor, with a median correlation of 0.16 (red line).

6.4.6 Validation using atrial tachycardia data

Atrial tachycardia (AT) data from two patients provided the opportunity to test the phase mapping algorithms on clinical data for which the activation times are known with more certainty. For the first patient, isochronal activation time maps created from unipolar and bipolar voltage recordings were compared to those created from unipolar and bipolar phase. This approach answers the question of whether activation times derived from phase match those from voltage in clinical AT data. For the second patient, a local activation time map was exported from the clinical electro-anatomic mapping system and the activation wavefront directions, calculated from these activation times, were compared with the direction computed by tracking phase wavefronts. The motivation for this analysis is that it is difficult to define activation time windows for analysis during fibrillation, meaning that isochronal mapping is difficult. With this in mind, a wavefront direction approach for phase mapping was developed and this was compared to wavefront directions calculated from activation times from voltage that were exported from the clinical system, using the techniques developed in Chapter 3.

Isochronal map comparison

Nine catheters of data were acquired during AT, for which each recording was between 22.7s and 33.0s (mean duration: 28.1s), with a mean of 111 beats of AT. Electrograms indicating poor contact with the tissue were removed from the isochronal map analysis. Activation times were tagged using a moving window in bipolar electrograms as locations of maximum absolute amplitude; in unipolar electrograms as locations of maximum negative slope; and in bipolar and unipolar phase as locations of phase 0. Activation times for unipolar and bipolar electrograms are in general simple to assign during AT using the standard definitions (Section 1.11.2) and so these are known with a degree of certainty. Locations of the twenty unipolar electrodes were converted to the two-dimensional co-ordinates that optimally preserve the geodesic distances between points, using the method described in Section 3.3.2. Bipolar electrode locations in two dimensions were taken to be the mid-points of unipolar electrode locations.

Time windows for constructing activation wavefronts were based on suitable time windows for bipolar voltage activation times. For each time window, isochronal maps were plotted for all four measures of activation time. For each map, the set of electrode locations with times within the window were used for interpolation, where the same interpolated mesh was used for each dataset. For each pair of maps, the correlation was calculated on the area corresponding to the intersection of all four maps.

This was necessary because electrodes may not have had an activation time within the window for bipolar phase, or unipolar recordings, and so the resulting maps may have been different sizes. The number of pixels contained in the intersection of each pair of maps was also calculated. The number of pixels contained in both maps under comparison is termed the *pixels overlap*. Example isochronal maps are shown in Fig. 6.31.

The resulting correlation of isochronal maps for bipolar voltage and phase measured across the entire recording for each catheter are shown in Fig. 6.32. All catheters show a high mean correlation (mean > 0.89) between maps from voltage and phase, and the average number of pixels overlapping between the two maps is moderate to high for all catheters ($57.2 - 99.5\%$). This suggests that the use of bipolar phase to construct activation maps gives spatially similar maps to those from bipolar voltage.

The average correlations for isochronal maps measured across the entire recording for each catheter between the different measurements are all strong: bipolar voltage and phase: 0.94 ± 0.06; bipolar phase and unipolar phase: 0.92 ± 0.09; bipolar voltage and unipolar voltage: 0.88 ± 0.11; unipolar voltage and unipolar phase: 0.94 ± 0.07. The average percentage of pixels overlap are also high: bipolar voltage and phase: $77.4\% \pm 14.3\%$; bipolar phase and unipolar phase: $70.0\% \pm 15.6\%$; bipolar voltage and unipolar voltage: $71.8\% \pm 15.7\%$; unipolar voltage and unipolar phase: $68.8\% \pm 15.8\%$. Thus the use of unipolar and bipolar phase to construct activation time maps perform similarly to voltage.

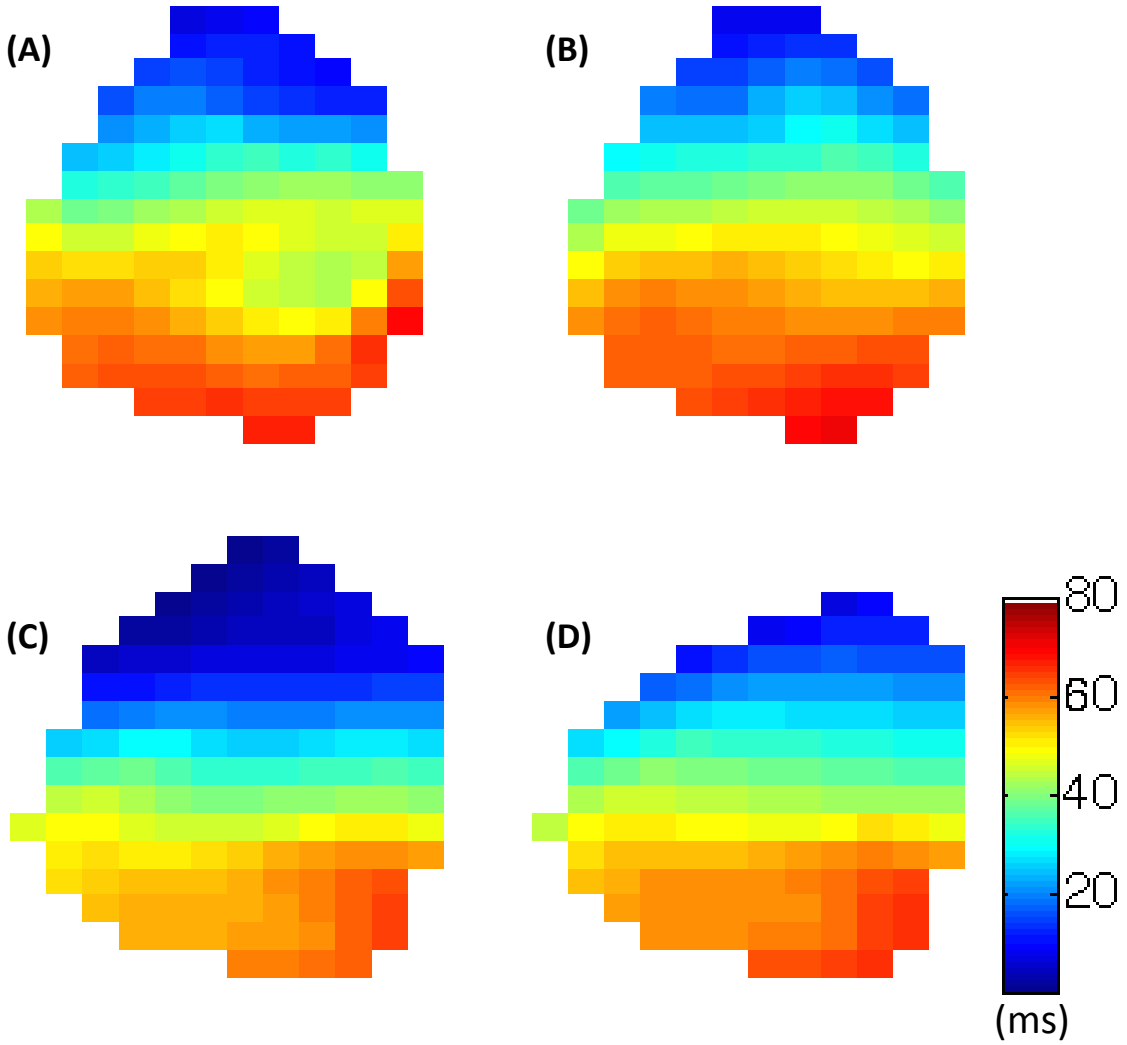

Figure 6.31: Example isochronal maps for validation of use of phase for atrial tachycardia data, in which the maps are seen to correlate well. Isochronal maps for data from: (A) Bipolar voltage; (B) Bipolar phase; (C) Unipolar voltage; (D) Unipolar phase. These maps correlate well with each other: A&B 0.98; A&C 0.95; C&D 0.99; B&D 0.98. The number of pixels in each map are also similar: A 129; B 129 ; C 137; D 121. This suggests that either unipolar or bipolar electrograms are suitable for use for constructing this isophase map. The maps cover different areas because bipolar electrode data are assigned to the mid-point location of unipolar electrogram recordings, and also electrodes may not have had an activation within the given window.

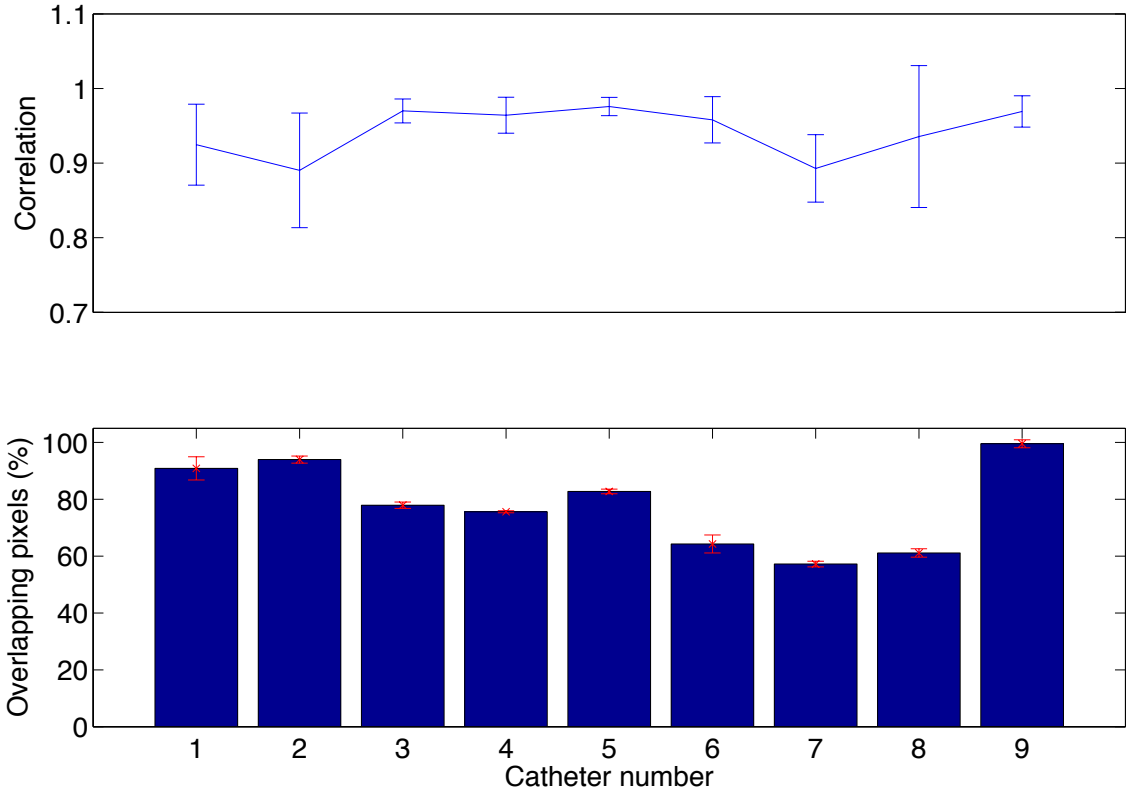

Figure 6.32: Isochronal map correlation and percentage of pixels overlapping are high for bipolar voltage and phase comparison, suggesting that bipolar phase gives similar activation maps to those from bipolar voltage.

Activation time map direction and phase wavefront direction comparison

As an additional investigation, conduction directions calculated from a local activation time map exported from Velocity electro-anatomic mapping system were compared to directions calculated from bipolar and unipolar phase wavefronts. A conduction velocity vector arrow was assigned to each of the thirty catheters analysed using the local activation times from the map exported from Velocity. The methods in Chapter 3 were used to calculate the conduction velocity vector, assuming a circular wavefront and using the two-dimensional representation that best preserves geodesic distances. The propagation map for which arrows were assigned using these directions was then compared to directions assigned using unipolar and bipolar phase.

Wavefront directions were assigned to either unipolar or bipolar phase by tracking the mid-points of lines of constant phase. Wavefronts were defined as lines of constant zero phase and the mid-point of each wavefront were stored and joined as paths if they belong to the same wave. Lines of constant phase were joined as a wavefront moving over time as a wave based on movement thresholds, where multiple wavefronts may coexist in any given frame. In more detail, wavefronts were defined as a connected path of at least three pixels and these were taken to be a part of the same wave if the number of pixels that were in both the wavefront in the current frame and the wavefront in the previous frame divided by the length of the current wavefront is greater than a threshold (10%). Each wavefront is traced to find the mid-point (the middle pixel). The movement of the mid-point of the wavefront over time then gives a line that is roughly perpendicular to the wave motion and indicates the direction over time. This is illustrated in Fig. 6.38. The paths of all wavefronts that give a satisfactory linear fit were stored. A line was then fit to the mid-point data from all of these wavefronts. Finally two points along this line (one quarter and three quarters along the line) were taken as the ends of the arrow for the wavefront direction for the catheter being analysed. Finally, these two points were mapped back to three dimensions using the techniques outlined in Section 3.3.2, in order to assign wavefront directions in three dimensions.

The calculated wavefront directions using the activation times for the thirty catheters of data, the bipolar phase of eighteen catheters and the unipolar phase of fifteen catheters are plotted in Fig. 6.33, in which it can be seen that the global activation patterns calculated using the different measures agree well since arrows are seen to overlap and follow the same pattern.

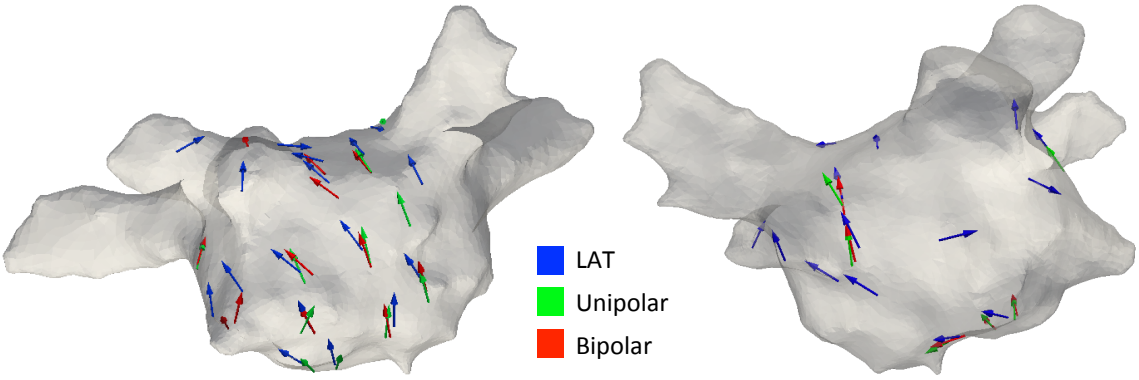

Figure 6.33: Directions measured using voltage (activation times, blue), unipolar electrogram phase (green) and bipolar electrogram phase (red) show a similar global pattern. One direction is assigned to each of the thirty catheters of data contained in the LAT map from the electroanatomic mapping system using the conduction velocity algorithm developed in Chapter 3. Unipolar arrows represent the average direction calculated from the unipolar phase of multiple beats of AT (99.9 ± 27.7 beats per catheter). Bipolar arrows represent the average direction calculated from the bipolar phase of multiple beats of AT (88.9 ± 19.7 beats per catheter).

6.4.7 Results: number of phase singularities

A simple comparison of the output from the unipolar electrogram and bipolar electrogram algorithms is whether the number of phase singularities calculated in each case is the same. Although the number does not address whether these phase singularities are found in the same location within the area of the catheter, it does give a useful measure of rotational content for a catheter, which should be the same regardless of whether unipolar or bipolar electrogram data are used. In order to address this question, interpolated unipolar and bipolar phase were analysed for each catheter to calculate the average number of phase singularities per frame.

In Fig. 6.34, example maps are shown for three patients for which the number of phase singularities per catheter is indicated by the colour scale. Visually, there is in general a good correspondence between catheter ordering by number of phase singularities for unipolar and bipolar phase. This was quantified in terms of the relationship between the average number of phase singularities per frame for each catheter for unipolar phase and bipolar phase; plotted in Fig. 6.35(A). The correlation coefficient between the mean number of phase singularities per frame for each catheter between unipolar and bipolar catheter recordings was 0.89. Overall, this shows that categorising catheters by degree of rotational content measured by the number of phase singularities is independent of data type.

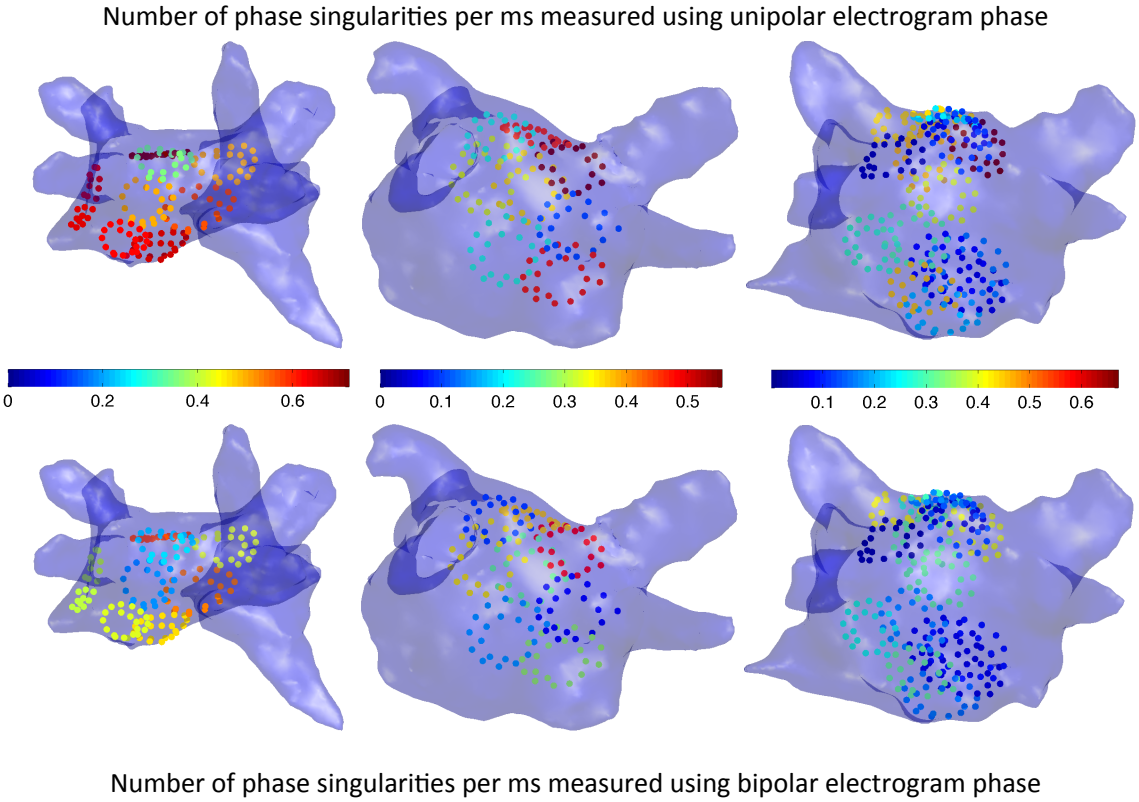

Figure 6.34: Agreement is typically seen between using unipolar and bipolar phase for identifying areas with high or low phase singularity content. Average number of phase singularities per frame is shown per catheter for both unipolar (top row) and bipolar (bottom row) phase for three patients.

Collating the data for all patients, the mean number of phase singularities per ms across all catheters was 0.36 ± 0.16 for bipolar electrogram phase and 0.47 ± 0.20 for unipolar electrogram phase. The histogram in Fig. 6.35 shows that there are more catheters in the bins representing a lower mean number of phase singularities per frame for bipolar phase than for unipolar phase. This is reflected in the mean of the differences in the number measured using each datatype per catheter which was -0.10 ± 0.09 per ms (bipolar minus unipolar), with a mean absolute difference of 0.11 phase singularities per ms.

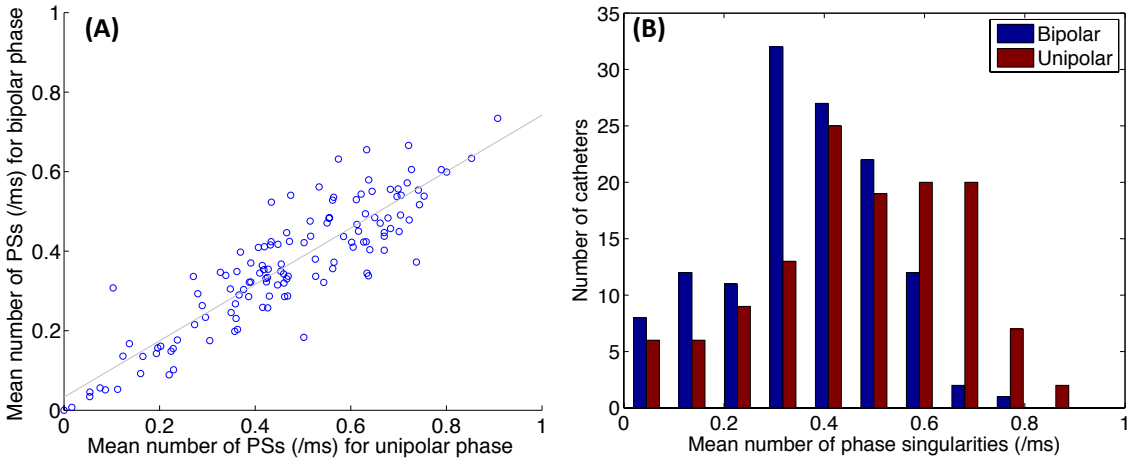

Figure 6.35: There is linear relationship between average number of phase singularities per frame per catheter for both unipolar and bipolar phase. (A) Scatter plot ($n = 127$; line of best fit is: $y = 0.03 + 0.71x$, with $R^2 = 0.79$.); (B) histogram.

6.4.8 Results: phase angle correlation

To assess whether the phase values calculated using unipolar and bipolar electrograms are similar, the phase angle correlation was calculated, as explained in Section 6.3.6. In order to obtain a measure of an acceptable correlation for clinical AF data, it was assumed that an agreement of 50% of the pixels was acceptable, with the justification that clinical data contains more noise and the signals are more fractionated; thus an exact correspondence is not expected and an agreement of half the array is deemed sufficient. To calculate the circular correlation coefficient expected for one such phase map, a random selection of 50% of the pixels were randomly permuted between these pixels to give a new phase map, and the circular correlation between these maps was calculated. This was repeated 100 times for each map and for 702 frames of AF. The median circular correlation for this test was 0.52 (mean

0.51, minimum -0.62, maximum 0.90). Thus a circular correlation of above 0.5 was considered acceptable.

An example plot showing the circular correlation between unipolar and bipolar phase for one catheter over the duration of the recording is demonstrated in Fig. 6.36(A). The correlation shows the activity varies in consistency between the data types over time, with some segments of agreement, and there are also segments for which the modalities do not agree. For this analysis, the median correlation per catheter are considered so as not to give undue weight to the low correlation time segments. For the example in Fig. 6.36(A), the median is 0.50, and the recordings show an acceptable correlation (> 0.50) 50% of the time. Segments that show a low correlation are investigated further in Section 6.4.10.

The median correlation per catheter are shown as a histogram plot across the 127 catheters in Fig. 6.36(B), in which it can be seen that there is a wide range of correlations ($0.21 - 0.92$), that are approximately normally distributed. This indicates that catheters show different degrees of agreement, which may depend on the amount of fractionation within the signal, whether there are any wavefront collisions and how planar the wave is. The median of the median correlations is 0.51, indicating that about half the catheters have a median correlation above the acceptable correlation threshold. The maximum p-value across the catheters was 0.02 (mean 5.29×10^{-4}), showing that there is a statistically significant relationship between unipolar and bipolar phase.

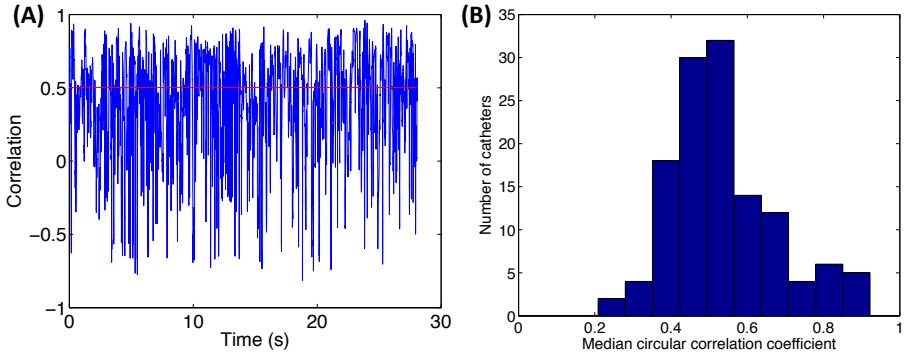

Figure 6.36: Correlation plot between unipolar and bipolar phase angles for an example catheter and histogram of median correlations for all catheters. (A) Correlation plot between unipolar and bipolar phase angles for an example catheter, where the median value is indicated by the red line. For this example catheter, the median correlation value is higher at 0.50 than the 10Hz amplitude based method for calculating unipolar phase for which the median correlation was 0.16 (compare to Fig. 6.30E). (B) Histogram to show the distribution of median circular correlation coefficient measured between bipolar and unipolar phase.

6.4.9 Results: activation time map correlation

Activation time maps indicate wavefront propagation so a further measure of the correspondence between unipolar and bipolar phase results is whether there is agreement between maps of activation time when constructed from phase. Activation time plots are difficult to construct during fibrillation due to the challenges associated with tagging activation times and also in choosing a suitable time window for representing the data. In this analysis, activation time maps were plotted for activity that was expected to show wavefronts that last at least 25ms. These time windows were selected based on wavefronts detected in the bipolar electrogram phase since bipolar electrogram phase was generally less noisy than unipolar electrogram phase.

The start and end times of each wavefront that lasted greater than 25ms were used as a time window to construct activation time maps from unipolar and bipolar phase (isophase value 0; an example is shown in Fig. 6.38). This was repeated for all wavefronts and the correlation between each pair of activation time maps were calculated. A histogram to show the median correlation for each catheter is shown in Fig. 6.37, where the overall median is 0.73.

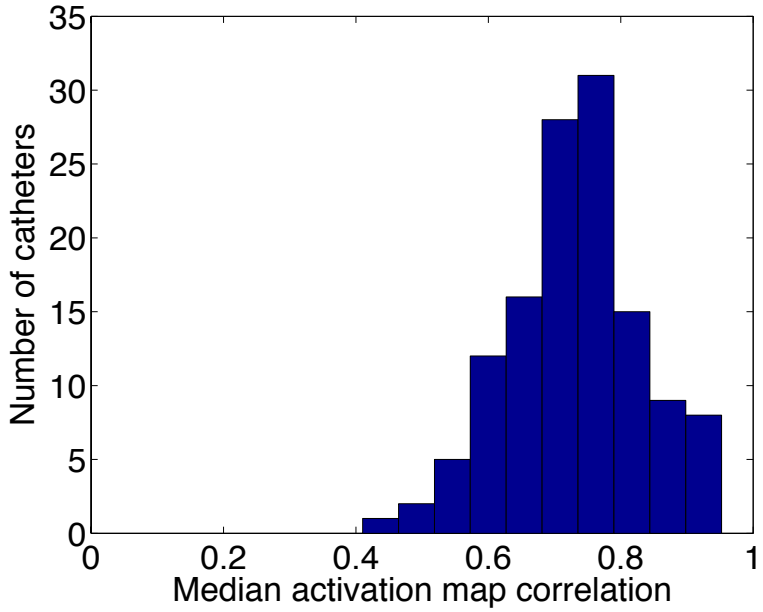

Figure 6.37: Histogram to show the median correlation coefficient measured between activation maps from bipolar and unipolar phase. The overall median is 0.73.

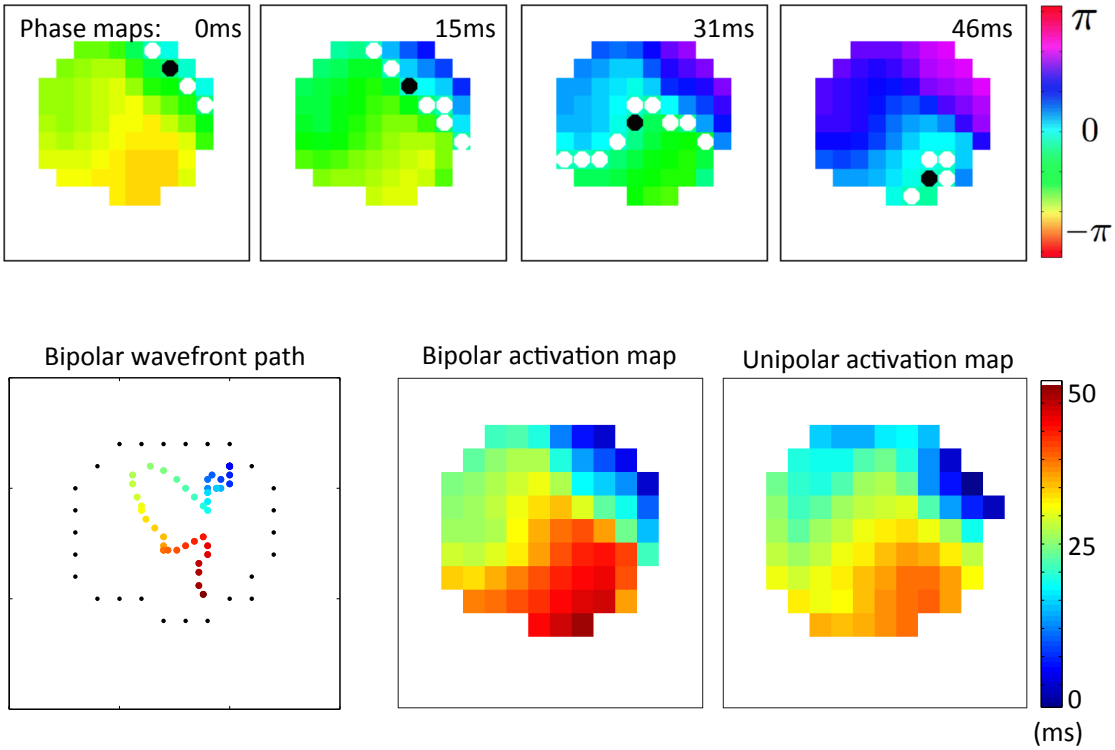

Figure 6.38: Methodology used to determine suitable time windows to construct activation time maps from unipolar and bipolar phase and to assess their correlation. Top: isophase maps with lines of isophase 0 (white dots) for which the mid-point of each wavefront is indicated as a black dot. These mid-points were joined and smoothed to show the bipolar wavefront path over time (bottom left), from blue to red. This line is roughly perpendicular to the wavefront. The time points corresponding to the start and end of this path were used as a time window for constructing activation time maps for bipolar and unipolar phase. These are seen to match well (correlation of 0.99).

6.4.10 Results: investigating segments of low correlation between unipolar and bipolar phase

As seen in Fig. 6.36(A), there are time segments for which unipolar and bipolar phase correlate poorly (10.4% of the recording has a circular correlation coefficient below 0, while 49.7% has one below the acceptable threshold of 0.5 circular correlation). These were investigated in more detail in order to identify any common occurrences leading to differences. Some instances of low correlation were due to a missed activation on the unipolar or bipolar electrogram. An example is shown in Fig. 6.39, for which a likely activation in the second unipolar electrogram is missed. This is difficult to assign in the absence of information from the other unipolar and bipolar electrograms. Other instances were due to a prolonged unipolar downstroke, in which case it is difficult to say where on the signal represents activation; an example is shown in Fig. 6.40.

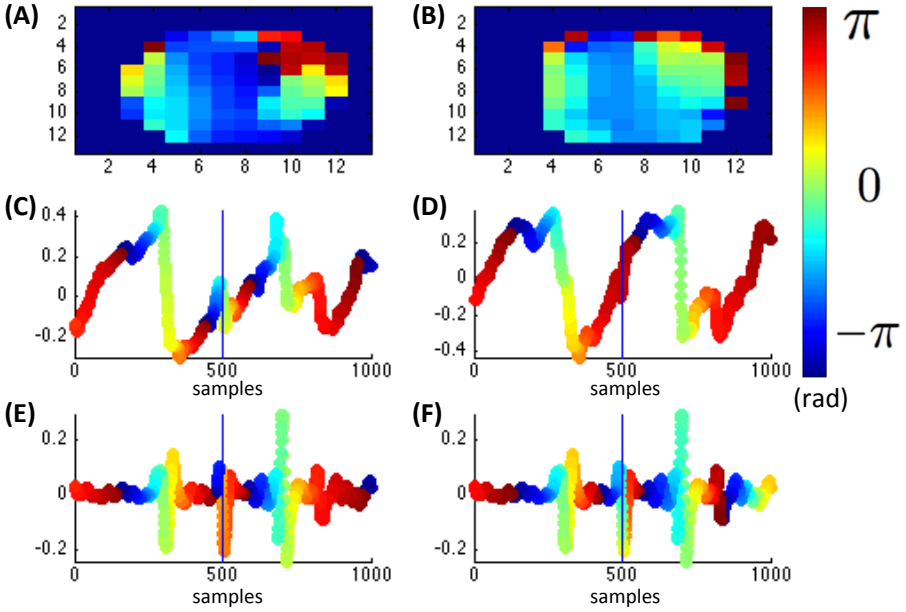

Figure 6.39: Causes of low correlation between unipolar and bipolar phase: missing detection on unipolar electrogram. (A) Isophase map for unipolar recording; (B) corresponding isophase map for bipolar recording, which correlate poorly. The average phase of each pair of unipolar electrograms is compared to the phase of the corresponding bipolar electrogram, and the electrogram showing the largest difference are plotted here, with the two unipolars coloured by their phase (C, D); the bipolar electrogram coloured by the average phase (of (C) and (D)) is shown in (E) and the actual bipolar phase in (F). It is likely that the differences at time point sample 500 are due to a missed activation in (D).

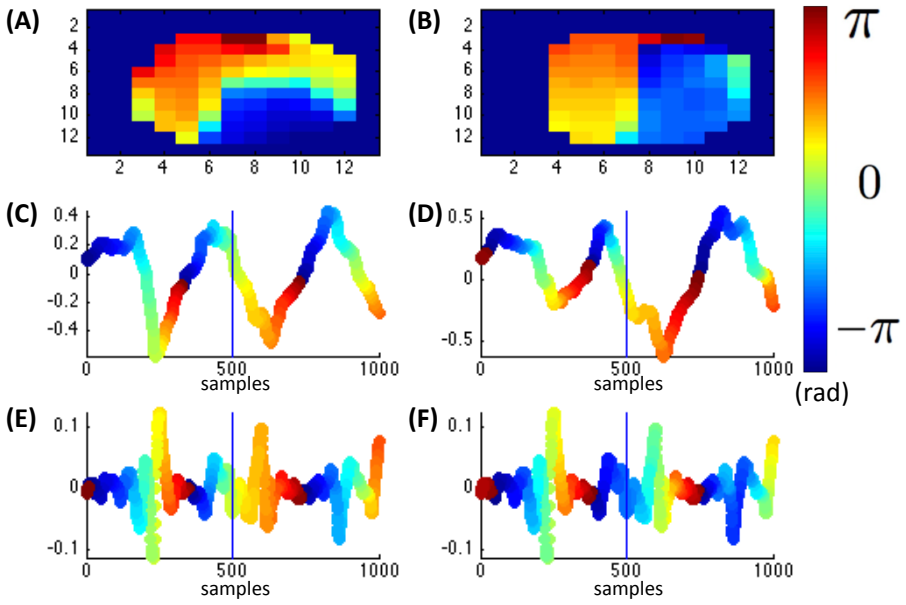

Figure 6.40: Reasons for segments of low correlation between unipolar and bipolar phase. (A)-(F) as per Fig. 6.39. Here the unipolar downstroke covers a long duration and it is difficult to assign where on the deflection activation occurs.

6.4.11 Summary of clinical findings

Clinical electrogram data analysis provided the most challenging of the environments, due to the addition of far-field noise, the difficulty with working on a complex atrial geometry, and an increased complexity of the underlying rhythm in which global propagation patterns are unknown. Several adaptations to the MEA unipolar phase algorithm were required. First of all, the far-field ventricular component of unipolar electrograms was removed using a method from the literature for QRS subtraction (Ng et al., 2007). In order to ensure that the unipolar algorithm selects activations as points of maximum negative slope, and not maximum positive slope, it was necessary to cap the derivative signal at 0 before filtering was applied. In addition, the step of identifying target times for MEA unipolar phase calculation was not required here. The bipolar electrogram phase calculation was unchanged from the MEA bipolar electrogram phase calculation. Overall, the same filtering and analysis steps were applied to the capped derivative of the QRS subtracted unipolar electrogram, in order to identify points of maximum negative slope; and the raw bipolar electrogram signal, in order to identify points of maximum amplitude.

An additional challenge for the clinical data was that electrograms were measured at points located in three dimensions. Catheter locations were projected to the two-dimensional plane of best fit or using geodesic distance preservation, in order to

perform phase singularity location analysis in two dimensions.

Atrial tachycardia validation studies

Clinical electrogram data exhibit a higher degree of complexity than simulated electrograms and *in vitro* electrograms, and as such a test to check whether the developed algorithms are appropriate for clinical data was performed using AT data. These data have the advantage that activation times and patterns can be assigned confidently using voltage, for comparison with the equivalent measures from phase. Activation time maps and wavefront directions matched well, indicating the validity of the technique. In particular, isochronal maps from bipolar or unipolar voltage or phase correlated well with each other, demonstrating the validity of phase for assigning activation times. One point to note is that calculated activation maps covered different areas since electrodes may not contain an activation time within the window analysed. The number of pixels overlapping between the maps was high, demonstrating that similar numbers of electrodes were included in the maps between the different measures of activation time (bipolar voltage, unipolar voltage, bipolar phase and unipolar phase). Activation windows were chosen from bipolar voltage, since these were the signals in which activation times could be assigned with the most confidence (least noise).

In addition, directions calculated from tracking unipolar or bipolar wavefronts using the calculated phase displayed a similar global activation pattern to directions calculated using the local activation times exported from the Velocity electroanatomic system, which provides a gold standard to compare the phase algorithms to. This validates the use of phase for assigning wavefront direction.

One point to note is that the phase calculation algorithm uses deflection tagging to create a zero-mean signal, and this tagging determines which deflections in the electrogram are present in the final phase. As such, activation times and directions from voltage are expected to match those from the resulting phase in AT data in which activation times are assigned with certainty. AF data offers the additional challenge of multi-component electrograms for which it is not always clear which deflections represent true activations, and so AT validation does not offer validation in the case of AF data.

Atrial fibrillation analysis

The average number of phase singularities measured using unipolar and bipolar phase during AF matched well on a catheter-by-catheter basis, showing that either method can be used for classifying areas by phase singularity content. The num-

ber of phase singularities exhibited a difference between catheters, indicating there is spatial variation in rotational content between catheters, which can be used to identify areas of high rotational content. A limitation is that the number of phase singularities does not indicate whether the distribution of phase singularities within the area of the catheter were the same. The circular correlation coefficient for the phase angle shows that the situation is more complicated, as this measures varies in time for each catheter, and there are time segments for which unipolar and bipolar phase do not correlate well. There are also differences in the median correlation coefficient measured for each catheter, with some catheters showing a higher correspondence than others. These catheters were observed to be those for which more of the wavefronts were planar, and consequently the phase was easier to assign.

Activation time maps correlated well during AF, showing that the wavefront propagation patterns detected using unipolar and bipolar phase were similar, so that both unipolar and bipolar phase measure similar activation wavefronts, even during fibrillation. One limitation of the method used to correlate activation time maps was that activation windows for the construction of the maps were based on wavefronts detected in bipolar phase that last at least 25ms. This technique circumvents the challenge of automatically choosing suitable activation windows during AF; however, it may bias the correlation score since only time segments corresponding to longer duration wavefronts are included. As such, short duration wavefronts, due to wavefront collision, may be excluded. Equally, time segments for which the phase is more noisy and wavefront patterns are unclear may be excluded based on the time duration threshold.

Time segments for which unipolar and bipolar phase did not correlate well were investigated on an individual basis. Although, the differences were on occasion because of a missed unipolar or bipolar deflection, for the majority of cases it was difficult to say which of the unipolar and bipolar deflections represent true activation.

6.5 Applying the clinical algorithms to left-atrial simulation data

Since the unipolar clinical algorithm differs substantially from the unipolar electrogram algorithm that was initially tested in simulated data in Section 6.2, a final simulation study was undertaken using an anatomically realistic MRI-derived left-atrial geometry for which unipolar and bipolar electrogram phase calculated using the clinical algorithms were compared to the results of using action potential phase. This simulation was performed using Nektar++ high-order spectral element solver

(Section 2.5), where the Courtemanche et al. (1998) human atrial ionic model was used, with changes representing electrical remodelling in AF (Courtemanche et al., 1999), and an S1-S2 pacing protocol was applied to induce two rotors.

Unipolar electrograms were calculated (Section 2.8) from voltage data at electrode locations representing nine Afocus catheters, for which each catheter was modelled as an Archimedean spiral with diameter 2cm as in Section 3.3.8. Spiral catheters were defined using the following steps:

1. The desired location for the catheter on the three-dimensional mesh was chosen.

2. The vertices within a bounding box of 1.5cm either side of the centre point were selected. This provided the three-dimensional co-ordinates for AP data.

3. These vertices were flattened to two dimensions using a distance-preserving mapping (see Sections 2.14, 3.3.2). This gave the two-dimensional co-ordinates for AP data.

4. An Archimedean spiral was defined in two dimensions centred about the centre of mass of the two-dimensional AP points. This gave the two-dimensional co-ordinates for unipolar electrogram data.

5. These points were projected back onto the mesh using barycentric co-ordinates (see Section 2.14).

6. Each of the points were projected 2mm endocardially, along the surface normal to the closest vertex, following Martínez et al. (2014). This gave the three-dimensional co-ordinates for unipolar electrogram data.

The unipolar catheters used for analysis are shown in the top row of Fig. 6.41. For each catheter, nineteen bipolar electrograms were calculated as the difference of the twenty adjacent pairs of unipolar electrograms, as in the clinical environment. Unipolar electrogram and bipolar electrogram phase were calculated for all of the catheters using the clinical algorithms, except QRS subtraction was not performed, since the simulation only included the left atrium. The phase of action potential data measured at each vertex on the mesh were also calculated.

Phase interpolation (see Section 2.12) was then performed using the two-dimensional co-ordinates of the action potential, unipolar electrogram or bipolar electrogram phase, and phase singularities were identified (see Section 2.11). Phase singularity trajectories were compared for a catheter located over a rotor-core, in terms of the

difference in the location of the centre of each trajectory and the frame wise differences in the phase singularity locations. The circular correlation co-efficient of the phase angle for each data type comparison (action potential, unipolar electrogram and bipolar electrogram) were calculated and averaged across the nine catheters.

Example isophase maps are shown in Fig. 6.41(B), along with the rotor-core trajectories. The centre locations were close together (distance between AP and bipolar centre 0.76mm; AP and unipolar centre 0.53mm; bipolar and unipolar centre 0.59mm). Frame-wise differences are also small (distance between AP and bipolar 2.43 ± 1.44mm; AP and unipolar 2.02 ± 1.10mm; bipolar and unipolar centre $1.74 \pm$ 0.99mm, Fig. 6.41(C)), and are not considered to be clinically relevant ($<$ 4mm ablation catheter). Median circular correlation coefficients were high across the nine catheters (Fig. 6.41(D)), showing that the calculated phase agree well between action potential, unipolar electrogram and bipolar electrogram data. Thus the algorithms used for the clinical analysis show similar results to the action potential gold standard results in simulated data; hence, demonstrating validity.

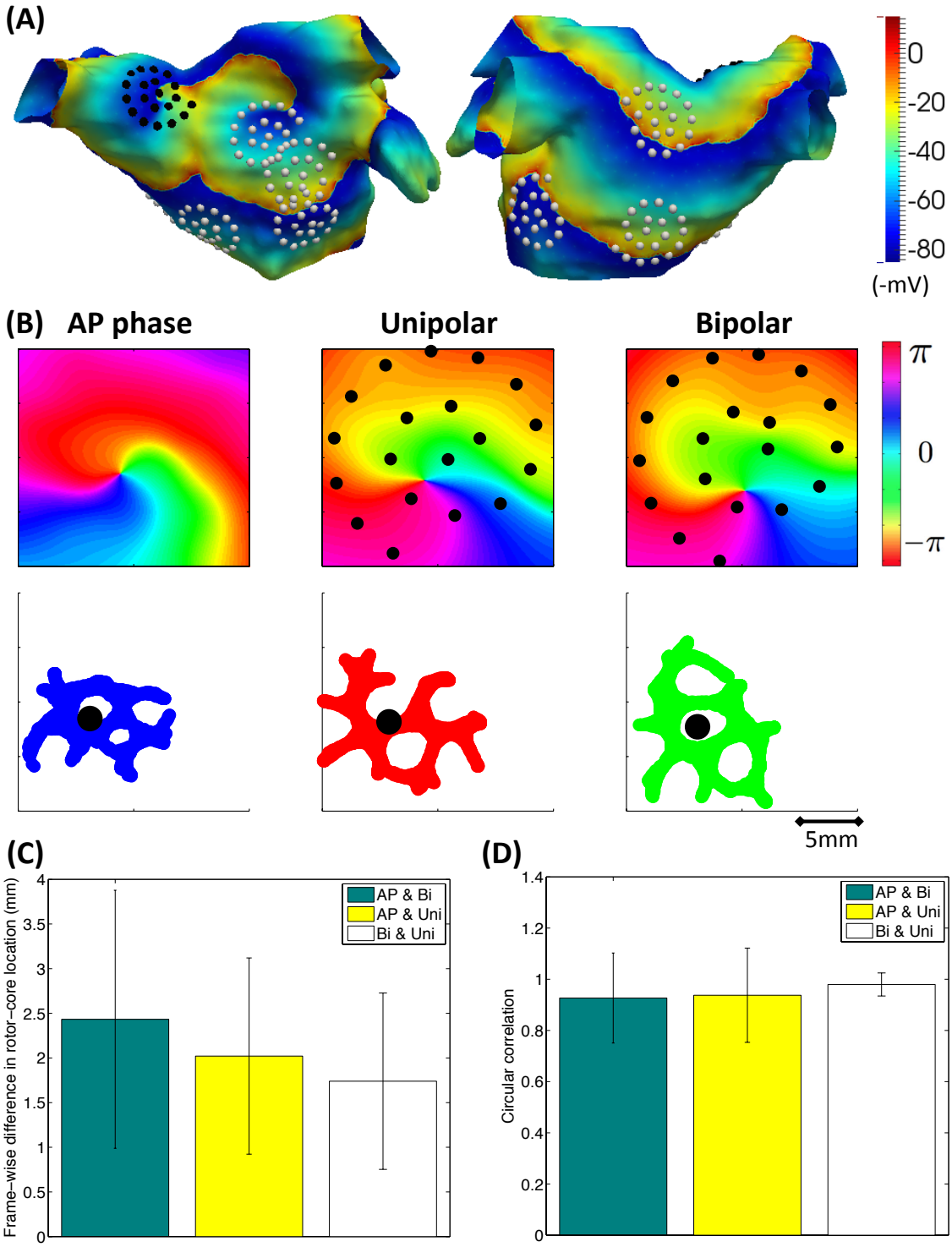

Figure 6.41: Differences in wavefront dynamics and PS positions computed using unipolar electrogram, bipolar electrogram and AP data were not clinically relevant in an MRI-derived left atrial simulation with two rotors. (A) Isopotential map with distribution of afocus catheters analysed. (B) Isophase maps and rotor trajectories for black catheter in (A) assessed using AP phase, unipolar electrogram phase and bipolar electrogram phase. (C) Mean frame-wise differences between rotor-core measured using different data types were small (< 4mm ablation catheter). (D) Circular correlation coefficients measured across nine catheters are high.

6.6 Discussion

6.6.1 Overview

In this chapter, methods were presented for phase mapping of unipolar electrogram and bipolar electrogram signals, which were initially developed for and tested on simulated data, and then adapted for and applied to experimental and clinical electrograms. Unipolar and bipolar phase were seen to perform similarly to AP phase in simulated data, and agreed well with each other in experimental data. In clinical data, phase calculated from unipolar and bipolar signals did not exhibit as strong a correlation, which is expected as the clinical signals are more complex and include far-field ventricular activation.

6.6.2 Comparison to action potential phase calculations

Whereas action potential phase captures both the depolarisation and repolarisation as separate stages of the action potential, electrogram phase is considered here to indicate activation and then progression within the cycle between activations. This is because stages of repolarisation are more difficult to identify for electrograms during AF. In addition, filters are required in order to make the electrogram data more sinusoidal so that phase analysis can be applied.

6.6.3 Comparison of simulated, experimental and clinical algorithms

Algorithms were first developed for calculating the phase of unipolar and bipolar electrograms in simulated data, for which it was possible to compare the calculated phase singularity locations to those from action potential data. These results showed that unipolar and bipolar phase can be used instead of action potential phase. However, the algorithms developed in simulated data required adaptations for use on experimental and clinical data. The most notable point was that the unipolar algorithm for simulated data, which determined activations by low-pass filtering the data at 10Hz and tagging activations based on amplitude, was not appropriate for experimental or clinical data. This was because of several reasons: filtering at 10Hz did not capture details of the fast depolarisation of MEA data; noise may be of larger amplitude than activations; unipolar activation assignment is gradient based rather than amplitude based, and as such a method assigning activations based on gradient is preferable. This motivated the development of a new unipolar phase calculation method that used the filters and steps applied to calculate bipolar phase

to the derivative of the unipolar electrogram. The final clinical methods were tested in simulated data, to provide validation against action potential phase.

The sequence of filters used in this study are commonly used for analysing bipolar electrograms. There are studies that investigate how these filters affect the bipolar electrogram and its frequency content (Castells et al., 2014). However, the application of these filters prior to phase analysis is novel, to the best of my knowledge. These filters make the signal more sinusoidal for phase analysis and also have the advantage that peaks within the filtered signal represent peaks in magnitude of the original signal, which agrees with the definition of activation time for bipolar electrograms. Using the same sequence of filters on the capped derivative of the unipolar electrograms worked well since peaks of maximum negative gradient were selected as activations. Use of these filters enabled the amplitude based approach of Bray and Wikswo (2002a) to be used to calculate phase.

6.6.4 Comparison with other published methodologies

Methods for assigning activation times

In this work, deflections were tagged based on a window length threshold. Alternatively, Ng et al. (2014) propose a technique for estimating cycle length from bipolar electrogram data in which deflections were tagged in order of decreasing amplitude until the mean and median cycle lengths were approximately equal. For the clinical data presented in this chapter, the method of Ng et al. (2014) was compared to the window length approach used for the analysis in this chapter on a subset of electrograms. The deflections chosen overlapped in most cases, as the window length was chosen to be close to the AF cycle length. In some instances, the approach of Ng et al. (2014) did not find a set of deflections for which the median and mean criteria were met in our data, in which case the window length approach was used by default.

Other approaches for assigning activation times to complex electrograms are discussed in Section 1.11 and these could be used for deflection tagging in order to calculate phase, to improve the robustness of this step of the algorithm. For example, the non-linear energy operator (Kaiser, 1990) could be used to guide which deflections to include in the bipolar phase calculation (see Section 1.11.3). Cross-correlation techniques may be challenging to apply in fibrillatory data due to the variation in morphology and degree of fractionation (see Section 1.11.4). It would be interesting to compare the effects of using each of these techniques for deflection tagging to the window length approach used in this chapter.

In addition, template matching is a technique for assigning activation times that works by comparing electrogram complexes to a library of deflection morphologies, for which a correlation function indicates the closeness of the signal to any given template (Houben et al., 2006; Houben and Allessie, 2006; Treo et al., 2013). Incorporation of this technique into the tagging deflections component of the phase calculation may improve the ability of the phase to capture true activations.

One challenge associated with the work presented here was determining what to do about uncertainty in activation times that occur in fractionated areas of the electrograms. Some studies reject fractionated electrograms from their analysis, or assign times of these signals manually depending on the surrounding electrograms (Ghoraani et al., 2013). The quantity of data analysed means that a manual approach was not feasible for the work in this chapter; however, the algorithm could be extended to calculate the local fractionation of a signal, and in cases of high fractionation, assign activation times automatically as an average of neighbouring electrodes.

Using phase to investigate wavefront dynamics

Phase was used in many ways to investigate wavefront dynamics in this chapter, including assessing the distribution of phase singularities and for tracking wavefronts. In addition, activation time maps were constructed from isophase values, as an alternative to tagging the original voltage signal. The approach of assigning activation at a constant value of a scalar field, such as phase angle, was also used by Mourad and Nash (2007) who developed a method for measuring conduction velocity that can be used with any scalar field for which a constant value represents activation.

The technique used in this chapter determines activation wavefronts by locating pixels at a constant phase value and takes the middle pixel along the line. Other methods have been developed for determining activation wavefronts; for example, Kay and Gray (2005) identify wavefronts using an isopotential line technique, applicable for transmembrane voltage data, and join them using a parametric spline. Their technique has the advantage that the conduction velocity can be defined analytically as normal to the spline. However, tracing an isopotential value is not appropriate for clinical data, which is very variable in amplitude; in addition the data are too noisy and the resolution is too low to perform a satisfactory spline fit. Thus our method is more appropriate for the clinical data used in this study.

Nanthakumar et al. (2004) define pixels as being part of an activation wavefront if the derivative with respect to time at that pixel is less than -0.25 at any point in a 15ms window of the time point, enabling the investigation of wavefronts during VF.

This method requires clean signals, or a reasonable amount of electrogram filtering, in order to ensure that the derivative is faithful to the signal. Their method is also expected to be applicable to the data used here.

Comparison with other methodologies for calculating phase

There are multiple clinical studies that use phase to assess rotational activity, including Haissaguerre et al. (2013) who use unipolar phase for identifying rotational activity from ECGi vest data, and Narayan et al. (2014) who use phase of unipolar and bipolar electrograms to identify rotors. However, to the best of my knowledge, there are no other published methodologies for calculating bipolar electrogram phase at the time of writing.

Kuklik et al. (2014) derive a sinusoidal recomposition method for atrial unipolar electrogram phase mapping in which the signal is first represented as a sum of sinusoidal wavelets of amplitude proportional to the negative slope of the electrogram. They include the additional criterion that a wavelet is only created if the derivative of the signal is negative. This sinusoidal reconstruction behaves well for phase mapping using the Hilbert Transform, and captures the timings of traditionally defined activation, because it is based on the size of the negative electrogram derivative. Wavefront maps constructed using activation times from phase and from voltage were compared and a good correspondence is seen. They also show that their method is superior to calculating the phase of the raw electrogram, where problems are hypothesised to arise due to the long isoelectric line between deflections. A similar phenomenon is noted by Pashaei et al. (2015) in which incorrect phase information arose in instances for which there were long periods between beats.

The method presented in this chapter also captures activation times at peaks of negative derivative. Problems with incorrect phase assignment between beats were not observed. In addition, the filtering and normalisation led to a sinusoidal signal of suitable amplitude and mean. The method developed here also shows a reasonably close correspondence with bipolar phase because the same sequence of filters and phase calculation techniques were applied to the bipolar electrogram that were applied to the derivative of the unipolar signal. Similar to the approach of Kuklik et al. (2014) in which wavelets were only generated where there is a negative gradient, the gradient of unipolar electrograms was capped at zero, before filtering, as this also prevented the algorithm from assigning activation at locations of steep positive gradient. It would be of interest to compare results from their sinusoidal recomposition technique to the techniques developed in this chapter.

For the method of Kuklik et al. (2014), the period of each sinusoidal wavelet is

equal to the mean of the cycle length of the signal. Their method has the disadvantage that it may not work well in the situation of varying cycle length. The method developed in this chapter also uses a window length in order to tag deflections and so may suffer similar limitations. A combination of window length and amplitude may be more appropriate.

Nash et al. (2006) analysed human VF dynamics using phase calculated from unipolar electrograms measured using an epicardial sock consisting of 256 electrodes. In their analysis, the used a quadratic detrending technique to ensure that the signal had mean zero, with activation times at voltage zero. This technique works well for unipolar electrograms during VF, however Kuklik et al. (2014) state that this technique may not perform as well on unipolar AF electrograms due to the longer isoelectric line. Umapathy et al. (2010) provide an extensive review of phase mapping techniques for electrogram data, although no methodology specific to atrial electrograms are presented.

Umapathy et al. (2008) also calculated phase from a monolayer of HL1 cells, demonstrating the suitability of the experimental model for phase analysis. However their phase analysis used pseudo-electrograms constructed from optical mapping data, rather than measured electrograms. An advantage of this is that optical mapping provides high resolution data; however, a disadvantage is that it does not use real electrograms. A comparison of recorded electrograms and pseudo-electrograms is of interest, as is the difference between phase calculated from these pseudo-electrograms to phase from the optical mapping data itself. Simultaneous optical mapping and MEA recordings would be required for this comparison.

Other methods for identifying rotor core location

In this chapter, the rotor-core location was determined based on phase singularity location. Other techniques based on features of the electrogram have been proposed for identifying rotor core locations, including Shannon entropy (Ganesan et al., 2013). Rottmann et al. (2014) compared different methods for estimating rotor tip location to the traditionally used phase singularity method, including local activation times, peak-to-peak amplitude (minimum at the rotor core), steepest negative slope in unipolar electrograms (maximum at the rotor core) and approximate entropy (maximum at the rotor core). Becerra et al. (2014) also used approximate entropy for rotor location, finding that accuracy reduced when the electrode resolution is reduced. Ganesan et al. (2015) also propose a method for moving a multipolar catheter towards a rotational source based on the location of the earliest activation time within the catheter. Ghoraani et al. (2013) investigated the existence of lo-

calised rotational in the left atrium and then determined whether CFAE and low voltage co-localised with these areas. Rotational activity in their study was defined for a circular catheter to be the sequential activation of bipoles, and these sites were common in persistent AF, but transient, and so unstable. It would be of interest to compare the techniques developed in this chapter to those in the literature.

6.6.5 Limitations and future work

The techniques developed in this chapter could be combined with the focal source estimation techniques developed in Chapter 3 in order to aid rotor tip localisation in a clinical environment. This approach would circumvent the problem of not being able to detect rotor-core location in the instance that the catheter is not placed over the rotor-core. This is discussed in more detail in the Conclusion, Chapter 8.

The techniques developed in this chapter could be used to overcome the major challenge in applying the CV algorithm to clinical AF data, which is picking a suitable time window for analysis, in which there is a single macroscopic wavefront. This could be achieved by identifying likely wavefronts, and the activation times of the electrodes that the wavefront passes over can then be defined within a window of time spanning the wavefront. Using these electrode locations and activation times as inputs for the CV and focal source estimation algorithm would then give an indication of the location that the wave originated from. In addition, it would overcome the limitation of the phase mapping algorithm, which is that it needs to be over a rotor core in order to detect it, since the focal source location estimation algorithm could guide the catheter towards the focal source, and once over the focal source or rotor core location, phase mapping could be performed. This circumvents an intrinsic limitation of local mapping.

The wavefronts calculated using the phase technique presented in this chapter could be further analysed using methods from the literature to assess the similarity of activation wavefronts. For example, Rogers et al. (1997) developed a technique for classifying the repeatability of VF wavefront patterns by computing the similarity between isolated wavefronts and clustering this information. They then defined a measure called *multiplicity* to be the numbered of clusters required to represent 90% of the wavefront directions.

One question not addressed in this chapter is to what extent differences in the results of the bipolar electrogram phase with different electrode spacings in the simulated data are due to differences in the electrogram morphology with changes in electrode spacing, compared to the effects of reducing the resolution.

One potential technique to improve the method would be to use the unipolar

and bipolar phase in tandem, such that time segments in which the unipolar and bipolar phase agree represent correctly tagged deflections, and times for which they disagree indicate that at least one of the electrograms is incorrectly tagged. Bipolar electrograms were observed to be less noisy than unipolar electrograms, and as such bipolar phase is hypothesised to give a more reliable representation of the wavefront dynamics. Unipolar electrograms could then be used to define activation time of an identified complex more accurately. The activation times calculated using phase assigned to fractionated electrograms should be compared to activation times chosen by an experienced clinician.

Chapter 7

Assessing the effects of spatial resolution on wavefront dynamics

7.1 Introduction

There is currently no consensus on the predominant mechanism for AF in humans. Various mechanisms have been proposed, which were based on recordings from modalities with different spatial scales, densities and resolutions, and it is possible that these differences could influence observations and hence the proposed mechanism. One example of a recording catheter used in clinical ablation cases is a 64-pole basket catheter, which gives simultaneous measurements from much of the endocardial surface, affording global coverage at a low resolution. Narayan et al. (2012b) used this basket catheter to identify rotors and focal sources, which were found to be stable, within a localised region for thousands of cycles (Swarup et al., 2014). A second recording modality is a noninvasive mapping technology consisting of 252 body surface electrodes, known as an ECGi vest (Haissaguerre et al., 2013). Using this technology, rotors were identified, but found to be transient, lasting at most eight rotations (Haissaguerre et al., 2014b). A third modality is a small high-resolution mapping device. Using this catheter in a human epicardial mapping study, Allessie et al. (2010) found no evidence for the presence of stable foci or rotors, and instead proposed a novel theory in which the endocardium and epicardium of the atrium become electrically dissociated and epicardial breakthrough leads to fibrillatory waves (de Groot et al., 2010).

Differences in the proposed mechanistic basis for human AF could also be partly due to the different methodologies used to analyse the wavefront dynamics. As well as providing various resolutions, data are analysed using many different techniques to understand the activation patterns in fibrillation. One such technique is phase

mapping in which phase singularities, which occur at the centres of rotational activity and the ends of wavefronts, are tracked to investigate wave dynamics. Phase mapping was originally developed for basic science optical mapping data, and has more recently been applied to unipolar electrogram VF data (Nash et al., 2006). In addition, phase mapping has been used to analyse AF data from both the basket catheter (Narayan et al., 2012c) and ECGi vest technologies (Haissaguerre et al., 2013).

Another technique used to analyse wavefront dynamics is plotting isochronal activation time maps. These can be arranged into maps showing individual wavefronts, or wave maps, to analyse data from a high-density mapping array (de Groot et al., 2010). Alternatively, activation times can be converted to conduction velocity (CV) vectors, and properties of the CV vector field can be calculated, including the divergence and curl, provided measurements are sufficiently dense. Fitzgerald et al. (2005) hypothesised that the divergence of the CV field can be used to locate ectopic foci (sources) and wavefront collisions (sinks), while the curl can be used to identify central obstacles in reentrant circuits.

To assess the resolution of the recording points required to identify stable rotors and focal sources from activation time maps, Rappel and Narayan (2013) used a theoretical approach to provide requirements in terms of the spatial separation between arms of spiral waves or focal impulses: the spatial wavelength (shown in Fig. 7.1). They consider a square grid of regularly spaced measuring points, and find that the required resolution is a grid spacing of λ/N, where λ is the spatial wavelength and N is the desired number of isochronal regions. They then provide a clinical demonstration that the resolutions used in their study are sufficient. Possible limitations of this study are that these assessments are visual, use activation time maps only and consider the case of a single rotor or focal source. In addition, for an experimentalist to employ the resolution requirement of λ/N, an experiment-specific measure of λ and a general recommended value of N are required, but these were not provided.

In this chapter, we extend the work of Rappel and Narayan (2013) to use both phase mapping and activation time mapping to identify numerically simulated rotors and focal sources automatically, using computational algorithms. The accuracy and reliability of the automated identification were assessed as a function of resolution, for activation patterns with different spatial wavelengths. A technique to estimate the spatial wavelength, λ, was developed and demonstrated using a small number of data points. Spatial resolution requirements are given as a function of the wavelength of the rhythm for rotors and focal sources. In this way, a recommended value for the number of isochronal regions, N, required for a given accuracy is provided, so

that it can be used in experiments. We assessed the extent to which differences in observed wavefront dynamics are due to the spatial scale, density and resolution of data, as well as the variety of post-processing techniques used.

Resolution requirements were initially assessed for a regular grid in Sections 7.2, 7.3 and then tested on more realistic catheter arrangements in Section 7.4. As such, this work extends our preliminary studies into the effects of resolution on observed wavefront dynamics presented in the Appendix, Section A.1.5.

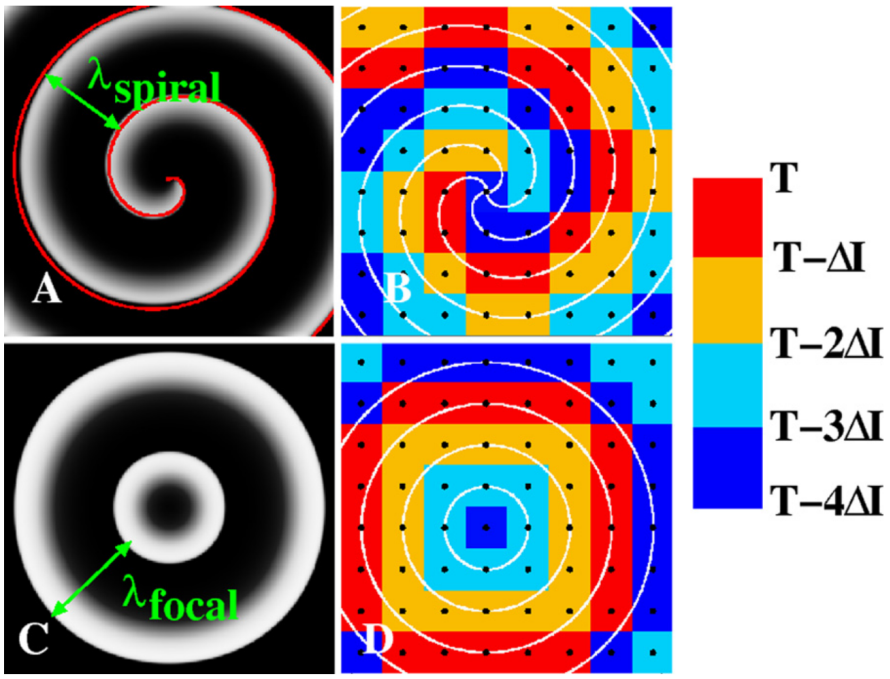

Figure 7.1: Definition of spatial wavelength and resolution requirement as a function of spatial wavelength. Spatial wavelength, λ, is defined as the distance between arms of a spiral wave (A) or focal source (C). The resolution required equals λ/N, where N is the number of isochronal regions. This is shown with $N = 4$ in (B) and (D). Reproduced from Rappel and Narayan (2013).

7.2 Methods for determining spatial resolution requirements assuming a regular grid

Spatial resolution requirements were initially determined as a function of spatial wavelength using regularly arranged grids of simulated data.

7.2.1 Simulation

To test the accuracy and reliability of the algorithms at different resolutions as a function of the spatial wavelength, simulations of rotors and focal sources were performed with a range of spatial wavelengths. The wavelength of a sinusoidal wave is the wave speed v divided by the wave frequency f, where the wave speed is taken to be constant. Spiral and focal source waves in the cardiac tissue simulations were assumed to be approximately sinusoidal, so that altering either the speed or frequency of propagation varied the spatial wavelength, via the formula $\lambda = v/f$.

For the simulations, the monodomain tissue model was used, with the Courtemanche et al. (1998) human atrial cell model to model the electrical activity, for a $10\,\text{cm} \times 10\,\text{cm}$ two-dimensional sheet of tissue. In order to change the conduction velocity (CV) of the wavefront (wave speed), the diffusion coefficient D was varied in the following monodomain equation:

$$\frac{\partial V}{\partial t} = -\frac{I_{\text{ion}} + I_{\text{stim}}}{C_m} + \nabla \cdot (D \nabla V)\,. \tag{7.1}$$

Three values of the diffusion coefficient were chosen ($D = 0.0005,\ 0.0010,\ 0.0015\,\text{cm}^2/\text{ms}$) based on preliminary simulations that showed that these values result in CVs within the physiological range observed in humans (Konings et al., 1994).

Electrical remodelling in AF was represented by reducing the ionic conductances of I_{to}, I_{Kur} and I_{CaL} (by 50%, 50% and 70% respectively), following Courtemanche et al. (1999). In addition, in order to modify the frequency of propagation for the spiral wave simulations, the conductance of I_{K1} was multiplied by 1.0, 1.5 or 2.0. Increasing this parameter has been shown to reduce the action potential duration (APD) and increase spiral wave stability in modelling studies (Pandit et al., 2005b).

Spiral wave simulations were run for parameter set combinations of the three diffusion coefficients with the three values of the I_{K1} conductance, resulting in nine different spiral wavelengths. This was repeated using the same parameter sets for a focal source stimulus with a stimulus applied at a frequency close to the corresponding spiral wave frequency. Initial conditions for each value of I_{K1} conductance and frequency were obtained by prepacing a single cell for 100 beats (Section 2.4.4).

The equations were solved using a finite-difference operator splitting scheme as in Qu and Garfinkel (1999), using Rush-Larsen for the gating variable ordinary differential equations (Rush and Larsen, 1978b), forward Euler for the voltage and ionic concentration equations, and an alternating-direction implicit scheme for the diffusion partial differential equation (Press et al., 2007), with a space step of 0.1mm and a time step of 0.01ms (see Chapter 2).

7.2.2 Data downsampling

To represent different spatial resolutions, subsets of voltage data were downsampled from the fully resolved case of 0.1mm to regular grid spacings ranging from 1mm to 25mm.

7.2.3 Phase singularity calculations

Phase of action potential data were calculated, and singularities were identified, using the techniques in Sections 2.10 and 2.11.

7.2.4 Phase interpolation

In order to assess the effects of spatial resolution on the observed wavefront dynamics, the phase calculated using the downsampled data (resolutions ranging from 1mm to 25mm) were interpolated to the full grid resolution (0.1mm) using the techniques detailed in Section 2.12 to perform exponential mapping and avoid the issue of interpolation across the phase angle branch cut. The data were interpolated using the Matlab `interp2` function, for which the following options were available as interpolation methods: linear, cubic or spline. The effects of the choice of method are shown in Fig. 7.2, where it can be seen that there are more false phase singularities detected for linear and cubic, than for spline interpolation. Hence in the work presented in this chapter, spline interpolation was used.

7.2.5 Conduction velocity

Conduction velocity measurements were used to locate focal sources using the divergence of the conduction velocity field (Section 7.2.6), and also in order to estimate the spatial wavelength. For each action potential, activation time was calculated as the point of maximum temporal gradient. The CV vectors were calculated by taking the differences of the activation times of four neighbouring points (Salama et al., 1994) (Fig. 7.3 B) and the magnitude indicated the conduction speed (Fig. 7.3 C). This finite difference method for calculating conduction velocity is explained in more detail in Section 1.12.2.

7.2.6 Divergence of conduction velocity

In order to locate focal sources in the conduction velocity field V, the divergence was calculated as in Fitzgerald et al. (2005) using the following equation: $\nabla \cdot V = \frac{\partial V}{\partial x} + \frac{\partial V}{\partial y}$. This is explained in more detail in Section 1.12.12. An outline of the

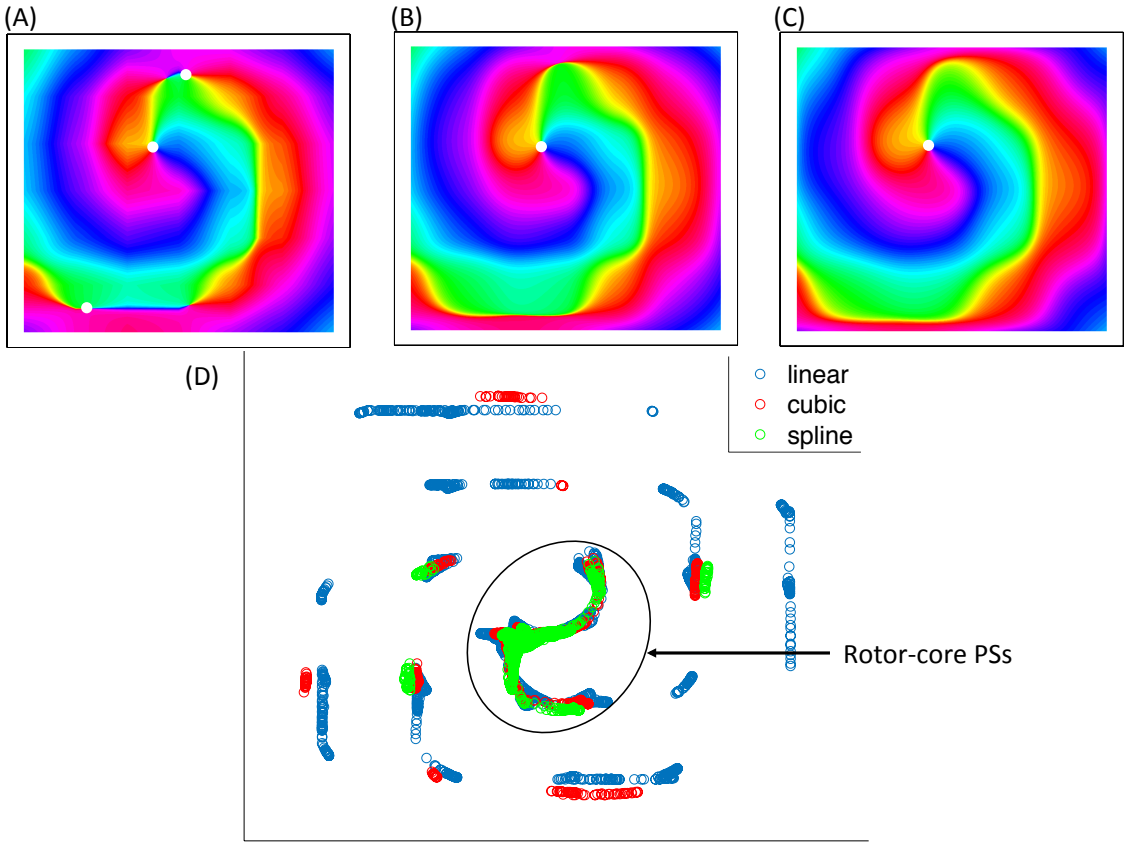

Figure 7.2: Comparison of isophase maps from linear, cubic and spline interpolation techniques: spline interpolation gives the fewest false detections. The data were interpolated from 15mm to 0.1mm resolution using: (A) linear, (B) cubic and (C) spline interpolation. There are extra phase singularities for the linear case compared to the cubic and spline interpolations. (D) Overall distribution of phase singularities; there are many more false detections for linear and cubic interpolations than for spline interpolation. These false detections tend to occur along the gridlines, outside of the marked rotor-core area.

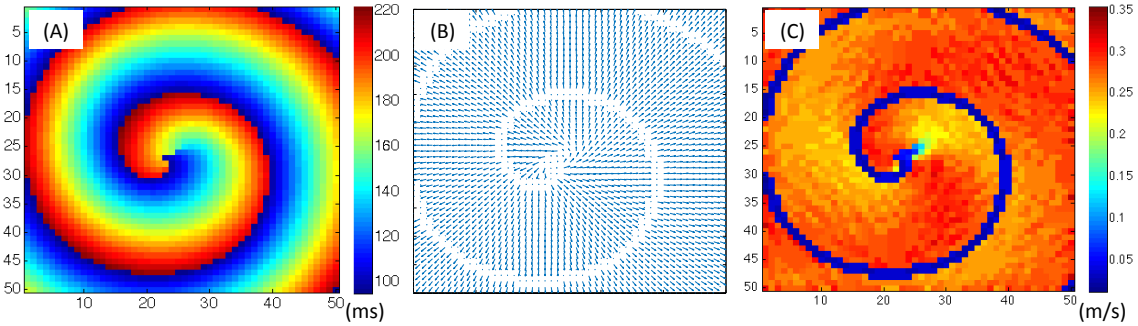

Figure 7.3: Finite difference technique for calculation of conduction velocity. (A) Activation time data at 2mm spacing; (B) CV vectors calculated by taking the differences of the activation times of four neighbouring points (Salama et al., 1994) (see Section 1.12.2). (C) The magnitude gives the conduction speed. In this example, the median conduction speed is 0.27m/s.

steps involved is shown in Fig. 7.4: the activation times (A) were downsampled to 2mm; an area corresponding to one focal beat was selected for analysis (B); the CV vectors were calculated as before and normalised (C); and the divergence of this field was calculated (D). The point of maximum divergence was used to identify the origin of focal sources, which is seen clearly in Fig. 7.4 (D). The CV vector field was normalised so that the divergence depended only on direction, and not speed.

For high resolution data (spacing below 2mm), the temporal resolution of 1ms limited the spatial resolution of the CV field because points closer together than 2mm may be assigned the same activation time measured to the closest millisecond. Hence, for these data it was necessary to downsample activation times to 2mm spacing (Figs. 7.3(A), 7.4(B)) before calculating CV vectors and the divergence.

For low resolution data (spacing greater than 2mm), the CV field was calculated as before (Fig. 7.5 (A), (B)). The components of the conduction velocity field V_x and V_y were then interpolated to the 2mm grid resolution and re-normalised to give the CV field in Fig. 7.5 (C); and finally the divergence of this field was calculated (Fig. 7.5 (D)). Hence, the final divergence field was at 2mm grid spacing for all initial data resolutions, to allow for comparison.

7.2.7 Calculating wavelength

To determine the relationship between spatial wavelength λ and required resolution (where resolution equals λ/N), the spatial wavelength was calculated using the full resolution data for each parameter set. For each spiral and focal source wave simulation, the wavelength was calculated using an automated algorithm that calculated the distance between arms of the spiral or focal source. For each frame that was

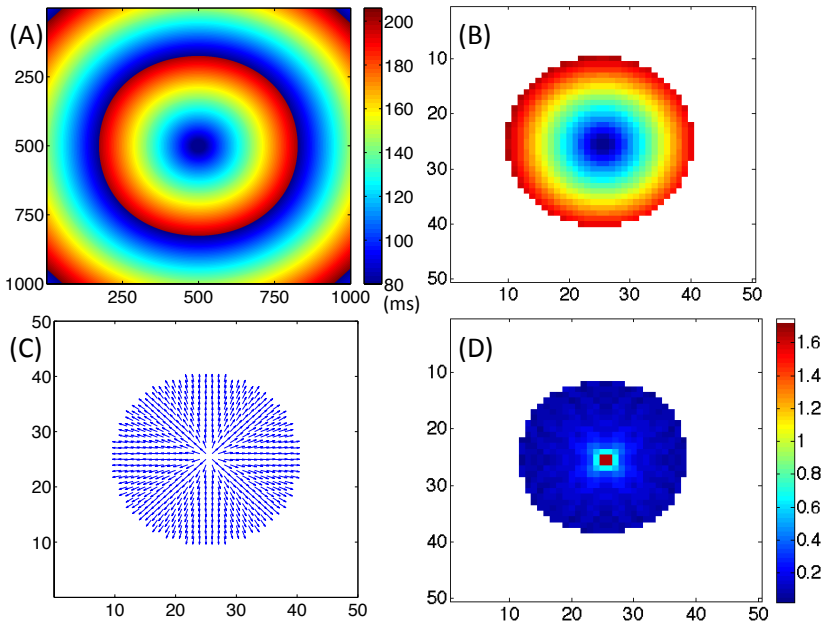

Figure 7.4: Steps involved in calculating divergence, where a peak is seen at the origin of the focal source. (A) Full resolution activation times; (B) activation times downsampled to 2mm and an area corresponding to one focal beat is selected for analysis; (C) CV vectors are calculated and normalised; (D) the divergence of this field is calculated. A peak is seen at the origin of the focal source.

analysed, an isopotential line was plotted (−60 mV). In order to create an acceptable isopotential line without interpolating the data, the method suggested by Kay and Gray (2005) was used, where points were selected for an isopotential line if firstly the potential of the node was less than the isopotential value and secondly between one and three of its four directly neighbouring nodes have an value greater than the isopotential value. Next the isopotential line was split into regions of positive and negative gradients. For spiral waves, the pixel where these meet was identified using a distance threshold (3-by-3 convolution operator) and taken to be the centre. Intersections of rays from this centre with the isopotential line with positive gradient were located, and in the instance that there was more than one intersection, the distance along the ray between points was stored. This was repeated every 10 degrees for frames every 10ms and the median and lower and upper quartile of these values were calculated. For focal sources, the calculation was similar but the centre was taken to be the point of maximum divergence. The method is demonstrated in Fig. 7.6.

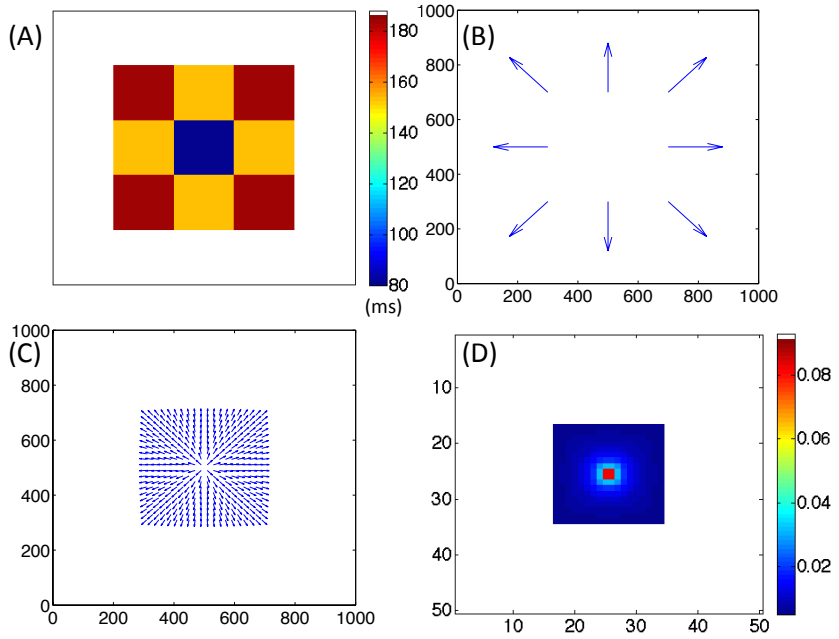

Figure 7.5: Calculation of the divergence of a downsampled focal source. (A) Activation time field in Fig. 7.4 is downsampled to 20mm spacing; (B) normalised CV vectors are calculated. (C) The velocity fields V_x and V_y are interpolated to give CV vectors at 2mm resolution. (D) Divergence; again the focal source origin is clearly identified from the divergence field.

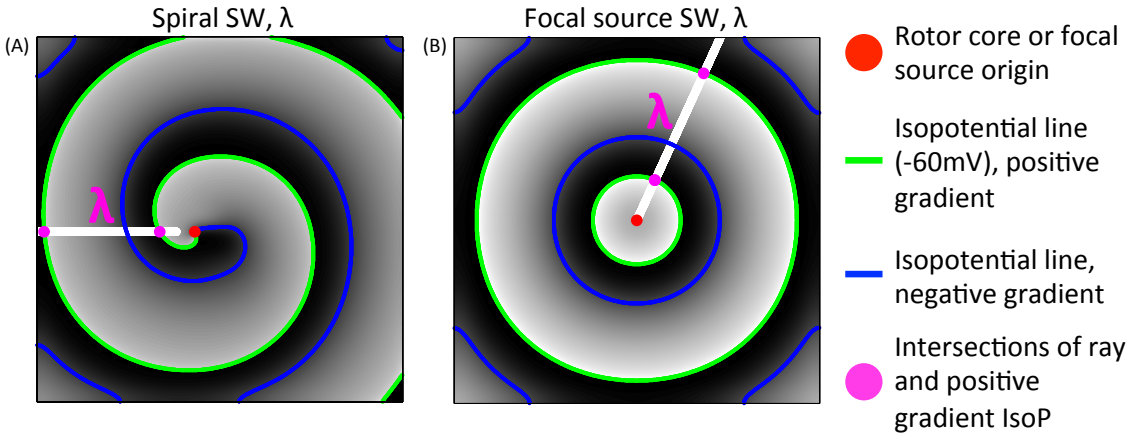

Figure 7.6: Calculation of the wavelength of a spiral (A) or focal (B) wavefront as the distance between isopotential lines. For the frame shown here, an isopotential line at -60 mV is traced, where positive gradient is shown in green and negative in blue. Intersections of the ray (white line), which extends from the phase singularity or focal source origin (red dot) to the edge of the domain, with the isopotential line are calculated (purple dots). In the case that there are two detections, the distance between the points, measured along the ray, is stored. This is repeated every 10 degrees and for frames every 10ms. The spatial wavelength (SW, λ) is taken to be the median of the stored values.

7.2.8 Estimating wavelength

In an experimental or clinical set-up, it is not possible to use the isopotential line method described in the previous section, and instead a method is developed here to estimate the spatial wavelength from limited data. In order to estimate the spatial wavelength, the CV and the wave period were calculated. The wave period is equivalent to the cycle length (CL).

The method used to estimate CV depends on the number and layout of recording points. For a regular grid of points, or in the case that the points were dense enough to get a reasonable interpolation, CV vectors were calculated using the method in Section 7.2.5. In the case of sparsely located, arbitrarily arranged points, the method developed in Section 3.2.6 was used to estimate CV. Briefly, the method works by fitting the parameters in an equation for the activation times of a circular wave measured at arbitrarily arranged points to the measuring locations and activation times. This CV equation works well for activation times on the same arm of a spiral, or circular ring of activation; however, the model breaks down when this is not the case. This is demonstrated in Fig. 3.10 and explained in Section 3.3.7. This places a limit on the diameter of the area over which CV is measured to be less than the wavelength. The wave period (cycle length) was estimated by calculating the average time difference between activation times (Fig. 7.7), and finally the spatial wavelength was estimated as the product of conduction velocity and cycle length.

The effects of the number of measuring points used to estimate wavelength were also investigated to give a recommended value for accurate and reliable measurement. To assess this, spatial wavelengths were estimated for between four and twenty measuring points from spiral wave simulations. These measuring points were random locations within a 2cm diameter box (chosen because high-density mapping catheters of 2cm diameter are typically used in human AF procedures, and this is less than the lowest spatial wavelength expected in human AF). The fits were repeated for ten choices of points, and for four locations of the box, to give forty trials. For each individual CV estimate, the activation times were chosen from a window shifted to give the fit with the lowest residual (Section 7.2.8, Fig. 3.10). The median CV of the forty estimates for twenty measuring points was used to calculate lower and upper limits to classify successful CV estimation for smaller numbers of points, with the lower limit taken to be the median CV minus 20% of the median CV and the upper limit taken to be the median CV plus 20% of the median CV. The proportion of the forty trials that were within these limits were calculated for each number of points and a threshold of 10% was used to define success or failure for each number of measuring points.

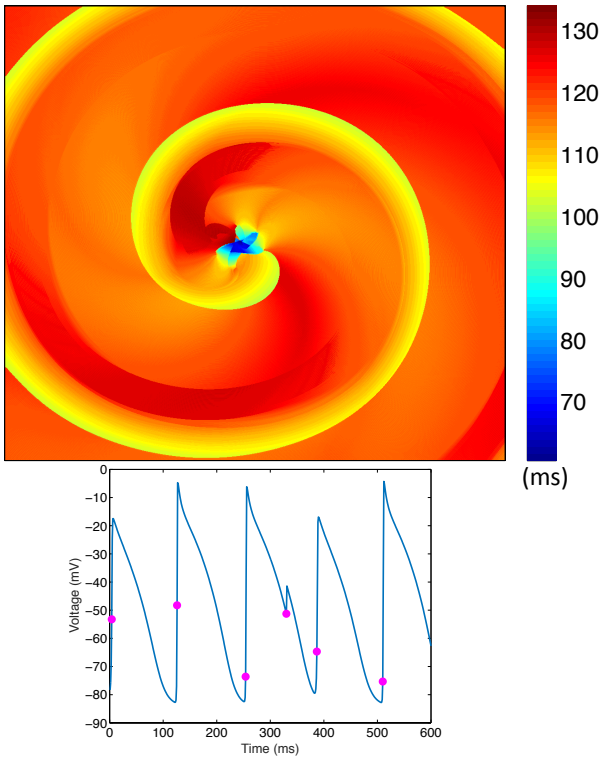

Figure 7.7: Estimation of median cycle length. Cycle lengths are shown as a spatial map (top), for which cycle lengths are calculated from activation times that are tagged using gradient thresholds (bottom). The median CL here is 117ms.

7.2.9 Selection criteria for determining required resolutions

Spiral wave (rotor) identification was assessed using three measures: visual identification; the amount of error in the centre of the rotor trajectory calculated using phase (*centre error*); and the number of false phase singularity detections. Fig. 7.8 demonstrates the centre error and number of false detections criteria for an example of a successful rotor core identification, as well as a failed identification. In the case of the error in the centre of the rotor trajectory, a 4mm threshold was used, such that errors below this count as a success, and errors larger than 4mm count as a failed identification using the centre error criterion. The value 4mm was chosen as it is the diameter of commonly used ablation catheters.

A methodology for determining an appropriate threshold for the number of permissible false detections was developed. This was necessary because using a simple percentage threshold does not contain information on the distribution of phase singularities, and as such does not indicate whether identification of the rotor core is likely to be possible. The developed method assessed the distribution of phase singularities by considering the number of phase singularities as a function of the distance from the downsampled rotor centre and plotting this distribution as a histogram. Again this score is binary and is termed a success when there is a single peak in the histogram, and a failure in the case that there are multiple peaks in the histogram. This is a sensible measure because a secondary peak of detections at a radii from the source may make it difficult to identify the true rotor core. The matlab function `ksdensity` was used in order to identify histogram peaks; an example of a single peak success and a double peak failure are shown in Fig. 7.8 C and F.

Focal source identification was assessed using two measures: visual identification; and error in centre location, identified using divergence. There were few false detections of positive divergence and so a measure of the number of false detections, equivalent to that for spiral waves and phase, was not appropriate.

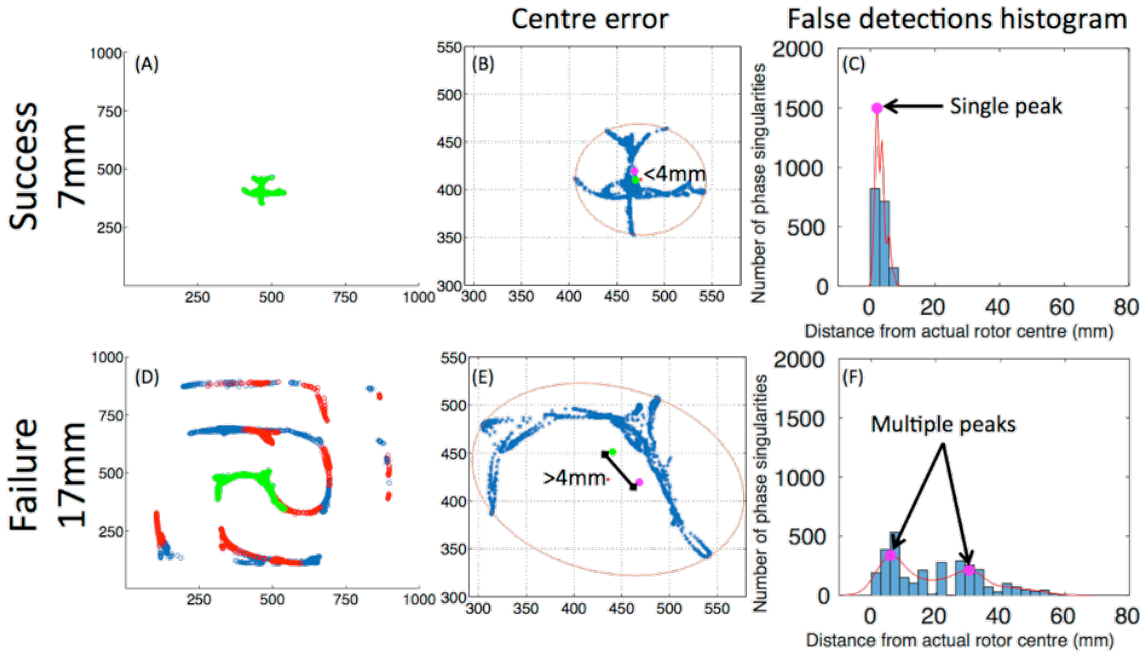

Figure 7.8: Methodology for defining success or failure of rotor core identification. In this example, the top row represents a successful rotor identification for all three criteria, whilst the bottom row represents a failure for all three criteria. This example is for $D = 0.0005\text{cm}^2/\text{ms}$, $g_{K1} = 0.09\text{nS/pF}$, where A-C are for 7mm spacing and D-F are for 17mm spacing. In this case, the rotor core centre location failed for 17mm spacing as it was greater than 4 mm (4.3mm, E), while it was within threshold for 7mm spacing (0.9mm, B). (The area of the bounding ellipse that contains the path marked out by the trajectory are 125.1, 439.5 mm^2 for 7 and 17mm respectively.) At 17mm spacing, this parameter set also failed the false detection threshold, as there were two peaks (marked by purple dots) in the histogram (F compared to C). This agreed with the percentage of false detections, which were 0.06% and 63.7%. (Other statistics are as follows: mean frame-wise error 3.4 ± 1.5, 7.9 ± 3.4mm; trajectory diameter 13.7, 27.5mm.)

7.3 Results for determining spatial resolution requirements, assuming a regular grid

Results are presented for the restitution characteristics of the parameters sets used to generate the tested range of spatial wavelengths, as well as the full resolution properties of the simulations. The results of estimating the spatial wavelengths of these simulations are then presented. Finally the resolution requirements, as a function of the spatial wavelength, are presented for both spiral waves and focal sources.

7.3.1 APD and CV restitution

The parameter sets used to generate the desired range of spatial wavelengths were determined based on the results of pacing in a one-dimensional cable. The parameters varied were the scaling factor for I_{K1} conductance and the diffusion coefficient. APD and CV restitution curves were calculated in order to find the range of APDs and CVs for each trialled parameter set. This enabled an estimate of the resulting wavelength in tissue, without running computationally demanding two-dimensional simulations.

The restitution curves for the nine parameter sets that were chosen for the resolution studies in this chapter are shown in Fig. 7.9 (combinations of diffusion coefficients of 0.0005, 0.001, 0.0015cm^2/ms with I_{K1} conductance equal to 0.09, 0.135, 0.18nS/pF). APD was found to depend on I_{K1} conductance but not on the choice of diffusion coefficient. CV was primarily affected by the diffusion coefficient, giving three families of restitution curves, although the I_{K1} conductance also had an effect.

7.3.2 Full resolution

The full resolution simulations represent the gold standard for each spatial wavelength. Differences in the rotor trajectories of each of the nine parameters sets were assessed, and the full resolution rotor trajectories are shown in Fig. 7.10. Doubling I_{K1} conductance from 0.09 to 0.18nS/pF roughly halved the rotor trajectory area for each diffusion coefficient (56.2%, 48.8%, 49.2% decrease in area for $D = 0.0005$, 0.001, 0.0015cm^2/ms). Increasing the diffusion coefficient threefold from $D = 0.0005$ to 0.0015cm^2/ms, approximately tripled the rotor trajectory area (173.6%, 204.7%, 217.4% increase in area for I_{K1} conductance, $g_{\mathrm{K1}} = 0.09$, 0.135, 0.18nS/pF, respectively). For these examples, rotor trajectory area is proportional to the diffusion coefficient and inversely proportional to I_{K1} conductance.

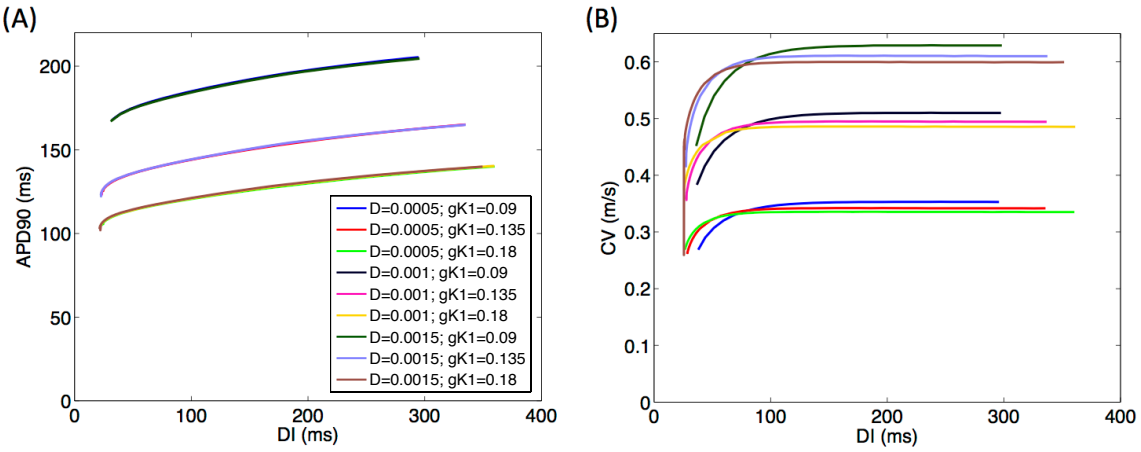

Figure 7.9: Restitution properties for a one-dimensional cable, where the parameter sets exhibit a range of APD and CV values seen in human AF. (A) APD restitution, where APD depended on I_{K1} conductance, and curves for the same I_{K1} conductance (but different diffusion coefficient) are seen to overlap; (B) CV restitution for the nine parameter sets (key as per A). These were calculated using the methods in Section 2.7.

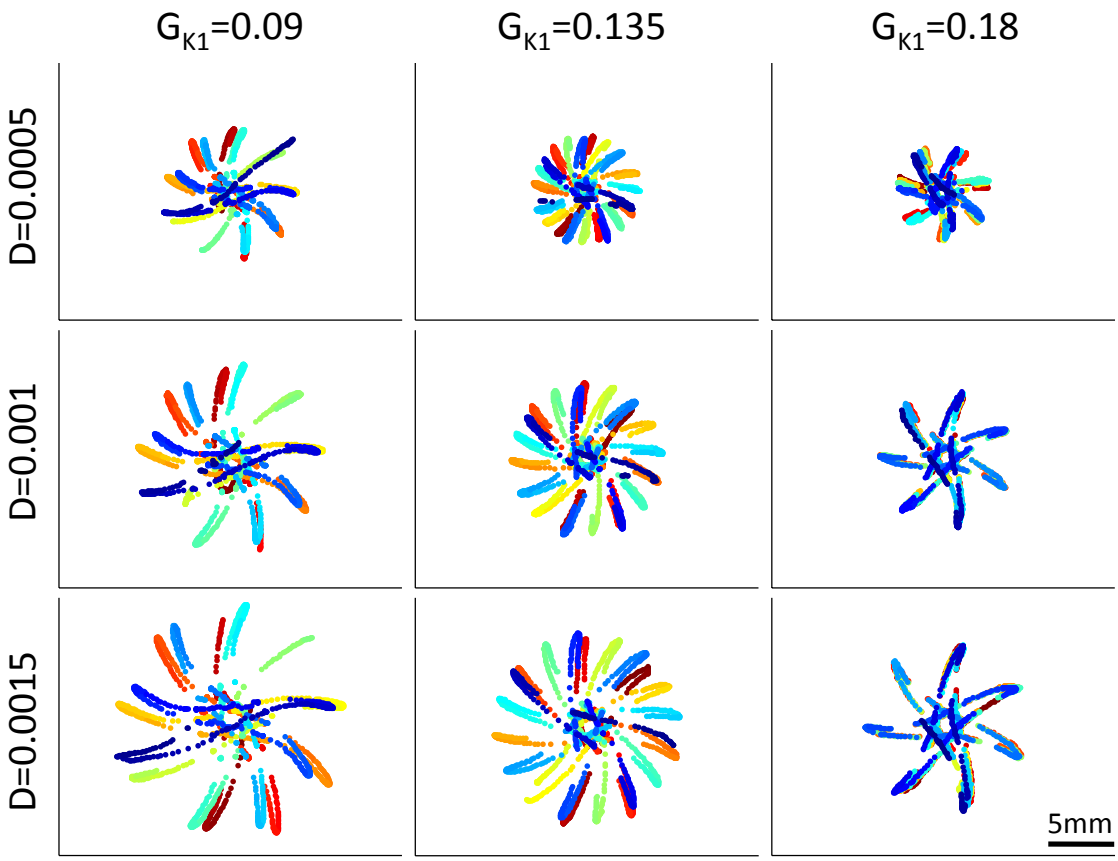

Figure 7.10: Full resolution rotor tip trajectories for the nine parameter sets. Areas of the bounding ellipse for each trajectory are as follows, from left-to-right: 160, 94, 70, 283, 188, 145, 439, 286, 223mm^2. Colour indicates time point during the simulation from blue through red.

7.3.3 Estimating wavelength

Wavelengths were initially calculated from the full grid of data using the isopotential technique (Section 7.2.7). The results for spiral wave simulations are shown in Table 7.1, and for focal source simulations in Table 7.2, in which results are quoted as median (lower quartile−upper quartile). Spiral wavelengths cover the range $33.56 - 78.32$mm, whilst focal sources cover the range $32.00 - 62.54$mm.

There were differences between the spatial wavelengths of the spiral wave simulations and focal source simulations for equivalent spatial wavelengths. These were particularly evident for $g_{K1} = 0.09$nS/pF and $g_{K1} = 0.135$nS/pF and occured because the cycle length of pacing applied in the focal source simulations was different to the spiral simulation periods. It was necessary to apply a pacing protocol with a longer cycle length in the focal source simulations because it was not possible to capture focal source pacing at the cycle length of the average spiral wave period, since the tissue was still refractory. In particular, for $g_{K1} = 0.09$nS/pF, the focal source pacing period was 20ms longer than the spiral wave cycle length, while for $g_{K1} = 0.135$nS/pF, it was 15ms longer, leading to longer wavelengths. The wavelengths for $g_{K1} = 0.18$nS/pF were similar between spiral and focal source simulations.

The wavelengths for three of the focal source parameter sets were too large to be measured within the 10cm by 10cm sheet used in these simulations (> 70mm, shown as NA in Table 7.2). The domain size was chosen based on a typical left-atrial surface area (100cm^2) and the parameter sets were chosen to give physiological wavelengths; thus, this is an expected limitation.

The method developed for estimating wavelengths using limited data was also applied and the results from this were compared to the wavelengths calculated using the full resolution isopotential method. Wavelengths were estimated as the product of CV and CL (Section 7.2.7); shown in Tables 7.1, 7.2.

Table 7.1: Wavelengths for spiral wave simulations. Top lines: full resolution calculated wavelengths (median and interquartile range); bottom lines: estimated wavelength (CV × CL).

D (cm^2/ms)	$g_{K1} = 0.09$ nS/pF	$g_{K1} = 0.135$ nS/pF	$g_{K1} = 0.18$ nS/pF
0.0005	**46.3** (44.5-49.0) 0.25m/s × 181ms=**44.9mm**	**38.0** (36.2-39.9) 0.26 × 142 = **36.6**	**33.6** (32.2-34.9) 0.27 × 117 = **31.7**
0.0010	**65.0** (62.7-68.9) 0.34 × 180 = **61.7**	**53.5** (51.3-56.5) 0.37 × 141 = **52.1**	**47.7** (46.1-49.6) 0.38 × 121 = **46.4**
0.0015	**78.3** (78.3-78.3) 0.42 × 182 = **76.7**	**66.6** (63.7-70.0) 0.46 × 141 = **65.6**	**58.5** (56.5-60.8) 0.47 × 121 = **56.7**

Table 7.2: Wavelengths for focal source simulations. Top lines: full resolution calculated wavelengths (median and interquartile range); bottom lines: estimated wavelength (CV × CL).

D (cm^2/ms)	$g_{K1} = 0.09$ nS/pF	$g_{K1} = 0.135$ nS/pF	$g_{K1} = 0.18$ nS/pF
0.0005	**51.1** (50.3-51.8) 0.26m/s × 203ms=**51.9mm**	**44.3** (43.9-44.6) 0.28 × 157 = **44.4**	**32.0** (31.7-32.2) 0.26 × 121 = **31.8**
0.0010	NA 0.36 × 202 = **72.3**	**62.5** (62.4-62.6) 0.40 × 156 = **62.4**	**45.1** (44.5-45.6) 0.38 × 122 = **45.9**
0.0015	NA 0.43 × 203 = **88.1**	NA 0.50 × 156 = **77.4**	**53.2** (52.1-55.0) 0.47 × 122 = **56.7**

For all spiral simulations, all wavelengths were underestimated compared to the full resolution median value (see Table 7.1). Overall, the full resolution estimates closely matched the calculated spatial wavelengths (Fig. 7.11). Comparing the estimated wavelengths to the full resolution wavelengths in detail, six of the nine estimated wavelengths were in the middle 50% of the full resolution wavelengths. Wavelengths were underestimated by between 1.52% and 5.54% compared to the full resolution median wavelength, with a mean difference of 3.25%. The spiral wavelengths that were too large to measure using the isopotential method are estimated as 72.28, 88.08 and 77.39mm. For focal source simulations, estimated wavelengths differed from the full resolution median wavelength by between −0.72% and 6.66%, with a mean error of 1.36%.

The dependence of the estimated spatial wavelength on the number of measuring points used for the estimation was tested for one short wavelength spiral wave simulation, one long wavelength spiral wave simulation, and one focal source simulation. For the short wavelength simulation ($D = 0.0005 cm^2/ms$, $g_{K1} = 0.18 nS/pF$, 33.56mm): using six measuring points, 20% of CV estimates were outside the CV range allowed ((median CV) ±(20% of median CV)), while using seven measuring points this dropped to 2.5%, thus here seven points were required. For the longer wavelength simulation ($D = 0.0015 cm^2/ms$, $g_{K1} = 0.09 nS/pF$, 78.32mm): using five measuring points 10% of CV estimates were outside the CV range allowed, while using six measuring points this dropped to 0%, thus here six points were required. This suggests fewer points are required for measuring longer wavelengths. For focal sources, for a wavelength of 53.19mm ($D = 0.0015 cm^2/ms$, $g_{K1} = 0.18 nS/pF$), seven points were required (12.5% outside range for six points; 7.5% outside range for seven points), suggesting resolution requirements are similar for spiral waves and focal sources. Close to the rotor core, the method broke down irrespective of the number of points used.

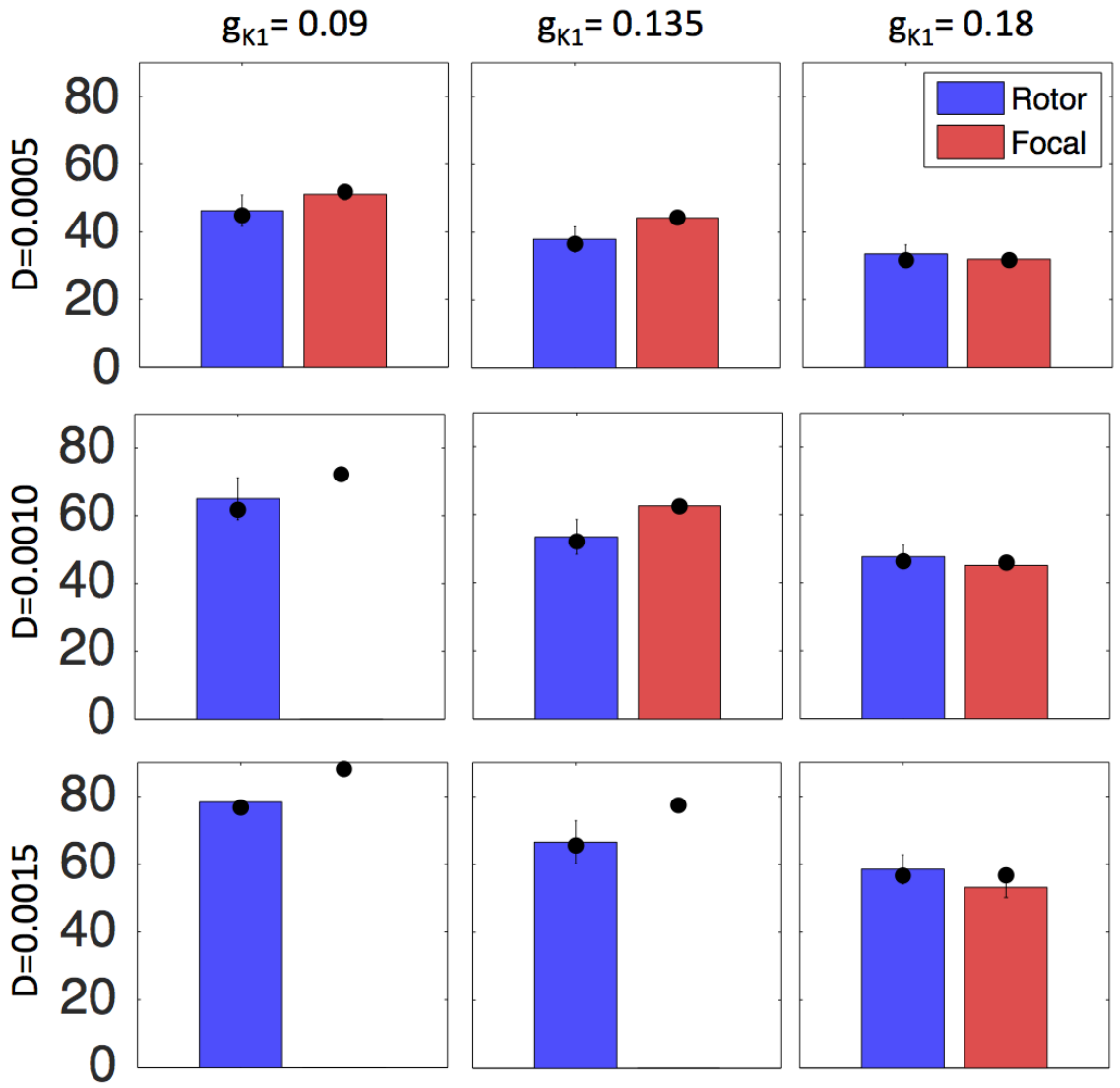

Figure 7.11: Estimated spatial wavelengths agree well with calculated spatial wavelengths and vary between parameter sets. Black dots indicate the estimated spatial wavelength for rotors (in blue) and focal sources (in red).

7.3.4 Error upon downsampling: spiral wave

To quantify how the error in estimated spiral wave dynamics changes with resolution, the following were assessed: visual identification; the error in mean rotor tip location compared to the full resolution mean location (*centre error*); the distribution of the number of false phase singularity detections as a histogram. A threshold of 4mm was used for the permissible distance error in the mean rotor core location of the down sampled spiral from the mean location of the full resolution trajectory, which was chosen because a 4mm diameter catheter is commonly used for ablation (for example, St. Jude Medical Therapy catheter), so this is a sensible cut-off threshold for success in rotor core location. Examples in which the rotor core location was identified successfully using the identification criteria are shown in Fig. 7.8 B, E. An example showing the critical resolution for which the rotor core location increased above the 4mm threshold is shown in Fig. 7.12.

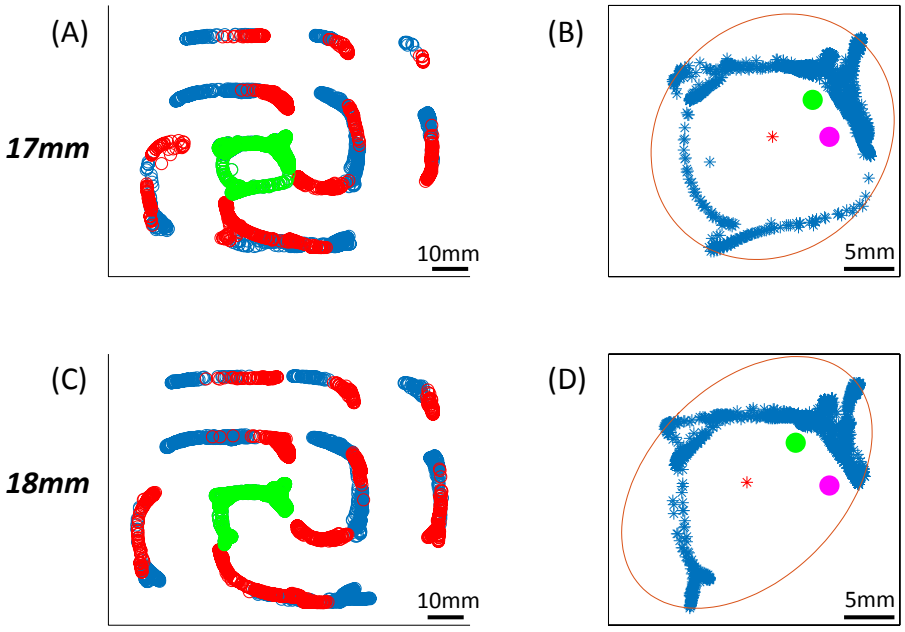

Figure 7.12: Phase singularity locations and rotor trajectories to show the resolution at which the error in the centre location exceeds the threshold. At a grid spacing of 17mm the centre of mass error is less than 4mm, while at a grid spacing of 18mm it is greater and so counts as a failure. (A), (C) rotor trajectory in green with other phase singularities in red and blue, by chirality. (B), (D) centre for this resolution in green, and full resolution centre in purple.

For each parameter set, the resolution for which visual identification failed were also found by watching the isopotential plots over time to determine if spiral wave activity could be identified with reasonable certainty. Examples to show how phase

singularity distributions change with resolution can be seen in Figs. 7.13, 7.14. At fixed point spacings, there are clear differences in the number of false detections for the different parameter sets; for example, at 15mm only the shorter wavelengths have a significant number of false phase singularities. An example showing the critical resolution for which the false detection histogram first has two peaks is shown in Fig. 7.15.

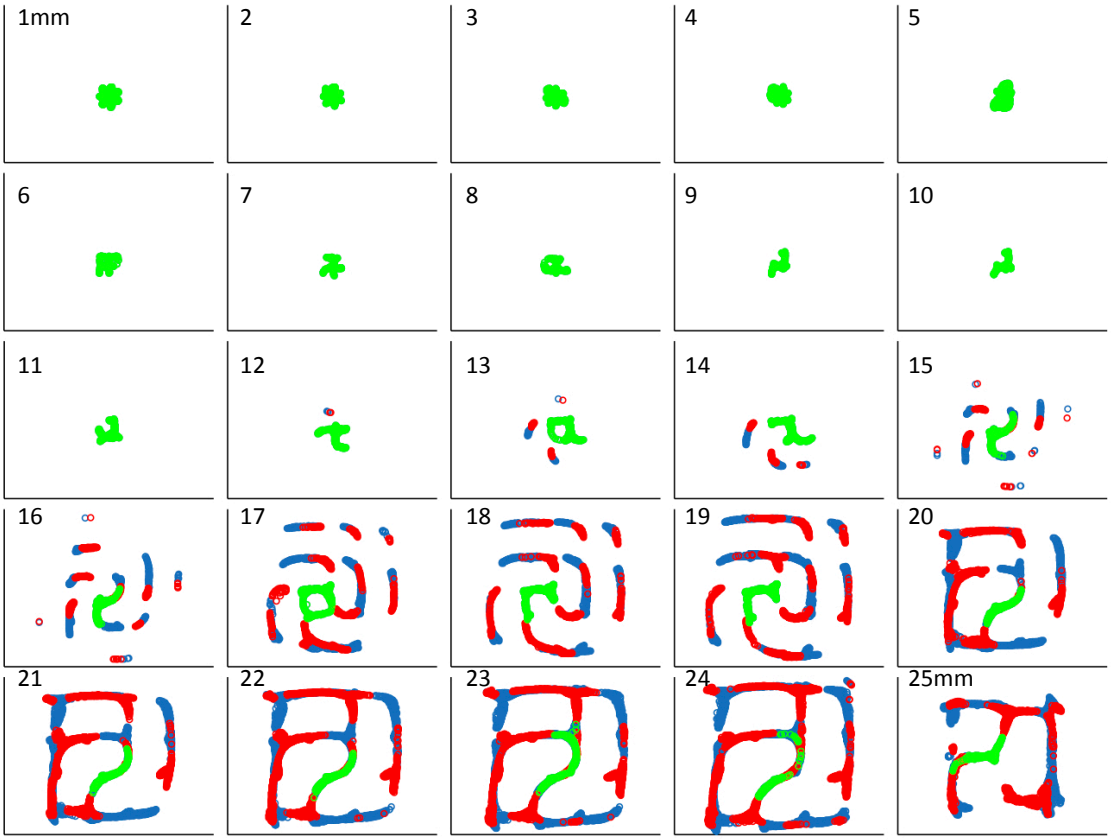

Figure 7.13: Number of false phase singularity detections increases as grid spacing is increased from 1 to 25mm, representing increased down-sampling. These results are for $D = 0.001\text{cm}^2/\text{ms}$ and $g_{K1} = 0.18\text{nS/pF}$, where the wavelength is 47.7mm. Visual identification requires 19mm and the distribution of phase singularities is seen to change from 19mm to 20mm; compare to: successful centre identification requires 17mm (Fig. 7.12); false detections histogram requires 16mm (Fig. 7.15). Green circles are rotor core phase singularities; blue and red circles are false phase singularity detections, coloured by chirality.

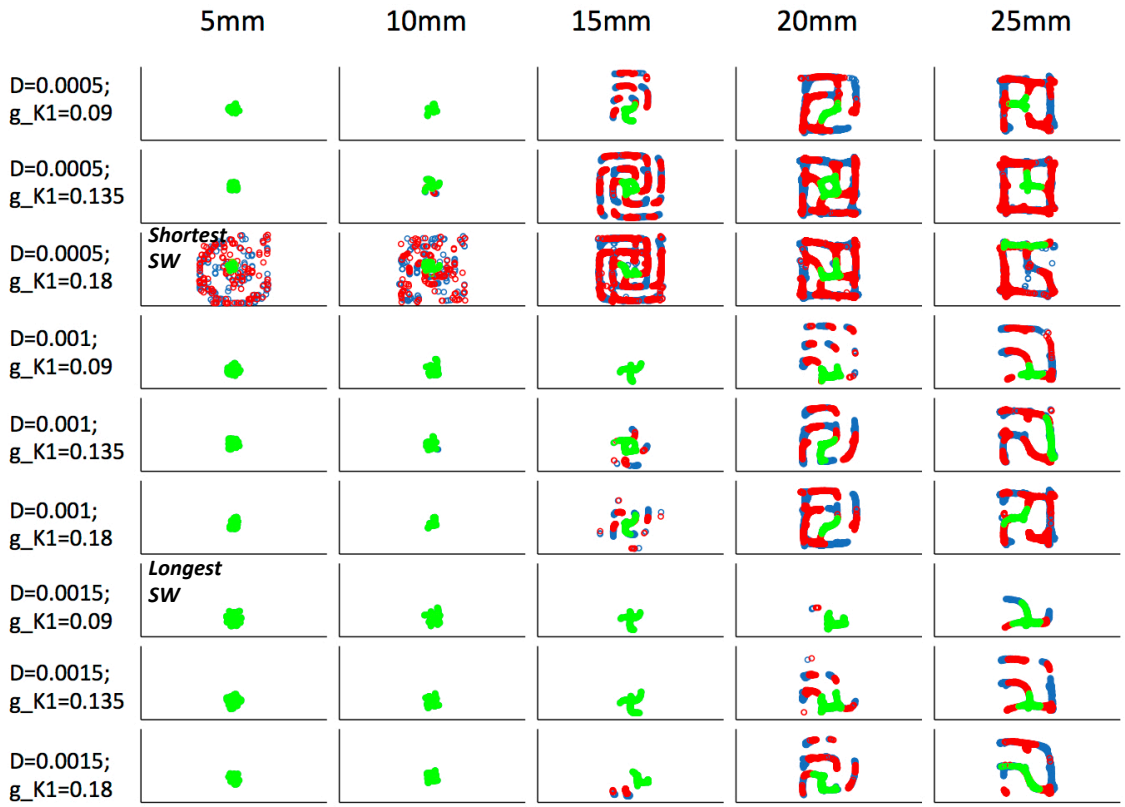

Figure 7.14: Phase singularity distributions at 5, 10, 15, 20 **and** 25**mm resolution for each spiral parameter set, where the number of false phase singularity detections is seen to vary with spatial wavelength.** There is a large difference between the number of false phase singularities in red and blue between the parameter sets for each fixed grid spacing, indicating that the resolution requirements for each parameter set are expected to be different. The parameter set corresponding to the shortest wavelength is shown in the third row, and it is clear that there are more false detections here at the smaller grid spacings. The parameter set corresponding to the longest wavelength (seventh row) has the fewest false detections.

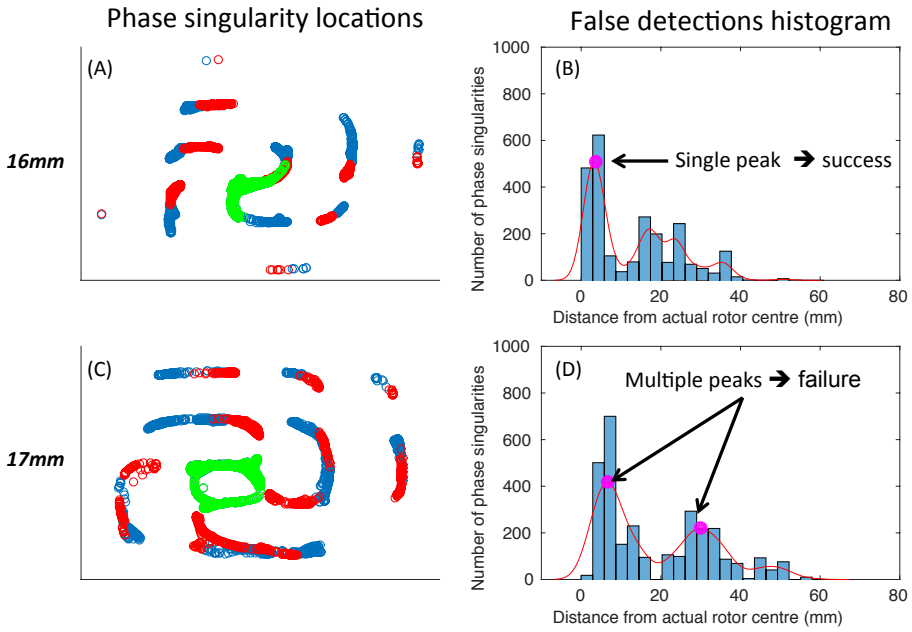

Figure 7.15: Phase singularity locations and histograms to show the resolution at which the number of false detections exceeded threshold due to multiple peaks in the histogram. At 16mm, there is only one detected peak in the histogram that is above the threshold, while at 17mm there are two, signifying a failed resolution.

For each of the identification criteria – visual, centre error and false detections histogram – the required resolution was quantified for each parameter set. The line of best fit was then calculated for each identification criterion, in order to give the linear relationship between the resolution required and the spatial wavelength. This is shown in Fig. 7.16, where the gradient of the lines are $1/N$ (since required resolution $= \lambda/N$). The values of N were as follows: 2.5 (visual identification), 2.7 (rotor centre location) and 3.1 (false detections histogram). Results for the three longest wavelengths (65.01, 66.59 and 78.52mm, Table 7.1) were excluded from this plot and the line of best fit as they were limited by the size of the domain. The equivalent parameter sets were also excluded for the focal source case as these were also too long for the domain size (Table 7.2: $D = 0.001\text{cm}^2/\text{ms}$ and $g_{K1} = 0.09\text{nS/pF}$, $D = 0.0015\text{cm}^2/\text{ms}$ and $g_{K1} = 0.09\text{nS/pF}$, $D = 0.0015\text{cm}^2/\text{ms}$ and $g_{K1} = 0.135\text{nS/pF}$).

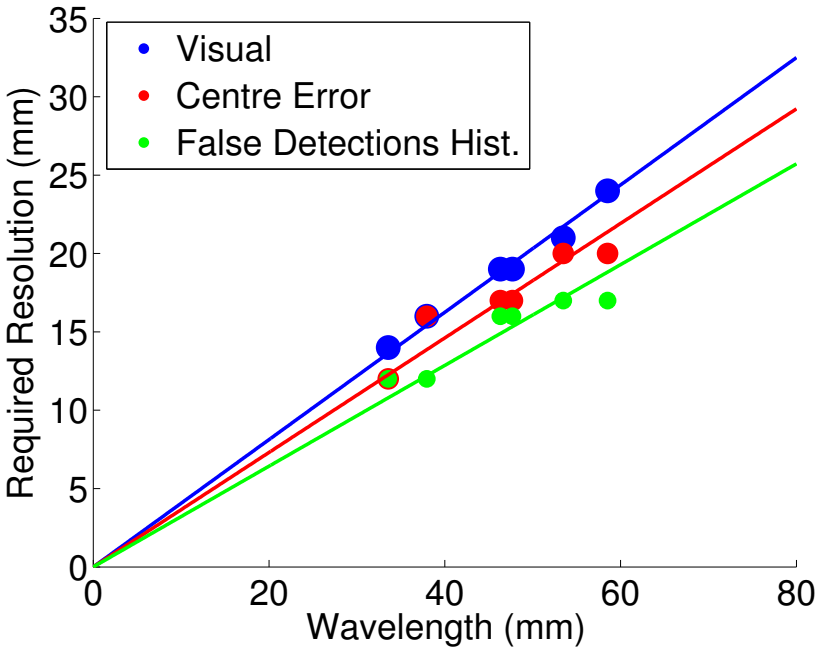

Figure 7.16: Required resolution for spiral wave detection as a function of the spatial wavelength: Minimum N necessary to identify a rotor were: 2.5 (visual), 2.7 (rotor core location) and 3.1 (false phase singularity detections histogram criterion). Minimum N were calculated as the reciprocal of the gradient of the lines of best fit, since required resolution is assumed to equal λ/N.

7.3.5 Error upon downsampling: focal source

To quantify the error in the case of a focal source, the following were calculated: success or failure of identification based visual identification or on the location of maximum divergence.

In order for successful focal source location using the maximum divergence, there must be a minimum of 3-by-3 measuring points within a single focal source wavefront. The cases tested here all had the focal source location at the centre of the sheet, so in this case, identification was successful if there were nine points within the domain from the activation front to the centre of the sheet (that is within the area corresponding to a circle centred at the focal source origin with radius equal to the spatial wavelength). This means that for shorter wavelengths a smaller grid spacing was necessary in order to provide these nine points. This is shown in Fig. 7.17.

As for the case of the spiral source, the resolution requirements for the different identification criteria were plotted as a function of the spatial wavelength (Fig. 7.18). Minimum N necessary to identify a focal source were: 3.3 (visual) and 1.6 (maximum divergence location).

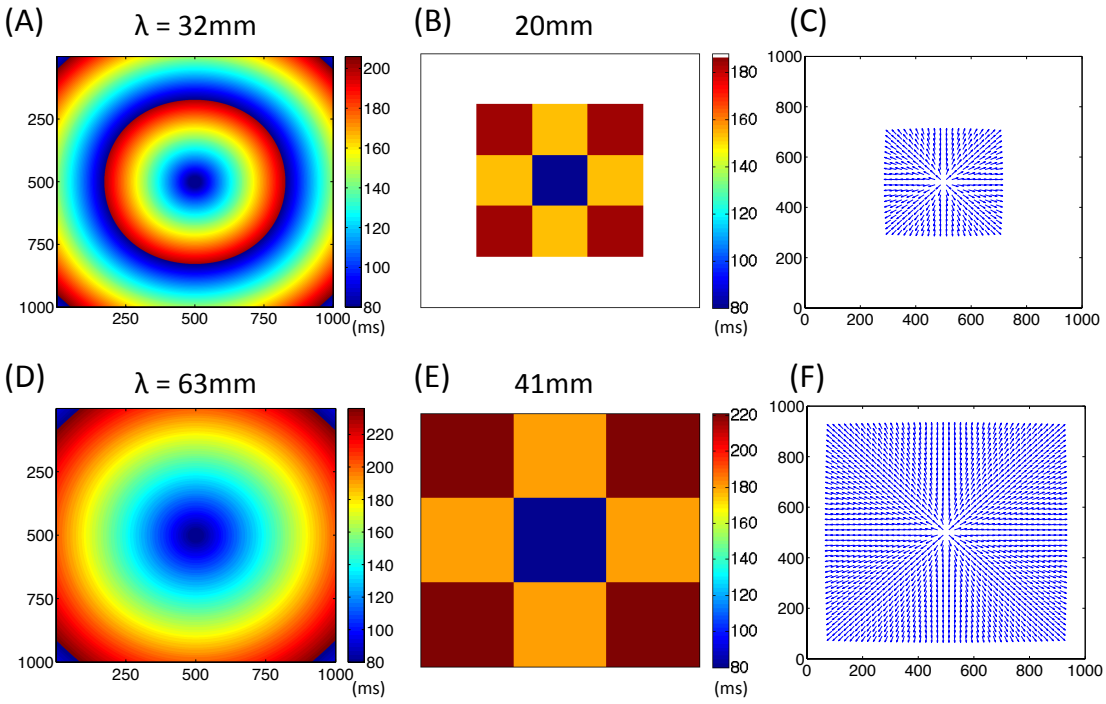

Figure 7.17: The effects of spatial wavelength on resolution requirements for a focal source: three-by-three points within a single wavefront are sufficient. This figure shows that having three-by-three points within a single focal source wavefront gives the minimum information required for successful identification of the location of maximum divergence. This means that a smaller grid spacing is required for shorter wavelengths. A-C are for a shorter wavelength of 32mm, for which a resolution of 20mm is required to give three grid points; while D-F are for a longer wavelength of 63mm, for which a resolution of 41mm is required. A, D show isochronal maps; B, E show the times used for the stated resolutions; C, F show the interpolated velocity fields from which the point of maximum divergence is located.

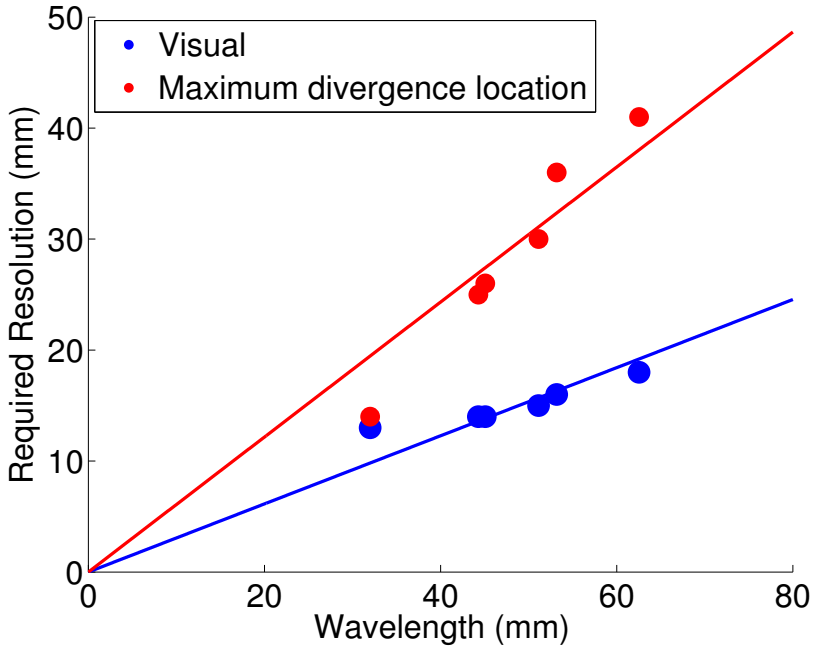

Figure 7.18: Required resolution for focal source detection as a function of the spatial wavelength: minimum N necessary to identify a focal source were: 3.3 (visual) and 1.6 (maximum divergence location). Again minimum N were calculated as the reciprocal of the gradient of the lines of best fit, since required resolution is assumed to equal λ/N.

7.4 Testing derived spatial resolution requirements using data from realistic catheter arrangements

7.4.1 Methods for modelling realistic catheter arrangements: Lasso, Afocus and PentaRay catheters

To determine whether the resolution requirements derived for a regular grid of points also apply to realistic clinical catheter arrangements, voltage data were analysed from points representing electrode recording points that are not on a regular grid. A circular (Lasso), spiral (Afocus) and five-spline (PentaRay) catheter were modelled using typical catheter diameters and interelectrode spacings (Fig. 7.19). Voltage data from the catheter electrode locations were post-processed as for the regular grid downsampled data, and the resulting phase singularity trajectories were compared to the full resolution gold standard (0.1mm spacing, regular grid).

For the modelled circular catheter, points were equally spaced on a circle of diameter 2cm. The spiral catheter was modelled as an Archimedean spiral (see Section 3.3.8 for more details). Two PentaRay catheter arrangements were modelled; one with an inter-electrode spacing of 2-6-2mm and one with equal spacing of 4-4-4mm along each of the equally-spaced five splines.

7.4.2 Results for modelling realistic catheter arrangements: Lasso, Afocus and PentaRay catheters

To confirm that clinically used catheter arrangements satisfy the resolution requirements found in this study, the effects of different catheter arrangements were compared for the spiral wave simulation with the shortest wavelength, with the justification that if the resolution and arrangement are satisfied for the shortest wavelength tested, then they will be for all of the wavelengths tested. Hence the results presented here are for a diffusion coefficient of 0.005cm^2/ms and I_{K1} conductance of 0.18nS/pF; giving a wavelength of 33.56mm.

Catheter comparison

The catheter arrangements tested were a circular (Lasso), spiral (Afocus) and two variations of a five-spline (PentaRay) arrangement, all of diameter 2cm (see Section 7.4.1). The effects of the number of points used for each catheter arrangement were also tested by considering 20 or 10 points, with the justification that these catheters consist of twenty unipoles, which can be paired as 10 bipoles (or 19, in

which case the difference in resolution is small). Isophase maps calculated by interpolating the phase at the twenty catheter recording points are shown in Fig. 7.19, along with the gold standard of 0.1mm spacing. The resulting trajectories from each of these arrangements are also shown. For twenty recording points, the PentaRay catheter with equally spaced recording points along each spline (4-4-4mm spacing arrangement; Fig. 7.19 D) gave the smallest error in the centre location of the rotor trajectory compared to the gold standard centre location, while the Lasso gave the largest (PentaRay arrangement two 0.28mm vs Lasso 3.53mm); the Afocus and PentaRay catheters gave similar centre errors (maximum difference 0.37mm), as can be seen in Fig. 7.19. The centre locations are shown on the gold standard PS trajectory in Fig. 7.19. The frame-wise errors in location compared to the gold standard trajectory were again similar for the Afocus and PentaRay catheters (maximum difference in mean values: 0.34mm), and again largest for the Lasso catheter (mean framewise error for Lasso is 84.7% larger than Afocus error; errors shown in Fig. 7.19).

Number of measuring points

The effects of reducing the number of measuring points to ten were investigated. For the ten point arrangement, the Afocus catheter gave the smallest errors compared to the gold standard locations, as can be seen in Fig. 7.19 (centre of mass error of Afocus smaller than Lasso by 2.70mm; PentaRay arrangement 1 by 0.56mm; PentaRay arrangement 2 by 0.35mm). The Afocus and Lasso catheters gave similar results whether twenty or ten points were used (changes of 0.07mm and -0.11mm respectively), while the PentaRay catheters become less accurate when the number of points were reduced (increase in error of 0.76mm and 0.79mm for arrangements 1 and 2 respectively).

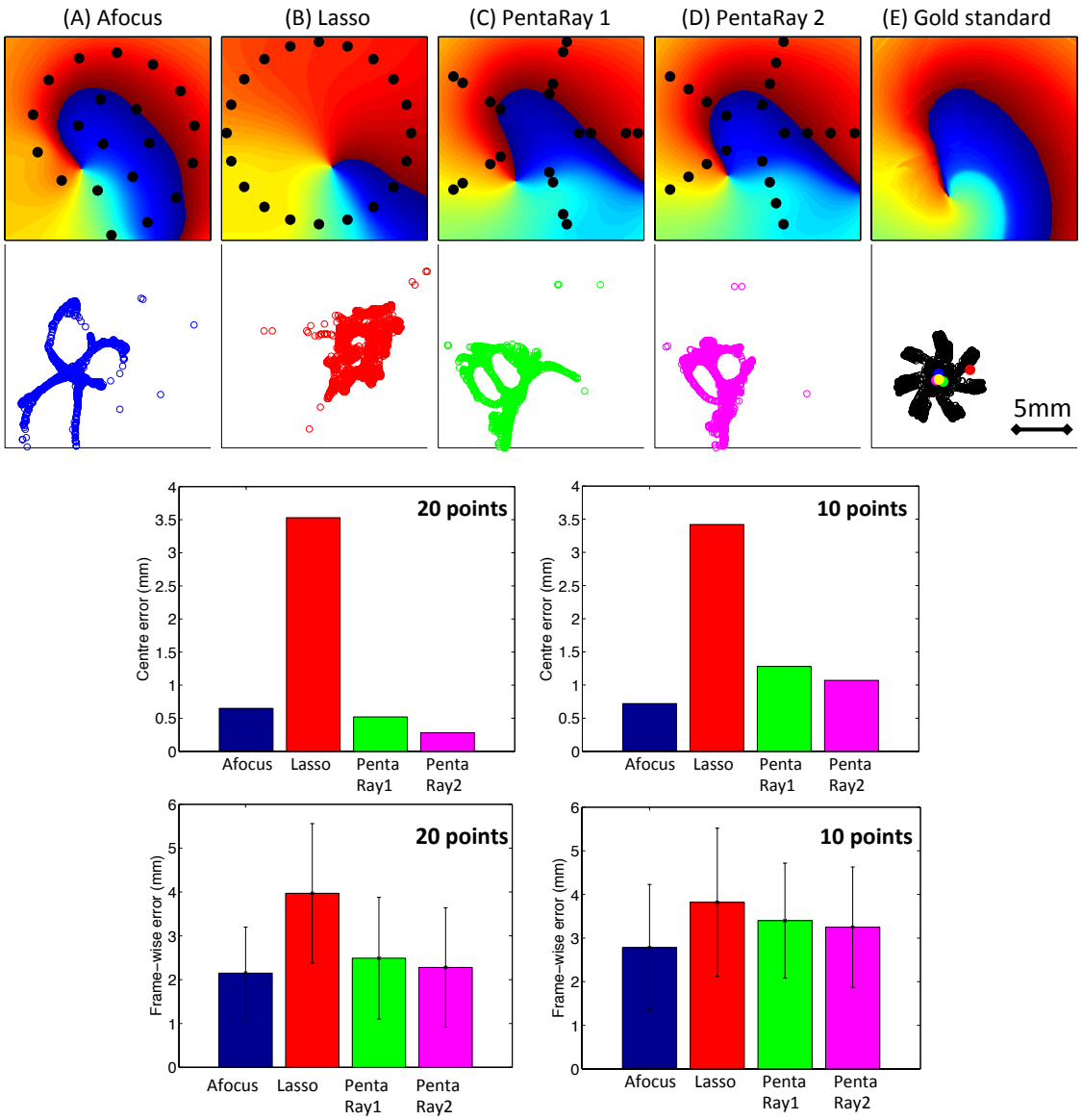

Figure 7.19: All multi-polar catheters offer sufficient resolution to locate a rotor-core, although the Lasso catheter is least accurate. Top: isophase maps from recording points shown in black are interpolated to the 0.1mm resolution of the gold standard arrangement (E). Second row: rotor trajectories calculated using the interpolated phase. For the gold standard (E) rotor trajectory, the centre of mass of each trajectory are marked (Afocus blue; Lasso red; PentaRay 1 green; PentaRay 2 magenta; gold standard yellow). For the twenty electrode arrangements here, the Lasso catheter has the largest error in the centre of mass location, which can be seen in the final panel in which the centre of mass of the Lasso catheter (red dot) is furthest from the gold standard location (yellow dot). Third row: errors in the centre location compared to the gold standard arrangement, using twenty or ten points. Bottom row: mean frame-wise difference in rotor location compared to the gold standard arrangement, using twenty or ten points. All centre errors are less than 4mm and so are not considered to be of clinically relevant magnitude.

7.4.3 Methods for modelling realistic catheter arrangements: patient geometry with basket catheter

As a final clinically relevant application, the effects of taking measuring points at locations representing the arrangement of a basket catheter (see Fig. 1.7 for a photograph) were assessed by simulating an anatomically realistic left atrial geometry with unipolar electrograms calculated at basket catheter measurement locations.

Creating the left-atrial mesh

The left-atrial geometry was derived from a patient MRI that was segmented using ITKsnap segmentation software (Yushkevich et al., 2006). The mesh was then trimmed along the four pulmonary veins, as well as at the mitral valve, using the software Blender (Blender, 2015). Finally the mesh was re-meshed using the software Gmsh (Geuzaine and Remacle, 2009), in order to create triangular elements of regular size. These steps in creating the geometry were performed by Dr Christopher Cantwell.

Modelling a basket catheter

In order to model a realistic representation of a basket catheter, the locations of the electrodes of a basket catheter were taken from a clinical case in which an electroanatomic mapping system was used. This basket catheter was 48mm in diameter and consisted of eight splines, with eight electrodes on each spline. Using Matlab, the electrode locations were shifted to be centred at the centre of the atrial mesh and rotated such that the largest gap between splines coincided with the mitral valve (Fig. 7.20 A). The electrode locations were then shifted to their closest vertex point (Fig. 7.20 B, C) and finally projected 0.2mm inside the geometry (Martínez et al., 2014), along the surface normal to the closest vertex. This ensured that all of the electrogram recording points for the simulation are endocardial and at a fixed distance of 0.2mm from the mesh.

Simulating a gold standard arrangement for error quantification

To produce a gold standard to compare the basket arrangement phase singularity results to, unipolar electrograms were calculated from the transmembrane voltage at every vertex of the mesh within the area of coverage of the basket catheter. Again the points were projected 0.2mm inside the geometry, along the surface normal to the vertex. The area of the mesh is marked in Fig. 7.20 B, C and the vertex points

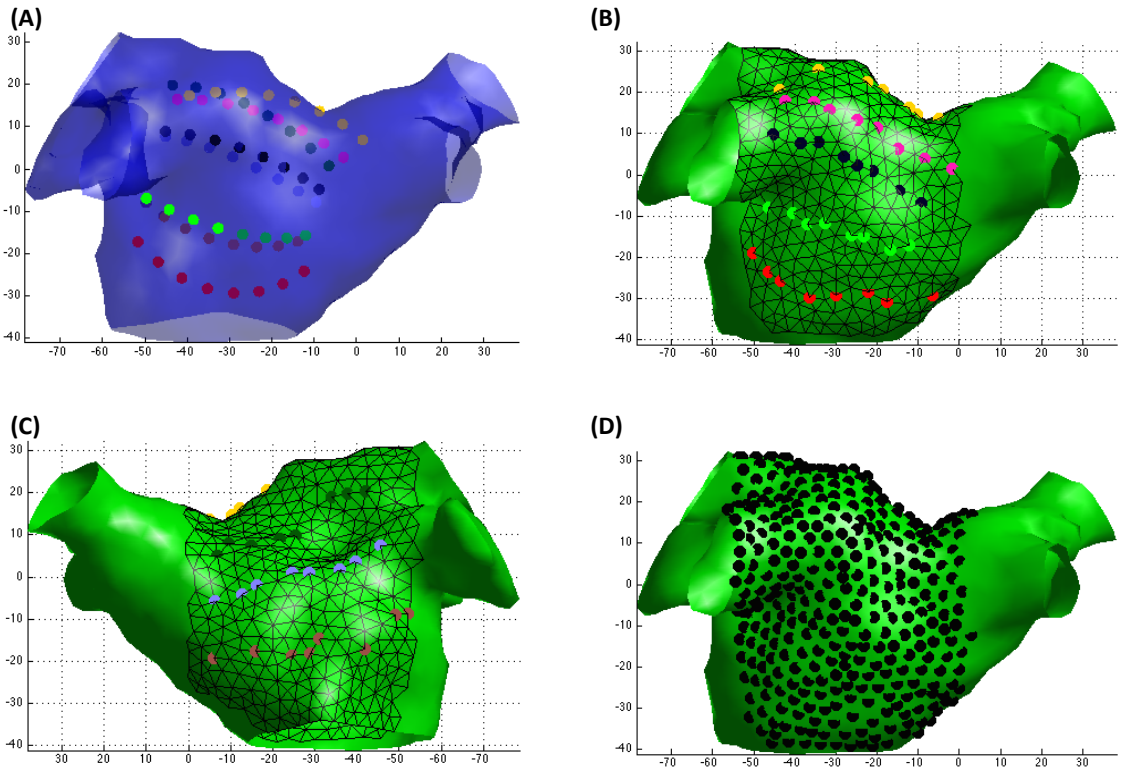

Figure 7.20: Basket catheter arrangement in human left atrial geometry: selection of electrode recording points. (A) The clinically acquired basket electrode locations were shifted and rotated to lie inside, or close to the left-atrial geometry, with the eight splines of the catheter shown as different colours. These locations were then shifted to the closest vertex point. (B) Posterior view; (C) anterior view. Vertices of the mesh were selected to give a domain containing the basket catheter that could be used for the geodesic flattening; this sub-selection is shown as the black edges (in (B), (C)). (D) Dense selection of surface points (black dots), where electrograms were calculated at endocardial points 2mm from each of the vertices in the sub-selected area.

are indicated in Fig. 7.20 D. The area was chosen such that the mesh is unconnected below the pulmonary veins, to allow the mesh to be flattened (Fig. 7.21 A, B).

Flattening the atrial mesh to 2D for visualisation and analysis purposes

This sub-selection of the atrial mesh was then flattened to two-dimensions using a method that optimally preserves geodesic distances (Zigelman et al., 2002). First of all, the geodesics distances between every pair of vertices on the mesh were calculated using Dijkstra's algorithm; an example path is shown in Fig. 7.21 B. These distances give a matrix of size equal to the number of vertices squared, and a classical scaling procedure (Zigelman et al., 2002) is then used to find the optimal two-dimensional representation. This method is explained in more detail in Section 2.14. The electrode locations are assumed to lie on vertices of the mesh for the flattening calculations.

The result of flattening the mesh from Fig. 7.20 A is shown in Fig. 7.21 C, where the dense mesh electrode locations are seen to cover a larger domain size than the basket electrode locations. In order to ensure that the dense electrode and basket electrode area for interpolation were the same, dense electrode locations were only included in the interpolation analysis if they were within a small distance threshold of the basket electrode location area (Fig. 7.21 D). This ensured that differences observed were due to spatial resolution rather than the area of coverage. The final selection of electrode locations used here are shown in Fig. 7.21 D.

Simulation details

Simulations were run with the Courtemanche et al. (1999) human atrial cell model as discussed in Section 7.2.1, using the Nektar++ finite element solver (Section 2.5). An extra-stimulus protocol was employed in order to generate spiral wave re-entry in the simulation. Unipolar electrograms were calculated at the electrode location points following Sato et al. (2009) (Section 2.8).

Unipolar electrogram phase calculation

In order to calculate the phase of each unipolar electrogram, the signal was first filtered using a series of filters commonly used for calculating the signal DF (Ng et al., 2006) (band-pass filter at $40 - 250$Hz, signal rectification, low-pass filter at 20Hz; Fig. 7.22). The maxima and minima of the signal were then tagged (Fig. 7.23 A) and joined with cubic splines(Fig. 7.23 B). The maxima and minima splines were then used to normalise the signal (Fig. 7.23 C), and this was then squared and the

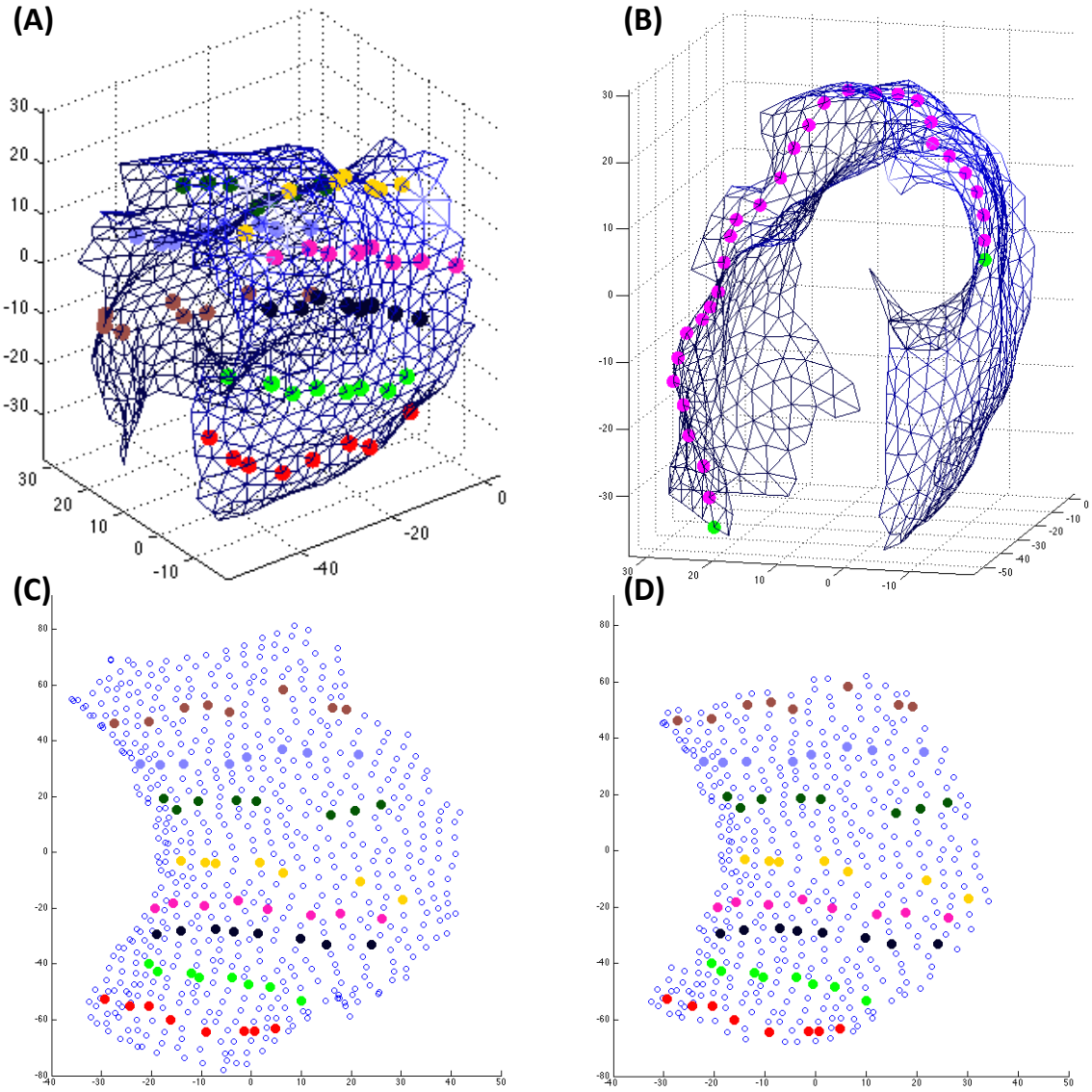

Figure 7.21: Flattening the left-atrial mesh to preserve geodesic distances. (A) Sub-selection of mesh, where the geodesic distance between all pairs of vertices were calculated. (B) Example shortest path (*geodesic*) is shown as the purple dots in between the vertices in green. (C) Two-dimensional arrangement that optimally preserves these distances, where the dense electrode points are blue circles and the basket electrodes are coloured by spline. (D) A subset of these points were used for the phase interpolation so that the area of coverage of the dense arrangement matches that of the basket catheter.

straight mean removed (Fig. 7.23 D). Finally the signal was plotted against the Hilbert transform of the signal to give full phase loops around the origin (Fig. 7.23 E), and the angle around this trajectory was the phase angle (Fig. 7.23 F). (See Chapter 6 for more detail.)

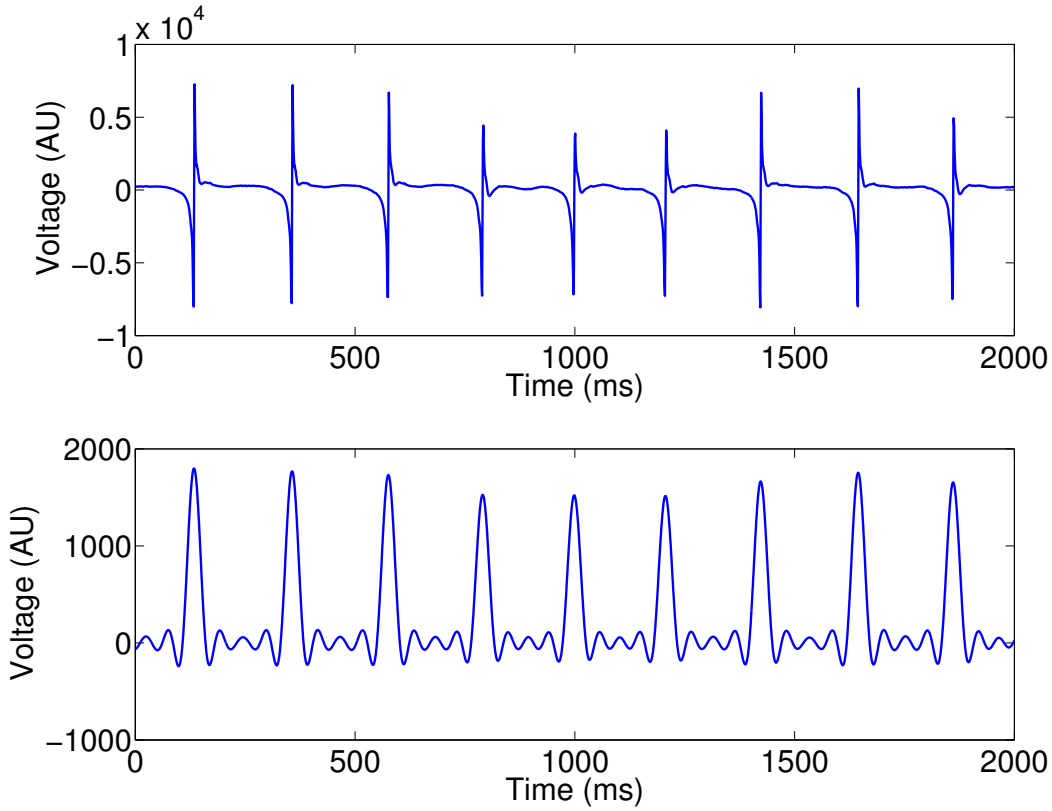

Figure 7.22: Filtering for unipolar simulated electrograms. The raw unipolar electrograms (top) were filtered using a band-pass filter (40-250 Hz), rectified, followed by a low-pass filter (20Hz) to give a sinusoidal signal suitable for phase analysis (bottom).

Phase interpolation and singularity detection

Finally the phase angle at the recording points were interpolated to give a regular grid of data. This was done for both the basket locations and for the dense arrangement of electrodes, where the interpolated basket grid points were every 2 mm and the dense arrangement interpolation grid points were every 0.5 mm. Interpolating the basket recording onto a finer grid than 2mm spacing caused artificial wavefront break-up. Phase angles were mapped as before (Section 7.2.4) and interpolated using the Matlab `griddata` function. Phase singularities were calculated as before

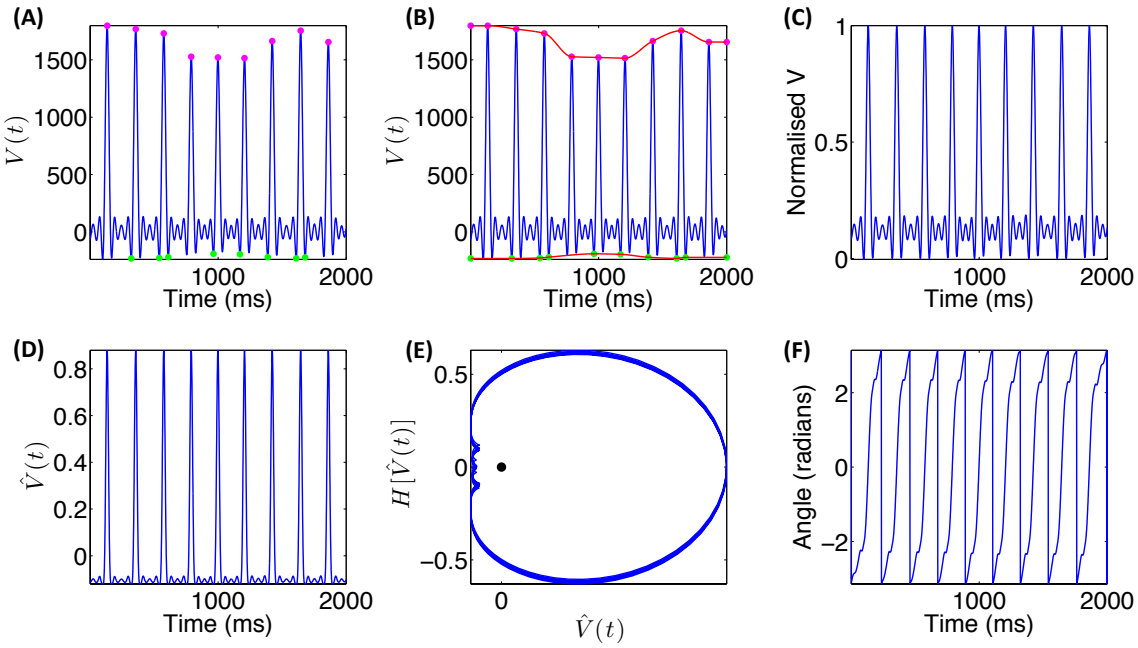

Figure 7.23: Steps for phase calculation for simulated unipolar electrograms. (A) Maxima and minima tagged; (B) joined with cubic splines; (C) maxima and minima lines used to normalise the signal; (D) signal squared and straight mean removed; (E) signal plotted against its Hilbert transform to give phase loop trajectories; (F) angle around the trajectory gives the phase angle.

(Section 7.2.3) for the dense arrangement (gold-standard) and the basket recording points, and the phase singularity locations were compared.

Calculating rotor trajectories using surface flattening techniques

In order to motivate the use of a two-dimensional representation for identifying phase singularities and displaying trajectories, the techniques detailed in Section 2.14 are used to convert three-dimensional phase to two dimensions. Trajectories, calculated from a simulation in which there were two rotors and re-entry around the left inferior pulmonary vein, are shown in Fig. 7.24. These are also shown on the corresponding three-dimensional geometry, in which one area of the re-entry is mostly out of view, demonstrating the advantage of the two-dimensional representation. The two-dimensional representation also allows the use of two-dimensional algorithms for calculating phase singularity locations using the topological charge, rather than requiring additional implementation to calculate this using the three-dimensional mesh elements.

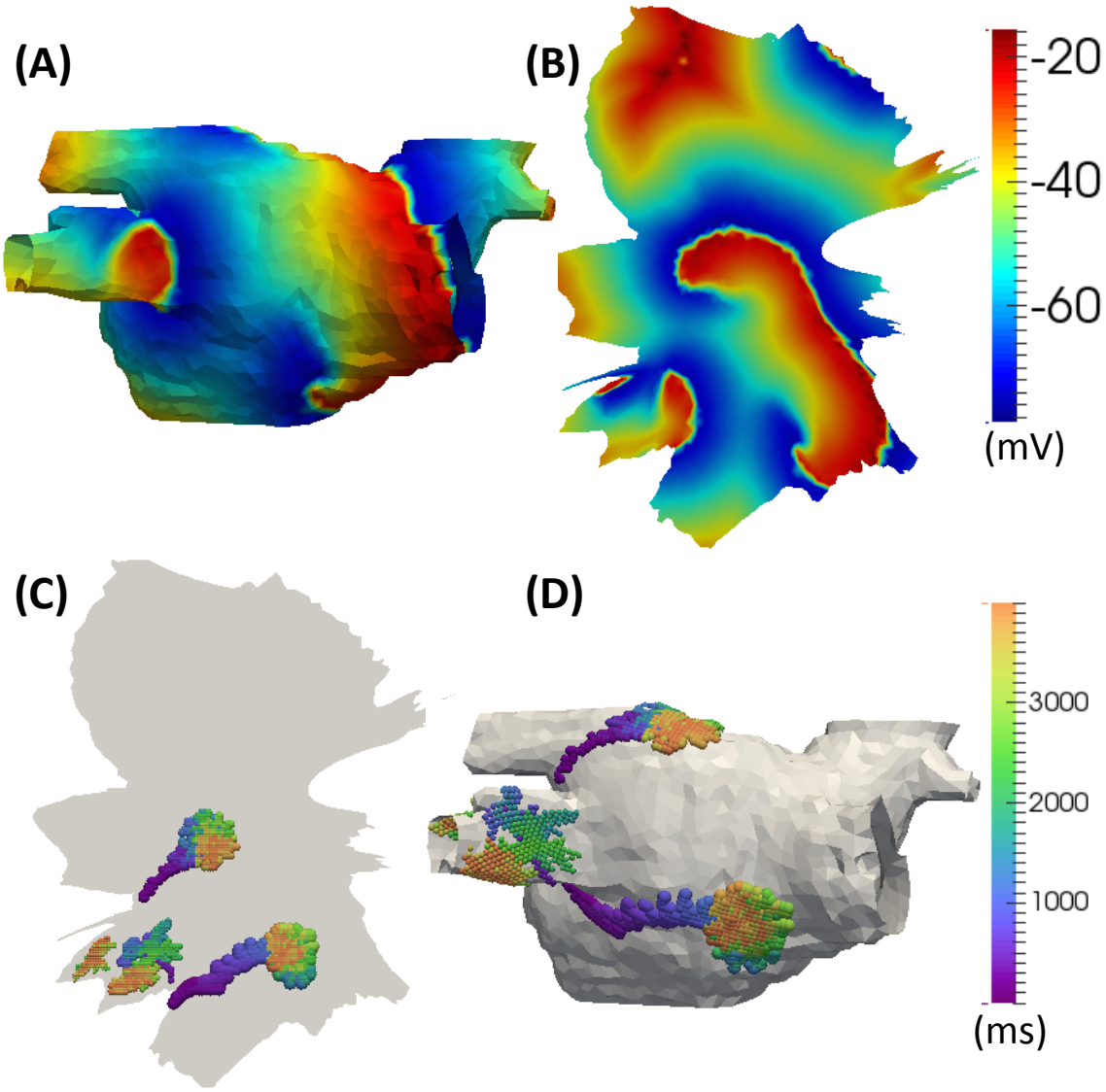

Figure 7.24: Calculating rotor trajectories using surface flattening techniques: re-entry is mostly out of view in three dimensions, demonstrating the advantage of the two-dimensional representation. Rotor tracking in simulated data: (A) Example isopotential map generated from action potential data sampled at mesh vertices in three-dimensions; (B) the corresponding two-dimensional representation. (C) Phase singularity trajectories for the two rotors and the re-entry observed in the simulation calculated in two-dimensions. (D) Trajectories displayed back on the three-dimensional mesh. The geometry of the atrium used here is the same as in Fig. 2.9.

7.4.4 Results for modelling realistic catheter arrangements: patient geometry with basket catheter

Basket simulations were run for thirty seconds of rotor activity for two parameter sets corresponding to one short and one long wavelength of activity. For both simulations, an S1-S2 protocol was used to generate two meandering rotors, of opposite chirality. In the following analysis, the two rotors were analysed individually by separating phase singularities by chirality (clockwise or counter-clockwise).

Estimated wavelength

For these simulations, the diffusion coefficient was $0.00953\text{cm}^2/\text{ms}$ (following Niederer et al. (2011)), resulting in CVs close to those for a diffusion coefficient of $0.001\text{cm}^2/\text{ms}$ for the two-dimensional simulations, specifically: for the longer wavelength simulation, median CV was 0.35m/s and for the shorter wavelength simulation it was 0.37m/s. For the long wavelength, I_{K1} conductance was 0.09nS/pF and the median CL was 218ms, resulting in an estimated wavelength of 75.2mm. For the short wavelength, I_{K1} conductance was 0.18nS/pF and the median CL was 123ms, resulting in an estimated wavelength of 45.2mm. Applying the most stringent resolution requirements for spiral wave identification from the three criteria, gives required resolutions of $75.2/3.11 = 24.4$mm and $45.2/3.11 = 14.5$mm.

Interelectrode distances for a basket catheter

In order to see whether these resolution requirements are met for the basket catheter, the 3D geodesic distances between each electrode and its four neighbouring electrodes were calculated. The median distance was 10.2mm, with a lower quartile of 5.87mm and upper quartile of 16.2mm (shown as a box and whiskers diagram in Fig. 7.25). Considering the full distribution allows the quantification of the percentage of distances that are less than the required resolution for a particular wavelength. Here 96.4% of distances between neighbouring electrodes were less than the longer wavelength resolution requirement of 24.4mm, and 64.0% of distances were less than the requirement for the shorter wavelength of 14.5mm.

Results overview

The percentage of inter-electrode distances between electrodes in the basket catheter within the resolution requirements for both the short and long wavelength simulations are satisfactory. In order to assess whether this is a good indication of the resolution adequacy, the ability of the basket electrode arrangement to identify

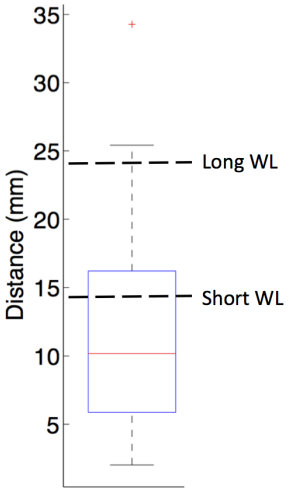

Figure 7.25: Box and whisker diagram to show the distances between electrodes in a basket catheter: both the long and short wavelength resolution requirements are met satisfactorily. The long and short wavelength resolution requirements are marked (96.4% less than the longer wavelength resolution requirement of 24.4mm, and 64.0% less than the requirement for the shorter wavelength of 14.5mm).

rotor-core location from the short and long wavelength simulations were tested. In each case, the error in the rotor core location and number of false detections were calculated. The methodology and example phase maps are shown in Figs. 7.26, and 7.27 where an isopotential map is shown along with the basket locations to show the inputs of the analysis. The dense arrangement of electrodes were used to generate the gold standard phase, where the dense electrode arrangement contained 7.67 times more points than the basket (491 vs. 64). The interpolated phase from the basket electrograms were qualitatively similar to the gold standard arrangement and the resulting PS trajectories overlap (see Figs. 7.26 and 7.27). For the longer wavelength, two rotor cores were present in the mapping area for much of the simulation and the gold-standard phase singularity locations are shown in Fig. 7.30. For the shorter wavelength, one rotor core was present inside the mapping area for the first ten seconds of the simulation, after which both rotor cores were outside of the mapping area.

Centre error and number of false detections for the long wavelength simulation

The phase singularity dynamics were analysed for the first ten seconds of rotor activity for the long wavelength. The rotor core locations are shown in Fig. 7.28 (A), where the basket rotor locations were taken to be the closest phase singularity

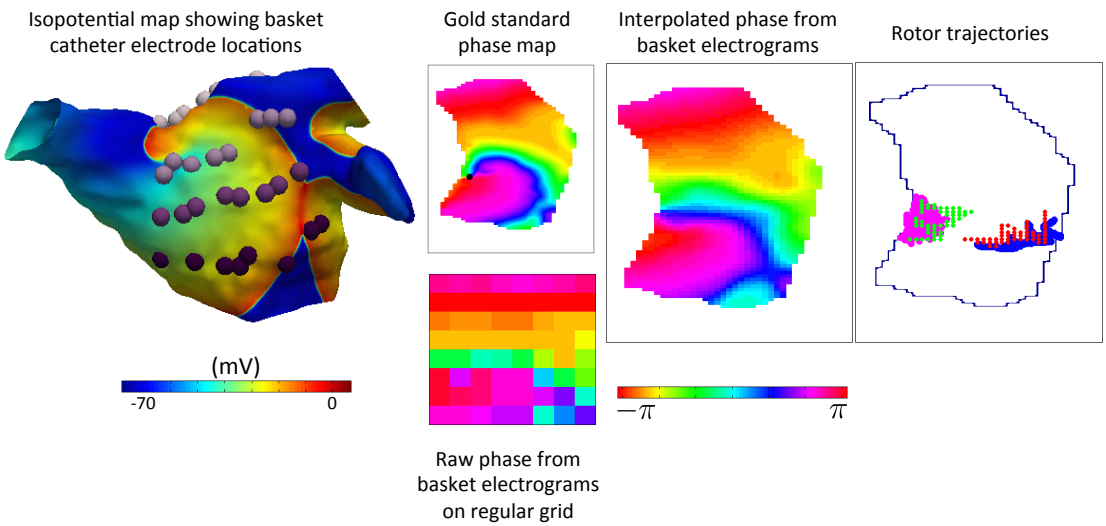

Figure 7.26: Realistic catheter arrangement: basket catheter in left-atrial geometry, results overview for longer wavelength. Example isopotential map for longer wavelength simulation (75.2mm) where the rotor tip for one of the rotors can be seen. The gold standard phase map is shown, generated from the phase of the dense arrangement of electrodes, with the phase singularity marked as a black dot. The phases as arranged on a regular 8-by-8 grid are also shown. The interpolated phase from the basket arrangement of electrodes is shown. Rotor trajectories for the two rotors of opposite chirality are shown for the first ten seconds of the simulation. The gold standard results are shown in blue and purple, and the basket results in red and green. The basket trajectories are seen to overlap with the gold standard trajectories. The full thirty second gold standard trajectories are shown in Fig. 7.30 and the analysis of these rotors is shown in Fig. 7.28.

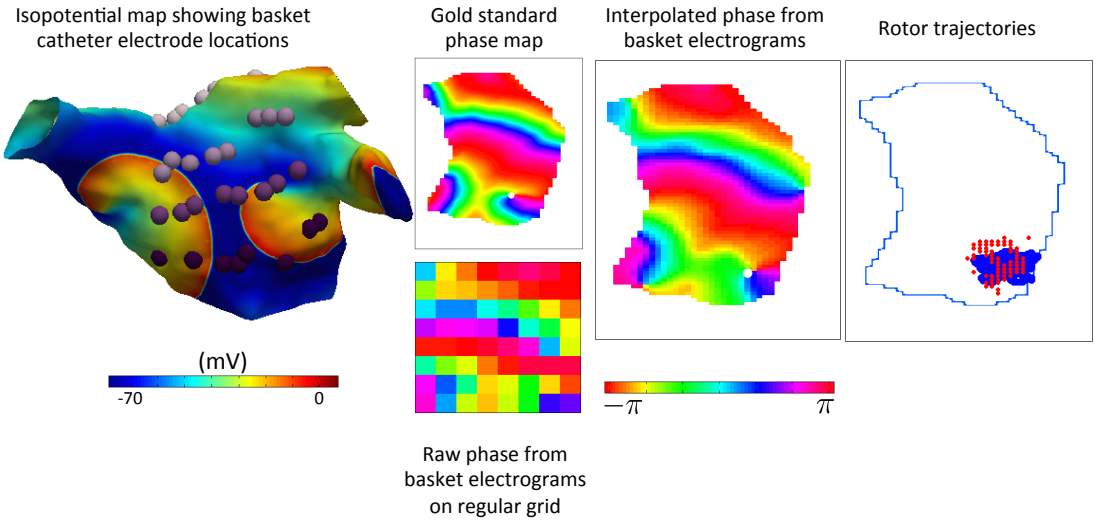

Figure 7.27: Realistic catheter arrangement: basket catheter in left-atrial geometry, results overview for shorter wavelength. Plots are as per Fig. 7.26. For this simulation, only one of the rotors was within the area of coverage of the basket catheter during the first ten seconds of the simulation.

location of the correct chirality that is within a 10mm distance threshold of the rotor core, on a frame-by-frame basis. All of the phase singularities for the basket arrangement are shown in Fig. 7.28 (B), where it can be seen that there are a large number of false detections. This is quantified using a histogram for the distribution of phase singularities depending on distance for the rotor centre in Figs. 7.28 (C), (D), where both have multiple peaks. This represents a failure of the false detection histogram criterion. The centre for the first rotor was located with sufficient accuracy (3.62mm, blue and red rotor) and this was also acceptable on a frame wise basis (3.54±2.01 per frame), and there were a small number of missing detections (2.56%). For the second rotor, the error in the centre of mass was greater than the 4mm threshold (5.36mm, purple and green rotor), and was also larger on a frame wise basis (5.45 ± 2.91mm). The number of missing detections was also large (40.16%) for the second rotor, since many of the phase singularities are along the edge of the dense domain and cannot be picked up by the basket arrangement.

Centre error and number of false detections for the short wavelength simulation

The equivalent analysis is shown for the shorter wavelength in Fig. 7.29, where there are two clear peaks in the false singularity histogram corresponding to the rotor core and an additional strip of phase singularities that aligns with where there is larger

inter-electrode spacing between electrodes in the vertical direction (see Fig. 7.21). This represents a failure of the false detection histogram criterion. On the other hand, the error in the centre of rotor core location is less than the 4mm threshold (1.33mm), while this error is greater than 4mm when considered on a frame wise basis (5.04±2.38mm). There are also a large number of missing rotor core detections for the basket compared to the dense arrangement (32.6%).

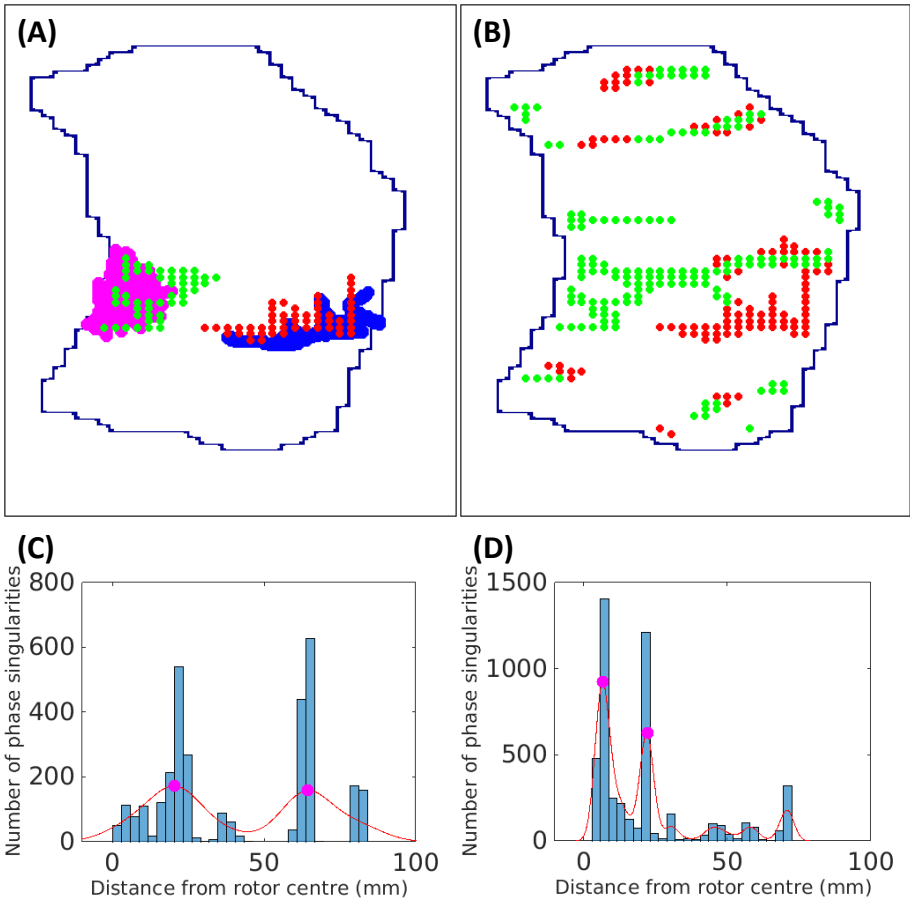

Figure 7.28: Rotor locations for gold-standard and basket electrodes and false detection histograms, for the first ten seconds of the long wavelength simulation, where there is a failure in the false detection criterion. (A) Rotor phase singularity locations for the gold standard resolution rotors (blue and magenta) and the basket electrode rotors (red and green). Here only the singularities that correspond to the two rotors are shown. (B) Basket phase singularity locations, in which all of the phase singularities are shown and it can be seen that there are a large number of false detections. (C) False singularity histogram for rotor number one (red); (D) false singularity histogram for rotor number two (green). For both rotors, the false detection histogram has two peaks, which signifies a failure in the false detection criterion at this wavelength.

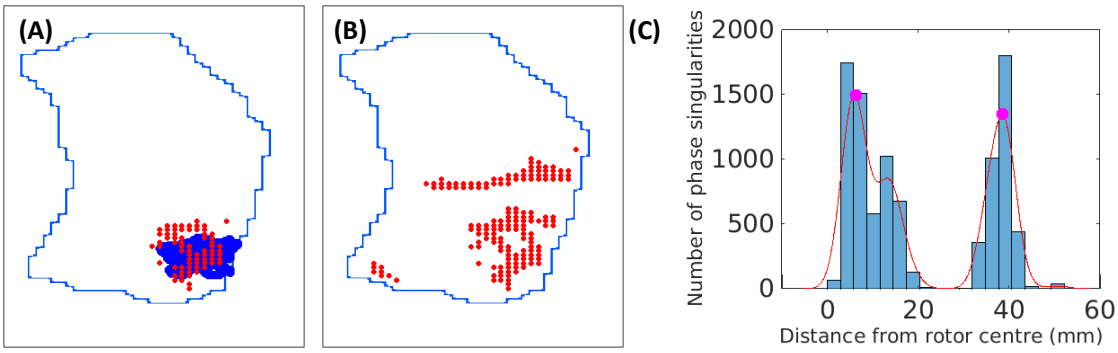

Figure 7.29: Rotor locations for gold-standard and basket electrodes and false detection histograms, for the first ten seconds of the short wavelength simulation, where there is a failure in the false detection criterion. (A) Rotor phase singularity locations for the gold standard resolution rotor (blue) and the basket electrode rotors (red). Again only the singularities that correspond to the two rotors are shown. (B) Basket phase singularity locations, in which all of the phase singularities are shown and it can be seen that there are a large number of false detections. (C) False singularity histogram, which again has two peaks, indicating a failure in the false detection criterion at this wavelength.

Comparing the meander trajectories to the gold standard case

In order to test the ability of the basket catheter arrangement to track meandering rotors, the dense and basket electrode arrangements were compared for the thirty second long wavelength simulation. During this simulation, there were two rotors that meandered over a reasonable area (Fig. 7.30). To compare the meander paths for the two rotors for the dense and basket arrangements, a rotor centre location was estimated using a moving window of length 1000ms that moved in 100ms shifts, where the average location was plotted for each window (Fig. 7.30). The paths are visually similar for both electrodes arrangements, where the average difference in the rotor centre path is 2.14 ± 1.18mm for the first rotor and 3.84 ± 2.06mm for the second rotor. The average path is therefore accurate, however the phase singularity trajectory shows a larger rotor meander area for the basket resolution than for the gold standard resolution. This is quantified by computing the area of the bounding ellipse of the trajectory for each window of data (1000ms). The basket trajectory areas are 327 ± 121mm^2 and 136 ± 184mm^2 larger than the gold standard for the two rotors respectively (diameter increased for basket compared to gold standard by: 8.71 ± 3.52mm and 3.44 ± 6.95mm respectively). The frame-wise errors were 4.89 ± 2.36mm for the first rotor and 4.12 ± 2.39mm for the second rotor.

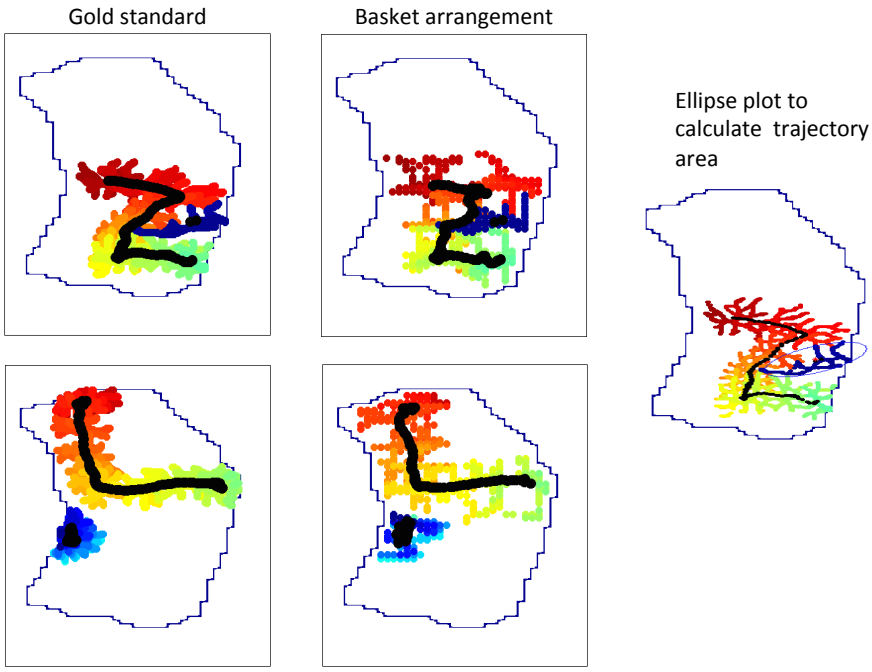

Figure 7.30: Phase singularity locations determined using the dense electrode arrangement and the basket arrangement for thirty seconds of the longer wavelength simulation (75.2mm), where the meander paths are visually similar, but the trajectory area is increased for the basket arrangement. Phase singularities are separated by chirality (top and bottom row) to show the locations of the two rotors over the simulation, where time is indicated by dark blue (0 seconds) through red (thirty seconds). Phase singularities are also shown for basket arrangement. In both cases, the location of the moving average is marked in black, and the moving average is seen to follow a similar path. The right hand sub plot shows an example bounding ellipse used to calculate the area of the trajectory path for a data window of 1000ms, where the window is then shifted in time along the trajectory.

7.5 Discussion

7.5.1 Main findings

A technique was devised to estimate wavelength from a small number of data-points so that the resolution requirements suggested by this study can be applied in an experimental or clinical setting. Spatial wavelength λ, the distance between successive wavefronts, was estimated accurately for focal sources and spiral waves using CV $\times$ CL. An estimate of the resolution requirements as a function of the spatial wavelength is also found for different identification criteria for spiral waves and focal sources. The required resolution was of the form λ/N, where values of N were found for a spiral wave to be 2.5 (visual), 2.7 (rotor core location) and 3.1 (false phase singularity detection), and for a focal source: 3.3 (visual) and 1.6 (maximum divergence location). The cases of more realistic catheter arrangements were then tested, where high-density mapping catheters were found to identify rotor core locations accurately. Finally the case of meandering rotors measured using a basket catheter was considered, for which identification was satisfactory.

7.5.2 New developments

In this chapter, a method to estimate spatial wavelength was developed. Spatial wavelength was measured using an automated algorithm to track the distance between isopotential lines. This method worked well for simulated data, however it is expected that the spatial wavelength estimation technique would need to be used instead in experimental and clinical data, due to the lower resolution and increased noise. The method to estimate spatial wavelength as CV $\times$ CL was found to be accurate, and the method to estimate the CV of spiral waves in an automated fashion, without the need for manual window length adjustment, worked well so long as the area over which measuring points are located is less than the spatial wavelength of the data. In addition, the technique to convert the three-dimensional electrode locations to the two-dimensional representation that best preserves geodesic distances (Section 2.14) works well for visualisation and also allowed the phase tracking techniques developed for two-dimensions to be applied here.

7.5.3 Expected spatial wavelengths in human AF

Spatial wavelength can be estimated as conduction velocity (CV) divided by dominant frequency (DF), and so considering the range of CVs and DFs seen in human AF provides an indication of the observed spatial wavelengths.

Many clinical studies have measured the DF during AF in either the left or right atrium, where a left-to-right frequency gradient is observed in some patients (Atienza et al., 2009). During paroxysmal AF, mean DF has been measured as: 5.7±0.9Hz (Jarman et al., 2012), 6.2±0.8Hz (Lazar et al., 2004) and 5.5±0.6Hz (Sanders et al., 2005). For persistent AF patients, the DF values from the same studies are as follows: 5.7±0.9Hz (Jarman et al., 2012), 6.1±0.7Hz (Lazar et al., 2004) and 6.4±0.6Hz (Sanders et al., 2005). Ng et al. (2006) compared DF measured using spectral analysis in the frequency domain to AFCL measured in the time domain for ten patients during AF and found that DF ranged from 4.8Hz to 8.6Hz (with a mean of 6.3±0.9Hz), while the mean activation rate ranged from 4.9Hz to 7.9Hz (mean 6.1±0.9Hz). Konings et al. (1994) measured AFCL for patients where they split the rhythms into three types with the following mean AFCLs: 174±28ms (type I, single broad wavefronts); 150±14ms (type II, one or two non-uniformly conducting wavefronts); 136±16ms (three or more wavefronts; highly fragmented).

Factors that affect DF include electrophysiological remodelling. Electrophysiological remodeling during AF consists of changes in the conductance of several of the ion channels including that of I_{K1}, which has been shown to increase in chronic AF (Vaquero et al., 2008; Workman et al., 2008; Voigt et al., 2010). Increasing I_{K1} conductance has been demonstrated to shorten APD as well as leading to a small hyperpolarization in the resting potential (Noujaim et al., 2007b). In addition, it has been suggested that I_{K1} plays the same role in AF and VF (Vaquero et al., 2008). I_{K1} conductance has been shown to affect DF through changes in APD and its restitution, refractory period and CV (Sánchez et al., 2012). Thus in this study, we varied I_{K1} conductance to produce a range of wavefront frequencies. The changes made were based on modelling studies by Gong et al. (2007), where the conductance was doubled with the justification given that this conductance is closer to the findings of Koumi et al. (1995), and Pandit et al. (2005b), where the conductance was again multiplied by two resulting in an increase in the DF and reduction in the tip meander (from 5.7Hz and tip meander 2.6cm, to 8.4Hz and tip meander 1.7cm). The DFs in the study by Pandit et al. (2005b) sit at the lower and upper end of the range of DFs in the literature for human AF, as detailed above. Hence to generate simulations with a range of DFs close to those observed in human AF, I_{K1} conductance was multiplied by 1.0, 1.5 and 2.0. For spiral wave simulations in this study, CLs were in the range $117-182$ms, giving a DF range of $5.5-8.5$Hz; and for focal source simulations, the CL range was $121-203$ms, giving a DF range of $4.9-8.3$Hz. Thus the simulations here cover the range seen in human AF.

CV is hard to measure during AF due to both difficulties in assigning activation

times of multi-component signals and in working out wavefront direction. Hence most human atrial CVs reported in the literature are for more simple rhythms including sinus rhythm (88±9cm/s (Hansson et al., 1998), 82.7±16.1cm/s (Kanagaratnam et al., 2002)), pacing (81±16cm/s (Hansson et al., 1998), 76.5±16.7cm/s (Kanagaratnam et al., 2002)) and flutter (74±3.6cm/s (Schilling et al., 2001)). CV limits can be inferred from CV restitution pacing protocols; for example, Weber et al. (2011) applied pacing at a range of CLs to five patients and found CVs in the range 35 to 115 cm/s. AF CVs may be at the lower edge of the CV range due to the short CLs observed in AF. Konings et al. (1994) measured CVs in sinus rhythm (73±5cm/s), paced rhythm (68±5cm/s), as well as for their three AF classifications: 61±6cm/s (type I AF), 54±4cm/s (type II AF) and 38±10cm/s (type III AF). In this study, CV was in the range $25 - 50$cm/s, representing the lower range of CVs observed in AF. However, CVs higher than this range will result in spatial wavelengths for which the domain size used here (10cm by 10cm) is too small to test the resolution requirements.

Dividing the range of values observed in the literature for CVs by the range of DFs, gives the following range of expected spatial wavelengths during human AF: $44 - 127$mm ($0.38/8.6 \times 1000$ to $0.61/4.8 \times 1000$). The wavelengths of the spiral waves in this study cover a subset of this range from $33 - 78$mm; larger wavelengths than this would require a larger domain size than the 10x10cm sheet used here. However, it is possible to extrapolate the results using the relationship between spatial wavelength and required resolution derived here to say that a spatial wavelength of 127mm requires a resolution of 41mm (using the largest requirement for the three identification criteria; that is 3.1).

7.5.4 Spatial wavelength scaling across species

In order to apply the findings here to other species, it is necessary to consider how spatial wavelength scales across species. Noujaim et al. (2007a) investigated cycle length (CL) during VF across eleven species of mammals to find that CL scaled with body mass (BM) such that: VF cycle length, VFCL ≈ 53 x $BM^{\frac{1}{4}}$, or equivalently VF dominant frequency, VFDF ≈ 18.9 x $BM^{-\frac{1}{4}}$. Species ranged in physical size from mouse (38Hz) to horse (6Hz), and included guinea pig (26Hz), rabbit (15Hz) and human (6.8Hz). Cardiac CV has been shown to correlate with fibre diameter, where larger cells generally result in faster CVs (Draper and Mya-Tu, 1959). Since myocardial fibre diameter is relatively uniform across species, CV is not expected to show great variation (van der Tweel et al., 1999). Thus, spatial wavelength will primarily vary due to changes in DF, following the body mass relation above.

Assuming a CV of 0.5m/s in AF (or VF) in order to give a suggested wavelength for each species, example spatial resolutions requirements indicated by this study are: mouse 4.2mm; guinea pig 6.2mm; rabbit 10.8mm; human 23.7mm (using N=3.1).

7.5.5 Required resolution for regular grids of data

This study aimed to extend the work of Rappel and Narayan (2013) who used a theoretical approach to determine that the resolution required to identify stable rotors and focal sources is λ/N, where λ is the spatial wavelength and N is the number of desired isochronal regions. In their study, wave patterns were identified visually and the required value of N was not quantitatively determined. In the study presented here, we find that the resolution requirements are linear in λ, suggesting that the resolution required does follow λ/N, with a best fit N of 2.5 (visual), 2.7 (rotor core location) and 3.1 (false phase singularity detections) for spirals; and 3.3 (visual) and 1.6 (maximum divergence location) for focal sources. In addition, this study uses phase and divergence to analyse the wavefront dynamics in an automated way, and a method is developed to estimate the spatial wavelength λ.

The spatial Nyquist criterion says that the inter-electrode spacing must be less than half the smallest spatial wavelength of interest (Bayly et al., 1998b), which would correspond to $N = 2$. Four of the identification criteria with the thresholds applied in this study suggest a slightly higher value of N is needed, while the maximum divergence location suggests a smaller value. The maximum divergence location criteria was applied for focal sources where the grid was centred over the focal source, which is the optimal arrangement; off-centre arrangements may require a higher value of N.

7.5.6 Using the conduction velocity divergence to identify focal sources

Masè et al. (2009) used divergence of a velocity vector field generated from a radial basis function interpolation of simulated PentaRay data to identify foci as maxima of the divergence and wavefront collision as areas of divergence minima. Their study interpolated the activation times from the fifteen points at locations representing five splines of a PentaRay catheter using radial basis interpolation, prior to calculating the divergence. In this study, no interpolation of activation times was performed; instead CV vectors were calculated from regular grids of downsampled data and the CV vector field components were then interpolated to the 2mm grid resolution. Since CV vectors were calculated using a finite difference method, focal source iden-

tification using divergence was limited to regular grids of data. Our study could be extended by employing radial basis function interpolation to activation times. Fitzgerald et al. (2005) also used divergence to locate ectopic foci.

7.5.7 Realistic mapping catheters – required resolutions

The effects of the number of measuring points and their arrangement as multipolar catheters has been investigated in several studies. Masè et al. (2009) simulated a PentaRay catheter composed of fifteen bipoles where foci and wavefront collision identification using radial basis function interpolation and the divergence was successful upon removal of eight or fewer bipoles, so long as these were from a random arrangement. Removing two entire splines reduced the ability of the divergence to identify foci. In this study, rotor tip location was successful for simulated PentaRay catheters with ten bipoles.

Weber (2011) simulated Lasso, Afocus and PentaRay catheters over a focal source and found that the Lasso catheter could not identify the focal source. Similarly, in Chapter 3, focal source location was identified successfully for Afocus and PentaRay catheters, but not for the Lasso catheter. This is because the Lasso catheter does not contain any radial information. In this chapter, the effects of catheter shape on rotor tip location was investigated and for twenty recording points, the Lasso catheter gave the largest error in estimated rotor centre location. Whereas focal source location was unsuccessful for the Lasso catheter placed over the focal source, the rotor tip location estimation was successful, although it was more inaccurate than for the other multipolar catheters.

Rottmann et al. (2014) compared different methods for estimating rotor tip location to the traditionally used phase singularity method, including local activation times, peak-to-peak amplitude (where the rotor core was at a minimum), steepest negative slope in unipolar electrograms (rotor core at maximum) and approximate entropy (rotor core at maxima). For the PentaRay catheter, peak-to-peak amplitude minimum and steepest negative slope maximum accurately located the rotor core (1.7mm and 0.7mm error respectively), and the activation time and approximate entropy also showed a good agreement. The results of using these methods were compared for a circular catheter arrangement (10 electrodes) and a PentaRay arrangement (20 electrodes), where the peak-to-peak amplitude method of location was not successful for the circular catheter, again due to the lack of information at the rotor core. In the work presented here, rotor core location was accurate using phase singularity location for the Lasso catheter with ten electrodes, suggesting it may offer advantages over peak-to-peak amplitude in this case. Becerra et al. (2014)

also used approximate entropy for rotor location, finding that accuracy reduces when the electrode resolution is reduced.

Martínez et al. (2014) investigated the effects of spatial resolution on rotor trajectory identification using a simulated electrode plaque, where the electrode spacing was either 1, 2 or 5mm and the distance between the plaque and the atrial wall was 0.2, 1, 2 or 5mm. They found that a stable rotor could be accurately identified when the electrode spacing was 1 or 2mm, so long as the distance between the plaque and the wall is less than 5mm. At 5mm, a rotor could be identified, but the measure of the area over which the rotor meandered was unreliable as the rotor core trajectory could not be identified accurately. An extension of their work is to consider a meandering rotor with a basket catheter to see how accurately the rotor core trajectory area is located with the basket catheter. In the work presented in this chapter, the case of a meandering rotor measured with a basket catheter is considered. For a wavelength of 75.2mm, the path of the average rotor tip location is accurate for the basket results, although the trajectory area is overestimated.

The area of coverage of the catheter is important in that rotor tip identification using phase requires the catheter to be located over the rotor tip. In the case that the catheter does not lie over the rotor core, the techniques developed in Chapter 3 could be used to direct the catheter towards the rotor core location.

7.5.8 Choice of interpolation method

Martínez et al. (2014) linearly interpolated voltage in order to compare results for different inter-electrode spacings. In contrast, in the work presented here, phase was interpolated using spline interpolation since it was found to result in fewer false phase singularity detections. Berenfeld and Oral (2012) make the point that phase interpolation may bias towards detecting reentrant behaviour. *Focal Impulse and Rotor Modulation* mapping technique (Narayan et al., 2012d) also uses interpolation of phase, however interpolation is linear; whereas, here it is cubic spline.

7.5.9 Feasibility of estimating wavelength to calculate resolution requirements

The spatial Nyquist criterion says that the interelectrode spacing must be less than half the smallest spatial wavelength of interest (Bayly et al., 1998b). In addition, the resolution requirements found in this study are in terms of the spatial wavelength. Thus, to determine the required resolution, it is necessary to estimate the smallest relevant spatial wavelength.

There are methods in the literature for estimating cardiac wavelength (Graux et al., 1998; Jacquemet et al., 2005; Botteron and Smith, 1996). Jacquemet et al. (2005) compared three methods from the literature: (1) dense activation map of CV × (APD + correction); (2) local measure of CV× *effective refractory period* (ERP) using two electrodes in paced rhythm (Graux et al., 1998); (3) space constant related to average wavelength from Graux et al. (1998). The estimated wavelength was found to depend on both the method and dynamics, where *a priori* information about the dynamics was required in order to properly interpret the estimated wavelength. In this study, the spatial wavelength was measured where possible and also estimated using CV×CL, rather than CV×ERP or CV×(APD + correction) used in previous studies. This gives a direct measure of the spatial wavelength (distance between successive wavefronts) rather than estimating the shortest possible wavelength approximated by CV×ERP. During AF, the measures of CV×CL and CV×ERP may be very close; however, in the vicinity of a focal source they may differ if the focal source pacing rate is slower than the fastest rate the tissue can support.

In this chapter, six or seven measuring points were required to give an accurate and reliable wavelength estimate using CV×CL, in the case that the measuring locations were taken from an area of a smaller diameter than the wavelength and away from a rotor core. A high-density mapping catheter (2cm diameter) would work well for this purpose, since wavelengths in human AF are estimated to be longer than 2cm.

7.5.10 Implications for various mapping modalities

Many centres only have the technology for sequential mapping; thus an important question is whether rotors can be located using sequentially collected data. The spatial resolution requirements found in this study suggest that the most stringent resolution requirement expected for the identification of spiral waves in human AF is $44/3.1 = 14.2$mm. The inter electrode spacing of all high-density mapping catheters is less than this (Afocus 4mm, Lasso 6mm, PentaRay 2, 4, or 6mm). However, it has to be kept in mind that the Lasso catheter does not provide radial information. Inter-electrode distances for the basket catheter used in the simulations here were median 10.2mm, lower quartile 5.87mm and upper quartile 16.2mm. 63.1% of the interelectrode distances are less than the resolution requirement of 14.2mm. (Berenfeld and Oral, 2012) comment that some areas of interpolation for basket mapping have interspline difference of greater than 20mm; here using the basket catheter and geodesic distances, 12.6% of inter electrode distances are greater than 2mm.

Ideker et al. (2009) consider the resolution of data required in order to distinguish between a focus and microreentry in the ventricle and find that an electrode spacing of 2mm is required. They suggest that in clinical studies where this resolution is not available, other information such as beat-to-beat variability could be used to differentiate between mechanisms.

7.5.11 Limitations and extensions

Possible limitations include that a linear relationship was assumed between required resolution and spatial wavelength. Spiral and focal sources were assumed to be sinusoidal to derive the relationship that spatial wavelength is conduction velocity multiplied by cycle length. In addition, resolution requirements for the regular grid studies were based on action potential data rather than electrogram data.

CV is assumed to be uniform within the area of interest, and a median CV is used to estimate the spatial wavelength. Regional heterogeneities in fibrosis and electrical remodelling may mean this is not the case. Equally, regional differences in frequency may lead to inaccurate estimates of spatial wavelength, in the case that the dominant frequency varies within an area.

In the basket simulation studies, all electrograms were noise-free, representing perfect data. In reality, electrograms will contain noise, signal artefacts and some may have unsatisfactory tissue contact (Berenfeld and Oral, 2012). An extension is to add noise to electrograms from the basket simulations or to remove subsets of electrograms from the basket simulation studies, to model noisy, or unsatisfactory data. The number of recording points within the basket necessary for rotor-core identification requires further study. In addition, electrodes may be a distance from the atrial wall, and the effects of this distance on the observed rotor dynamics requires investigation. Phase interpolation was performed using the two-dimensional locations that best preserve the geodesic distances; the reduction in accuracy associated with placing the measuring points on a regular 8-by-8 grid should also be considered. Finally, the difficulty in assigning success and failure in rotor identification was highlighted in the basket simulations, since two of the three rotors failed the centre of mass criterion, and all failed the false detection histogram criterion; however, the average rotor path was defined adequately. This suggests that the overall rotor path is observable; however, care should be taken in the analysis, due to the large number of false singularity detections, which though transient, could affect algorithm.

The parameter sets used in the regular grid simulations had CVs towards the lower range of CVs seen in AF; however, higher CVs will result in spatial wavelengths

for which the domain size used here is too small to test the resolution requirements. Further simulations with a large domain size could be run to check whether the extrapolation of the results is correct, although the domain size of 10cm-by-10cm does represent realistic atrial dimensions.

Chapter 8

Conclusions

The overall motivation of this thesis was to address some of the challenges associated with arrhythmia interpretation, by developing and testing techniques for analysing cardiac electrical wavefront dynamics applied to simulated, experimental and clinical data. Novel techniques were developed to measure conduction velocity, estimate focal source location, create phase maps from electrogram data and to analyse arrhythmia data. In addition, the questions of the measurements required, the most appropriate post-processing protocols and the influence of parameter choice within analysis protocols were investigated. This chapter summarises the key findings and future directions of this work.

8.1 Summary of key findings

In Chapter 3, an algorithm was developed to rapidly estimate conduction velocity (CV) and the location of the origin of a focal source, for either a planar or circular wavefront measured from any arbitrary arrangement of recording points. Both the planar and circular algorithms with an arbitrary arrangement of points performed well for a range of simulated focal sources and catheter locations, and for two out of the three clinical data sets considered. The three dimensional catheter electrode locations were converted to two-dimensions by either projecting to the two-dimensional plane of best fit, or by finding the locations which best preserve the geodesic distances between the electrode points on the mesh. The geodesic method was found to be superior in the case of increased surface curvature, or when the source location and recording catheter were not on the same side of the geometry. This technique was applied successfully to atrial tachycardia data for two patients.

In the case of spiral wave or focal source propagation data, it can be difficult to assign an appropriate time window corresponding to a single wavefront. An

automated approach to finding the CV and focal source location using the time window with the lowest residual was developed, so that the algorithm can be used without the need to pre-specify a time window. The circular wavefront algorithm provided an estimate of the location of where the focal wave originated from. This was applied to simulated focal sources and spiral waves to show the applicability of the technique in estimating the location of a focal source or the core of rotational activity. In the case that the catheter was placed over a focal source, five-spline and spiral catheters were able to predict the source location; however, the location estimation was unsuccessful in the case of a circular catheter, due to the lack of radial information.

In Chapter 4, a protocol was developed for analysing wavefront dynamics in optical mapping data, including phase singularities and frequency analysis. This required the development of a methodology, which is robust to noise, to identify and track phase singularities and to calculate their number of rotations. The sensitivity of the algorithm to filtering and post-processing parameters was investigated in terms of the resulting dominant frequency (DF) maps and phase singularity durations, number of rotations and distributions. The following values were chosen following the sensitivity analysis: spatial bin size for voltage (9-by-9 pixels); temporal filter for voltage (125% of the dominant frequency); moving mean window length (90% of the median cycle length) and amplitude deletion threshold (15% of the median amplitude) for phase calculation; spatial bin size for phase (9-by-9 pixels); spatial bin size for phase singularity distribution map (3-by-3 pixels); duration or number of rotations threshold for inclusion in heat map (0.5 rotations).

In Chapter 5, the optical mapping protocol from Chapter 4 was applied to four experimental preparations, and a methodology was developed for assessing the mechanisms maintaining fibrillation in each of the preparations, by calculating the number and distributions of phase singularities and new wavefront initiation sites. Each of the following were shown to exhibit stability over time: dominant frequency maps; the spatial distribution of phase singularities; and the spatial distribution of new wavefront initiation locations. Regions of high phase singularity density were found to exist, with low phase singularity density on the septal region of all preparations. There were preferential regions for new wavefront initiations in three of the four preparations, where two of the preparations had a single site that was responsible for maintaining the arrhythmia, whilst the third preparation had multiple sites of new wavefront initiations. For the preparation without preferential sites for new wavefront initiation, there was also a lower incidence of electrical quiescence in the mapping field and a higher incidence of rotors, suggesting that AF was maintained by

rotational activity on the endocardium. Hence differences were quantified between the preparations in order to determine the mechanisms for maintaining arrhythmia.

In Chapter 6, methodologies were developed for phase mapping of both unipolar electrogram and bipolar electrogram signals, which were tested against action potential phase from simulated data; and then applied to experimental and clinical electrograms. Phase values and singularity locations were similar across the three modalities (action potential data, unipolar electrogram data and bipolar electrogram data) in simulated data, and unipolar and bipolar electrogram phase agreed well in experimental data. The number of phase singularities assessed using clinical unipolar and bipolar electrograms matched well, as did activation times calculated for time windows assigned using wavefronts calculated from bipolar phase. For each catheter, there were times when the unipolar and bipolar phase did not correlate as closely due to differences in the activation assignment between the signals, which occurred in cases where the signals were fractionated or of longer duration.

In Chapter 7, the effects of spatial resolution on the identification of rotors and focal sources were determined as a function of the distance between successive wavefronts (the spatial wavelength, λ). A technique was presented to estimate spatial wavelength from a small number of measuring points, providing experimental and clinical utility. Spatial wavelength was estimated as conduction velocity $\times$ cycle length, for which seven measuring points were required. The required resolution was of the form λ/N, and values of N were calculated for a regular grid of points using several identification criteria. Values of N were found for a spiral wave to be 2.5 (visual), 2.7 (rotor core location) and 3.1 (false phase singularity detection), and for a focal source to be 3.3 (visual) and 1.6 (maximum divergence location). In order to determine whether these resolution requirements also hold for irregular arrangements of points, high-density mapping catheter arrangements were simulated (circular, spiral and five-spline formations), and these were found to identify rotor core locations accurately. In addition, the case of meandering rotors measured using a basket catheter was considered, for which identification was satisfactory.

In this thesis, novel techniques were developed for the following:

1. visualising three-dimensional left atrial cardiac activation data in two dimensions, with minimal distance distortion;

2. estimating conduction velocity and the location of the origin of a focal source, for either a planar or circular wavefront, measured from any arbitrary arrangement of recording points;

3. assessing the spatio-temporal distribution of dominant frequency, phase sin-

gularities and new wavefront initiation locations in order to gain insight into arrhythmia mechanisms

4. calculating phase and tracking phase singularities from simulated, cell culture and clinically acquired electrogram data;

5. estimating spatial wavelength.

In addition, the following questions were investigated:

1. the effects of post-processing techniques and the importance of parameter choice in phase mapping;

2. the relationship between resolution requirements and wavefront spatial wavelength for identifying rotors and focal sources.

These techniques and investigations, relating to the analysis and interpretation of cardiac wavefront dynamics, are discussed in the following sections.

8.2 Novel techniques

8.2.1 Visualising three-dimensional left atrial cardiac activation data in two dimensions with minimal distance distortion

A technique to visualise the left atrium in three dimensions with minimal distance distortion was applied to MRI and electro-anatomic mapping data, and the effects of different cuts in the mesh were investigated (Section 2.14). This methodology is superior to existing methods in the literature for surface flattening in situations in which distance preservation is important; for example, for calculating conduction velocity (see Fig. 3.4.9 for an example activation time map). A further advantage of the method is that it enables the use of two-dimensional algorithms, such as interpolation and phase mapping; as well as offering easier visualisation of phase singularity trajectories (see Fig. 7.24). The method was based on that of Zigelman et al. (2002), who applied a surface flattening technique to arbitrary surfaces that minimises distance distortions, but did not specifically assess its use for the cardiac anatomy.

Karim et al. (2014) also presented a method for mapping the left atrium to two dimensions; however, they aimed to preserve area and angles, rather than distance.

In addition, they applied boundary conditions to fit the atrium to a square; whereas, the method presented in Section 2.14 allowed a free boundary in order to minimise distance distortion. The choice of cuts made in order to flatten the mesh affected the two-dimensional representation, and the most appropriate choice depends on the application. For example, cutting along the pulmonary vein sleeves and removing them to the level of the atrial body minimised the distance distortion due to their high curvature. Thus this is preferred in clinical studies in which data are only collected on the atrial body. However, for some studies the pulmonary veins are required in the two-dimensional map (for example, simulation studies into the effects of the pulmonary veins on AF). Removing the veins without including additional cuts along the sleeves resulted in a two-dimensional map with holes representing the pulmonary veins, and this choice of cut was found to be most similar to the technique of Karim et al. (2014). Extensions to this work include weighting interpolation points by the degree of distance distortion, in order to minimise these effects on the final interpolation.

8.2.2 Estimating conduction velocity and the location of the origin of a focal source, for either a planar or circular wavefront, measured from any arbitrary arrangement of recording points

Any arrangement of measuring points

The cosine-fit technique of Weber et al. (2010) was initially developed for a circular catheter of measuring points. The extension presented in this thesis, which allows an arbitrary arrangement of two-dimensional points, means the algorithm can also be used on spiral and PentaRay catheters.

Many CV methodologies impose constraints on measuring point locations, and so are not suitable for use with an arbitrary arrangement of points. These include finite difference techniques (Section 1.12.2), which require measuring locations to be on a regular grid; and the cosine-fit method of Weber et al. (2010) (Section 1.12.5), which assumes points are located on a circular catheter. CV techniques suitable for use with an arbitrary arrangement of points include triangulation (Section 1.12.1), which requires the construction of triangles of points; polynomial surface fitting techniques, which require the choice of a spatial and temporal window for points to be included in the surface fit (Section 1.12.4); and radial basis function techniques,

which are computationally demanding (Section 1.12.8). The algorithm developed in Chapter 3 overcomes these limitations, since it is computationally efficient, and can be applied to an arbitrary arrangement of points on a catheter and so no further selection criteria are necessary.

Required resolution of the CV vector field versus accuracy

On the one hand, a dense CV vector field provides detailed information for assessing spatial heterogeneity in CV and complicated activation patterns. The CV technique developed in this thesis can be applied to three measuring points in the case of a planar fit, in which case, a large number of CV vectors can be assigned to each catheter. Similarly, triangulation is based on triads of points, resulting in an increased CV vector field resolution (Cantwell et al., 2014a). As such, heterogeneity in CV across the tissue covered by a catheter and localised correlations with other measures can be analysed using triangulation (Ali et al., 2014). However, in this case, each CV direction is sensitive to noise content, as only three points are involved in the calculation. On the other hand, errors in activation time assignment may necessitate a technique that fits to a larger number of points, or a technique to assign activation times based on neighbouring activation times (Dubois et al., 2012). The technique developed in this thesis is designed to assign one direction per multipolar catheter of data, and to give a more global measure of CV, which is less sensitive to errors in activation time assignment and quick to apply. Overall, the choice of the most appropriate technique depends on the required balance between the density of the CV field, and the number of points required for each estimate in order to reduce the effects of noise.

Focal source and spiral core location estimation

The technique developed in this thesis was able to accurately and reliably estimate focal source and spiral core location in simulated data, and also worked well in two out of three clinical cases tested for which the wavefront originated from a paced location. As such, the technique can be used to guide a catheter towards a focal source or a rotor core.

Vector field analysis is a further technique that can be used to locate focal sources in the case that data are recorded over the source, by calculating the divergence and curl (Sections 1.12.12, 7.2.6) (Rousakov et al., 1999; Fitzgerald et al., 2005; Masè et al., 2009). In addition, spiral core location estimation can be performed by locating phase singularities in the case that data are available over the rotor core

location (Sections 2.10, 2.11). Other techniques that are applicable in the case that the catheter is not over the focal source or rotor core location include the study of Ganesan et al. (2015), which investigated how electrogram characteristics vary with distance from a rotor core location; however, their study does not give an explicit measure of the distance towards the source.

Calculating CV without the need to specify a time window in the case of focal or rotational wavefronts

A technique was proposed in order to automatically select a suitable time window for calculating CV for a focal or rotational wavefront. This circumvents the major problem of the selection of a time window for activation time assessment during tachycardias and fibrillation. Other mapping techniques that do not require a manual selection of a window of interest include ripple mapping (Linton et al., 2009).

8.2.3 Assessing the spatio-temporal distribution of dominant frequency, phase singularities and new wavefront initiation locations in order to gain insight into arrhythmia mechanisms

The methodology presented in Chapter 5 for calculating the dominant frequency, the number and distribution of phase singularities and the distribution of new wavefront initiation sites, highlighted the differences in these properties between experimental preparations. There was a low correlation between the three measures, suggesting that all three measures are required to elucidate the mechanisms sustaining AF. For example, in three of the four preparations studied, there were preferential regions for new wavefront initiations, which were not identified during visual inspection of the phase propagation videos. For two of the preparations, there was a single site that was responsible for maintaining the arrhythmia within the mapping field. These sites were not seen on dominant frequency or phase singularity distribution maps. For the preparation without preferential sites of new wavefront initiation, it was more important to calculate the phase singularity density maps. Hence, multiple measures should be considered in combination.

Identifying new wavefronts from phase

Similar to the studies of Rogers (2004) and Nash et al. (2006), wavefronts were defined in Chapter 5 as lines of constant phase. New wavefronts were then identified in the case that there were no active pixels within a neighbourhood in the preceding frame. This technique has the advantage that it does not require any activation time assignment. In addition, the technique worked well with signals of variable amplitude, which would pose a problem for isopotential line techniques (Kay and Gray, 2005). Stability was observed in new wavefront location in three of the preparations, demonstrating efficacy of the technique.

Phase singularity tracking can also be performed by tracking wavefronts, since phase singularities are located at the ends of wavefronts (Rogers, 2004). However, this approach was not used in this thesis because noise in phase led to wavefront mis-identification in some cases (for an example, see Fig. 4.21). This suggests the wavefront identification technique in Section 5.2.1 could be improved using techniques similar to those employed for phase singularity detection in Chapter 4 (for example, adding a number of missing frames threshold to the algorithm).

Comparison with other studies

Dominant frequency (DF) was found to be stable in the preparations studied here, which agrees with the findings of Sanders et al. (2005). Multiple frequency domains were observed in the preparations, which is a similar finding to those presented in the study of Sarmast et al. (2003). Phase singularity density maps were also found to exhibit a degree of stability over time, which agrees with the clinical studies of Narayan et al. (2012d) and Haissaguerre et al. (2013). New wavefront initiation locations were also shown to exhibit a degree of stability over time in three of the four preparations studied here. Likewise, Filgueiras-Rama et al. (2011) detected organised focal wavefronts located at the same site and with the same direction over four or more sequential beats. In contrast, Eckstein et al. (2013) reported that new wavefronts due to endocardial-epicardial dissociation are not found in repeated locations.

There was very little correlation between dominant frequency, PS distribution maps and new wavefront sites in the preparations investigated in this thesis, which is surprising since focal or reentrant drivers are thought to coincide with areas of high-frequency (Mansour et al., 2001; Filgueiras-Rama et al., 2012). PS trajectories were included in the PS distribution map in the case that the trajectory lasted at least 0.5 rotations; varying this threshold may affect this correlation, although

the studies performed in Chapter 4 indicate this change is likely to be small. The definition of rotor in terms of the number of rotations required differs among the literature (Kay and Rogers, 2006; ten Tusscher et al., 2007, 2009), and so parameter sensitivity studies such as the one presented in Chapter 4 are important to gauge the effects of this.

The effects of acetylcholine concentration on the wavefronts observed in AF are complicated (Sarmast et al., 2003), and its application in the experiments analysed in this thesis led to unphysiological frequencies. Despite this, the optical mapping data provided a useful dataset for testing the ability of the developed methodology to analyse arrhythmia wavefront dynamics. The source of new wavefronts in this study were unknown, since analysed data were from the endocardium only; this is discussed in more detail in Section 8.5.1.

8.2.4 Calculating phase and tracking phase singularities from simulated, cell culture and clinically acquired electrogram data

Phase mapping techniques were developed for unipolar and bipolar electrogram signals, where in contrast to action potential phase, for which both activation and recovery of the tissue were represented, phase of electrograms indicated activation only, due to the difficulty in identifying repolarisation within the electrogram signals.

Development approach

The approach here for the development of the electrogram phase mapping method was to start with the simplest data type (simulated data) and then to build in complexity (experimental and clinically acquired electrograms). With each extension, multiple adaptations of the algorithms were required. The final clinical algorithms were significantly different from the initial algorithms, so the final algorithm was tested on simulated data (a gold standard dataset) to ensure that the later modifications had not affected the correspondence with action potential phase. The challenges associated with analysing clinical data necessitated this iterative approach of increasing model complexity; and retesting the final model against the original simplest data set was an important step in model validation.

Assigning activation to complicated signals

Electrogram phase mapping appears to circumvent the challenge of explicitly assigning activation times to fractionated signals; however, the step of the algorithm in which maxima and minima were selected in order to normalise the signal determined which deflections were given a full progression of phase, and hence which deflections were defined as activations. As such, this step is equivalent to assigning activation times, and determining an isophase value equivalent to activation will enable recovery of these times from the phase signal. There are multiple techniques in the literature for assigning activation times that may offer an improved phase calculation, including selecting times such that the mean and median cycle length converge (Ng et al., 2014); template matching (Houben et al., 2006); and assigning times based on neighbouring locations (Dubois et al., 2012).

Use of unipolar phase and bipolar phase in tandem

The combined use of unipolar phase and bipolar phase may offer an improved measure of activation patterns. The circular correlation measured between unipolar and bipolar phase was low in cases where different deflections within unipolar and bipolar electrogram complexes were selected as representing activation. As such, these periods of low correlation indicated times of uncertainty in phase assignment; whereas, more confidence could be placed in phase assignment in the case that the signals agreed. The areas of uncertainty could be subjected to further analysis.

Comparison with other techniques for phase mapping

Kuklik et al. (2014) recently published a methodology for calculating phase of unipolar atrial electrograms, which shares a number of similarities with our technique. Both capture activation times at peaks of negative derivative of unipolar electrograms; both include a step in the methodology to enforce that activations are assigned at locations of steep negative gradient only; and both create a sinusoidal signal suitable for use with the Hilbert transform and for phase analysis. A disadvantage of the method of Kuklik et al. (2014) is that the period of each sinusoidal wavelet is equal to the mean of the cycle length (the time between activations) of the signal; thus, the method may perform sub-optimally in the situation of varying cycle length. Similarly, the method developed in this thesis used a window length in order to tag deflections and so may suffer similar limitations. A combination of window length and amplitude may be more appropriate. Our method has the advantage

that it will work with any set of tagged maxima, and as such, the technique used to initially assign deflections as activations could be adjusted for the individual signal.

Our method uses the approach suggested by the pseudo-empirical mode decomposition technique of Bray and Wikswo (2002a) to normalise the filtered bipolar or filtered derivative of the unipolar signal using maxima and minima splines. It would not be appropriate to apply this to the unipolar signal directly because far-field signals may be of higher amplitude than local deflections, which is discussed in Kuklik et al. (2014). However, the technique is applicable to the derivative of the unipolar signal, where steep negative slopes indicate activation.

Other techniques for phase mapping of electrograms include that used by Nash et al. (2006) to analyse human VF dynamics of epicardial unipolar electrograms. They used a quadratic detrending technique to ensure that the signal had mean zero, with activation times at voltage zero, which performed well. However, Kuklik et al. (2014) stated that this technique may not be suitable for unipolar AF electrograms due to the longer isoelectric line.

To the best of my knowledge, the application of the set of filters commonly used for dominant frequency analysis (Ng et al., 2006; Castells et al., 2014) prior to phase analysis is a novel application, and there are no other published methodologies for calculating bipolar electrogram phase at the time of writing.

Additional techniques for identifying rotor core location

Rotor cores can be located as phase singularities in the case that the measuring device is placed over the rotor core. When this is not the case, the CV technique developed in this thesis could be used to direct the catheter towards the rotor core, or to estimate the rotor core location (Section 3.4.7), and then phase mapping could be used in order to determine a more accurate location. Other techniques for identifying rotor cores using electrogram characteristics include measuring entropy (Ganesan et al., 2013; Becerra et al., 2014); and peak-to-peak amplitude (Rottmann et al., 2014).

8.2.5 Estimating spatial wavelength

Resolution requirements were determined as a function of spatial wavelength, and so an estimate of the spatial wavelength is required in order to apply these requirements in an experimental or clinical recording environment. Spatial wavelength λ is the distance between successive wavefronts, and for sinusoidal waves is the wave speed v divided by the wave frequency f, or CV $\times$ cycle length (CL). This differs from

the various methods in the literature for estimating cardiac wavelength (the shortest possible wavelength) as CV $\times$ (APD + correction) or CV$\times$ effective refractory period (ERP) (Jacquemet et al., 2005; Graux et al., 1998). During fibrillation, CV$\times$CL and CV$\times$ERP are likely to be similar in value; however, close to a focal source they may differ if the focal source activation rate is slower than the fastest rate the tissue can support.

The method used to estimate CV will affect the estimated spatial wavelength. In the case of arbitrarily arranged recording points, the method developed in Chapter 3 is recommended. Estimation was found to require seven points and must be measured away from a rotor core.

8.3 Questions addressed

8.3.1 Effects of post-processing techniques and importance of parameter choice for rotor tracking analysis

Choice of rotor core identification method and parameters

Preliminary studies presented in Appendix A indicated that rotor-core location trajectories depended on the method used to identify them and the parameter choices within the method. The two methods used were the isopotential line method (Section 2.13) and the phase singularity method (Section 2.9).

Optical mapping: parameter sensitivity analysis for DF and phase singularity analysis

The optical mapping analysis protocol outlined in Chapter 4 contained many data-specific thresholds (see Figs. 4.3, 4.31), and the sensitivity of the final output of the dominant frequency and phase singularity measures on a subset of these parameters were determined. The true DF and phase singularity distributions were unknown, since there was no gold standard (see Section 8.5.2 for further discussion), and so the output from the various parameter combinations were compared to each other.

Variation of the high-band of the band-pass filter within the range of $100-200\%$ of the estimated DF did not have a large effect on the calculated phase singularities; whereas, the choice of spatial bin size was found to have a larger effect. The filter settings here were lower (125% is equivalent to 35.7Hz) than the 100Hz recommen-

dation of Laughner et al. (2012) (with their justification being that all of the relevant physiological frequencies in the frequency spectrum are below 100Hz). Rodrigo et al. (2014) found that filtering at the highest DF allowed the identification of rotors that would otherwise be hidden by irregular activity at other frequencies, in a clinical and computational study of surface mapping data.

The phase calculation method used for calculating the phase of action potential signals is an extension of the technique of Bray and Wikswo (2002a), to work with both a window length threshold for tagging extrema of the signal and an amplitude threshold for determining which of the small amplitude detections to delete. The study of Bray and Wikswo (2002a) uses a window length of 50% of the estimated cycle length, in order to include double potentials that occur during reentry in the final phase signal. However, for the data analysed here, window lengths smaller than 90% of the estimated median cycle length were found to include too many additional deflections within the signal. This indicates that experiment specific thresholds are required for an optimal algorithm.

Spatial distributions of drivers (focal sources or rotors) are used clinically by centres using the non-invasive ECGi technology to determine ablation targets, for which the atria are divided into seven regions for regional analysis (Haissaguerre et al., 2013, 2014a). Similarly, our analysis was regional; however, this was for the purpose of comparison with histological data. Additional differences include that focal sources (new wavefronts) and rotors (phase singularities) were considered separately for our investigations.

Parameter sensitivity analysis should be performed for the electrogram phase mapping of clinical electrograms presented in Chapter 6, particularly with regards to the effects of the window length threshold for tagging deflections in the phase calculation.

8.3.2 Determining the relationship between resolution requirements and wavefront spatial wavelength for identifying rotors and focal sources

This work aimed to extend the study of Rappel and Narayan (2013) who showed that the theoretical resolution required in order to identify a spiral or focal source is the distance between successive wavefronts (the spatial resolution) divided by the number of desired isochronal regions, N, per wavefront. Extensions presented in this thesis were to determine the value of N for different identification requirements, and

to provide a method to estimate spatial wavelength, so that the resolution requirements can be used by other researchers to inform their data sampling strategies and catheter design. These requirements were initially determined for a regular grid of data, and then tested on arrangements representing clinical catheters. Analysis of the basket simulations for this work (Section 7.4.3) required the use of surface flattening techniques (Section 2.14) and the calculation of unipolar electrogram phase (Chapter 6), demonstrating the use of several of the techniques developed in this thesis in order to address a clinically relevant question.

Comparison of measurement criteria to the spatial Nyquist criterion

Successful rotor identification was assessed using three measures, which required different numbers of measuring points: visual assessment; error in the centre of the rotor core location; false phase singularity detections. The visual identification criterion was found to require the smallest number of measuring points (2.5), whilst the number of false detections criterion required the largest (3.1). These requirements are larger than the 2 points required by the theoretical spatial Nyquist criterion (Bayly et al., 1998a). Visual identification is subjective, and it is possible that another user may have chosen resolution cut-offs closer to a requirement of 2 points per spatial wavelength. The criterion of an accurate rotor core location ($<$ 4mm error) and an acceptable number of false detections are expected to require more grid points than identification only, explaining the larger values for N.

Successful focal source identification required 3.3 points for the visual criterion and 1.6 for the focal source divergence. The simulated focal sources were perfectly circular, and the grid of points used for the maximum divergence location criteria was centred over the focal source; resulting in an optimal arrangement and the smallest possible value of N. The effects of non-symmetric propagation and the case in which the points are not centred over the source should be considered.

Implications for mapping modalities

The spatial resolution requirements determined in this thesis suggest that the most stringent resolution requirement expected for the identification of spiral waves in human AF is $44/3.1 = 14.2$mm (using the shortest wavelength expected and the highest number of points requirement). All high-density mapping catheters have an inter-electrode distance much smaller than this (Afocus 4mm, Lasso 6mm, PentaRay 2, 4, or 6mm), suggesting they provide sufficient data to identify a rotor or focal source in the case that they are located over the source. One point to note is that

the Lasso catheter does not provide radial information, making this interpretation more difficult. The basket catheter used in simulation studies here (48mm diameter) had a median inter-electrode distance of 10.2mm, a lower quartile of 5.87mm and an upper quartile of 16.2mm, and 63.1% of the inter-electrode distances were less than the resolution requirement of 14.2mm. Simulation studies suggested that the rotor trajectory mean path was accurate for the basket catheter; however, there were a large number of false phase singularity detections, indicating that care has to be taken for the analysis of phase maps created from basket catheter data.

8.4 Open problems and challenges

There are a number of open problems and challenges relating to this work, including:

1. measuring and interpreting the three-dimensional nature of atrial fibrillation;
2. algorithm validation in the absence of a suitable gold standard measurement;
3. calculating conduction velocity during fibrillation;
4. locating drivers of atrial fibrillation from sequential data measurements;
5. the spatial resolution required to distinguish between mechanisms of atrial fibrillation.

These are discussed in more detail along with other study limitations and future extensions in the following sections.

8.5 Study limitations

8.5.1 Limitations of recording techniques: two-dimensional measurements of a three-dimensional substrate

Most experimental and clinical recording techniques do not record data through the thickness of the atrial wall. For example, the clinical data analysed to calculate conduction velocity in Chapter 3 were from the endocardial surface. The three-dimensional electrode locations were mapped to two dimensions, by either projecting to the plane of best fit or using a geodesic mapping, and then the two-dimensional CV algorithms were applied. The CV algorithms could be extended to work with

three-dimensional co-ordinates as input; however, since the available data are on a surface manifold, and data are not available through the volume of the tissue, this is not appropriate.

In Chapter 5, new wavefront initiation sites were found to be functionally important in sustaining AF in three of the four preparations investigated. However, it is unknown whether these new wavefronts represented triggered activity (Burashnikov and Antzelevitch, 2003), transmural conduction (Verheule et al., 2010), or rotors with U or O shaped filaments (Berenfeld et al., 2014). Simultaneous optical (Gutbrod et al., 2015) or electrogram (Eckstein et al., 2013) mapping of both surfaces would aid this interpretation (Yamazaki et al., 2012). The optimal dataset would be one measured through the atrial thickness (Walton et al., 2011; Barnette et al., 2000), in order to interpret intramural wavefront dynamics. The techniques presented in Chapter 4 could be extended to work with scroll waves if three-dimensional data were available.

8.5.2 The lack of gold standard measurement

A problem inherent to much of the work presented in this thesis was the difficulty in choosing a gold standard to compare the findings to. In particular, for the parameter sensitivity analysis of optical mapping data in Chapter 4, results from the various parameter sets were compared to each other to determine the sensitivity; however, the true dynamics of the system were unknown. The final parameter set were chosen as those that were reasonable and showed a degree of stability upon local variation. Similarly, in Chapter 6, the results from unipolar and bipolar AF phase mapping were compared to each other for the experimental and clinical data sources, as for these data a gold standard AF dataset was not available. Final testing of the data using an anatomically accurate simulation for which action potential data of the model were available represents testing the algorithms against a gold standard in the simplest data environment. In Chapter 7, resolution requirements were determined using simulated data, since this provided a high-resolution, noise free dataset as a gold standard to compare the results for reduced datasets to. However, clinical data provides the additional challenge of poor electrogram contact, increased noise and heterogeneous wavefront propagation, which may affect resolution requirements.

8.5.3 Requirement of a single macroscopic wavefront under the recording points for the conduction velocity algorithm

The developed CV algorithm assumes a single macroscopic wavefront under the measuring points. In the case that a set of activation times exist such that the activation times of each of the measuring points are from the same propagating wavefront, the technique presented in Section 3.3.7 would select these points, in order to give the correct calculation of conduction velocity. However, this is not possible in the case of colliding wavefronts under the measuring catheter. This also imposes the constraint that the diameter of the tissue where CV is measured must be less than the spatial wavelength (see Section 7.2.8).

Triangulation also assumes a single wavefront (Kojodjojo et al., 2006), and so suffers from similar limitations. In contrast, radial basis function interpolation (see Section 1.12.8) and polynomial surface fitting algorithms (see Section 1.12.4) can capture multiple wavefronts.

8.6 Future directions

8.6.1 Calculating conduction velocity and estimating locations of sources using sequentially collected data in fibrillation

Measuring CV during AF is particularly difficult due to number of wavefronts and the propagation complexity. The techniques developed in Chapter 6 could be combined with the conduction velocity estimation techniques developed in Chapter 3 in order to address this challenge. In particular, the techniques in Chapter 6 could be used to identify likely wavefronts. For each of these wavefronts, the activation times for the wavefront, along with the electrode locations that the wavefront passes over, can be used as inputs for the CV algorithm, in order to estimate the CV of each wavefront. This step would overcome a major challenge in applying the CV algorithm to clinical AF data, which is picking a suitable time window for analysis, in which there is a single macroscopic wavefront.

In addition, this combination of techniques could be used in the same way in order to aid rotor tip localisation in a clinical environment. For each wavefront identified

using the techniques in Chapter 6 (see Fig. 6.38 for an example), the focal source estimation algorithm could be applied to give an indication of the location that the wave originated from. This would overcome a significant limitation of the phase mapping algorithm, which is that it needs to be over a rotor core in order to detect it, since the focal source location estimation algorithm could guide the catheter towards the focal source, and once over the focal source or rotor core location, phase mapping could be performed.

Conduction velocity measured during AF could provide important functional information, and an interesting application would be a study into the relationship between CV heterogeneity in sinus rhythm, in AF and in pacing-dependent properties.

8.6.2 Extending the spatial resolution requirement investigations

The work presented in Chapter 7 could be extended in several ways. The question of the resolution required to distinguish between a focus and a microrentry was not addressed, although this has been considered by Ideker et al. (2009) for the ventricles. Furthermore, techniques could be used to distinguish between rotors and focal sources by the combined use of divergence, curl and phase singularities. In addition, the case of a non-circular propagating wavefront could be considered. Further extensions include incorporating the effects of electrode spacing into the resolution requirements, using Section 6.2.

8.7 Concluding remarks

In conclusion, in this thesis techniques for analysing cardiac wavefront dynamics were developed and tested. These included techniques for visualisation of three-dimensional left atrial cardiac activation data in two dimensions; for estimating conduction velocity and focal source location for an arbitrary arrangement of recording points, assuming a planar and circular wavefront; for electrogram phase mapping; for assessing arrhythmia mechanisms by comparing distributions and timings of phase singularities and new wavefronts; and for estimating spatial wavelength. In addition, the following questions were investigated: the effects of post-processing techniques and the importance of parameter choice in phase mapping; and the relationship between resolution requirements and wavefront spatial wavelength for identifying

rotors and focal sources.

Overall, the challenge of analysing electrical signals during fibrillation is still very much an open one, due to the noise, variability and availability of data (the resolution and area of coverage). Analysis techniques should be developed with the constraints of measurement techniques in mind.

References

Ahmad, a., Salinet, J. L., Brown, P., Tuan, J. H., Stafford, P., Ng, G. A., and Schlindwein, F. S. (2011). QRS subtraction for atrial electrograms: flat, linear and spline interpolations. *Medical & biological engineering & computing*, 49(11):1321–8. 266

Ali, R. L., Cantwell, C. D., Roney, C. H., Qureshi, N. A., Lim, P. B., Siggers, J. H., Sherwin, S. J., and Peters, N. S. (2014). A novel method for quantifying localised correlation of late-gadolinium intensity with conduction velocity. *CINC - Computing in Cardiology*, pages 193–196. 32, 42, 132, 360

Aliev, R. R. and Panfilov, A. V. (1996). A simple two-variable model of cardiac excitation. *Chaos Solitons Fractals*, 7(3):293–301. 46

Allessie, M. a., de Groot, N. M. S., Houben, R. P. M., Schotten, U., Boersma, E., Smeets, J. L., and Crijns, H. J. (2010). Electropathological substrate of long-standing persistent atrial fibrillation in patients with structural heart disease: longitudinal dissociation. *Circulation. Arrhythmia and electrophysiology*, 3(6):606–15. 9, 10, 301

Arbelo, E., Guiu, E., Ramos, P., Bisbal, F., Borras, R., Andreu, D., Tolosana, J. M., Berruezo, a., Brugada, J., and Mont, L. (2014). Benefit of Left Atrial Roof Linear Ablation in Paroxysmal Atrial Fibrillation: A Prospective, Randomized Study. *Journal of the American Heart Association*, 3(5):e000877–e000877. 26

Ashihara, T., Haraguchi, R., Nakazawa, K., Namba, T., Ikeda, T., Nakazawa, Y., Ozawa, T., Ito, M., Horie, M., and Trayanova, N. a. (2012). The role of fibroblasts in complex fractionated electrograms during persistent/permanent atrial fibrillation: implications for electrogram-based catheter ablation. *Circulation research*, 110(2):275–84. xxv, 63, 64, 423

Aslanidi, O. V., Colman, M. A., Stott, J., Dobrzynski, H., Boyett, M. R., Holden, A. V., and Zhang, H. (2011). 3D virtual human atria: A computational platform for studying clinical atrial fibrillation. *Progress in Biophysics and Molecular Biology*, 107:156–168. 22

Atienza, F., Almendral, J., Jalife, J., Zlochiver, S., Ploutz-Snyder, R., Torrecilla, E. G., Arenal, A., Kalifa, J., Fernández-Avilés, F., and Berenfeld, O. (2009). Real-time dominant frequency mapping and ablation of dominant frequency sites

in atrial fibrillation with left-to-right frequency gradients predicts long-term maintenance of sinus rhythm. *Heart rhythm : the official journal of the Heart Rhythm Society*, 6(1):33–40. 347

Atienza, F., Almendral, J., Moreno, J., Vaidyanathan, R., Talkachou, A., Kalifa, J., Arenal, A., Villacastín, J. P., Torrecilla, E. G., Sánchez, A., Ploutz-Snyder, R., Jalife, J., and Berenfeld, O. (2006). Activation of inward rectifier potassium channels accelerates atrial fibrillation in humans: evidence for a reentrant mechanism. *Circulation*, 114(23):2434–42. 204, 225

Banville, I. and Gray, R. a. (2002). Effect of action potential duration and conduction velocity restitution and their spatial dispersion on alternans and the stability of arrhythmias. *Journal of cardiovascular electrophysiology*, 13(11):1141–9. 12

Bär, M. and Eiswirth, M. (1993). Turbulence due to spiral breakup in a continuous excitable medium. *Physical Review E*, 48(3):1635–1638. 46

Barkley, D., Kness, M., and Tuckerman, L. (1990). Spiral wave dynamics in a simple model of excitable media: The transition from simple to compound rotation. *Physical Review ....* 53

Barnette, a. R., Bayly, P. V., Zhang, S., Walcott, G. P., Ideker, R. E., and Smith, W. M. (2000). Estimation of 3-D conduction velocity vector fields from cardiac mapping data. *IEEE transactions on bio-medical engineering*, 47(8):1027–35. 35, 43, 44, 110, 370

Barr, R. C., Gallie, T. M., and Spach, M. S. (1980). Automated production of contour maps for electrophysiology. II. Triangulation, verification, and organization of the geometric model. *Computers and biomedical research, an international journal*, 13(2):154–170. 32

Bassingthwaighte, J., Hunter, P., and Noble, D. (2009). The Cardiac Physiome: perspectives for the future. *Experimental physiology*, 94:597–605. 21

Bayer, J. D., Narayan, S. M., Lalani, G. G., and Trayanova, N. a. (2010). Rate-dependent action potential alternans in human heart failure implicates abnormal intracellular calcium handling. *Heart rhythm : the official journal of the Heart Rhythm Society*, 7(8):1093–101. 13, 19

Baykaner, T., Lalani, G. G., Schricker, A., Krummen, D. E., and Narayan, S. M. (2014). Mapping and ablating stable sources for atrial fibrillation: summary of the literature on Focal Impulse and Rotor Modulation (FIRM). *Journal of interventional cardiac electrophysiology : an international journal of arrhythmias and pacing*. 25, 27

Bayly, P. V., KenKnight, B. H., Rogers, J. M., Hillsley, R. E., Ideker, R. E., and Smith, W. M. (1998a). Estimation of conduction velocity vector fields from epicardial mapping data. *IEEE transactions on bio-medical engineering*, 45(5):563–71. 34, 36, 37, 44, 133, 368

Bayly, P. V., KenKnight, B. H., Rogers, J. M., Johnson, E. E., Ideker, R. E., and Smith, W. M. (1998b). Spatial organization, predictability, and determinism in ventricular fibrillation. *Chaos (Woodbury, N.Y.)*, 8(1):103–115. 349, 351

Beaumont, J., Davidenko, N., Davidenko, J. M., and Jalife, J. (1998). Spiral waves in two-dimensional models of ventricular muscle: formation of a stationary core. *Biophysical journal*, 75(1):1–14. 53

Becerra, M. A., Murillo-escobar, J., Palacio, L. C., Zuluaga, C. T., Universitaria, I., and Metropolitano, I. T. (2014). Noise and Spatial-resolution Effect of Electrode Array on Rotor Tip Location during Atrial Fibrillation : A Simulation Study Materials and methods Kalman filter. *Computing in Cardiology (CinC)*, pages 797–800. 298, 350, 365

Benharash, P., Buch, E., Frank, P., Share, M., Tung, R., Shivkumar, K., and Mandapati, R. (2015). Quantitative Analysis of Localized Sources Identified by Focal Impulse and Roter Modulation Mapping in Atrial Fibrillation. *Circulation: Arrhythmia and Electrophysiology*. 27

Berenfeld, O. and Oral, H. (2012). The quest for rotors in atrial fibrillation: different nets catch different fishes. *Heart rhythm : the official journal of the Heart Rhythm Society*, 9(9):1440–1. 351, 352, 353

Berenfeld, O., Yamazaki, M., Filgueiras-Rama, D., and Kalifa, J. (2014). Surface and intramural reentrant patterns during atrial fibrillation in the sheep. *Methods of Information in Medicine*, 53(4):314–319. 204, 227, 370

Berens, P. (2012). Circular Statistics Toolbox (http://www.mathworks.com/matlabcentral/fileexchange/10676-circular-statistics-toolbox–directional-statistics-/content//circ_corrcc.m). 261

Biermann, M., Shenasa, M., Borggrefe, M., Hindrick, G., Haverkamp, W., and Breithardt, G. (2003). The interpretation of cardiac electrograms in "Cardiac Mapping". *Cardiac Mapping. Elmsford, NY: Blackwell Publishing/Futura Division*, 2nd ed.:15–39. 7

Biktashev, V. N., Holden, A. V., and Zhang, H. (1994). Tension of Organizing Filaments of Scroll Waves. 53

Blender (2015). Blender - a 3D modelling and rendering package. 331

Botteron, G. W. and Smith, J. M. (1996). Quantitative Assessment of the Spatial Organization of Atrial Fibrillation in the Intact Human Heart. *Circulation*, 93:513–518. 352

Bradley, C. P., Clayton, R. H., Nash, M. P., Mourad, A., Hayward, M., Paterson, D. J., and Taggart, P. (2011). Human ventricular fibrillation during global ischemia and reperfusion: Paradoxical changes in activation rate and wavefront complexity. *Circulation: Arrhythmia and Electrophysiology*, 4:684–691. 226, 228

Bray, M.-A. and Wikswo, J. (2002a). Considerations in phase plane analysis for nonstationary reentrant cardiac behavior. *Physical Review E*, 65(5):051902. xviii, xxv, 49, 51, 73, 74, 88, 197, 238, 295, 365, 367, 421

Bray, M.-A. and Wikswo, J. P. (2002b). Use of topological charge to determine filament location and dynamics in a numerical model of scroll wave activity. *IEEE transactions on bio-medical engineering*, 49(10):1086–93. 52, 77, 78, 153, 198

Brown, R., Sidorowich, J., and Tsimring, L. S. (1993). The analysis of observed chaotic data. *Reviews of Modern Physics*, 65. 49

Bub, G., Shrier, A., and Glass, L. (2002). Spiral wave generation in heterogeneous excitable media. *Physical review letters*, 88:058101. 20

Bueno-Orovio, A., Cherry, E. M., and Fenton, F. H. (2008). Minimal model for human ventricular action potentials in tissue. *Journal of theoretical biology*, 253(3):544–60. 20

Burashnikov, A. and Antzelevitch, C. (2003). Reinduction of atrial fibrillation immediately after termination of the arrhythmia is mediated by late phase 3 early afterdepolarization-induced triggered activity. *Circulation*, 107(18):2355–60. 227, 370

Burdumy, M., Luik, A., Neher, P., Hanna, R., Krueger, M. W., Schilling, C., Barschdorf, H., Lorenz, C., Seemann, G., Schmitt, C., Doessel, O., and Weber, F. M. (2012). Comparing measured and simulated wave directions in the left atrium - a workflow for model personalization and validation. *Biomedizinische Technik. Biomedical engineering*, 57(2):79–87. 30, 38, 40, 44, 132

Byrd, G. D., Prasad, S. M., Ripplinger, C. M., Cassilly, T. R., Schuessler, R. B., Boineau, J. P., and Damiano, R. J. (2005). Importance of geometry and refractory period in sustaining atrial fibrillation: testing the critical mass hypothesis. *Circulation*, 112(9 Suppl):I7–13. 136

Campbell, K., Calvo, C. J., Mironov, S., Herron, T., Berenfeld, O., and Jalife, J. (2012). Spatial gradients in action potential duration created by regional magnetofection of hERG are a substrate for wavebreak and turbulent propagation in cardiomyocyte monolayers. *The Journal of physiology*, 590(Pt 24):6363–79. 135

Cantwell, C., Moxey, D., Comerford, A., Bolis, A., Rocco, G., Mengaldo, G., Grazia, D. D., Yakovlev, S., Lombard, J.-E., Ekelschot, D., Jordi, B., Xu, H., Mohamied, Y., Eskilsson, C., Nelson, B., Vos, P., Biotto, C., Kirby, R., and Sherwin, S. (2015a). Nektar++: An open-source spectral/hp element framework. *Computer Physics Communications*. 21

Cantwell, C., Roney, C., Ng, F., Siggers, J., Sherwin, S., and Peters, N. (2015b). Techniques for automated local activation time annotation and conduction velocity estimation in cardiac mapping. *Computers in Biology and Medicine*. xviii, 6, 29, 34

Cantwell, C. D., Roney, C. H., Ali, R. L., Qureshi, N. A., Phang Boon Lim, and Peters, N. S. (2014a). A software platform for the comparative analysis of electroanatomic and imaging data including conduction velocity mapping. *Conference proceedings : Annual International Conference of the IEEE Engineering in Medicine and Biology Society. IEEE Engineering in Medicine and Biology Society. Annual Conference*, 2014:1591–4. 32, 44, 360

Cantwell, C. D., Yakovlev, S., Kirby, R. M., Peters, N. S., and Sherwin, S. J. (2014b). High-order spectral/hp element discretisation for reaction-diffusion problems on surfaces: Application to cardiac electrophysiology. *Journal of Computational Physics*, 257:813–829. 70, 84, 109

Cappato, R., Calkins, H., Chen, S.-A., Davies, W., Iesaka, Y., Kalman, J., Kim, Y.-H., Klein, G., Natale, A., Packer, D., Skanes, A., Ambrogi, F., and Biganzoli, E. (2010). Updated worldwide survey on the methods, efficacy, and safety of catheter ablation for human atrial fibrillation. *Circulation. Arrhythmia and electrophysiology*, 3(1):32–8. 8

Castells, F., Cervigón, R., and Millet, J. (2014). On the preprocessing of atrial electrograms in atrial fibrillation: understanding Botteron's approach. *Pacing and clinical electrophysiology : PACE*, 37(2):133–43. 295, 365

Cerqueira, M. D., Weissman, N. J., Dilsizian, V., Jacobs, A. K., Kaul, S., Laskey, W. K., Pennell, D. J., Rumberger, J. a., Ryan, T. J., and Verani, M. S. (2002). Standardized Myocardial Segmentation and Nomenclature for Tomographic Imaging of the Heart. *Journal of Cardiovascular Magnetic Resonance*, 4:203–210. 83

Chen, J., Mandapati, R., Berenfeld, O., Skanes, a. C., Gray, R. a., and Jalife, J. (2000). Dynamics of wavelets and their role in atrial fibrillation in the isolated sheep heart. *Cardiovascular research*, 48(2):220–32. 198

Cherry, E. and Fenton, F. (2004). Suppression of alternans and conduction blocks despite steep APD restitution: electrotonic, memory, and conduction velocity restitution effects. *American Journal of Physiology- ...*, 11549:2332–2341. 19, 412

Cherry, E. M. and Evans, S. J. (2008). Properties of two human atrial cell models in tissue: restitution, memory, propagation, and reentry. *Journal of theoretical biology*, 254(3):674–90. xviii, xxv, 55, 56, 64, 72, 422

Cherry, E. M. and Fenton, F. H. (2008). Visualization of spiral and scroll waves in simulated and experimental cardiac tissue. *New Journal of Physics*, 10(12):125016. xviii, 18, 53, 54

Choi, B.-R. and Salama, G. (2000). Simultaneous maps of optical action potentials and calcium transients in guinea-pig hearts: mechanisms underlying concordant alternans. *The Journal of Physiology*, 529(1):171–188. 409

Clayton, R. H. (2008). Vortex filament dynamics in computational models of ventricular fibrillation in the heart. *Chaos*, 18(2008). 54

Clayton, R. H. (2013). Models of ventricular arrhythmia mechanisms. *Proceedings of the Annual International Conference of the IEEE Engineering in Medicine and Biology Society, EMBS*, pages 1526–1529. 229

Clayton, R. H., Bailey, a., Biktashev, V. N., and Holden, a. V. (2001). Re-entrant cardiac arrhythmias in computational models of long QT myocardium. *Journal of theoretical biology*, 208:215–225. 54

Clayton, R. H., Bernus, O., Cherry, E. M., Dierckx, H., Fenton, F. H., Mirabella, L., Panfilov, a. V., Sachse, F. B., Seemann, G., and Zhang, H. (2011). Models of cardiac tissue electrophysiology: progress, challenges and open questions. *Progress in biophysics and molecular biology*, 104(1-3):22–48. 19, 20

Clayton, R. H. and Holden, A. V. (2002a). A method to quantify the dynamics and complexity of re-entry in computational models of ventricular fibrillation. *Physics in medicine and biology*, 47:225–238. 53, 228

Clayton, R. H. and Holden, A. V. (2002b). A method to quantify the dynamics and complexity of re-entry in computational models of ventricular fibrillation. *Physics in Medicine and Biology*, 47(2):225–238. 198

Clayton, R. H. and Holden, A. V. (2002c). Dynamics and interaction of filaments in a computational model of re-entrant ventricular fibrillation. *Physics in medicine and biology*, 47:1777–1792. 228

Clayton, R. H. and Holden, A. V. (2003). Effect of regional differences in cardiac cellular electrophysiology on the stability of ventricular arrhythmias: a computational study. *Physics in medicine and biology*, 48:95–111. 53

Clayton, R. H. and Holden, A. V. (2004). Filament Behavior in a Computational Model of Ventricular Fibrillation in the Canine Heart. *IEEE Transactions on Biomedical Engineering*, 51(1):28–34. 201

Clayton, R. H. and Nash, M. P. (2015). Analysis of cardiac fibrillation using phase mapping. *Cardiac Electrophysiology Clinics*, 7(1):49–58. 204

Clayton, R. H., Zhuchkova, E. a., and Panfilov, a. V. (2006). Phase singularities and filaments: simplifying complexity in computational models of ventricular fibrillation. *Progress in biophysics and molecular biology*, 90(1-3):378–98. 55, 204, 231

Colli Franzone, P., Pavarino, L. F., and Taccardi, B. (2005). Simulating patterns of excitation, repolarization and action potential duration with cardiac Bidomain and Monodomain models. *Mathematical biosciences*, 197(1):35–66. 21, 59

Coronel, R., de Bakker, J. M. T., Wilms-Schopman, F. J. G., Opthof, T., Linnenbank, A. C., Belterman, C. N., and Janse, M. J. (2006). Monophasic action potentials and activation recovery intervals as measures of ventricular action potential duration: Experimental evidence to resolve some controversies. *Heart Rhythm*, 3(9):1043–1050. 7, 8

Courtemanche, M., Ramirez, R. J., and Nattel, S. (1998). Ionic mechanisms underlying human atrial action potential properties: insights from a mathematical model. *The American journal of physiology*, 275(1 Pt 2):H301–21. x, xviii, 55, 56, 59, 61, 62, 63, 64, 69, 109, 232, 291, 304

Courtemanche, M., Ramirez, R. J., and Nattel, S. (1999). Ionic targets for drug therapy and atrial fibrillation-induced electrical remodeling: insights from a mathematical model. *Cardiovascular research*, 42(2):477–89. 17, 55, 62, 232, 291, 304, 333, 409

Davidenko, J. M., Kent, P. F., Chialvo, D. R., Michaels, D. C., and Jalife, J. (1990). Sustained vortex-like waves in normal isolated ventricular muscle. *Proceedings of the National Academy of Sciences of the United States of America*, 87(22):8785–9. 9

Davidenko, J. M., Pertsov, A. V., Salomonsz, R., Baxter, W., and Jalife, J. (1992a). Stationary and drifting spiral waves of excitation in isolated cardiac muscle. *Nature*, 355:349–351. 53, 135

Davidenko, J. M., Pertsov, A. V., Salomonsz, R., Baxter, W., and Jalife, J. (1992b). Stationary and drifting spiral waves of excitation in isolated cardiac muscle. *Nature*, 355:349–351. 53

de Carvalho, A. P., Hoffman, B. F., and de Carvalho, M. P. (1969). Two components of the cardiac action potential. I. Voltage-time course and the effect of acetylcholine on atrial and nodal cells of the rabbit heart. *The Journal of general physiology*, 54(5):607–635. 227

de Groot, N., Houben, R., Smeets, J., Boersma, E., Schotten, U., Schalij, M., Crijns, H., and Allessie, M. (2010). Electropathological Substrate of Longstanding Persistent Atrial Fibrillation in Patients With Structural Heart DiseaseClinical Perspective Epicardial Breakthrough. *Circulation*, pages 1674–1682. 10, 228, 301, 302

Delaunay, B. (1934). Sur la sphére vide. *Bull. Acad. Sci*, USSR (VII)(7):793–800. 32

Dhillon, P. S., Gray, R., Kojodjojo, P., Jabr, R., Chowdhury, R., Fry, C. H., and Peters, N. S. (2013). Relationship between gap-junctional conductance and conduction velocity in mammalian myocardium. *Circulation. Arrhythmia and electrophysiology*, 6(6):1208–14. 29

Dias, P. (2011). *Influence of Connexin Expression / Co-Expression Levels on Electrical Impulse Propagation Investigated in the HL-1 Cell Model*. PhD thesis, Imperial College London. 265

Doshi, R. N., Wu, T. J., Yashima, M., Kim, Y. H., Ong, J. J., Cao, J. M., Hwang, C., Yashar, P., Fishbein, M. C., Karagueuzian, H. S., and Chen, P. S. (1999). Relation between ligament of Marshall and adrenergic atrial tachyarrhythmia. *Circulation*, 100:876–883. 136

Dössel, O., Krueger, M. W., Weber, F. M., Wilhelms, M., and Seemann, G. (2012). Computational modeling of the human atrial anatomy and electrophysiology. *Medical & biological engineering & computing*, 50(8):773–99. 22

Draper, M. and Mya-Tu, M. (1959). A comparison of the conduction velocity in cardiac tissues of various mammals. *Experimental Physiology*, 44(1)(July):91–109. 348

Dubois, R., Labarthe, S., Coudiere, Y., Hocini, M., and Haissaguerre, M. (2012). Global and Directional Activation maps for cardiac mapping in electrophysiology. *Computers in Cardiology (CinC)*, pages 3–6. 39, 44, 360, 364

Echebarria, B. and Karma, a. (2007). Mechanisms for initiation of cardiac discordant alternans. *The European Physical Journal Special Topics*, 146(1):217–231. 13, 19

Eckstein, J., Maesen, B., Linz, D., Zeemering, S., van Hunnik, A., Verheule, S., Allessie, M., and Schotten, U. (2011). Time course and mechanisms of endo-epicardial electrical dissociation during atrial fibrillation in the goat. *Cardiovascular research*, 89(4):816–24. 14

Eckstein, J., Verheule, S., de Groot, N. M., de Groot, N., Allessie, M., and Schotten, U. (2008). Mechanisms of perpetuation of atrial fibrillation in chronically dilated atria. *Progress in biophysics and molecular biology*, 97(2-3):435–51. xxv, 9, 416

Eckstein, J., Zeemering, S., Linz, D., Maesen, B., Verheule, S., van Hunnik, A., Crijns, H., Allessie, M. a., and Schotten, U. (2013). Transmural conduction is the predominant mechanism of breakthrough during atrial fibrillation: evidence from simultaneous endo-epicardial high-density activation mapping. *Circulation. Arrhythmia and electrophysiology*, 6(2):334–41. 204, 205, 227, 362, 370

Efimov, I. R., Krinsky, V. I., and Jalife, J. (1995). Dynamics of Rotating Vortices in the Beeler-Reuter Model of Cardiac Tissue. *Chaos, Solitons & Fractals*, 5(3/4):513–526. 53

Efimov, I. R., Nikolski, V. P., and Salama, G. (2004). Optical imaging of the heart. *Circulation research*, 95(1):21–33. 15, 45

Eitel, C., Hindricks, G., Dagres, N., Sommer, P., and Piorkowski, C. (2010). EnSite Velocity cardiac mapping system: a new platform for 3D mapping of cardiac arrhythmias. *Expert review of medical devices*, 7(2):185–92. 24, 109, 110

El Haddad, M., Houben, R., Stroobandt, R., Van Heuverswyn, F., Tavernier, R., and Duytschaever, M. (2013). Algorithmic detection of the beginning and end of bipolar electrograms: Implications for novel methods to assess local activation time during atrial tachycardia. *Biomedical Signal Processing and Control*, 8(6):981–991. 30

Engelman, Z. J., Trew, M. L., and Smaill, B. H. (2010). Structural heterogeneity alone is a sufficient substrate for dynamic instability and altered restitution. *Circulation. Arrhythmia and electrophysiology*, 3(2):195–203. 14

Estner, H. L., Hessling, G., Ndrepepa, G., Luik, A., Schmitt, C., Konietzko, A., Ucer, E., Wu, J., Kolb, C., Pflaumer, A., Zrenner, B., and Deisenhofer, I. (2008). Acute effects and long-term outcome of pulmonary vein isolation in combination with electrogram-guided substrate ablation for persistent atrial fibrillation. *The American journal of cardiology*, 101(3):332–7. 26

Ezekowitz, M. D. and Levine, J. a. (1999). Atrial Fibrillation. *The Nurse Practitioner*, 24(11):108. 8

Falcke, M., Hudson, J. L., Camacho, P., and Lechleiter, J. D. (1999). Impact of mitochondrial Ca2+ cycling on pattern formation and stability. *Biophysical journal*, 77:37–44. 45

Fast, V. G. and Ideker, R. E. (2000). Simultaneous Optical Mapping of Transmembrane Potential and Intracellular Calcium in Myocyte Cultures. *Journal of cardiovascular electrophysiology*, 11(1):547–557. 409

Fenton, F. and Karma, A. (1998). Vortex dynamics in three-dimensional continuous myocardium with fiber rotation: Filament instability and fibrillation. *Chaos (Woodbury, N.Y.)*, 8(1):20–47. 19, 20, 52, 53, 81

Fenton, F. H., Cherry, E. M., Hastings, H. M., and Evans, S. J. (2002). Multiple mechanisms of spiral wave breakup in a model of cardiac electrical activity. *Chaos (Woodbury, N.Y.)*, 12(3):852–892. 53, 81

Filgueiras-Rama, D., Martins, R. P., Ennis, S. R., Mironov, S., Jiang, J., Yamazaki, M., Kalifa, J., Jalife, J., and Berenfeld, O. (2011). High-Resolution Endocardial and Epicardial Optical Mapping in a Sheep Model of Stretch-Induced Atrial Fibrillation. *Journal of Visualized Experiments*, 53(53):1–7. 227, 362

Filgueiras-Rama, D., Price, N. F., Martins, R. P., Yamazaki, M., Avula, U. M. R., Kaur, K., Kalifa, J., Ennis, S. R., Hwang, E., Devabhaktuni, V., Jalife, J., and Berenfeld, O. (2012). Long-term frequency gradients during persistent atrial fibrillation in sheep are associated with stable sources in the left atrium. *Circulation. Arrhythmia and electrophysiology*, 5(6):1160–7. 228, 362

Fitzgerald, T., Rhee, E., Brooks, D., and Triedman, J. (2001). Estimation of cardiac conduction velocities using small data sets. *Computers in Cardiology (CinC)*. 31, 36, 42, 44

Fitzgerald, T. N., Brooks, D. H., and Triedman, J. K. (2005). Identification of cardiac rhythm features by mathematical analysis of vector fields. *IEEE transactions on bio-medical engineering*, 52(1):19–29. 42, 302, 305, 350, 360

Fitzhugh, R. (1961). Impulses and Physiological States in Theoretical Models of Nerve Membrane. *Biophysical journal*, 1(6):445–466. 47

Fox, J., Bodenschatz, E., and Gilmour, R. (2002). Period-Doubling Instability and Memory in Cardiac Tissue. *Physical Review Letters*, 89(13):138101. 11

Ganesan, A. N., Kuklik, P., Lau, D. H., Brooks, A. G., Baumert, M., Lim, W. W., Thanigaimani, S., Nayyar, S., Mahajan, R., Kalman, J. M., Roberts-Thomson, K. C., and Sanders, P. (2013). Bipolar electrogram shannon entropy at sites of rotational activation: implications for ablation of atrial fibrillation. *Circulation. Arrhythmia and electrophysiology*, 6(1):48–57. 231, 298, 365

Ganesan, P., Cherry, E. M., Arkady, M., and Ghoraani, B. (2015). Characterization of Electrograms From Multi-polar Diagnostic Catheters During Atrial Fibrillation. *BioMed Research International*, In press. 133, 298, 361

Garfinkel, a., Kim, Y. H., Voroshilovsky, O., Qu, Z., Kil, J. R., Lee, M. H., Karagueuzian, H. S., Weiss, J. N., and Chen, P. S. (2000). Preventing ventricular fibrillation by flattening cardiac restitution. *Proceedings of the National Academy of Sciences of the United States of America*, 97(11):6061–6. 12

Geuzaine, C. and Remacle, J.-F. (2009). Gmsh: a three-dimensional finite element mesh generator with built-in pre- and post-processing facilities. *International Journal for Numerical Methods in Engineering*, 79:1309–1331. 331

Gharaviri, A., Verheule, S., Eckstein, J., Potse, M., Kuijpers, N. H. L., and Schotten, U. (2012). A computer model of endo-epicardial electrical dissociation and transmural conduction during atrial fibrillation. *Europace : European pacing, arrhythmias, and cardiac electrophysiology : journal of the working groups on cardiac pacing, arrhythmias, and cardiac cellular electrophysiology of the European Society of Cardiology*, 14 Suppl 5:v10–v16. 411

Ghoraani, B., Dalvi, R., Gizurarson, S., Das, M., Ha, a., Suszko, a., Krishnan, S., and Chauhan, V. S. (2013). Localized rotational activation in the left atrium during human atrial fibrillation: Relationship to complex fractionated atrial electrograms and low-voltage zones. *Heart rhythm : the official journal of the Heart Rhythm Society*, 10(12):1830–8. 296, 298

Gong, Y., Xie, F., Stein, K. M., Garfinkel, A., Culianu, C. a., Lerman, B. B., and Christini, D. J. (2007). Mechanism underlying initiation of paroxysmal atrial flutter/atrial fibrillation by ectopic foci: a simulation study. *Circulation*, 115(16):2094–102. 72, 347

Grandi, E., Pandit, S. V., Voigt, N., Workman, A. J., Dobrev, D., Jalife, J., and Bers, D. M. (2011). Human atrial action potential and Ca2+ model: sinus rhythm and chronic atrial fibrillation. *Circulation research*, 109(9):1055–66. 55

Graux, P., Carlioz, R., Rivat, P., Bera, J., Guyomar, Y., and Dutoit, a. (1998). Wavelength and atrial vulnerability: an endocavitary approach in humans. *Pacing and clinical electrophysiology : PACE*, 21(1 Pt 2):202–8. 352, 366

Gray, R., Pertsov, A., and Jalife, J. (1998). Spatial and temporal organization during cardiac fibrillation. *Nature*, 393(May):75–78. xviii, xxv, 45, 48, 231, 420

Gray, R. a. and Jalife, J. (2001). Video imaging of cardiac fibrillation. In Rosenbaum, D. S. and Jalife, J., editors, *Optical Mapping of Cardiac Excitation and Arrhythmias*, chapter 14, pages 245–264. Futura Publishing Company. 49

Gutbrod, S. R., Walton, R., Gilbert, S., Meillet, V., Jais, P., Hocini, M., Haissaguerre, M., Dubois, R., Bernus, O., and Efimov, I. (2015). Quantification of the Transmural Dynamics of Atrial Fibrillation by Simultaneous Endocardial and Epicardial Optical Mapping in an Acute Sheep Model. *Circulation: Arrhythmia and Electrophysiology*. 204, 227, 370

Haissaguerre, M., Hocini, M., Denis, a., Shah, a. J., Komatsu, Y., Yamashita, S., Daly, M., Amraoui, S., Zellerhoff, S., Picat, M.-Q., Quotb, a., Jesel, L., Lim, H., Ploux, S., Bordachar, P., Attuel, G., Meillet, V., Ritter, P., Derval, N., Sacher, F., Bernus, O., Cochet, H., Jais, P., and Dubois, R. (2014a). Driver Domains in Persistent Atrial Fibrillation. *Circulation*. 25, 27, 199, 367

Haissaguerre, M., Hocini, M., Denis, A., Shah, A. J., Komatsu, Y., Yamashita, S., Daly, M., Amraoui, S., Zellerhoff, S., Picat, M.-Q., Quotb, A., Jesel, L., Lim, H., Ploux, S., Bordachar, P., Attuel, G., Meillet, V., Ritter, P., Derval, N., Sacher, F., Bernus, O., Cochet, H., Jais, P., and Dubois, R. (2014b). Driver domains in persistent atrial fibrillation. *Circulation*, 130(7):530–8. 301

Haissaguerre, M., Hocini, M., Shah, A. J., Derval, N., Sacher, F., Jais, P., and Dubois, R. (2013). Noninvasive panoramic mapping of human atrial fibrillation mechanisms: a feasibility report. *Journal of cardiovascular electrophysiology*, 24(6):711–7. xxv, 10, 25, 27, 28, 199, 203, 226, 227, 231, 297, 301, 302, 362, 367, 418

Haïssaguerre, M., Jaïs, P., Shah, D. C., Takahashi, a., Hocini, M., Quiniou, G., Garrigue, S., Le Mouroux, a., Le Métayer, P., and Clémenty, J. (1998). Spontaneous initiation of atrial fibrillation by ectopic beats originating in the pulmonary veins. *The New England journal of medicine*, 339(10):659–66. 25

Haïssaguerre, M., Shah, D. C., Jaïs, P., Hocini, M., Yamane, T., Deisenhofer, I., Garrigue, S., and Clémenty, J. (2000). Mapping-guided ablation of pulmonary veins to cure atrial fibrillation. *The American journal of cardiology*, 86(9A):9K–19K. 25

Halbach, M. D., Egert, U., Hescheler, J., and Banach, K. (2003). Estimation of action potential changes from field potential recordings in multicellular mouse cardiac myocyte cultures. *Cellular Physiology and Biochemistry*, 13:271–284. 15, 16

Hansson, a., Holm, M., Blomström, P., Johansson, R., Lührs, C., Brandt, J., and Olsson, S. B. (1998). Right atrial free wall conduction velocity and degree of anisotropy in patients with stable sinus rhythm studied during open heart surgery. *European heart journal*, 19(2):293–300. 348

Heeringa, J., van der Kuip, D. a. M., Hofman, A., Kors, J. a., van Herpen, G., Stricker, B. H. C., Stijnen, T., Lip, G. Y. H., and Witteman, J. C. M. (2006). Prevalence, incidence and lifetime risk of atrial fibrillation: the Rotterdam study. *European heart journal*, 27(8):949–53. 8

Hiromoto, K., Shimizu, H., Furukawa, Y., Kanemori, T., Mine, T., Masuyama, T., and Ohyanagi, M. (2005). Discordant Repolarization Alternans-Induced Atrial Fibrillation is Suppressed by Verpamil. *Circulation Journal*, 69(November):1368–1373. 12

Hodgkin, A. and Huxley, A. (1952). A quantitative description of membrane current and its application to conduction and excitation in nerve. *The Journal of physiology*, pages 500–544. 17

Horner, S., Vespalcova, Z., and Lab, M. (1997). Electrode for recording direction of activation, conduction velocity, and monophasic action potential of myocardium. *American Physiological Society*. 39, 44

Houben, R. P. M. and Allessie, M. A. (2006). Processing of intracardiac electrograms in atrial fibrillation: Diagnosis of electropathological substrate of AF. 296

Houben, R. P. M., de Groot, N. M. S., Lindemans, F. W., and Allessie, M. a. (2006). Automatic mapping of human atrial fibrillation by template matching. *Heart rhythm : the official journal of the Heart Rhythm Society*, 3(10):1221–8. 296, 364

Huang, N. E., Shen, Z., Long, S. R., Wu, M. C., Shih, H. H., Zheng, Q., Yen, N.-C., Tung, C. C., and Liu, H. H. (1996). The empirical mode decomposition and the Hilbert spectrum for nonlinear and non-stationary time series analysis. *The Royal Society*, 454:903–995. 51

Ideker, R. E., Rogers, J. M., Fast, V., Li, L., Kay, G. N., and Pogwizd, S. M. (2009). Can mapping differentiate microreentry from a focus in the ventricle? *Heart rhythm : the official journal of the Heart Rhythm Society*, 6(11):1666–9. 352, 372

Iyer, A. N. and Gray, R. a. (2001). An Experimentalist's Approach to Accurate Localization of Phase Singularities during Reentry. *Annals of Biomedical Engineering*, 29(1):47–59. xviii, xxv, 46, 47, 49, 79, 153, 198, 419

Jacquemet, V. (2010). An eikonal approach for the initiation of reentrant cardiac propagation in reactiondiffusion models. *IEEE Transactions on Biomedical Engineering*, 57:2090–2098. 20

Jacquemet, V., Virag, N., and Kappenberger, L. (2005). Wavelength and vulnerability to atrial fibrillation: Insights from a computer model of human atria. *Europace : European pacing, arrhythmias, and cardiac electrophysiology : journal of the working groups on cardiac pacing, arrhythmias, and cardiac cellular electrophysiology of the European Society of Cardiology*, 7 Suppl 2:83–92. 352, 366

Jadidi, A. S., Duncan, E., Miyazaki, S., Lellouche, N., Shah, A. J., Forclaz, A., Nault, I., Wright, M., Rivard, L., Liu, X., Scherr, D., Wilton, S. B., Sacher, F., Derval, N., Knecht, S., Kim, S. J., Hocini, M., Narayan, S., Haïssaguerre, M., and Jaïs, P. (2012). Functional nature of electrogram fractionation demonstrated by left atrial high-density mapping. *Circulation. Arrhythmia and electrophysiology*, 5(1):32–42. 27

Jahnke, W., Skaggs, W., and Winfree, A. (1989). Chemlcal Vortex Dynamics in the Belousov-Zhabotlnsky Reaction and in the Two-Variable Oregonator Model. *The Journal of Physical Chemistyr*, 93(2):740–749. 53

Jalife, J., Berenfeld, O., and Mansour, M. (2002). Mother rotors and fibrillatory conduction: a mechanism of atrial fibrillation. *Cardiovascular research*, 54(2):204–16. 9, 10

Jammalamadaka, S. R. and Sengupta, A. (2001). *Topics in circular statistics*, volume 6. World Scientific. 261

Jarman, J. W. E., Wong, T., Kojodjojo, P., Spohr, H., Davies, J. E., Roughton, M., Francis, D. P., Kanagaratnam, P., Markides, V., Davies, D. W., and Peters, N. S. (2012). Spatiotemporal behavior of high dominant frequency during paroxysmal and persistent atrial fibrillation in the human left atrium. *Circulation. Arrhythmia and electrophysiology*, 5(4):650–8. 28, 347

Kadish, A., Johnson, D., Choe, W., Goldberger, J., and Horvath, G. (2003). Characterization of fibrillatory rhythms by ensemble vector directional analysis. *American journal of physiology. Heart and circulatory physiology*, 285(4):H1705–19. 39, 44

Kadish, a. H., Spear, J. F., Levine, J. H., Hanich, R. F., Prood, C., and Moore, E. N. (1986). Vector mapping of myocardial activation. *Circulation*, 74(3):603–615. 39, 44

Kaiser, J. (1990). On a simple algorithm to calculate the 'energy' of a signal. *Acoustics, Speech, and Signal Processing, 1990. ...*, 2(10):381–384. 30, 295

Kanagaratnam, P., Rothery, S., Patel, P., Severs, N. J., and Peters, N. S. (2002). Relative expression of immunolocalized connexins 40 and 43 correlates with human atrial conduction properties. *Journal of the American College of Cardiology*, 39(1):116–23. 116, 348

Karim, R., Ma, Y., Jang, M., Housden, R. J., Williams, S. E., Chen, Z., Ataollahi, A., Althoefer, K., Rinaldi, C. A., Razavi, R., O'Neill, M. D., Schaeftter, T., and Rhode, K. S. (2014). Surface flattening of the human left atrium and proof-of-concept clinical applications. *Computerized medical imaging and graphics : the official journal of the Computerized Medical Imaging Society*, 38(4):251–66. 83, 88, 89, 358, 359

Karma, A. (1994). Electrical alternans and spiral wave breakup in cardiac tissue. *Chaos (Woodbury, N.Y.)*, 4(3):461–472. 11

Kawara, T., Derksen, R., de Groot, J. R., Coronel, R., Tasseron, S., Linnenbank, a. C., Hauer, R. N., Kirkels, H., Janse, M. J., and de Bakker, J. M. (2001). Activation Delay After Premature Stimulation in Chronically Diseased Human Myocardium Relates to the Architecture of Interstitial Fibrosis. *Circulation*, 104(25):3069–3075. 14, 29, 91

Kay, M., Walcott, G., Gladden, J. D., Melnick, S. B., and Rogers, J. M. (2006). Lifetimes of epicardial rotors in panoramic optical maps of fibrillating swine ventricles. *American journal of physiology. Heart and circulatory physiology*, 35294:1935–1941. 226

Kay, M. W. and Gray, R. a. (2005). Measuring curvature and velocity vector fields for waves of cardiac excitation in 2-D media. *IEEE transactions on bio-medical engineering*, 52(1):50–63. xviii, 40, 44, 80, 81, 82, 206, 296, 308, 362, 406

Kay, M. W. and Rogers, J. M. (2006). Epicardial rotors in panoramic optical maps of fibrillating swine ventricles. *Conference proceedings : ... Annual International Conference of the IEEE Engineering in Medicine and Biology Society. IEEE Engineering in Medicine and Biology Society. Conference*, 1:2268–71. 363

Kazbanov, I. V., Clayton, R. H., Nash, M. P., Bradley, C. P., Paterson, D. J., Hayward, M. P., Taggart, P., and Panfilov, A. V. (2014). Effect of Global Cardiac Ischemia on Human Ventricular Fibrillation: Insights from a Multi-scale Mechanistic Model of the Human Heart. *PLoS Computational Biology*, 10(11):e1003891. 229

Keener, J. and Sneyd, J. (2009). *Mathematical Physiology*. Springer, Interdisciplinary Applied Mathematics. 66

Kim, Y. H., Garfinkel, a., Ikeda, T., Wu, T. J., Athill, C. a., Weiss, J. N., Karagueuzian, H. S., and Chen, P. S. (1997). Spatiotemporal complexity of ventricular fibrillation revealed by tissue mass reduction in isolated swine right ventricle. Further evidence for the quasiperiodic route to chaos hypothesis. *The Journal of clinical investigation*, 100(10):2486–500. 53

Kjolbye, A. L., Dikshteyn, M., Eloff, B. C., Deschênes, I., and Rosenbaum, D. S. (2008). Maintenance of intercellular coupling by the antiarrhythmic peptide rotigaptide suppresses arrhythmogenic discordant alternans. *American journal of physiology. Heart and circulatory physiology*, 294:H41–H49. 14

Kléber, A. G. and Rudy, Y. (2004). Basic mechanisms of cardiac impulse propagation and associated arrhythmias. *Physiological reviews*, 84(2):431–88. 14

Knecht, S., Hocini, M., Wright, M., Lellouche, N., O'Neill, M. D., Matsuo, S., Nault, I., Chauhan, V. S., Makati, K. J., Bevilacqua, M., Lim, K. T., Sacher, F., Deplagne, A., Derval, N., Bordachar, P., Jaïs, P., Clémenty, J., and Haïssaguerre, M. (2008). Left atrial linear lesions are required for successful treatment of persistent atrial fibrillation. *European Heart Journal*, 29(19):2359–2366. 26

Kneller, J., Zou, R., Vigmond, E. J., Wang, Z., Leon, J., and Nattel, S. (2002). Cholinergic Atrial Fibrillation in a Computer Model of a Two-Dimensional Sheet of Canine Atrial Cells With Realistic Ionic Properties. *Circulation Research*, 90(9):73e–87. 204

Koivumäki, J. T., Korhonen, T., and Tavi, P. (2011). Impact of sarcoplasmic reticulum calcium release on calcium dynamics and action potential morphology in human atrial myocytes: a computational study. *PLoS computational biology*, 7(1):e1001067. 55

Kojodjojo, P., Kanagaratnam, P., Markides, V., Davies, W., and Peters, N. (2006). Age-Related Changes in Human Left and Right Atrial Conduction. *Journal of cardiovascular electrophysiology*, pages 10–15. 32, 44, 371

Kondo, M., Nesterenko, V., and Antzelevitch, C. (2004). Cellular basis for the monophasic action potential. Which electrode is the recording electrode? *Cardiovascular research*, 63(4):635–44. 8

Konings, K. T., Kirchhof, C. J., Smeets, J. R., Wellens, H. J., Penn, O. C., and Allessie, M. a. (1994). High-density mapping of electrically induced atrial fibrillation in humans. *Circulation*, 89(4):1665–1680. 304, 347, 348

Konings, K. T., Smeets, J. L., Penn, O. C., Wellens, H. J., and Allessie, M. A. (1997). Configuration of unipolar atrial electrograms during electrically induced atrial fibrillation in humans. *Circulation*, 95:1231–1241. 26

Koumi, S., Backer, C. L., and Arentzen, C. E. (1995). Characterization of inwardly rectifying K+ channel in human cardiac myocytes. Alterations in channel behavior in myocytes isolated from patients with idiopathic dilated cardiomyopathy. *Circulation*, 92:164–174. 347

Krueger, M. W., Schmidt, V., Tobón, C., Weber, F. M., Lorenz, C., Keller, D. U. J., Barschdorf, H., Burdumy, M., Neher, P., Plank, G., Rhode, K., Seemann, G., Sanchez-Quintana, D., Saiz, J., Razavi, R., and Dössel, O. (2011). Modeling atrial fiber orientation in patient-specific geometries: A semi-automatic rule-based approach. In *Lecture Notes in Computer Science (including subseries Lecture Notes in Artificial Intelligence and Lecture Notes in Bioinformatics)*, volume 6666 LNCS, pages 223–232. 23

Krüger, M. (2012). *Personalized Multi-Scale Modeling of the Atria*, volume 19. KIT Scientific Publishing. 35, 36

Krummen, D. E., Bayer, J. D., Ho, J., Ho, G., Smetak, M. R., Clopton, P., Trayanova, N. a., and Narayan, S. M. (2012). Mechanisms of human atrial fibrillation initiation: clinical and computational studies of repolarization restitution and activation latency. *Circulation. Arrhythmia and electrophysiology*, 5(6):1149–59. 55

Kuklik, P., Zeemering, S., Maesen, B., Maessen, J., Crijns, H., Verheule, S., and Schotten, U. (2014). Reconstruction of instantaneous phase of unipolar atrial contact electrogram using a concept of sinusoidal recomposition and Hilbert transform. *IEEE transactions on bio-medical engineering*. 232, 297, 298, 364, 365

Kurotobi, T., Shimada, Y., Kino, N., Ito, K., Tonomura, D., Yano, K., Tanaka, C., Yoshida, M., Tsuchida, T., and Fukumoto, H. (2014). Residual Arrhythmogenic Foci Predict Recurrence in Longstanding Persistent Atrial Fibrillation Patients Following Sinus Rhythm Restoration Ablation. *Canadian Journal of Cardiology*. 227

Langston, M. A., Pieper, C. F., and Pacifico, A. (1994). Spectral analysis of activation time sequences. *PACE - Pacing and Clinical Electrophysiology*, 17(7):1288–1299. 30

Lau, D. H., Maesen, B., Zeemering, S., Kuklik, P., van Hunnik, A., a.R. Lankveld, T., Bidar, E., Verheule, S., Nijs, J., Maessen, J., Crijns, H., Sanders, P., and Schotten, U. (2015). Indices of Bipolar Complex Fractionated Atrial Electrograms Correlate Poorly with Each Other and Atrial Fibrillation Substrate Complexity. *Heart Rhythm*, pages 1–9. 26

Laughner, J. I., Ng, F. S., Sulkin, M. S., Arthur, R. M., and Efimov, I. R. (2012). Processing and analysis of cardiac optical mapping data obtained with potentiometric dyes. *American journal of physiology. Heart and circulatory physiology*, 303(7):H753–65. 33, 37, 44, 135, 140, 142, 196, 197, 367

Lazar, S., Dixit, S., Marchlinski, F. E., Callans, D. J., and Gerstenfeld, E. P. (2004). Presence of left-to-right atrial frequency gradient in paroxysmal but not persistent atrial fibrillation in humans. *Circulation*, 110(20):3181–6. 347

Lee, S., Sahadevan, J., Khrestian, C. M., Durand, D. M., and Waldo, A. L. (2013). High density mapping of atrial fibrillation during vagal nerve stimulation in the canine heart: restudying the Moe hypothesis. *Journal of cardiovascular electrophysiology*, 24(3):328–35. 203

Legland, D. (2015). Matlab file exchange - geom3d. 108

Levick, R. J. (2009). *An Introduction to Cardiovascular Physiology*. CRC Press. 8

Linton, N. W. F., Koa-Wing, M., Francis, D. P., Kojodjojo, P., Lim, P. B., Salukhe, T. V., Whinnett, Z., Davies, D. W., Peters, N. S., O'Neill, M. D., and Kanagaratnam, P. (2009). Cardiac ripple mapping: a novel three-dimensional visualization method for use with electroanatomic mapping of cardiac arrhythmias. *Heart rhythm : the official journal of the Heart Rhythm Society*, 6(12):1754–62. 361

Lloyd, C. and Noble, P. (1998). Ionic mechanisms underlying human atrial action potential properties: insights from a mathematical model. 72

Lloyd, C. M., Lawson, J. R., Hunter, P. J., and Nielsen, P. F. (2008). The CellML Model Repository. *Bioinformatics (Oxford, England)*, 24(18):2122–3. 17, 63, 70

Lou, Q., Ripplinger, C., Bayly, P., and Efimov, I. (2008). Quantitative Panoramic Imaging of Epicardial Electrical Activity. *Annals of biomedical . . .*, 36(10):1649–1658. 83

MacCannell, K. A., Bazzazi, H., Chilton, L., Shibukawa, Y., Clark, R. B., and Giles, W. R. (2007). A mathematical model of electrotonic interactions between ventricular myocytes and fibroblasts. *Biophysical journal*, 92:4121–4132. 21, 63, 64, 410

Maclachlan, M. C., Sundnes, J., and Spiteri, R. J. (2007). A comparison of non-standard solvers for ODEs describing cellular reactions in the heart. *Computer methods in biomechanics and biomedical engineering*, 10(5):317–26. 69

Mahnkopf, C., Badger, T. J., Burgon, N. S., Daccarett, M., Haslam, T. S., Badger, C. T., Mcgann, C. J., Akoum, N., Kholmovski, E., Macleod, R. S., and Marrouche, N. F. (2010). Evaluation of the left atrial substrate in patients with lone atrial fibrillation using delayed-enhanced MRI : Implications for disease progression and response to catheter ablation. *HRTHM*, 7(10):1475–1481. 14

Maleckar, M., Greenstein, J., Giles, W., and Trayanova, N. a. (2009). K+ current changes account for the rate dependence of the action potential in the human atrial myocyte. *American Journal of . . .*, pages 1398–1410. 55

Mansour, M., Mandapati, R., Berenfeld, O., Chen, J., Samie, F. H., and Jalife, J. (2001). Left-to-Right Gradient of Atrial Frequencies During Acute Atrial Fibrillation in the Isolated Sheep Heart. *Circulation*, 103(21):2631–2636. 28, 135, 228, 362

Marcus, G. M., Yang, Y., Varosy, P. D., Ordovas, K., Tseng, Z. H., Badhwar, N., Lee, B. K., Lee, R. J., Scheinman, M. M., and Olgin, J. E. (2007). Regional left atrial voltage in patients with atrial fibrillation. *Heart rhythm : the official journal of the Heart Rhythm Society*, 4(2):138–44. 231

Marsh, M. E., Ziaratgahi, S. T., and Spiteri, R. J. (2012). The secrets to the success of the Rush-Larsen method and its generalizations. *IEEE transactions on biomedical engineering*, 59(9):2506–15. 69

Martínez, L., Romero, L., Tobón, C., Ferrero, J. M., Jalife, J., Berenfeld, O., Saiz, J., Valencia, U. P. D., and Metropolitano, I. T. (2014). Accurate Characterization of Rotor Activity during Atrial Fibrillation Depends on the Properties of the Multi-electrode Grid. *Computing in Cardiology (CinC)*. 291, 331, 351

Masè, M., Greco, M. D., Marini, M., and Ravelli, F. (2009). Velocity Field Analysis of Activation Maps in Atrial Fibrillation A Simulation Study. In *IFMBE Proceedings 25/IV*, pages 1014–1017. 39, 40, 42, 44, 349, 350, 360

Masé, M. and Ravelli, F. (2010). Automatic reconstruction of activation and velocity maps from electro-anatomic data by radial basis functions. *Conference proceedings : ... Annual International Conference of the IEEE Engineering in Medicine and Biology Society. IEEE Engineering in Medicine and Biology Society. Conference*, 2010:2608–11. 40, 44

Mazeh, N., Haines, D. E., Kay, M. W., and Roth, B. J. (2013). A Simplified Approach for Simultaneous Measurements of Wavefront Velocity and Curvature in the Heart Using Activation Times. *Cardiovascular Engineering and Technology*, 4(4):520–534. 41, 44

McDowell, K. S., Vadakkumpadan, F., Blake, R., Blauer, J., Plank, G., MacLeod, R. S., and Trayanova, N. a. (2012). Methodology for patient-specific modeling of atrial fibrosis as a substrate for atrial fibrillation. *Journal of electrocardiology*, 45(6):640–5. 23

Moe, G. and Abildskov, J. (1959). Atrial Fibrillation as a Self-Sustaining Arrhythmia Independent of Focal Discharge. *American heart journal*. 10

Moe, G., Rheinboldt, W., and Abildskov, J. (1964). A computer model of atrial fibrillation. *American heart journal*. 10, 20, 203

Moreno, J. D., Zhu, Z. I., Yang, P.-C., Bankston, J. R., Jeng, M.-T., Kang, C., Wang, L., Bayer, J. D., Christini, D. J., Trayanova, N. a., Ripplinger, C. M., Kass, R. S., and Clancy, C. E. (2011). A computational model to predict the effects of class I anti-arrhythmic drugs on ventricular rhythms. *Science translational medicine*, 3(98):98ra83. 19

Mourad, A. and Nash, M. (2007). Method for quantifiying conduction velocity during ventricular fibrillation. *Physical Review E*, 75(1):011914. 41, 44, 296

Nademanee, K., McKenzie, J., Kosar, E., Schwab, M., Sunsaneewitayakul, B., Vasavakul, T., Khunnawat, C., and Ngarmukos, T. (2004). A new approach for catheter ablation of atrial fibrillation: mapping of the electrophysiologic substrate. *Journal of the American College of Cardiology*, 43(11):2044–53. 26, 231

Nanthakumar, K., Walcott, G. P., Melnick, S., Rogers, J. M., Kay, M. W., Smith, W. M., Ideker, R. E., and Holman, W. (2004). Epicardial organization of human ventricular fibrillation. *Heart rhythm : the official journal of the Heart Rhythm Society*, 1(1):14–23. 296

Narayan, S., Wright, M., Derval, N., Jadidi, A., Forclaz, A., Nault, I., Miyazaki, S., Sacher, F., Bordachar, P., Clémenty, J., Jais, P., and Haissaguerre, M. (2011a). Classifying fractionated electrograms in human atrial fibrillation using monophasic action potentials and activation mapping: evidence for localized drivers,. *Heart Rhythm*, 8(2):244–253. 26

Narayan, S. M. (2002). Alternans of Atrial Action Potentials During Atrial Flutter as a Precursor to Atrial Fibrillation. *Circulation*, 106(15):1968–1973. 12

Narayan, S. M., Baykaner, T., Clopton, P., Schricker, A., Lalani, G. G., Krummen, D. E., Shivkumar, K., and Miller, J. M. (2014). Ablation of rotor and focal sources reduces late recurrence of atrial fibrillation compared with trigger ablation alone: extended follow-up of the CONFIRM trial (Conventional Ablation for Atrial Fibrillation With or Without Focal Impulse and Rotor Modulat. *Journal of the American College of Cardiology*, 63(17):1761–8. 297

Narayan, S. M., Franz, M. R., Clopton, P., Pruvot, E. J., and Krummen, D. E. (2011b). Repolarization alternans reveals vulnerability to human atrial fibrillation. *Circulation*, 123(25):2922–30. 8, 11, 12

Narayan, S. M., Kazi, D., Krummen, D. E., and Rappel, W.-J. (2008). Repolarization and activation restitution near human pulmonary veins and atrial fibrillation initiation: a mechanism for the initiation of atrial fibrillation by premature beats. *Journal of the American College of Cardiology*, 52(15):1222–30. 8, 11

Narayan, S. M., Krummen, D. E., Enyeart, M. W., and Rappel, W.-J. (2012a). Computational mapping identifies localized mechanisms for ablation of atrial fibrillation. *PloS one*, 7(9):e46034. 27

Narayan, S. M., Krummen, D. E., and Rappel, W.-J. (2012b). Clinical mapping approach to diagnose electrical rotors and focal impulse sources for human atrial fibrillation. *Journal of cardiovascular electrophysiology*, 23(5):447–54. 9, 10, 25, 27, 203, 226, 227, 301

Narayan, S. M., Krummen, D. E., Shivkumar, K., Clopton, P., Rappel, W.-J., and Miller, J. M. (2012c). Treatment of atrial fibrillation by the ablation of localized sources: CONFIRM (Conventional Ablation for Atrial Fibrillation With or Without Focal Impulse and Rotor Modulation) trial. *Journal of the American College of Cardiology*, 60(7):628–36. 302

Narayan, S. M., Patel, J., Mulpuru, S., and Krummen, D. E. (2012d). Focal impulse and rotor modulation ablation of sustaining rotors abruptly terminates persistent atrial fibrillation to sinus rhythm with elimination on follow-up: a video case study. *Heart rhythm : the official journal of the Heart Rhythm Society*, 9(9):1436–9. 45, 351, 362

Nash, M. P., Mourad, A., Clayton, R. H., Sutton, P. M., Bradley, C. P., Hayward, M., Paterson, D. J., and Taggart, P. (2006). Evidence for multiple mechanisms in human ventricular fibrillation. *Circulation*, 114(6):536–42. 50, 83, 204, 227, 228, 231, 298, 302, 362, 365

Ndrepepa, G., Caref, E. B., Yin, H., El-Sherif, N., and Restivo, M. (1995). Activation time determination by high-resolution unipolar and bipolar extracellular electrograms in the canine heart. *Journal of cardiovascular electrophysiology*, 6:174–188. 7

Nerbonne, J. and Kass, R. (2005). Molecular physiology of cardiac repolarization. *Physiological reviews*, pages 1205–1253. xviii, 4, 5

Neu, J. C. and Krassowska, W. (1993). Homogenization of syncytial tissues. *Critical reviews in biomedical engineering*, 21:137–199. 59

Ng, J., Kadish, A. H., and Goldberger, J. J. (2006). Effect of electrogram characteristics on the relationship of dominant frequency to atrial activation rate in atrial fibrillation. *Heart Rhythm*, 3:1295–1305. 235, 333, 347, 365

Ng, J., Kadish, A. H., and Goldberger, J. J. (2007). Technical considerations for dominant frequency analysis. *Journal of cardiovascular electrophysiology*, 18(7):757–64. 266, 268, 288

Ng, J., Sehgal, V., Ng, J. K., Gordon, D., and Goldberger, J. J. (2014). Iterative method to detect atrial activations and measure cycle length from electrograms during atrial fibrillation. *IEEE transactions on bio-medical engineering*, 61(2):273–8. 295, 364

Niederer, S. a., Fink, M., Noble, D., and Smith, N. P. (2009). A meta-analysis of cardiac electrophysiology computational models. *Experimental physiology*, 94(5):486–95. 19

Niederer, S. a., Kerfoot, E., Benson, A. P., Bernabeu, M. O., Bernus, O., Bradley, C., Cherry, E. M., Clayton, R., Fenton, F. H., Garny, A., Heidenreich, E., Land, S., Maleckar, M., Pathmanathan, P., Plank, G., Rodríguez, J. F., Roy, I., Sachse, F. B., Seemann, G., Skavhaug, O., and Smith, N. P. (2011). Verification of cardiac tissue electrophysiology simulators using an N-version benchmark. *Philosophical transactions. Series A, Mathematical, physical, and engineering sciences*, 369(1954):4331–51. 21, 339

Noble, D. (1960). Cardiac action and pacemaker potentials based on the Hodgkin-Huxley equations. *Nature*. 17

Noble, P. (2015). CellML: Ionic mechanisms underlying human atrial action potential properties: insights from a mathematical model. 63

Nolasco, J. and Dahlen, R. (1968). A graphic method for the study of alternation in cardiac action potentials. *Journal of applied physiology*, 25(2):191–196. 12

Noujaim, S. F., Berenfeld, O., Kalifa, J., Cerrone, M., Nanthakumar, K., Atienza, F., Moreno, J., Mironov, S., and Jalife, J. (2007a). Universal scaling law of electrical turbulence in the mammalian heart. *Proceedings of the National Academy of Sciences of the United States of America*, 104(52):20985–9. 348

Noujaim, S. F., Pandit, S. V., Berenfeld, O., Vikstrom, K., Cerrone, M., Mironov, S., Zugermayr, M., Lopatin, A. N., and Jalife, J. (2007b). Up-regulation of the inward rectifier K+ current (I K1) in the mouse heart accelerates and stabilizes rotors. *The Journal of physiology*, 578(Pt 1):315–26. 347

Nygren, A., Fiset, C., Firek, L., Clark, J. W., Lindblad, D. S., Clark, R. B., and Giles, W. R. (1998). Mathematical model of an adult human atrial cell: the role of K+ currents in repolarization. *Circulation research*, 82:63–81. xviii, 55, 56

O'Hara, T., Virág, L., Varró, A., and Rudy, Y. (2011). Simulation of the undiseased human cardiac ventricular action potential: model formulation and experimental validation. *PLoS computational biology*, 7(5):e1002061. 19

Oral, H. (2002). Pulmonary Vein Isolation for Paroxysmal and Persistent Atrial Fibrillation. *Circulation*, 105(9):1077–1081. 26

Packard, N. H., Crutchfield, J. P., Farmer, J. D., and Shaw, R. S. (1980). Geometry from a time series. *Physical Review Letters*, 45(9):712–716. 46

Pálsson, E. and Cox, E. C. (1996). Origin and evolution of circular waves and spirals in Dictyostelium discoideum territories. *Proceedings of the National Academy of Sciences of the United States of America*, 93:1151–1155. 45

Pandit, S. V., Berenfeld, O., Anumonwo, J. M. B., Zaritski, R. M., Kneller, J., Nattel, S., and Jalife, J. (2005a). Ionic determinants of functional reentry in a 2-D model of human atrial cells during simulated chronic atrial fibrillation. *Biophysical journal*, 88(6):3806–21. 14

Pandit, S. V., Berenfeld, O., Anumonwo, J. M. B., Zaritski, R. M., Kneller, J., Nattel, S., and Jalife, J. (2005b). Ionic determinants of functional reentry in a 2-D model of human atrial cells during simulated chronic atrial fibrillation. *Biophysical journal*, 88(6):3806–21. 232, 304, 347

Pandit, S. V. and Jalife, J. (2013). Rotors and the dynamics of cardiac fibrillation. *Circulation research*, 112(5):849–62. 52

Pashaei, A., Bayer, J., Meillet, V., Dubois, R., and Vigmond, E. J. (2015). Computation and Projection of Spiral Wave Trajectories During Atrial Fibrillation: A Computational Study. *Cardiac Electrophysiology Clinics*, 7(1):37–47. 297

Paskaranandavadivel, N., O'Grady, G., Du, P., Pullan, A. J., and Cheng, L. K. (2012). An improved method for the estimation and visualization of velocity fields from gastric high-resolution electrical mapping. *IEEE transactions on bio-medical engineering*, 59(3):882–9. 33, 37

Pastore, J. M., Girouard, S. D., Laurita, K. R., Akar, F. G., and Rosenbaum, D. S. (1999). Mechanism Linking T-Wave Alternans to the Genesis of Cardiac Fibrillation. *Circulation*, 99(10):1385–1394. 2, 11

Peyre, G. (2015). Toolbox Fast Marching. 84

Pieper, C. F., Blue, R., and Pacifico, A. (1993). Simultaneously collected monopolar and discrete bipolar electrograms: comparison of activation time detection algorithms. *Pacing and clinical electrophysiology : PACE*, 16:426–433. 30

Pitt-Francis, J., Pathmanathan, P., Bernabeu, M. O., Bordas, R., Cooper, J., Fletcher, A. G., Mirams, G. R., Murray, P., Osborne, J. M., Walter, A., Chapman, S. J., Garny, A., van Leeuwen, I. M. M., Maini, P. K., Rodríguez, B., Waters, S. L., Whiteley, J. P., Byrne, H. M., and Gavaghan, D. J. (2009). Chaste: A test-driven

approach to software development for biological modelling. *Computer Physics Communications*, 180:2452–2471. 21

Plank, G., Burton, R. A. B., Hales, P., Bishop, M., Mansoori, T., Bernabeu, M. O., Garny, A., Prassl, A. J., Bollensdorff, C., Mason, F., Mahmood, F., Rodriguez, B., Grau, V., Schneider, J. E., Gavaghan, D., and Kohl, P. (2009). Generation of histo-anatomically representative models of the individual heart: tools and application. *Philosophical transactions. Series A, Mathematical, physical, and engineering sciences*, 367:2257–2292. 22

Pop, M., Sermesant, M., Mansi, T., Crystal, E., Ghate, S., Peyrat, J. M., Lashevsky, I., Qiang, B., McVeigh, E., Ayache, N., and Wright, G. A. (2011). Correspondence between simple 3-D MRI-based computer models and in-vivo EP measurements in swine with chronic infarctions. *IEEE Transactions on Biomedical Engineering*, 58:3483–3486. 22

Press, W. H., Teukolsky, S. A., Vetterling, W. T., and Flannery, B. P. (2007). *Numerical Recipes: The Art of Scientific Computing*, volume 29. Cambridge University Press. 67, 68, 304

Pruvot, E. J., Katra, R. P., Rosenbaum, D. S., and Laurita, K. R. (2004). Role of calcium cycling versus restitution in the mechanism of repolarization alternans. *Circulation research*, 94(8):1083–90. 13

Qu, Z. and Garfinkel, a. (1999). An advanced algorithm for solving partial differential equation in cardiac conduction. *IEEE transactions on bio-medical engineering*, 46(9):1166–8. 66, 304

Rappel, W.-J. and Narayan, S. M. (2013). Theoretical considerations for mapping activation in human cardiac fibrillation. *Chaos (Woodbury, N.Y.)*, 23(2):023113. 302, 303, 349, 367

Ravelli, F., Masè, M., del Greco, M., Marini, M., and Disertori, M. (2011). Acute atrial dilatation slows conduction and increases AF vulnerability in the human atrium. *Journal of cardiovascular electrophysiology*, 22(4):394–401. 32, 44

Reppel, M., Pillekamp, F., Lu, Z. J., Halbach, M., Brockmeier, K., Fleischmann, B. K., and Hescheler, J. (2004). Microelectrode arrays: A new tool to measure embryonic heart activity. In *Journal of Electrocardiology*, volume 37, pages 104–109. xxv, 16, 417

Rodrigo, M., Guillem, M. S., Climent, A. M., Pedrón-Torrecilla, J., Liberos, A., Millet, J., Fernández-Avilés, F., Atienza, F., and Berenfeld, O. (2014). Body surface localization of left and right atrial high-frequency rotors in atrial fibrillation patients: A clinical-computational study. *Heart rhythm : the official journal of the Heart Rhythm Society*, 11(9):1584–91. 197, 199, 200, 367

Rogers, J. M. (2004). Combined phase singularity and wavefront analysis for optical maps of ventricular fibrillation. *IEEE transactions on bio-medical engineering*, 51(1):56–65. 50, 55, 154, 198, 227, 362

Rogers, J. M., Usui, M., KenKnight, B. H., Ideker, R. E., and Smith, W. M. (1997). Recurrent wavefront morphologies: a method for quantifying the complexity of epicardial activation patterns. *Annals of biomedical engineering*, 25(5):761–8. 299

Roney, C. H., Cantwell, C. D., Qureshi, N. A., Ali, R. L., Chang, E. T. Y., Lim, P. B., Sherwin, S. J., Peters, N. S., Siggers, J. H., and Ng, F. S. (2014a). An automated algorithm for determining conduction velocity, wavefront direction and origin of focal cardiac arrhythmias using a multipolar catheter. In *2014 36th Annual International Conference of the IEEE Engineering in Medicine and Biology Society*, pages 1583–1586. Ieee. 44, 91

Roney, C. H., Cantwell, C. D., Siggers, J. H., Ng, F. S., and Peters, N. S. (2014b). A Novel Method for Rotor Tracking Using Bipolar Electrogram Phase. In *Computing in Cardiology (CinC)*, pages 233–236. 231

Rosenbaum, D. and Jalife, J. (2001). *Optical Mapping of Cardiac Excitation and Arrhythmias*. Futura Publishing Company. 49

Rotter, M., Dang, L., Jacquemet, V., Virag, N., Kappenberger, L., and Haïssaguerre, M. (2007). Impact of varying ablation patterns in a simulation model of persistent atrial fibrillation. *PACE - Pacing and Clinical Electrophysiology*, 30:314–321. 23

Rottmann, M., Keller, M. W., Oesterlein, T., Seemann, G., and Do, O. (2014). Comparison of Different Methods and Catheter Designs to Estimate the Rotor Tip Position – A Simulation Study. *Computing in Cardiology (CinC)*, pages 133–136. 298, 350, 365

Rousakov, S., Wikswo, J., and Aliev, R. (1999). Wave vector analysis of cardiac activation patterns. *Proceedings of the First Joint BMES/EMBS Conference. 1999 IEEE Engineering in Medicine and Biology 21st Annual Conference and the 1999 Annual Fall Meeting of the Biomedical Engineering Society (Cat. No.99CH37015)*, 1:161. 42, 360

Ruchat, P., Dang, L., Schlaepfer, J., Virag, N., von Segesser, L. K., and Kappenberger, L. (2007). Use of a biophysical model of atrial fibrillation in the interpretation of the outcome of surgical ablation procedures. *European journal of cardio-thoracic surgery : official journal of the European Association for Cardio-thoracic Surgery*, 32(1):90–5. 23

Rudy, Y. and Messinger-Rapport, B. J. (1988). The inverse problem in electrocardiography: solutions in terms of epicardial potentials. *Critical reviews in biomedical engineering*, 16:215–268. 25

Rush, S. and Larsen, H. (1978a). A Practical Algorithm for Solving Dynamic Membrane Equations. *Biomedical Engineering, IEEE Transactions ...*, pages 389–392. 64

Rush, S. and Larsen, H. (1978b). A Practical Algorithm for Solving Dynamic Membrane Equations. *Biomedical Engineering, IEEE Transactions ...*, pages 389–392. 232, 304

Rutherford, S. L., Trew, M. L., Sands, G. B., Legrice, I. J., and Smaill, B. H. (2012). High-resolution 3-dimensional reconstruction of the infarct border zone: Impact of structural remodeling on electrical activation. *Circulation Research*, 111:301–311. 22

Sachse, F. B., Moreno, A. P., Seemann, G., and Abildskov, J. A. (2009). A model of electrical conduction in cardiac tissue including fibroblasts. *Annals of Biomedical Engineering*, 37:874–889. 21

Saitoh, H., Bailey, J. C., and Surawicz, B. (1988). Alternans of action potential duration after abrupt shortening of cycle length: differences between dog Purkinje and ventricular muscle fibers. *Circulation Research*, 62(5):1027–1040. 13

Salama, G., Kanai, a., and Efimov, I. R. (1994). Subthreshold stimulation of Purkinje fibers interrupts ventricular tachycardia in intact hearts. Experimental study with voltage-sensitive dyes and imaging techniques. *Circulation Research*, 74(4):604–619. 33, 44, 305, 307

Salinet, J. a. L., Tuan, J. H., Sandilands, A. J., Stafford, P. J., Schlindwein, F. S., and André Ng, G. (2014). Distinctive patterns of dominant frequency trajectory behavior in drug-refractory persistent atrial fibrillation: preliminary characterization of spatiotemporal instability. *Journal of cardiovascular electrophysiology*, 25(4):371–9. 203, 225

Salinet, J. L., Madeiro, J. P. V., Cortez, P. C., Stafford, P. J., André Ng, G., and Schlindwein, F. S. (2013). Analysis of QRS-T subtraction in unipolar atrial fibrillation electrograms. *Medical & biological engineering & computing*, 51(12):1381–91. 266

Sánchez, C., Corrias, A., Bueno-Orovio, A., Davies, M., Swinton, J., Jacobson, I., Laguna, P., Pueyo, E., and Rodríguez, B. (2012). The Na+/K+ pump is an important modulator of refractoriness and rotor dynamics in human atrial tissue. *American journal of physiology. Heart and circulatory physiology*, 302(5):H1146–59. 14, 347

Sanders, P., Berenfeld, O., Hocini, M., Jaïs, P., Vaidyanathan, R., Hsu, L.-F., Garrigue, S., Takahashi, Y., Rotter, M., Sacher, F., Scavée, C., Ploutz-Snyder, R., Jalife, J., and Haïssaguerre, M. (2005). Spectral analysis identifies sites of high-frequency activity maintaining atrial fibrillation in humans. *Circulation*, 112(6):789–97. 203, 225, 231, 347, 362

Sandrini, L., Faes, L., Ravelli, F., Antolini, R., and Nollo, G. (2002). Morphology-based measurement of activation time in human atrial fibrillation. *Computers in Cardiology*, pages 593–596. 30

Sarmast, F., Kolli, A., Zaitsev, A., Parisian, K., Dhamoon, A. S., Guha, P. K., Warren, M., Anumonwo, J. M. B., Taffet, S. M., Berenfeld, O., and Jalife, J. (2003). Cholinergic atrial fibrillation: I(K,ACh) gradients determine unequal left/right atrial frequencies and rotor dynamics. *Cardiovascular research*, 59(4):863–73. 199, 225, 226, 362, 363

Sato, D., Xie, L.-H., Sovari, A. A., Tran, D. X., Morita, N., Xie, F., Karagueuzian, H., Garfinkel, A., Weiss, J. N., and Qu, Z. (2009). Synchronization of chaotic early afterdepolarizations in the genesis of cardiac arrhythmias. *Proceedings of the National Academy of Sciences of the United States of America*, 106:2983–2988. 70, 73, 233, 333

Sawa, A., Shimizu, A., Ueyama, T., Yoshiga, Y., Suzuki, S., Sugi, N., Oono, M., Oomiya, T., and Matsuzaki, M. (2008). Activation patterns and conduction velocity in posterolateral right atrium during typical atrial flutter using an electroanatomic mapping system. *Circulation Journal*, 72(March):384–391. 32, 44

Schilling, C., Nguyen, M. P., Luik, A., Schmitt, C., and Dossel, O. (2009). Non-Linear Energy Operator for the Analysis of Intracardial Electrograms. *IFMBE Proc. World Congr. Med. Phys. Biomed. Eng*, 25(4):872–875. 30

Schilling, R. J., Peters, N. S., and Davies, D. W. (1998). Simultaneous endocardial mapping in the human left ventricle using a noncontact catheter: comparison of contact and reconstructed electrograms during sinus rhythm. *Circulation*, 98:887–898. 24

Schilling, R. J., Peters, N. S., Goldberger, J., Kadish, a. H., and Davies, D. W. (2001). Characterization of the anatomy and conduction velocities of the human right atrial flutter circuit determined by noncontact mapping. *Journal of the American College of Cardiology*, 38(2):385–93. 348

Schoenwald, A., Sahakian, A., and Swiryn, S. (1994). A method for determining local activation direction in the atrium. *IEEE*, pages 1–2. 39, 44

Schoenwald, a. T., Sahakian, a. V., Sih, H. J., and Swiryn, S. (1998). Further observations of "linking" of atrial excitation during clinical atrial fibrillation. *Pacing and clinical electrophysiology : PACE*, 21(1 Pt 1):25–34. 39

Schuessler, R. B., Grayson, T. M., Bromberg, B. I., Cox, J. L., and Boineau, J. P. (1992). Cholinergically mediated tachyarrhythmias induced by a single extrastimulus in the isolated canine right atrium. *Circulation Research*, 71(5):1254–1267. 204

Schuessler, R. B., Rosenshtraukh, L. V., Boineau, J. P., Bromberg, B. I., and Cox, J. L. (1991). Spontaneous tachyarrhythmias after cholinergic suppression in the isolated perfused canine right atrium. *Circulation Research*, 69(4):1075–1087. 227

Sharifov, O. F., Zaitsev, A. V., Rosenshtraukh, L. V., Kaliadin, A. Y., Beloshapko, G. G., Yushmanova, A. V., Schuessler, R. B., and Boineau, J. P. (2000). Spatial distribution and frequency dependence of arrhythmogenic vagal effects in canine atria. *Journal of cardiovascular electrophysiology*, 11:1029–1042. 227

Shenasa, M., Hindricks, G., Borggrefe, M., Breithardt, G., and Josephson, M. E. (2013). *Cardiac Mapping*. Wiley-Blackwell, 4th edition. 5, 7

Shkurovich, S., Sahakian, a. V., and Swiryn, S. (1998). Detection of atrial activity from high-voltage leads of implantable ventricular defibrillators using a cancellation technique. *IEEE transactions on bio-medical engineering*, 45(2):229–34. 266, 268

Shors, S., Sahakian, A., Sih, H. J., and Swiryn, S. (1996). A Method for Determining High Resolution Activation Time Delays in Unipolar Cardiac Mapping. *IEEE transactions on biomedical engineering*, 43(12):1192–1196. 31

Shumaker, J. M., Clark, J. W., and Giles, W. R. (1993). Simulations of passive properties and action potential conduction in an idealized bullfrog atrial trabeculum. *Mathematical biosciences*, 116:127–167. 204

Spach, M. S. and Kootsey, J. (1985). Relating the Sodium Current and Conductance to the Shape of Transmembrane and Extracellular Potentials by Simulation : Effects of Propagation Boundaries. *IEEE transactions on biomedical engineering*, 32(10). 5

Spiteri, R. J. and Dean, R. C. (2008). On the performance of an implicit-explicit Runge-Kutta method in models of cardiac electrical activity. *IEEE Transactions on Biomedical Engineering*, 55:1488–1495. 64, 69

Steinhaus, B. M. (1989). Estimating cardiac transmembrane activation and recovery times from unipolar and bipolar extracellular electrograms: a simulation study. *Circulation Research*, 64(3):449–462. 30

Stevens, C., Remme, E., LeGrice, I., and Hunter, P. (2003). Ventricular mechanics in diastole: Material parameter sensitivity. *Journal of Biomechanics*, 36:737–748. 21

Stinstra, J., MacLeod, R., and Henriquez, C. (2010). Incorporating histology into a 3D microscopic computer model of myocardium to study propagation at a cellular level. *Annals of Biomedical Engineering*, 38:1399–1414. 20

Sung, D., Omens, J. H., and McCulloch, a. D. (2000). Model-based analysis of optically mapped epicardial activation patterns and conduction velocity. *Annals of biomedical engineering*, 28(9):1085–92. 37, 44, 83

Swarup, V., Baykaner, T., Rostamian, A., Daubert, J. P., Hummel, J., Krummen, D. E., Trikha, R., Miller, J. M., Tomassoni, G. F., and Narayan, S. M. (2014). Stability of Rotors and Focal Sources for Human Atrial Fibrillation: Focal Impulse and Rotor Mapping (FIRM) of AF Sources and Fibrillatory Conduction. *Journal of Cardiovascular Electrophysiology*, 25(12):1284–92. 301

Takens, F. (1981). Detecting strange attractors in turbulence. *Dynamical systems and turbulence, Lecture Notes in Mathematics*, 898:366–381. 46

Tan, R. C. and Joyner, R. W. (1990). Electrotonic influences on action potentials from isolated ventricular cells. *Circulation Research*, 67(5):1071–1081. 14

Tanaka, K., Zlochiver, S., Vikstrom, K. L., Yamazaki, M., Moreno, J., Klos, M., Zaitsev, A. V., Vaidyanathan, R., Auerbach, D. S., Landas, S., Guiraudon, G., Jalife, J., Berenfeld, O., and Kalifa, J. (2007). Spatial distribution of fibrosis governs fibrillation wave dynamics in the posterior left atrium during heart failure. *Circulation research*, 101(8):839–47. 14

ten Tusscher, K. H. W. J., Hren, R., and Panfilov, A. V. (2007). Organization of ventricular fibrillation in the human heart. *Circulation Research*, 100. 22, 226, 363

ten Tusscher, K. H. W. J., Mourad, A., Nash, M. P., Clayton, R. H., Bradley, C. P., Paterson, D. J., Hren, R., Hayward, M., Panfilov, A. V., and Taggart, P. (2009). Organization of ventricular fibrillation in the human heart: experiments and models. *Experimental physiology*, 94:553–562. 22, 204, 226, 363

ten Tusscher, K. H. W. J., Noble, D., Noble, P. J., and Panfilov, a. V. (2004). A model for human ventricular tissue. *American journal of physiology. Heart and circulatory physiology*, 286(4):H1573–89. 19

ten Tusscher, K. H. W. J. and Panfilov, a. V. (2003). Reentry in heterogeneous cardiac tissue described by the Luo-Rudy ventricular action potential model. *American journal of physiology. Heart and circulatory physiology*, 284(2):H542–8. 14

ten Tusscher, K. H. W. J. and Panfilov, A. V. (2006). Alternans and spiral breakup in a human ventricular tissue model. *American journal of physiology. Heart and circulatory physiology*, 291:H1088–H1100. 19

Trayanova, N. (2006). Defibrillation of the heart: insights into mechanisms from modelling studies. *Experimental physiology*, 91:323–337. 21

Treo, E. F., Cervantes, D. O., and Ciaccio, E. J. (2013). Automated detection and mapping of electrical activation when electrogram morphology is complex. *Biomedical Signal Processing and Control*, 8(1):41–49. 296

Trew, M., Le Grice, I., Smaill, B., and Pullan, A. (2005). A finite volume method for modeling discontinuous electrical activation in cardiac tissue. *Ann Biomed Eng*, 33:590–602. 21

Umapathy, K., Masse, S., Kolodziejska, K., Veenhuyzen, G. D., Chauhan, V. S., Husain, M., Farid, T., Downar, E., Sevaptsidis, E., and Nanthakumar, K. (2008). Electrogram fractionation in murine HL-1 atrial monolayer model. *Heart rhythm : the official journal of the Heart Rhythm Society*, 5(7):1029–35. 298

Umapathy, K., Nair, K., Masse, S., Krishnan, S., Rogers, J., Nash, M. P., and Nanthakumar, K. (2010). Phase mapping of cardiac fibrillation. *Circulation. Arrhythmia and electrophysiology*, 3(1):105–14. 73, 74, 135, 298

Vadakkumpadan, F., Arevalo, H., Prass, A. J., Chen, J., Kickinger, F., Kohl, P., Plank, G., and Trayanova, N. (2010). Image-based models of cardiac structure in health and disease. *Wiley Interdisciplinary Reviews: Systems Biology and Medicine*, 2:489–506. 21

van der Tweel, L. H., Strackee, J., Stokhof, a. a., Wassenaar, C., and Meijler, F. L. (1999). ECG of the "newborn" mouse (Mus domesticus) with specific reference to comparative AV transmission. *Journal of cardiovascular electrophysiology*, 10(2):168–73. 348

Vaquero, M., Calvo, D., and Jalife, J. (2008). Cardiac fibrillation: from ion channels to rotors in the human heart. *Heart rhythm : the official journal of the Heart Rhythm Society*, 5(6):872–9. 9, 347

Varela, M. and Aslanidi, O. V. (2014). Role of Atrial Tissue Substrate and Electrical Activation Pattern in Fractionation of Atrial Electrograms : a Computational Study. *Computing in Cardiology (CinC)*, pages 1587–1590. 73

Verheule, S., Tuyls, E., van Hunnik, A., Kuiper, M., Schotten, U., and Allessie, M. (2010). Fibrillatory conduction in the atrial free walls of goats in persistent and permanent atrial fibrillation. *Circulation. Arrhythmia and electrophysiology*, 3(6):590–9. 10, 203, 204, 370

Vetter, F. J. and McCulloch, A. D. (1998). Three-dimensional analysis of regional cardiac function: a model of rabbit ventricular anatomy. *Progress in biophysics and molecular biology*, 69:157–183. 21

Vigmond, E. J., Aguel, F., and Trayanova, N. a. (2002). Computational techniques for solving the bidomain equations in three dimensions. *IEEE transactions on bio-medical engineering*, 49(11):1260–9. 21

Vigmond, E. J., Hughes, M., Plank, G., and Leon, L. (2003). Computational tools for modeling electrical activity in cardiac tissue. *Journal of Electrocardiology*, 36:69–74. 21

Vigmond, E. J. and Leon, L. J. (1999). Electrophysiological basis of monophasic action potential recordings. *Medical & biological engineering & computing*, 37(3):359–65. 8

Vigmond, E. J., Tsoi, V., Yin, Y., Pagé, P., and Vinet, A. (2009). Estimating atrial action potential duration from electrograms. *IEEE transactions on bio-medical engineering*, 56(5):1546–55. 7

Voigt, N., Trausch, A., Knaut, M., Matschke, K., Varró, A., Van Wagoner, D. R., Nattel, S., Ravens, U., and Dobrev, D. (2010). Left-to-right atrial inward rectifier potassium current gradients in patients with paroxysmal versus chronic atrial fibrillation. *Circulation. Arrhythmia and electrophysiology*, 3(5):472–80. 347

Walker, M. L. and Rosenbaum, D. S. (2005). Cellular alternans as mechanism of cardiac arrhythmogenesis. *Heart rhythm : the official journal of the Heart Rhythm Society*, 2(12):1383–6. 13

Walmsley, J., Mirams, G., Bahoshy, M., Bollensdorff, C., Rodriguez, B., and Burrage, K. (2010). Phenomenological modeling of cell-to-cell and beat-to-beat variability in isolated Guinea Pig ventricular myocytes. *Conference proceedings : ...*

Annual International Conference of the IEEE Engineering in Medicine and Biology Society. IEEE Engineering in Medicine and Biology Society. Conference, 2010:1457–60. 20

Walton, R. D., Bernus, O., and Dubois, R. (2013). A novel approach for deriving global activation maps from non-averaged cardiac optical signals. *Conference proceedings : ... Annual International Conference of the IEEE Engineering in Medicine and Biology Society. IEEE Engineering in Medicine and Biology Society. Annual Conference*, 2013:1772–5. 39

Walton, R. D., Smith, R. M., Mitrea, B. G., White, E., Bernus, O., and Pertsov, A. M. (2012). Extracting surface activation time from the optically recorded action potential in three-dimensional myocardium. *Biophysical journal*, 102(1):30–8. 15

Walton, R. D., Xavier, C. D. L., Tachtsidis, I., and Bernus, O. (2011). Experimental validation of alternating transillumination for imaging intramural wave propagation. *Proceedings of the Annual International Conference of the IEEE Engineering in Medicine and Biology Society, EMBS*, pages 1676–1679. 370

Wan, X., Laurita, K. R., Pruvot, E. J., and Rosenbaum, D. S. (2005). Molecular correlates of repolarization alternans in cardiac myocytes. *Journal of molecular and cellular cardiology*, 39(3):419–28. 13

Weber, F. (2011). *Personalizing Simulations of the Human Atria: Intracardiac Measurements, Tissue Conductivities, and Cellular Electrophysiology*, volume 12. KIT Scientific Publishing. 40, 131, 133, 350

Weber, F., Schilling, C., Seemann, G., Luik, A., Schmitt, C., and Dossel, O. (2010). Wave direction and conduction-velocity analysis from intracardiac electrograms - a single-shot technique. *IEEE transactions on bio-medical engineering*, 57(10):2394–2401. 30, 37, 38, 40, 44, 92, 93, 130, 132, 359

Weber, F. M., Luik, A., Schilling, C., Seemann, G., Krueger, M. W., Lorenz, C., Schmitt, C., and Dossel, O. (2011). Conduction velocity restitution of the human atrium–an efficient measurement protocol for clinical electrophysiological studies. *IEEE transactions on bio-medical engineering*, 58(9):2648–55. 38, 42, 44, 348

Weiss, J. N., Chen, P.-S., Qu, Z., Karagueuzian, H. S., and Garfinkel, a. (2000). Ventricular Fibrillation : How Do We Stop the Waves From Breaking? *Circulation Research*, 87(12):1103–1107. 12

Weiss, J. N., Karma, A., Shiferaw, Y., Chen, P.-S., Garfinkel, A., and Qu, Z. (2006). From pulsus to pulseless: the saga of cardiac alternans. *Circulation research*, 98(10):1244–53. 11

Wilhelms, M., Hettmann, H., Maleckar, M. M., Koivumäki, J. T., Dössel, O., and Seemann, G. (2012). Benchmarking electrophysiological models of human atrial myocytes. *Frontiers in physiology*, 3(January):487. 55

Workman, A. J., Kane, K. a., and Rankin, A. C. (2008). Cellular bases for human atrial fibrillation. *Heart rhythm : the official journal of the Heart Rhythm Society*, 5(6 Suppl):S1–6. 14, 347

Wu, T.-J., Yashima, M., Xie, F., Athill, C. a., Kim, Y.-H., Fishbein, M. C., Qu, Z., Garfinkel, a., Weiss, J. N., Karagueuzian, H. S., and Chen, P.-S. (1998). Role of Pectinate Muscle Bundles in the Generation and Maintenance of Intra-atrial Reentry : Potential Implications for the Mechanism of Conversion Between Atrial Fibrillation and Atrial Flutter. *Circulation Research*, 83(4):448–462. 53

Yamazaki, M., Mironov, S., Taravant, C., Brec, J., Vaquero, L. M., Bandaru, K., Avula, U. M. R., Honjo, H., Kodama, I., Berenfeld, O., and Kalifa, J. (2012). Heterogeneous atrial wall thickness and stretch promote scroll waves anchoring during atrial fibrillation. *Cardiovascular Research*, 94(1):48–57. 370

Yu, Y., Santos, L. M., Mattiace, L. A., Costa, M. L., Ferreira, L. C., Benabou, K., Kim, A. H., Abrahams, J., Bennett, M. V. L., and Rozental, R. (2012). Reentrant spiral waves of spreading depression cause macular degeneration in hypoglycemic chicken retina. 45

Yushkevich, P. A., Piven, J., Hazlett, H. C., Smith, R. G., Ho, S., Gee, J. C., and Gerig, G. (2006). User-guided 3D active contour segmentation of anatomical structures: Significantly improved efficiency and reliability. *NeuroImage*, 31:1116–1128. 83, 331

Zhang, H. and Holden, A. (1995). Chaotic meander of spiral waves in the FitzHugh-Nagumo system. 53

Zigelman, G., Kimmel, R., and Kiryati, N. d. (2002). Texture mapping using surface flattening via multidimensional scaling. *IEEE Transactions on Visualization and Computer Graphics*, 8:198–207. 83, 84, 86, 88, 106, 333, 358

Appendix A

Preliminary investigations into the choice of method and parameter choices for rotor core location identification

A.1 Preliminary findings

Preliminary investigations were performed into the effects of choice of method and measurement used (for example transmembrane voltage or calcium data) for locating the rotor core. The effects of heterogeneities on the rotor tip trajectory were also investigated. Finally initial studies into the effects of spatial resolution were performed. These findings motivated and informed the methods used in the main body of the thesis.

A.1.1 Effects of rotor tip identification method

Rotor core location can be identified using methods other than phase singularity identification. The effects of using the isopotential line method (Section 2.13) or using phase singularities (Section 2.11)) to locate the rotor tip were investigated. The choice of isopotential value for the isopotential line method affects the rotor trajectory as can be seen in Fig. A.1.

The choice of the threshold for the amplitude of deflections to be included in the moving mean used for the phase calculation (Section 2.10, Fig. 4.9), also affects the rotor trajectory, as seen in Fig. A.2.

The differences between the isopotential line method, for different choices of isopotential value, and the phase method, with different deflection exclusion thresholds are presented in Fig. A.3.

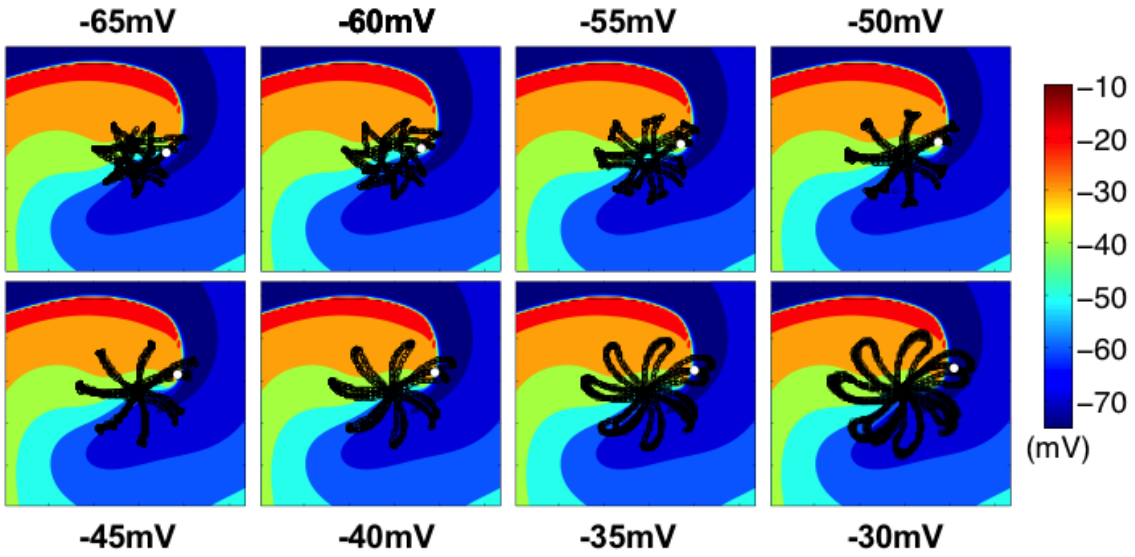

Figure A.1: Spiral tip trajectories vary with the choice of isopotential line. The method of Kay and Gray (2005) was used to identify the isopotential line, and the neighbourhood method was used to classify points as either wavefront or waveback to find the point of wave break. The differences in the trajectories are quantified in Fig. A.3.

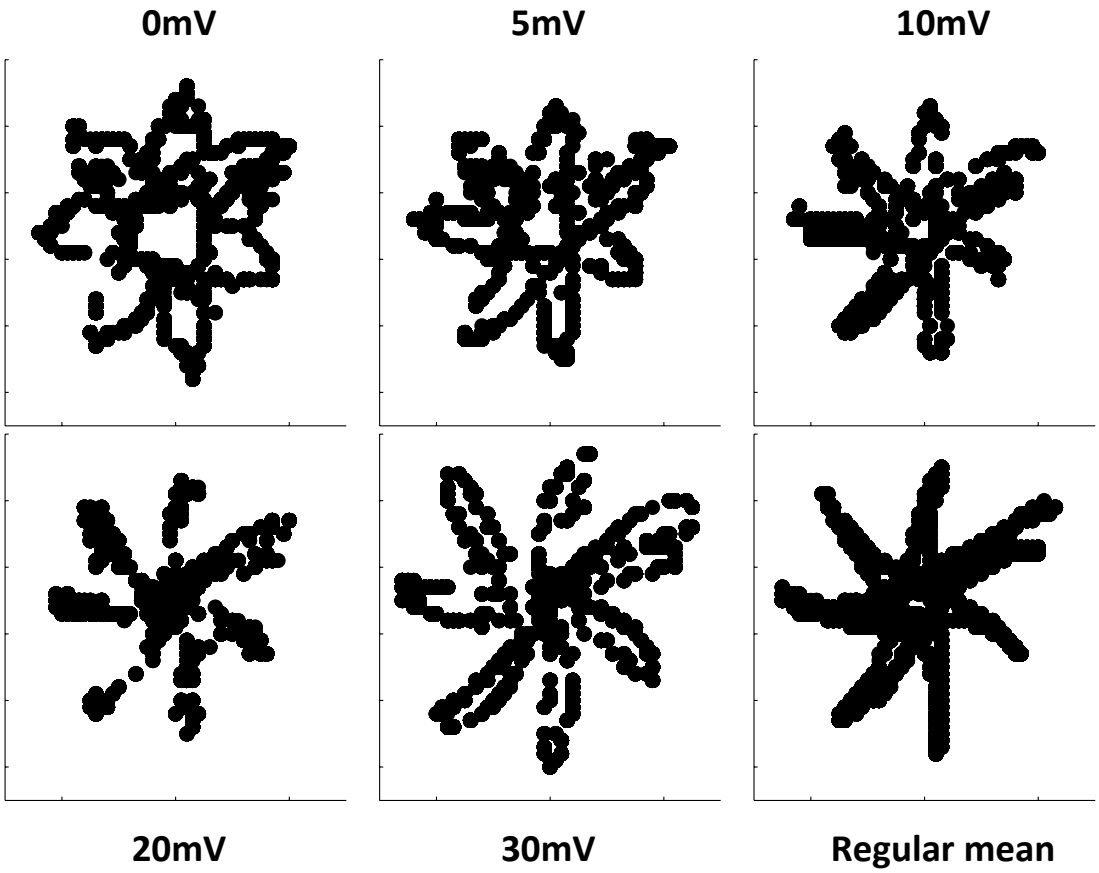

Figure A.2: Rotor tip trajectories identified as phase singularities for different amplitude deletion thresholds. The trajectories are seen to vary with the choice of amplitude deletion threshold, which was varied from 0mV (no deletion) to 30mV, and these differences are quantified in Fig. A.3. The trajectory using a overall mean is also shown for comparison.

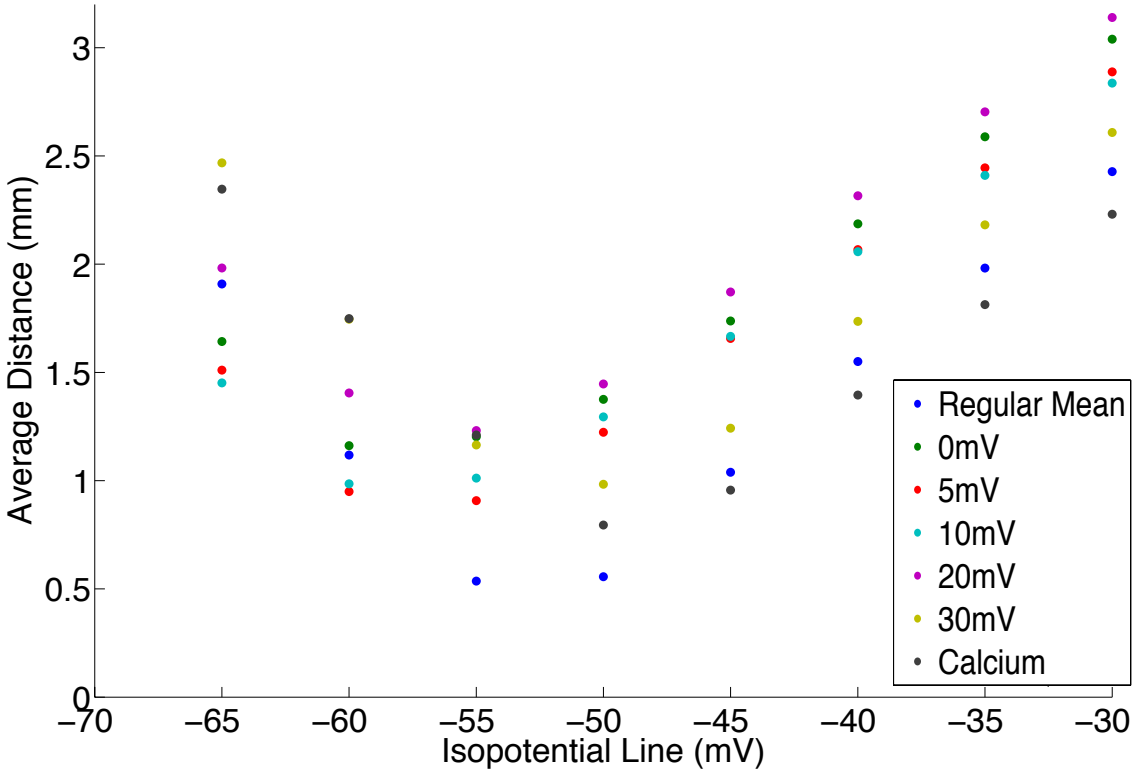

Figure A.3: The mean distance per frame between rotor tip locations calculated using different parameter choices within the two methods. For each choice of isopotential line, the mean distance from the rotor core location found using the isopotential line method is compared to the phase singularity location for phase using different amplitude thresholds. Results for using a regular mean in the phase calculation, or using calcium instead of voltage are also shown.

A.1.2 Voltage-Calcium mapping in simulated data

State space analysis requires the choice of a second variable, such as a time shifted signal (Section 1.13.2). An alternative choice for the second variable is calcium concentration. Dual optical mapping uses two fluorescent dyes in order to record both voltage and calcium signals (Choi and Salama, 2000; Fast and Ideker, 2000), and many biophysical cell models contain an intracellular calcium transient, so this technique has potential applicability.

As a preliminary study, the effects of using calcium data for phase were compared to voltage phase. The locations of phase singularities found by using calcium are compared to those using voltage for simulation results using the (Courtemanche et al., 1999) AF cell model. An overall mean is used for calculating calcium phase. The effects of using calcium phase compared to voltage phase on the rotor tip trajectory are shown in Fig. A.4, in which it can be seen that the trajectories are qualitatively similar. The quantitative differences in the rotor tip locations calculated using calcium phase compared to voltage with the isopotential line method are shown in Fig. A.3.

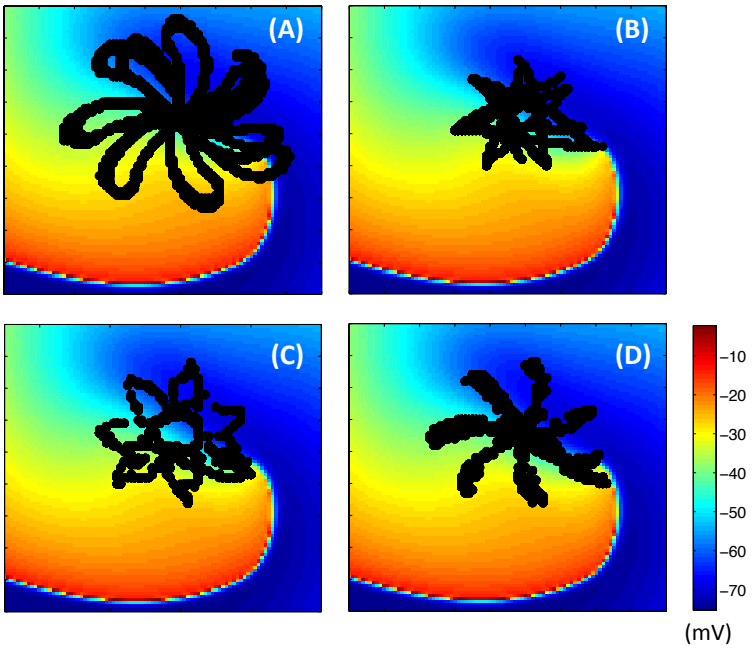

Figure A.4: Rotor tip locations for the isopotential line method and voltage and calcium phase. (A) Isopotential line of −30mV; (B) isopotential line of −65mV; (C) action potential phase singularities, with 0 amplitude deletion; (D) calcium phase singularities.

A.1.3 Calcium mapping in HL1 cells

Phase singularity locations were calculated using phase mapping of calcium fluorescence from five monolayers of HL1 cells in which reentry occurred (see Fig. A.5). Due to the noise in the signal, a larger contour integral size was used in order to calculate the topological charge, and phase singularities were determined based on a threshold number of neighbouring pixels for which the topological charge integral was a threshold from ± 1 (compare to Section 4.2.5).

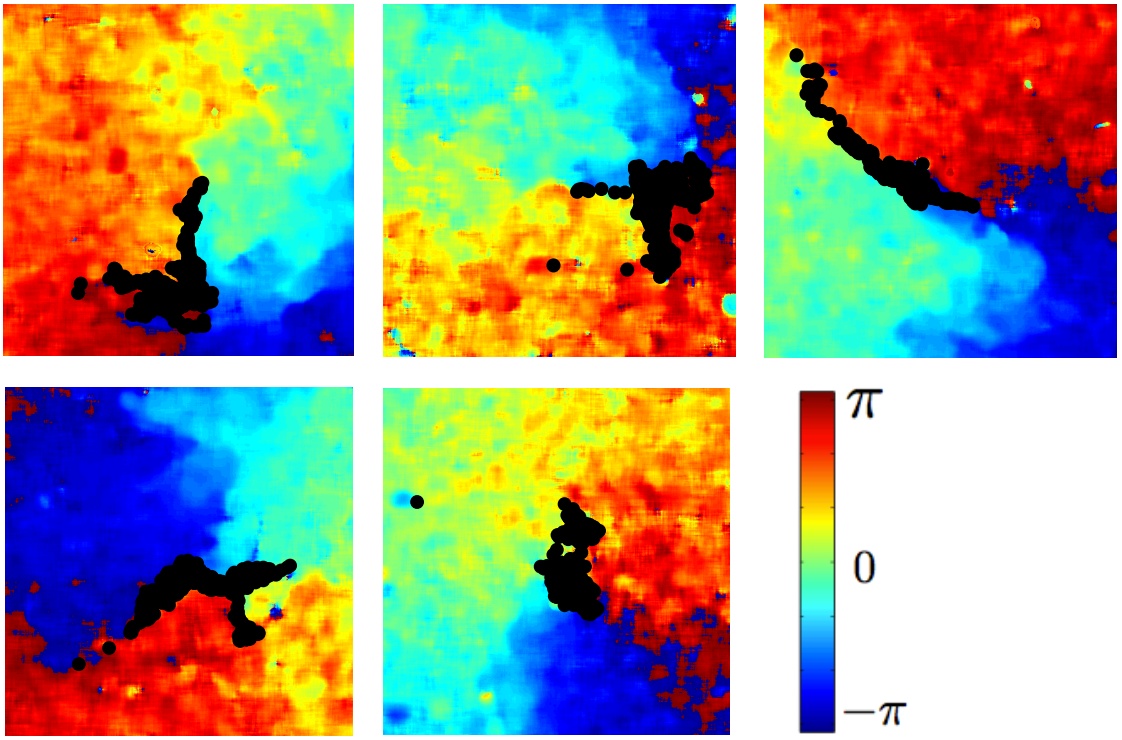

Figure A.5: Phase singularity locations (black circles) calculated from optical mapping of intracellular calcium concentration for five monolayers of HL1 cells. For the third plate, the phase singularity is seen to move along a line of block, demonstrating a linear core.

A.1.4 Effects of fibroblast coupling

The effects of coupling to fibroblasts on rotor core location were investigated by coupling each atrial myocyte to between one and four fibroblast cells modelled using the MacCannell et al. (2007) model. Results are shown in Fig. A.6, in which it can be seen that including fibroblast coupling in this way does not have a large effect on the rotor trajectory.

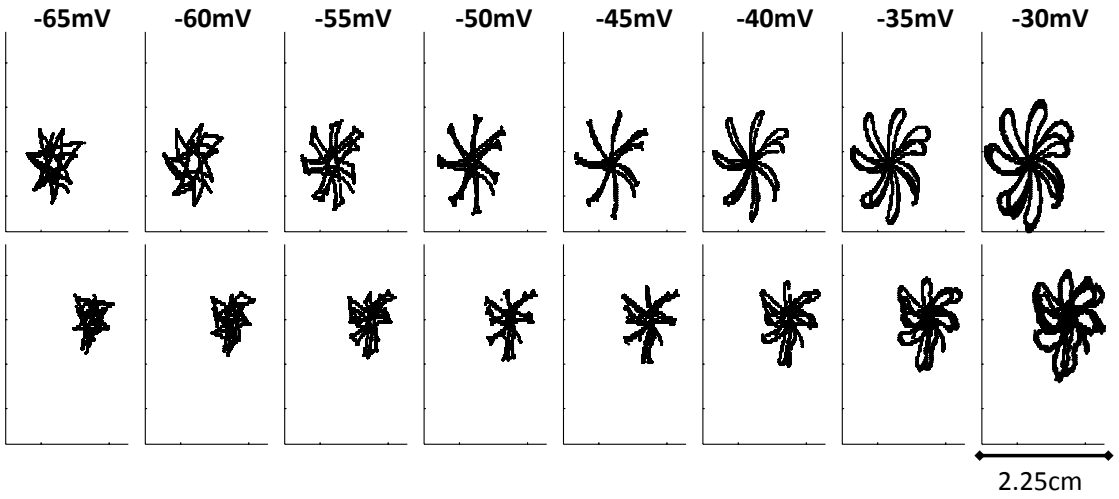

Figure A.6: The effects of fibroblast coupling on rotor tip locations. Top: homogeneous atrial myocytes; Bottom: heterogeneous fibroblast coupling.

A.1.5 Effects of resolution

In order to gauge the effects of resolution on the interpretation of various mechanisms of AF, simulations of rotors, focal sources and multiple wavelets were analysed using downsampled subsets of data. The resolution of data was found to affect whether identification of rotors and focal sources were successful, either visually or by identifying phase singularities (Fig. A.7). For this simulation, two 2D sheets were coupled by adding a linear term that is proportional to the difference in the voltage between the two sheets. The influence of this term was scaled spatially using the sum of two-dimensional Gaussians to simulate breakthrough sites on the sheets, using an approach similar to Gharaviri et al. (2012).

In addition, at increased grid spacings, the ability to identify small wavefronts in multiple wavelets simulations decreased (Fig. A.8).

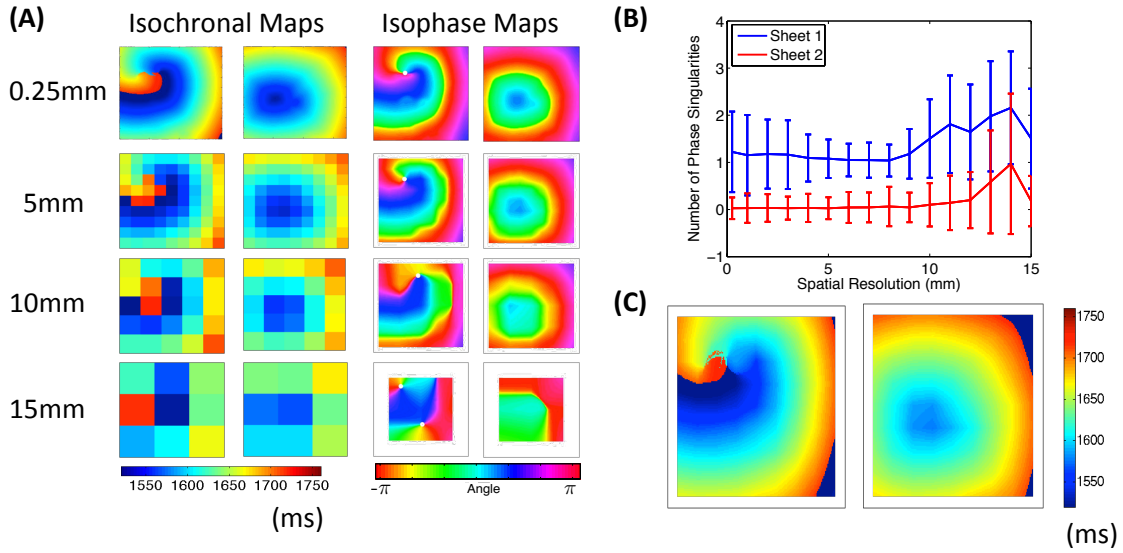

Figure A.7: A rotor and focal source were identifiable down to 15mm, when it became difficult to visually distinguish between a spiral and focal source. (A) For two coupled sheets: rotor tip and focal source were clearly identified at 10mm resolution, but no longer at 15mm. (B) For sheet 1 (stable rotor) and sheet 2 (focal source), decreasing the spatial resolution >10mm increased the number of false phase singularities detected. (C) Activation times from 5mm resolution interpolated phase.

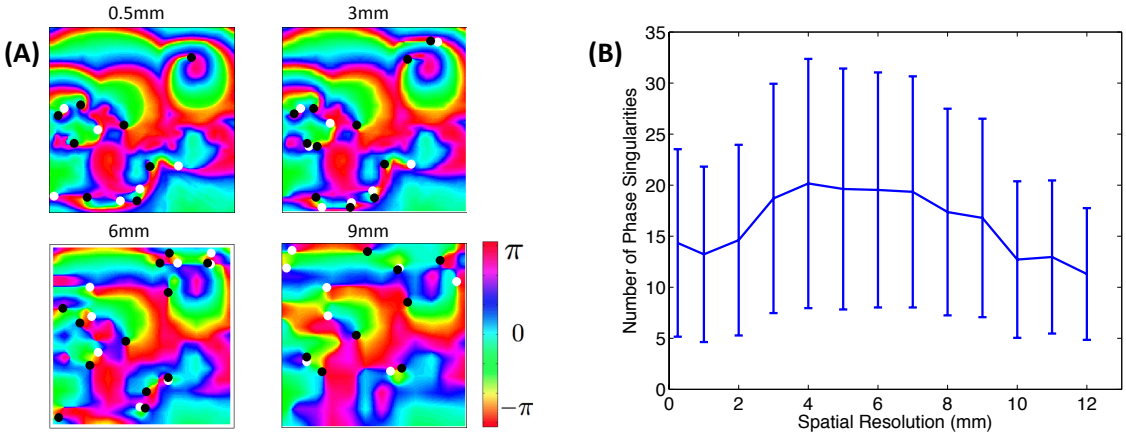

Figure A.8: Complex wavefront interactions were lost at 9mm, in a multiple wavelet simulation using the Cherry and Fenton (2004) cell model. (A) Phase with phase singularities marked at different grid spacings: fewer wavefronts and phase singularities detected at 9mm. (B) Mean and standard deviation of number of phase singularities per frame of the simulation: number initially increases as the number of false detections increases, then decreases as small wavefronts are lost.

A.1.6 Summary

In this appendix, the effects of the choice of spiral wave tip identification technique and associated parameters were found to be important in the determining the calculated spiral tip trajectory. For the chapters in the main body of the thesis, the phase mapping method was used to identify rotor tips because it can be applied to different data modalities, including action potentials and electrograms; whereas, the isopotential line method is limited to action potential data. The effects of parameter choices were investigated further for optical mapping data in Chapter 4.

The preliminary investigations presented in this chapter suggest that resolution is important for the correct interpretation of cardiac wavefront dynamics; however, these findings need to be generalised in terms of the distance between successive wavefronts because this will affect the required grid spacing. That is, the number of grid points required depends on the spacing between the underlying wavefronts and so any resolution requirements should be given in terms of this distance. This generalisation was performed in Chapter 7.

Appendix B

Permissions to use figures

Permissions to republish copyrighted figures from the literature in this thesis are included in this appendix.

To view this email as a web page, go here.

Do Not Reply Directly to This Email

To ensure that you continue to receive our emails,
please add rightslink@marketing.copyright.com to your address book.

This email was sent to: **caroline.roney10@imperial.ac.uk**

Please visit Copyright Clearance Center for more information.

This email was sent by Copyright Clearance Center
222 Rosewood Drive Danvers, MA 01923 USA

To view the privacy policy, please go here.

Figure B.1: Permission to use Fig. 1.4, from Eckstein et al. (2008).

To view this email as a web page, go here.

Do Not Reply Directly to This Email

To ensure that you continue to receive our emails,
please add rightslink@marketing.copyright.com to your address book.

RightsLink | Copyright Clearance Center

Thank You For Your Order!

Dear Ms. Caroline Roney,

Thank you for placing your order through Copyright Clearance Center's RightsLink service. Elsevier has partnered with RightsLink to license its content. This notice is a confirmation that your order was successful.

Your order details and publisher terms and conditions are available by clicking the link below:
http://s100.copyright.com/CustomerAdmin/PLF.jsp?ref=45219519-c836-41fd-b07a-22ca507697db

Order Details
Licensee: Caroline Roney
License Date: Jun 1, 2015
License Number: 3640181432427
Publication: Journal of Electrocardiology
Title: Microelectrode arrays: A new tool to measure embryonic heart activity
Type Of Use: reuse in a thesis/dissertation
Total: 0.00 GBP

To access your account, please visit https://myaccount.copyright.com.

Please note: Online payments are charged immediately after order confirmation; invoices are issued daily and are payable immediately upon receipt.

To ensure that we are continuously improving our services, please take a moment to complete our customer satisfaction survey.

B.1:v4.2

+1-855-239-3415 / Tel: +1-978-646-2777
customercare@copyright.com
http://www.copyright.com

This email was sent to: **caroline.roney10@imperial.ac.uk**

Please visit Copyright Clearance Center for more information.

This email was sent by Copyright Clearance Center
222 Rosewood Drive Danvers, MA 01923 USA

To view the privacy policy, please go here.

Figure B.2: Permission to use Fig. 1.5, from Reppel et al. (2004).

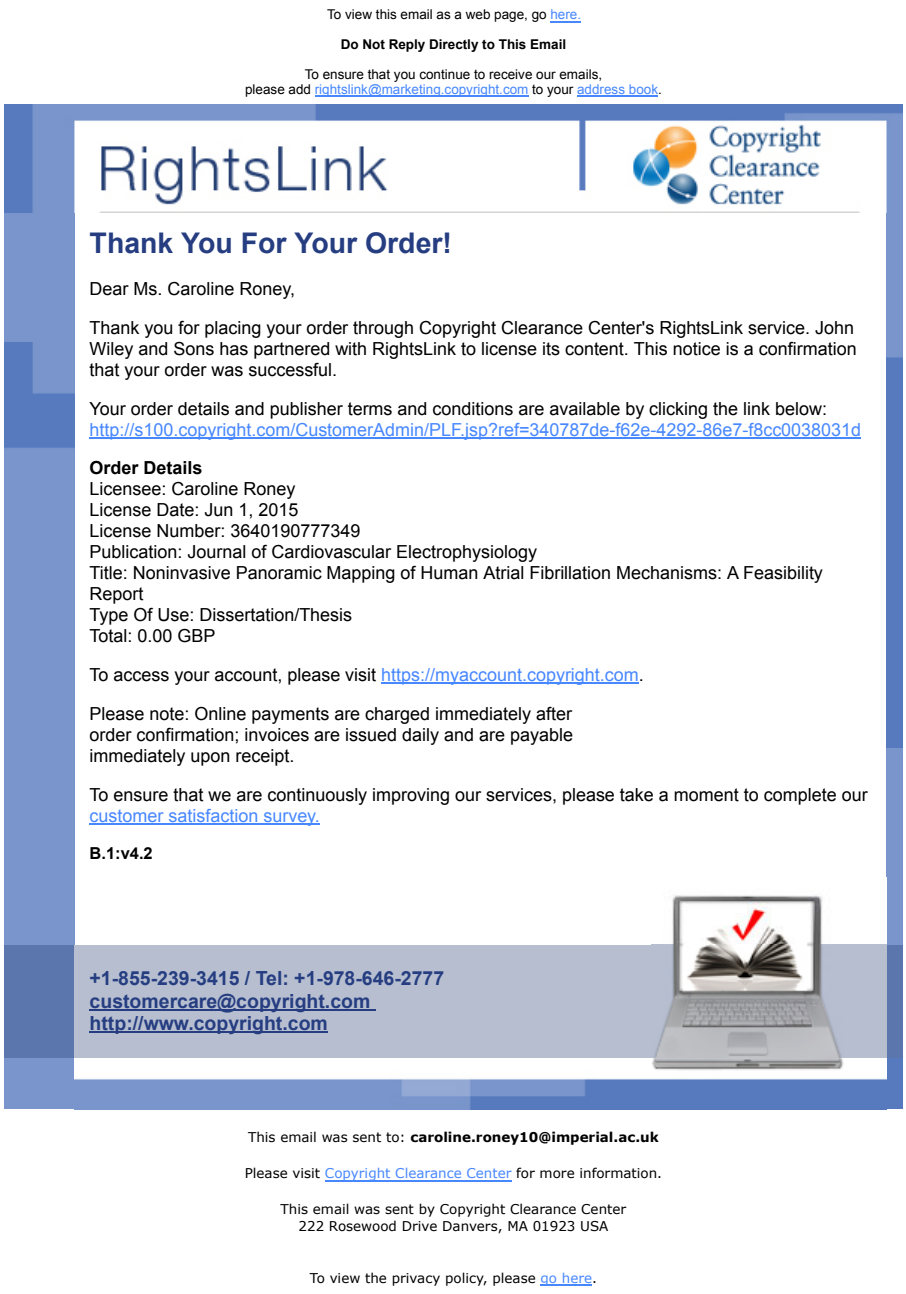

To view this email as a web page, go here.

Do Not Reply Directly to This Email

To ensure that you continue to receive our emails,
please add rightslink@marketing.copyright.com to your address book.

RightsLink | Copyright Clearance Center

Thank You For Your Order!

Dear Ms. Caroline Roney,

Thank you for placing your order through Copyright Clearance Center's RightsLink service. John Wiley and Sons has partnered with RightsLink to license its content. This notice is a confirmation that your order was successful.

Your order details and publisher terms and conditions are available by clicking the link below:
http://s100.copyright.com/CustomerAdmin/PLF.jsp?ref=340787de-f62e-4292-86e7-f8cc0038031d

Order Details
Licensee: Caroline Roney
License Date: Jun 1, 2015
License Number: 3640190777349
Publication: Journal of Cardiovascular Electrophysiology
Title: Noninvasive Panoramic Mapping of Human Atrial Fibrillation Mechanisms: A Feasibility Report
Type Of Use: Dissertation/Thesis
Total: 0.00 GBP

To access your account, please visit https://myaccount.copyright.com.

Please note: Online payments are charged immediately after order confirmation; invoices are issued daily and are payable immediately upon receipt.

To ensure that we are continuously improving our services, please take a moment to complete our customer satisfaction survey.

B.1:v4.2

+1-855-239-3415 / Tel: +1-978-646-2777
customercare@copyright.com
http://www.copyright.com

This email was sent to: **caroline.roney10@imperial.ac.uk**

Please visit Copyright Clearance Center for more information.

This email was sent by Copyright Clearance Center
222 Rosewood Drive Danvers, MA 01923 USA

To view the privacy policy, please go here.

Figure B.3: Permission to use Fig. 1.8, from Haissaguerre et al. (2013).

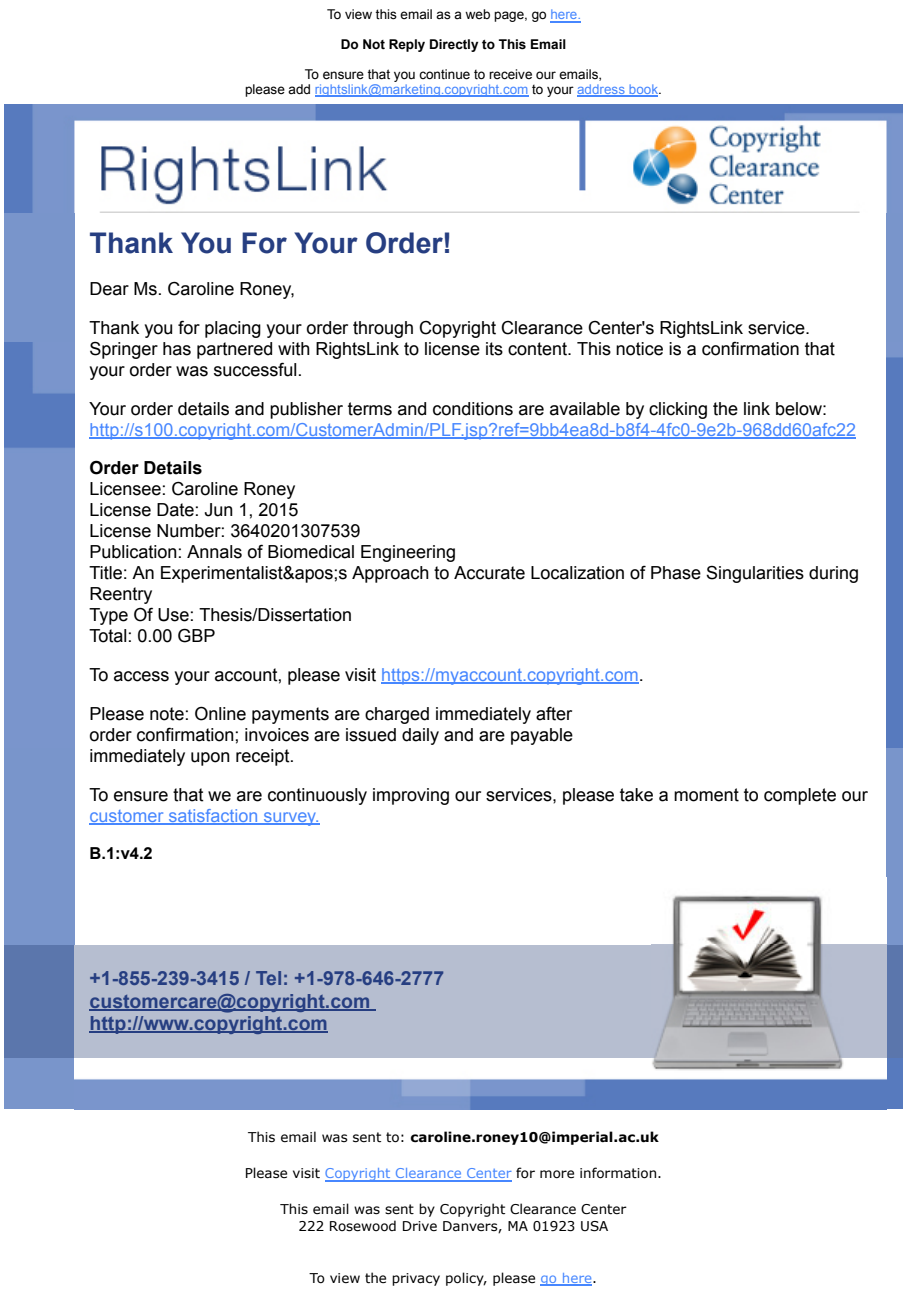

To view this email as a web page, go here.

Do Not Reply Directly to This Email

To ensure that you continue to receive our emails,
please add rightslink@marketing.copyright.com to your address book.

RightsLink | Copyright Clearance Center

Thank You For Your Order!

Dear Ms. Caroline Roney,

Thank you for placing your order through Copyright Clearance Center's RightsLink service. Springer has partnered with RightsLink to license its content. This notice is a confirmation that your order was successful.

Your order details and publisher terms and conditions are available by clicking the link below:
http://s100.copyright.com/CustomerAdmin/PLF.jsp?ref=9bb4ea8d-b8f4-4fc0-9e2b-968dd60afc22

Order Details
Licensee: Caroline Roney
License Date: Jun 1, 2015
License Number: 3640201307539
Publication: Annals of Biomedical Engineering
Title: An Experimentalist's Approach to Accurate Localization of Phase Singularities during Reentry
Type Of Use: Thesis/Dissertation
Total: 0.00 GBP

To access your account, please visit https://myaccount.copyright.com.

Please note: Online payments are charged immediately after order confirmation; invoices are issued daily and are payable immediately upon receipt.

To ensure that we are continuously improving our services, please take a moment to complete our customer satisfaction survey.

B.1:v4.2

+1-855-239-3415 / Tel: +1-978-646-2777
customercare@copyright.com
http://www.copyright.com

This email was sent to: **caroline.roney10@imperial.ac.uk**

Please visit Copyright Clearance Center for more information.

This email was sent by Copyright Clearance Center
222 Rosewood Drive Danvers, MA 01923 USA

To view the privacy policy, please go here.

Figure B.4: Permission to use Fig. 1.11, from Iyer and Gray (2001).

To view this email as a web page, go here.

Do Not Reply Directly to This Email

To ensure that you continue to receive our emails,
please add rightslink@marketing.copyright.com to your address book.

RightsLink | Copyright Clearance Center

Thank You For Your Order!

Dear Ms. Caroline Roney,

Thank you for placing your order through Copyright Clearance Center's RightsLink service. Nature Publishing Group has partnered with RightsLink to license its content. This notice is a confirmation that your order was successful.

Your order details and publisher terms and conditions are available by clicking the link below:
http://s100.copyright.com/CustomerAdmin/PLF.jsp?ref=54afc89c-3790-4fbb-a442-ad7af5615d3c

Order Details
Licensee: Caroline Roney
License Date: Jun 1, 2015
License Number: 3640210467585
Publication: Nature
Title: Spatial and temporal organization during cardiac fibrillation
Type Of Use: reuse in a dissertation / thesis
Total: 0.00 GBP

To access your account, please visit https://myaccount.copyright.com.

Please note: Online payments are charged immediately after order confirmation; invoices are issued daily and are payable immediately upon receipt.

To ensure that we are continuously improving our services, please take a moment to complete our customer satisfaction survey.

B.1:v4.2

+1-855-239-3415 / Tel: +1-978-646-2777
customercare@copyright.com
http://www.copyright.com

This email was sent to: **caroline.roney10@imperial.ac.uk**

Please visit Copyright Clearance Center for more information.

This email was sent by Copyright Clearance Center
222 Rosewood Drive Danvers, MA 01923 USA

To view the privacy policy, please go here.

Figure B.5: Permission to use Fig. 1.12, from Gray et al. (1998).

To view this email as a web page, go here.

Do Not Reply Directly to This Email

To ensure that you continue to receive our emails,
please add rightslink@marketing.copyright.com to your address book.

RightsLink | Copyright Clearance Center

Thank You For Your Order!

Dear Ms. Caroline Roney,

Thank you for placing your order through Copyright Clearance Center's RightsLink service. American Physical Society has partnered with RightsLink to license its content. This notice is a confirmation that your order was successful.

Your order details and publisher terms and conditions are available by clicking the link below:
http://s100.copyright.com/CustomerAdmin/PLF.jsp?ref=f216f23c-ec6c-4f8e-b92c-c2caa1592441

Order Details
Licensee: Caroline Roney
License Date: Jun 1, 2015
License Number: 3640260633615
Publication: Physical Review E
Title: Considerations in phase plane analysis for nonstationary reentrant cardiac behavior
Type Of Use: Thesis/Dissertation
Total: 0.00 GBP

To access your account, please visit https://myaccount.copyright.com.

Please note: Online payments are charged immediately after order confirmation; invoices are issued daily and are payable immediately upon receipt.

To ensure that we are continuously improving our services, please take a moment to complete our customer satisfaction survey.

B.1:v4.2

+1-855-239-3415 / Tel: +1-978-646-2777
customercare@copyright.com
http://www.copyright.com

This email was sent to: **caroline.roney10@imperial.ac.uk**

Please visit Copyright Clearance Center for more information.

This email was sent by Copyright Clearance Center
222 Rosewood Drive Danvers, MA 01923 USA

To view the privacy policy, please go here.

Figure B.6: Permission to use Fig. 1.13, from Bray and Wikswo (2002a).

To view this email as a web page, go here.

Do Not Reply Directly to This Email

To ensure that you continue to receive our emails,
please add rightslink@marketing.copyright.com to your address book.

RightsLink | Copyright Clearance Center

Thank You For Your Order!

Dear Ms. Caroline Roney,

Thank you for placing your order through Copyright Clearance Center's RightsLink service. Elsevier has partnered with RightsLink to license its content. This notice is a confirmation that your order was successful.

Your order details and publisher terms and conditions are available by clicking the link below:
http://s100.copyright.com/CustomerAdmin/PLF.jsp?ref=0ac13736-e494-4cf4-a6a0-606923513509

Order Details
Licensee: Caroline Roney
License Date: Jun 1, 2015
License Number: 3640231152298
Publication: Journal of Theoretical Biology
Title: Properties of two human atrial cell models in tissue: Restitution, memory, propagation, and reentry
Type Of Use: reuse in a thesis/dissertation
Total: 0.00 GBP

To access your account, please visit https://myaccount.copyright.com.

Please note: Online payments are charged immediately after order confirmation; invoices are issued daily and are payable immediately upon receipt.

To ensure that we are continuously improving our services, please take a moment to complete our customer satisfaction survey.

B.1:v4.2

+1-855-239-3415 / Tel: +1-978-646-2777
customercare@copyright.com
http://www.copyright.com

This email was sent to: **caroline.roney10@imperial.ac.uk**

Please visit Copyright Clearance Center for more information.

This email was sent by Copyright Clearance Center
222 Rosewood Drive Danvers, MA 01923 USA

To view the privacy policy, please go here.

Figure B.7: Permission to use Fig. 1.15, from Cherry and Evans (2008).

To view this email as a web page, go here.

Do Not Reply Directly to This Email

To ensure that you continue to receive our emails,
please add rightslink@marketing.copyright.com to your address book.

RightsLink | Copyright Clearance Center

Thank You For Your Order!

Dear Ms. Caroline Roney,

Thank you for placing your order through Copyright Clearance Center's RightsLink service. Wolters Kluwer Health, Inc. has partnered with RightsLink to license its content. This notice is a confirmation that your order was successful.

Your order details and publisher terms and conditions are available by clicking the link below:
http://s100.copyright.com/CustomerAdmin/PLF.jsp?ref=ecd7eb7b-e67c-408d-9e1f-3d6aa56cb5cf

Order Details
Licensee: Caroline Roney
License Date: Jun 1, 2015
License Number: 3640231415329
Publication: Circulation Research
Title: The Role of Fibroblasts in Complex Fractionated Electrograms During Persistent/Permanent Atrial Fibrillation: Implications for Electrogram-Based Catheter Ablation
Type Of Use: Dissertation/Thesis
Total: 0.00 GBP

To access your account, please visit https://myaccount.copyright.com.

Please note: Online payments are charged immediately after order confirmation; invoices are issued daily and are payable immediately upon receipt.

To ensure that we are continuously improving our services, please take a moment to complete our customer satisfaction survey.

B.1:v4.2

+1-855-239-3415 / Tel: +1-978-646-2777
customercare@copyright.com
http://www.copyright.com

This email was sent to: **caroline.roney10@imperial.ac.uk**

Please visit Copyright Clearance Center for more information.

This email was sent by Copyright Clearance Center
222 Rosewood Drive Danvers, MA 01923 USA

To view the privacy policy, please go here.

Figure B.8: Permission to use Fig. 2.1(B), from Ashihara et al. (2012).